NASA Conference Publication 3202

Magnetic Suspension Technology Workshop

NASA Conference Publication 3202

Magnetic Suspension Technology Workshop

Edited by
Claude R. Keckler
and Nelson J. Groom
Langley Research Center
Hampton, Virginia

Colin P. Britcher
Old Dominion University Foundation
Norfolk, Virginia

Proceedings of a workshop sponsored by the
National Aeronautics and Space Administration,
Washington, D.C., and held at
Langley Research Center
Hampton, Virginia
February 2–4, 1988

NASA
National Aeronautics and
Space Administration
Office of Management
Scientific and Technical
Information Program
1993

PRIMARY

INTRODUCTION

A Workshop on Magnetic Suspension Technology was held at the Langley Research Center in Hampton, Virginia, on February 2-4, 1988. The workshop was sponsored by the Langley Research Center in coordination with NASA Headquarters and was hosted by the Spacecraft Controls Branch of the Guidance and Control Division at Langley Research Center. The workshop was chaired by the following people:

Claude R. Keckler, General Chairman
NASA Langley Research Center
Hampton, VA 23681-0001

David B. Eisenhaure, Technical Chairman
SatCon Technology Corporation
12 Emily Street
Cambridge, MA 02139-4507

Virginia B. Marks, Executive Chairman
NASA Langley Research Center
Hampton, VA 23681-0001

The goal of the workshop was to identify the state of magnetic suspension technology in such areas as rotating systems, pointing of experiments or subsystems, and payload isolation. An additional goal was to review recent developments in superconducting materials and to examine their impact on magnetic suspension system technology. The workshop was attended by members of industrial, academic, and government organizations. A list of attendees is included as a part of this document.

The first two days of the workshop were dedicated to presentations. There were five technical sessions in which a total of 24 papers were presented. The technical sessions covered the areas of modelling and control, rotating systems, superconductors, and pointing, isolation, and measurement. This publication contains copies of the papers which were presented. The last half-day of the workshop was set aside for discussions between members of the general audience and a panel of experts to address questions of near-term technology, technology shortfalls and their resolution, and finally the impact of superconductivity developments on magnetic suspension systems. The panel members were

Dr. Paul Allaire
University of Virginia

Dr. Dan DeBra
Stanford University

Mr. Crawford Meeks
Hughes Aircraft Co.

Dr. Robert Mokadam
Sundstrand Corp.

Mr. Michael Superczinski
David Taylor Research Center

Dr. Jack Crowe
Temple University

A transcript of the panel discussions was not available at the time of publication.

The use of trade names of manufacturers in this report does not constitute an official endorsement of such products or manufacturers, either expressed or implied, by the National Aeronautics and Space Administration.

CONTENTS

SESSION 4—Rotating Systems

Co-Chairman—Nelson J. Groom, NASA Langley Research Center
Co-Chairman—James F. Wilson, Honeywell Inc.

SESSION 5—Superconductors

Chairman—David B. Eisenhaure, SatCon Technology Corporation

omit

Session 1

Application Surveys

Chair: Rhonda C. Raffi

SatCon Technology Corporation

omit

Magnetic Actuator Concepts and Applications

John Kroeger, Satellite Systems Division, Honeywell Inc.

omit

Magnetic Bearings - Fifty Years of Progress

Michael K. Swann, Proto-Technology Corporation

51-18
163481
P-11

MAGNETIC SUSPENSION ACTUATOR CONCEPTS AND APPLICATIONS

John Kroeger
Honeywell Inc.
Satellite Systems Division
Glendale, Arizona

N93-27555

SUMMARY

The fundamental aspect which makes magnetic suspension systems possible is the magnetic phenomena by which significant forces can be generated. Each of these force-producing phenomena has unique characteristics and is implementable in a unique fashion, such that each performs the magnetic suspension task differently than the others.

This paper provides a practical overview of the force-producing concepts, their unique characteristics, and their typical methods of application.

INTRODUCTION

Magnetic suspension systems have become the focus of intense interest and development in recent years. Applications for these magnetic suspensions vary widely but may be grouped into two rather broad classifications.

The first classification would be a spinning shaft group of applications including momentum wheels, energy storage wheels and rims, and gimbals. In this application group, the magnetic suspension ideally duplicates the stiffness performance of the conventional ball or roller bearing and is substituted for the conventional bearing, either to achieve longer life due to the absence of contact wear or to eliminate the thermal conduction path inherent with direct contact. Although not spinning, reciprocating applications, such as cryogenic refrigerators, would also be included in this group, since performance equivalent to a linear roller bearing would be the ideal.

The second application group would be the suspended platforms, characterized by the desire to vibration isolate and/or point the payload or experiment on the platform with respect to a second (reference or stationary) body. In this group, the magnetic suspension is ideally very stiff or rigidly controlled in the low-frequency pointing region and soft in the frequency region where vibration isolation is desired.

ACTUATOR CONCEPTS

This section will introduce and discuss the magnetic suspension actuator concepts which would be considered and could be utilized in normal ground and space environments (typically one atmosphere pressure to hard vacuum and a temperature range from -50 to +80°C). In a later section, alternate concepts and design modifications for cryogenic temperatures will be discussed.

The fundamental basis which makes magnetic suspension systems possible is the magnetic phenomenon where significant forces can be generated between mechanically isolated bodies. Each of these force-producing phenomena has unique characteristics and, therefore, has unique methods of implementation and areas of application.

The force concept, which is the basis for two distinctly different actuators, is the minimum reluctance principle. This principle states that, when a magnetic flux flows between two bodies separated by a gap, a force is generated between those bodies in a direction to reduce the gap reluctance.

One actuator, based on this concept, is the ferromagnetic attraction actuator. In its simplest form, it is a single horseshoe electromagnet operating against a magnetic steel armature plate (fig. 1(a)) and producing unidirectional force on the armature plate. The addition of a second electromagnet (stator), operating against the other side of the armature, creates an actuator capable of bidirectional force, with the stators controlled differentially (fig. 1(b)). This actuator is an active actuator since active control of the excitations to the two stators is required to obtain the desired force characteristics and to maintain stability.

The second type of actuator, based on the minimum reluctance principle, is the variable reluctance actuator in which a magnetic field passes between two bodies, with the gap surface of each body consisting of a matched series of teeth and grooves (fig. 2). The force generated is always in a direction to align the teeth on the movable element (armature) to those on the stator. The field may be generated by either permanent magnets or by a coil as in the electromagnet. The more common configuration uses a permanent magnet to create the field, resulting in a completely passive actuator; then, should a variable force actuator be desired, a coil is utilized to modulate the permanent magnet field.

A second force concept commonly employed in a vast array of magnetic devices is the Lorentz (or D'Arsonval) force principle. In this concept, a current-carrying conductor in and perpendicular to a magnetic field has a force exerted upon it which is perpendicular to both the field and the current (fig. 3(a)). Magnetic suspension actuators of this type are very similar in operation and construction to the common speaker actuator or voice coil (fig. 3(b)). This actuator obviously requires active control to obtain the force magnitude desired.

The third force concept that can be used is the repulsion force created between like poles of permanent magnets. When configured as a radial actuator (fig. 4), it produces a net radial force in a direction opposing any radial offset of the movable rotor element with respect to the stator. It is a passive actuator and performs in a manner similar to the variable reluctance actuator.

ACTUATOR ATTRIBUTES AND APPLICATIONS

The ideal magnetic suspension would provide all of its advantages: long life, no contact, no wear debris, and vibration isolation, with no penalty in weight, power or complexity compared to its mechanical counterpart. However, this is never achieved, and the magnetic suspension system and its actuators must be optimized to the application in order to be competitive with alternate devices, such as bearings, flexures, and dampers. Then, at the onset of magnetic system design, the requirements must be evaluated and a careful selection of the type of system, actuators, and control scheme must be performed.

Prior to discussing actuator attributes, several terms, which will be used in that discussion, require definition.

- Stiffness - will be used to denote the restoring force per unit deflection of the passive-type actuators. K_A will denote the axial stiffness of a passive axial actuator, and K_R will denote the radial stiffness of a passive radial actuator. The term "stiffness" will also be used for active actuators, based on measurable deflection levels, for comparison purposes.

- Unbalance Stiffness - will be used to denote the force per unit deflection, which acts in a direction to increase the deflection, such as in the cross-axis direction of the passive actuators. For example, K_{UA} will denote the axial unbalance stiffness of a passive radial actuator.

Table 1 provides a qualitative attribute summary for the four actuator types. These attributes are further explained and quantized in the following sections.

Active Actuators

The electromagnet actuator is applicable to both the spinning shaft and suspended platform application groups. In spinning shaft applications, where passive radial support is preferred for simplicity, the electromagnet actuator is used to provide control of the unstable axial axis. This can be accomplished by integrating it into the passive suspension, as shown in a simplified configuration in figure 5, or by incorporating it as a separate component. The electromagnet can be, and has been, used to provide the radial support in these applications. With high-resolution position sensors and an appropriate control system, it is capable of much higher radial stiffness than the passive actuators for a given weight and envelope. However, the added complexity of the control system for four degrees of freedom (DOF) (two radial and two angular) usually eliminates it from consideration.

The electromagnet actuator is the principal candidate for suspended platform applications. These payload pointing and vibration applications typically consist of five or six actuators, depending on the number of DOF to be controlled, located around or under the platform. The actuator is required to provide its full force capability (several newtons to several thousand newtons) over a significant motion range (a few millimeters to several centimeters). The force requirement usually decreases with increasing frequency but may be significant out to several thousand hertz.

The electromagnet actuator's competition for suspended platforms is the voice coil actuator. When traded off against the voice coil, one of the electromagnet's

disadvantages is that its output force is nonlinear to both excitation current and gap flux density and varies as the inverse square of armature motion (gap), thus requiring complex control systems. Other weak points include its relatively high inductance (due to the iron core which can limit high frequency force generation or require very high voltage supplies), torques generated due to armature rotation (or tilt) about the two cross axes, and the fact that some power, although slight, is dissipated in the armature. On the other side of the trade-off, the electromagnet's passive armature, which is located on the suspended element, is light compared to the passive (magnet/return path) element of the voice coil; cross-axis translations are accommodated by the armature overlap where, in the voice coil, large magnetic gap clearances are required; and most important, for practically every set of force/motion requirements, the electromagnet is substantially lighter and lower in power than the voice coil.

The cross-axis torque produced by the electromagnet actuator becomes less of a problem as the actuator location radius increases, since the torques are generated as functions of the actuator pole spacing and pole face area and decrease in relative magnitude with increasing location radius. The force and torque errors of the electromagnet have been the subject of significant study and modelling at Honeywell in recent years, are reasonably well-understood, and are routinely incorporated into the system error budget from the onset of a suspension system design.

Configurations of the electromagnet that have been used in Honeywell suspension system designs include the horseshoe, as shown in figure 1(b), four horseshoes in a single component (similar to a motor stator), and the cup core consisting of a single coil with a pole in the coil center and a return pole around the coil outer diameter.

Sizing the electromagnet actuator is an iterative process based on the requirements flow-down from the system-level requirement set. Size, weight, and power increase with increasing force and gap motion requirements. They are also highly dependent on the type of feedback system employed (gap, force, gap flux and combinations) and the degree of required conformance to the force-proportional-to-current-squared and force-proportional-to-inverse-gap-squared relationships. Honeywell's more recent systems utilize gap flux density feedback, with the flux density squared closely approximating the actual force produced; thus, several error sources (hysteresis and current and gap square law errors), which previously required the use of low flux density core material and increased magnetic gap, are now eliminated. This allows the use of a high flux density core material, which reduces the core size and, since weight and power can be traded off against each other, results in a lower power and weight actuator.

The voice coil actuator has already been partially discussed in comparing it against the electromagnet actuator. It becomes a serious competitor only in applications where full force capability above approximately 20 Hz or significant forces above approximately 100 Hz are required or where extreme freedom from force and torque errors can offset the weight and power penalties incurred.

One application area to which the voice coil actuator is ideally suited is the control of fast steering mirrors where forces to 2000 Hz and higher may be required.

When selected for its low error capability, the configuration must be modified from the simple voice coil in figure 3(b), with magnets located only at the inner

diameter of the gap. That configuration typically yields a gap flux density distribution, as shown in figure 6(a), and radial and angular coil motions in the gap result in force scale factor and cross-axis force/torque errors. Locating magnets at both the inner and outer diameters of the gap will result in the more balanced flux density distribution of figure 6(b) and thus minimize motion-induced errors.

Table 2 shows a portion of the trade-offs between active actuator types for a recent program. For this application, the electromagnet actuator, using the low-weight, high-flux density material, was the selected option primarily because of weight and the fact that the other options were 1.5 to 4 times more expensive to build.

Passive Actuators

As previously mentioned in the discussion of spinning shaft applications, passive radial suspension is preferred because of the simplicity it affords. With the two radial DOF and the two angular axes (orthogonal to the rotational axis) passive, the only penalties it incurs, relative to the ball-bearing system, are one DOF active control, added weight, and reduced stiffness. The advantages, of course, are the absence of contact and resultant wear particles, elimination of lubrication concerns, potential for longer life, constant drag level over life, and higher reliability.

The variable-reluctance passive actuator, in addition to a high weight-to-stiffness ratio (table 3), usually has a high unbalance stiffness (K_U)-to-radial stiffness (K_R) ratio. In most configurations, this K_U/K_R ratio is in the range of 5 to 10. This has disadvantages and advantages. Assuming a passive-radial, active-axial system, the high axial unbalance stiffness requires a very tight loop (high bandwidth) be closed on the axial axis, and stability is often difficult to achieve. The unbalance stiffness can be used to an advantage; in ground-based applications or in space applications where ground testing is required, it provides support for the weight of the suspended body in an axial 1g gravitational field. The technique uses the active axial actuator to offset the passive radial actuators axially to the point where the axial unbalance force equals the suspended weight; the active axial suspension then maintains this position, where its average power is almost zero. Because of problems caused by the high K_U, including larger active portions to provide initial liftoff from the stops, Honeywell has recently been evaluating alternate configurations whose K_U/K_R ratios are in the range of 0.5 to 2. Build and test of hardware based on this configuration will occur this year.

The other passive actuator, using permanent magnets operating in repulsion, is also being investigated. In the designs evaluated to date, this actuator suffers a weight penalty of almost 2 to 1, compared to the variable-reluctance type, and the K_U/K_R ratio is in the 1.0-to-1.5 range. A distinct disadvantage is that, with two magnetic fields in repulsion, the fields are very uncontained, which results in significant stray external fields. This is in comparison to all the previously discussed actuator types whose magnetic circuits are closed and whose fields are reasonably well-contained.

Table 3 provides a comparison of the four actuator types for an assumed rotating wheel application with a small motion range requirement. This example is chosen to demonstrate an application where the active and passive concepts are reasonably competitive and the choice is not obvious but is more related to desired performance.

ACTUATORS AND CRYOGENIC APPLICATIONS

Current investigations of cryogenic applications and the impact of using actuators at or near cryogenic temperatures lead to the following preliminary conclusions.

- Core materials, in general, do not suffer serious degradation at cold temperatures, although there are some notable exceptions, such as 49 percent nickel iron which reportedly loses about 45 percent of its permeability at -150°C and 75 percent of its permeability at 40°K.
- Impregnants usually used for the 25 ± 75°C range are not applicable to cold temperatures, but alternate materials exist.
- Power consumption in active actuators can be reduced to near zero, using superconducting cable, but the complexity of active control still exists.
- The negative temperature coefficient of the samarium cobalt class of magnets could result in up to 60 percent strength increase, but this requires verification.
- Actuators based on the diamagnetic principle may now become a practical alternative.

Diamagnetic actuators utilize the property that diamagnetic materials are repelled by an external magnetic field. The main disadvantage of these actuators is the low load capacity per unit volume of material. The low load capacity, in the room ambient temperature range, is due to the relative permeability of the diamagnetic materials being only slightly less than one. Superconducting materials are a limiting case of diamagnetic materials, with relative permeabilities approaching zero. Now, with the development of materials that are superconducting above the temperature of liquid nitrogen (77°K), one element of the magnets-in-repulsion actuator may be replaced with a superconductor yielding another actuator alternative for low-temperature applications. Honeywell's finite-element modelling of the permanent magnets-in-repulsion actuator will probably be extended to include this actuator.

CONCLUSIONS

An overview of magnetic suspension actuators has been presented. Although certainly not complete, we have covered the main attributes of each actuator type and provided some insight into the trade-offs to be considered in the selection and design process.

We see the low-temperature and cryogenic applications area as one where magnetic suspensions incur additional advantages over mechanical suspensions, specifically because the mechanical isolation yields both partial thermal isolation and freedom from lubricant problems.

TABLE 1. - ACTUATOR COMPARISONS

Actuator Type	Electromagnet	Voice Coil	Variable Reluctance	P/M Repulsion
Active or Passive	Active	Active	Passive	Passive
Force Function	$F \propto I^2$ $F \propto I/G^2$	$F \propto I$	$F \propto$ Offset	$F \propto$ Offset
Cross-Axis Forces	Minimal	~ Negligible	Substantial	Substantial
Cross-Axis Torques	Significant	Minimal	Substantial	Substantial
Sensors Required	Postion and/or Flux	Position	None	None

TABLE 2. - ACTIVE ACTUATOR TRADE-OFFS FOR A SPECIFIC APPLICATION*

Actuator Type	Weight (kg)	Peak Power (watts)	Pk. Torque Error Due to Motions (N•m)	Hysteresis (N)
Electromagnet Low B and Hyst. Mat'l.	400	350	65	15
Electromagnet High B and Hyst. Mat'l.	125	225	50	160
Voice Coil Single Magnet (ID only)	400	850	130	--
Voice Coil Dual Magnets (ID and OD)	500	850	44	--

*Requirements
Force = 6500 N (1460 lbs)
Motion = ±2.5 mm Linear, ± 1 m Radian Rotation
Actuators located on 6.5 m diameter

TABLE 3. - COMPARISON OF THE FOUR ACTUATOR TYPES FOR SPECIFIC APPLICATION*

Actuator Type→ Parameter↓	Electromagnet	Voice Coil	Variable Reluctance	P/M Repulsion
Position Sensor	Yes	Yes	No	No
Radial Stiffness (K_R)	1 x 10^6 N/m(at 50μm) 10 x 10^6 N/m(at 5μm)	1 x 10^6 N/m(at 50μm) 10 x 10^6 N/m(at 5μm)	1 X 10^6 N/m	1 x 10^6 N/m
Radial Force	50 N (Full Range)	50 N (Full Range)	50 N (at 50μm)	50 N (at 50μm)
Axial Unbalance Stiffness (K_U)	~0	~0	0.5 x 10^6 N/m	1.5 x 10^6 N/m
Total Weight (per end)	0.6 kg	1.4 kg	0.5 kg	0.9 kg
Suspended Portion Weight	0.15 kg	1.3 kg	0.1 kg	0.4 kg
Peak Power	15 watts	50 watts	None	None
NOTES	Added Complexity But Higher Stiffness at Small Motions		Require Upsized Active Axial Support to Accommodate K_U	

*Assumed Application: Radial support of gimbal or wheel (per end)
Required radial stiffness (K_R) = 1 x 10^6 N/m (11.4 x 10^3 lb/in)
Radial motion range = ± 50 μm (± 0.002 in)
Minimum clearance = 200 μm (0.008 in)
Assumed position sensor resolution (where used) = 5 μm (0.0002 in)

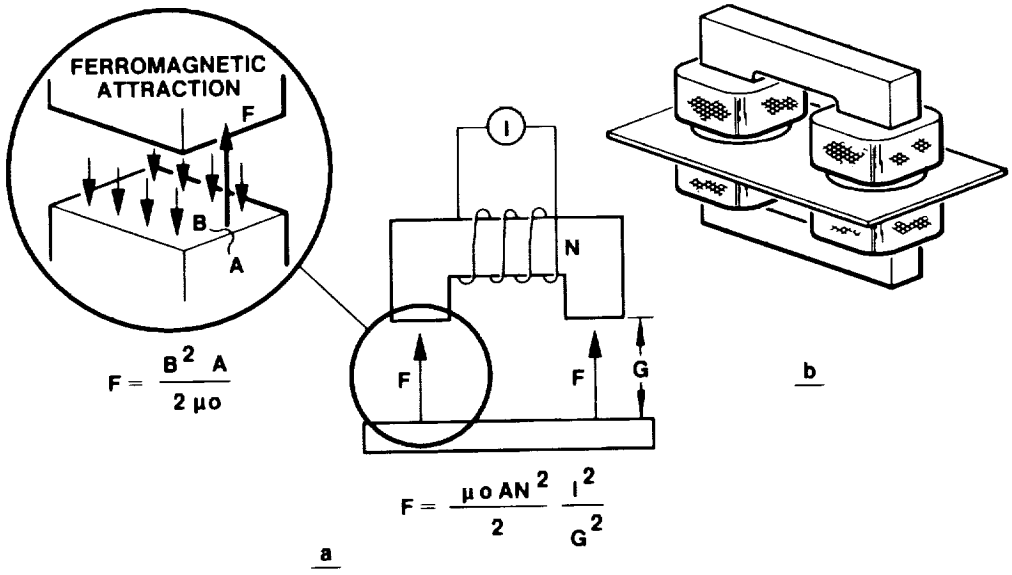

Figure 1. - Electromagnetic Attraction

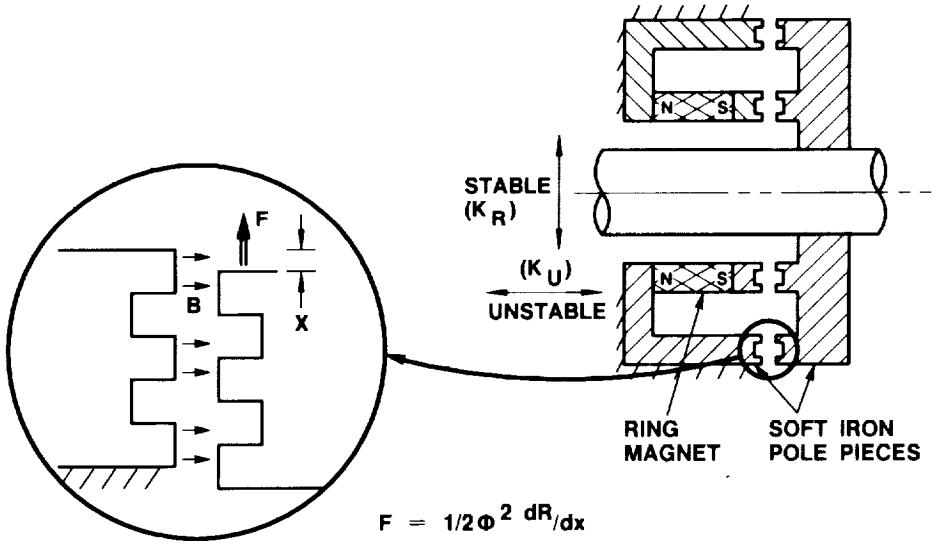

Figure 2. - Variable Reluctance Actuator

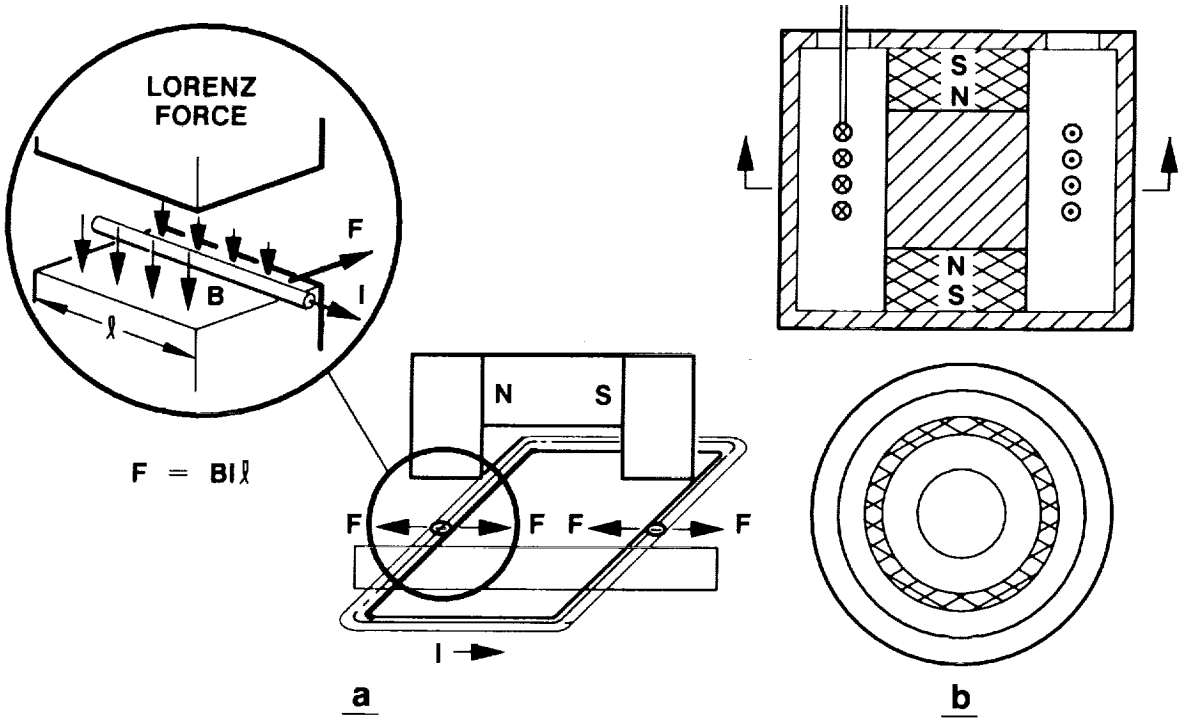

Figure 3. Voice Coil Actuator

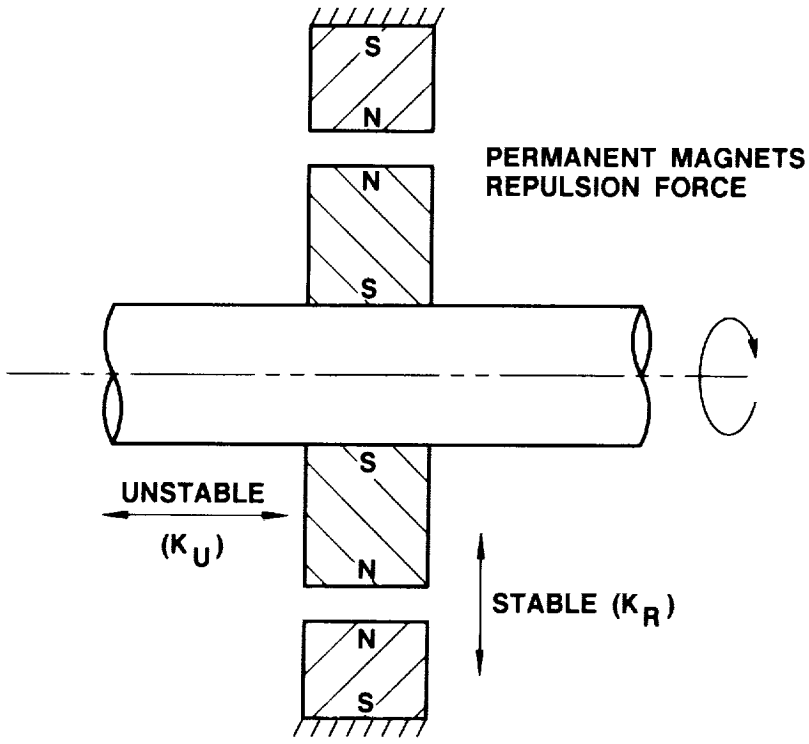

Figure 4. Permanent magnet (PM) Repulsion Actuator

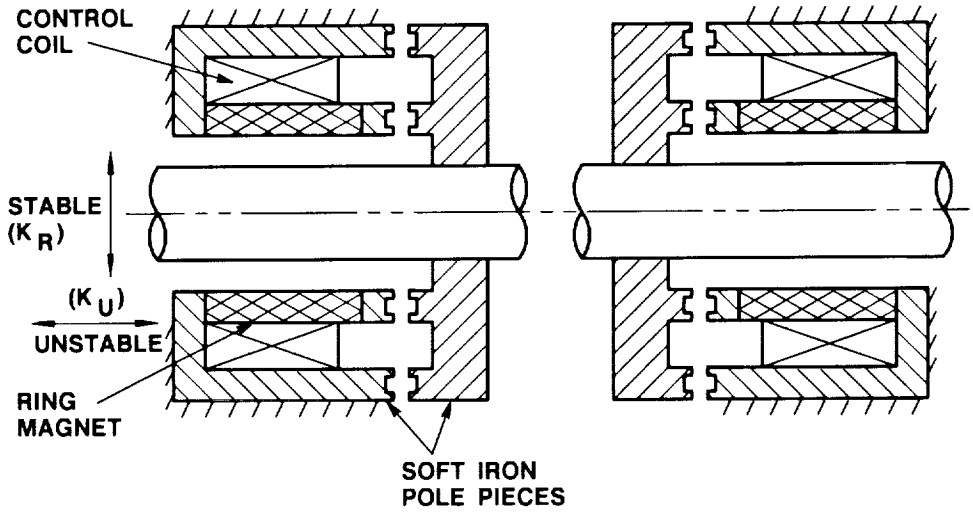

VARIABLE RELUCTANCE, PASSIVE RADIAL SUSPENSION WITH INTEGRATED ELECTROMAGNET ACTUATOR FOR ACTIVE CONTROL OF THE UNSTABLE AXIAL AXIS (SIMPLIFIED CONFIGURATION)

Figure 5. Integrated Passive Radial, Active Axial Suspension

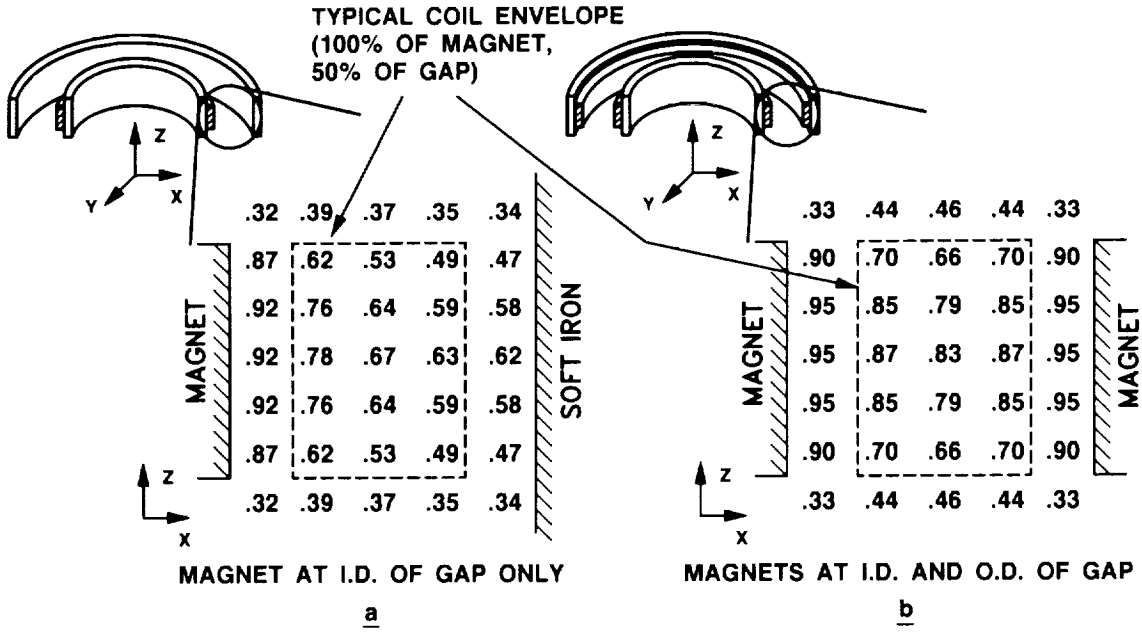

Figure 6. Voice Coil Actuators - Magnetic Field Distribution

S2-37
163482

MAGNETIC BEARINGS - FIFTY YEARS OF PROGRESS

N93-27556

Michael K. Swann
Proto-Technology Corporation
Groton, Connecticut

SUMMARY

Magnetic bearings are just beginning to be flown in spacecraft systems, but their development spans more than 50 years. The promise of completely non-contacting, unlubricated rotating systems operating at speeds substantially beyond the range of conventional bearings, and with no wear and virtually no vibration, has provided the incentive to develop magnetic bearing technology for many diverse applications. The idea is seductive indeed!

Earnshaw theorized in 1842 that stable magnetic suspension is not possible in all three spatial directions unless the magnetic field is actively controlled. Since that time, researchers have attempted to successfully support spinning rotors in a stable manner. Development of magnetic suspension systems over the past fifty years has included progress on both passive (permanent magnet) and active (electromagnet) systems. The improvements in bearing load capacity, stiffness and damping characteristics are traced in this report. The trends in rotor size, rotational kinetic energy and improvements in active control system capabilities are also reviewed. Implications of superconductivity on suspension system design and performance are discussed.

INTRODUCTION

The idea of magnetic suspension is not a new one. Man has long dreamed of magnetic levitation of spinning rotors as a means to the elimination of mechanical wear and the achievement of indefinite life to rotating machinery. Magazine covers in years past have depicted the day when high speed trains would smoothly criss-cross this country with absolutely no contact with the track beneath; levitation and propulsion would be provided by a magnetic field generated by electromagnets contained in the track bed. The energy shortages in the 1970's gave researchers new incentive to usher in a solar age when large photovoltaic arrays would collect the sun's energy for storage in large flywheels supported by frictionless magnetic bearings to provide near perfect conservation of energy for later use. Recent progress in the last few years in the field of superconductivity seems to herald the day when all of these dreams will come to fruition.

However, practical commercial applications of magnetic suspension have flourished for over ten years now without the use of superconducting materials. Rotating equipment ranging from high-speed, lightweight momentum wheels for satellites and electrospindles for precise positioning of cutting tools used in manufacturing industries to large turbomachinery including steam turbines, compressors and pumps

have been successfully developed and operated with magnetic bearing systems. The successful development of this technology spans more than fifty years of effort fraught with many ingenious ideas that were doomed to ultimate failure. Not until the development of semiconductor and integrated circuit technologies was success of these same ideas possible.

The attractiveness of magnetic bearings for spacecraft applications is apparent. The elimination of lubrication requirements means that spinning rotor systems can run at speeds only limited by material strength considerations with minimal power losses and vibration. For precision pointing systems, the elimination of lubrication means that these systems can operate with no lubricant debris generation resulting in very low runout errors and drag torque. For both types of systems, non-contacting suspension eliminates mechanical wear and provides a good interface between the rotor and stator for thermal management purposes, especially in cryogenic applications. Exceptional reliability of the magnetic bearing systems promises that these systems may operate for many years in space applications without a failure.

SUSPENSION TYPES

In 1842 Earnshaw published the fundamental theorem (ref. 1) that governs all forms of magnetic suspension. Now bearing his name, this theorem essentially asserts that a body may not be stably supported in a magnetic field in all three spatial directions without dynamic control or diamagnetic effects; at least one axis of instability (negative stiffness) must exist. Except for some minor peculiarities, this theorem has not been disproved despite more than a century of experimentation and testing of different suspension arrangements. These various arrangements can be classified into three groups: diamagnetic (passive), permanent magnetic (passive), electromagnetic (active).

The early work was in passive suspensions of permanent magnetic and diamagnetic types due to their inherent simplicity. These types are termed passive since no control of the magnetic field is provided; mechanical restraint in at least one direction is required. Permanent magnet suspensions may be either attractive or repulsive depending on the magnet arrangement, but the early researchers soon discovered that no real success could be achieved without at least one axis of active control or physical restraint.

Diamagnetism is the effect created by a material with a relative permeability with respect to a vacuum of less than one which results in an opposing magnetic field being induced by a magnetomotive force (mmf) source. A diamagnetic body is repelled in a magnetic field and can thus be passively suspended. Under normal temperature conditions, known diamagnetic materials such as bismuth and antimony exhibit too weak an effect for other than very lightweight suspension systems.

The recent strides in superconductivity have promoted new interest in this type of magnetic suspension since a strong diamagnetic effect can be induced in a superconductor by virtue of the currents which arise to oppose introduction of a magnetic field (Meissner effect). This is the same effect which gives rise to conventional eddy currents except that superconductivity promotes currents which are sufficiently strong to counter induced mmf without additional excitation. The only physical limitation to application of this type of suspension is the critical

value of magnetic field strength which disrupts superconductivity thus limiting the repelling forces.

The four types of electromagnetic suspensions as presently conceived are ac resonant, eddy-current, simple attractive, and simple repulsive. The ac resonant suspension provides attractive mode suspension of a ferromagnetic object by employing electromagnets tuned such that increasing air gap shifts the inductance of the electromagnetic circuit towards resonance with the excitation frequency thereby increasing coil current and restoring force. This suspension type provides intrinsic rotor position feedback but little or no damping.

The eddy-current suspension provides repulsive mode suspension of a non-magnetic, electrically conducting object by diamagnetic effects induced by ac electromagnets. Supporting forces are developed by inducing currents in the suspended body. Thus, high power consumption and heating of the body results. This type of suspension differs from the diamagnetic suspension discussed earlier in that external excitation is required to produce currents strong enough to counter the induced mmf.

In a simple attractive or repulsive suspension electromagnets are driven in response to discretely sensed feedback of the position, velocity, or acceleration of a ferromagnetic suspended object. The simple attractive or repulsive suspension requires active feedback control on one or more axis. Thus, a general system with five independent degrees of freedom (figure 1) will require five feedback control loops.

Despite this complexity, the advantage of active control on an axis is that gain and phase lead of the control loop can provide variable stiffness and damping characteristics for the rotor support, thus allowing influence of rotor dynamics. These considerations have favored the simple attractive or repulsive mode suspensions. Virtually all practical applications of electro-magnetic suspensions have been of either the simple attractive or repulsive modes. Successful applications of ac resonant and eddy-current suspensions have been, for the most part, limited to the laboratory.

Early researchers found all four types of electromagnetic suspension to require large power inputs and bulky structure to support the loads carried by the electromagnets. The large power input losses to the electromagnets arise from joule, hysteresis, and eddy currents. Since eddy currents and hysteresis losses are more significant in an ac systems, dc systems have certain inherent advantages when applied in the simple attractive or repulsive suspension. Furthermore, ac systems impose a higher drag on the suspended body compared to dc systems.

Repulsive mode suspension offers several advantages as compared to active mode suspension: the foundation can carry the vertical load instead of the machine frame; the mode is inherently stable since the repulsive force increases as the gap decreases, and less power is required. Nevertheless, despite the inherent instability of the attractive mode (force increases as gap decreases), it is more important commercially since higher bearing loads can be achieved, the magnetic leakage flux is less, and better stiffness and damping characteristics can be obtained.

DESIGN EVOLUTION

The realization of true contact free suspension of a rotor has been achieved in the last four decades with radially passive/axially active, radially active/axially passive, or active control on all axes. The first known successful work in magnetic bearings was performed by J.W. Beams at the University of Virginia. In 1937 his team successfully suspended a small spinning rotor up to 60,000 rpm using a radially passive/axially active arrangement, figure 2. Later work culminated in the achievement of the world's rotational speed record, 2.7 x 10^7 rpm, a record that still stands today. This early work was performed by servoing only one axis of the rotor in a simple proportional feedback loop in which the rotor's position was measured with a light beam. Comparison of the feedback signal with a reference input produced a control signal proportional to the signal difference to null the output (ref. 2). F. T. Backers (ref. 3) later employed permanent magnets in the radial direction to provide the first known successful hybrid arrangement of active and passive suspension elements in the late 1950's.

The complexity of actively controlling five axes for a typical two bearing rotor system was prohibitive for these early efforts. Furthermore, these early systems suffered from poor stiffness and damping characteristics: two physical parameters required for application to practical rotating systems. Poor availability of suitable power amplifiers for providing sufficient current for driving the electromagnets made these early achievements spectacular. All of the early work with these active and hybrid systems, including that of Beams, was performed using vacuum tube and magnetic amplifiers. The invention of the transistor in the Bell Laboratories in the early 1950's ushered in the present era of rapid advancement in magnetic bearing technology predominated by active and hybrid suspension arrangements.

Most of the important work in magnetic bearings in the sixties and early seventies was performed for spacecraft and satellite applications. Much of the current success in magnetic bearing technology is directly traceable to this effort despite the fact that actual use in space of this technology did not occur until 1983. This effort was largely centered around attitude control system development. Typically, these systems are comprised of (1) low speed reaction wheels, one for each axis; (2) two control moment gyros, each of which is capable of controlling two axes; or (3) momentum wheels capable of passive gyroscopic torques in two axes and active control in a third axis. Magnetic bearings were sought for these applications to resolve the lubrication design problems, power losses, and limited reliability that plagued the applications of conventional bearings.

The Cambridge Thermionic Corporation was the first to develop magnetic suspensions for these aerospace applications after scrapping their earlier work with ac resonance systems in favor of active systems. An eighteen month development effort culminated in 1970 with the delivery to NASA's Goddard Space Flight Center (GSFC) of two magnetically suspended motorized rotors of this type. These rotors weighed 3 kg and ran at speeds up to 12,000 rpm (ref. 4). However successful the demonstration of the technology feasibility, optimism was dampened by the fact that 3 kilograms of weight and 40 watts of power were being used to replace a conventional bearing weighing one thousandth as much and using very little power.

The development of hybrid designs employing permanent magnets and electromagnets for spacecraft applications was initiated at the same time with the introduction of the first designs by Studer at GSFC in 1970. These early hybrid suspensions were developed to reduce the power requirement by employing permanent magnets to supply the steady state magnetic flux for suspension with electromagnetic modulation of the flux in a common air gap. Furthermore, these designs served to reduce the weight requirement by reducing the amount of iron in the magnetic circuit and the required load capacity of the external structure used to support the electromagnet coils. In addition, the parallel PM (permanent magnet) and EM (electromagnet) circuits aided in linearizing the bearing force with control current.

Subsequent effort by Lyman at the Cambridge Thermionic Corporation resulted in the development of the "VZP (virtually zero power) Controller" for a hybrid suspension arrangement (ref. 5). This controller positioned the rotor at its force center rather than its geometric center of the working air gap. This feature forced the permanent magnets to carry the steady-state loads thus further reducing power and weight.

In the early 1970's other concerns, including Sperry Flight Systems and General Electric were also active in the development of flight prototype magnetic bearing systems for spacecraft and satellite applications. Figure 3 is a momentum wheel design derived from this effort. Designs that typify the development of the technology during this time period are illustrated in figures 4 through 6. Figure 7 is the result of a more recent design effort for a two degree of freedom system (ref. 6).

A noteworthy design in the development of magnetic suspension occurred in early 1975 when a unique satellite momentum wheel (ref. 7) appeared that represented a geometric configuration possible only with magnetic suspension, figure 8. A combination of permanent magnets and electromagnets were used to support the flywheel from three points near the periphery with no spokes or axle. Axial and radial servo control was provided at each of the three locations. This design marked the realization of one more important advantage available to rotating equipment with the use of magnetic bearings.

These early design concepts were successful in demonstrating the applicability of magnetic bearing technology to reaction and momentum satellite wheels. However, application to larger wheels or rotor systems operating above critical speeds was not feasible due to the inability to influence rotor dynamics because of limited stiffness and damping values.

On the other hand, as these researchers noted, the alternative, radially active suspension, requires high control bandwidth, with possible noise and structural interaction problems, and the added complexity of speed-dependent compensation to accommodate phasing and gyroscopic effects (ref. 8). These considerations delayed the start of large scale hardware development of the first totally active suspension until the late 1960's although a French company, Hispano-Suiza, filed a patent that used electromagnetic bearings and inductive rotor position sensors in 1957.

While all of this activity in application of magnetic bearings for satellite momentum and reaction wheels was taking place, efforts to apply magnetic bearings to other earthbound and space flight hardware including various sensors and energy storage flywheel systems was being pursued. A 1979 GSFC energy storage demonstration unit is shown in figure 9. This promising work continues (refs. 9 and 10). Another notable development was a magnetically suspended helium circulator for a spacecraft thermal control subsystem (ref. 11).

Comsat Laboratories decided to make a major commitment to magnetic **bearing** technology based on some of their own work with Cambion and the successful developments at GSFC. International competition brought support from both the German and French governments. In France, the exploratory work on spacecraft applications by Societe Europeenne de Propulsion (SEP) starting in 1969 culminated in 1976 with the formation of Societe de Mecanique Magnetique (S2M) in a joint effort with SKF to develop and market totally active systems internationally.

The first known commercial application of this technology appeared at an Italian exhibit of thread spinning machinery in 1975. By the next year, S2M had completed its first application of industrial equipment. In parallel efforts, development work on aerospace applications continued with the first use in space of active magnetic bearings coming in November 1983 with the launch of the Space Shuttle with the European Spacelab on board. Spacelab was equipped with a vacuum pump suspended on active magnetic bearings. The first known use of magnetic bearings in attitude control system flight hardware was in the SPOT satellite launched by an ARIANE booster on February 21, 1986 (ref 6).

In the last eleven years the trend in commercial applications has been to higher speeds and larger rotors as the availability of transistors capable of switching larger dc currents at higher frequencies has evolved. The rotational kinetic energy which magnetic bearings have been capable of supporting in commercial applications has increased from 10^3 to 10^7 N-m in these few years. Analog systems employing the classical proportional-integral-derivative (PID) control loop have been behind the success of these systems. The range in key system performance and size parameters is listed in Table 1.

Despite the success of some of these systems, attention has recently turned to digital control because of the developments in this field. Analog has been viewed as suffering from noise and drift problems and the inability to reconfigure components for changing system operating conditions. Since 1980 several digital controllers have been designed and built for laboratory studies. However, a case may be made that stable suspension of many of the cited commercial applications would not be possible with present digital technology because of data rate problems.

THE PID ANALOG CONTROLLER

Typical analog controllers consist of a chain of linear or operational amplifiers providing the signal conditioning and phase lead necessary for stable suspension of the rotor. A block diagram representation of the controller is presented in figure 10. Stability problems for a system can become quite complex when dealing with multiple shaft resonances, gyroscopic effects, rotor induced whirl due to rotor internal dumping, and the inherent negative stiffness of the bearing (attractive mode). For a hybrid design using permanent magnets, the magnetic break frequency above which the electrical gain falls off must be reckoned with (ref. 8).

The rotor dynamic performance and stability of the many commercial magnetic bearing applications is attributable, in a large way, to the capability in the PID controller to adjust bearing stiffness and damping parameters over a large range. The integral action of the controller is responsible for the elimination of system drift required to achieve high rotor positioning accuracies. While many systems have been built and tested, the classic PID controller continues to provide superior stiffness and damping characteristics. Static stiffness values up to 10^{10}N/m (ref. 12) have been achieved, thus surpassing that of conventional bearings. More typically, dynamic values in the range of 10^6 to 10^7N/m are obtained. Of course, the upper limit on achievable stiffness values is determined by system stability considerations; simple gain increases to achieve higher stiffness would otherwise be straightforward. Achievable damping values are significantly better than conventional bearings, and typically are optimized to provide maximum damping when crossing critical speeds by providing positive phase lead as described below.

The stiffness characteristics of conventional mechanical bearing systems including rotor mass have been approximated in the Bode plot form for a rigid rotor and a flexible rotor in figures 11 and 12 ,respectively. The phase advance, not shown, is minimal for conventional bearing systems.

In contrast, the stiffness and damping characteristics of active magnetic bearing systems, figures 13 and 14, exhibit the classical PID attributes: the proportional effort providing a positive spring-like stiffness, the integral effect providing high stiffness values at low frequencies to preclude drift, and the derivative effect providing damping by control loop phase lead. As described in ref. 13, position sensor information from a pair of radial bearings can be processed to readily control the two rigid body modes of the rotor.

Notice in figure 14 how the phase lead can be controlled to cover a large frequency band providing positive damping at multiple resonant frequencies. However, it is generally ill advised to provide positive phase lead at the frequency of the first bending mode by opening up the bandwidth due to noise considerations which may saturate the power amplifiers. A preferred method is to provide the ideal 90^o phase lead in a very narrow frequency band in the region of the critical speed, Figure 15. This is accomplished through an inner control loop that resolves the rotor position sensor information to a rotating coordinate system.

This same rotating coordinate system is also used to provide rotor "automatic balancing", the feature which allows the rotor to seek its inertial axis within the stator air gap. A conventional rotor system constrains the rotor to its geometric axis thus resulting in the transmission of unbalance forces to the stator. The rotating reference system allows the bearing stiffness to be cancelled at the rotational frequency, Figure 16. The opposite of this feature is "peak of gain" which drives the electronic gain to a maximum value in a narrow frequency range, thus providing excellent rotational accuracy for pointing systems.

Other analog techniques for achieving some of these same results are just developing. The "rotating force control" (ref. 14) method provides stable magnetic suspension and the automatic balance feature through the use of velocity and accleration observers which avoids analog differentiation. Reported stiffness and damping values are not as high as those attainable with the classical PID controller.

SUPERCONDUCTIVITY IMPLICATIONS OF MAGNETIC BEARING DEVELOPMENT

Future improvements in magnetic bearing system performance may be tied closely to breakthroughs in superconducting materials. Recent progress (ref. 15) in this research has led to the discovery of a class of rare earth oxides with transition temperatures above 90°K. Cooling may now be achieved with relatively inexpensive liquid nitrogen at 77°K instead of liquid helium at 4.2°K. This development represents a four fold increase in the transition temperature for superconductivity in the past year and heralds the advent of practical, cost effective superconducting devices.

This recent progress has been achieved with type II superconductors. The Abrikosov theory of type II superconductors (ref. 16) shows that for certain materials a magnetic field exceeding a lower critical field would penetrate the superconductor in a regular array of flux tubes each confined by a vortex of current. For other materials, the Meissner effect of ordinary, type I superconductors prevails whereby all flux is excluded. The condition of superconductivity exists only within parameters defining critical temperature, current density and magnetic field intensity.

The relevancy of superconductivity to magnetic bearings is at least twofold: electromagnet and control system design. Sensor technology is a possible third area where superconductivity may play a role in future improvements.

The application of these new materials in the design of the electromagnet coils used for magnetic suspension is obvious. Bearings of increased load capacity and reduced weight can be achieved by utilizing superconducting coils without any iron core. Presently available bearings operate with a magnetic field of about 1 tesla at room temperature. One present type II superconductor, $PbMo_6S_8$, has an upper critical field of up to 55 tesla at 4.2°K. Since the force producing capability and stored energy of a magnetic bearing varies directly with the square of the magnetic field, superconducting bearing power of over a thousand times that of a normally conducting device should be possible in future magnetic bearing systems.

The high critical current density possible in a superconductor (on the order of 10^8 A/m^2) and the lack of any requirement for field shaping iron combine to promise a compact, light bearing system for future spacecraft applications.

Current limitations governing the use of these materials in bearing systems include the quenching problem, high Lorentz forces, poor ductility, and high cooling requirements. Operation without an iron core requires that other means be provided for a structure to support the Lorentz force of the magnetic field. The

Lorentz forces become manifested as varying conductor stresses which store large amounts of mechanical energy. Small fractions of this energy are dissipated in the rapidly varying field needed to provide dynamic control of a spinning rotor. Since most conductors have very small enthalpies of solids at cryogenic temperatures, this energy dissipation can cause a "quench" or local transition to the normal conducting state. Current design provisions to prevent this occurence include dividing the superconductor into many fine filaments and embedding them in a copper matrix. In this manner, electromagnetic disturbances associated with the magnetic field gradient in the conductor itself are minimized while providing an adequate heat sink. Poor ductility properties are being resolved by continuing improvements in fabrication techniques.

Control system design will be impacted by advances in superconductivity that improve the overall energy density of magnetic bearings. Both analog as well as digital systems will be affected. The discovery of tunneling of particles between superconductors has led to ongoing development of tunnel junctions (e.g. Josephson juctions) for use in applications requiring high speed, low power signal processing. Present efforts are producing tunnel junctions with response rates in excess of 1THz (ref. 16). Development of other solid state superconducting devices will be used in amplifiers at presently unimaginable switching speeds to further enhance magnetic bearing load capacity and dynamic control capabilities.

Further potential applications of tunnel junctions are for use in advanced magnetic bearing sensor designs for both rotor position (displacement) and electromagnet coil flux. Today, rotor position accuracy of 10-6m total indicated runout has been achieved (ref. 12) using inductive position sensors on certain electrospindle applications. Currently projected spacecraft applications of spinning rotor systems require similar radial accuracies and certain pointing applications require angular positioning to within 5 microradians (ref. 17). Further improvements in these capabilities may be achieved by using SQUID (superconducting quantum interference devices) technology. Presently being developed for a host of applications from mapping of the magnetic field emanating from the human brain to the detection of submicroscopic motions of gravity wave detectors, these devices rely on superconducting Josephson junctions for operation. Non-contacting SQUID's may find their way into magnetic bearing sensor technology for precise rotor position and coil magnetic flux control.

ACKNOWLEDGMENTS

The author wishes to thank Mr. Philip Studer for his helpful review of the historical accuracy of this paper.

REFERENCES

1. Earnshaw, S.: On the Nature of the Molecular Forces. Transactions of the Cambridge Philosophical Society, Vol. 7, 1842, pp 97-112.

2. Beams, J. W.: High Speed Rotation. Physics Today, July 1959, pp 20-27.

3. Backers, F.T.: A Magnetic Journal Bearing. Philips Technical Review, Vol. 22, 1960, pp 232-238.

4. Studer, Philip A.: Magnetic Bearings for Spacecraft. NASA Goddard Space Flight Center, January 1972.

5. Development of a DC Motor with Virtually Zero Powered Magnetic Bearing. NASA-CR-130225, Cambridge Thermionic Corporation.

6. Gautheir, M. and J. P. Roland: An Advanced and Low Cost 2 Degrees of Freedom Magnetic Bearing Flywheel, AIAA, 1987.

7. Henrikson, Carl H. et al: Magnetically Suspended Momentum Wheels for Spacecraft Stabilization. AIAA 12th Aerospace Sciences Meeting, 1974, AIAA Paper No. 74-128.

8. Reistad, K. et al: Magnetic Suspension for Rotating Equipment. Phase 1, National Science Foundation, 1980.

9. Eisenhaure, D.B. et al: A Combined Attitude, Reference, and Energy Storage System for Satellite Applications, AIAA 22nd Aerospace Sciences Meeting, Reno, NV, January 9-12, 1984.

10. Nikolajsen, J.L.: An Electromagnetic Bearing for Flywheel Energy Storage in Space. Workshop on Magnetic Suspension Technology, NASA CP-3202 . 1993.

11. Fujii, R.C. et al: A Helium Circulator for Spacecraft Thermal Control Using Magnetic Bearings, Aerojet Electrosystems, AIAA-80-0146.

12. Weise, D.A.: Active Magnetic Bearings and Their Industrial Applications. Fifth Annual Rotating Machinery and Controls Industrial Research Conference, 1985

13. Habermann, H. and M. Brunet: The Active Magnetic Bearing Enables Optimum Damping of Flexible Rotor, ASME paper 84-GT-117.

14. Chen, H. M. and M. S. Darlow: Magnetic Bearings With Rotating Force Control, ASME. 1987.

REFERENCES (cont.)

15. Khurana, A.: Superconductivity Seen Above the Boiling Point of Nitrogen. Physics Today. April 1987, pp. 17-23.

16. Tinkham, M.: Superconductivity. Physics Today. March 1986.

17. Andres, J.: Cryogenic Magnetic Gimball Bearing, Honeywell Inc., AIAA 18th Aerospace Sciences Meeting, Pasadena, CA, January 14-16, 1980.

TABLE 1. CLASSIC PID CONTROLLER RANGE OF COMMERCIAL APPLICATIONS

Rotor mass	:	$3x10^{-2}$ - $7x10^{3}$ Kg
Rotational Speed	:	0 - $8x10^{5}$ rpm
Bearing Diameter	:	$1.5x10^{-2}$ - 1.2 m
Ambient Temperature	:	20 - 720 °K

FIGURE 1. SUSPENSION PRINCIPLE

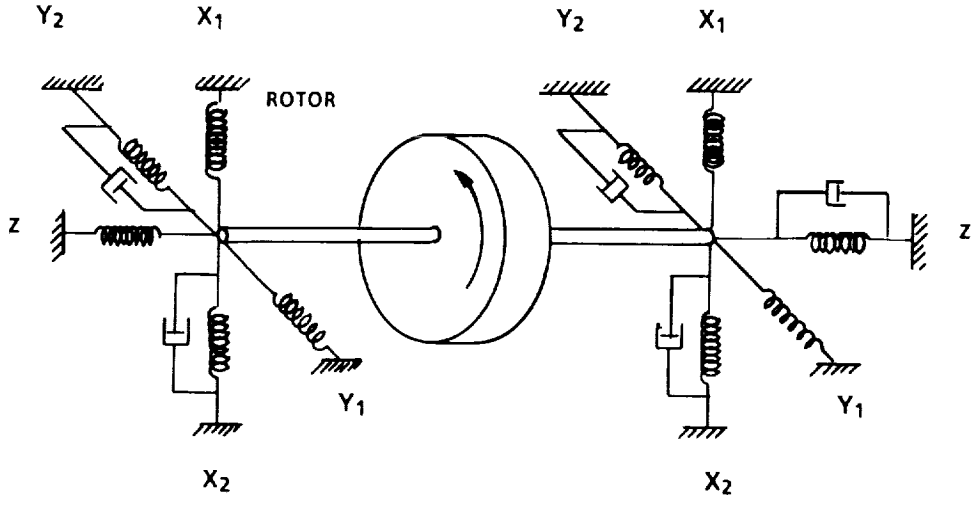

FIGURE 2. FIRST RECOGNIZED MAGNETIC SUSPENSION SYSTEM, BEAMS, CIRCA 1937

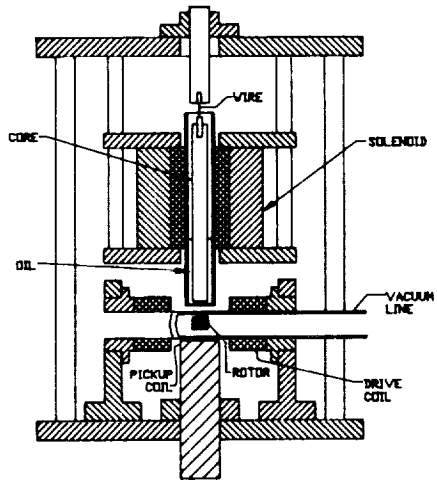

FIGURE 3. MAGNETICALLY SUSPENDED MOMENTUM WHEEL, 1973

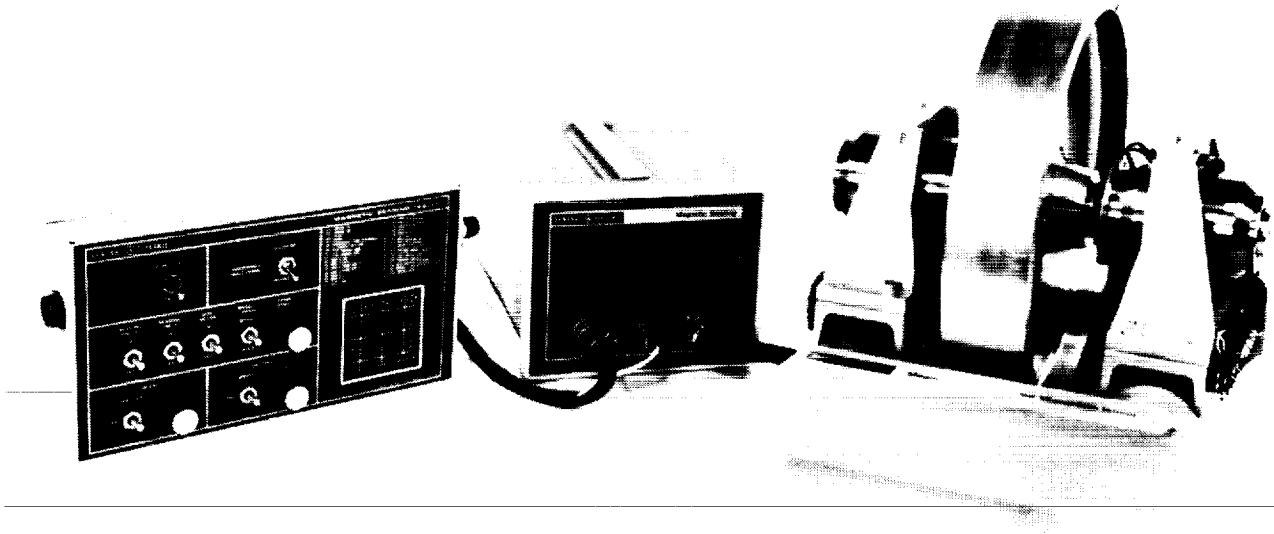

FIGURE 4. PM SUPPLEMENTED MAGNETIC BEARING

- PARALLEL PATH FOR CONTROL FLUX
- RELUCTANCE OF PM PATH CONSTANT FOR MOTION OF SUSPENDED ROTOR

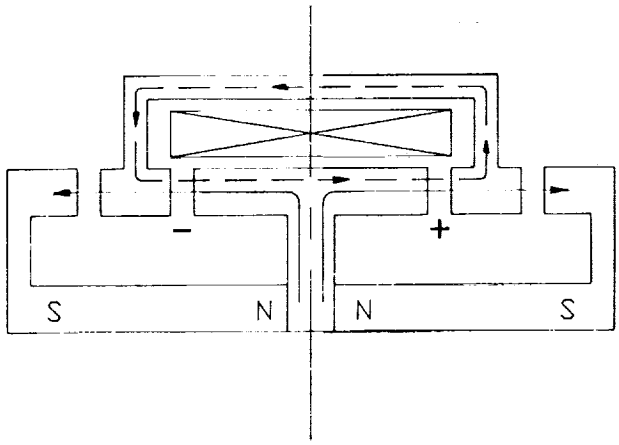

FIGURE 5. "PANCAKE" BEARING

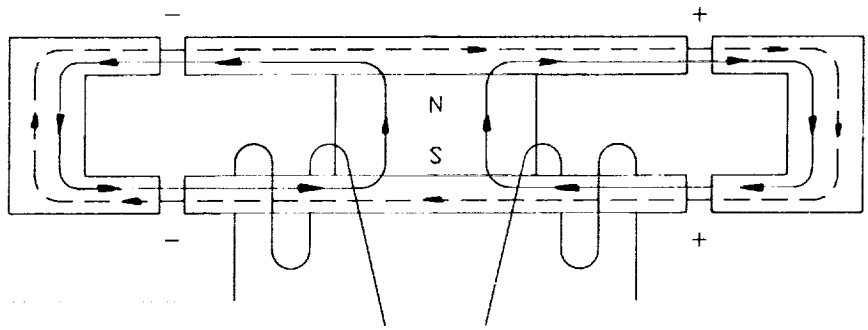

- PARALLEL PATH FOR CONTROL FLUX.
- MINIMAL PM CIRCUIT RELUCTANCE CHANGE.
- PM AND CONTROL COILS ON STATOR.

U.S. Patent No. 4,000,929.

FIGURE 6. EXTERNAL STATOR BEARING

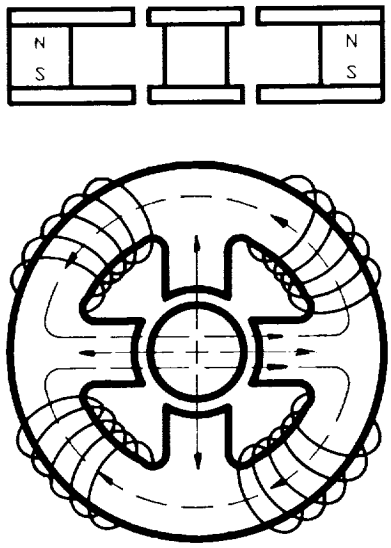

- PARALLEL PATH
- SMALL RELUCTANCE CHANGE
- STATIONARY WINDINGS AND PERMANENT MAGNETS

Patent No. 4,381,875

FIGURE 7. LOW COST 2DOF BEARING

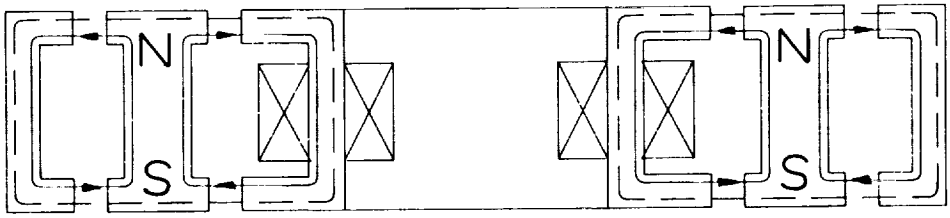

- PARALLEL PATH
- MINIMAL RELUCTANCE CHANGE
- OUTER RING PROVIDES STABILITY FOR RADIAL AND AXIAL MOTION

FIGURE 8. ANNULAR MOMENTUM CONTROL DEVICE, 1977

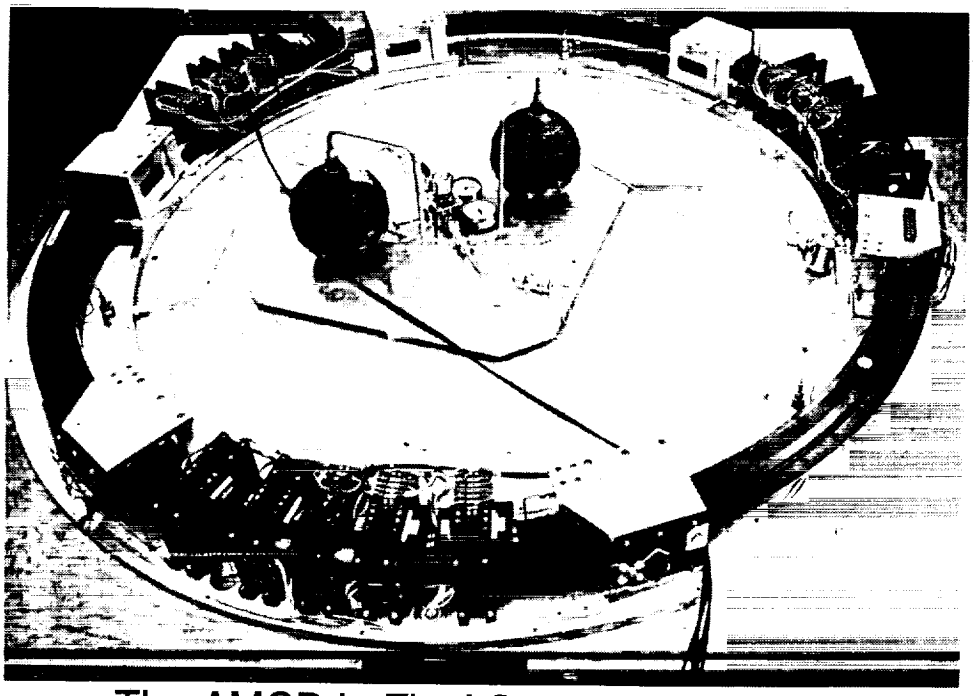

The AMCD in Final Stages of Assembly

FIGURE 9. NASA ENERGY STORAGE DEMONSTRATION, 1979

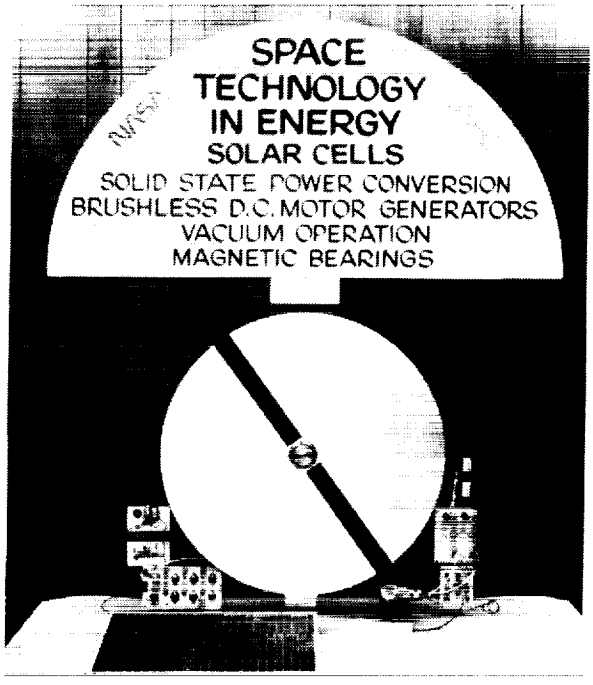

FIGURE 10. ACTIVE MAGNETIC BEARING CONTROL SYSTEM

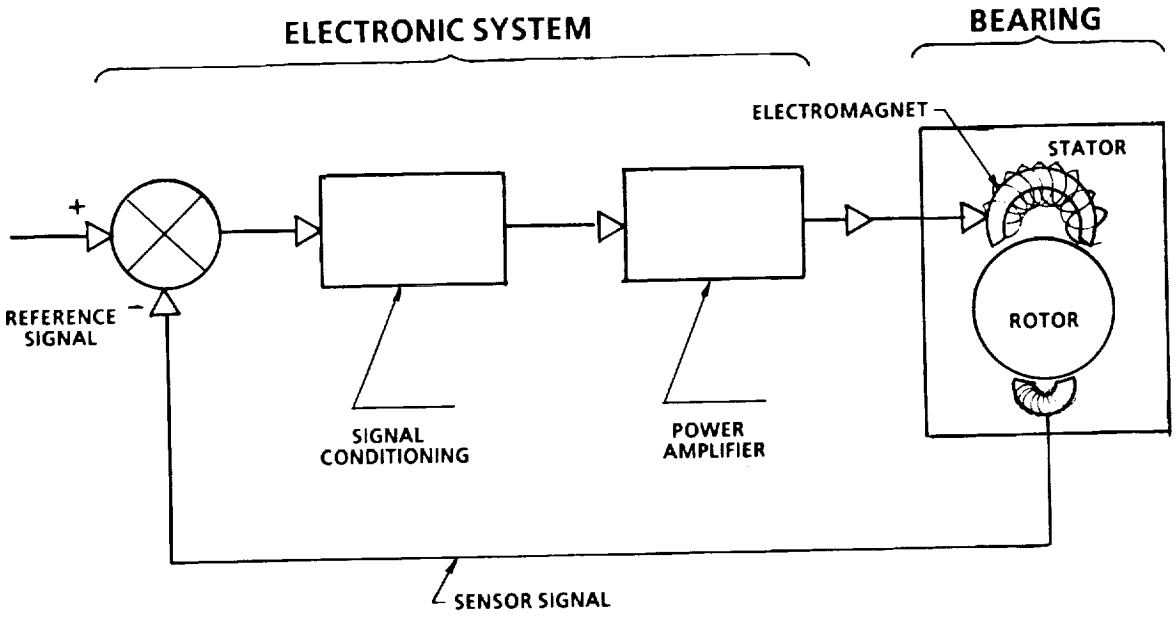

FIGURE 11. CONVENTIONAL BEARING STIFFNESS CHARACTERISTIC--RIGID SHAFT

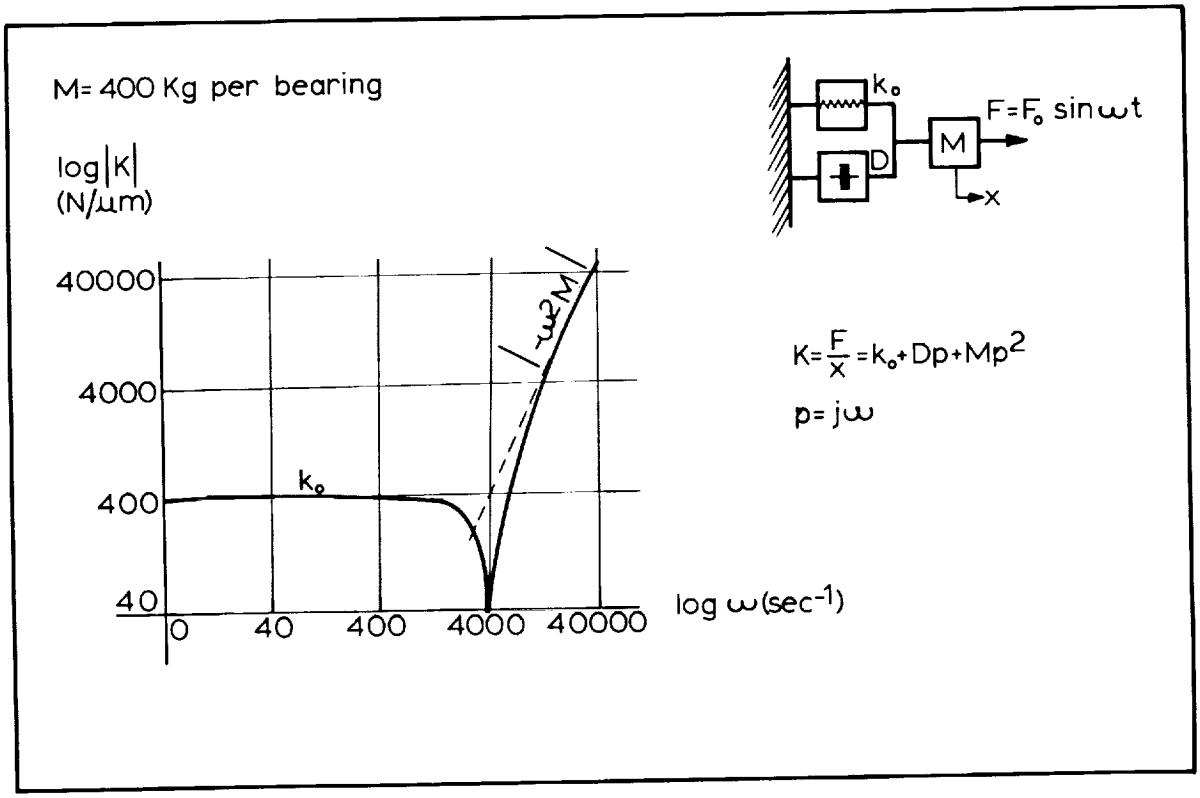

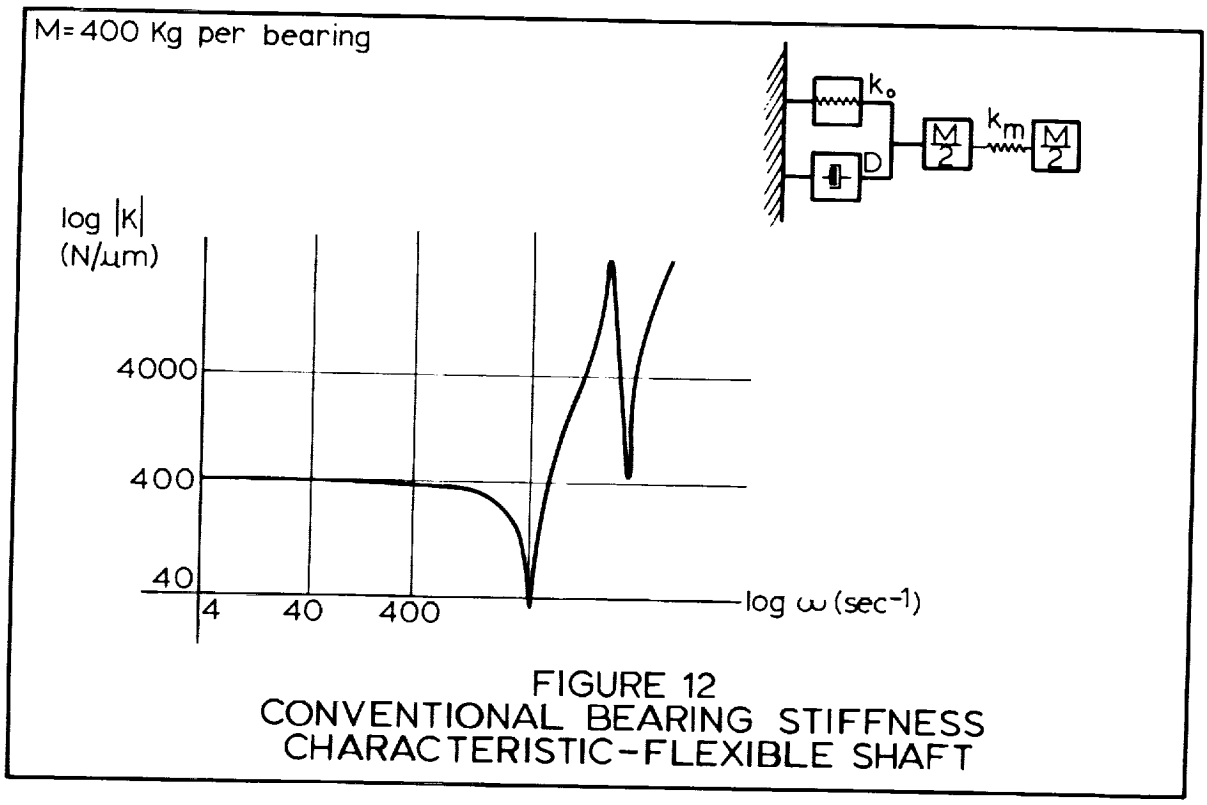

FIGURE 12
CONVENTIONAL BEARING STIFFNESS
CHARACTERISTIC-FLEXIBLE SHAFT

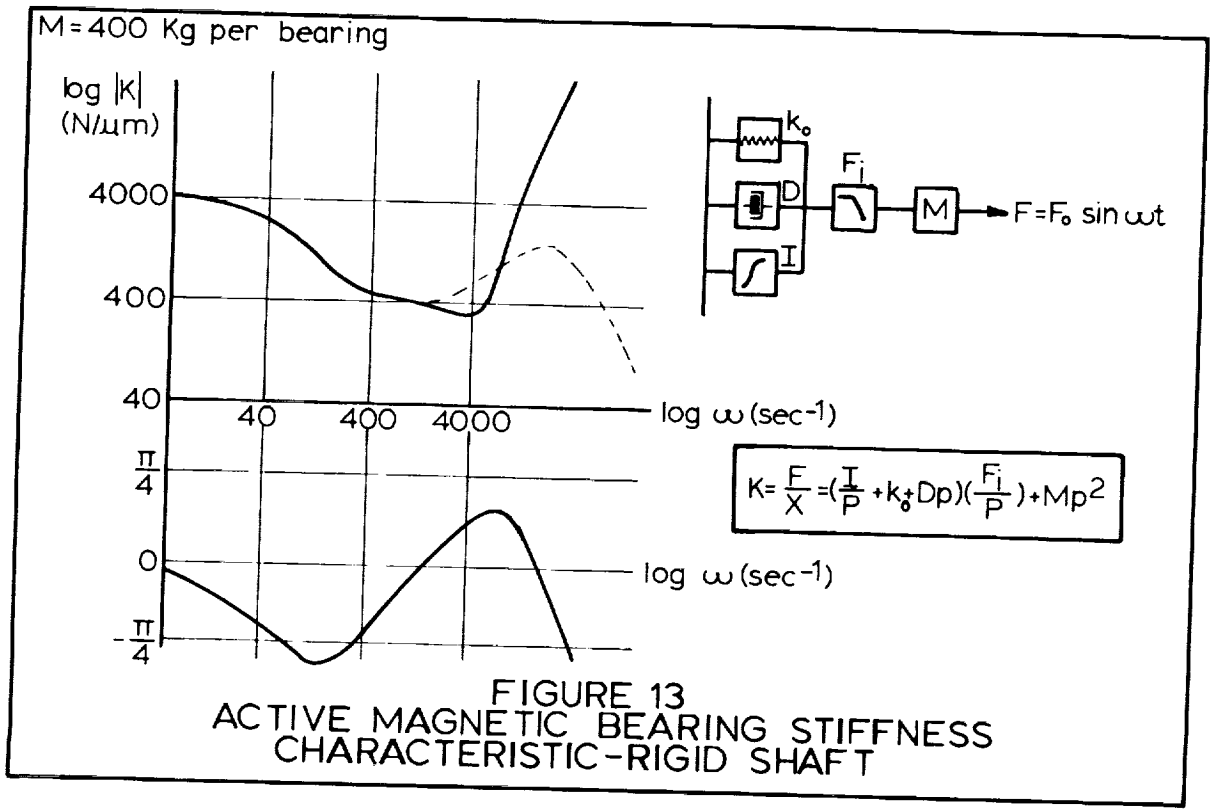

FIGURE 13
ACTIVE MAGNETIC BEARING STIFFNESS
CHARACTERISTIC-RIGID SHAFT

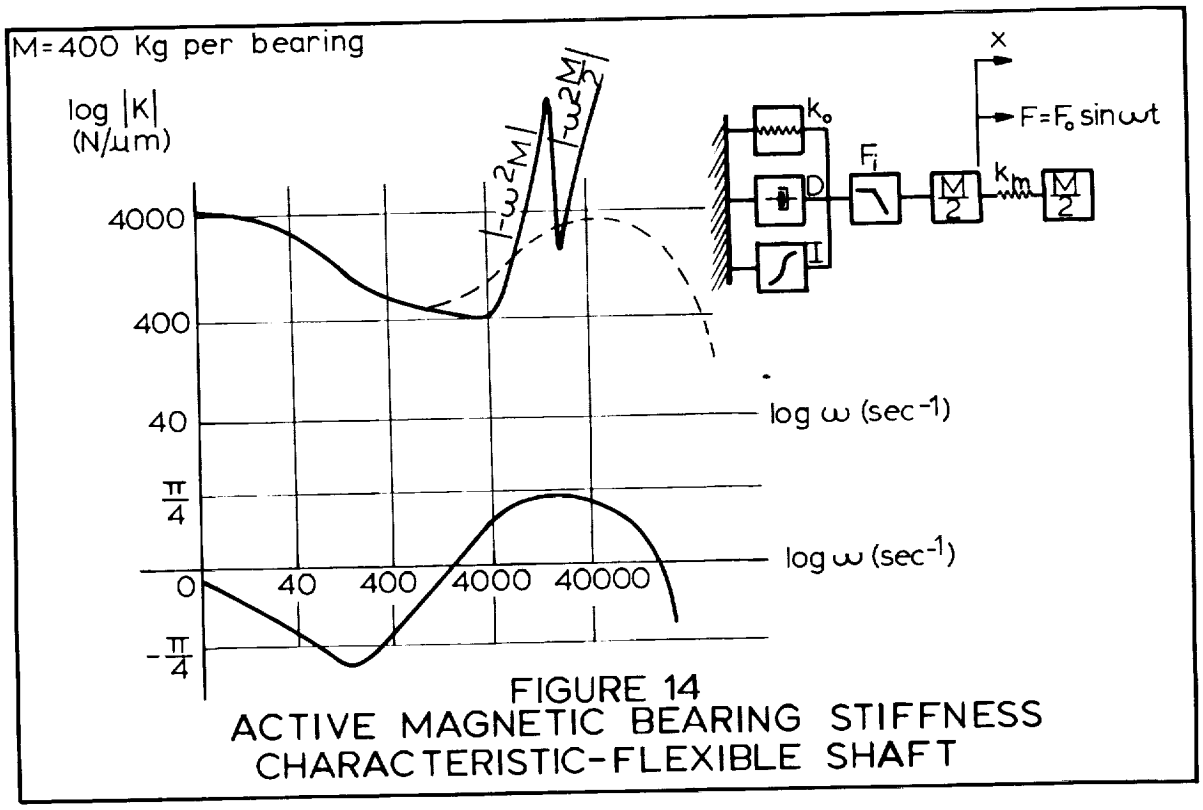

FIGURE 14
ACTIVE MAGNETIC BEARING STIFFNESS
CHARACTERISTIC-FLEXIBLE SHAFT

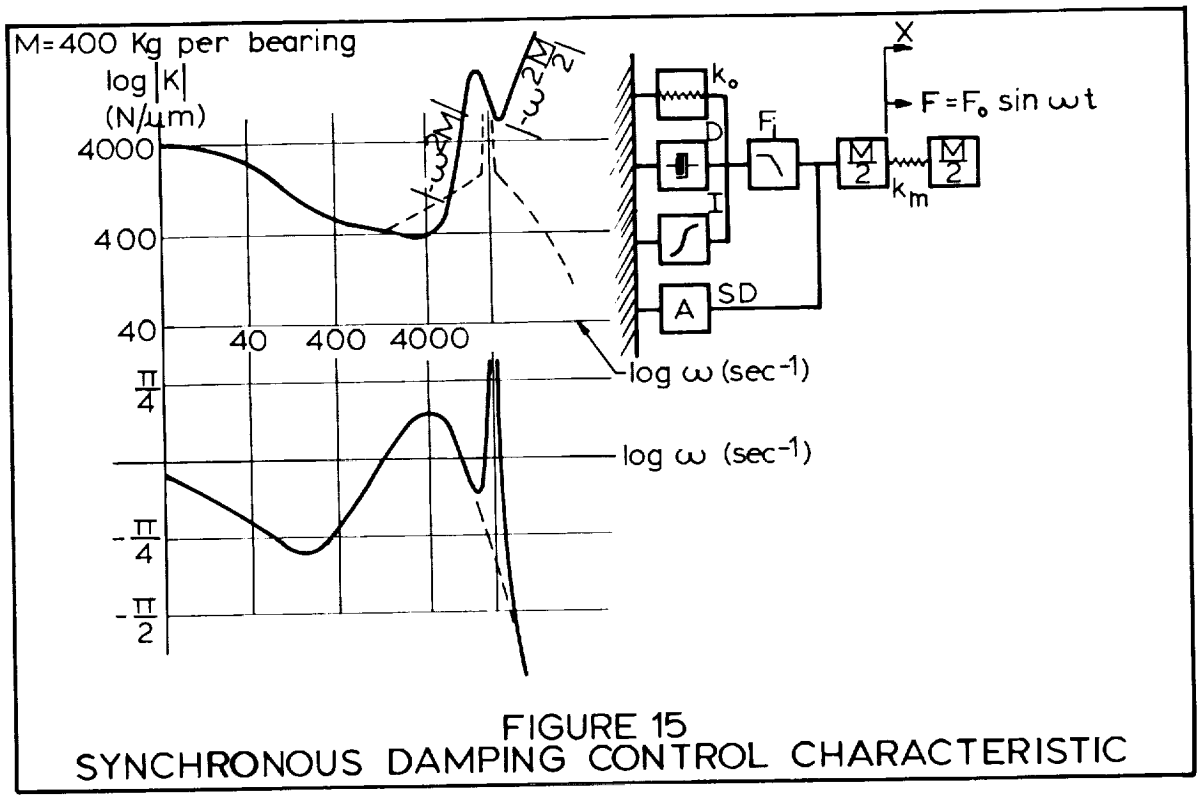

FIGURE 15
SYNCHRONOUS DAMPING CONTROL CHARACTERISTIC

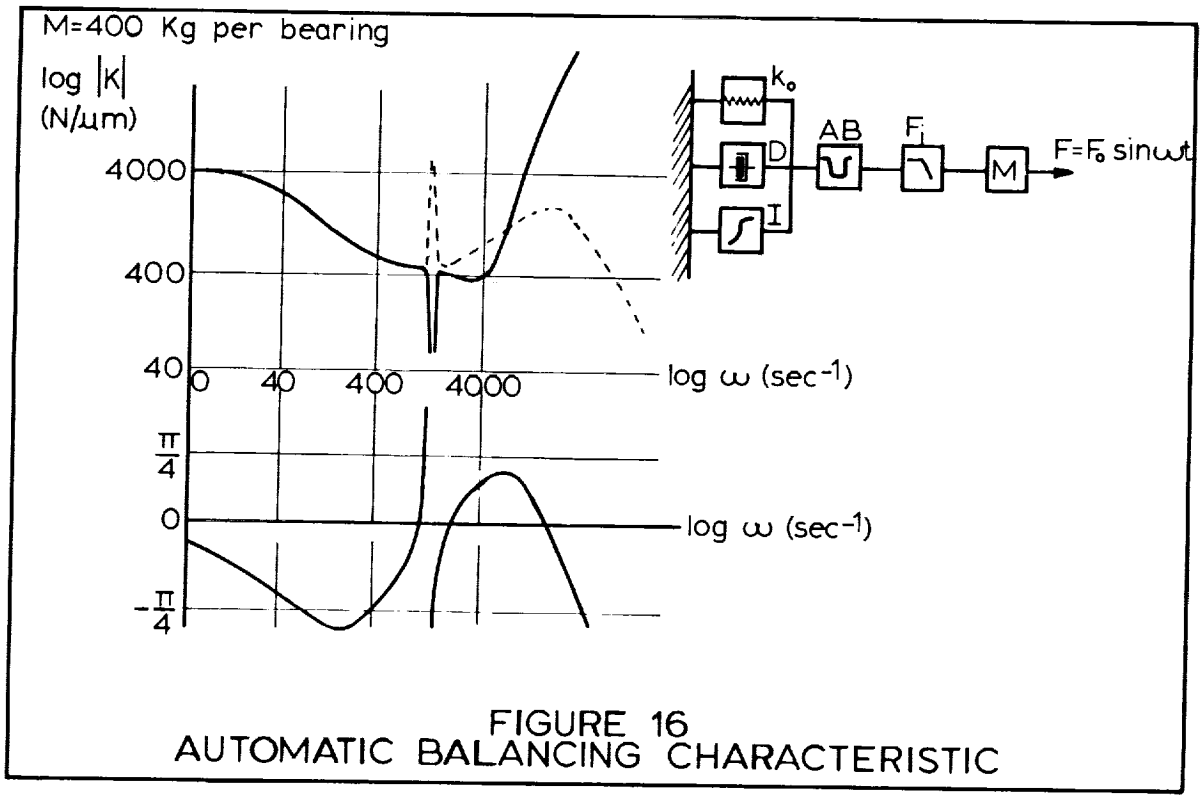

FIGURE 16
AUTOMATIC BALANCING CHARACTERISTIC

OMIT

Magnetic Bearing Turbo-Machinery Case Histories and Applications for Space-Related Equipment

David A. Weise, Magnetic Bearings Inc.

MAGNETIC BEARING TURBOMACHINERY CASE HISTORIES AND APPLICATIONS FOR SPACE RELATED EQUIPMENT

David A. Weise
Magnetic Bearings, Inc.
Radford, Virginia

SUMMARY

The concept of magnetic levitation is not a new one and can be easily traced back to the 1800's. (1) It is only recently, however, that the congruous technologies of electronic control systems, power electronics and magnetic materials have begun to merge to make the magnetic suspension device a viable product.

The following paper provides a brief overview of an active magnetic bearing technology.(2) Case histories of various turbomachinery in North America presently operating on magnetic bearings are reviewed. Finally, projections are made as to the space related machinery that may be benefited by incorporating magnetic bearings into the equipment design.

BACKGROUND

In theory, the principle is quite basic. An electromagnet will attract any piece of ferrous material. By using a stationary electromagnet (stator) and a rotating ferrous material (rotor) a shaft can be suspended in a magnetic field while maintaining accurate position under varying loads. This can be accomplished given a small space (air gap) between the stator and rotor and proper electronic control of the electromagnet. In the following case of the active magnetic bearing, this concept is utilized for both radial and axial configurations. It must be noted that the bearing system described here always operates in an attraction mode and never repulsion.

The radial and axial bearing rotors make use of a ferrous laminated sleeve and solid disc respectively.(3) Applying ferrous rotor elements to the shaft allows the shaft material to be constructed from a non-magnetic metal or composite material. While the radial bearing requires laminations due to the number of flux reversals during rotation, the axial rotor disc can be solid since the magnetic flux level is changing but the polarity is not.

As with any type of electromagnet, a wound field stator is required to produce a force output. Both the radial and axial bearing stators incorporate laminations to minimize stray losses and improve the bearing response time. The radial bearing stator is wound to provide four independently controllable quadrants for maximum rotor stability. The axial bearing, attracting the rotor in only one plane, requires the use of two stators, one on either side of the rotor disc, to provide double acting control.

Inductive position sensors are used to detect the exact radial and axial location of the shaft. Similar to the bearings, these sensors utilize a ferrous rotor and a wound field stator. As the air gap at the sensors changes with shaft disturbances the inductance bridge of the sensor also changes. It is this change in inductance with air gap variation that provides the position feedback signal required for closed loop servo control.

Figure 1 shows an isometric view of both a radial and double acting axial bearing with their associated position sensors.

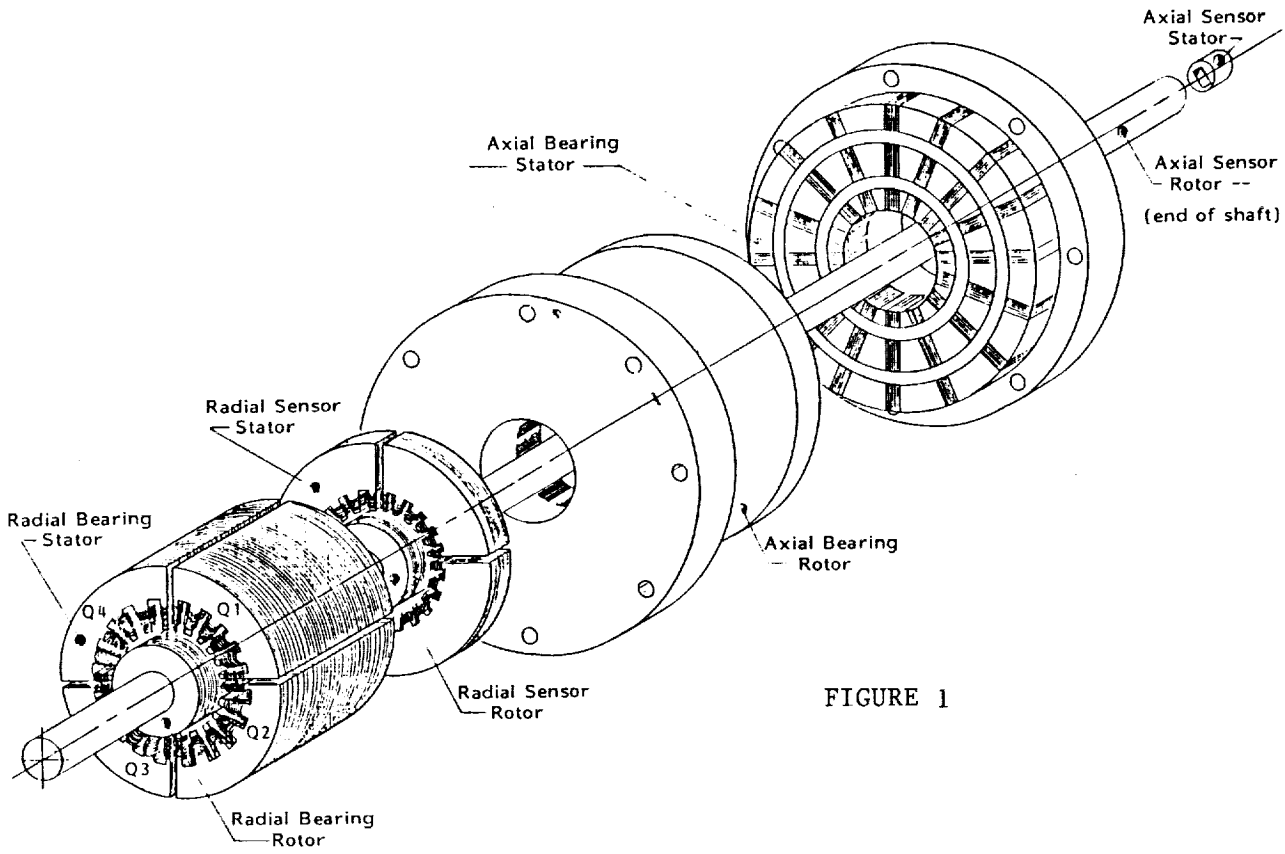

FIGURE 1

Control electronics are required to process the position signal and power the appropriate bearing coils. The exact shaft location is detected by the position sensors, and a DC voltage is generated which is relating to rotor displacement. This DC voltage (where the shaft is) is compared to the position reference signal (where the shaft should be). Any difference between these two signals generates an error signal which is used to maintain control of the rotor. This signal is then amplified, filtered, and conditioned prior to commanding the specified power amplifier(s). Current is increased or decreased in the appropriate bearing coil(s) to maintain the rotor at equilibrium. Figure 2 shows a basic block diagram of the closed loop servo control.

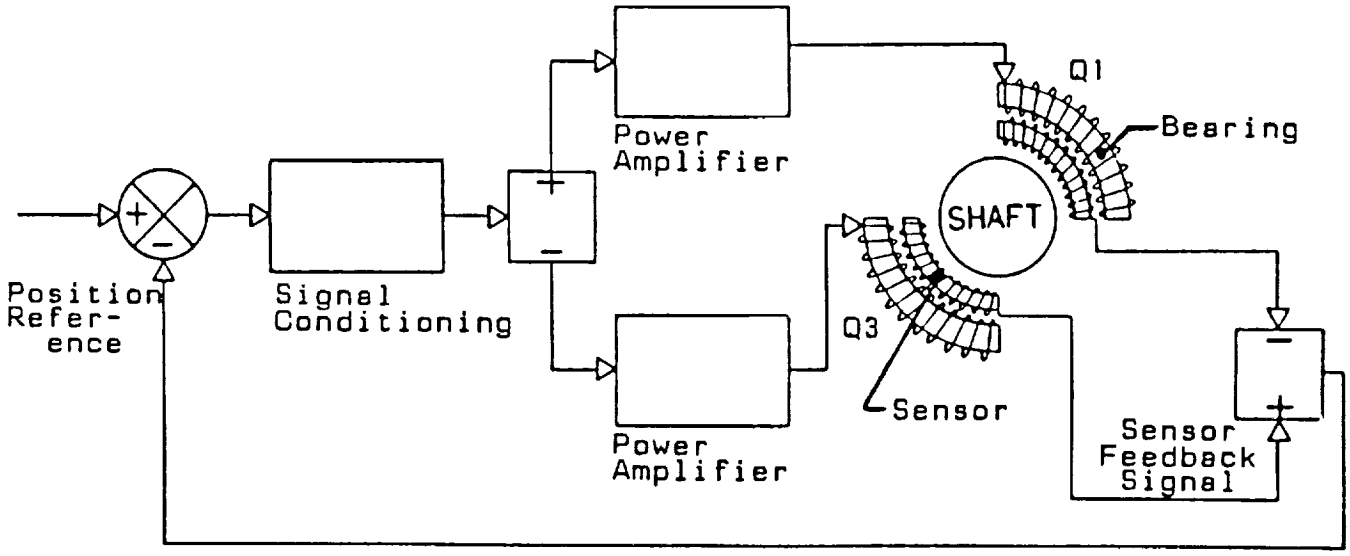

Figure 2

RADIAL BEARING CONFIGURATION

CASE HISTORIES

At the time of this writing, there are presently nine industrial machines in North America operating on this type of magnetic bearing system. Table 1 provides a listing of these units including basic machinery data.

TABLE 1

MACHINE	TYPE	SERVICE	DUTY	COMM	ROTOR WEIGHT LB	THRUST LOAD LB	SPEED RPM	JOURNAL DIAMETER	RATING HP	OPERATING HOURS (*)
CDP-230	CENT COMP	PIPELINE	SEASONAL	1985	3200	12000	5250	10.6"	14650	6800
CDP-416	CENT COMP	PIPELINE	SEASONAL	1986	280	3370	14500	3.7"	4150	6700
1B26	CENT COMP	PIPELINE	CONTINUOUS	1986	780	4050	11000	6.5"	5540	4800
1B26	CENT COMP	PIPELINE	CONTINUOUS	1987	780	4050	11000	6.5"	5540	300
CBF-842	CENT COMP	REFINERY	CONTINUOUS	1987	1420	4590	10250	6.0"	4500	750
8DD-300	CENT COMP	LAB	INTERMIT	1980	850	3150	13000	7.5"	5360	750
B15/1000	SPIN TESTER	PROD/TEST	INTERMIT	1985	17	17	60000	2.5"	20	375
7CK148	TEST RIG	LAB	INTERMIT	1980	675	2700	12000	5.9"	1800	610
	TEST RIG	LAB	INTERMIT	1985	350	300	10000	7.5"	40	50
HSNC-CN1	NEUTRON CHOPPER	LAB	INTERMIT	1984	33	33	48000	2.4	4	250

*AMB CABINET OPERATING HOURS AS OF DECEMBER 15, 1987

To date all of the above mentioned equipment have operated with a very high level of performance. The limited failures incurred have been attributed to human error (i.e.. wire rubbing on shaft after final machine assembly) or electrical component failure and not to design or technology flaws.

Reasons for utilizing magnetic bearings in rotating machinery vary with each particular application, although many common threads are evident. Heavy equipment users, typically employing oil lubricated tilting pad bearings, see many advantages, including efficiency and safety in eliminating the oil lubrication system.[4] Such a system utilizes external lube oil pumps, piping, reservoirs and filters which are also costly elements to install and maintain. In many cases, more heavy equipment down time is attributable to failures in machinery subsystems than actual machinery failure itself. Other users of magnetic bearings site higher speeds, harsh environment operation and optimized rotor dynamic characteristics[5] as reasons for using magnetic bearings.

While researching the operating histories of the previously mentioned machinery it became apparent that discussing each unit in depth would become monotonous. Following the commissioning of each machine multiple starts and stops have occurred and operating hours have accrued with very little attention brought by the fact that it is a "magnetic bearing" machine. In every case, there have been few or no equipment shutdowns attributable to the magnetic bearings. Those that have been were previously mentioned. Therefore, it was decided to expand from Table 1 only the one machine with the most operational hours.

The machine researched is an Ingersoll-Rand pipeline compressor model number CDP-230. The unit is part of the NOVA natural gas pipeline system in Alberta, Canada and was put into service at the Hussar compressor station in 1970. This train is ISO rated at 14,650 Hp and consists of a General Electric LM-1500 gas generator exhausting into an Ingersoll-Rand GT-51 power turbine dry coupled to the compressor. The normal operating speed range is from 3000 to 5250 rpm.

As originally supplied, this compressor incorporated oil film seals and bearings. In 1982 the conventional oil seal system was replaced by a mechanical dry gas seal.[6] Three years later conversion of this unit to the world's first oil free compressor of its type in production service was completed with the retrofit of the oil film bearings to active magnetic bearings.[7]

Following the installation of the magnetic bearings extensive dynamic testing took place. Two bearing resonant frequencies were identified at 28 and 42 Hz with first three shaft modes occurring at 89, 142 and 190 Hz. It can be seen that the first bending mode at 89 Hz (5,340 rpm) is very near the maximum operating speed of 5,250. However, the bearing control system maintained shaft movements no less than 0.8 mils peak-to-peak with no noticeable excess current draw during operation. Bearing parameters were monitored under various load conditions and data collected as per Table 2.

TABLE 2 — TEST VALUES - CURRENT, BEARING LOADS AND POWER CONSUMPTION

BEARING LOCATION		STATIC TESTING (0 RPM) CASING PRESSURIZED	NORMAL OPERATION 3600 RPM Δ P = 112 PSI	CHOKE CONDITION 4500 RPM ΔP = 12 PSI	SURGE CONDITION 4100 RPM Δ P = 152 PSI	IN-SERVICE 12-15-87 4280 RPM	
OUTBOARD RADIAL BEARING	UPPER (2) QUADRANTS	17.6	18.3	17.7	18.0	17.2	CURRENT (AMPS)
	(AVERAGE)	1370	1460	1370	1439	1339	LOAD (LBS)
	LOWER (2) QUADRANTS	5.0	5.0	5.0	5.0	5.0	CURRENT (AMPS)
	(AVERAGE)	112	112	112	112	112	LOAD (LBS)
INBOARD RADIAL BEARING	UPPER (2) QUADRANTS	21.0	20.2	20.1	21.0	19.3	CURRENT (AMPS)
	(AVERAGE)	1933	1798	1776	1933	1705	LOAD (LBS)
	LOWER (2) QUADRANTS	5.0	5.0	5.0	5.0	5.0	CURRENT (AMPS)
	(AVERAGE)	112	112	112	112	112	LOAD (LBS)
THRUST BEARING	OUTBOARD	11.8	5.0	41.5	5.0	19.2	CURRENT (AMPS)
		679	112	8610	112	1790	LOAD (LBS)
	INBOARD	5.0	15.8	5.0	18.8	5.0	CURRENT (AMPS)
		112	1259	112	1753	112	LOAD (LBS)
TOTAL BEARING POWER CONSUMPTION (Hp)		4.7	5.1	5.4	5.1	4.8	

Subsequent evaluations of the operating history of this machine provided additional economic and performance data.[8] While most of this data includes improvement from the installation of both the gas seal and the magnetic bearings, it is representative of the benefits associated with a lubrication free machine.

By total elimination of the oil system, parasitic and oil shear horsepower losses improved the units output power by approximately 2%. The magnetic bearing system on the compressor uses about 5 Hp of energy. This compares to 302 Hp lost in the conventional bearing and seal oil system.

Maintenance savings were also calculated and determined to be a rather substantial figure. With the total absence of contacting stationary and rotating components no wear related maintenance was seen. Also maintenance to the lubrication and seal oil subsystems was eliminated. Overall machinery maintenance, call outs, and downtime have been reduced by 85%. With the total average scheduled maintenance cost for the compressor and associated equipment of $41,250 and $22,500 typically related to call outs and unscheduled maintenance, an annual maintenance savings of $54,187 was calculated.

Based on these maintenance savings and the additional savings associated with oil consumption and oil and pipeline contamination a payback period of 4.4 years is anticipated for this retrofit. Installation of magnetic bearings and dry gas seals in a new compressor where the initial bearing and seal costs are partially offset by not purchasing a bearing and seal oil system can improve the payback period to less than one year.

Lubrication free equipment capable of harsh environment operation is definitely seen as the future for many types of rotating machinery. At the time of this writing, the author's company is actively involved in the installation or commissioning of magnetic bearings in fourteen machines encompassing five different areas of application.

SPACE RELATED EQUIPMENT

If it can be stated that commercial applications are just now beginning to grow, it is safe to say that space related applications are still in their infancy. Most of the investigations and applications to date have been related to gyroscopes and momentum wheels.[9][10] While these are indeed good applications of magnetic bearings which have proven to be successful to the space program, the real benefits can be gained by utilizing magnetic bearings in machinery with more of a production output.

With the potential seen today in zero-gravity space experiments and the possibility of specific production products being made in space, equipment requiring no lubrication and minimal maintenance is very attractive. Some equipment has already been developed with this particular application in mind. A turbomolecular vacuum pump having a magnetic bearing supported rotor has been developed for experimentation requiring a constant vacuum.[11] Where total vibratory isolation of a test table is required a magnetic suspension device to provide damping and stabilization could be incorporated.[12]

Further benefits can be gained by utilizing magnetic bearings in the power plant and life support systems of such projects as the upcoming space lab. Some of the advantages of high horsepower commercial equipment have already been discussed. By adopting magnetic bearings in the original design of equipment such as environmental control units for cabin pressurization and air circulation, these units output per weight ratio can be substantially increased. Smaller and lighter equipment, electric motor driven and operating at very high speeds (50,000 to 80,000 RPM) can now provide the same output as larger previous equipment typically less efficient and requiring some type of external lubrication system.

Work in the field of magnetic bearings has not gone unnoticed by NASA and indeed in many ways has been enhanced by them. Over the years, NASA has generated multiple patent activity relating to various magnetic bearing configurations.[13][14] Additionally, some actual equipment, including a Stirling cycle cryogenic cooler operating on magnetic bearing, has been designed by NASA.[15]

CONCLUSION

The operational history of machinery utilizing magnetic bearings has uncovered many benefits provided to ground based equipment. With the advances continually being made in the areas of electronic components and control systems, magnetic alloys and superconducting materials, the field of magnetic levitation will continue to grow as fast as its associated technologies will allow. Investigation and applications work should be continued to fully understand and exploit the total potential of magnetic suspension devices for the United States space program.

REFERENCES

1. Earnshaw, S.: "On the Nature of the Molecular Forces:. Trans. Cambridge Phil. Soc. 7, 97-112, 1842.

2. Weise, David A.: Active Magnetic Bearings Provide Closed Loop Servo Control for Enhanced Dynamic Response. Presented at the 27th IEEE Machine Tool Conference, October, 1985.

3. Weise, David A.: Present Industrial Applications of Active Magnetic Bearings. 22nd IECEC'87 Philadelphia, Pennsylvania, August 10-14.

4. Cataford, G.F.and Lancee, R.P.: Oil Free Compression on a Natural Gas Pipeline. ASME Paper No. 86-GT-293.

5. Hustak, J.F., Kirk, R.G. and Schoeneck, K.A.: Analysis and Test Results of Turbocompressors Using Active Magnetic Bearings. ASLE Preprint No. 86-AM-1A-1, May 12-15, 1986.

6. Hesje, R.C. and Peterson, R.A.: Mechanical Dry Seal Applied to Pipeline (Natural Gas) Centrifugal Compressors. ASME Paper No. 84-GT-3.

7. Foster, E.G., Kulle, V. and Peterson R.A.: The Application of Active Magnetic Bearings to a Natural Gas Pipeline Compressor. ASME Paper No. 86-GT-61.

8. Uptigrove, S.O., Harris, T.A. and Holzner, D.O.: Economic Justification of Magnetic Bearings and Mechanical Dry Seals for Centrifugal Compressors. ASME Paper No. 87-GT-174.

9. Habermann et al.: Devices Including Rotating Members Supported by Magnetic Bearings. United States Patent No. 3,787,100, Jan 22, 1974.

10. Gauthier, M., Roland, R.P.: An Advanced and Low Cost 2 Degrees of Freedom Magnetic Bearing Flywheel. American Institute of Aeronautics and Astronautice, Inc. Paper No. 879447, 1987.

11. Bachler et al.: Turbomolecular Vacuum Pump Having a Magnetic Bearing-Supported Rotor. United States Patent No. 4,023,920, May 17, 1977.

12. Habermann: Device for the Horizontal Stabilization of a Vertically Supported Mass. United States Patent No. 4,244,629, Jan. 13, 1981.

13. Studer: Magnetic Bearing and Motor. United States Patent No. 4,381,875, May 3, 1983.

14. Studer: Radial and Torsionally Controlled Magnetic Bearing. United States Patent No. 4,634,191, Jan. 6, 1987.

15. Gasser et al.: Stirling Cycle Cryogenic Cooler. United States Patent No. 4,389,849, June 28, 1983.

Session 2

Modelling and Control

Chairman: Suresh M. Joshi

NASA Langley Research Center

Digital Control of Magnetic Bearings Supporting a Multimass Flexible Rotor

F. Joseph Keith, Ronald D. Williams, Paul E. Allaire, University of Virginia

R. Michael Schafer, Tell Labs Inc.

DIGITAL CONTROL OF MAGNETIC BEARINGS SUPPORTING A MULTIMASS FLEXIBLE ROTOR

F. J. Keith, Research Associate (1)
R. D. Williams, Assistant Professor (1)
P. E. Allaire, Professor (2)
R. M. Schafer, Senior Research Engineer (3)

(1) Electrical Engineering Department
Thornton Hall
University of Virginia
Charlottesville, VA

(2) Mechanical and Aerospace Engineering Department
Thornton Hall
University of Virginia
Charlottesville, VA

(3) Tell Labs Research Center
Tell Labs, Inc.
Bldg. No. 2, Suite 101
3702 North Main St.
Mishawaka, Indiana

ABSTRACT

This paper considers the characteristics of magnetic bearings used to support a three mass flexible rotor operated at speeds up to 14,000 RPM. The magnetic components of the bearing are of a type reported in the literature previously, but the earlier analog controls have been replaced by digital ones. Analog-to-digital and digital-to-analog converters and digital control software were installed in an AT&T PC. This PC-based digital controller was used to operate one of the magnetic bearings on the test rig. Basic proportional-derivative control was applied to the bearings, and the bearing stiffness and damping characteristics were evaluated. Particular attention is paid to the frequency dependent behavior of the stiffness and damping properties, and comparisons are made between the actual controllers and ideal proportional-derivative control.

INTRODUCTION

This paper discusses the development of digital controls for magnetic bearings. An analog controlled magnetic bearing developed by the Rotating Machinery and Controls Laboratory at the University of Virginia has been described in several articles [1-4]. A PC-based digital controller has been implemented for the same magnetic components and flexible rotor.

Magnetic bearings are coming into increasing commercial use in rotating machinery. Uses include industrial applications such as compressors, turbines and pumps, and space related applications such as momentum wheels, turbomolecular pumps and attitude control devices. Magnetic suspension devices can also be used in other applications such as wind tunnels. A full literature review for all magnetic bearings is beyond the scope of this paper - the emphasis here is on digital controls for magnetic bearings.

Single-axis digital control has been reported by several authors. Hisatani, et al. [5] described the magnetic support of a 1 kg vertical rotor supported by a digitally controlled axial active magnetic bearing. They noted that the particular digital control algorithm used was successful but not quite as qood as the corresponding analog one. Carmichael, et al. [6] reported the use of digital controls in a single axis vertical support for a 1 in diameter ball. Scudiere, et al. [7] employed a microprocessor based digital control system to support small steel spheres and small vertical rotors with masses up to 90 grams.

Digital control of magnetic suspension and balance systems for wind tunnels has been described by Britcher, et al. [8,9]. Like magnetic bearings, these suspension systems are inherently unstable. Digital controls provide the means to stabilize them with a much greater degree of flexibility than analog controls. The system employed for the wind tunnels is much more complicated than the single axis control systems indicated above because many axes are involved. A PDP 11/84 minicomputer was chosen for implementing the digital controller.

A theoretical treatment of digital control for radial bearings was given by Schweitzer and Ulbrich [10] but not tested. Bleuler and Schweitzer [11] analyzed the use of decentralized control for radial magnetic bearings as preparation for the application of microprocessor-based digital controls. Gondhalekar and Holmes [12] developed a magnetic bearing for control of transmission shaft vibrations. Traxler, et al. [13] described a radial bearing using a microprocessor-based digital control. The microprocessor software consisted of a main program and an interrupt handler. Also, a magnetic bearing with digital control has been developed utilizing a rotational interrupt [14]. The system was employed on a single-mass rotor supported at one end. Orbit and other vibration plots indicated successful operation of the bearing.

The purpose of this paper is to demonstrate the relationships between the analog and digital controllers used to stabilize the magnetic bearing and the resulting bearing stiffness and damping properties. Earlier work on this test rig [ref. 1] has shown the effect of control algorithms similar to those reported here; this work will extend the earlier work, with particular attention paid to the frequency dependence of the magnetic bearing dynamic properties. Comparison is made between the actual controllers and equivalent ideal controllers which do not exhibit this frequency dependence. Both analog and digital control systems are shown to be effective for controlling vibrations of the test rotor and for exerting a great deal of control over the dynamic properties of the magnetic bearing.

NOMENCLATURE

A/D	Analog-to-digital convertor
A_g	area of air gap perpendicular to magnetic flux
C	Capacitance
$C_{eq}(\omega)$	Frequency dependent damping characteristic of magnetic bearing
D/A	Digital-to-analog converter (see ZOH)
D(z)	Digital control algorithm
F	Force
F_{ext}	Externally applied force
g	length of the air gap
G	Nominal undeflected gap length (y=0)
G(s)	Continuous domain transfer function
I_{bx}, I_{by}	Bias current in magnet coil
i_{px}, i_{py}	Perturbation current in magnet coil
K_a	Power amplifier transconductance
$K_{A/D}$	A/D converter gain (counts/volt)
$K_{D/A}$	D/A converter gain (volts/count)
K_d	First derivative feedback gain constant
$K_{eq}(\omega)$	Frequency dependent stiffness characteristic of magnetic bearing
K_g	Analog proportional feedback gain constant
K_{ix},K_{iy}	Actuator gain of magnetic bearing in x and y directions
K_{myy},K_{mxx}	Magnetic position stiffness (i, j = x or y)
K_p	Proportional feedback gain constant
K_{pert}	Perturbation input gain of power amplifier
K_r	Analog derivative feedback gain constant
K_s	Position probe sensitivity
K_t	Loop gain for analog PD controller
m	Mass
N	Number of coil turns per pole pair
PD	Proportional-derivative
R	Resistance
s	Laplace variable, $s = j\omega$
SR	Sampling rate
T	Sampling period
W	Weight
z	Z-transform variable, $z = e^{sT}$
ZOH	Zero-order-hold device (see D/A)
β	sensitivity of the air gap to shaft displacement: $\frac{\partial g}{\partial x}$
μ_0	Permeability of free space
μ_r	Relative permeability
μ	Permeability, $\mu = \mu_0\mu_r$
τ_a	Power amplifier LPF time constant
$\tau_{A/D}$	A/D conversion time
τ_{comp}	Computation time of digital control algorithm
τ_{in}	Input LPF time constant (digital controller)
τ_{out}	Output LPF time constant (different for analog and digital controllers)
τ_s	Position probe LPF time constant
Φ	Magnetic Flux
ω	Frequency (rad/sec)

SECTION 1 - Description of Magnetic Bearing

The magnetic bearings used to support the flexible rotor in this work consist of four electromagnets arranged radially around the shaft as shown in Figure 1. Varying the currents in the magnet coils determines the forces on the bearing journal (the magnetic laminations), thus determining the static and dynamic properties of the magnetic bearing. Maslen, et al. [ref. 15] present the governing equation for a bearing of this type, which for small displacements about $y = 0$, can be linearized as

$$F_y = K_{iy} i_{py} - K_{myy} y \tag{1}$$

where

$$K_{iy} = \frac{\mu_0 A_g N^2 I_{by} \beta}{G^2} \tag{2}$$

and

$$K_{myy} = -\frac{\mu_0 A_g N^2 I_{by}^2 \beta^2}{G^3} \tag{3}$$

K_{iy} and K_{myy} are referred to as the *actuator gain* and the *position stiffness* , respectively.

SECTION 2 - Controller Configuration and Block Diagram

We now wish to incorporate these force relationships (K_{myy} and K_{iy}) into a block diagram configuration of the magnetic bearing. The equation of motion for the bearing journal is (see Figure 2):

$$f_{ext} = m\ddot{y} + K_{myy} y + K_{iy} i_{py} \tag{4}$$

if we assume that i_{py_0} is chosen so that $K_{iy} i_{py_0} = -W$, and that i_{py} has been redefined about the operating point i_{py_0} (allowed here since K_{iy} is a linear function of i_{py}).

Taking the Laplace transform gives the steady state solution:

$$F_{ext} = (ms^2 + K_{myy}) Y(s) + K_{iy} I_{py}(s) \tag{5}$$

Re-arranging this equation gives:

$$\frac{Y(s)}{F_{ext} - K_{iy} I_{py}(s)} = \frac{1}{ms^2 + K_{myy}} \tag{6}$$

where $F_{ext} - K_{iy} I_{py}(s)$ represents the total exogenous force applied to the rotor (see Figure 3).

Inspection of the characteristic equation of this transfer function reveals that the system is open-loop unstable, since $K_{myy} < 0$. Thus, we must employ active feedback control to stabilize the system. Designating the controller as G(s), a controller which relates rotor position y (or x) to actuator current i_{py} (or i_{px}), we have the configuration shown in Figure 4.

The CLTF (closed loop transfer function) for the magnetic bearing system with this feedback is

$$\frac{Y(s)}{F_{ext}} = \frac{1}{ms^2 + K_{myy} + K_{iy} G(s)}, \quad K_{myy} < 0 \tag{7}$$

which can also be written:

$$Y(s)[ms^2 + K_{myy} + K_{iy} G(s)] = F_{ext} \tag{8}$$

We are interested in the relationships between the controller G(s) and the stiffness and damping properties of the magnetic bearing. For the single degree-of-freedom (SDOF) bearing model shown in Figure 5, the equation of motion is:

$$Y(s)[ms^2 + C_b s + K_b] = F_{ext} \tag{9}$$

Thus, we wish to relate the SDOF stiffness and damping coefficients K_b and C_b to the feedback controller G(s).

This relationship must be made with care, however. It is important to realize that, because the forces generated by a magnetic bearing are a function of, among other things, a frequency dependent transfer function, G(s), the stiffness and damping properties experienced by the bearing journal (and hence the rotor) will be different for different radial excitation frequencies. We introduce frequency dependent stiffness and damping coefficients, $K_{eq}(\omega)$ and $C_{eq}(\omega)$, to replace terms K_b and C_b for realizable controllers. It is important to note that ω does not refer to the rotational frequency of the rotor, but rather the radial vibration frequency of the bearing journal.

Now, we combine equation (8) and equation (9) as follows:

$$Y(s)[ms^2 + K_{myy} + K_{iy}G(s)] = Y(s)[ms^2 + C_{eq}(\omega)s + K_{eq}(\omega)] \tag{10}$$

Cancelling like terms, substituting $s = j\omega$ and separating real and imaginary parts of the equations gives:

$$K_{eq}(\omega) = K_{myy} + K_{iy}\mathrm{Re}\{G(j\omega)\} \tag{11}$$

$$C_{eq}(\omega) = K_{iy}\frac{\mathrm{Im}\{G(j\omega)\}}{\omega} \tag{12}$$

Thus, for the SDOF model of the magnetic bearing/rotor system, we have a relationship between the bearing stiffness and damping characteristics and the controller transfer function.

SECTION 3 - Analog implementation of PD control

The Routh criterion [ref. 16] dictates that the system described by equation (7) is open-loop unstable. Stabilization requires that both proportional and derivative terms be present in G(s), the controller transfer function. Without considering stability, earlier works have demonstrated the utility of derivative feedback for reducing vibration in rotating systems [ref. 17]. This suggests a transfer function of the form:

$$G(s) = K_p + K_d s \tag{13}$$

Combining with the expressions for $K_{eq}(\omega)$ and $C_{eq}(\omega)$ (equations 11 and 12) leads to:

$$K_{eq}(\omega) = K_{myy} + K_{iy}K_p \tag{14}$$

$$C_{eq}(\omega) = K_{iy}K_d \tag{15}$$

In other words, the bearing stiffness is a linear function of K_p (the proportional feedback coefficient), and the bearing damping is a linear function of K_d (the derivative feedback coefficient).

As it turns out, this controller cannot be implemented perfectly. In particular, an infinite bandwidth differentiator will exacerbate the effects of any extraneous noise in the system; high frequency poles must be included in the actual design to avoid this problem. Also, the proximity probes and power amplifiers employed in a real control system will have finite bandwidth and will introduce additional poles into the controller transfer function, G(s). The analog controller reported in this work is represented by:

$$G(s) = \frac{0.01K_sK_iK_a[R_1C(0.1K_r)s + K_g(1+RCs)(1+R_1C_1s)]}{(1+\tau_s s)(1+RCs)(1+R_1C_1s)(1+\tau_{out}s)(1+\tau_a s)} \tag{16}$$

Figure 6 shows a block diagram of this controller. Note that for the actual analog controller, the proportional feedback gain coefficient is denoted by K_g and the derivative feedback gain coefficient is written K_r. Values for the various system parameters described in this paper are presented in Appendix A.

SECTION 4 - Digital Implementation of PD Control

The digital implementation of proportional-derivative feedback is quite similar to the analog one. The proximity probes and power amplifier used with the analog controller are retained in the digital design; after all, the interface between any control system and a physical device must ultimately be analog in nature. The difference between the analog and digital systems lies mainly with the core elements of the system: while the analog controller employs resistors and capacitors to realize continuous differential equations, the transfer function of the digital controller results from repeated evaluation of a difference equation. The periodic rate at which the computer evaluates this difference equation is called the *sampling rate*.

Figure 7 is a block diagram of the digital controller. As mentioned earlier, it shares many features with its analog counterpart - namely, the proximity probe interface and the power amplifier. There are, however, notable differences. Before a signal can be processed by a difference equation, it must be converted to a numerical value, thus requiring the presence of an Analog-to-Digital converter between the position signal input and the digital computer. Likewise, the periodic stream of numbers generated by successive solutions of the difference equations must be converted back to analog voltage signals by a Digital-to-Analog converter prior to power amplification.

Proportional-derivative control is achieved digitally by converting the analog PD algorithm [equation (13)] to its discrete equivalent. The approximation used here is the backwards difference rule for approximating the Laplace variable s. The resulting equivalence is

$$s = \frac{(z-1)}{Tz} \tag{17}$$

where T is the sampling period (inverse of sampling rate) and $z = e^{sT}$. Substituting for s in equation (13) and taking the inverse z-transform yields the difference equation:

$$c_n = K_p r_n + \frac{K_d}{T}(r_n - r_{n-1}) \tag{18}$$

where r_n and c_n are points in the input and output data streams of the digital computer, respectively. Note that the backwards difference rule approximates the derivative of the incoming signal by determining the slope of a straight line intersecting the most recent two data points in the input stream. Detailed discussion of z-transform theory and other approximation rules can be found in Franklin & Powell [ref. 18].

The digital controller discussed in this paper was implemented on an AT&T PC6300 personal computer (IBM PC/XT compatible). Even though this computer has an 8 MHz system clock and is outfitted with the Intel 8087 math co-processor, its computational abilities are somewhat limited. Thus, in order to achieve the highest possible sampling rate for the controller, the software that actually performs the difference equation calculations is written in 8086/8087 assembly language. Admittedly, assembly language programming is a somewhat tedious task; unfortunately, high-level languages (such as Pascal or Fortran) generate machine-level programs that are much longer, and hence much slower to execute, than an equivalent assembly language program. Given the computational constraints imposed by the PC, assembly language implementation of the digital PD algorithm is the only reasonable approach. The maximum sampling rate achieved for this software is 2.86 kHz (T = 350 μS).

SECTION 5 - Frequency Dependence of Stiffness and Damping Characteristics

In Section 3 it was shown that implementation of ideal PD control produced a system in which the stiffness and damping properties of the magnetic bearing could be determined by choice of two controller parameters K_p and K_d. In practice, however, such an ideal controller cannot be built. Thus, we investigate the effects of finite-bandwidth controllers on the bearing's stiffness and damping properties [$K_{eq}(\omega)$ and $C_{eq}(\omega)$].

Figures 8A, 8B, 9A and 9B present calculated values of $K_{eq}(\omega)$ and $C_{eq}(\omega)$ for the analog controller as functions of the radial excitation frequency encountered at the bearing location. The ideal curves represent the expected behavior of the ideal PD controller postulated in equation (13); the actual curves show the calculated stiffness and damping properties of the controller actually tested for this work [equation (16)]. Note that at low frequencies, the ideal and actual controllers behave quite similarly. As the excitation frequency is increased, however, the high frequency limitations of the actual controller are no longer negligible, and their presence starts to degrade the performance of the magnetic bearing. In addition, the independent behavior of the ideal stiffness and damping properties as functions of K_p and K_d is not fully realized with the actual controller: varying K_g has a slight effect on the damping curve (Figure 8B), and changes in K_r can be seen in the stiffness properties (Figure 9A).

Similar stiffness and damping curves are presented in Figures 10A, 10B, 11A and 11B for the digital PD controller, although for these curves, definition of an 'ideal' controller is a somewhat arbitrary task. In general, higher sampling rates result in improved controller performance, so our ideal digital controller is defined as one which has a sampling rate of 1 MHz (roughly 400 times faster than the actual digital controller presented here). Once again, the bandwidth limitations of the actual controller are clear: bearing performance is degraded at high

frequencies, and the relationships between the controller parameters (K_p, K_d) and the stiffness and damping properties are not completely independent.

While there is clearly some deviation from ideal controller behavior at high frequencies, we note that both the analog and digital controllers behave in a very similar fashion, in spite of the fact that the resistor-capacitor network that makes up the analog control system is obviously quite different from the regularly re-evaluated difference equation in the digital control system. This similarity results from the imperfect high frequency derivative calculations performed by both controllers: analog differentiator performance is limited by the presence of the high frequency poles mentioned earlier, and the straight-line derivative approximation used in the digital control system becomes progressively less accurate as the input signal frequency is increased. Note that a faster sampling rate would improve the high frequency performance of the digital controller, as increasing the roll-off points of the poles associated with the analog differentiator would increase the usable bandwidth of the analog controller.

SECTION 6 - Experimental Results

The test rig used to evaluate bearing performance is shown in Figure 12. Three shaft masses were mounted on the 1/2 inch diameter flexible shaft as shown; the magnetic bearing journals each weigh 5.12 N (1.15 lb), and the center mass weighs 7.88 N (1.77 lb). For all of the experimental results gathered, the inboard bearing was controlled by the analog controller with parameter settings K_g=2.0 and K_r=4.0. Two sets of tests were performed: the stiffness of the bearing was varied while the damping was held constant, and the damping was adjusted while the stiffness remained unchanged. These tests were run for both the analog and digital PD controllers, and the results presented represent the vertical vibration response at the outboard bearing (outboard horizontal responses were very similar to the vertical results).

The effect of varying the proportional feedback (stiffness) for both controllers is presented in Figures 13A and 13B. The curves represent the vertical amplitude response of the rotor as observed at the outboard bearing (similar results were obtained for the inboard bearing and are not presented here). The curves clearly indicate that bearing stiffness is increasing with greater amounts of proportional feedback: for frequencies below the first critical speed (about 1800 RPM), the amplitude of vibration is reduced as the proportional feedback is increased.

At higher frequencies, there are two other peaks (critical speeds) at about 3700 RPM and 5500 RPM. Changes in the bearing stiffness have little effect on the second critical because the rotor has a conical mode shape for this critical. It is nearly a rigid body mode shape with the ends rotating 180 degrees out of phase, and the center is a node point, so the bearing damping effectively keeps this peak small. The third critical is quite different. It is a bending mode with the end masses (bearing magnetic laminated disks) out of phase with the center mass. Apparently, increasing the bearing stiffness increases the peak vibration level, a result which is counter to intuition. What seems to be happening is that the magnetic force is applied at the disk location and probably does decrease the shaft motion at the bearing location, but the sensor is located a small distance away from the disk center and reports an apparent increase in the peak vibration level. Thus, the measured amplitude of motion increases with increasing K_p.

Rotor responses in the presence of various amounts of bearing damping are presented in Figures 14A and 14B. For both the analog and digital controllers, the measured results confirm the expectations for this test: as the bearing damping is increased by increasing the derivative feedback, the peak amplitude responses at the critical speeds are significantly reduced, and the critical frequencies themselves are moved to higher frequencies (this last effect is most noticable at the third critical speed, which varies from 4600 RPM to 5600 RPM as K_d is increased from 2.0 to 3.5 via the digital controller).

SECTION 7 - Conclusions

A PC-based digital control system has been designed and tested for controlling a radial magnetic journal bearing. Implementation of a proportional-derivative control algorithm on the digital computer has been shown to yield similar results to those obtained with an analog PD controller. For both controllers, varying the proportional gain coefficient altered the stiffness of the magnetic bearing, and varying the derivative gain changed the effective damping of the magnetic bearing.

The frequency dependent nature of the effective stiffness and damping properties of the magnetic bearing has been investigated. High frequency poles present in the actual analog controller introduced phase-lag into the control signal, and degraded operation of the magnetic bearing system at higher frequencies. Computational delays and zero-order-hold effects in the digital controller were seen to have effects similar to those produced by the high frequency poles present in the analog system.

Both the analog and digital controllers were effective at altering the dynamic properties of the bearing under test. Judicious choice of the controller parameters (K_g & K_r for the analog controller, K_p & K_d for the digital controller) allows significant alteration of the vibration amplitudes and critical speeds of the rotor system.

The introduction of digital control into a magnetic bearing system offers the potential for evaluation and testing of algorithms much more complex than would be possible with an analog controller. For example, addition of an integrator to the controller creates a system which rejects static loads on the rotor. This addition is a somewhat tedious chore with an analog system, but with a digital controller it can be accomplished by merely installing a different software program on the computer. Also, complex digital control algorithms which can 'shape' the $K_{eq}(\omega)$ and $C_{eq}(\omega)$ curve to meet certain specifications can be developed and tested. Analog realization of such algorithms would be very difficult, if it were even possible. Thus, digital control provides bearing designers a flexible tool with which they can design bearings exhibiting dynamic properties unlike those of any passive bearings.

The authors would like to thank the Center for Innovative Technology of the Commonwealth of Virginia and the Army Research Office for partial support of this project.

This material is based upon work supported under a National Science Foundation Graduate Fellowship. Any opinions, findings, conclusions or recommendations expressed in this publication are those of the authors and do not necessarily reflect the views of the National Science Foundation.

REFERENCES

1. Humphris, R. R., Kelm, R. D., Lewis, D. W., and Allaire, P. E., "Effect of Control Algorithms on Magnetic Journal Bearing Properties," Journal of Engineering for Gas Turbines and Power, Trans. ASME, Vol. 108, October, 1986, pp. 624-632.

2. Allaire, P. E., Humphris, R. R., Kasarda, M. E. F., and Koolman, M. I., "Magnetic Bearing/Damper Effects on Unbalance Response of Flexible Rotors," Proc. AIAA Conference, Philadelphia, PA., August 10-14, 1987.

3. Allaire, P. E., Humphris, R. R., and Barrett, L. E., "Critical Speeds and Unbalance Response of a Flexible Rotor in Magnetic Bearings," Proceedings of European Turbomachinery Symposium, October 27-28, 1986.

4. Allaire, P. E., Humphris, R. R., and Imlach, J., "Vibration Control of Flexible Rotors with Magnetic Bearings Supports," AFOSR/ARO Conference, Non-Linear Vibrations, Stability and Dynamics of Structures and Mechanisms, Virginia Tech, Blacksburg, Virginia, March 23-25, 1987.

5. Histani, M., Inoue, Y. and Mitsui, J., "Development of Digitally Controlled Magnetic Bearing," Bulletin of JSME, Vol. 29, No. 247, January 1986, pp. 214-220.

6. Carmichael, A. T., Hinchliffe, S., Murgatroyd, P. N. and Williams, I. D., "Magnetic Suspension Systems with Digital Controllers," Review of Scientific Instuments, Vol. 58, No. 8, August 1986, pp. 1611-1615.

7. Scudiere, M. B., Willems, R. A. and Gilles, G. T., "Digital Controller for a Magnetic Suspension System," Review of Scientific Instruments, Vol. 58, No. 8, August 1986, pp. 1616-1626.

8. Britcher, C. P., "Progress Toward Magnetic Suspension and Balance Systems for Large Wind Tunnels," AIAA Journal of Aircraft, April, 1985.

9. Britcher, C. P., Goodyer, M. J., Eskins, J., Parker, D. and Halford, R. J., " Digital Control of Wind Tunnel Magnetic Suspension and Balance Systems," Proceedings of the ICIASF Record - International Conference on Instrumentation in Aerospace Simulation Facilities, Williamsburg, VA, June 22-25, 1987.

10. Schweitzer, G. and Ulbrich, H., "Mangetic Bearings - A Novel Type of Suspension," Institution of Mechanical Engineers, Second International Conference on Vibrations in Rotating Machinery, Cambridge, September 1980, Paper C 273/80.

11. Blueler, H., Schweitzer, G., "Dynamics of a Magnetically Syspended Rotor With Decentralized Control," First IASTED International Symposium on Applied Control and Identification, Copenhagen, Denmark, June 28-July 1, 1983, pp. 17-22.

12. Gondhalekar, V. and Holmes, R., "Design of an Electromagnetic Bearing for the Vibration control of a Flexible Transmission Shaft," Rotor Dynamic Instability Problems in High Performance Turbomachinery, Texas A&M University, May 1984.

13. Traxler, A., Meyer, F. and Murbach, H. P., "Fast Digital Control of a Magnetic Bearing with a Microprocessor," International Kongress Mikroelektonik, Munich, November 13-15, 1984.

14. Nagai, B., Okada, Y., and Shimane, T., "Digital Control of Magnetic Bearing with Rotationally Synchronized Interrupt," Ibaraki University.

15. Maslen, E., Hermann, P., Scott, M., and Humphris, R. R., "Practical Limits to the Performance of Magnetic Bearings: Peak Force, Slew Rate and Displacement Sensitivity.," Presented at the NASA Workshop on Magnetic Suspension Technology, February 2-4, 1988, NASA CP- 3202, 1993.

16. D'Azzo, J. J., and Houpis, C. H., *Linear Control System Analysis and Design,* McGraw-Hill Book Company, 1981.

17. Allaire, P. E., Lewis, D. W., and Knight, J. D., "Active Vibration Control of a Single Mass Rotor on Flexible Supports," Journal of the Franklin Institute, Vol. 315, No. 3, 1983, pp. 211-22.

18. Franklin, G. F., and Powell, J. D., *Digital Control of Dynamic Systems,* Addison-Wesley Publishing, 1981.

APPENDIX A - Parameters for Magnetic Bearing Control System

A_g:	0.53 in^2 (3.42 cm^2)	N:	1840 turns per pole pair
G:	39 mils (0.99 mm)	RC:	220 μS (720 Hz)
I_{bx}, I_{by}:	250 mA	R_1C:	22 mS
K_a:	0.5 A/V	R_1C_1:	100 μS (1.6 kHz)
$K_{A/D}$:	4096 counts/10 volts	τ_a:	100 μS (1.6 kHz)
$K_{D/A}$:	5 volts/4096 counts	$\tau_{A/D}$:	25 μS
K_d:	0 to 10	τ_{comp}:	175 μS for PD controller
K_g:	0 to 10	τ_{in}:	10.3 μS (15 kHz)
K_p:	0 to 10	τ_{out} (analog):	47 μS (3.4 kHz)
K_{pert}:	0.11 A/V	τ_{out} (digital):	155 μS (1.0 kHz)
K_r:	0 to 10	τ_s:	56 μS (2.8 kHz)
K_s:	200 mV/mil (7.87 V/mm)		
K_t:	0 to 10		

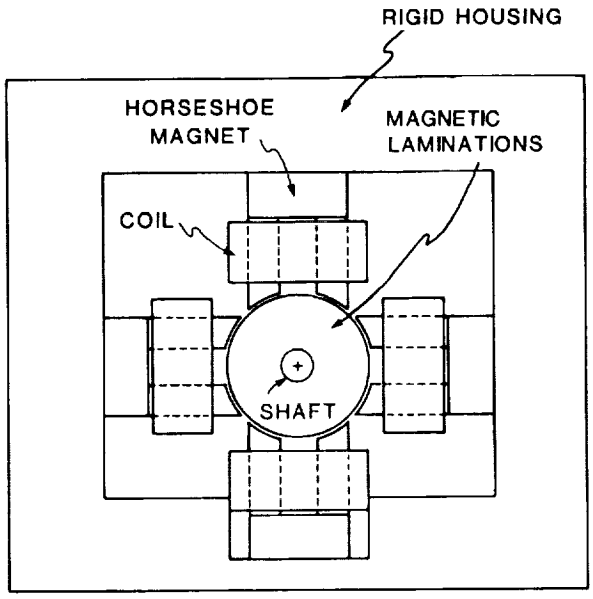

Figure 1 - Magnetic Bearing Configuration

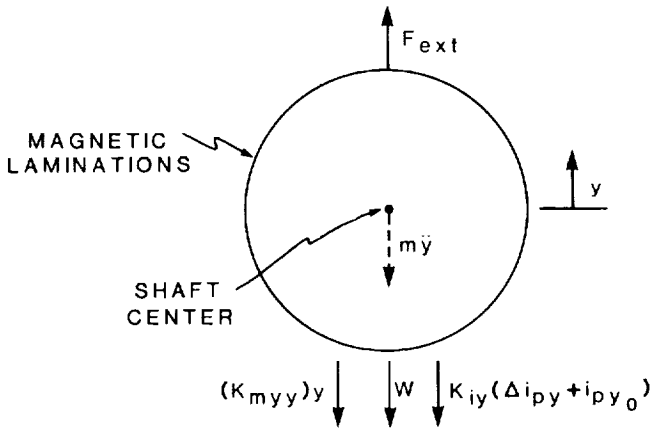

Figure 2 - Forces on Magnetic Bearing Journal

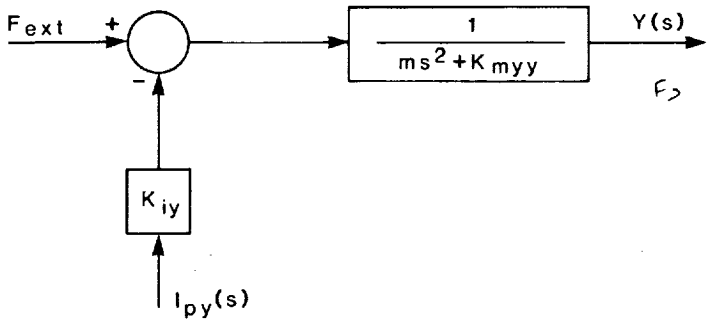

Figure 3 - Open-loop Magnetic Bearing System

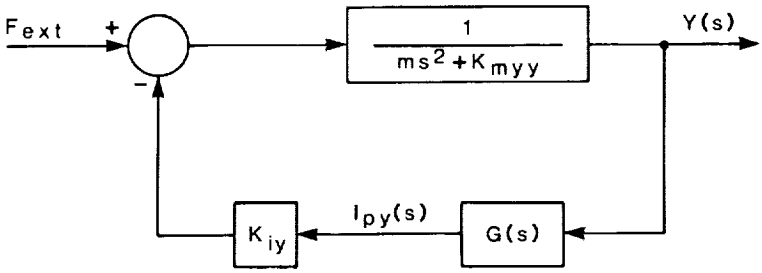

Figure 4 - Closed-loop Magnetic Bearing System

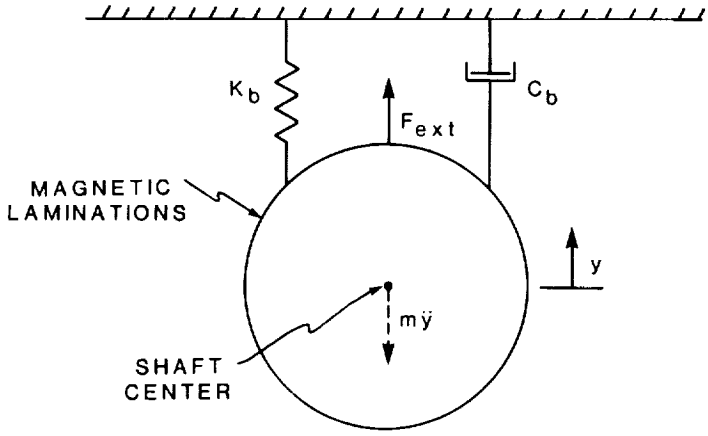

Figure 5 - Single Degree-of-Freedom Bearing Model

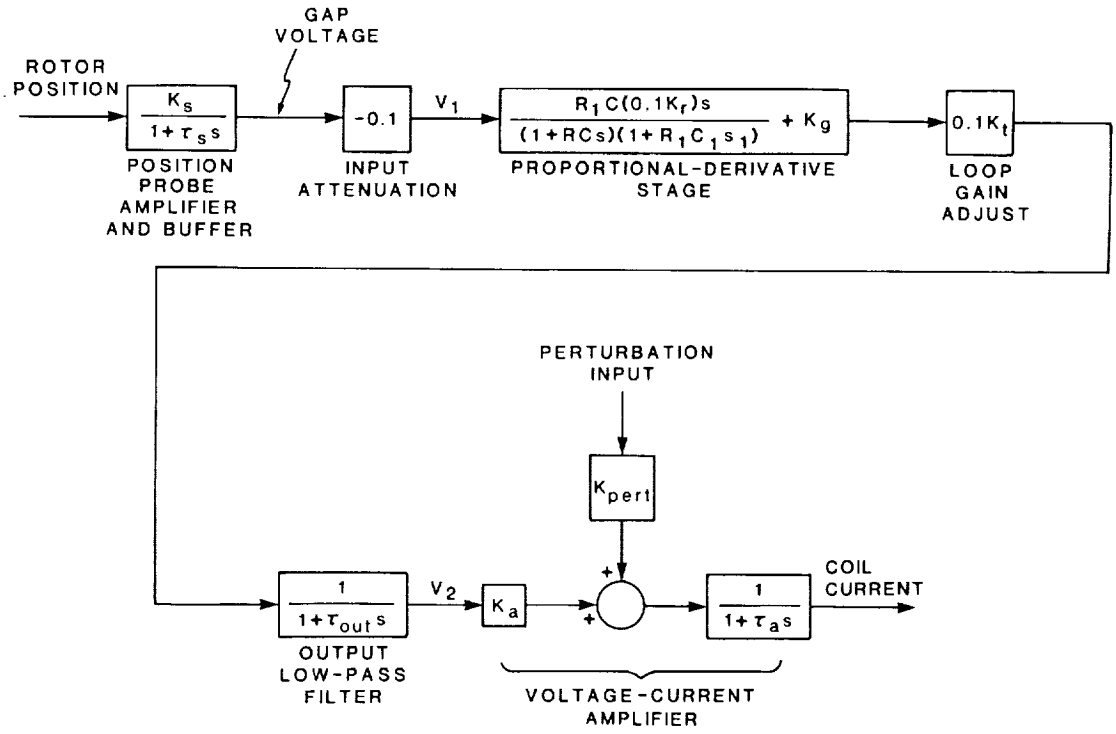

Figure 6 - Analog Controller (Block Diagram)

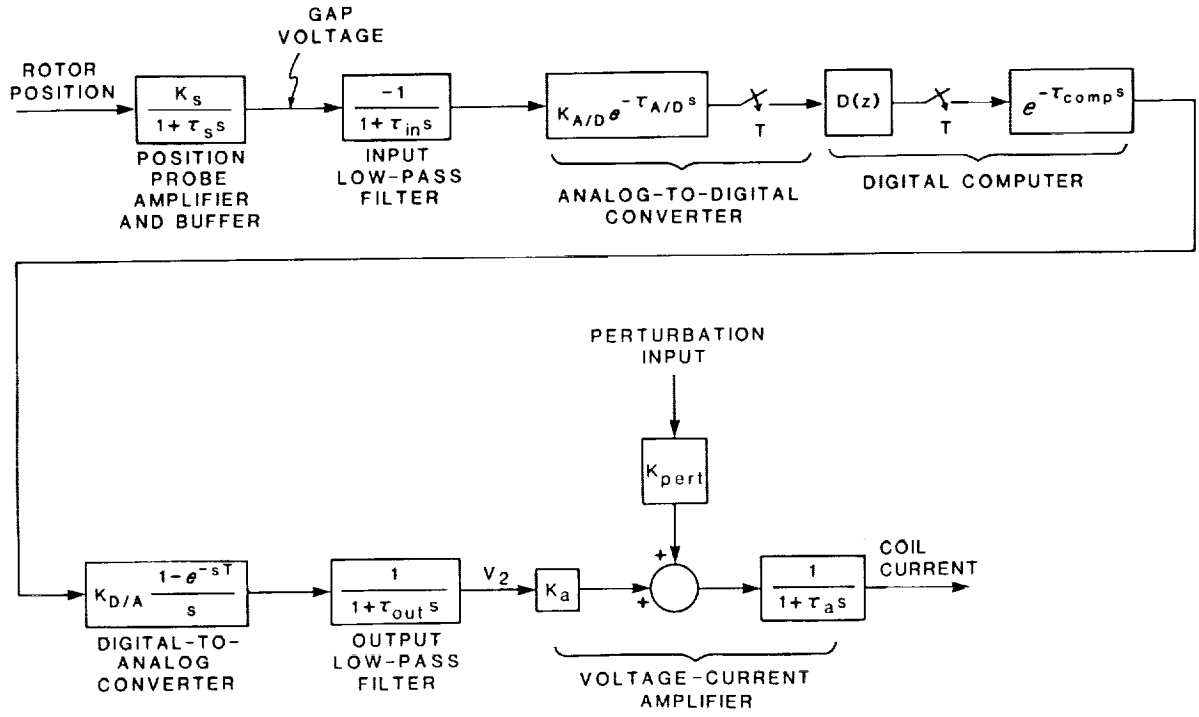

Figure 7 - Digital Controller (Block Diagram)

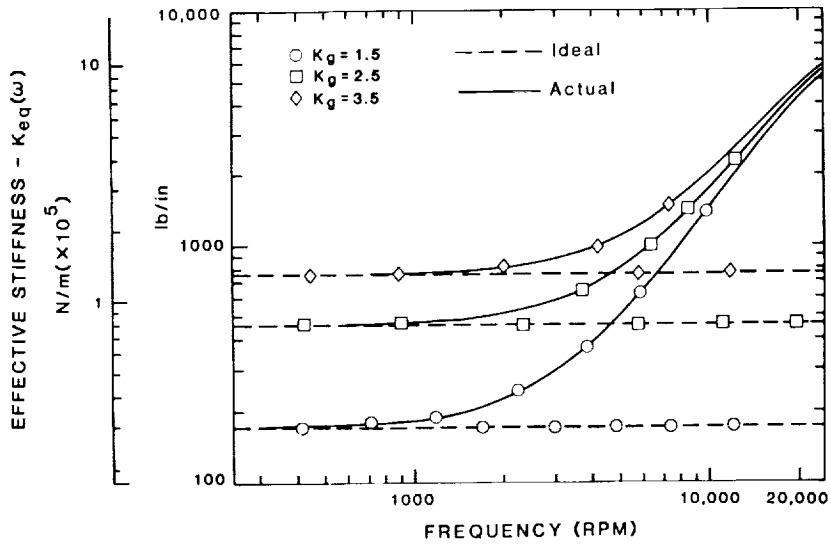

(A)

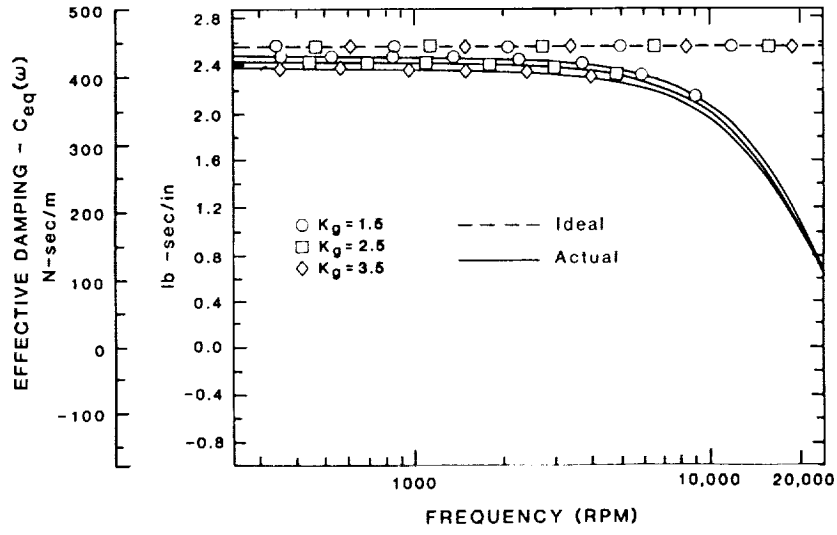

(B)

Figures 8A & 8B - $K_{eq}(\omega)$ and $C_{eq}(\omega)$
Varying Proportional Feedback (Analog)

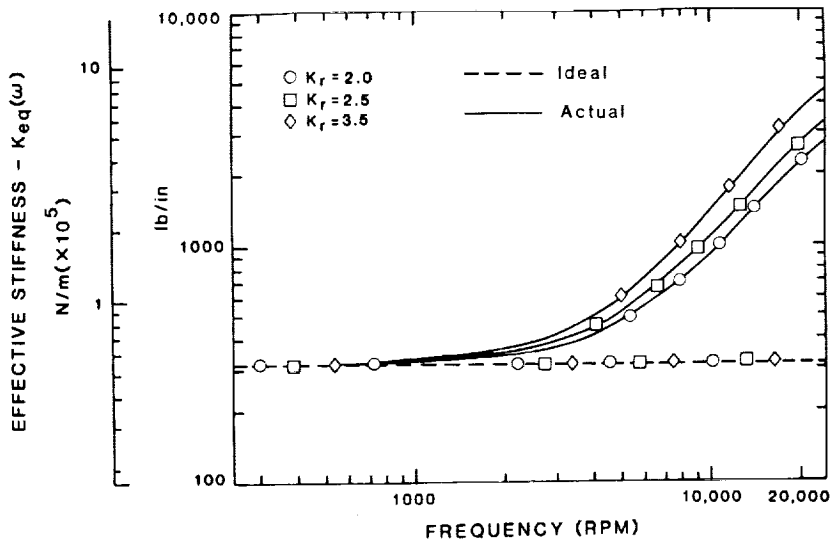

(A)

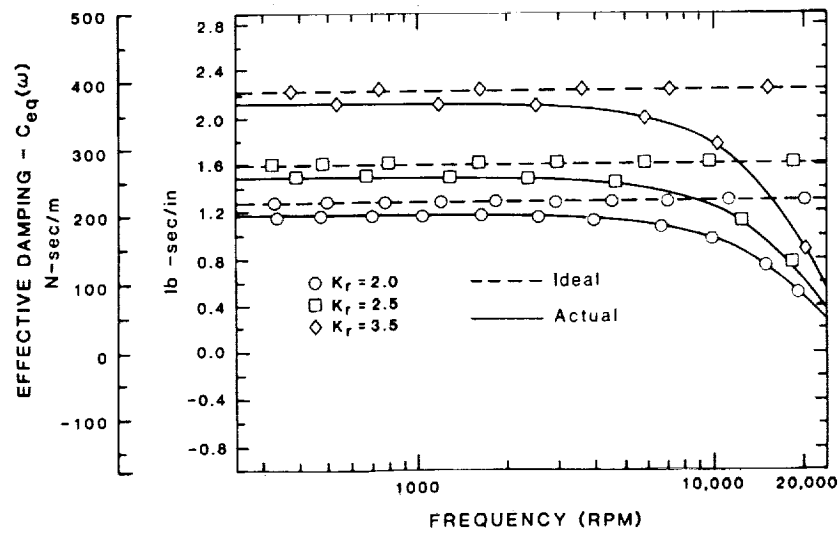

(B)

Figures 9A & 9B - $K_{eq}(\omega)$ and $C_{eq}(\omega)$
Varying Derivative Feedback (Analog)

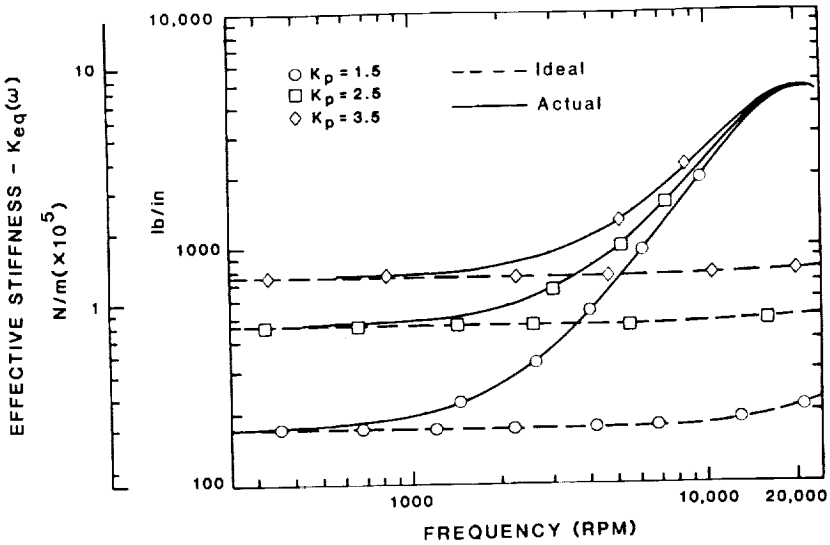

(A)

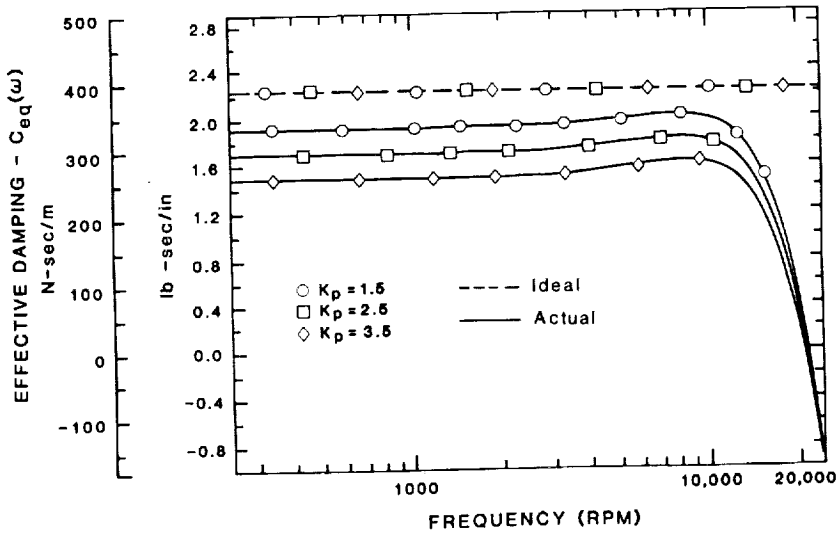

(B)

Figures 10A & 10B - $K_{eq}(\omega)$ and $C_{eq}(\omega)$
Varying Proportional Feedback (Digital)

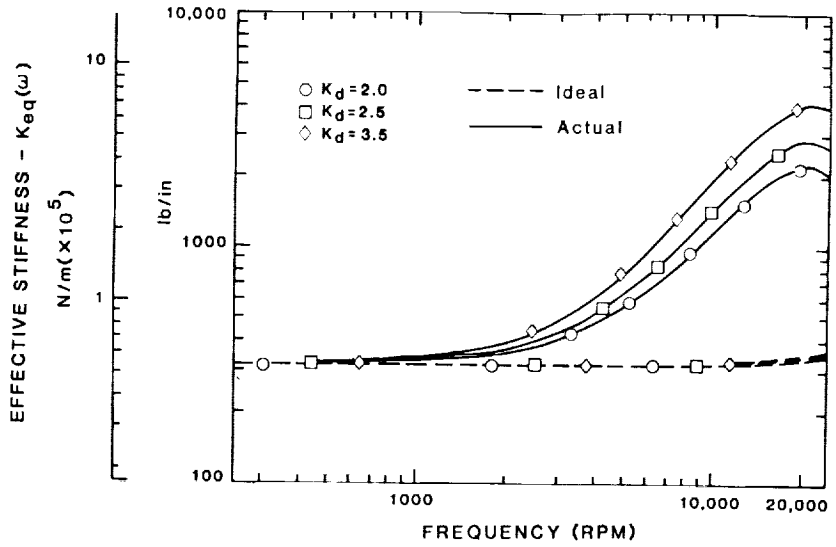

(A)

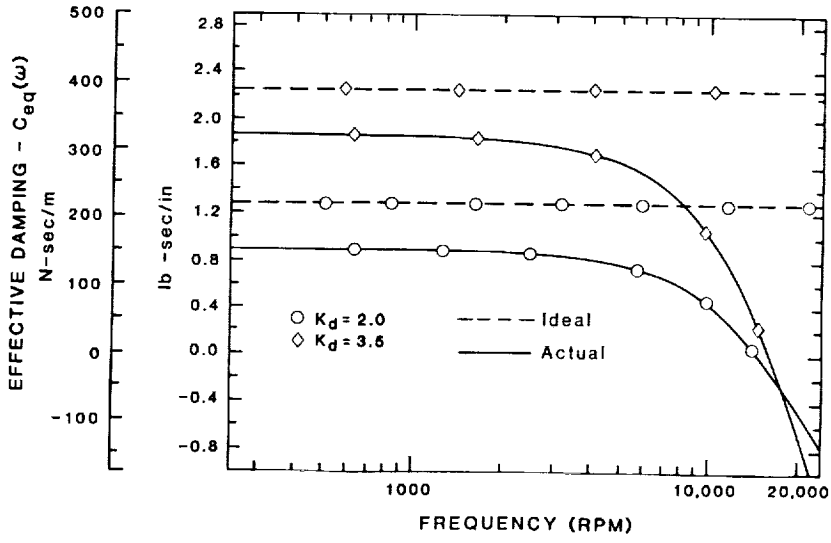

(B)

Figures 11A & 11B - $K_{eq}(\omega)$ and $C_{eq}(\omega)$
Varying Derivative Feedback (Digital)

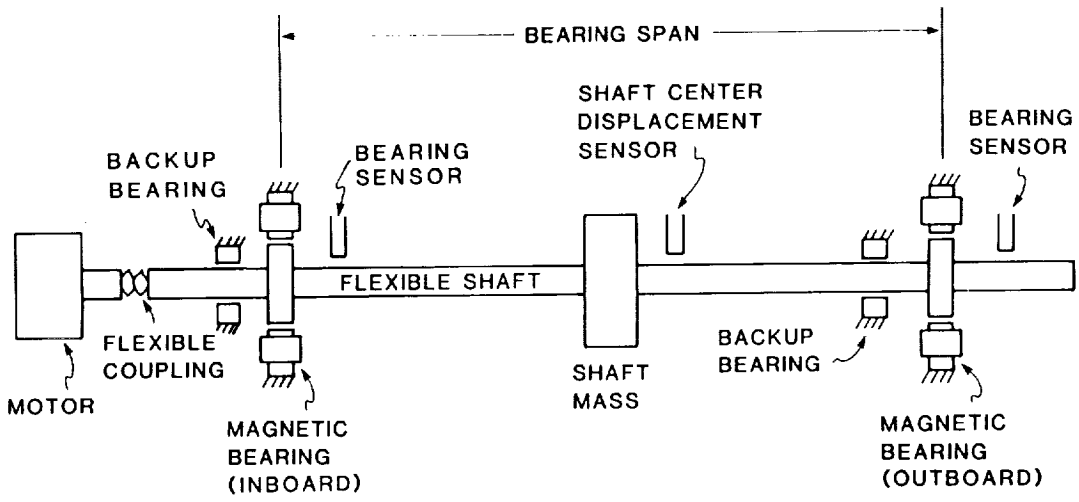

Figure 12 - Experimental Apparatus

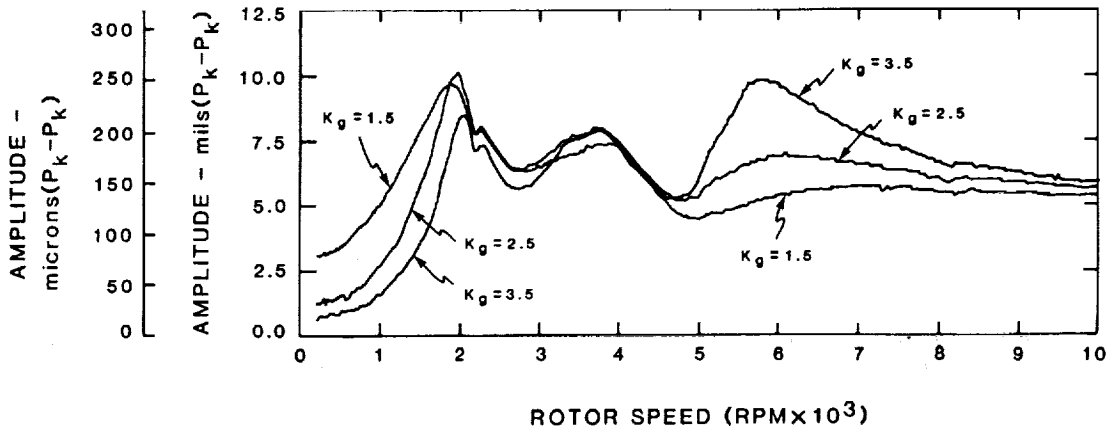

Figure 13A - Bearing Vertical Displacement - Varying Proportional Feedback (Analog Controller)

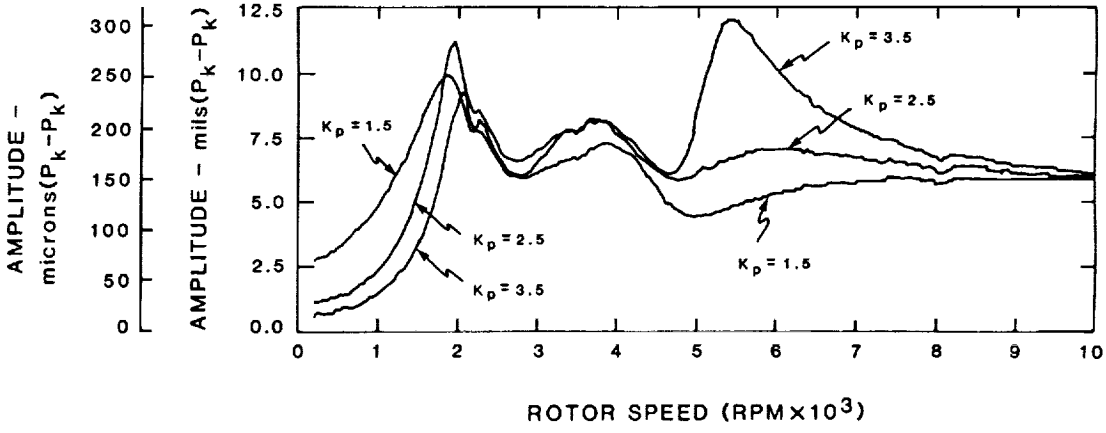

Figure 13B - Bearing Vertical Displacement - Varying Proportional Feedback (Digital Controller)

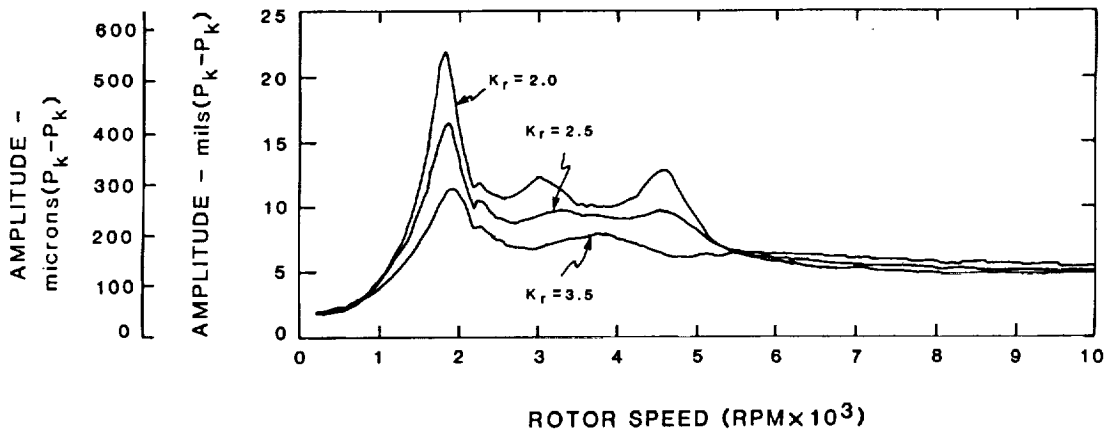

Figure 14A - Bearing Vertical Displacement - Varying Derivative Feedback (Analog Controller)

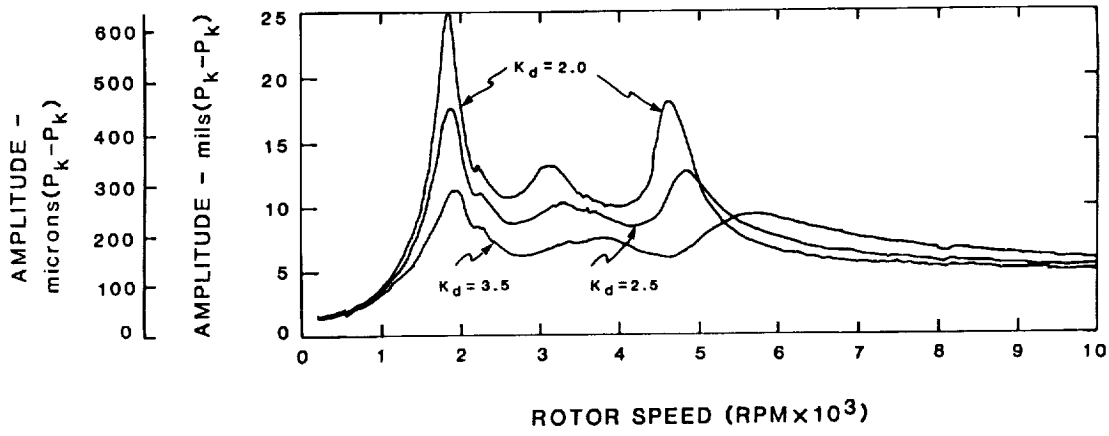

Figure 14B - Bearing Vertical Displacement - Varying Derivative Feedback (Digital Controller)

omit

Six Degrees-of-Freedom Vibration Isolation Using Electromagnetic Suspension

Sang-il Lee, Daniel B. DeBra, Peter F. Michelson,

Robert C. Taber, John C. Price, Stanford University

SIX DEGREES OF FREEDOM VIBRATION ISOLATION USING ELECTROMAGNETIC SUSPENSION

Sang-il Lee[1], Daniel B. DeBra[2], Peter F. Michelson[3],
Robert C. Taber[4], John C. Price[4]

ABSTRACT

Experimental data are presented for modelling an electromagnet. Control laws are considered with and without flux feedback and with position and orientation information of the suspended body. Base motion and sensor noise are the principal disturbances. Proper selection of the geometrical operating point minimizes the passive coupling above the bandwidth of the control and filtering can attenuate the high frequency content of sensor noise. Six electromagnets are arranged in a configuration which optimizes the load support and provides control over all six degrees of freedom of the suspended body. The design is based on experimental data generated with a specially designed test facility. Application for suspension of a gravity wave antenna is discussed.

INTRODUCTION

Isolation from base motion is frequently required. On the ground, precise instruments must be isolated from the cultural and natural seismic motion of the earth. In orbit, the motion of a spacecraft may be significant due to moving machinery, thrusters or the presence of man [1,2]. Many techniques are available. Mechanical devices such as coil springs, air cushions or compliant materials offer the advantage of simplicity and reliability. By using stacks of such devices, rapid attenuation with frequency can be achieved. But the mechanical link remains and when internal resonances, cross coupling of degrees of freedom and nonlinearity exist, the idealized attenuation hoped for is not always achieved. Passive or active feedback techniques using magnetic or electrostatic fields can remove the mechanical link and permit an improved degree of isolation. Examples include the electrostatic gyro [3] which can achieve spin down time constant of hundreds of years, passively suspended superconducting proof masses for a principle of equivalence experiment [4] and an eddy current suspension for gradiometers [5] and many forms of active and passive magnetic suspension reviewed by Jayawant [6]. An interesting variant is to shield a proof mass on orbit and use it as a reference thus producing a drag free satellite [7], which has achieved average disturbances of less than 5×10^{-12}g.

For an active isolation system, the suspended body follows its reference within the bandwidth of the feedback control. Thus isolation only occurs for frequencies above the bandwidth (natural frequency) of the control. Though the mechanical link is gone, displacement dependence of the force may remain and produces coupling which cannot be influenced by the feedback. Thus one desires to design an actuator which has no spatial dependence on force or has a local extremum so that the small-motion dependence is small. We will give an example later. The force used for suspension is generated as a function of measurements. These measurements are noisy and produce a component of force which is a disturbance. But the frequency content of this disturbance is under the control of the designer by appropriate filtering.

Certainly the most exquisitely sensitive instruments ever developed are the gravity wave antennas. Current bar antennas are capable of detecting strains of 10^{-18} and it is hoped bars can reach 10^{-20}

---

1. Graduate student, Dept. of Mechanical Engineering, Stanford University
2. Professor, Dept. of Aeronautics and Astronautics, Stanford University
3. Assistant Professor, Dept. of Physics, Stanford University
4. Research Associate, High Energy Physics Laboratory, Stanford University

with several improvements including better vibration isolation [8]. Optical measurements hold promise of reaching 10^{-22} strain [9]. The success with the existing bars has been achieved with an air cushion in combination with stacks of rubber and steel, producing an extremely sharp attenuation with frequency and an isolation in the frequency band from 500 to 1 kHz to levels below the Brownian noise in the bar. Vacuum and low temperature necessary for adequate isolation and sensitivity make the introduction of a large stack of isolators difficult, so an optimization has been performed to achieve the greatest isolation in a fixed volume [10].

For ultra-low temperature gravity wave antennas, it will be desirable to enclose the principal portions of the isolation system within the ultra-low (~ 100 mK) temperature region. If these structures are installed without adequate damping, nonlinear behavior can be expected. On the other hand, provision of an adequate degree of passive damping at these temperatures is challenging. Thus we have been looking at active means to provide magnetic suspension or quiet damping to an isolation stack. The results reported here are preliminary work on active magnetic suspension. We have followed an approach similar to the work of Rainer Weiss (Physic, MIT), where they are developing a 3 DOF active and 3 DOF passive suspension using Hall effect flux and optical fiber displacement feedback.

SYMBOLS

A	area
B	magnetic flux density
B_D	desired magnetic flux density
D	disturbance
f	frequency
F	force
F_D	desired force
$\mathfrak{I}$	magnetomotive force
g	gravitational acceleration
H	magnetic field intensity
i	current
i_D	desired current
l	length of the flux path in the solid
m	mass of the suspended body
N	number of turns
$\mathfrak{R}$	reluctance
$\mathfrak{R}_s$	reluctance due to solid magnetic circuit
s	Laplace transform variable
$S_i(f)$, $S_o(f)$	mean square spectral density
W	weight
z	air gap

z_D	desired air gap
z_g	ground motion
δ	error
ϕ	magnetic flux
μ_o	permeability of the air

THE ELECTROMAGNET

The force F between two parallel ferromagnetic surfaces with uniform magnetic flux density B between them is

$$F = - \frac{B^2 A}{2\mu_o} \tag{1}$$

where the minus sign signifies an attractive force, A is the area and μ_o is the permeability of the air (Figure 1). The magnetomotive force $\Im$ is due to permanent magnetism Hl and current in coils Ni. The flux ϕ and reluctance $\Re$ of the magnetic circuit which is dominated by the air gap then relate the flux density to current and gap

$$\Im = Hl + Ni \tag{2}$$

$$B = \frac{\phi}{A} = \frac{\Im}{\Re A} \tag{3}$$

$$\Re = \frac{z}{\mu_o A} + \Re_s \tag{4}$$

$$B = \frac{(Hl + Ni)\mu_o}{z(1 + \Re_s \mu_o A/z)} \tag{5}$$

To produce a desired control force F from (1), one must have a measure of B or use (2) with measures of the gap z and current i to produce B and thus F. The control is the current. An actual electromagnet has magnetic lines near the edge of its gap which are hard to calculate. Furthermore, the side force dependence on lateral deflection which we want to use for control is not easily calculated. So an electromagnet and two degrees of freedom test fixture was built to measure these quantities.

The experimental equipment shown in Figure 2 was designed to suspend a 10 pound mass. The set-up is mainly composed of two parts. The upper part is an electromagnet which has an annular cross section with core and can rotate about a vertical axis A-A offset from it. An annulus with a center core made of ferromagnetic material was chosen for the geometry of the electromagnet in order to minimize the loss and to provide the complete closed path of the magnetic flux. Magnetic flux density is measured by a Hall effect sensor located at the bottom of the center core in the upper housing which has a hole for the leads of the Hall effect sensor. The lower part is a cantilevered plate which can rotate about a horizontal axis B. At an equilibrium condition, the lower part

maintains a gap of 1 mm with respect to the upper part. The counterpart of the upper solenoid is made of the same ferromagnetic material, and the magnetic flux is supposed to pass through both of them. To reduce the dynamic range of the control current, a permanent magnet is used to provide the nominal flux and the control current provides only the small variations needed to maintain the average gap spacing. With two independent axes of rotation, vertical and horizontal motions can be measured by use of a displacement sensor when the magnetic flux density or the suspended mass is changed.

If the counterpart of the lower plate (Fig. 2) is flat and of uniform permeability, no lateral force develops with lateral displacement. By limiting the extent of the ferromagnetic material or introducing steps so that the geometry of the housing and counterpart match, more shearing of the field results. Static lateral force for the case of a step around the lower counterpart was investigated. Vertical interaction between the upper housing and the lower plate was eliminated by fixing the elevation of the lower plate. Figure 3 shows the experimental data of the relationship between the lateral force and the displacement as the current (and thus flux density) increases with 1 mm constant air gap. The lateral force increases until about 1.5 mm from the center, which corresponds to 60% of the thickness of the step and 150% of the gap and then decreases gradually. The slope of each curve at a certain point gives the lateral stiffness. If we wish to use two actuators to provide active control laterally each would be biased and a value of 0.75 mm would be of great interest. This combines passive stable performance and also active control. But for astatized pure feedback control, one might want to be at 1.5 mm. Figure 4 shows the experimental result on the vertical force according to the change in the vertical displacement. Fig. 3 and Fig. 4 are the data for passive behavior above the bandwidth of servos on both flux density and vertical displacement, which will be explained later.

VERTICAL MOTION CONTROL

As a consequence of Earnshaw's theorem [11], systems using permanent magnet or electromagnets (AC or DC) without the control of current are inherently unstable. In order, therefore, to achieve stable suspension it is necessary to devise a means of regulating the current in an electromagnet using position feedback, or others, of the object to be suspended. Two typical ways of stabilizing the system by use of an electromagnet are discussed by other researchers [12]. One is a pure feedback using only the gap information detected by a proximity sensor, and the other is a state feedback using the inertial information obtained by an accelerometer in addition to the gap information. As is stated earlier, one wants the supported element to be essentially attached to the foundation within the low frequency bandwidth of the feedback. Position feedback provides this link. Above the bandwidth of this control, one hopes to have complete isolation. A magnetic structure would have a constant force if the flux stayed constant. However, the reluctance changes as the gap changes and typically results a change in force. Thus one is motivated to remove this gap dependence above the bandwidth of the position feedback in order to reduce the coupling and linearize the outer loop. Flux feedback, which would keep the gap flux density constant, should do this. If a flux density transducer is introduced and used in conjunction with a feedback control loop to control the magnet current in such a manner that the gap flux density remains constant over the operating range of airgaps, the nonlinear force-displacement characteristics will be very linear. Figure 5 shows a block diagram with position and flux feedback for vertical motion control. Here PID control is used in the outer loop. An integrator is needed in the inner loop because there are no dynamics to reduce the magnitude of the feedback signal with frequency and therefore naturally cause a crossover which would limit the bandwidth. However, a sensor can only measure the flux density locally and even if spread throughout the gap, will miss the fringing flux. The flux density feedback should have a very wide bandwidth to reduce the gap dependent force to relatively high frequencies. The bandwidth reported by another study was 5 kHz [13]. In Figure 5, three possible noise sources are included. They are Hall effect sensor noise, displacement sensor noise and the ground motion as an external disturbance. The effects of these on the system response, especially on acceleration, are of great importance. Using the transfer function from each noise

source to the output acceleration, the effect of noise contents can be seen by the following equation if the frequency spectrum of the sensor noise is measured.

$$S_o(f) = |\text{Transfer Function}|^2 \, S_i(f) \tag{6}$$

Here $S_i(f)$ and $S_o(f)$ are the input and output mean square spectral densities as functions of frequency.

CONTROL FOR SIX DEGREES OF FREEDOM

A configuration shown in Figure 6 and Figure 7 uses 3 sets of two electromagnets displaced from their centers in opposite directions. The geometrical operating point is the flat spot on the lateral force vs. displacement curve which for this electromagnet is 1.5 mm for a 1 mm gap. The lateral forces cancel when there is equal current but they do not when the current is unequal. The vertical force can be changed without disturbing the horizontal motion and by keeping the sum of the vertical forces constant the lateral force can be changed by increasing one while the other is reduced. When an electromagnet is displaced radially there is a radial force change. But the symmetry of the device insures there is no tangential force. Therefore the two horizontal directions for the suspended body have neutral passive stability for constant current and in principle there is no coupling above the bandwidth of the control for small amplitude vibrations of the ground.

The control of the six degrees of freedom can be accomplished with the six measurements shown in Fig. 6. Because the sensors are not at the center of the actuators one should use all six to provide precise information on the height and shear of each pair. But the sensor coupling is small and poses no threat to the stability of the system. The control coupling is about $1/\sqrt{3}$ and the sensor coupling can be made small by moving the sensor closer to the center point between each pair of actuators. Furthermore there is no resonant gain in the dynamics. The control can be calculated for each pair separately, estimating the force needed to restore the body to the correct gap and a centered lateral position. We are presently working on ways to reduce the slope of the vertical force with gap. A sketch in Figure 8 suggests a positive slope can be added to the vertical force dependence but at the expense of the horizontal slope. Earnshaw's theorem indicates a limit but we are currently studying actuator geometries that will provide the static forces for a given current needed for control as indicated above and at the same time minimize the slope of the force displacement curves for all degrees of freedom to minimize coupling above the control bandwidth.

CONCLUSIONS

Experimental data for force displacement relationship in the horizontal and vertical direction of an electromagnet were presented. Control laws were proposed with and without flux feedback in addition to position loop for the suspended body. Proper design of an electromagnet can give a passive zero stiffness operating region where the passive coupling above the bandwidth of the control can be minimized. The effect of base motion and sensor noise as principal disturbances to the vibration isolation must be minimized for example in the sense of minimizing the mean square spectral density of output acceleration. A control scheme for six degrees of freedom vibration isolation has been developed by use of the experimental model of an electromagnet and improved actuator characteristics are being developed to minimize high frequency passive coupling.

ACKNOWLEDGEMENT

This work is partially supported by the U.S. National Science Foundation under grants PHY85-13525 and PHY85-15856.

REFERENCES

1. N.Searby, "Effect of Science Laboratory Centrifuge on Space Station Environment," NASA/MSFC Workshop Proc. on "Measurement and characterization of the acceleration environment on board the space station," Guntersville, AL, Aug 1986

2. O.K.Garriott and D.B.DeBra, "A Simple Microgravity Table for the Orbiter or Space Station," Earth-Orient. Applic. Space Technol. Vol. 5, No. 3, 1985

3. R.A. Van Patten, "Flight Suspension for the Relativity Gyro," Marcel Grossman Conference, Sanghi, China, 1982

4. P.W.Worden, "Measurement of small forces with superconducting magnetic bearings," Precision Engineering Vol. 4, No. 3, July 1982

5. D.Sonnabend, "Mechanical Isolation for Gravity Gradiometers," NASA/MSFC Workshop Proc. on "Measurement and characterization of the acceleration environment on board the space station," Guntersville, AL, Aug 1986

6. B.V.Jayawant, "Electromagnetic suspension and levitation," IEE Proc., Vol. 129, Part A, No. 8, November 1982

7. Space Dept. of the Johns Hopkins University Applied Physics Lab. and Guidance & Control Lab. of Stanford University, "A Satellite Freed of all but Gravitational Forces: 'Triad I'," J. Spacecraft, Vol. 11, No. 9, Sept. 1974

8. P.F.Michelson, J.C.Price, R.C.Taber, "Resonant-Mass Detectors of Gravitational Radiation," Science, Vol. 237, 1987

9. A.D.Jeffries et al., "Gravitational Wave Observatories," Scientific American, Vol. 256, No. 6, June 1987

10. P.F.Michelson et al., "The Stanford Gravitational Wave Detection Program: A Plan for Observing the Next Supernova," The International Symposium on Experimental Gravitational Physics, Guang Zhou, PRC, 1987

11. S.Earnshaw, "On the nature of molecular forces which regulate the constitution of luminiferous ether," Trans. Camb. Phil. Soc., 1842, 7, pp. 97-112

12. J.K.Hedrick and D.N.Wormley, "Active suspensions for Ground Transport Vehicles - A State of the Art Review," Mechanics of Transportation Suspension Systems, The Winter Annual Meeting of ASME 1975

13. B.J.Hamilton, J.H.Andrus and D.R.Carter, "Pointing Mount with Active Vibration Isolation for Large Payloads," 10th annual AAS Guidance and Control Conference, 1987

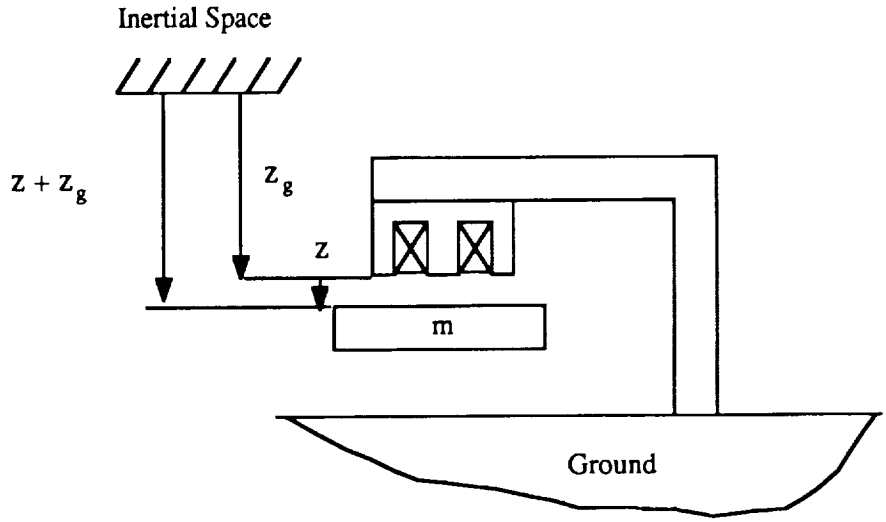

Figure 1 Coordinate System

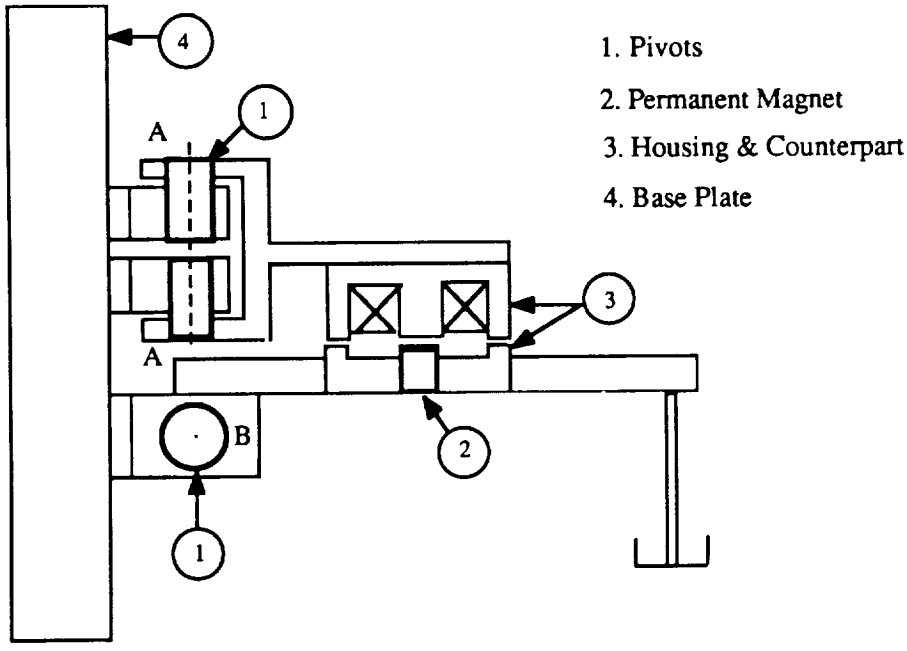

Figure 2 Schematic Diagram of Experimental Equipment

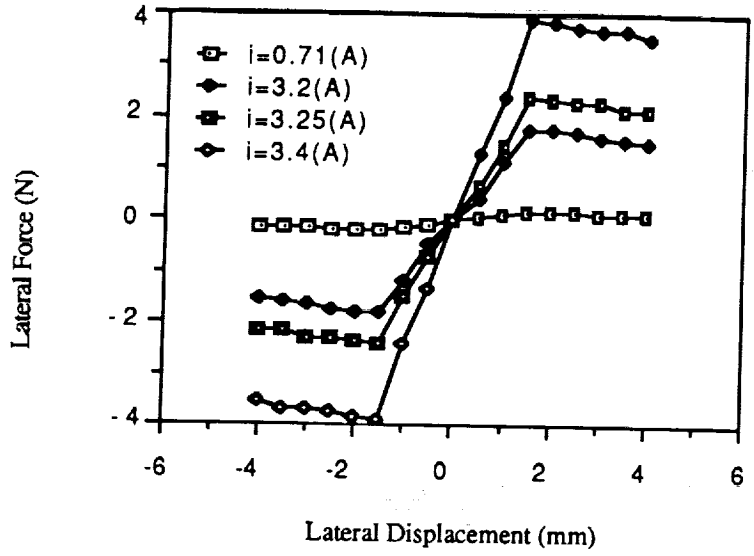

Figure 3 Lateral Force-Displacement Relation

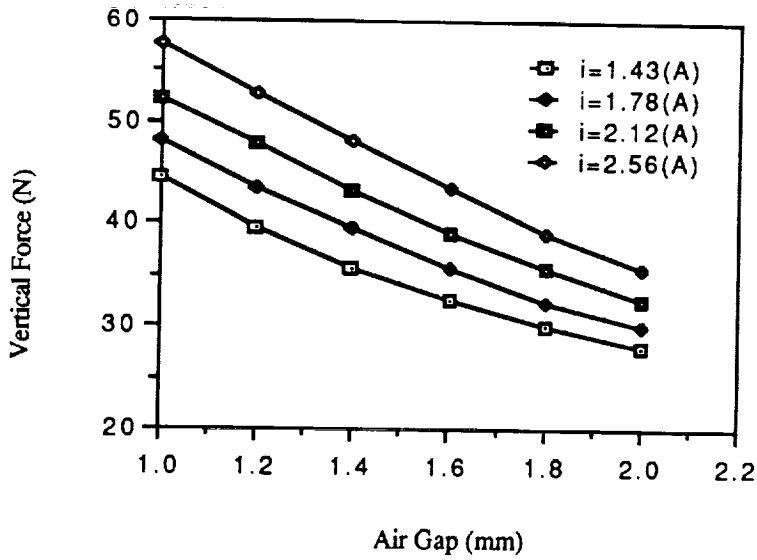

Figure 4 Vertical Force-Air Gap Relation

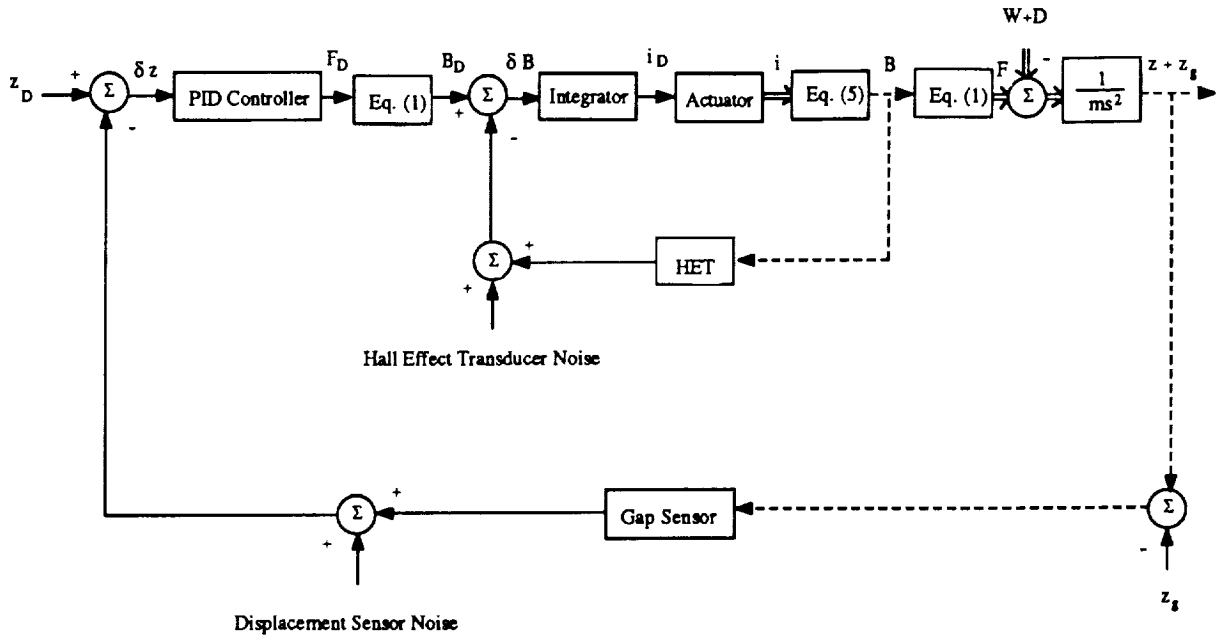

Figure 5 Block Diagram with Position and Flux Density Loop

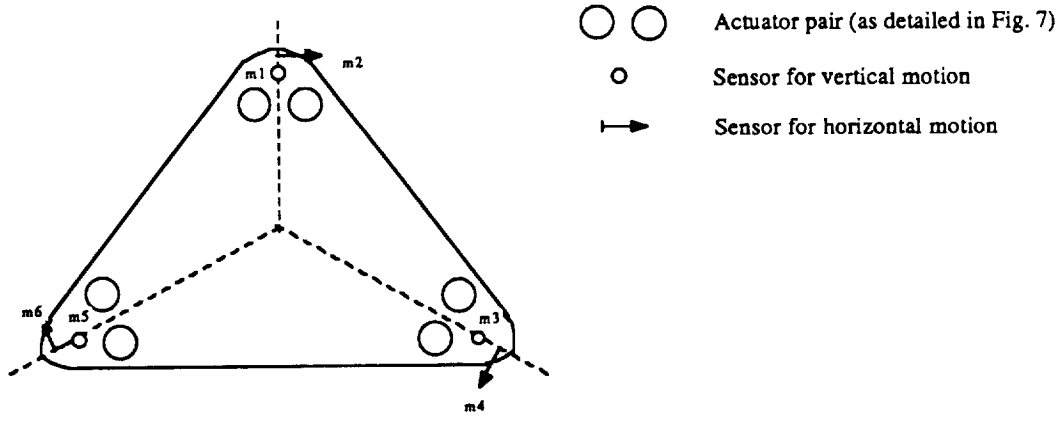

Figure 6 Configuration of Six Actuators and Sensors

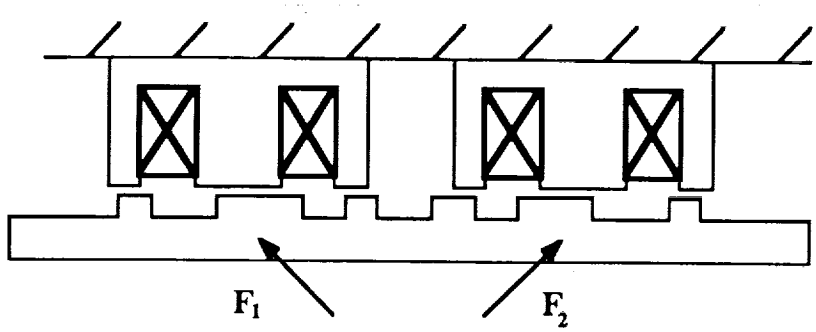

Figure 7 Two displaced electromagnets

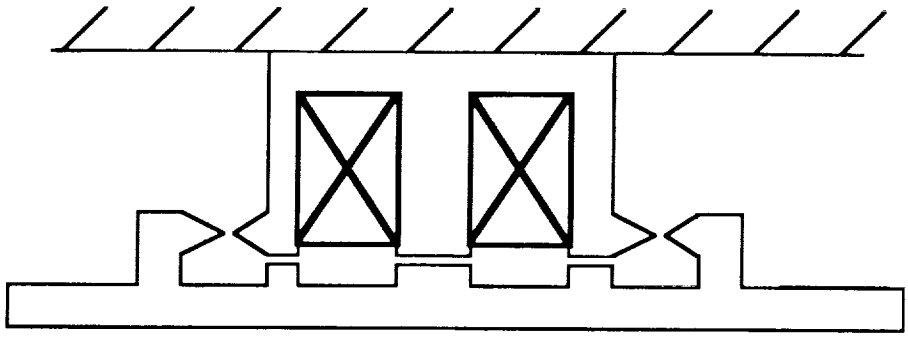

Figure 8 An actuator design with minor flux path with restoring force in vertical direction

omit

A Constitutive Model for the Forces of a Magnetic Bearing Including Eddy Currents

Dean L. Taylor, K.V. Hebbale, Cornell University

A Constitutive Model for the Forces of a Magnetic Bearing Including Eddy Currents[1]

D. L. Taylor, Associate Professor
K. V. Hebbale [2], Graduate Research Assistant

Sibley School of Mechanical and Aerospace Engineering
Cornell University, Ithaca, New York

ABSTRACT

A multiple magnet bearing can be developed from N individual electromagnets. This paper presents the constitutive relationships for a single magnet in such a bearing. Analytical expressions are developed for a magnet with poles arranged circumferencially. Maxwell's field equations are used so the model easily includes the effects of induced eddy currents due to the rotation of the journal. Eddy currents must be included in any dynamic model because they are the only speed dependent parameter and may lead to a critical speed for the bearing. The model is applicable to bearings using attraction or repulsion.

INTRODUCTION

Research and development activity on passive, active, and combination magnetic bearing systems spans over 150 years beginning with Earnshaw in 1839. The authors will not attempt to summarize the history for this workshop but will simply note research in magnetic bearings, magnetic dampers, and magnetic levitation for vehicles. High speed magnetic bearings are a commercial reality, being used in grinding and polishing machinery, vacuum pumps, compressors, turbines, generators, and centrifuges.

Passive systems using permanent magnets in repulsion are usually incapable of generating sufficient load carrying capacities. Two electromagnetic levitation methods have met with success: direct, position feedback control techniques; and ac modulated or indirect feedback methods. The latter suffers from high eddy current losses and a small range of stable air gaps. Early experiments with fully active systems (1957) were largely thwarted by the then high cost and large size of control system components. Since active magnetic bearings provide both damping and support, and with the reduction in cost and size of sophisticated electronics, the choice is clear. Subsequent efforts for load bearing situations have concentrated on active magnetic bearings.

However, the dynamics of direct feedback magnetic bearings have not been as thoroughly analyzed as have journal bearings. Most of the available literature deals with empirical ideas and concentrates on reliability of the bearing, reducing the size, weight and complexity of the devices. The authors have completed an extensive investigation of the dynamics of an active magnetic bearing [1,2,3,4] in terms of equilibrium points, transient response, on-set of instability, limit cycle size, and forced response. The only speed dependent effect was the change in forces due to eddy currents. This change leads to a critical speed, a Hopf bifurcation with subcritical unstable limit cycles. The reader is referred to [3,4] for a description of the dynamic analysis and results.

The purpose of this paper is to present the eddy current analysis. Although a good analytical model has not previously been available for eddy currents due to shaft rotation, a number of authors have calculated the eddy current effects in other geometrical configurations using a hypothetical simplified model and finite element methods [5,6]. Studies on linear induction motors are available [7,8] which can be extended to magnetic bearings by several assumptions and manipulations. In the above studies, the current density vector is cross multiplied to calculate the induced forces, which does not take care of the attractive force when the moving material is ferromagnetic. In this paper, the forces are calculated using the Maxwell's stress tensor approach which in one calculation gives all the forces involved. Matsumara [9] has derived the fundamental equations for a horizontal shaft magnetic bearing taking into account the rolling, pitching, and yawing of the rotor. In deriving the equations of motion, he assumes that the journal consists of a laminated core and consequently no eddy currents are generated in the material.

FOUR MAGNET BEARING

Consider a bearing using four magnets as shown in Fig. 1. The shaft has high permeability and high conduc-

[1] This work was supported in part by the Office of Naval Research under Contract No. N0014-80-C-0618.

[2] Presently at General Motors Research Laboratories.

tivity and is not laminated. (Lamination would serve to inhibit eddy currents.) Purely for simplicity, all of the four electromagnets are identical, modelled as a coil of N turns on a laminated core of high permeability. Each magnet applies a flux density B_i and the dead weight is suspended by the difference in forces exerted by top and bottom magnets. All magnets generate a flux density which can be adjusted to vary the equilibrium gap lengths under the magnets. This fully energized configuration was chosen so that the magnets could generate the effect of repulsion by decreasing the attraction. The shaft displacement is measured by two coordinates (ξ, η) as shown in Fig. 1, measured from the center of the clearance space in the horizontal and vertical directions respectively when the journal is spinning under the magnets.

If the shaft is not laminated, motion of the conducting shaft through the supporting magnetic fields will induce eddy currents. These eddy currents create two kinds of force on the rotor: drag forces which lead to additional power dissipation and coupling of motions of the journal in two perpendicular directions; and repulsive forces which tend to counter balance the attractive forces and shift the equilibrium point.

The following geometrical assumptions are made. The journal always remains perfectly aligned within the bearing (no tilting). Under small displacements the surfaces of the journal and the magnet pole faces are assumed to remain parallel. Since the individual poles are located at angles $\pm\theta$ relative to the control of the magnet, it is assumed that when the rotor moves vertically a distance η, the change in gap length for the vertical magnets is $\eta cos\theta$. Similarly, when the rotor moves horizontally by a distance ξ, the change in gap length for the horizontal magnets is $\xi cos\theta$. Any other translational motion of the rotor can be written as a superposition of the motions in ξ and η directions. The effect of unequal gap lengths under a vertical magnet caused by a rotor motion in the horizontal direction or vice versa is neglected because the total gap length under that magnet remains constant.

EQUATIONS OF MOTION

The differential equations of motion describing the response of the rotor system require the vectorially combined magnetic forces from all the magnets $\Sigma\vec{F}_{mag}$ at a station along the rotor axis.

$$\sum \vec{F}_{mag} = f(\xi, \eta, \dot{\xi}, \dot{\eta}, B_1, B_2, B_3, B_4) \tag{1}$$

Most rotordynamics codes linearize this to provide the eight bearing coefficients.

$$\begin{pmatrix} F_\xi \\ F_\eta \end{pmatrix} = \begin{bmatrix} c_{\xi\xi} c_{\xi\eta} \\ c_{\eta\xi} c_{\eta\eta} \end{bmatrix} \begin{pmatrix} \dot{\xi} \\ \dot{\eta} \end{pmatrix} + \begin{bmatrix} k_{\xi\xi} k_{\xi\eta} \\ k_{\eta\xi} k_{\eta\eta} \end{bmatrix} \begin{pmatrix} \xi \\ \eta \end{pmatrix} \tag{2}$$

It is immediately obvious that the dynamic characteristics of the bearing are determined by the control system which produces the changes in magnetic flux density. This system may be simply local, represented by

$$B_i = f(\Delta_i, \dot{\Delta}_i) \tag{3}$$

or coupled

$$B_i = f(\xi, \eta, \dot{\xi}, \dot{\eta}) \tag{4}$$

The design of the control system will not be discussed here. Both pole placement methods [4,10] and linear quadratic regulator theory [1] can be used to design state variable controllers.

Each magnet force will be expressed as resolutes normal and tangential to the magnet center line. These forces will include steady state attraction forces and eddy current forces (both repulsion and drag). Only spin velocity is assumed to generate eddy currents. Motion of the journal center $(\dot{\xi}, \dot{\eta})$ doesn't generate eddy currents. The force resolutes are only functions of flux density, gap, and journal speed.

$$F_{ni} = f(\Delta_i, \Omega, B_i) \tag{5}$$

$$F_{ti} = f(\Delta_i, \Omega, B_i) \tag{6}$$

Each magnet gap can be determined from the journal location

$$\Delta_i = f(\xi, \eta) \tag{7}$$

It can then be shown that unless the control is based on velocities

$$c_{\xi\xi} = c_{\xi\eta} = c_{\eta\xi} = c_{\eta\eta} = 0 \tag{8}$$

and the eddy current drag forces produce bearing cross stiffness terms.

Assuming the controller is determined, the general procedure is to:

(a) Determine the equilibrium location for a given spin speed (This assumes no journal velocity, $\dot{\xi} = \dot{\eta} = 0$);
(b) Linearize magnetic forces about equilibrium locations;
(c) Form system dynamic equations, extract eigenvalues, determine stability;
(d) Perform parameter study to locate system bifurcations;
(e) Apply center manifold theorem to determine large amplitude behavior of any bifurcation points;

The usual parameter study would be to follow the equilibrium location and stability as functions of spin speed. Note that due to nonlinearities, the bearing coefficients must be determined at each different parameter value.

MAGNETIC FORCES INCLUDING EDDY CURRENT EFFECTS

The complete eddy current analysis for 4 magnets as shown in Fig. 1 with unequal gap lengths is analytically intractable. (It is probably amenable to finite element techniques.) The following approximations are required.

First, the problem is assumed two dimensional.

Second, the problem will be unwrapped and considered as periodic on a half-space. However, before net forces are calculated, the surface tractions predicted by Maxwell's stress tensor will be wrapped around a circular shaft. As the shaft starts spinning, the eddy currents tend to repel the applied magnetic field and the skin depth of penetration becomes very small. This motivates a semi infinite assumption in the radial direction. The velocity will be treated as constant with respect to y, although it actually decreases linearly as the center is approached. $V = \Omega(\frac{D}{2} + \Delta - y)$. This assumption is supported by the very small skin depth.

Third, each magnet will be considered separately, and the magnetic field for each magnet will be determined individually. The net force of each magnet is then determined, leading to 4 vector forces which are then summed vectorially. An alternative (more complex) solution is discussed later in the paper. Fig. 2 shows the approximate problem to be solved for each magnet.

Fourth, the square wave applied flux density is expanded as a Fourier series

$$B_m(x) = \sum_i \frac{2B_o}{\pi i}[cos(\frac{2bi}{D}) - cos(\frac{2ai}{D})]sin(\frac{2ix}{D}) \tag{8}$$

or

$$B_m(x) = \sum_i B_i sin(k_i x) \tag{9}$$

The field density and current density distributions within the moving material solve a linear problem, and hence the principle of superposition can be invoked and each harmonic handled separately. Figure 3 shows a single harmonic applied to the semi-infinite medium.

The equation that describes the distribution of the magnetic field in the conducting medium is derived from Maxwell's field equations.

$$-\frac{1}{\mu\sigma}\nabla^2\vec{B} + \frac{\partial\vec{B}}{\partial t} = \nabla \times (\vec{V} \times \vec{B}) \tag{10}$$

where $\vec{B} = B_x\vec{e}_x + B_y\vec{e}_y$ ($\vec{e}_x$ and $\vec{e}_y$ being unit vectors in x and y directions respectively). The y component B_y is determined from the y component of (10) The remaining component B_x can be determined from the relation $\nabla \cdot B = 0$. The magnetic field is driven by the applied magnetic field density, and so solutions with the same traveling wave dependence on (x, t) are assumed. That is, it is assumed that the flux density takes the form

$$\vec{B} = [B_x(y)\vec{e}_x + B_y(y)\vec{e}_y]e^{j(kx-\omega t)} \tag{11}$$

The solution form in the y-direction is $e^{\pm qy}$ where

$$q_i = k_i\sqrt{1+js} = k_i\sqrt{1+j\frac{\mu\sigma V}{k_i}} \tag{12}$$

Eqn (12) can be used to predict the skin depth.

The solution domain is divided into two regions, denoted by subscripts 1 and 2 respectively: Region (1), the air gap where $\sigma = 0 (0 \leq y \leq \Delta)$; and Region (2), the moving conducting medium ($\Delta \leq y \leq \infty$). The solutions within each region have two constants of integration, determined from the following 4 boundary conditions:

(1) the applied flux density at $y = 0$;

(2) the solution cannot grow as $y \rightarrow \infty$ (one constant is zero);

(3) conservation of flux at the interface $y = \Delta$ ($\nabla \cdot B = 0$, using the divergence theorem, this leads to $B_{y1} = B_{y2}$).

(4) at the interface, $\nabla \times H = 0$ (using Stokes theorem, this leads to $H_{x1} = H_{x2}$).

Hence, the flux density distribution throughout both regions can be determined.

In the air gap, the solution is

$$\vec{B}_{1i} = \left((D_1 e^{k_i y} + D_2 e^{-k_i y})\vec{e}_x + (D_1 e^{k_i y} - D_2 e^{-k_i y})\vec{e}_y\right) e^{j(k_i x - wt)} \tag{13}$$

where

$$D_1 = \frac{(1 - \frac{\mu_0}{\mu}\frac{q_i}{k_i}) B_i e^{-k_i \Delta}}{2[cosh(k_i \Delta) + \frac{\mu_0}{\mu}\frac{q_i}{k_i} sinh(k_i \Delta)]} \tag{14}$$

$$D_2 = \frac{(1 + \frac{\mu_0}{\mu}\frac{q_i}{k_i}) B_i e^{k_i \Delta}}{2[cosh(k_i \Delta) + \frac{\mu_0}{\mu}\frac{q_i}{k_i} sinh(k_i \Delta)]} \tag{15}$$

In the journal, the solution is

$$\vec{B}_{2i} = \left(\frac{q_i}{jk_i}\vec{e}_x + \vec{e}_y\right) D_3 e^{-q_i y} e^{j(k_i x - wt)} \tag{16}$$

where

$$D_3 = \frac{B_i e^{q_i \Delta}}{[cosh(k_i \Delta) + \frac{\mu_0}{\mu}\frac{q_i}{k_i} sinh(k_i \Delta)]} \tag{17}$$

The forces acting on the conducting medium are calculated by Maxwell's stress tensor. For magnetic problems with currents and no charges, the forces acting on a body are given by

$$\vec{F} = \int_\Sigma \frac{1}{\mu}[\vec{B}\vec{B} \cdot \vec{n} - \frac{1}{2}\vec{B}^2 \vec{n}] dA \tag{18}$$

where Σ is any closed surface surrounding the body and not containing any other body and B is the value of the field on the closed surface. Choosing a closed surface Σ such that it extends from $-\infty$ to ∞ and includes only the conducting medium, the integration is carried out with $\vec{n} = -\vec{e}_y$.

The complete flux density distribution in the whole region of Fig. 2 due to all the applied sinusoidal waves is determined by superposing the individual fields. Each component of the field (B_x, B_y) is an infinite series in sine or cosine terms. The value of the $\vec{B}$ field at the interface, which is required for calculating the forces, is calculated by substituting $y = \Delta$. It is interesting to note that the integral and the summation are interchangable in order. That is, the force for each component of the Fourier series can be determined and then summed or the fields summed and the force determined. This is perhaps surprising because the problem is nonlinear, but the infinite series for B_x and B_y are made up of sine and cosine terms which are orthogonal to one another and all the cross terms drop out during integration over one period.

The total flux can also be calculated and compared with that predicted by magnetic circuit theory (Appendix A). For the numerical example which follows, the more detailed solution is about 8% lower, showing the effects of magnetic circuit assumptions (uniform field density and no leakage in air gap). For comparison to classical problems, the forces for the problem in Fig. 2 will be determined, although the reader is cautioned to go on Eqn. (23) for a bearing problem. Substituting for $\vec{B}$ and evaluating the integrals, the drag and lift forces per unit area acting on the material turn out to be

$$\vec{F}_{drag} = -\frac{1}{4\mu_0}\frac{\mu_0}{\mu}\sum_i \frac{B_i^2}{(n_{1i}^2 + n_{2i}^2)} \frac{s_i}{Re\sqrt{1 + js_i}} \tag{19}$$

$$\vec{F}_{lift} = -\frac{1}{4\mu_0}\sum_i \frac{B_i^2}{(n_{1i}^2+n_{2i}^2)}[1-(\frac{\mu_0}{\mu})^2\sqrt{1+s_i^2}] \tag{20}$$

where

$$s_i = \frac{\mu\sigma V}{k_i} \tag{21}$$

and n_1 and n_2 are the real and imaginary parts of γ_i.

$$\gamma_i = [cosh(k_i\Delta) + \frac{\mu_0}{\mu}\frac{q_i}{k_i}sinh(k_i\Delta)] \tag{22}$$

As expected, when no currents are induced in the slab (V=0,s=0), there is no drag force and the lift is the magnetic attractive force. There is an optimum value of V at which the maximum force per unit area $\vec{F}_x$ is produced. The lift force decreases as V is increased, at some value of V the lift force becomes zero, and at higher values the lift force acts in the opposite direction (repulsion). At very high values of V there is no drag because all the flux is excluded from the material and the repulsion force reaches an asymptotic value irrespective of the permeability of the material.

For the magnetic bearing, the forces acting on a rotating shaft are calculated by wrapping one period of the B field distribution back onto the circular shaft. Choosing a closed surface $\sum$ on the circumference of the rotor and simplifying the integral in Eq. (18) give the forces acting on the rotor per unit width as

$$F_t = -\frac{1}{\mu_0}\int_{-\frac{\pi D}{2}}^{\frac{\pi D}{2}} \tilde{B}_x\tilde{B}_y cos(\frac{2x}{D})dx - \frac{1}{2\mu_0}\int_{-\frac{\pi D}{2}}^{\frac{\pi D}{2}} (\tilde{B}_y^2-\tilde{B}_x^2)sin(\frac{2x}{D})dx \tag{23}$$

$$F_n = -\frac{1}{\mu_0}\int_{-\frac{\pi D}{2}}^{\frac{\pi D}{2}} \tilde{B}_x\tilde{B}_y sin(\frac{2x}{D})dx - \frac{1}{2\mu_0}\int_{-\frac{\pi D}{2}}^{\frac{\pi D}{2}} (\tilde{B}_y^2-\tilde{B}_x^2)cos(\frac{2x}{D})dx \tag{24}$$

where

$$\tilde{B}_x = B_{x1}(y)\Big|_{y=\Delta} = \sum_i -\frac{1}{\gamma_i}\frac{\mu_0}{\mu}\frac{q_i}{k_i}B_i e^{jk_i x} \tag{25}$$

$$\tilde{B}_y = B_{y1}(y)\Big|_{y=\Delta} = \sum_i \frac{1}{\gamma_i}\frac{q_i}{k_i}B_i e^{jk_i x} \tag{26}$$

The parameters in Table 1 were used in the following numerical examples. Figure 4 shows the flux distribution at zero speed and Figure 5 shows the convection effect and decrease in skin depth as velocity increases. Integrating the total flux within the air gap and within the journal, Figure 6 shows how the flux is compressed out of the journal as eddy currents increase. Fig. 7 shows the variation in lift and drag forces. Observe the change over to repulsion at 50,000 rpm. The drag force peaks at a value of 1100 Nt at $\Omega = 10^8 rpm$.

The effect on the values of the forces of the number of terms used in the Fourier series was investigated. The magnetic forces were calculated at different spinning speeds using 10, 25, 50, 100, and 500 terms in the series. Figure 8 shows the variation of the lift force. There is very little change in the results when the number of terms used in the series is 50 or more. There is approximately 3% change in the lift force when the number of terms is increased from 10 to 25 or from 25 to 50. This large number of harmonics is reasonable if the Fourier approximation to the applied square wave is plotted. The drag force effectively converged within 10 harmonics. The authors typically use 25 harmonics in dynamic analysis.

An alternative approach is developed in [2] to find net magnetic field for all four magnets as a single system (simultaneously). The problem is posed in Fig. 9, which shows all four B fields. This complex boundary condition is expanded in a Fourier series and the previous equations applied. However, this approach requires the assumption that all the gaps are equal. At low spinning speeds there is no difference between the two methods as shown in Fig. 10. Only at very high speeds do the two differ. (For parameters in this paper, 4% at 10^5 rpm). Researchers may wish to pursue this method.

CONCLUSION

A very general analytical expression for bearing forces has been presented. The model is applicable to journals made of permeable or nonpermeable material and to DC fields or AC fields. Both kinds of eddy current repulsion bearings are included. The predicted loss of lift (about 30% at 12500 rpm), agrees approximately with experimental results of Yamamura [11]. The expression for the drag force under a single sinusoidal field density wave is the same as that obtained by Meisenholder [9].

Without considering eddy current effects, there is no speed dependent term in the constitutive model for a magnetic bearing. Eddy currents cause a loss of effective lift which can be viewed as an external load and may cause a change in equilibrium point, and change bearing coefficients. More importantly, eddy current drag causes coupling between (x, y). Any change in the x gap affects the drag force in the y direction. Other work has shown this coupling effects bearing stability.

A final comment applies to bearing coefficients (equivalent stiffness and damping matrices). The situation for a magnetic bearing is different from that of journal bearings. It is not possible to determine the 8 classical coefficients just by differentiating the force expressions with respect to $\xi, \eta, \dot{\xi}, \dot{\eta}$. The design of the control system may introduce state variables within the controller. In that case the dynamics of the electrical components must also be incorporated. Some subspace reduction might be possible, but it is impossible to determine even approximate coefficients without a completely designed control system.

REFERENCES

1. Bartlett, R.A.: *Active Vibration Control of Flexible Rotors using Magnetic Bearings*, M.S. Thesis, Cornell University, January 1984.
2. Hebbale, K.V.: *A Theoretical Model for the Study of Nonlinear Dynamics of Magnetic Bearings*, Ph.D. Dissertation, Cornell University, January, 1985.
3. Hebbale, K. and Taylor, D. L.: "Dynamics of a Ferromagnetic Suspension System", proceedings of the 1986 Joint Automatic Control Conference, June 18-20, 1986, Vol. 1, pp. 216-223.
4. Hebbale, K. and Taylor, D. L.: "Nonlinear Dynamics of Attractive Magnetic Bearings", Proceedings of the 1986 Workshop on Bearing Stability, June 2-4, 1986, Texas A&M.
5. Chari, M.V.K.; Silvester, P.P.: "Finite Elements in Electrical and Magnetic Field Problems", John Wiley and Sons, Inc., New York, 1980.
6. Yoshimoto, T.: "Eddy Current Effect in a Magnetic Bearing Model", *IEEE Transactions on Magnetics*, Vol. MAG-19, n5, September, 1983.
7. Meisenholder, S.G.; Wang, T.C.: "Dynamic Analysis of an Electromagnetic Suspension System for a Suspended Vehicle System", TRW Systems Group, Prepared for Federal Railroad Administration, 1972.
8. Wang, T.C.; et. al.: "Single-Sided Linear Induction Motor", Sixth Annual IEEE-IGA Meeting, October, 1971.
9. Matsumara, F.; et. al.: "Fundamental Equation for Horizontal Shaft Bearing and its Control System Design", *Electrical Engineering in Japan*, Vol 101, n3, pp. 123, May-June 1981.
10. Woodson, H.H.; Melcher, J.R.: "Electromechanical Dynamics Part I, Part II", John Wiley and Sons, Inc., New York, 1968.
11. Yamamura, S.; Ito, T.: "Analysis of Speed Characteristics of Attractive Magnet for Magnetic Levitation of Vehicles", *IEEE Transactions on Magnetics*, Vol. MAG-11, n5, Spetember, 1975.

NOMENCLATURE

a	Distance of magnet pole corner (near) from center line
A	Area of magnet pole face.
b	Distance of magnet pole corner (far) from center
B	Magnetic flux density
B_0	Magnetic flux density under the magnet pole
D	Diameter of journal
$\vec{e}$	Unit vectors
F_{mag}	Magnetic force
H	Magnetic field intensity
j	$\sqrt{-1}$
k	Wave number
L	Inductance of circuit

L_i	Flux path length
n_1, n_2	Real and imaginary parts of γ
N	Number of turns in coil
q	Complex wave number
R	Resistance of coil
s_i	Nondimensional velocity
t	Time
$\vec{V}$	Velocity vector
V	Velocity (magnitude)
W_d	Field energy density
W_f	Field energy stored
ξ	shaft displacement
η	shaft displacement
γ	Complex number $= \cosh k\Delta + \mu_0 q/\mu k \sinh k\Delta$
Δ	Gap length
Γ	Magnetomotive force
θ	Magnet pole angle with respect to magnet axis
λ	Flux linkage
μ, μ_r	Permeability
σ	Electrical conductivity of journal material
Σ	Closed surface, Summation sign
Φ	Magnetic flux
Ω	Spin speed of rotor

APPENDIX A
ESTIMATION OF MAGNETIC LIFT FORCE USING CIRCUIT THEORY

If eddy currents are neglected, magnetic circuit theory can be used to approximate the magnetic lift force of a single magnet. The following assumptions are made in deriving the expressions for the magnetic lift force:

1. Field fringing is neglected.
2. Magnetization curve is linear ($B = \mu H$).
3. Magnetic flux density B and field intensity H are uniform over cross-sections of the core, gap, or journal.

An electromagnetic circuit is considered whose elements are gap, core, and journal. Each element has constant crossection A_i and length L_i. The magnetic flux ϕ is assumed constant throughout the circuit, and Γ is the total magnetomotive force within the circuit elements.

The density relationship $\phi = BA$ and the constitutive law $B = \mu H$ can be used to express field intensity in the ferromagnetic material in terms of the field intensity within the air gap.

By definition $\Gamma = \int H dl$ Integrating around the circuit and equating Γ to the current linked (NI) results in an equation for field intensity within the air gap. The field energy is determined within each element $w = \frac{1}{2}\mu H$ and the total field energy is obtained by a volume integral over all the elements.

By definition, the force is the rate of change of stored field energy with respect to the mechanical displacement.

$$F_{mag} = \frac{\mu_0 N^2 A I^2}{(2x + \frac{L_1}{\mu_{r1}} + \frac{L_2}{\mu_{r2}})^2} \tag{A.1}$$

In addition, the total flux ϕ, the magnetic field density B, the magnetic flux linkage λ, and the inductance L can be expressed in terms of the gap length x and current I as:

$$\phi = \frac{\mu_0 N I A}{(2x + \frac{L_1}{\mu_{r1}} + \frac{L_2}{\mu_{r2}})} \tag{A.2}$$

$$B = \frac{\mu_0 N I}{(2x + \frac{L_1}{\mu_{r1}} + \frac{L_2}{\mu_{r2}})} \tag{A.3}$$

$$\lambda = \frac{\mu_0 N^2 I A}{(2x + \frac{L_1}{\mu_{r1}} + \frac{L_2}{\mu_{r2}})} \tag{A.4}$$

$$L = \frac{\mu_0 N^2 A}{(2x + \frac{L_1}{\mu_{r1}} + \frac{L_2}{\mu_{r2}})} \tag{A.5}$$

TABLE 1
Four Magnet Bearing Parameters

JOURNAL		
	Diameter of journal D	= 0.15 m
	Path length in journal L_2	= 0.05 m
	Relative permeability of journal material μ_{r2}	= 100.0
	Electrical conductivity of journal material σ	= 1.0 E+07 mho/m
MAGNET		
	Pole angle	= 15 degrees
	Path length in core L_1	= 0.28 m
	Relative permeability of core material μ_{r1}	= 10000.0
	Area of pole face A	= 0.00025 m^2
	Width of pole face W	= 0.008333 m
	Number of turns N	= 800.0
	Distance of pole corner a	= 0.0075 m
	Distance of pole corner b	= 0.0375 m
	Resistance of coil R	= 3.0 ohms
	Permeability of free space μ_0	= 4π E - 07 H/m

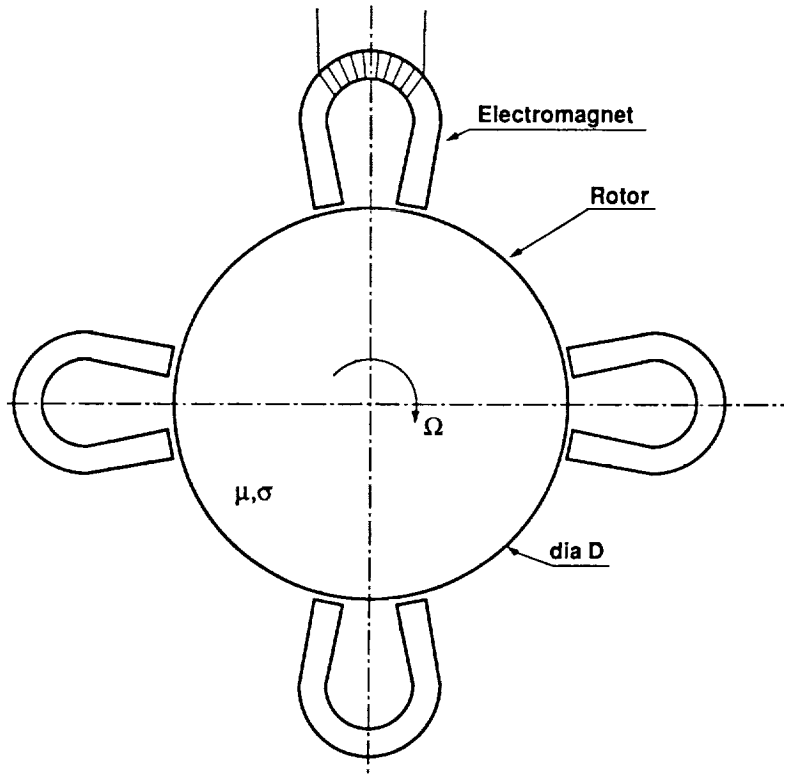

Figure 1. Four magnet bearing.

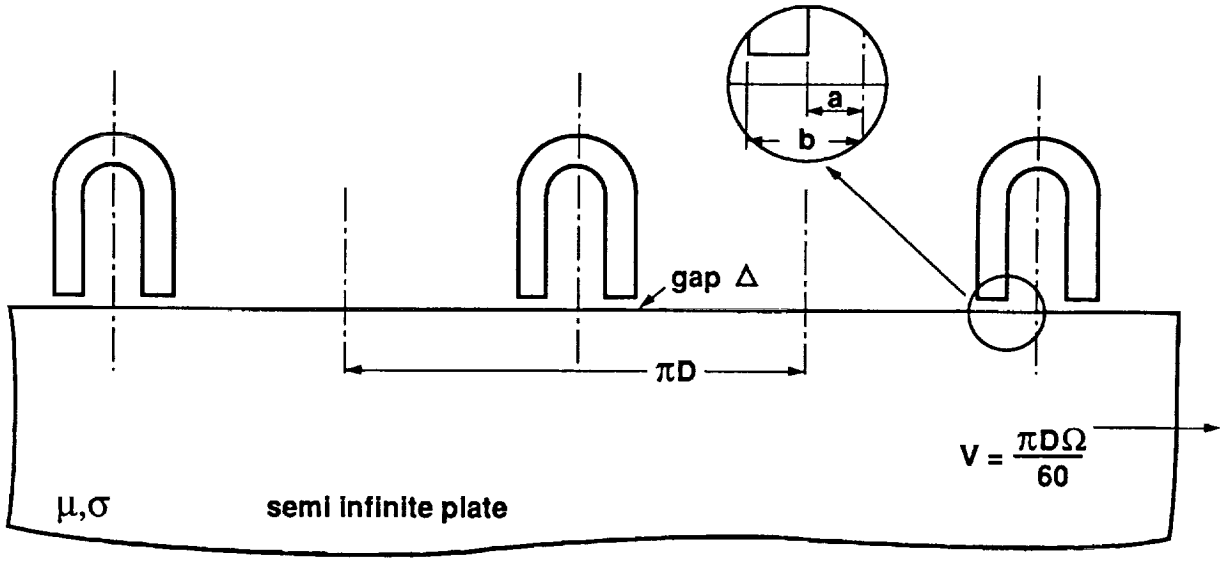

Figure 2. Semi-infinite plane under a series of electromagnets.

C-2

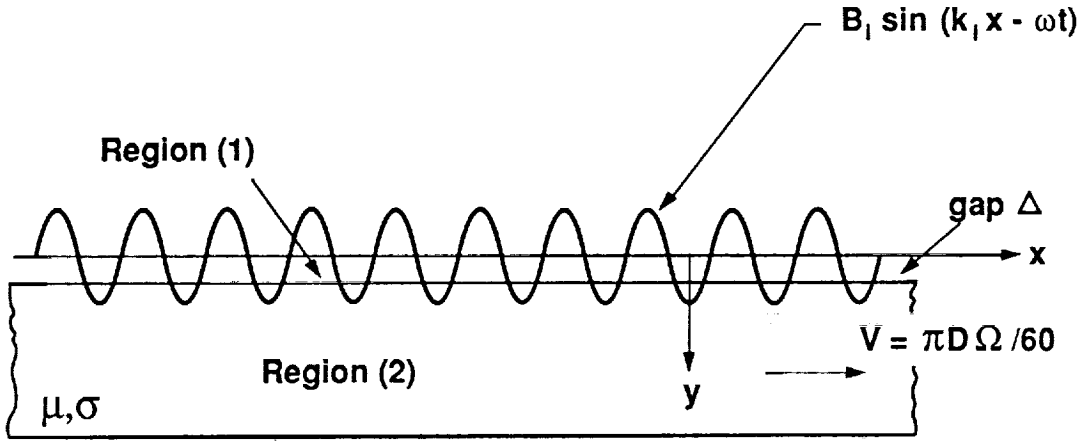

Figure 3. Moving conductive medium under an applied flux density wave.

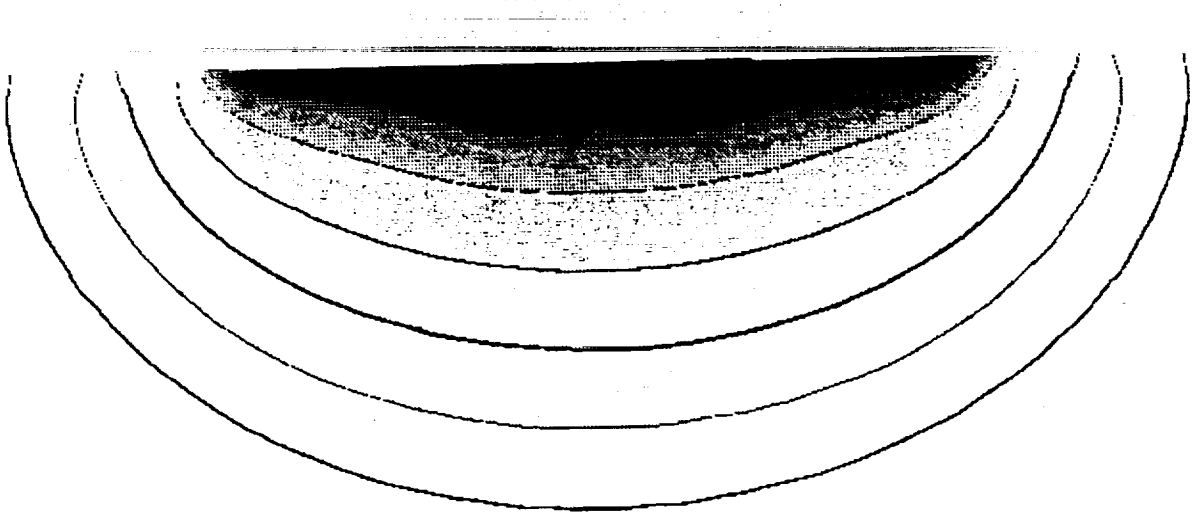

Figure 4. Flux distribution inside stationary conducting medium.

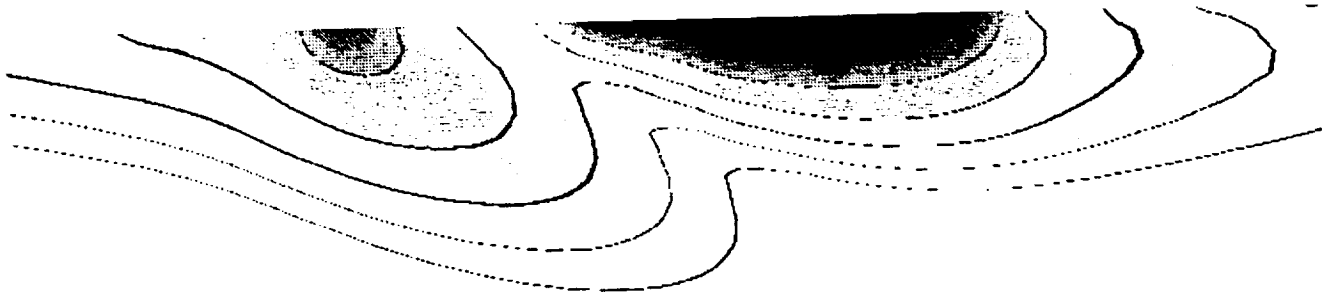

Figure 5. Flux distribution inside moving conducting medium.

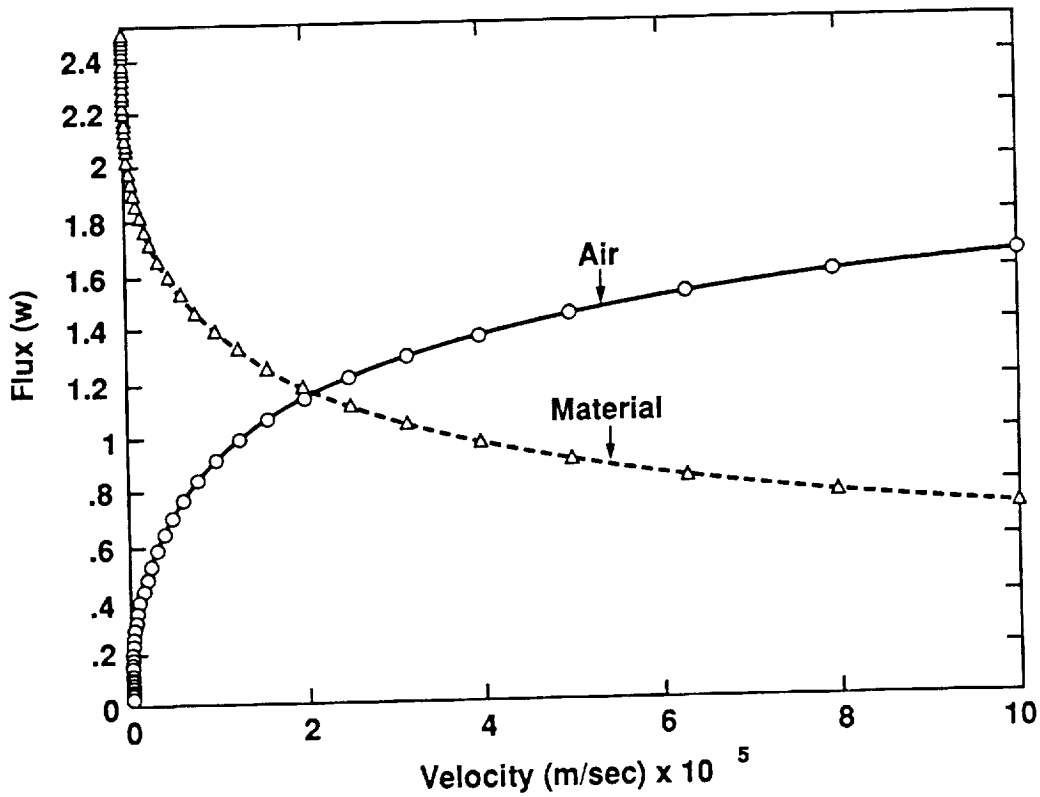

Figure 6. Flux distribution between air gap and journal.

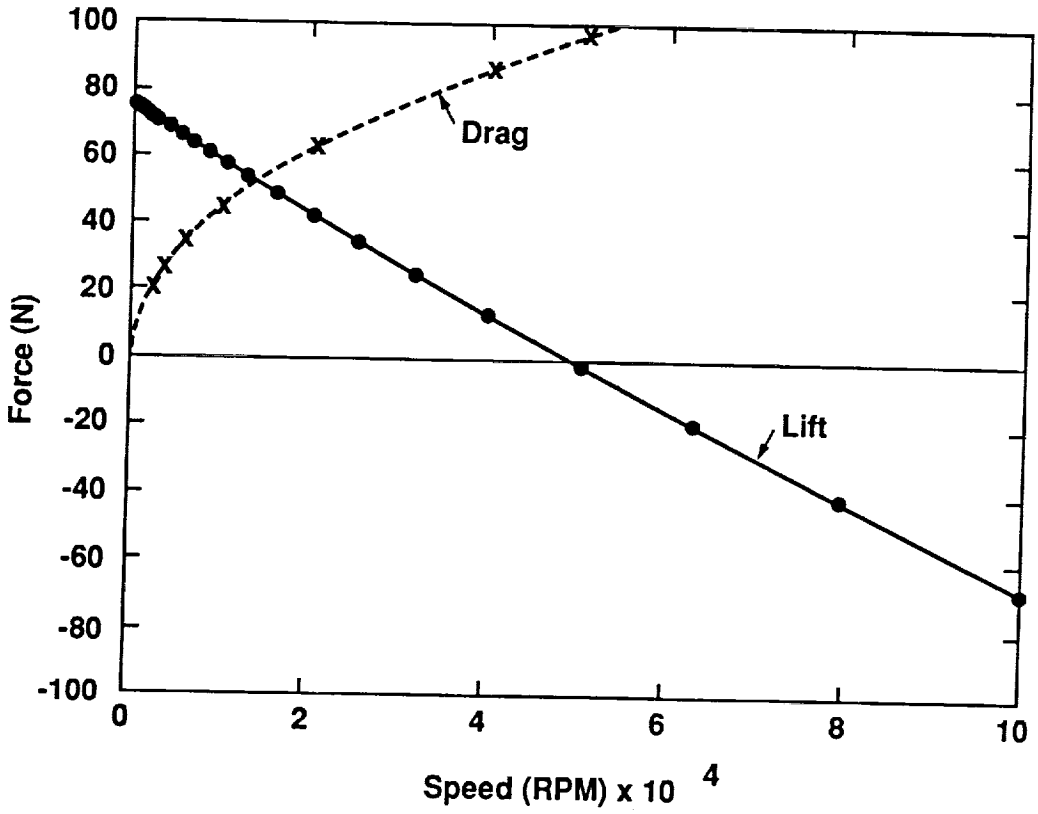

Figure 7. Lift and drag as a function of speed.

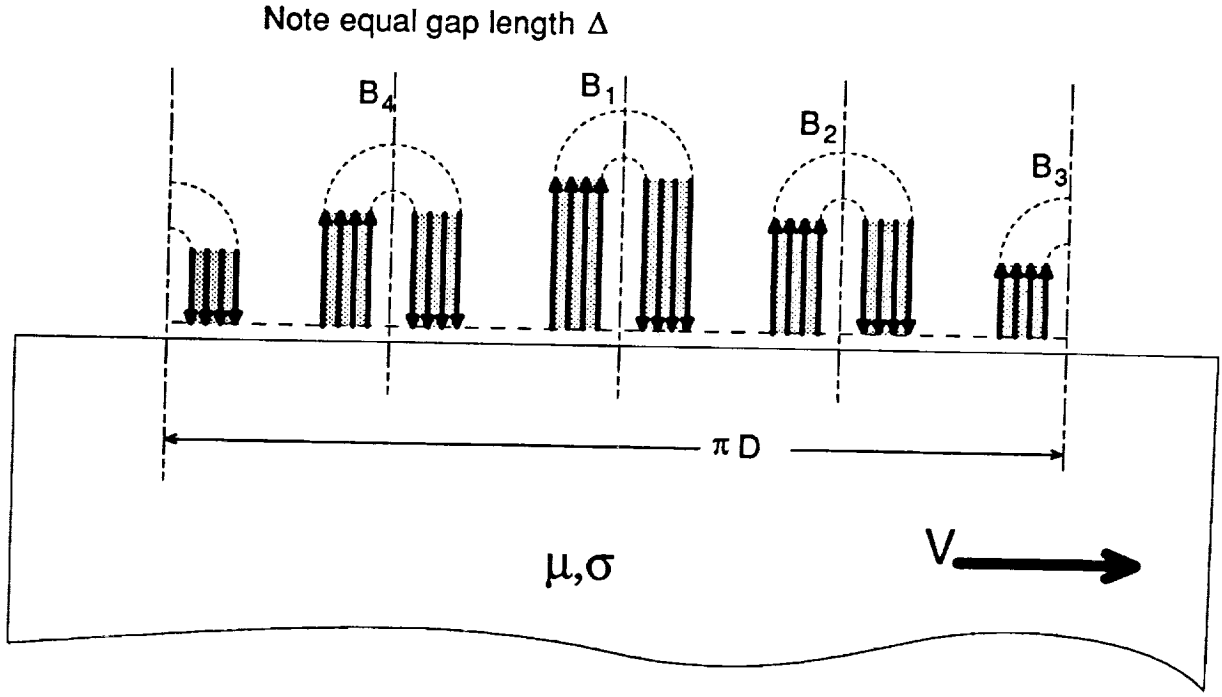

Figure 8. Effect of number of harmonics on lift force.

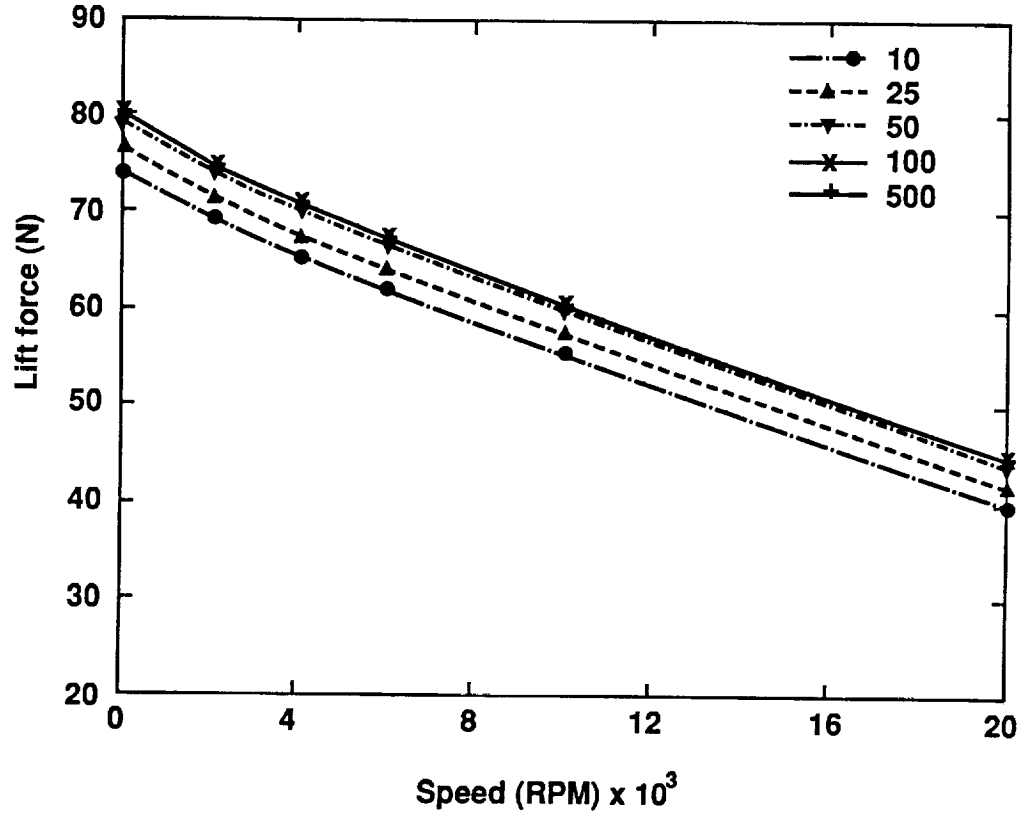

Figure 9. Equivalent problem for multiple magnet case.

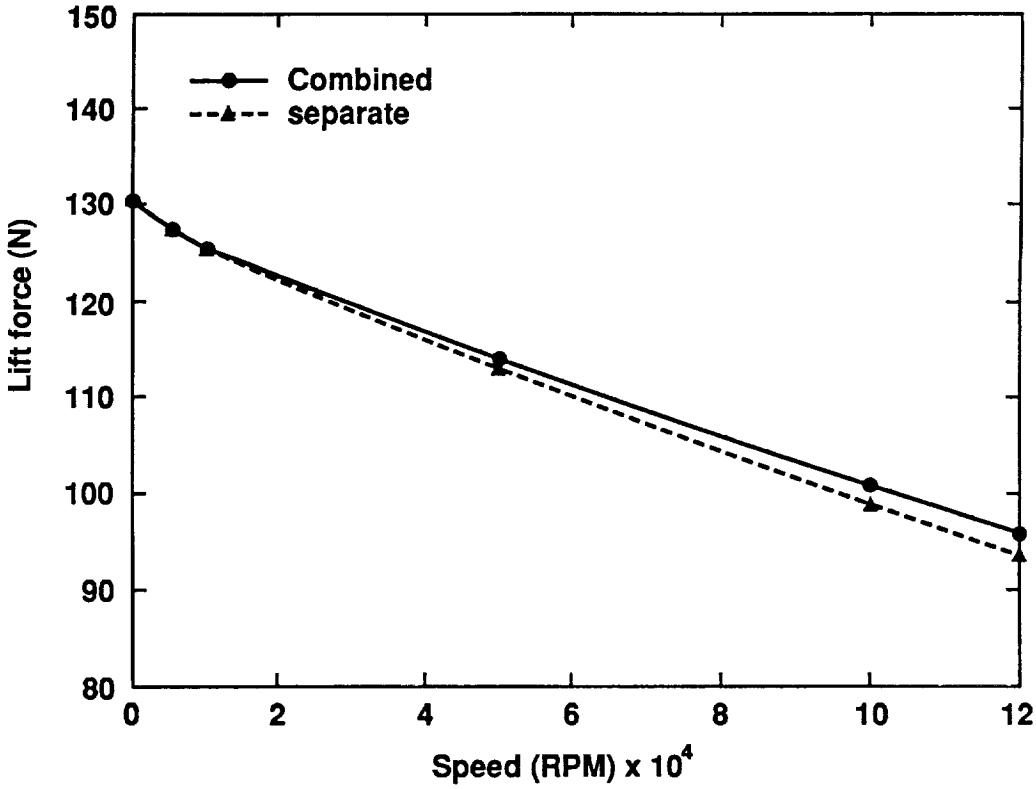

Figure 10. Effect of superposition of lift force.

omit

Session 3

Pointing, Isolation, and Measurement

Chairman: Claude R. Keckler

NASA Langley Research Center

omit

Magnetic Suspension Characteristics of Electromagnetic Actuators

Dantam K. Rao, James Dill, Edward Zorzi, Mechanical Technology Inc.

MAGNETIC SUSPENSION CHARACTERISTICS OF ELECTROMAGNETIC ACTUATORS

by

Dantam K. Rao
J. Dill
E. Zorzi

Mechanical Technology, Inc.
Advanced Technology Dept.
Latham, New York

ABSTRACT

Electromagnetic actuators that use a current-carrying coil (which is placed in a magnetic field) to generate mechanical force are conceptually attractive components for active control of rotating shafts. In one concept that is being tested in the laboratory, the control forces from such actuators are applied on the flexibly supported bearing housings of the rotor. Development of this concept into a practical reality requires a clear and thorough understanding of the role of electromechanical parameters of these actuators in delivering the right amount of control force at the right phase into the rotor. The electromechanical parameters of the actuators investigated in this paper are the mass of the armature, stiffness of its suspension, electrical resistance and inductance of the coils. Improper selection of these parameters can result in degradation in their performance, leading to mistuning between the actuator and the rotor. Through a simple analysis, this paper shows that use of such mistuned actuators could result in sharp fluctuations in the phase of the control force delivered into the rotor around the critical speeds. These sharp fluctuations in phase, called "Phase Glitches", are undesirable. Hence, future designs of controllers should take into account the undesirable mistuning effects between the actuator and the rotor caused by the Phase Glitches.

1. INTRODUCTION

Active control of structural vibrations has received considerable attention in the past few decades. Essentially, as shown in Fig. 1, the concept of active control implies that the sensed vibrations are used to generate and apply control forces f_{c1}, f_{c2}, ..., on the structure in such a manner that they either create some favorable characteristics, such as stability, or they counter some undesirable influence of any existing external forces f_1, f_2, ... on the structure. The structures whose vibrations are to be controlled can be broadly classified into (a) Stationary Structures, such as Large Space Structures, (b) Moving Structures, such as mechanically levitated Trains or (c) Rotating Structures, such as the shafting in momentum wheels, gyros, compressors, etc. In this paper we restrict ourselves to active control of structures which have one

rotational degree of freedom, such as a compressor rotor or machine tool spindle. There are a number of mechanisms by which control forces could be exerted on these rotating shafts, such as fluid film pressure control, "active-swirl," electro-magnetic forces etc. We focus our attention to only the magnetic or electromagnetic means of force generation. Earnshaw (Ref. 1) has shown that passive suspension of a rotor by magnetic means is unstable, and hence we deal only with active magnetic suspensions herein.

Historically, a number of Control Force Generation Mechanisms that use magnetic means have been examined by various authors with varied degree of success. As summarized by Geary (Ref. 2), most of these mechanisms could be traced directly or indirectly to (a) forces of attraction or repulsion induced solely by magnetic sources, such as electromagnets, permanent magnets, superconducting magnets, diamagnets, ferromagnetic materials, etc., or (b) those induced by interaction between magnetic and electric fields, such as the forces exerted on a current carrying coil that is placed across a magnetic field. The control forces of type (a) will be proportional to the square of the ratio of current and gap (when electromagnets are used) whereas those of type (b) are proportional to the current flowing in the coils. This latter principle of generation of mechanical forces, herein called the Lorentz Force Principle, is most often used in common energy conversion devices such as generators, motors, etc. It is also used in the construction of various vibration excitation devices such as electrodynamic exciters, shakers, linear motors, and electromagnetic actuators. Application of such electromagnetic actuators to control the vibrations of rotors forms the subject matter of this study.

2. ELECTROMAGNETIC ACTUATORS AS CONTROL-FORCE GENERATORS

The electromagnetic actuators have been used recently by Ulbrich (Refs. 3,4) and Nonami (Ref. 5) to actively control the vibrations of an experimental rotating shaft, as shown in Fig. 2. A similar demonstration model has also been reported (Ref. 6) at Case Western Reserve University as a NASA funded activity. In this setup (Fig. 2), the rotor is mounted in two roller bearings. The housings of these roller bearings are flexibly supported from the ground so as to meet the controllability criterion. Electromagnetic actuators symmetrically attached around the housings of these flexibly supported roller bearings deliver the control forces. Thus, the control forces are transmitted into the rotor through the roller bearings. Additional suspensions that support the armature of the actuator are built into the housing of the actuator. A PID type controller generates appropriate control signal using the vibrations of the rotor sensed by some noncontacting type transducer; this control signal is fed into the electromagnetic actuator through power amplifiers to generate the required control forces.

When electromagnetic actuators are so used to generate the control forces, the interaction between the actuator and the rotating structure (rotor) needs to be understood clearly in order to precisely characterize the stability and performance limitations of the closed loop system. This interaction between the actuator and rotor could be broadly classified into (a) Mechanical Interaction that describes the influence of mechanical quantities such as mass of armature m_a, stiffness of its suspension k_a, as well as any mechanical damping in the coil assembly, and (b) electrical interaction that describe the effect of electrical quantities such as resistance R, self inductance L and back emf generated in the electrical circuit that sends in electrical power into the actuator.

3. OBJECTIVES OF THE INVESTIGATION

The mechanical interaction between the electromagnetic actuator (also called 'Linear Momentum Exchange Device'(LMED) or 'Proof Mass Actuator' (PMA) has been analyzed extensively as applied to active control of Large Space Structures (Ref. 7). Basically, it has been shown that damping in the actuator has a beneficial effect in controlling the vibrations of the space structure, but the stroke reversals impose some performance limits on the controller. In a parallel development, the electrical interactive effects have been studied by Rao (Ref. 8) when these actuators are used to excite a structure and measure its frequency response function. Essentially, Rao (Refs. 8,9) has shown that "glitches" (i.e. local variations in the amplitude of force transmitted) could be produced around the structural resonance frequency, and these glitches are influenced by electrical parameters. Review of previous literature (Ref. 8) on the use of exciters in the Experimental Modal Analysis area has established the importance of electromechanical interactive effects between the actuator and the structure as applied to stationary structures. Similar effects are bound to occur when these electromagnetic actuators are used to actively control the vibrations of rotating structure, such as that shown in Fig. 2. But this effect of electrical parameters seems to have not been investigated so far in the literature dealing with active control of rotating structures that use electromagnetic actuators.

The objective of this investigation is, therefore, to identify the electromechanical parameters and analyze their influence on the control force generated and transmitted into the rotor. To this end, we first list the major assumptions of the analysis. We then develop simple coupled equations of motion that include both the mechanical force balance (Newton's laws) and voltage balance (Kirchhoff's laws). We solve these coupled electromechanical equations and determine the control force generated by the actuator on the rotor. We express this control force as a function of nondimensional electromechanical parameters, and then discuss how mistuning between the actuator and the rotor could lead to a phenomenon called "Phase Glitches" around the critical speeds of the rotor.

4. ASSUMPTIONS OF THE ANALYSIS

Since our objective is to understand clearly how both the Mechanical as well as the Electrical parameters of the electromagnetic actuator affect the characteristics of the system, our mathematical model should be simple enough to bring out the essential nature and character of electromechanical interactions but not so complicated that the essence of this electro-mechanical interaction is lost in the complex structural modeling, controller analysis and higher order effects. With this philosophy in mind, we develop a simple mathematical model on the basis of the following assumptions:

1. The mechanical character of the electromagnetic actuator is described by its rigid armature mass m_a and its suspension stiffness k_a. This stiffness k_a includes the stiffness of suspension of the bearing housing as well as the stiffness of suspension of armature. Its mechanical motion is described by a small linear displacement x(t) along the axial

direction of the actuator. These assumptions imply that we neglect all other five degrees of rigid body motion of the armature. We also ignore its internal flexibility and the distributed nature of mass and stiffness of the armature. We also neglect the distributed character of suspension springs. Of particular importance is that we neglect the parasitic motions such as oil canning of the table, micromotions generated by the radiated sound, distortions induced by thermal unbalances, and helical coil effects due to the coils being spread along the length of the armature.

2. The electrical character of this actuator is described by a resistance R (which includes the resistance of coil and any other resistance in the circuit) and self inductance L. We assume that the electrical motion is described by the current i(t). These assumptions imply that we neglect the variations of these quantities with temperature and frequency. We also neglect other parasitic electrical effects like hysteretic losses, eddy currents, I^2R heat loss effects, magnetic saturation effects, internal capacitances and hysteretic losses.

3. We assume that the housing body of the actuator acts as an ideal, infinitely rigid ground that remains stationary while absorbing the reaction force generated in the coils. We further assume that this body does not transmit any part of the reaction force back into the rotating structure through the support platform.

4. We assume that the bearing housing is described with sufficient accuracy by a rigid mass m_b. We thus neglect its flexibility and assume that it acts as a 'simple support' to the rotating structure.

5. We assume that the rotating structure is described by a rigid mass m and complex stiffness k^*. This complex stiffness is expressed as $k^* = k\ (1 + j\eta)$ where η denotes the structural loss factor of the rotor. They could be its modal or effective values. Implicit in this assumption is that we are dealing with situations when rotor's behavior could be simplistically described by a single degree of freedom.

5. EQUATIONS OF MOTION

Based on the aforementioned assumptions, a simplified model that accounts for both mechanical as well as electrical behavior of the system is shown in Fig. 3. In this model, the electromagnetic actuator's armature is rigidly attached to the bearing housing (m_a denotes the combined effective mass of bearing housing and armature). This actuator's armature is driven by a signal source from a controller through the electrical circuit shown, where R and L denote the effective resistance and self-inductance of the coils. The back emf $k_B\dot{x}_a$ denotes the emf voltage induced into the electrical circuit due to the motion of the coil velocity $\dot{x}_a$ in the magnetic field. Here k_B denotes the back emf constant of proportionality that depends on the flux density. We assume that the energy conversion process is lossless.

The electromagnetic force generated in the coils of the armature is k_Bi. Some part of this force is 'expended' in overcoming the inertia of the bearing housing and armature mass; another part of it is transmitted into the ground through

the stiff suspension spring; only the remaining part is transmitted into the rotor to control its motion.

Newton's law applied to the mechanical part of the system yields the following equation of motion:

$$\begin{aligned} m\ddot{x} + k^{*}x + k_b(x - x_a) &= f \\ m_a\ddot{x} + k_a x_a + k_b(x_a - x) &= k_B i \end{aligned} \tag{1}$$

Similarly, the Kirchhoff's voltage law applied to the electrical circuit yields following voltage balance equation:

$$k_B \dot{x}_a + (R + L d_t) i = e(t) \tag{2}$$

Here e(t) denotes the signal voltage generated by the contoller and power amplifier combinations that drives the electrical circuit. This could, in practice, depend upon the sensed motion. In PD type of controller, when e(t) will be proportional to the motion x and velocity x of the rotor.

Since we want to focus our attention only on the interactive effects between the electromagnetic actuator and the rotor, we make following additional assumptions: (a) the stiffness of roller bearings is very large relative to that of the rotor so that motion of the bearing follows closely that of the rotor, and (b) the rotor is free of synchronous excitations such as unbalances. Under these assumptions, the combined system that consists of the rotor, bearing, and electromagnetic actuator simplifies to that shown in Fig. 4. The equation (2) governing the electrical part remains unaffected by these assumptions. The mechanical part of equation of motion as obtained by Newton's law is modified to:

$$(m + m_a)\ddot{x} + (k^{*} + k_a)x - k_B i = 0 \tag{3}$$

6. EFFECT OF ACTUATOR DYNAMICS ON CRITICAL SPEED

The preceding equation shows that the critical speed of the shaft now will be affected by the mass m_a and stiffness k_a of the actuator. Normally the mass of the armature is negligible. Hence the major parameters influencing the plant's critical speeds are (a) the mass of the bearing housing and, (b) the combined stiffness of the bearing and the armature suspension.

From Eq. (3), it is clear that the performance of the plant is degraded if the natural frequency of the bearing housing mass m_a that is sprung on the suspension stiffness k_a is smaller than the critical speed of the rotor. This condition leads to a reduction in the critical speed of the combined system that consists of rotor, bearing and the electromagnetic actuator (the plant).

Hence it is clear that proper matching of an electromagnetic actuator to the rotor requires that it satisfy the following condition:

$$\frac{k_a}{m_a} >> \frac{k}{m}$$

When this condition is satisfied, the critical speed of the total system will be higher than the critical speed of the rotor.

7. EFFECT OF ACTUATOR DYNAMICS ON CONTROL FORCE

From equation (3) it is clear that not all of the force ($k_B i$) that is generated in the coils of the actuator is utilized as control force on the rotor. Part of this force is used to overcome the inertia of the bearing housing and armature masses m_a, while part of it is transmitted through the suspension stiffness into the ground. Thus the control force exerted on the rotor is

$$f = k_B i - m_a \ddot{x} - k_a x \tag{4}$$

We assume uniform sinusoidal voltage excitation, $e = e_o \cos \omega t$, and solve equations (2) and (3) for resulting displacement $x = x_o \cos \omega t$ and currents $i = i_o \cos \omega t$ where x_o and i_o denotes complex amplitudes. We substitute these amplitudes into (4). We thus arrive at the following expression for the control force as a function of the electromechanical actuator parameters:

$$f_o = \frac{k^* + k_a}{k^*} \frac{(k^* - \omega^2 m) R}{\{[k^* + k_a - \omega^2 (m + m_a)][R + j\omega L] + j\omega k_B^2\}} \tag{5a}$$

Here f_c denotes the force that would be transmitted into the rotor if it were to be stationary and non-rotating (i.e., $\omega = o$).

8. IDENTIFICATION OF ELECTROMECHANICAL PARAMETERS OF ACTUATOR

Assuming that the bearing stiffness k_a is negligible relative to the structure's stiffness, the preceding expression for control force could be expressed in nondimensional form as:

$$f_o = \frac{(1 - \Omega^2 + j\eta)}{\{(1 - a\Omega^2 + j\eta)(1 + j 2\zeta\Omega/K) + j 2\zeta\Omega\}} \tag{5b}$$

where the excitation frequency parameter that governs the control force is

$$\Omega = \frac{\omega}{\omega_N} = \frac{\text{excitation frequency}}{\text{critical speed } \sqrt{k/m}}$$

The mechanical parameters influencing the control force are the armature mass parameter, which is defined by

$$M_a = \frac{m_a}{m} = \frac{\text{mass of armature + bearing}}{\text{mass of rotor}}$$

The electrical parameters that influence the control force can be expressed as equivalent mechanical damping and stiffness quantities. They are presented herein as ratios of corresponding rotor's critical damping and stiffness quantities, and are

$$K = \frac{k_B^2/L}{k} = \frac{\text{electircal stiffness of actuator}}{\text{mechanical stiffness of rotor}}$$

$$\mathcal{J} = \frac{k_B^2/R}{2\sqrt{km}} = \frac{\text{electrical damping of actuator}}{\text{critical damping of the rotor}} \qquad (6)$$

Further, the quantity a denotes $(1 + M_a)$

9. THE PHENOMENON OF "PHASE GLITCHES"

The importance of mechanical parameters of the actuator has been recognized and analyzed by Zimmerman (Ref. 7) and others in the literature dealing with space structures. However, as shown above, there are electrical parameters that need to be considered before a proper integration between the actuator and the rotor is achieved. Since the mechanical effects have already been well investigated, we analyze now only the effect of electrical parameters of the actuator on the control force around the critical speed.

Fig. 5 shows the variation of amplitude of control force as a function of electrical resistance damping parameter ζ. As can be expected, this figure shows that the control force reaches a maximum value at a frequency called peak frequency (P) which corresponds to the pole in equation (5). This peak frequency is associated thus with the resonance of the total system that consists of the actuator, its electrical circuit, the bearing housing and the rotor. Immediately after this, the force falls sharply to a minimum value at a frequency called notch frequency (N), that corresponds to the zero of Eq. (5). This notch frequency refers to the critical speed of the rotor. This figure also shows that a lower coil resistance (R) increases the electrical damping; this in turn reduces the control force transmitted into the rotor.

Fig. 6 shows how the coil resistance influences the phase of the control force. This diagram shows that the single peak-notch (P-N) present in the previous force-amplitude diagram could possibly be split into two peak-notches on the force-phase diagram. Thus, depending on the value of coil resistance, the phase could show one sharp drop and rise around the peak frequency; or it could show an additional sharp drop and arise around the Notch frequency. These sharp variations in the phase are called herein the "Phase Glitches." These phase glitches are undesirable, and could cause mistuning between the combined

controller circuit and actuator and rotor plant electromechanical system. These possible mistuning effects should be taken into account by future designs of controllers.

The effect of coil inductance on the amplitude of control force is also shown in Fig. 7. As expected, a reduction in the inductance of the coil increases the electrical contribution to the stiffness of the suspension. This increased stiffness implies siphoning of an increased part of force generated by the coils into the suspension, and hence less force is transmitted into the rotor. This results in a reduction in the peak value of the control force as shown in Fig. 7.

Fig. 8 shows the effect of coil inductance on the phase of the control force. As observed above, the phase glitch is present around the critical speed even when inductance is varied. These phase glitches also need to be taken into account in future design of controllers and power amplifiers.

The simplified analysis presented herein has the major aim of emphasizing the fact that a mechanical designer of a magnetic bearing can ill-afford to ignore the electromechanical interactive effects of the actuator. These interactive effects are generated because of electromechanical coupling in the medium that converts the electrical signal into mechanical force. Various approaches are available to address these electromechanical coupling issues and they will be the subject matter of future investigations.

CONCLUSIONS

In this paper we have discussed the conceptual approaches of active control of a rotating shaft's vibrations using electromagnetic actuators. We outlined the basic assumptions normally made in modeling the electrodynamic transduction of the actuator and developed simple equations of motion of a rotor controlled by the electrodynamic actuator through a P-D type feedback. We then derived expression for the control force transmitted into the rotor through the bearing. We showed that this control force displays sharp fluctuations in the phase around the resonance frequency. These fluctuations, called "Phase Glitches," are undesirable. They need to be taken into account in future designs of controllers that use electromagnetic actuators.

REFERENCES

1. Earnshaw, S., "On the Nature of Molecular Forces Which Regulate The Construction of Luminiferous Ether," Trans. Cambridge Phil. Soc., Vol. 7, 1842, pp. 97-112.

2. Geary, P.J., "Magnetic and Electric Suspension, 1964 Survey of Instruments, Part 6," SIRA Research Report No. R314, British Scientific Instrument Res. Assoc., 1964.

3. Ulbrich, H., "Control of Flexible Rotors by Active Elements," in Rotating Machinery Dynamics, ASME Publ. No. H0400, 1987.

4. Ulbrich, H., "Dynamik and Regelung von Rotorsystemen," Fortschr. Ber., VDI, Reihe II, Nr 86, 1986.

5. Nonami, K., "Vibration Control of Rotor Shaft Systems by Active Control Bearings," ASME Paper No. 85-DET-126, 1985.

6. Adams, M.L., Private Communication, 1988.

7. Zimmerman, D.C., and Inman, D.J., "Actuator/Structure Interactions," Presented at the 2nd NASA/DOE Conf. on Control-Structure Interaction, Colorado Springs, Oct. 1987.

8. Rao, D.K., "On The Glitches In The Force Transmitted By An Electrodynamic Exciter To A Structure," Proc. 58th Shock and Vibration Symposium, Huntsville, Ala., Oct. 13-15, 1987, pp. 1142-1150.

9. Rao, D.K., "Electrodynamic Interaction Between A Resonating Structure And An Exciter," Proc. 5th Int. Conf. on Modal Analysis, London, April 6-9, 1987, pp. 245-255.

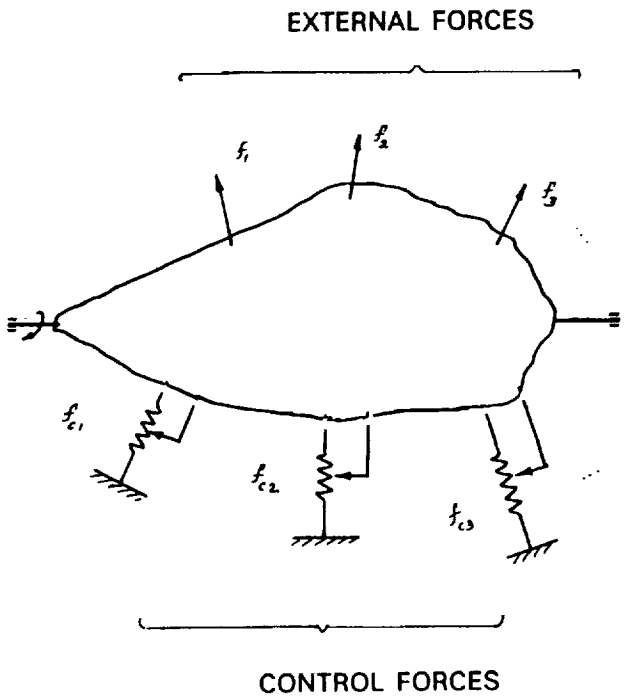

Figure 1. General magnetic suspension problem involves study of response characteristics of an unconstrained structure under external forces and control forces.

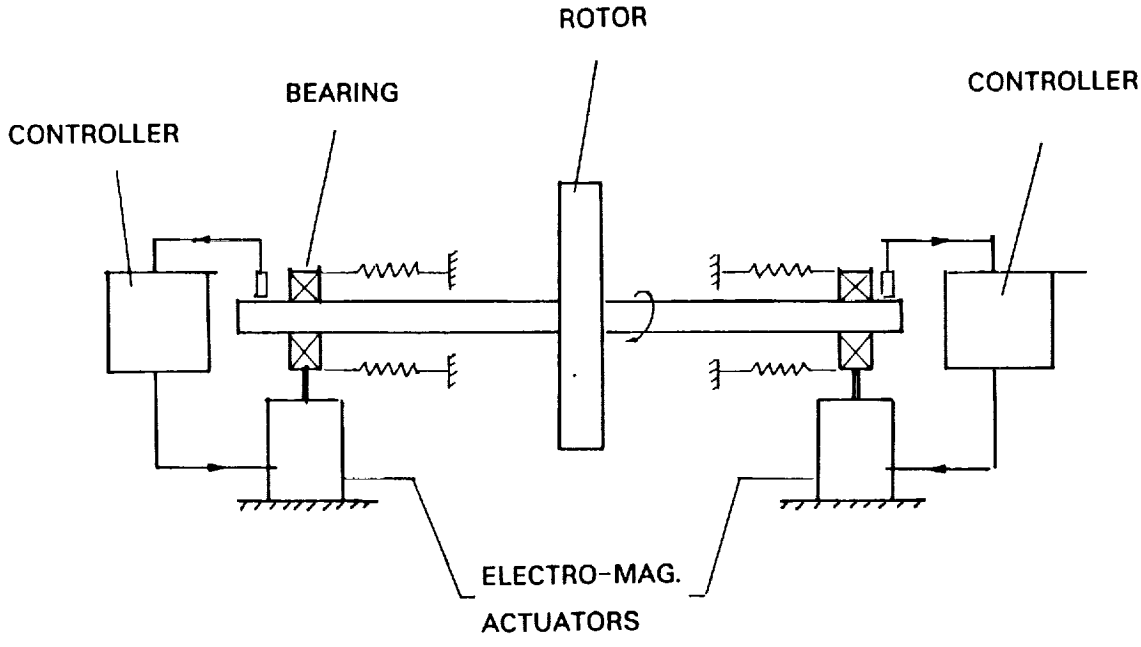

Figure 2. Concept of using electromagnetic actuators to exert control forces on the bearing housing of a rotating shaft.

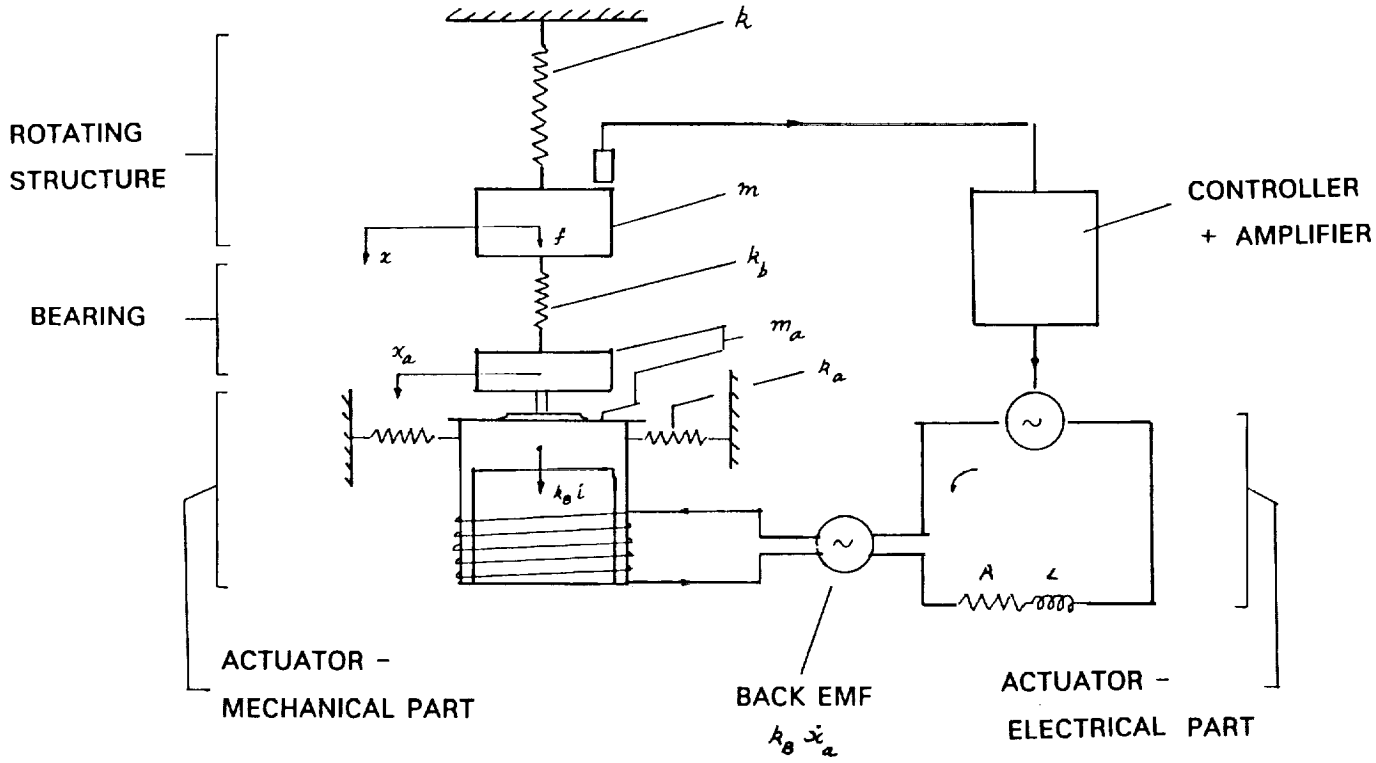

Figure 3. Simplified electromechanical model of an electromagnetic actuator applying control force on the bearing housing of a rotating shaft.

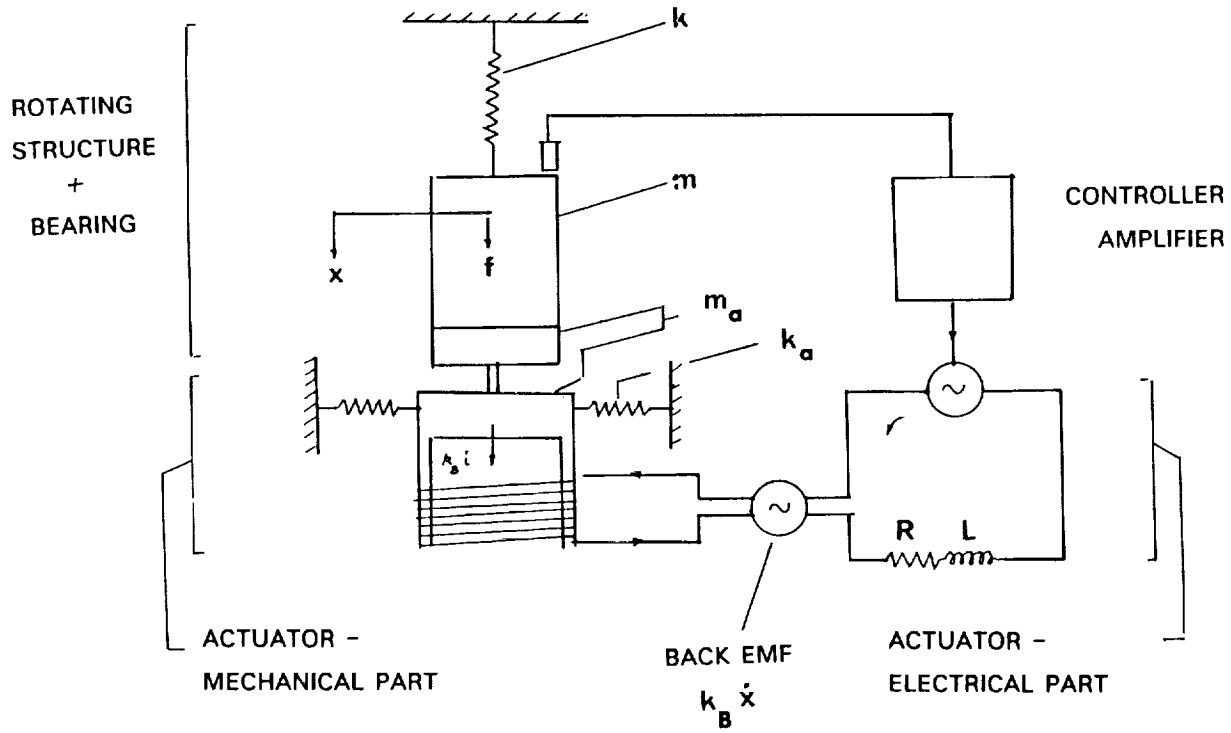

Figure 4. Basic electromechanical model of electromagnetic actuator + rotating structure.

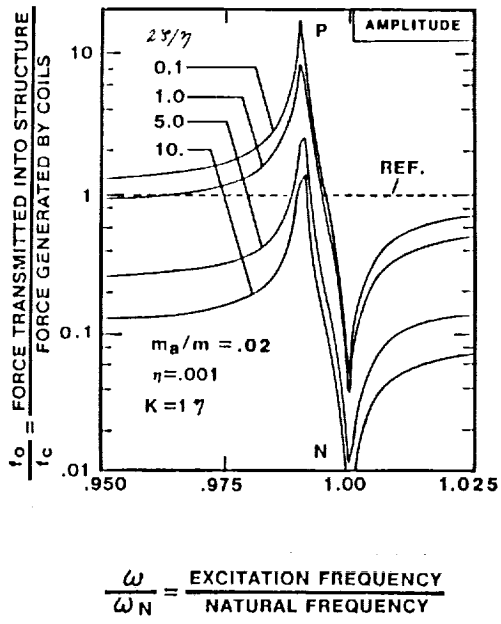

Figure 5. Effect of coil resistance on the amplitude of control force.

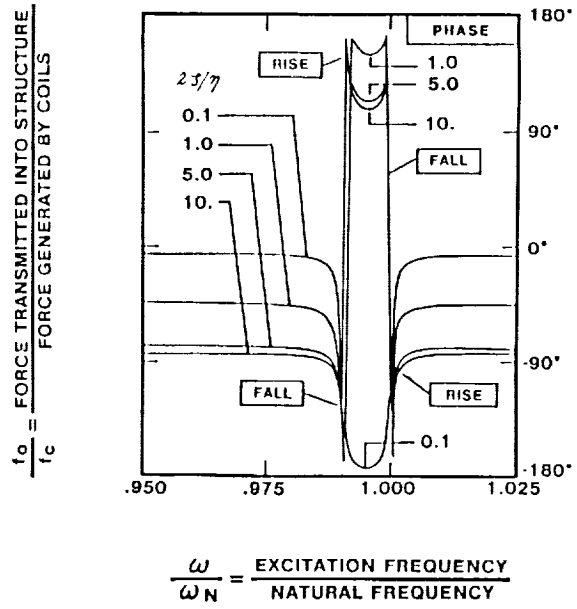

Figure 6. Effect of coil resistance on the phase of control force.

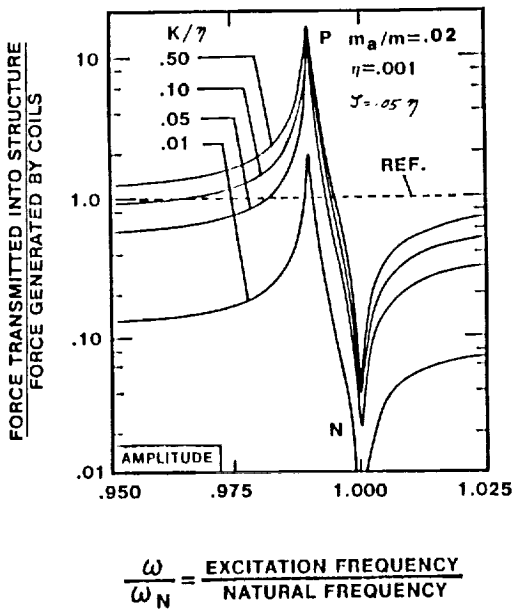

Figure 7. Effect of coil inductance on the amplitude of control force.

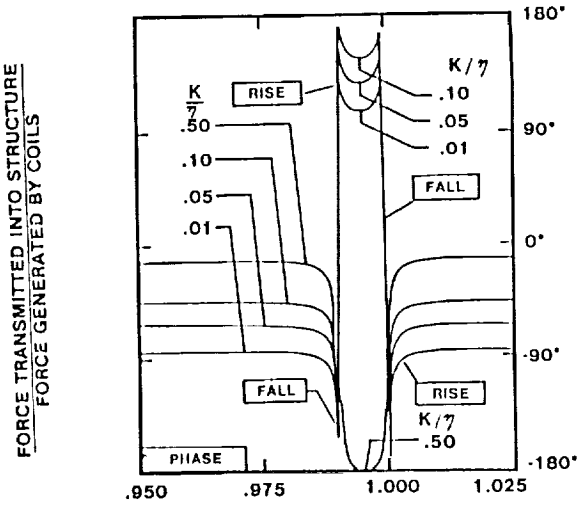

Figure 8. Effect of coil inductance on the phase of control force.

omit

Design Considerations for Ultra-Precision Magnetic Bearing Supported Slides

Alexander H. Slocum, Massachusetts Institute of Technology

David B. Eisenhaure, SatCon Technology Corporation

DESIGN CONSIDERATIONS FOR ULTRA-PRECISION MAGNETIC BEARING SUPPORTED SLIDES[1]

Alexander H. Slocum
Massachusetts Institute of Technology
Cambridge Massachusetts

David B. Eisenhaure
SatCon Technology Corporation
Cambridge Massachusetts

SUMMARY

This paper describes development plans for a prototype servo-controlled machine with 1 Ångstrom resolution of linear motion and 50 mm range of travel. Two such devices could then be combined to produce a two dimensional machine for probing large planar objects with atomic resolution, the Ångstrom Resolution Measuring Machine (ÅRMM).

INTRODUCTION

Several Ångstrom resolution devices currently exist. Scanning electron microscopes (STMs) are flexural linkage structures with Ångstrom resolution and range of motion only on the order of one micron [1]. Because of its small range of motion, an STM can be made small enough to make it virtually immune to thermal and vibration problems that would plague a machine with centimeter range of motion. Researchers at the National Physical Laboratories (NPL) in England have built a linear stage with 1 Å smoothness of motion over a range of centimeters. The stage uses Rulon™ pads as bearings that are arranged kinematically on a Vee way [2]. However, questions regarding long term stability of the plastic bearings and controllability in the presence of sliding friction remain unanswered. Current designs of other precision machines such as wafer steppers and diamond turning machines [3] are principally performance limited by mechanical contact between moving parts, misalignment between actuators and bearings, bearing stability, and attainable temperature control [4,5,6]. To help overcome these problems, coarse-fine positioning system have evolved as shown in Figure 1. Although they can

[1] This work was supported by the Center for Manufacturing Engineering of the National Bureau of Standards.

be effective, they are mechanically cumbersome and are intrinsically difficult to control. The design envisioned for the ÅRMM would address these issues by way of its kinematic magnetic bearing design.

The design of the ÅRMM evolved into the crossed axis design shown in Figures 2-4. A two axis version only requires fabrication and installation of a "mirror image" of the first axis. The resultant two axis machine would have a spherical or cubic shape to maximize structural efficiency with respect to stiffness and thermal stability. The axis' moving structural members would be mirror finished and be used as reflectors for the laser interferometers that provide position feedback signals to magnetic bearings[2]. The magnetic bearing actuators would be configured kinematically: Five magnetic bearing actuators positioned to control five degrees-of-freedom.

TEMPERATURE CONTROL

Controlling system temperature without introducing large gradients could be achieved by using constant or low power devices[3], operating the system at a steady thermal state, and configuring the system as a sphere hanging inside another temperature controlled evacuated sphere. The two spheres would be radiantly coupled with the outer sphere cooled by a high velocity coolant source[4].

Temperature control by radiant coupling can be effective and is not as prone to the formation of gradients as convective cooling is. Consider the heat transferred between two bodies by radiation:

$$Q_{net} = F_{1\text{-}2}\,\sigma A_1(T_1^4\text{-}T_2^4) \qquad (1)$$

If 10 watts of waste heat are to be removed from 1.0 or 0.5m diameter spheres, and temperature is to be maintained at 20°C (293 °K), then Equation 1 can be used to determine that corresponding outer spheres must be kept at 19.440407°C and 17.742068°C respectively.

Assuming steady state conditions, small deviations δT (less than 0.1°C) in the temperature of the outer sphere will affect the amount of power retained by the inner spheres by:

$$\Delta Q_{watts\ @\ 0.25m,\ 17.742068\ C} = 4.378*\delta T \qquad (2)$$

$$\Delta Q_{watts\ @\ 0.5m,\ 19.440407\ C} = 17.820*\delta T \qquad (3)$$

---

2 The axis would be designed so servo forces from the bearings and the weight of the part caused less than 0.1 Å deformation.

3 For example, magnetic bearings with heaters, piezoelectric actuators, and laser interferometers.

4 The inner sphere cannot be cooled directly because the high velocities needed to eliminate gradients also generate turbulence and vibration.

If deviations in the outer sphere temperature occur with a time constant much faster than that of the inner sphere, then the thermal mass of the inner sphere will prevent it from being affected by these variations.

In order to make a first order evaluation of various materials for the ÅRMM structure, consider the time it takes the inner sphere (δT_i) to reach a new equilibrium temperature given a step change in the outer sphere temperature. Assume that the new equilibrium temperature is $T_{inominal} + \delta T_i$, where δT_i is the change in temperature that causes 0.1Å thermal growth in a 0.25m segment of the structure. Given a change in the outer sphere temperature of δT_o, then to the first order the time it takes the inner sphere to change its temperature by δT_i via radiant coupling is

$$t = \frac{R_1 C_p \delta T_i}{3F_{1-2}\sigma[T_{inom}^4 - T_{onom}^4 - (T_{inom}+\delta T_i)^4 + (T_{onom}+\delta T_o)^4]} \quad (4)$$

Table 1 illustrates this change for various candidate materials. Based on the time evaluation, Zerodur or Invar should be used. If the thermal diffusivity is considered, a material such as copper should be used in order to minimize gradients[5].

By tuning power dissipation and the equivalent black body view factor with the size of the sphere, it may be possible to utilize an inexpensive accurate temperature control process (i.e. a phase change process) for controlling the inner sphere's temperature. For example, assume the outer sphere is contained in an ice water bath and the temperature of the outer sphere is fine tuned with an electric heater. If the inner sphere still needs to dissipate 10 Watts of power, the diameter of the inner sphere should be about 0.1758 m if the spheres still behave like black bodies.

This preliminary analysis gives a good indication of where to start the design process, although it does not include transient affects nor does it model hot spots within the sphere. Hot spots can be prevented if the structure is suitably instrumented and zone temperature control is used.

BEARING DESIGN

The properties desirable in a bearing for the ÅRMM include: 1) repeatability, 2) low friction, and 3) high stiffness. Only magnetic bearings have the potential to meet these requirements, *and allow for easy adjustment of performance after fabrication.*

[5] Zerodur, Invar, Copper, Aluminum, Beryllium and Cast Iron are all known to have very stable forms [7].

A simple magnetic bearing control system is shown in Figure 5 and is characterized by the gain (stiffness) which relates errors in position to applied magnetic force and the bandwidth which indicates the frequency range over which the magnetic force may be applied to reject disturbance forces. The magnets have negative spring constants which lead to a minimum required system bandwidth for stability of about 10 Hz for many suspensions. Maximum achievable bandwidths range from 100 Hz for a simple attractive-type system to 40 KHz or higher for systems implemented with ferrite or voice coil actuators.

At low frequencies, performance is determined almost completely by the ability of the controller to cancel disturbances. The primary control system parameter affecting disturbance cancellation is the controller gain which determines suspension stiffness. The higher the suspension stiffness, the greater the ability to reject force disturbances. Depending on the nature of the source, at high frequencies, the disturbance forces are generally absorbed by the platten's inertia and internal damping characteristics.

Figures 6 and 7 show the achievable resolution at various disturbance force levels as a function of suspension stiffness and bandwidth, respectively. The disturbance force represented is modeled as a broad band disturbance over the entire frequency range of interest. For the simple control system considered, the bandwidth is equal to the natural frequency of the system.

The principal disturbance forces acting on the slide in a laboratory environment are caused by air currents, acoustic disturbances, ground plane motion, and linear actuator error motions. Figures 8 and 9 show the disturbance forces for impinging air flow and acoustic disturbances respectively. Figure 10 shows the disturbance forces as a function of base motion for various suspension gaps. A comparison of Figures 8 through 10 shows that base motion is the largest single contributor to slide disturbance force[6]. If necessary, the sensitivity to base motion could be reduced by one order of magnitude by incorporating magnetic flux feedback in the control loop and by two orders of magnitude by employing voice coil-type actuators. Even without these changes, the total disturbance force level should be kept below about 0.01 N (0.005 lb).

Capacitance probes or laser interferometers can be used to make ultra precision measurements of the magnetic bearing gap. Regardless of

[6] The current state of the art of vibration control centers on active (servo) control of vibrations [8,9,10,11], and commercially available servo-controlled systems capable of keeping table motion amplitudes below 100Å @ 10 Hz have recently become available from Barry Control and Newport Corp.

the system used, however, *a through the bearing measurement method* must be used. This maintains accuracy of the kinematic model and provides for checking measurement closure should direct measurement of the position and orientation of a region of the slide also be made.

If a laser interferometer system is used as a position feedback sensor, as shown in Figure 11, then the platten must be polished to optical quality. The cost of a laser interferometric measurement system is on the order of $10,000 per measurement axis. It is envisioned that in the near future the resolution of differential plane mirror interferometers will approach the one Ångstrom level[7]. Hence a single magnetic bearing supported slide would require $50,000 worth of laser interferometers.

For substantially less cost, on the order of $3,000 per axis, capacitance probes, also shown in Figure 11, could be used. They have the advantage of not requiring the surface of the slide to be optically polished. The finite area of their measuring tips creates an averaging effect which reduces the effect of surface finish errors on the gap measurement. However, on the Ångstrom level, long term drift problems may render the probes inadequate for continuous operation of the system over a period of days.

ACTUATORS

There are numerous actuator possibilities for the ÅRMM, especially if one considers combinations of macro and micro motion systems. However, because of the complexity of a coarse-fine actuator system, only linear electric motors, and piezoelectric inchworm translators are considered here.

Linear electric motors have had a practical resolution limit on the order of 10 microinches, based on the fact that mechanical coupling and thermal errors in existing systems begin to dominate at this resolution. If a kinematic transmission system could filter out thermal and mechanical errors from a linear motor, then advanced measurement and control techniques may increase their applicability to ultra precision machines. Typically, linear motors are controlled by current feedback from the motor and position feedback of the slide. However, current feedback can only provide clean motor force resolution on the order of 1/4,096 - 1/65,536. Also for current feedback to be useful, the motor needs to be rigidly coupled to the slide, but this permits mechanical and thermal errors to be transmitted to the slide. Instead of current feedback from the motor, the position of both ends of the transmission system should be measured with a laser interferometer.

[7] Discussions with Carl Zanoni, VP. Eng., Zygo Corp., Middlefield, Connecticut.

Piezoelectric inchworm devices are high resolution actuators with large ranges of motion. Their resolution is a function of the increment of each step, which can be on the order of 10^{-11} meters, and how the device clamps between steps; a jerky clamping action will induce errors. Currently available piezoelectric inchworm actuators typically have a thick force transmission bar which a circumferential piezoelectric element clamps onto. Unfortunately the bar also transmits lateral "noise" forces from the actuator to the platten, and the bar can never be aligned perfectly with the platten. Typical axial resolution is on the order of 50 Ångstroms, although lateral errors can amount to microns. Cost of this system is on the order of $1,700, excluding a precision power supply[8,9].

As shown schematically in Figure 12, the wire-piezo inchworm actuator designed for the ÅRMM can deliver 0.1 Ångstrom axial resolution with less than 0.1 Ångstrom lateral error motion. Cost to manufacture this system is on the order of $6,000, excluding a precision power supply.

Design of a control system to achieve smooth jerk-free motion from any inchworm actuator is potentially very difficult. On the other hand, the advantages offered by piezoelectric inchworm devices include essentially zero thermal energy generation and virtually infinite resolution.

KINEMATIC TRANSMISSION SYSTEMS

The purpose of a kinematic transmission system is to negate the effect of non-axial motion components on the motion of a linear slide[10] by allowing members to move (i.e. slide or deflect) in non-sensitive directions. There are two principal types of kinematic transmissions: active and passive. Active systems are those that use low or zero friction bearings to accomodate errors while maintaining high axial stiffness; however, these would be too complex for use on the ÅRMM. Passive systems, on the other hand, use flexural elements to accomodate error motions, and include beam, membrane, and wire type elements as shown in Figure 13.

A wire transmission, as shown in Figure 13, is the simplest form of a kinematic transmission system and can be accurately modeled as a simple linear spring. The axial stiffness of the wire is a function of the cross sectional area A of the wire, the length of the wire ℓ, and Young's Modulus of elasticity, E: $K_{axial} = AE/\ell$. The lateral stiffness of the wire transmission, which should be minimal, is a function of the tension in the wire, the

8 New Micropositioning Products. Burleigh Instruments, Fisher, NY.

9 Physik Instrumente: The PI System Catalog. Physik Instrumente (PI) GmbH & Co. West Germany. 8/86.

10 It should also help to reduce the amount of heat transfer from the actuator to the slide via its thin cross section.

lateral error motion ε, and the length ℓ of the wire: $K_{lateral} = 2T/\ell$. By measuring the lateral motion of the wire, the ability of the transmission system to prevent non-axial forces from acting on the slide can be determined.

Typically, the tension in the wire will be on the order of 4-5N (1.0 lb), just enough to keep it taught and prevent backlash. The error motion the wire may be required to compensate for could be as large as 25μm (0.001 in), and the length of the wire on the order of 12-13 cm (5 in). With these parameters, the lateral force transmitted to the slide is only on the order of 0.0018N (0.0004 lb). If the slide has an axial stiffness on the order of 180 x 10^6 N/m (10^6 lb/in), the resultant error motion will only be on the order of 0.1 Ångstroms. However, in order for the linearized expression for lateral stiffness to be valid, the length to diameter ratio for the wire should be on the order of 500:1. Thus the axial stiffness is limited to: $K_{axial} = \pi \ell E/2.5 \times 10^5$. For the previous example, K_{axial} = 330KN/m (1900 lb/in). In order to increase the apparent stiffness, software based control techniques are needed.

Much work has been done on control of flexible systems in an effort to control more degrees of freedom than are directly measured. For example, controlling mode shapes of large flexible structures with application to robotic and space structures [12,13]. Subsequent work focused on controlling motions of cantilevered robotic structures with the assumption that only position feedback from the joints was available. The essence of this work consisted of using analysis of joint torques to predict and correct for deformations of the robot's structural members [14,15,16,17]. This is a similar problem to that faced by kinematic transmissions; however, these control techniques could not assume the robot had end-point feedback and thus had to rely on the use of observers. The accuracy of these techniques was only a few percent which is not acceptable for precision applications. Research has also been directed at increasing the performance of monolithic piezoelectric actuator-bearing combinations, similar to ones used on STMs, but it has not addressed the issue of using the actuators in combination with very compliant flexural couplings [18, 19].

Figure 14 shows a first-order model of a linear slide, actuator, and flexural kinematic transmission system. The actuator is modeled as a force source that acts on the damped mass of the actuator and the transmission. The transmission is the dominant spring in the system which connects the motor (mass) to the slide, which is also modeled as a mass and damper. The position of the slide cannot be controlled directly as the force output from the actuator is divided amongst accelerating the motor mass, overcoming friction, and deforming the kinematic transmission spring. The

only way to accurately determine the force in the spring (transmission) with high resolution is to measure the deflection of the spring (transmission) using a laser interferometer or a capacitance probe.

SENSOR SYSTEMS

There are four principal sensor systems that need to be designed for the ÅRMM:

1) Environmental. Temperature, pressure, and humidity all need to be monitored to enable the environment to be controlled to ensure accuracy of the machine. It is anticipated that temperature control good to 0.01-0.001°C/cm will be required for the ÅRMM. In order to achieve such high resolution and accuracy, a Mach-Zehnder interferometer will probably be used.

2) Large range of motion, high resolution. For example, the axial position of the platten has to be measured with a resolution on the order of 1.0-0.1Å over a range of motion on the order of 50 mm. Differential plane mirror interferometers will probably be used for this application. Existing technology allows for resolution to $\lambda/512$ (about 10 Ångstroms).

3) Small range of motion, ultra-high resolution. For example, the lateral position of the platten, the magnetic bearing gap, needs to be measured with a resolution of 0.1-0.01Å over a range of motion on the order of 1μm. A Fabry-Perot interferometer with the capability to resolve to $\lambda/10^6$ could even be used for this type of application where one of the reference optics is moving orthogonal to the distance being measured.

4) Measuring location of atoms. For example, scanning tunneling probes need to be adapted for use on the ÅRMM. Existing technology developed for the STM could be used; however, a single probe would take many thousands of years to map a 50 mm diameter specimen. Thus multiple probe techniques would be needed.

MOTION CONTROL SYSTEM

The resolution of the signal sent by the controller to the magnetic bearing affects the total force acting on the platten. If ηx100% of the mass M of the platten is supported against gravity by permanent magnets or a constant voltage supplied to the windings, then the downward acceleration of the platten will be $(1 - \eta)Mg$. If we assume that the magnetic bearings must be able to exert at least twice the force required to levitate the mass (sans force provided by permanent magnets), in the time t between servo update times with an N bit ADC, the platten will fall an amount δ:

$$\delta = \frac{(1 - \eta)gt^2}{2^{N-2}} \qquad (5)$$

If $\eta = 0.9$, $\delta = 0.1$Å, and $N = 14$, then the maximum servo update time is 204 microseconds; and if a 32 bit DSP is dedicated to each bearing, these times are achievable. Even with a 14 bit ADC, which generally precludes the occurrence of electrical noise problems[11], 0.1Å resolution motion control is feasible.

In order to achieve even higher resolutions, superconducting coils powered by a ultra-high-accuracy microwave-superconducting-Josephson junction power supply could be used. This type of power supply has been shown by NBS researchers to produce voltages with part-per-billion resolution. Using available superconductors that operate at liquid nitrogen temperatures would require the bearings to be wrapped in an insulating blanket, liquid nitrogen passed around the coils, and an electric heater used to balance the heatflow into the structure.

CONCLUDING REMARKS

The tools for the development of the ÅRMM currently exist, and it would take about two years to construct a single axis prototype. By careful design, resolution will be increased not by a change in the mechanical design, but by advances and changes in sensor, control system, and control algorithm designs. Perhaps with the introduction of "warm" (20-30°C) superconductor technologies, new sensors and devices will become available that will push resolution limits even further.

REFERENCES

[1] G. Binnig and H. Rohrer, "Scanning Electron Microscopy", Helvitica Physica Acta, Vol. 55 (1982) pp 726-735.

[2] Lindsey, K. and Steuart, P. "NPL Nanosurf 2: A Sub-nanometer Accuracy Stylus-based Surface Texture and Profile Measuring System with a Wide Range and Low Environmental Susceptibility," 4th Int. Precision Engr. Sem. Cransfield Inst. of Tech., U.K. 11-14 May 1987 p15.

[3] R. Donaldson, S. Patterson, "Design and Construction of a Large Vertical-Axis Diamond Turning Machine", paper presented at SPIE's 27th Annual International Technical Symposium and Instrument Display, August 21-26, 1983.

---

[11] High frequency electrical noise would be damped out by the inductance of the coils and the mass of the platten. Low frequency noise would be compensated for by the closed loop position servo.

[4] W. Moore, Foundations of Mechanical Accuracy. The Moore Special Tool Company, Bridgeport, CT, 1970, (e.g. pp 24-28).
[5] J. Biesterbos et al, " A Submicron I-Line Wafer Stepper", Solid State Technology, Feb. 1987, pp 73 - 76.
[6] M. Nuhn, S. Yao, B. Avrit, "I-Line Wafer Stepper Used for Low Volume Production of 0.5 Micrometer GaAs Integrated Circuits", Solid State Technology, Feb. 1987, pp 81 - 84.
[7] J. Berthold, S. Jacobs, M. Norton, "Dimensional Stability of Fused Silica, Invar, and Several Ultra-low Thermal Expansion Materials:, Metrologia 13, pp 9-16, 1977
[8] P. R. Saulson, "Vibration Isolation for Broadband Gravitational Antennas", Rev. Sci. Instrum., Vol. 55 No. 8, August 1984, pp 1315-1320.
[9] J.C. Dankowski, "Vibration-Isolation Bench for testing in Vacuum" NASA Tech Briefs, Summer 1983, p 421.
[10] J. Sandercock et al, "A Dynamic Antivibration Support", RCA Review, Vol. 46, March 1985, pp 70 - 80.
[11] R.L. Rinker, and J.E. Faller, "'Super Spring' - A Long Period Vibration Isolator", Precis. Meas. and Fund. Const., Natl. Bur. Stds. (US) Spec. Publ. 617 (1984), pp 411 - 417.
[12] W.J. Book et al, "Feedback Control of Two-Beam Two-Joint System with Distributed Flexibility," ASME Jou. Dynamic Sys. Meas. and Con. Dec. 1975, pp 424-431.
[13] R.C. Burrows, T.P. Adams, "Control of a Flexibly Mounted Stabilized Platform," ASME Jou. Dynamic Sys. Meas. and Con. Sept. 1977, pp 174-182.
[14] R. Luh et al, "Resolved Acceleration Control of Mechanical manipulators", IEEE Tans. Auto. Cont., Vol. AC-25, 1980, pp 468-474.
[15] J. Slotine and S. Sastry, "Tracking Control of Nonlinear Systems using sliding surfaces with applications to robot manipulators", Int. Jou. Cont., Vol. 38 1983, pp 465-492.
[16] L. Sweet and M. Good, "Re-definition of the Robot Motion Control Problem: Effects of Plant Dynamics, Drive Systems Constraints, and User Requirements", Proc. 23rd IEEE Conf. Decis. and Cont., Las Vegas Nev., Dec. 1984, pp 724-731.
[17] E. Rivin, "Effective Rigidity of Robot Structure: Analysis and Enhancement", Proc. 1985 Amer. Cont. Conf., Boston, Mass., June 1985.
[18] P.D. Atherton, et al, "An Infinitely Stiff Very High Precision Actuator, Proc. of the 1987 Precision Engineering Conference, Cranfield UK.
[19] J.R. Leteurte, "Capacitance Based Sensing and Servo Control to Angstrom Resolution", Proc. of the 1987 Precision Engineering Conference, Cranfield UK.

Table 1 Properties of various materials and relative time for temperature change in a 1m diameter inner sphere caused by disturbance of 0.001°C in the outer temperature control envelope to cause 0.1Å thermal expansion in a 0.25m segment[1]

Material	ρ (kg/m^3)	E (Gpa)	$\alpha_{expansion}$ ($\mu m/m\text{-}^oK$)	K ($w/m\text{-}^oK$)	C_p ($J/Kg\text{-}^oK$)	t (secs)	ΔT ($^oCx10^{-6}$)	α ($m^2/sx10^{-6}$)
Aluminum	2707	69	22.0	231	900	130	1.8	94.8
Beryllium	1848	275	11.6	190	1,886	352	3.4	54.5
Copper	8954	115	17.0	398	384	237	2.3	116
Grey cast iron	7200	80	11.8	52	420	300	3.4	17.2
Invar	8000	150	0.9	11	515	5533	44.4	2.7
Lead	11373	14	26.5	35	130	65	1.5	23.7
Zerodur	2550	90	0.15	6	821	22,733	266	2.9

[1]For the small temperature excursions considered here, the time t is proportional to the diameter of the sphere and inversely proportional to the temperature excursion of the outer sphere.

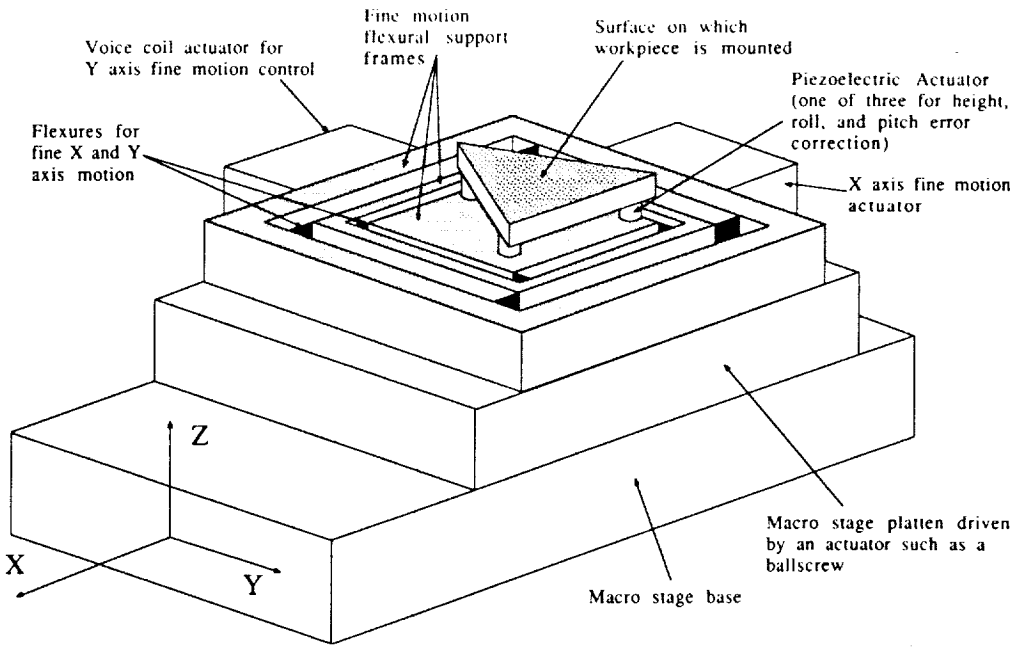

Figure 1 Example of a coarse-fine positioning system used to correct for slide errors caused by errors in slide geometry and forces caused by a misaligned actuator

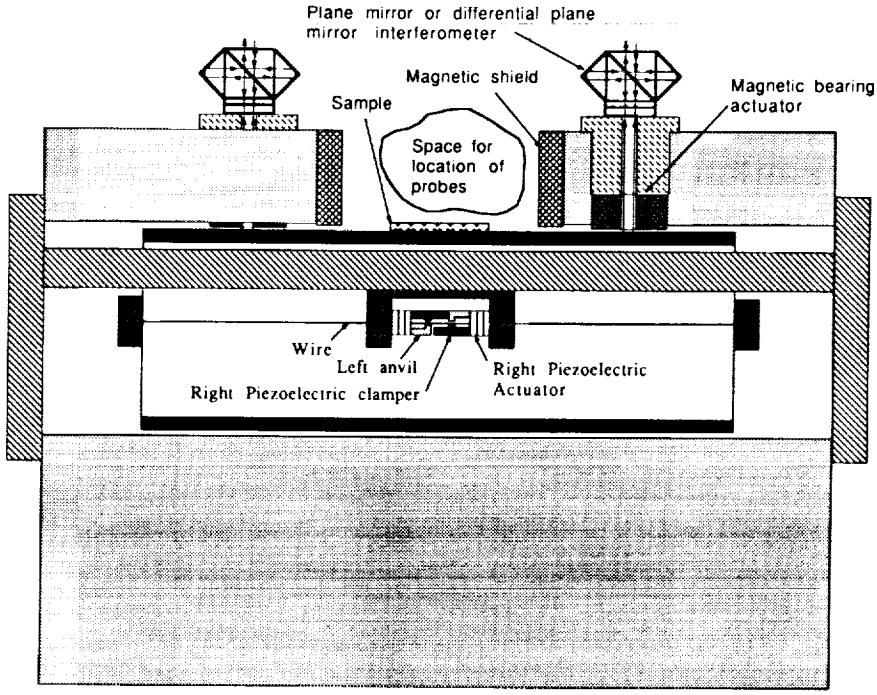

Figure 2 Cutaway side view of Atomic Resolution Measuring Machine (ARMM)

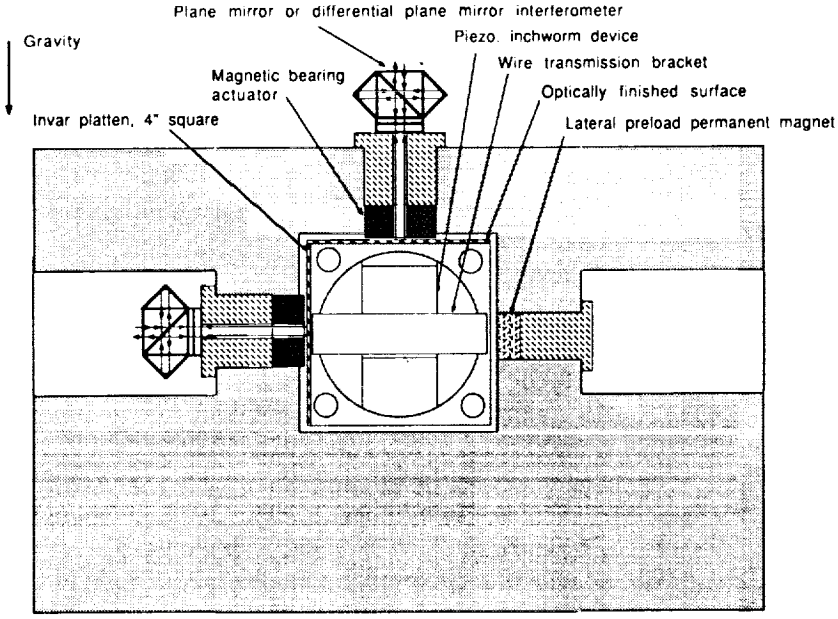

Figure 3 Cutaway right end view of Atomic Resolution Measuring Machine (ARMM)

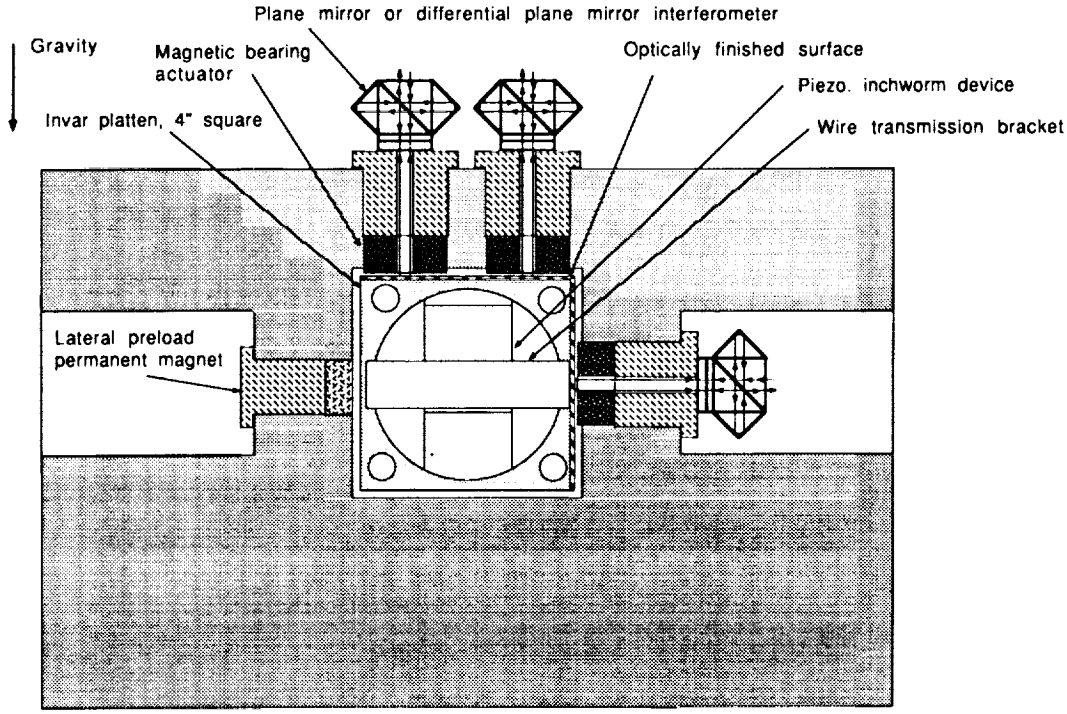

Figure 4 Cutaway left end view of Atomic Resolution Measuring Machine (ARMM)

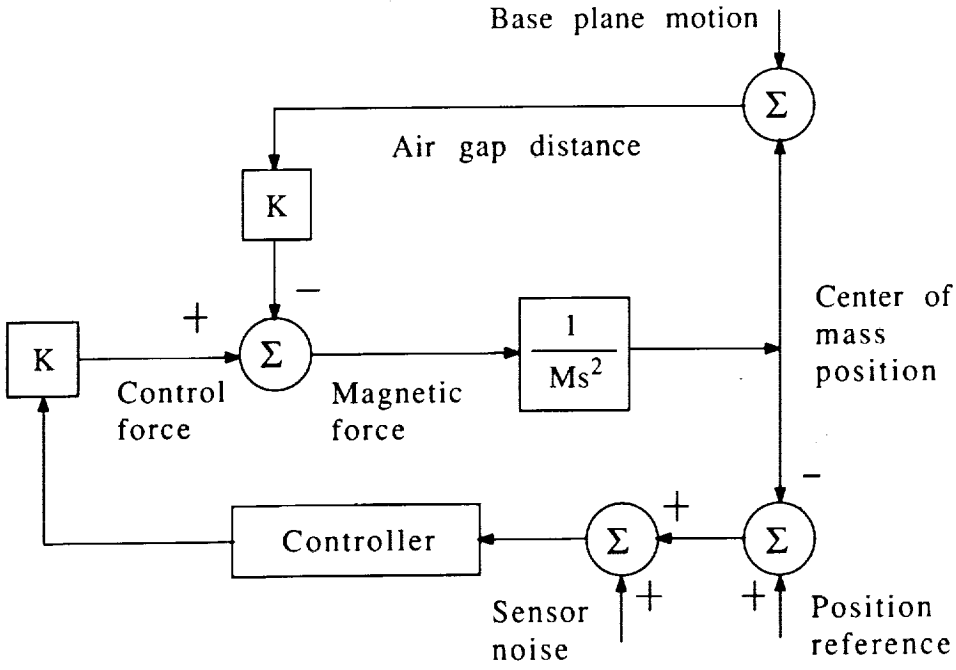

Figure 5 Basic magnetic suspension block diagram

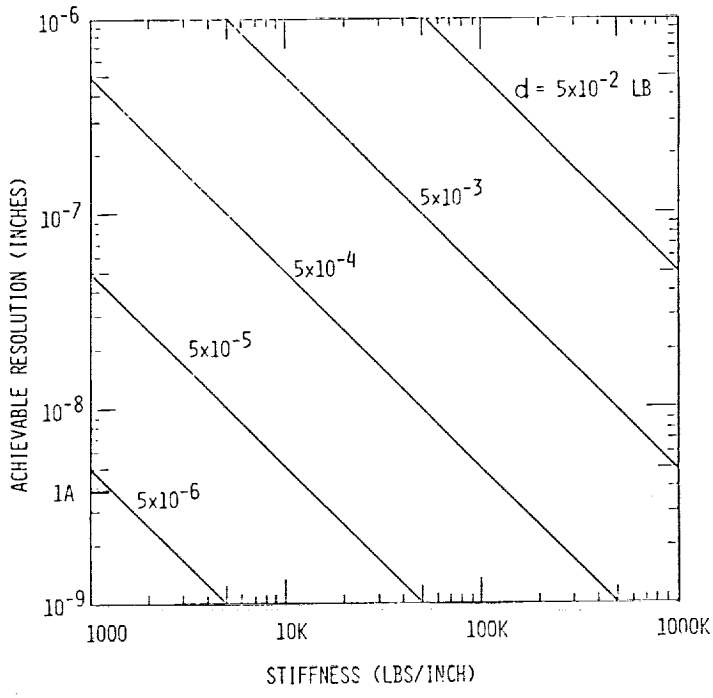

Figure 6 Achievable suspension resolution vs. suspension stiffness

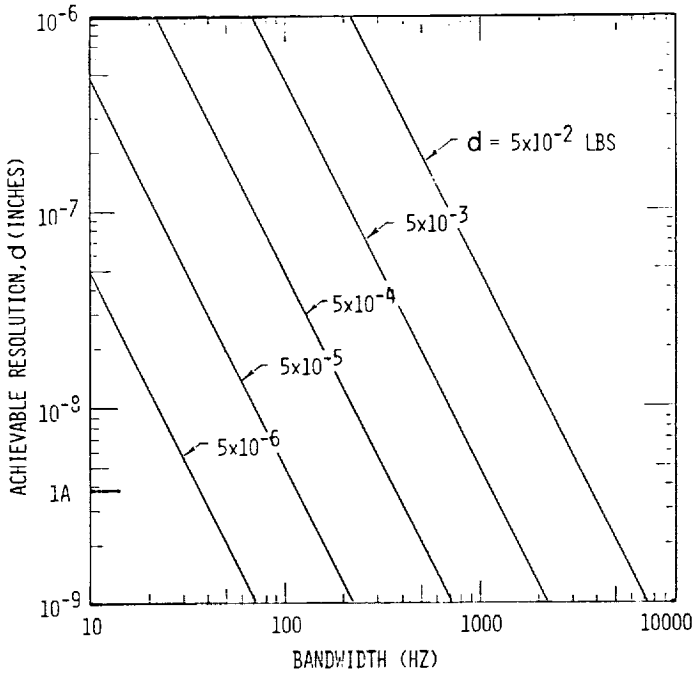

Figure 7 Achievable suspension resolution vs. suspension stiffness

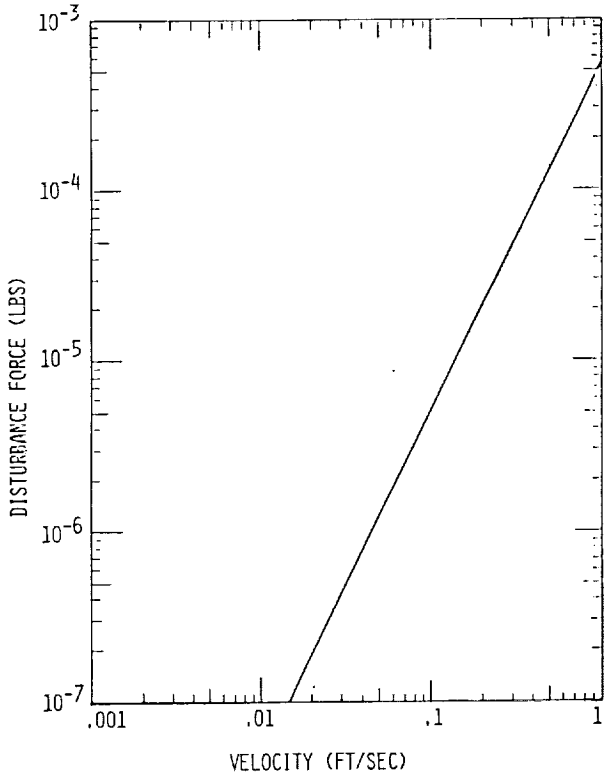

Figure 8 Slide disturbance force as a function of impinging air flow

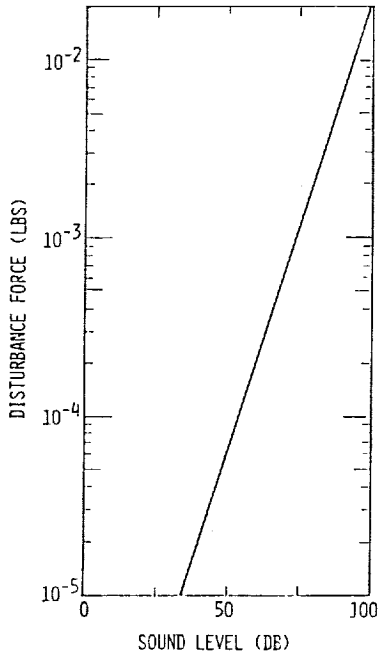

Figure 9 Slide disturbance force vs. acoustic noise level

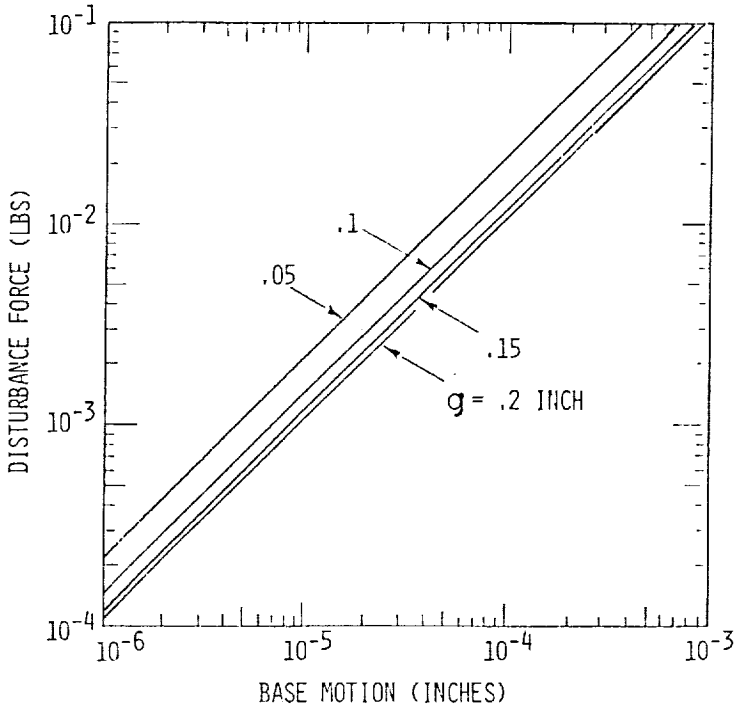

Figure 10 Slide disturbance force as a function of base plane motion

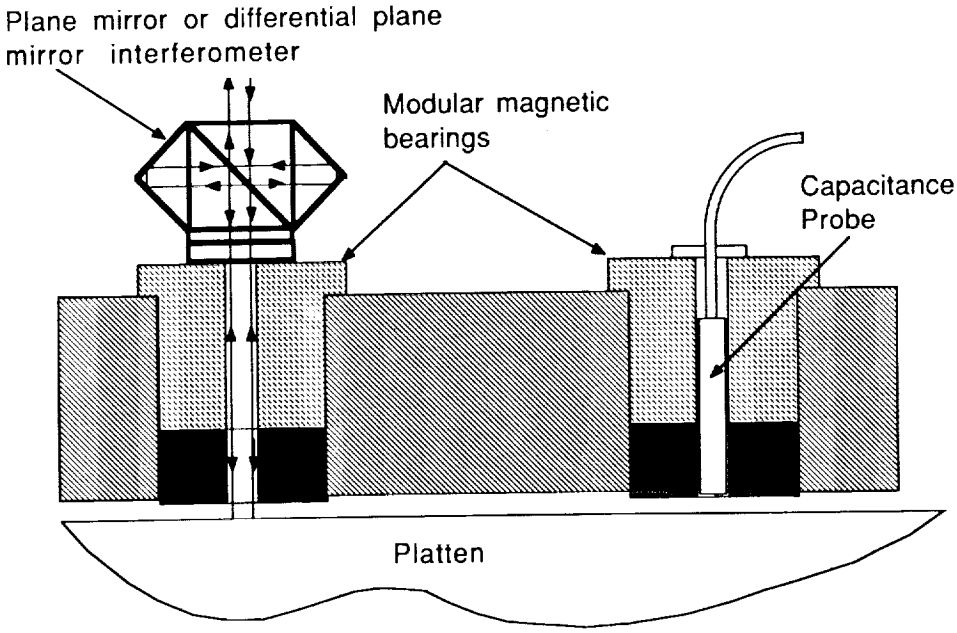

Figure 11 Possible sensor arrangements for precision "through the bearing measurement"

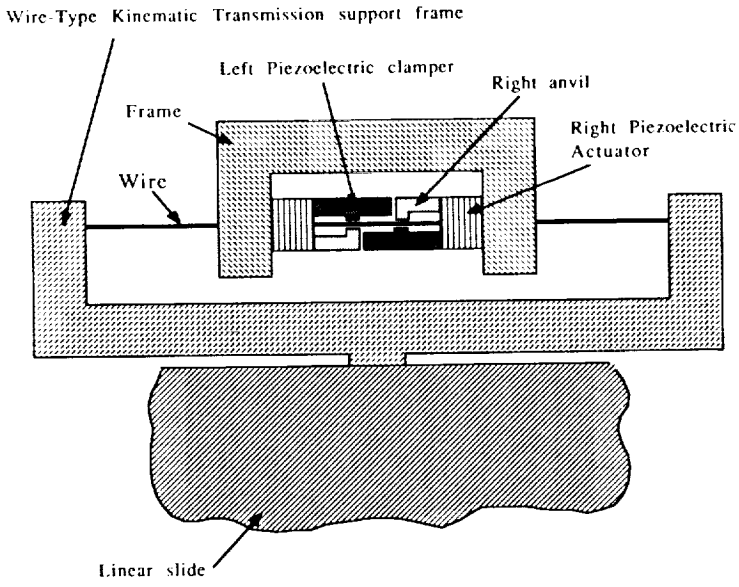

Figure 12 Schematic design of the Wire-Type Kinematic Transmission/Piezoelectric Inchworm Actuator designed for the Molecular Measuring Machine

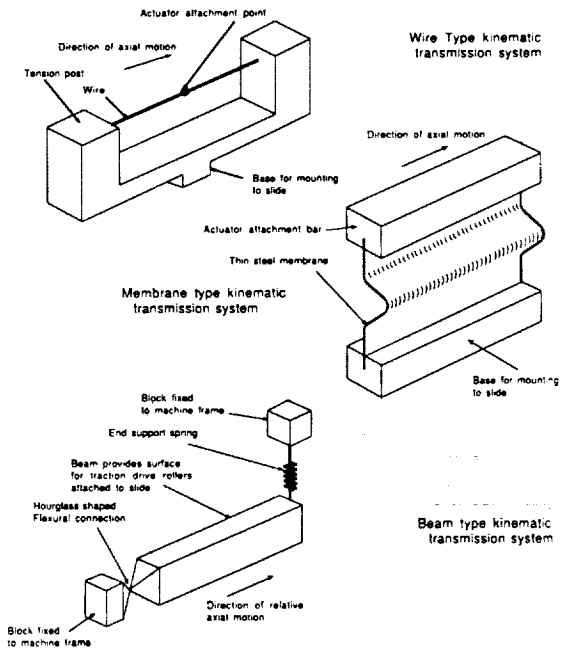

Figure 13 Types of flexural kinematic transmissions

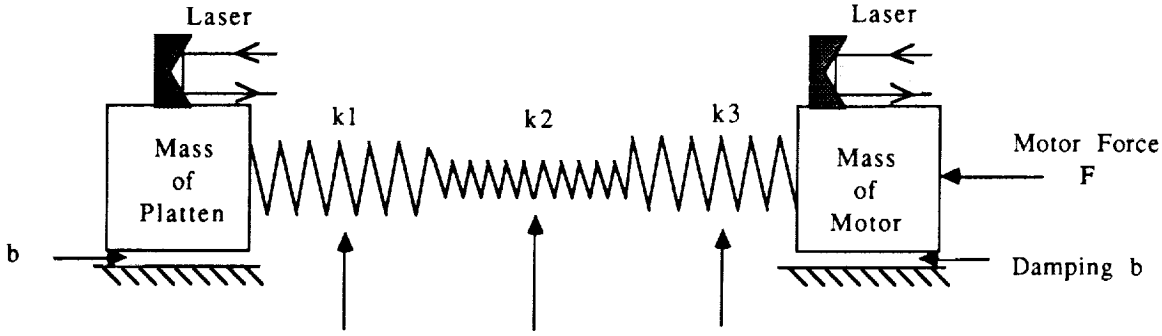

$$\frac{1}{k1} + \frac{1}{k2} + \frac{1}{k3} = \frac{1}{k} \approx \frac{1}{k2}$$

Figure 14 Dynamic system model of a wire-type kinematic transmission

OMIT

A Magnetic Isolation and Pointing System for the Astrometric Telescope Facility

William Hibble, Patrick J. Wolke, Honeywell Satellite Systems

Marcie Smith, NASA Ames Research Center

A MAGNETIC ISOLATION AND POINTING SYSTEM FOR THE ASTROMETRIC TELESCOPE FACILITY*

William Hibble and
Patrick J. Wolke
Satellite Systems Division
Honeywell Inc.

Marcie Smith
NASA Ames Research Center

SUMMARY

The astrometric telescope facility (ATF), a 20-meter telescope designed for long-term detection and observation of planetary systems outside of the solar system, is scheduled to be a major user of the Space Station's payload pointing system (PPS) capabilities. However, because the ATF has such a stringent pointing stability specification (as low as 0.01 arcsec error over the frequency range from 5 to 200 hertz) and requires +/- 180-degree roll rotation around the telescope's line of sight, the ATF's utilization of the PPS requires the addition of a mechanism or mechanisms to enhance the basic PPS capabilities. This paper presents the results of a study conducted to investigate the ATF pointing performance achievable by the addition of a magnetic isolation and pointing (MIPS) system between the PPS upper gimbal and the ATF, and separately, by the addition of a passive isolation system between the Space Station and the PPS base. In addition, the study has produced requirements on magnetic force and gap motion as a function of the level of Space Station disturbance. These results have been used to support the definition of a candidate MIPS.

Pointing performance results from the study indicate that an MIPS can meet the ATF pointing requirements in the presence of a PPS base transitional acceleration of up to 0.018g, with reasonable restrictions placed on the isolation and pointing bandwidths. By contrast, the passive base isolator system must have an unrealistically low isolation bandwidth on all axes (less than 0.1 hertz) to meet ATF pointing requirements.

The candidate MIPS, described in this paper, is based on an assumed base translational disturbance of 0.01g. The system fits within the available annular region between the PPS and ATF while meeting power and weight limitations and providing the required payload roll motion. Payload data and power services are provided by noncontacting transfer devices.

---

*This work was performed for NASA Ames Research Center under Contract No. NAS2-12525.

INTRODUCTION

The astrometric telescope facility (ATF) is a single-mirror optical telescope whose primary purpose is to search for extrasolar planetary systems (ref. 1). The ATF will measure the positions of selected nearby stars relative to sets of distant reference stars with an accuracy of 10 microarcseconds. By analyzing the motion of these stars over several years, it will be possible to infer the presence or absence of planetary systems.

The accuracy of the measurement is determined by the requirement to detect Uranus/Neptune-size planets orbiting solar-size stars up to 10 parsecs from Earth. To make this measurement, the target star and reference stars' signals in the focal plane are modulated by passing the collected light through a moving grating, called a Ronchi ruling. The ruling modulation frequency can be commanded between 10 and 100 hertz.

The ATF is designed to be an attached payload on the Space Station (SS) and uses many SS services. Because the mission span is long (20 years), the advantages of the low operating costs associated with the SS are great. As well as using the station power and data systems, the ATF requires use of one of the SS PPS for orienting the telescope relative to the station. The PPS will provide three-axis pointing with 1 arcmin pointing accuracy and 15 arcsec jitter.

The telescope design is shown in figure 1. The ATF has a 1.25-meter-diameter paraboloid mirror and a focal ratio of 13. The tube, itself, is 1.85 meters in diameter and 20 meters long, including the sun shade. The mass of the telescope is 3340 kilograms. The telescope uses about 1.0 kilowatts power continuously and has a 1.75 Mbps downlink data rate.

Although the dimensions of the PPS allow for motion of the telescope to view all stars, the PPS, alone, will not satisfy the pointing and isolation requirements of the ATF. The ATF requires 1 arcsec pointing accuracy and has stringent frequency-dependent jitter requirements. The most severe requirement is to control the jitter of the image at the Ronchi ruling to 0.01 arcsec in a bandwidth between one half and two times the ruling frequency (5 - 200 hertz). For frequencies below 5 hertz, the jitter must be less than 1 arcsec; for frequencies above 200 hertz, it must be less than 0.1 arcsec.

Space Station disturbance accelerations and motions are expected to generate PPS pointing error levels, even for a center-of-gravity mounted payload, that are significantly above ATF specifications. Additionally, although the PPS provides three axes of active pointing, the telescope still must be able to roll +/- 180 degrees to allow measurement of star positions in two dimensions. To meet these requirements, the ATF preliminary design concept places an annular vibration isolation/vernier pointing system between the ATF and the PPS, which includes a roll mechanism to position the telescope about the line of sight.

This paper presents the results of a study which had as its primary objective the determination of ATF pointing performance achievable by adding a magnetic isolation and pointing system (MIPS) between the PPS and the ATF. The MIPS provides a noncontacting interface between the PPS gimbal system and the ATF. Magnetic actuators, similar to the one illustrated in figure 2, are used to point the ATF inertially and to isolate the ATF from PPS translational motions. The stators of the actuators are connected to the PPS; the armatures are attached to the ATF.

The magnetic system pointing performance results were primarily parametric in nature, defining pointing performance as a function of the level of input disturbance from the Space Station and of allowable control bandwidths, for both pointing and isolation functions.

The secondary objections of the ATF study include: 1) the comparison of the MIPS performance with that obtained by adding a passive isolation system to the base of the PPS and, 2) the definition of a candidate MIPS which would serve as a basis for establishing system power, weight, and size budgets. The proposed magnetic system design is based on Honeywell's activities over the past decade in developing similar MIPS for space and ground test applications (ref. 2-16).

SPACE STATION DISTURBANCE CHARACTERIZATION

The major sources of ATF pointing errors are expected to be the SS motions and accelerations generated at the base of the PPS. The translational accelerations at the PPS control center (intersection of the gimbal axes in figure 1), resulting from both translational and angular accelerations at the PPS base, produce a disturbance torque to the PPS control loop that is proportional to the offset between the control point and the payload center of gravity. Similarly, the SS rotational motion is coupled into the PPS control loops by the gimbal bearing friction and by any fluid couplings or electrical cabling required for the payload.

By adding an isolator below the PPS, the disturbance levels into the pointing loops are reduced. Alternatively, the MIPS, by adding a noncontacting interface between the PPS and the ATF, removes the effect of the rotational coupling to the payload, attenuates the translational disturbances transmitted through the PPS, and makes payload pointing control very insensitive to the gimbal-to-payload center of gravity, since the magnetic system provides the pointing control. In addition, the magnetic system isolates the payload from disturbances produced by the PPS itself.

Ideally, models of the SS and its disturbance forces and torques would be used to generate an estimate of the PPS base motions and accelerations. However, the Space Station is not defined well enough to allow this option. Thus, disturbances at the PPS base were assumed to consist of discrete spectrums of sinusoidal rotations and translational accelerations.

Meaningful study performance results were obtained by limiting the spectrum to two frequencies, one above 5 hertz and the other below 5 hertz. The two frequencies were selected to provide worst-case pointing errors in these respective frequency ranges. In this ATF study, a conservative value of 0.01g translation acceleration magnitude was assumed for the linear disturbance levels, both below and above 5 hertz. For rotational disturbance, a one-arcmin rotational magnitude was used.

PASSIVE BASE ISOLATOR COMPARISON

Evaluation of ATF pointing performance, assuming a PPS with passive base isolation, was performed with a simple planar model. The model included the PPS azimuth and elevation gimbals and assumed the cross-elevation gimbal would be replaced with a roll mechanism. The PPS pointing loop bandwidth was considered limited to 5 radians per second by the lowest gimbal structural mode of 5 hertz. The isolator system was comprised of spring-fluidic damper elements.

Results of the study indicated that to meet the ATF pointing requirements with the specified disturbance inputs, the isolation bandwidth had to be extremely low, (less than 0.3 radians per second. Such an isolator would require an extremely large stroke (over 0.3 meter). Since the estimated upper limit on actuator deflection for a reasonably sized isolator element of the space telescope reaction wheel isolator variety (ref. 17) is about 0.03 meter, no additional hardware studies with this configuration were pursued, and emphasis was placed on the MIPS.

MAGNETIC ISOLATION AND POINTING PERFORMANCE MODEL

To define a model of the PPS-magnetic system, some basic assumptions about the system's physical characteristics and operations are required. The following items summarize the assumptions made for the ATF study.

- Only the bottom two gimbals of the PPS configuration of figure 1 (azimuth and elevation) are retained. The space required for the magnetic system with roll gimbal does not provide room for the cross-elevation yoke.
- The magnetic system stators are mounted to the elevation gimbal yoke. Exact placement is unimportant for preliminary performance evaluation.
- The control point for the magnetic system is placed as close as possible to the ATF center of gravity.
- Inertial pointing control of the ATF is accomplished with the magnetic actuators. PPS gimbal control is used to orient the actuator stators so as to follow the angular motion of the armature ring.

Figure 3 illustrates a configuration based on these assumptions. The bottom view in the figure looks along the payload X-axis normal to both the line of sight of the payload (Z-axis) and the elevation gimbal axis. It shows two actuators, oriented parallel to the payload axis, which can provide pointing control around the

X-axis and translational isolation along the Z-axis. Pointing control of the elevation yoke around the X-axis (following payload motion on this axis) is achieved using the azimuth gimbal.

The pointing performance of the proposed MIPS was evaluated using a planar three-degree-of-freedom (3 DOF) simulation based on the configuration in figure 3 (the simulation was developed using the MATRIX-x™ design and analyses program from Integrated Systems Inc.). The 3 DOFs in the performance model include:

- Payload inertial angular motion around the payload X-axis, θp
- PPS elevation yoke angular motion around the X-axis, θ_G
- Translational motion of the payload normal to the pointing control axis, Z_p

As figure 3 makes clear, the elevation yoke rotation around the X-axis is determined by the azimuth gimbal rotation and by the PPS base rotation normal to the two gimbal axes, θ_N. This latter parameter is viewed as a disturbance input to the model. The selected planar model was chosen because it allows major disturbance sources, including θ_N, to be evaluated without the complexity and cost of an 8-DOF model.

The functional block diagram of the planar model is given in figure 4. The control loops corresponding to θp, Z_p, and θ_G are labelled inertial pointing loop, isolation loop, and PPS gimbal follow-up loop, respectively. Other details of the model include:

- Two magnetic actuators for inertial pointing and isolation. Actuator models are included to show high-frequency isolation response.
- Interface stiffness and damping (K and B) due to cabling across the azimuth gimbal
- Bearing breakaway friction torque on the azimuth gimbal (T_{fmax}) with linear spring, K_F, up to breakaway
- Effect of payload and PPS rotations (θp, θ_G) and payload and base translation (Z_p, Z_b) on the gap motion (armature-to-stator relative motion) at each actuator.
- Errors in knowledge of payload center of gravity offset from the two actuators; actual R_1 versus assumed R_1; same for R_2.
- Errors in knowledge of gimbal rotation axis offset from the two actuators; ΔR_{B1}, ΔR_{B2}.
- Disturbance inputs due to base translations (Z_b), base rotation around the azimuth gimbal (θ_{AZ}), and base normal axis rotation (θ_N).

Table 1 lists the compensation forms and control bandwidths for the control loops appearing in figure 4. The inertial pointing loop bandwidth limit, 10 rad/s, is conservatively consistent with the assumed first mode frequency of the ATF telescope, i.e. 20 hertz. The form of the isolation compensation is chosen to

produce a very fast ideal high-frequency roll off, (-100 dB/decade). As simulation results show, however, the actuator dynamics limit the frequency range over which the -100-db roll-off is actually produced. Table 2 lists numeric values for several of the model parameters.

POINTING STUDY RESULTS

The primary results of the study conducted with the model of figure 4 relate to the payload pointing errors obtained in response to base acceleration disturbances, Z_b, and base rotational motions, θ_{AZ} and θ_N. In addition to pointing performance results, however, the model was used to define system response characteristics required to specify magnetic actuator force and gap parameters. These characteristics include required control force and actuator gap motion. The three items below summarize these study objectives.

- Define pointing performance for magnetic pointing system (high and low frequency disturbances) as a function of input disturbance level and pointing and isolation bandwidths.
- Define the peak actuator gap motion as a function of input disturbance level and isolation and pointing loop bandwidths.
- Define the control force requirements as a function of input disturbance level.

As described above, pointing performance for the ATF MIPS has been defined by the pointing error generated by single-frequency sinusoidal disturbances (both linear acceleration and base rotations) in the frequency regions below and above 5 hertz. Pointing error levels are determined, using the model of figure 4, by generating the magnitude frequency response curves for the transfer functions from the various disturbance sources to θ_p. At any particular frequency (corresponding to the frequency of the disturbance input), the magnitude of θ_p depends on the magnitude of the disturbance input and the bandwidths of the pointing and isolation control loops.

Figure 5 shows frequency response curves for the $\ddot{Z}_b$ to θ_p transformation. The different curves reflect a variation in pointing loop bandwidth from 5 to 10 rad/s. As indicated in the figure label, the $\ddot{Z}_b$ magnitude used in generating the curves is 0.01g and the isolation bandwidth is 7 rad/s.

The curves of figure 5 show that peak pointing error below 5 hertz is significantly affected by pointing loop bandwidth, while at higher frequencies, pointing error is unaffected by changes in this parameter. By contrast, a variation in isolation bandwidth produces little pointing error change below 5 hertz. This result is due to the fact that pointing error produced by base translational accelerations is proportional to the isolator transmissibility.

Frequency response curves similar to those of figure 5 were also generated for rotational disturbance motions around the azimuth and normal axes. Results from these curves are summarized in Table 3. As indicated, the input disturbance level is 0.3 millrad (or approximately 1 arcmin). For each disturbance and at each

pointing loop bandwidth, the error levels are more than two orders of magnitude below the required specification values.

The major factors influencing payload-to-base relative translational motion, $(Z_B - Z_p)$ in figure 4, and, thus, actuator gap requirements, are isolator bandwidth and level of base translational motion. Frequency response curves for the transformation from $\ddot{Z}_B$ to $(Z_B - Z_p)$, assuming a 0.01g disturbance level and various levels of isolator bandwidth, were generated using the performance model to evaluate these sensitivities. The peak relative motions from these frequency response curves were then used to generate the parameterization curves of figure 6. In this figure, gap motion is plotted against translational disturbance level for various isolation bandwidths. The curves indicate that a 0.5-inch motion limit can be maintained out to 0.02g if the isolation bandwidth is set above 6 rad/s.

The following items summarize the results from the MIPS performance study.

- Low-frequency pointing performance is affected most by pointing loop bandwidth-high frequency performance by the isolator.
- A 10 rad/s pointing bandwidth and 6 rad/s isolation bandwidth satisfy low- and high- frequency pointing requirements for single-axis disturbances <0.018g.
- For the nominal disturbance input level, 0.01g, gap motion is less than 0.5 inch (1.27cm).
- Angular motion disturbances at the 1 arcmin level are insignificant in their effect on pointing error.

MAGNETIC ISOLATION AND POINTING SYSTEM (MIPS) DESIGN

A candidate ATF MIPS, including all potential sources of power and weight, was defined to establish a power, weight, and size budget for such a system. In addition, system reliability was addressed. To place a limit on the peak force required of the magnetic actuators, a peak control force of 80 lbs (356 N), corresponding to a 0.01 translational disturbance acceleration input, was assumed.

The following items summarize the requirements and assumptions imposed on the magnetic system design,

- A 356 N control force can be required in any direction.
- A 34 N.m control torque is required normal to the ATF line of sight.
- Relative motion at any actuator is limited to ±0.5 inch (1.27cm).
- A full ring armature attached to the ATF is required to provide ±200 degrees roll motion.
- A noncontacting roll motor providing 7 N.m (5 ft-lbs) of roll torque is required.

- The magnetic system must fit within an annular region between the PPS and ATF that has a 1.8-meter inside diameter and a 2.5-meter outside diameter.

- The system must provide noncontacting power and signal transfer to the ATF.

Several actuator configurations were considered for the design. The number of actuators in the configuration is important because a large number of actuators implies a small peak actuator force and, thus, a small actuator. A small actuator makes it easier to fit the system into the available radial space. However, each actuator requires separate drive electronics, gap sensors, and flux sensors. Since it is undesirable to make the system any more complicated than necessary, a balance is found between accommodating the radial space limitation and minimizing the number of actuators. While five actuators and a roll motor are adequate for providing ATF control, eight actuators (plus roll motor) were selected for the MIPS, as shown in figures 7, 8, and 9.

A simple model was developed which related peak (of the eight actuators) single actuator force to control force and torque magnitudes and directions to the inclination angle of the armature from the plane of the actuator system. An optimization procedure was implemented to minimize the maximum peak single actuator force and torque. The peak force requirement was determined to be 156 N (35 lbs) at an inclination angle of 52 degrees.

To provide force margin, a peak actuator force of 220 N (or 50 lbs) was chosen for the system. Figure 10 shows the results of the actuator force sizing process carried out for other values of control force. The circled point on the graph corresponds to the nominal configuration values (80 lb, 50 lb or 356 N, 220 N). This places the nominal actuator design in an array of possible actuator force, motion, peak power, and weight options. The curves in the figure relate total system actuator weight (eight actuators) to peak actuator force for different levels of actuator gap motion and single actuator peak power. The curves can be used to determine how an increase in actuator force and motion, or an emphasis on power rather than weight, can be expected to affect the actuator system weight.

The quiescent and peak power requirements for a single actuator were determined to be 5 and 200 watts, respectively. The quiescent power requirement corresponds to the situation where the force command to the actuator is zero and the armature is centered in the actuator gap, i.e. no gap motion. The peak power is required when the actuator is driven to its peak force level while the gap motion is at its limit. In normal operation, an actuator's power requirement, determined by the command force and gap motion, is somewhere in between these extremes. The actuator system's power requirement is, of course, the sum of the individual values.

To define operational power needs of the proposed actuator configuration, a simulation was developed to compute the power for each of the configuration actuators as a function of its commanded force and gap motion. The command forces and gap motions were based on the payload control forces and torques (magnitudes and directions) and on the relative motion between the ATF payload and the actuator stator ring. The maximum operational power was determined to be approximately 450 watts.

Based on the actuator dimensional parameters, a mechanical layout for the proposed magnetic system was generated (figs 7, 8, and 9) that show that the system can fit easily into the available radial space. The cross section in figure 8 also indicates how the actuators might be placed relative to the optical signal coupler channel, the rotary power transformer, and a power-off caging mechanism. The coupler and transformer are described below. The caging mechanism has not been defined. Presumably it would operate on an annular ring and operate when power is lost or on command. A similar cross section of the roll motor placement, with respect to the same armatures used by the pointing and isolation actuators, is shown in figure 9.

ATF roll control is provided by two ac induction motors reacting against the two actuator rings. The motors are placed as indicated in figure 7 to balance disturbance forces produced by the motors. Each motor produces a torque of 3.4 N.m (2.5 ft-lbs).

The rotary transformer designed to transfer power to the ATF from the PPS, is illustrated in figure 8. The majority of the weight is placed on the stator side of the transformer. The transformer is designed to supply 2400 watts peak at 120 volts and 20 kilohertz. The efficiency is 94 percent.

The concept design for signal transfer between the PPS and ATF is also shown in figure 8. The device consists of a reflective channel around the ATF, with optical transmitters (LEDs) and receivers (photodetectors) placed on both rotor and stator sides of the channel. Information is transmitted as sequences of optical pulses, from the ATF to the PPS and vice versa. Multi-information channels can be supported by multiplexing on both sides of the channel.

Support and drive electronics are required for each of the magnetic system components described above: control actuators, roll motors, rotary transformer, and optocoupler. In addition, gap sensor and support electronics are required to support the isolation and PPS follow-up control. Finally, an ATF processor is required to connect all of the functions. All electronics are redundant. Figure 11 is the hardware and signal block diagram which shows this redundancy for the processor, actuator, and roll drive electronics.

Table 4 supplies an estimated breakdown of total system weight and operational power. The values in parentheses refer to changes in power and weight resulting from a change to 100-watt peak power actuators (without a change in motion limit or maximum actuator force). No dimensional layouts were defined to determine whether or not the larger system will actually fit in the available radial space.

The intended 20-year operational life of the ATF experiment mandates that all major electronic components of the MIPS be redundant. A summary of the system component failure rates is provided in Table 5. The redundant electronics components are nonoperational prior to a primary component failure and therefore are assigned a failure rate of 1/10 of the primary failure rate. A single actuator failure is viewed as a system failure. Fewer than eight actuators can be used to control the ATF (with modification to the control software), but the system was sized assuming eight actuators. Thus, an actuator failure may result in unacceptably degraded performance.

The magnetic actuator failure rate listed in table 5, 0.015, assumes a single coil with discrete insulation between coil windings. The failure rate can be improved to 0.00285 by adding redundant coils, but the effect on overall system reliability is very small. A decision to add redundant coils might be made based on the difficulty of exchanging a failed actuator.

CONCLUSION

A magnetic suspension system design, with greater than ±180-degree roll capability, has been generated which will provide the precise pointing and isolation required of the ATF in the presence of a 0.01g Space Station disturbance. The design fits in the available annular space and is estimated to weigh less than 900 kilograms (2000 lbs). Power requirements for the system are dominated by the magnetic actuator and roll motor requirements. Power numbers presented for these systems do not represent the peak possible power for the system. They do, however, represent the anticipated peak operational power. Based on these peak numbers, the total system power requirement is estimated to be < 800 watts. The full redundancy of the system, except actuator coils, provides a reasonable mean time between system failures (defined by system nonoperation or performance degradation).

REFERENCES

1. "Astrometric Telescope Facility: Preliminary Systems Definition Study", NASA TM 89429, Washington, DC: NASA, March 1987.

2. Cunningham, D.C., Gismondi, T.P., and Wilson, G.W.: System Design of the Annular Suspension and Pointing System (ASPS). AIAA Paper 78-1311, Palo Alto, CA, August 1978.

3. Cunningham, D.C., et al: Design of the Annular Suspension and Pointing System. NASA CR-3343, January 1980.

4. Hamilton, B.J.: Laboratory Evaluation of the Pointing Stability of the ASPS Vernier System. NASA CR-159307, June 1980.

5. VanRiper, R.V.: A Precision Pointing System for Shuttle Experiment Payloads. 17th Space Congress, May 1980.

6. Hamilton, B.J.: Experiment Pointing with Magnetic Suspension. SPIE Paper 265-13, Los Angeles Technical Symposium, February 1981.

7. VanRiper, R.V.: High-Stability Shuttle Pointing System. SPIE Paper 265-12, Los Angeles Technical Symposium, February 1981.

8. Hamilton, B.J.: Vibration Attenuation Using Magnetic Suspension Isolation. 1981 Joint Automatic Controls Conference, Charlottesville, VA, June 1981.

9. Hamilton, B.J.: Stability of Magnetically Suspended Optics in a Vibration Environment. SPIE Paper 295-21, San Diego Technical Symposium, August 1981.

10. Hamilton, B.J.: Magnetic Suspension: The Next Generation in Precision Pointing. AAS Paper 82-034, Rocky Mountain Guidance and Control Conference, February 1982.

11. Hamilton, B.J., Samario, E. and Waldman, M.: Talon Gold Control System Architecture. 9th DARPA Strategic Space Symposium, October 1983.

12. Hamilton, B.J. and Keckler, C.: A System for Load Isolation and Precision Pointing. SPIE Advanced Technology Optical Telescopes II, London, England, September 1983.

13. Havenhill, D. and Kral, K.: Payload Isolation Using Magnetic Isolation. AAS Paper 85-014, Rocky Mountain Guidance and Control Conference, February 1985.

14. Hamilton, B.J., Wolke, P. J. and Aldrich, J.: Characterization of VIPS Magnetic Force Actuator. AIAA Paper 85-1988-CP, AIAA Guidance and Control Conference, Snowmass, CO, August 1985.

15. Hamilton, B.J., Andrus, J.H., and Carter, D.R.: Pointing Mount with Active Vibration Isolation For Large Payloads. AAS Paper 87-033, Rocky Mountain Guidance and Control Conference, February 1987.

16. Andrus, J.H.: Cryogenic Magnetic Gimbal Bearing. AIAA Paper 879446, 22nd Intersociety Energy Conversion Engineering Conference, August 1987.

17. Rodden, J.J., Dougherty, H.J., Reschke, L.F., Hasha, M.D., and Davis, L.P.: Line-of-Sight Performance Improvement with Reaction Wheel Isolation. AAS Paper 86-005, Rocky Mountain Guidance and Control Conference, February 1986.

TABLE 1.- SIMULATION MODEL COMPENSATION FORMS

Compensation Description	Form	Open-Loop Bandwidth
Pointing Loop	$\frac{K_R S^2 + K_P S + K_P K_I}{S}$	<10 rad/s
Isolation Loop	$\frac{\frac{\omega_C^3}{32}\left(\frac{S}{(\omega_C/4)} + 1\right)\left(\frac{S}{(\omega_C/8)} + 1\right)}{S\left(\frac{S^2}{(5\omega_C)^2} + \frac{S}{5\omega_C} + 1\right)^2}$	ω_C between 7 and 4 rad/s
Gimbal Follow-up Loop	$\frac{K_{PG} S + K_{PG} K_{IG}}{S\left(\frac{S}{\omega_{LAG}} + 1\right)}$	1 rad/s
Actuator Bandwidth	2nd-order Low Pass	3140 rad/s

TABLE 2.- SIMULATION PARAMETERS

Parameter	Description	Value
θ_P	Payload Interial Angular Motion	
θ_G	Gimbal Angular Motion	
Z_B	Base Translational Motion on Z-Axis	
Z_P	Payload Translational Motion on Z-Axis	
θ_N	Base Rotational Motion Normal Axis	
θ_{AZ}	Base Rotational Motion Azimuth Axis	
K_R	Pointing Compensation Parameters for	10.0
K_P	10 rad/s open-loop crossover	35
K_I		1.7
ω_C	Isolation Compensation, Open Loop Bandwidth	
ω_{LAG}	Gimbal Followup Compensation	4
K_{PG}	Parameters	0.25 * I_{AZ}
K_{IG}		0.25
I_P	Payload Inertia	160,000 kg-m^2
M_P	Payload Mass	3660 kg
I_{AZ}	Azimuth Gimbal Inertia-PPS Only	2050 kg-m^2
$\hat{L}$	Actuator Span	1.85 m
L	Estimate of L	1.85 m
$(R_1 - \hat{R}_1)$	Misknowledge in Payload CG Offset	2 cm
$\Delta R_{B1}, \Delta R_{B2}$	Misknowledge in Location of Magnetic Actuator Force Application Points with Respect to the Gimbal Control Axis	5 cm
EL	Elevation Angle	45°
K	Azimuth Gimbal Interface Stiffness	1700 N•m/rad
B	Azimuth Gimbal Damping Factor	23,000 (N•m-s)/rad

TABLE 3.- ERROR RESPONSE TO 1 ARCMIN AZIMUTH AND NORMAL AXIS ROTATION DISTURBANCES
(Isolator Bandwidth = 5 rad/s)

Pointing Loop Bandwidth (rad/s)	Pointing Error with 1 Arcmin Disturbance			
	θ_{AZ} (arcsec)		θ_N (arcsec)	
	Below 5 Hz	At 5 Hz	Below 5 Hz	At 5 Hz
5	0.0011	0.0001	0.0012	0.0003
7	0.0009	0.0001	0.0011	0.0003
8	0.0009	0.0001	0.0011	0.0003
9	0.0008	0.0001	0.0010	0.0003
10	0.0008	0.0001	0.0010	0.0003

TABLE 4.- MIPS WEIGHT-POWER PREDICTION

Component Description	Max Op Power (W)	Total Weight	
		(lbs)	(Kg)
Actuators (100-W Actuators)	450 (225)	1000 (1400)*	454 (636)
Roll Motors	125	160	72.7
Suspension Electronics (Redundant)	100	120	54.5
Processor	16	32	14.5
Optical Coupler	16	40	18.2
Roll Motor Electronics (Based on 60% Roll Motor operation)	80	50	22.7
Structure	-	225 (325)	103.3 (147.7)
Rotary Transport	(94% Efficient)	310	140.9
System Total (with 100-W Actuators)	787 (562)	1937 (2437)	880.5 (1107.7)

* Power and weight values corresponding to the use of magnetic actuators requiring 100 watts peak power.

TABLE 5.- MIPS ESTIMATED RELIABILITY

Component Description	Quantity	Failures per million hours of operation (λ)			
		Individual	Total	Primary Electronics	Redundant Electronics
MAGNETIC ACTUATOR ELECTRONICS				8.29	0.829
Drive Electronics	8	0.49	3.92		
Standby Electronics	1	3.86	3.86		
Flux Sensor	8	0.002	0.016		
Gap Sensor	8	0.062	0.496		
MAGNETIC ACTUATOR	8	0.015		0.12	
ROLL MOTOR	2	0.03		0.06	
ROLL MOTOR ELECTRONICS				4.64	0.464
Drive Electronics	2	1.05	2.10		
Standby Electronics	1	2.29	2.29		
Gap Sensor	4	0.062	0.25		
OPTOCOUPLER	8	0.3		2.40	0.24
COMPUTER	1	2.4		2.40	0.24
ROTARY TRANSFORMER	1	0.06		0.06	
TOTAL MTBF				17.97	
Probability of Success					
5-year mission				0.455	0.905
10-year mission				0.207	0.711

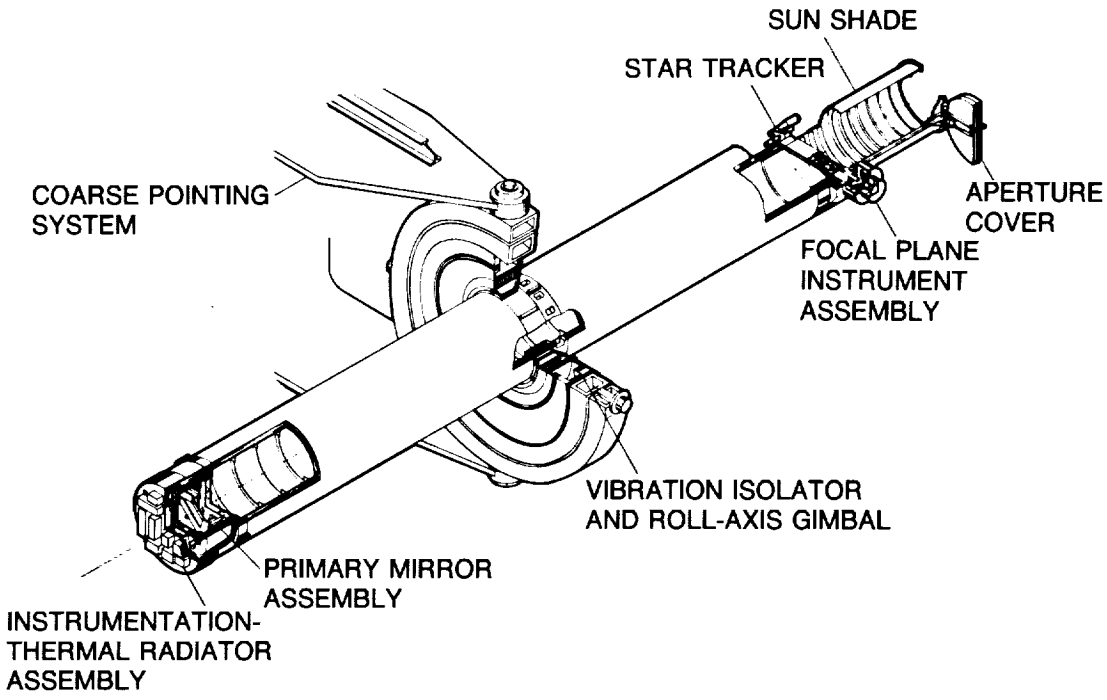

Figure 1. Mission and System Description and Requirements ATF/CPS Mounting Interface Concept

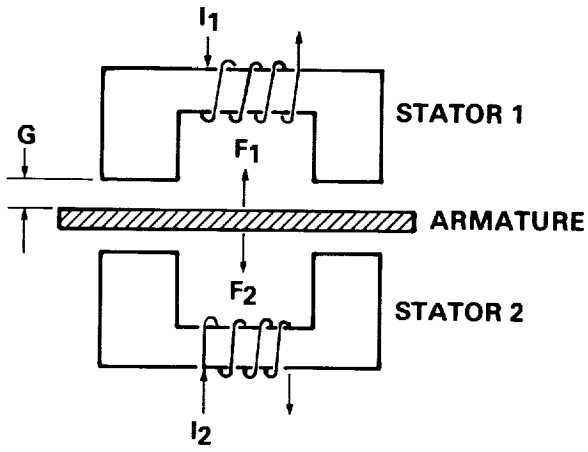

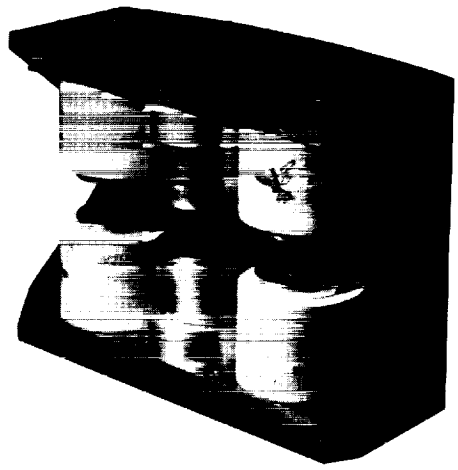

- Attractive Force F_1 and F_2
- F Insensitive to Armature Rotation and Cross Axes Translation
- Armature Isolated From Stator Disturbance Forces

- $F \sim I^2$
- $F \sim G^{-2}$
- Moving Armature Is Passive

Figure 2. Magnetic Actuator

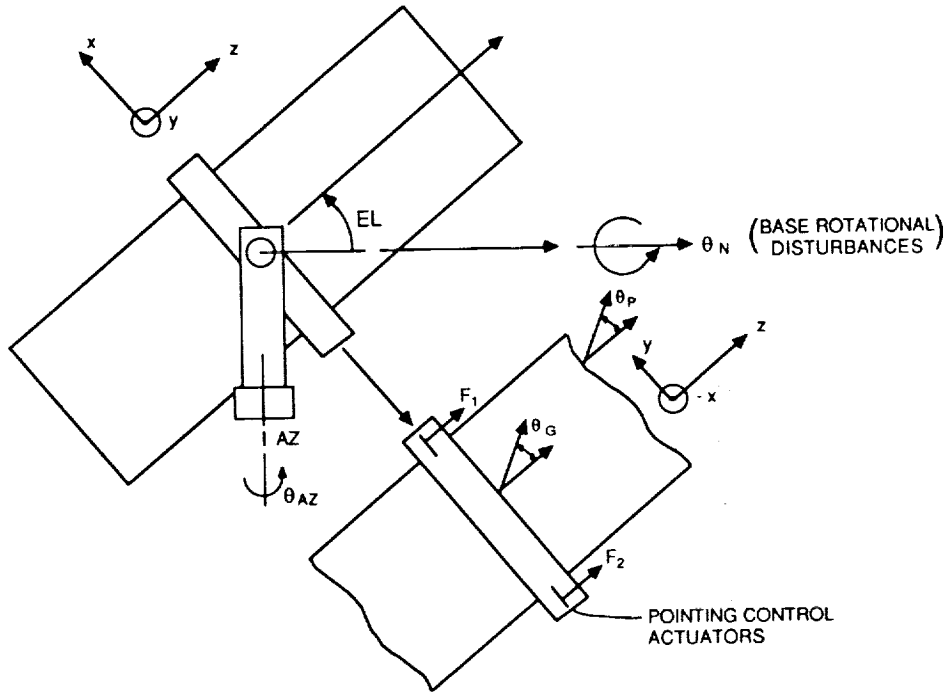

Figure 3. ATF Magnetic Isolation and Pointing Physical Configuration

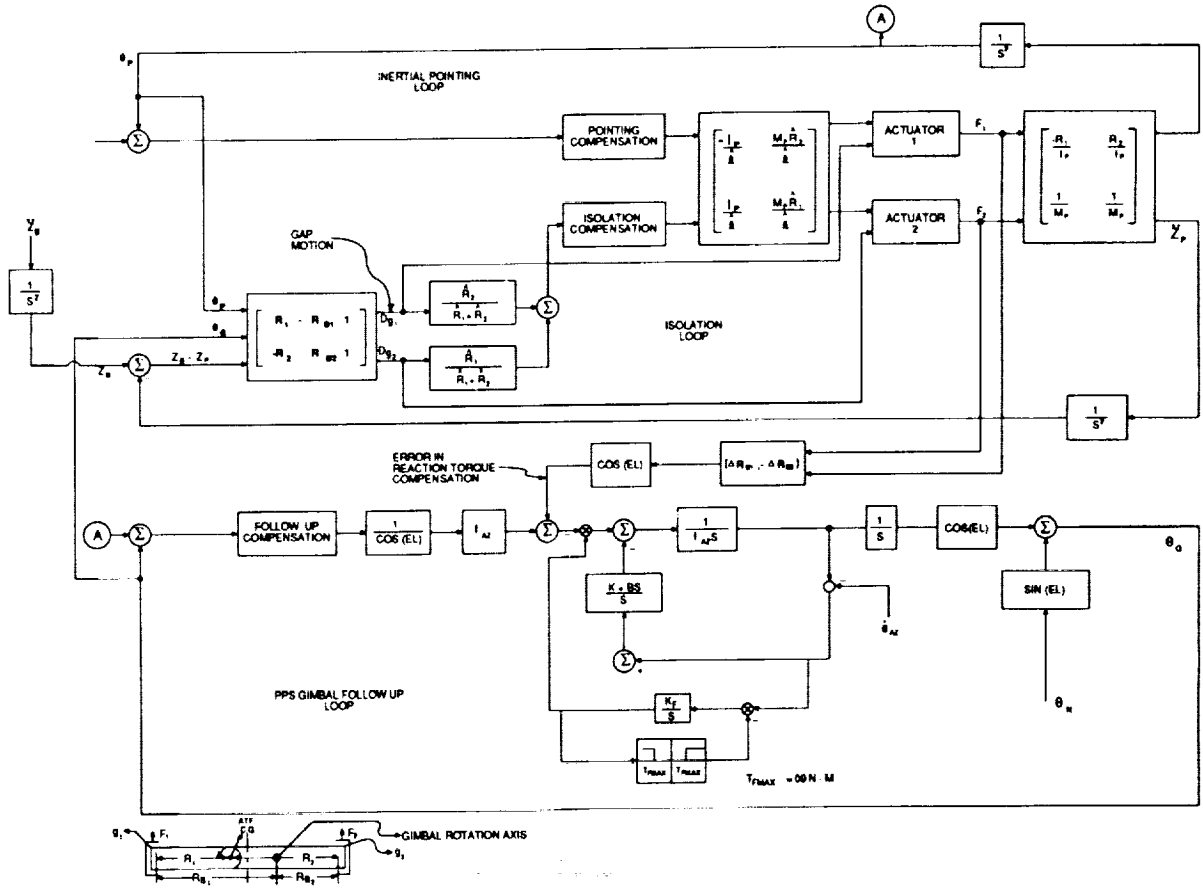

Figure 4. Magnetic Isolation and Pointing Block Diagram

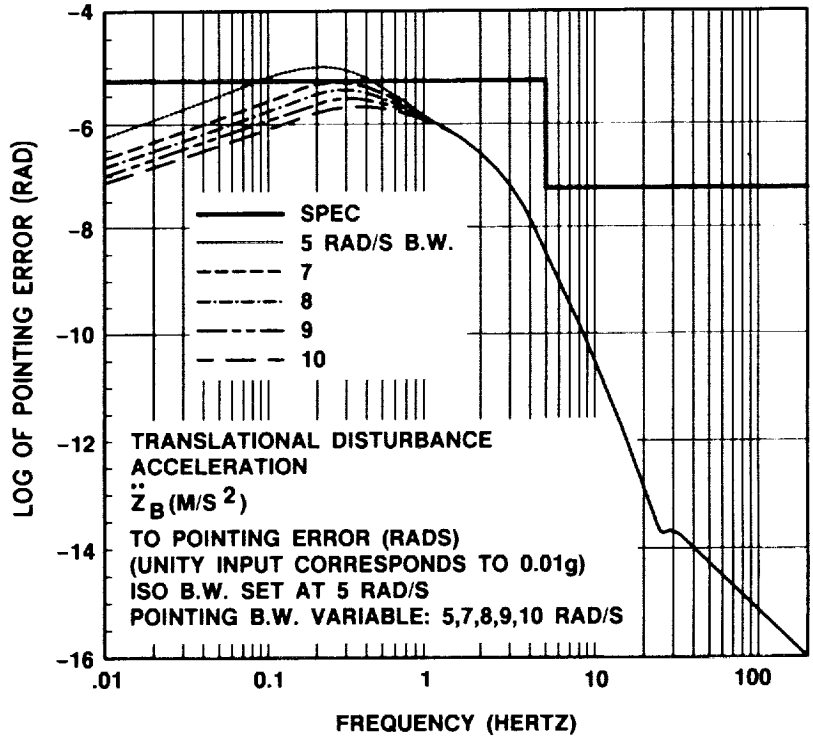

Figure 5. Frequency Response Curves, Translational Disturbance Acceleration to Pointing Error - Isolation Bandwidth = 5 rad/s

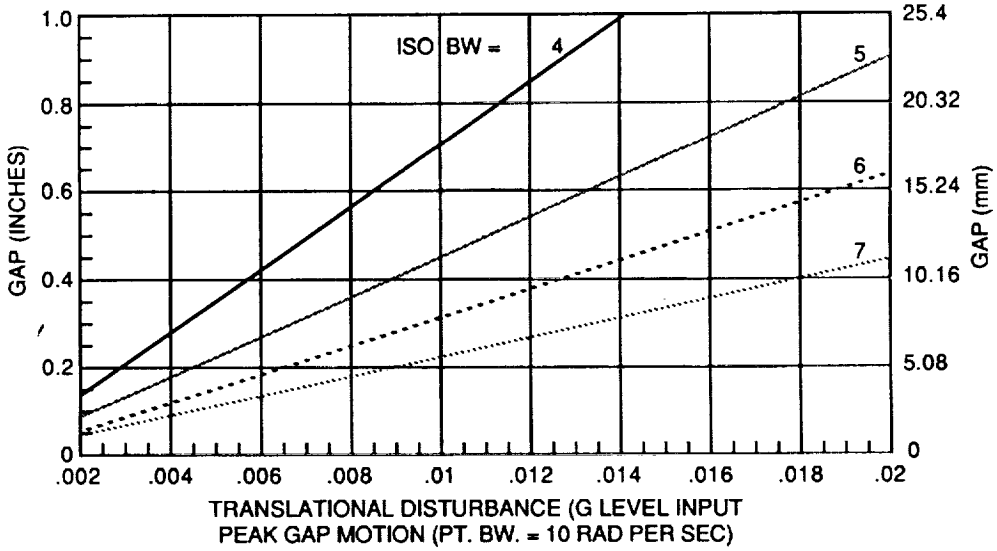

Figure 6. Actuator Gap Motion Requirements Versus Linear Acceleration Disturbance Level, Isolation Bandwidth-Variable

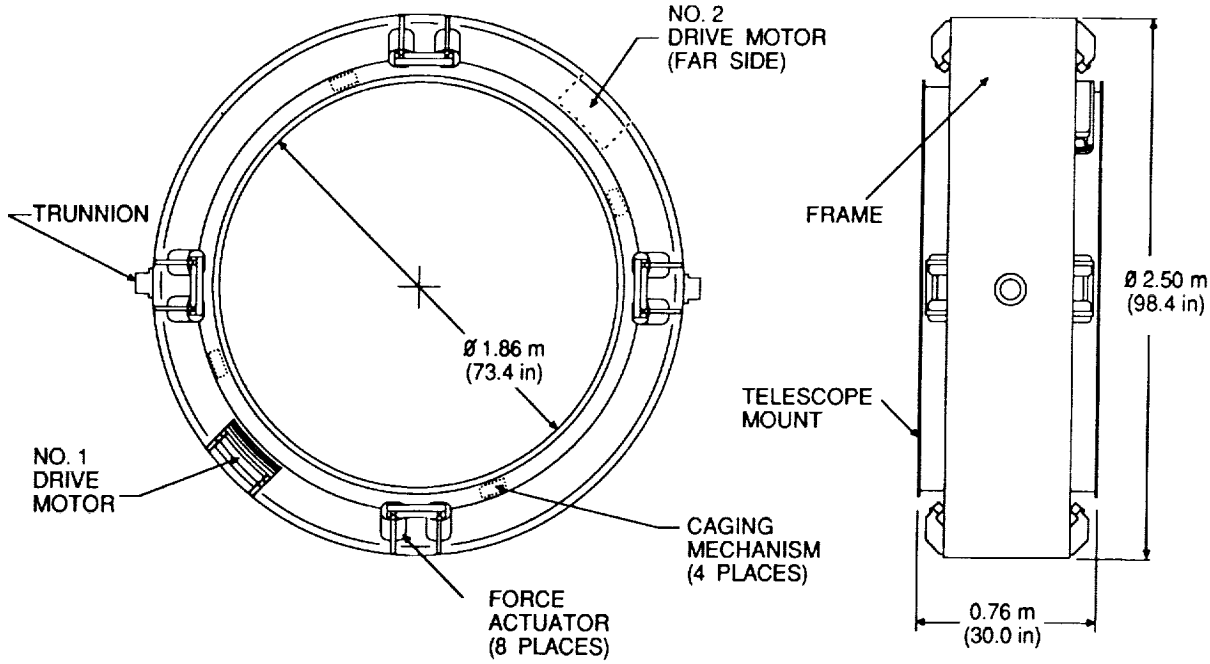

Figure 7. Actuator Layout

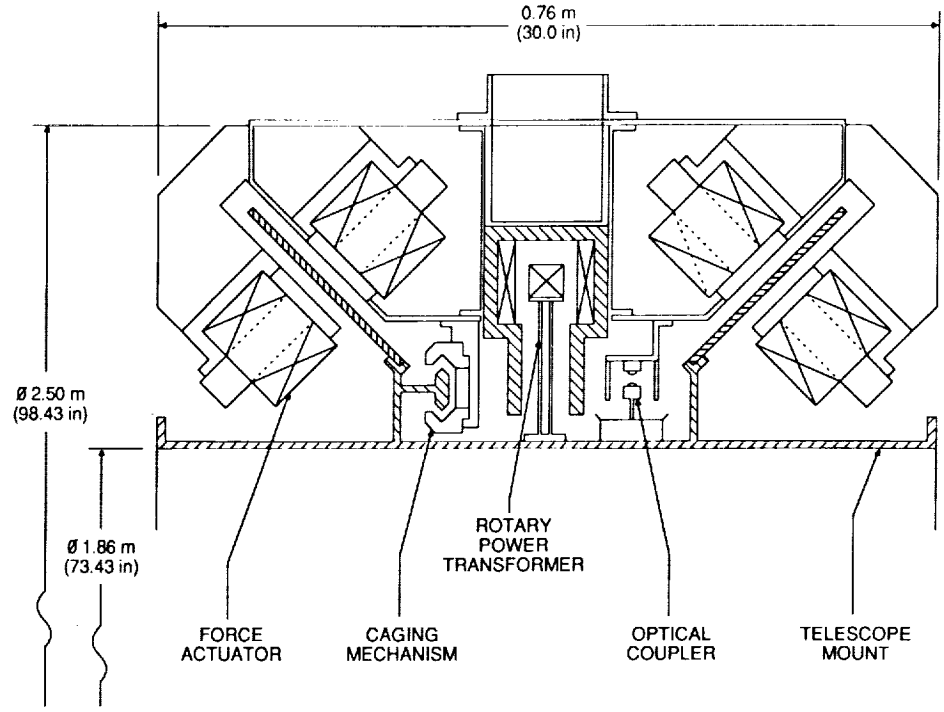

Figure 8. Actuator Cross Section

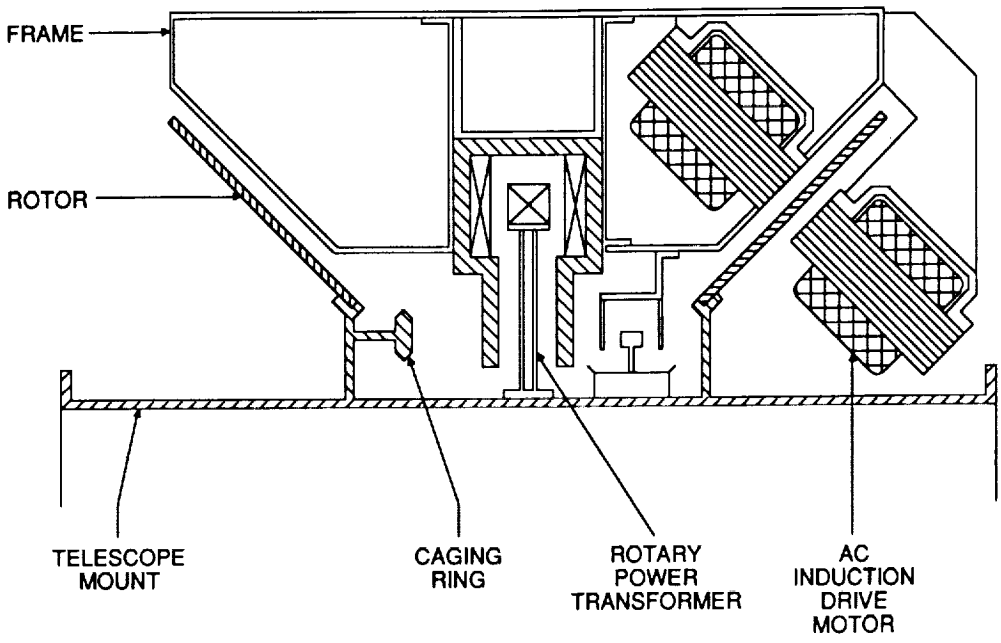

Figure 9. Roll Motor Cross Section

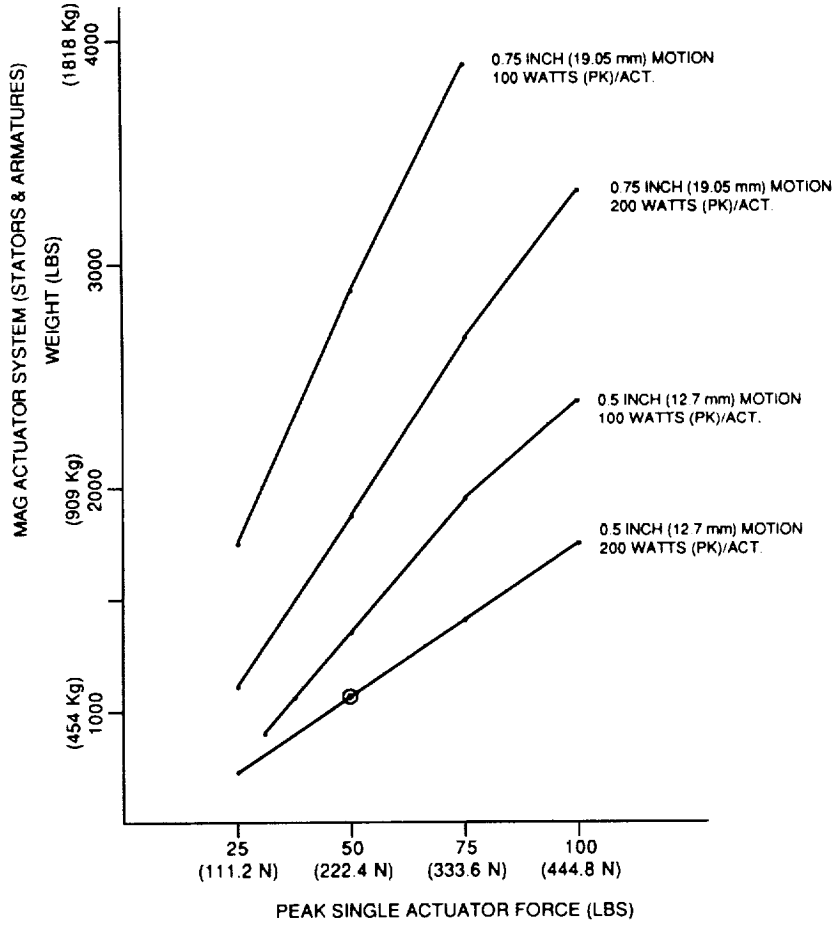

Figure 10. Actuator System Weight Versus Actuator Force

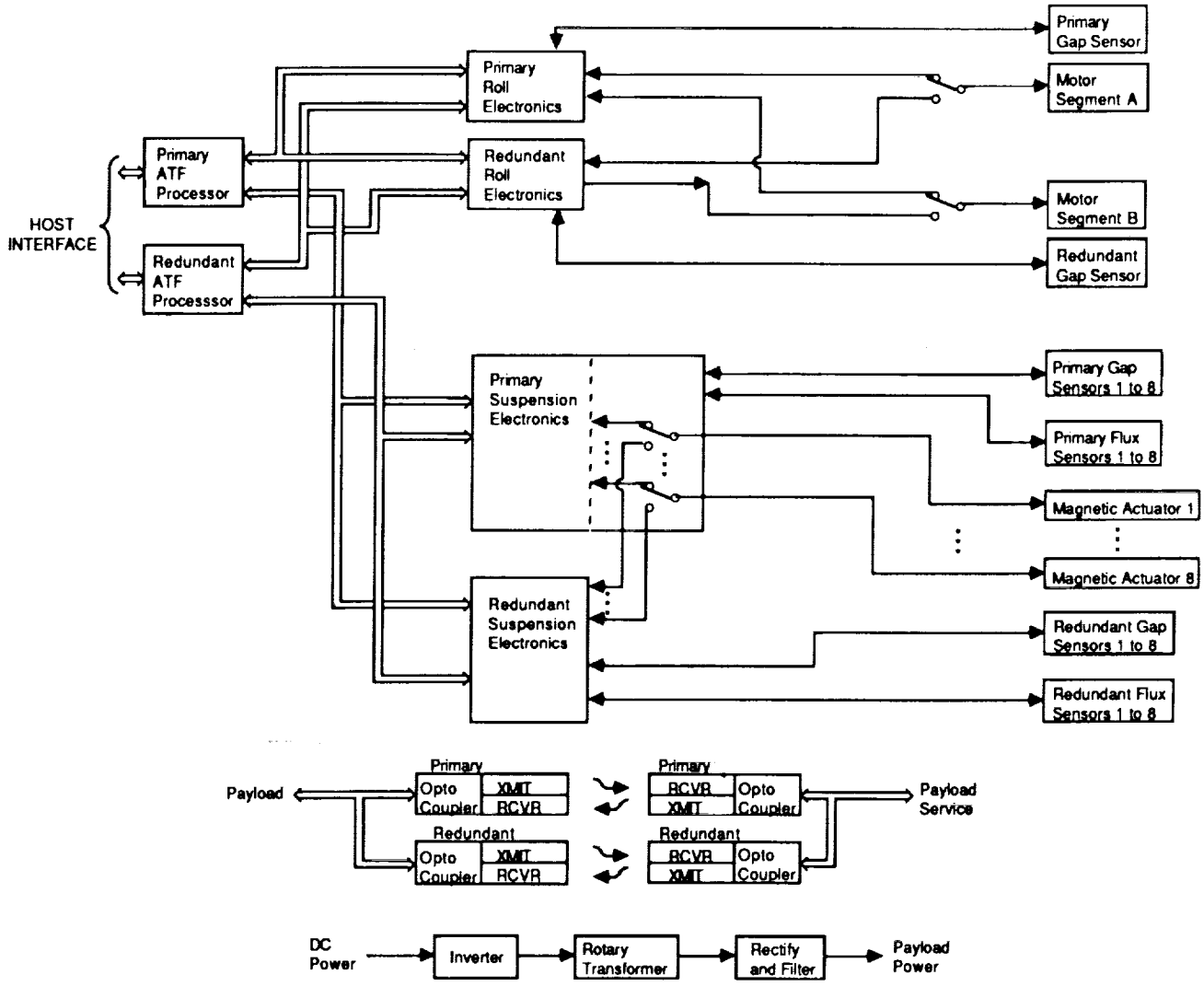

Figure 11. ATF MIPS Equipment

OMIT

Magnetic Gimbal Proof-of-Concept Hardware Performance Results

Keith O. Stuart, Innovative Information Systems, Aura Systems Company

MAGNETIC GIMBAL PROOF-OF-CONCEPT HARDWARE PERFORMANCE RESULTS

Keith O. Stuart
Innovative Information Systems
An Aura Systems Company
Los Angeles, California

1.0 SUMMARY

This report discusses the Magnetic Gimbal Proof-of-Concept Hardware activities, accomplishments, and test results. The Magnetic Gimbal Fabrication and Test (MGFT) program addressed the feasibility of using a magnetic gimbal to isolate an Electro-Optical (EO) sensor from the severe angular vibrations induced during the firing of divert and attitude control system (ACS) thrusters during space flight. The MGFT effort was performed in parallel with the fabrication and testing of a mechanically gimballed, flex pivot based isolation system by the Hughes Aircraft Missile Systems Group. Both servo systems supported identical E-O sensor assembly mockups to facilitate direct comparison of performance. The results obtained from the MGFT effort indicate that the magnetic gimbal exhibits the ability to provide significant performance advantages over alternative mechanically gimballed techniques.

2.0 INTRODUCTION

The MGFT effort was funded by the U. S. Air Force under the SDI KEW Program, formally known as the Kinetic Kill Vehicle (KKV) Program. The hardware proof-of-concept study was conducted from March to November, 1986.

The specifications imposed on the magnetic gimbal required the angular vibrations transmitted to the E-O sensor's optical path be less than 100 microradians, even during 10 g lateral divert maneuvers. A series of environmental tests were to be conducted at the Hughes MSG facility where the performance of the magnetic suspension system was to be evaluated. These tests included mounting of the MGFT hardware onto shaker tables and measuring the E-O sensor mockup's line-of-sight (LOS) while specific vibration profiles were produced.

A parallel effort involving the flex pivot gimbal fabrication and test was performed and this system was subjected to similar specifications and evaluations.

A detailed structural analysis of the E-O sensor mockup was provided to the control system engineers responsible for the two efforts to aid in the design of the respective servo systems.

2.1 DESCRIPTION OF MGFT HARDWARE AND SOFTWARE

Figure 2.1 shows the completed MGFT hardware. Hardware components that were designed, fabricated or procured, and integrated into the system are listed below.

1. Dual magnetic bearings (see figure 2-2 for a photograph of one of the bearings during characterization testing)
2. Bearing support fixtures
3. Rotary actuator
4. Automatic autocollimator (for LOS servo position feedback)
5. E-O Sensor assembly structural mockup
6. Custom 5-channel digital servo processing board based on a Motorola 68020 Microprocessor and 12 bit A/D and D/A convertors.

These items represent the necessary components involved in the various servo loops that control the magnetic suspension and line-of-sight of the E-O sensor mockup.

The magnetic bearings, one of which is shown in figure 2-2, were designed to utilize Simarian Cobalt (SmCo) permanet magnets to linearize the relationship between coil current and force exerted across the gap. Figure 2-3 shows a layout of the bearing used for the MGFT Program.

The bearing support fixtures were designed for structural rigidity. No size requirements were imposed.

The automatic autocollimator provided a highly accurate analog angular position reference to the E-O sensor LOS servo.

The E-O sensor mockup was provided to IIS by Hughes and was outfitted with optical quality mirrors used during the measurement of vibration rejection and for closure of the LOS position servo.

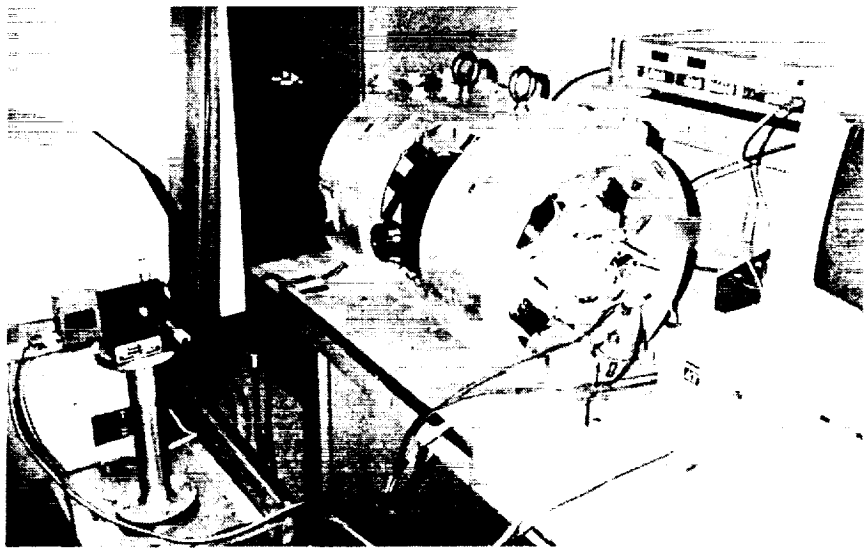

FIGURE 2-1. MAGNETIC SUSPENSION AND POINTING SYSTEM DEVELOPMENT FOR PHASE 1 RISK REDUCTION EFFORT

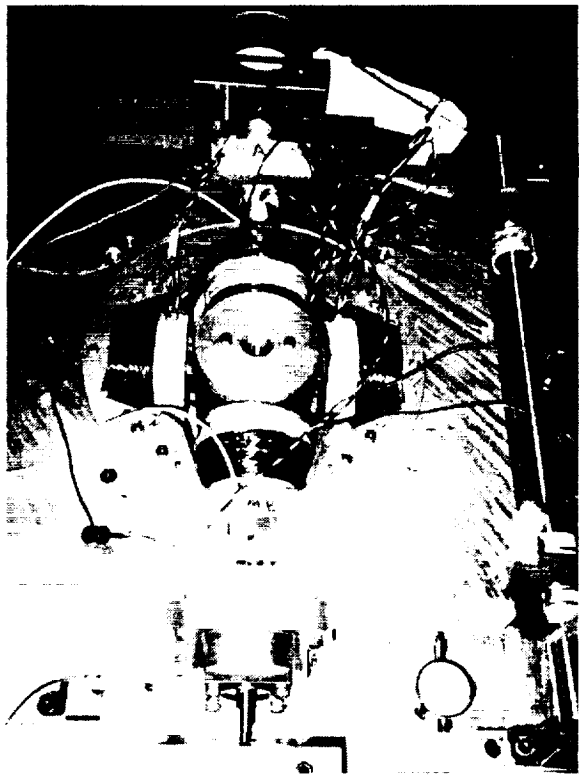

FIGURE 2-2. MAGNETIC BEARING IN TEST FIXTURE

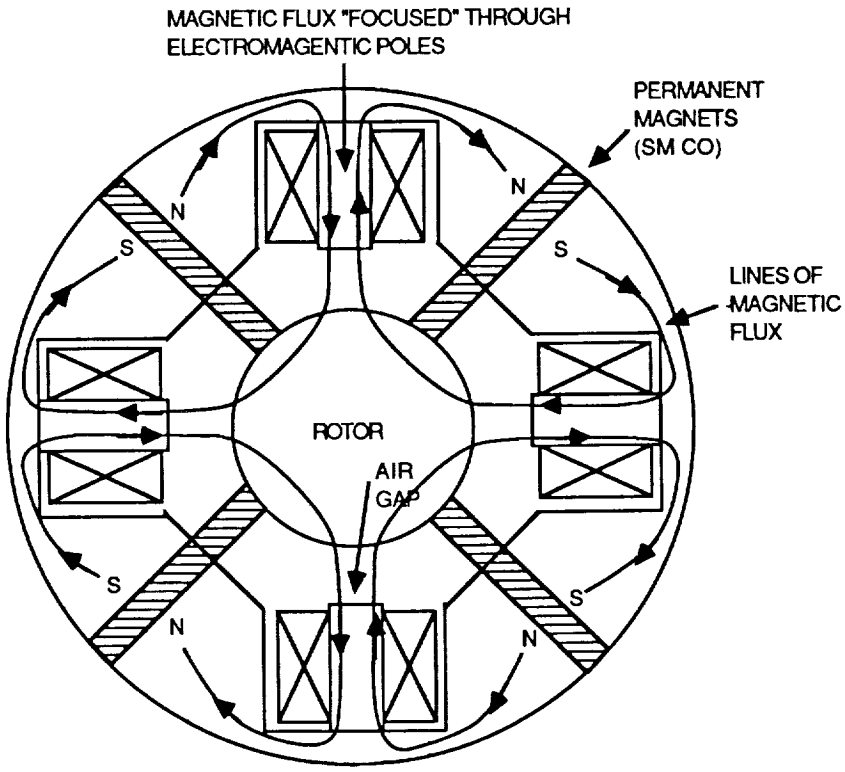

FIGURE 2-3. MAGNETIC CIRCUIT USED FOR PAYLOAD EXPERIMENT

The following digital servo systems were implemented in software on the 68020 and developed for the MGFT Program during the months of May to September, 1986.

a. Four digital magnetic suspension servos
b. One digital pointing control servo (LOS servo)
c. One digital acceleration feedforward compensator

The digital servo algorithms are serviced serially by the 68020 to provide the magnetic suspension and control the angular position of the seeker structural model.

The digital servo processing board is mounted in an IBM PC/AT compatible computer for ease of program development and downloading, and to allow real-time monitoring and modification of servo parameters. A real-time servo monitor and modification program was developed, allowing the controls engineer to observe and modify important servo parameters during operation. This interactive servo parameter modification software drastically reduces the time required for servo performance optimization. This technique is applicable to automated servo optimization, where a host computer can vary servo parameters to achieve specific performance requirements via a pre-determined rule-based algorithm.

3.0 SUMMARY OF TEST RESULTS

The vibration testing to be preformed for the MGFT Program followed as closely as possible the testing done for the flex pivot gimbal system. Two vibration tests were performed: torsional vibrations and linear vibrations. Figure 3-1 shows how each type of motion was induced.

The objective of the test sequences was to infer the line-of-sight stability of the KKV seeker assembly during the terminal portion of flight. This objective was met by disturbance definition, seeker geometry, test set-up and procedure and the vibration isolation system. Hughes Missile System group provided the first 3 items, and IIS provided the last item.

Each test involved the measurement of the level of motion disturbance which passed through to the isolated gimbal system due to a predefined vibration disturbance induced by a shaker table. Both shaker table vibration and the vibration motion transmitted to the seeker assembly was measured with optical measurement equipment (Optrons and Autocollimators). The data from these devices was recorded by a Hewlett Packard frequency analyser. All testing was done in the Hughes Missile System Group's Vibration Lab located in Canoga Park, California. The vibration testing was done on a Unholtz-Dickie model 1000 shaker table controlled with a Hewlett Packard computer system. The optical sensing equipment was placed on an air-bag table next to the shaker table to isolate them from unwanted vibrations. A photograph of the torsion table set-up can be found in figure 3-2.

Both torsional and lateral test sequences were performed. The following sections summarize the results of those test sequences.

3.1 TORSIONAL VIBRATION TESTING

A diagram of the torsional test set-up can be found in figure 3-3. A total of 4 different tests were performed: Simulated Thruster Pulses test, Amplitude Sweep, Frequency Sweep, and Lateral Suspension Stiffness test.

3.1.1 Simulated Thruster Pulses Test

The Simulated Thruster Pulses test examined the gimbal's ability to isolate motion waveforms representing realistic worst-case torsional disturbances produced by the firing of the missile's divert and ACS thrusters. These motion waveforms were provided by Hughes Aircraft Missile Systems Group.

A total of 4 different torsional waveshapes were tested. Each of these disturbance waveshapes had a fundamental frequency of 10 Hz. In each of the four pulses tested, the gain of the pointing control servo was reduced gradually until completely eliminated, allowing the suspended sensor's own inertia to stabilize it's LOS. This is only possible due to the frictionless nature of the magnetic suspension, since no mechanical coupling occurs between the sensor and the outside world. The reduction of the pointing servo gain had the effect of reducing the servo's closed loop bandwidth, an effect verified during the frequency-analysis phase of the servo development.

Figure 3-4 contains the reduced data for each of the four torsional pulse shapes. In summary, the level of vibration isolation between the high pointing servo bandwidth case (60 Hz closed loop bandwidth) and no pointing servo is very close, yielding rejection ratios from -50 dB to -60 dB depending on the waveshape. When the pointing servo bandwidth approached the disturbance waveform's fundamental frequency, a peaking of the transmitted disturbance resulted. This resonance phenomena can be explained by the increase of the closed loop servo gain (gain overshoot) just prior to roll-off.

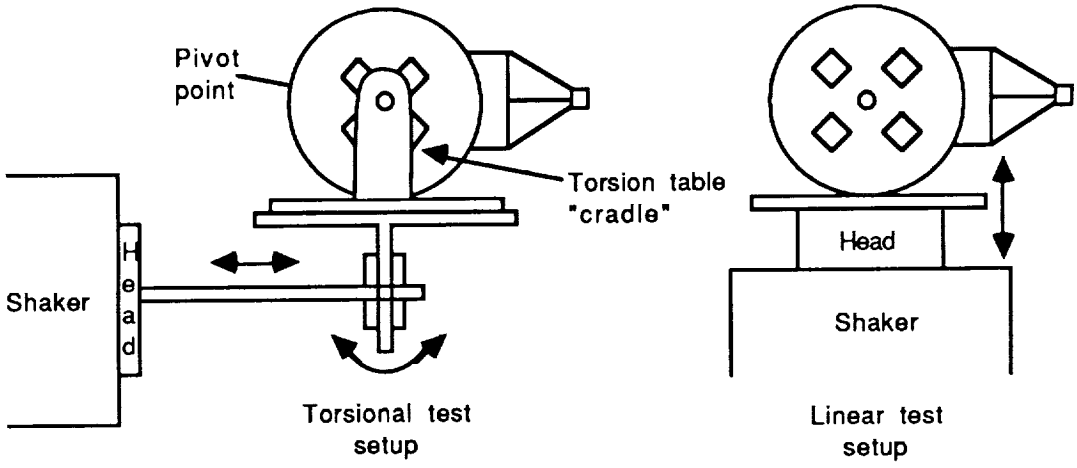

FIGURE 3-1. MECHANICAL METHODS OF INDUCING VIBRATIONAL DISTURBANCES

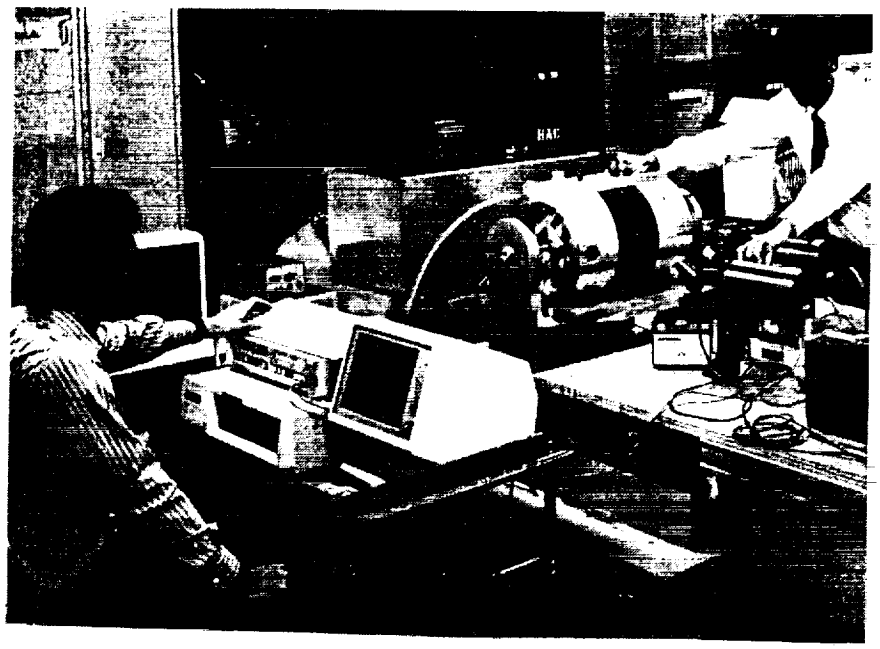

FIGURE 3-2. PAYLOAD EXPERIMENT TEST SETUP AT HUGHES VIBRATION LABORATORY

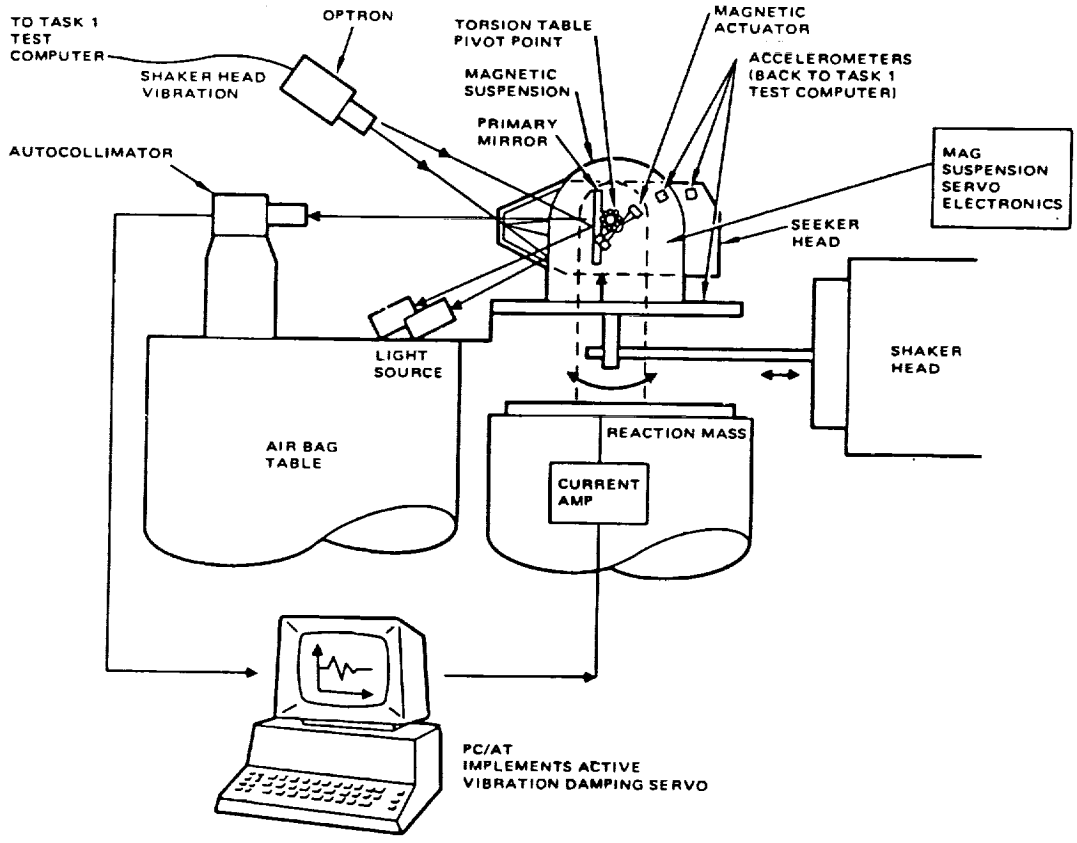

FIGURE 3-3. TORSIONAL TEST SET

CONTROL SERVO BANDWIDTH, Hz	DISTURBANCE AMPLITUDE, MILLIRAD	TRANSMITTED ANGULAR VIBRATIONS, μrad	REJECTION RATIO	
			ABSOLUTE	DB
60*	3.9	4.1	956.0	59.6
60*	3.9	3.1	1247.0	61.9
60*	3.9	5.0	775.2	57.8
45	3.9	6.9	564.8	55.0
23	3.9	13.6	286.8	49.2
12	3.9	10.9	358.5	51.1
0	3.9	5.1	764.8	57.7

*GAIN VARIED FOR FIRST 3 CASES. SEE APPENDIX A

a) Pulse 1
FIGURE 3-4. TORSIONAL TEST

CONTROL SERVO BANDWIDTH, Hz	DISTURBANCE AMPLITUDE, MILLIRAD	TRANSMITTED ANGULAR VIBRATIONS, μrad	REJECTION RATIO	
			ABSOLUTE	DB
60	5.6	5.2	1082.6	60.6
60	5.6	7.02	801.9	58.1
60	5.6	12.7	441.0	52.9
45	5.6	17.7	318.0	50.0
23	5.6	18.3	306.3	49.7
12	5.6	18.3	306.3	49.7
0	5.6	6.1	918.8	59.2

b) Pulse 2
FIGURE 3-4B TORSIONAL TEST RESULTS

POINTING SERVO BANDWIDTH, Hz	DISTURBANCE BANDWIDTH, Hz	TRANSMITTED ANGULAR VIBRATIONS, μrad	REJECTION RATIO	
			ABSOLUTE	DB
60	3.5	4.2	838.6	58.5
60	3.5	4.5	787.8	57.9
60	3.5	4.7	742.8	57.4
45	3.5	5.1	694.1	56.8
23	3.5	10.2	346.6	50.8
12	3.5	8.8	400.0	52.0
0	3.5	6.4	554.6	54.8

c) Pulse 3
FIGURE 3-4. TORSIONAL TEST RESULTS

POINTING SERVO BANDWIDTH, Hz	DISTURBANCE AMPLITUDE, MILLIRAD	TRANSMITTED ANGULAR VIBRATIONS, μrad	REJECTION RATIO	
			ABSOLUTE	DB
60	3.2	5.6	571.9	55.1
60	3.2	6.2	516.2	54.3
60	3.2	9.9	325.3	50.2
45	3.2	15.7	204.0	46.3
23	3.2	15.3	209.6	46.4
12	3.2	13.6	267.8	48.5
0	3.2	7.8	410.2	52.3

d) Pulse 4

FIGURE 3-4. TORSIONAL TEST RESULTS

The amount of vibration transmitted to the seeker when the pointing servo overshoot frequency was away from the primary vibrational resonance frequency varied between 4.2 microradians to 7.8 microradians peak-to-peak, which averages about a factor of 20 below the 100 microradian specification limit. The resonance frequency vibrations climbed as high as 15.7 microradians peak-to- peak, or about a factor of 6 below the spec limit.

Figure 3-5 shows a comparison of the angular vibration isolation test results of the flex pivot gimbal and the IIS magnetic gimbal. The upper graph shows the transmitted vibration of both the magnetic gimbal and flex pivot with the same input disturbance, shown in the lower graph. The peak-to-peak vibration transmitted to the seeker with the flex pivot is 125 microradians, giving a rejection ratio of -35 dB. The peak-to-peak vibrations transmitted through the magnetic suspension for the same disturbance input is 5.2 microradians, achieving a rejection ratio of -60.6 dB.

3.1.2 Amplitude Sweep Test

The amplitude sweep test was performed to study the correlation between input disturbance amplitude and disturbance transmitted through the magnetic gimbal. The amplitude of a 10 Hz sinusoidal angular motion was increased from 10 milliradians peak-to-peak to over 77 milliradians peak-to-peak. The results of the test is shown in figure 3-6.

With an amplitude disturbance of 10.0 milliradians, the amount of transmitted vibration was 5.1 microradians (-65.8 dB rejection). An amplitude of 77 milliradians produced a transmitted vibration of 8.5 microradians (-79.1 db rejection). The conclusion reached was that the amount of vibration transmitted through the magnetic suspension system is essentially independent of the amplitude of the disturbance.

3.1.3 Frequency Sweep Test

The frequency sweep test was performed to study the correlation between input disturbance frequency and disturbance transmitted through the magnetic gimbal. The frequency of a sinusoidal angular motion disturbance with a constant input angular acceleration of 48 rad/sec^2 was increased from 10 Hz to 200 Hz. The results of the test is shown in figure 3-7.

The amount of vibration transmitted over the 10 Hz to 200 Hz frequency sweep varied from 5.3 microradians (at 200 Hz) to 12.7 microradians (at 20 Hz). This increase at 20 Hz corresponded to the pointing control servo overshoot frequency of 30 Hz. The conclusion reached from this test is that the amount of transmitted vibration is independent of disturbance frequency except around the pointing servo overshoot frequency. This problem can be solved by designing the pointing servos to place the overshoot frequency far away from the thrusters primary pulse frequency.

3.1.4 Lateral Suspension Stiffness Test

The lateral suspension stiffness test was performed to study the correlation between the closed-loop bandwidth of the digital suspension servo (which is a function of the "stiffness" of the magnetic bearings) and the disturbance transmitted through the magnetic gimbal. The closed loop bandwidth of the suspension servos were modified by increasing the servo gain from a point where it was almost unstable due to lack of gain to the point where it was almost unstable due to too much gain. As with the pointing servo, the effect of the variation of gain on the closed loop bandwidth was verified during the frequency analysis portion of the servo development.

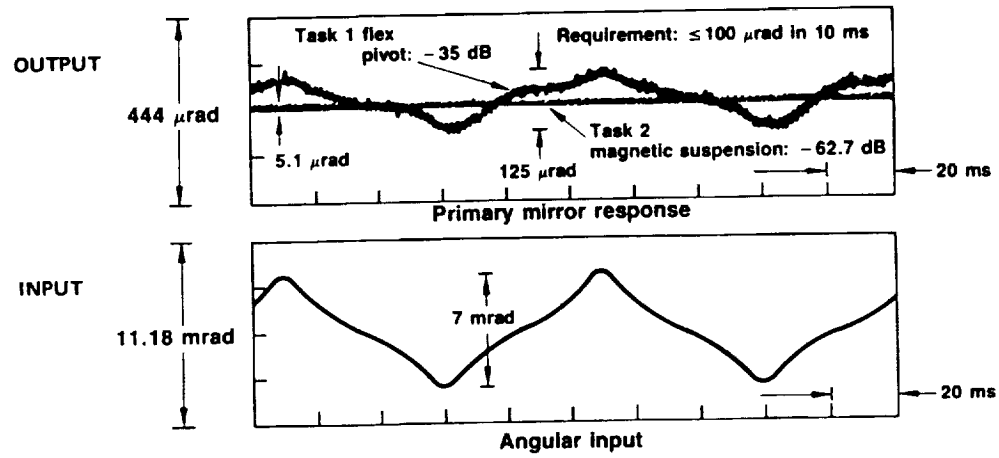

FIGURE 3-5. ANGUALAR VIBRATION ISLOATION TEST RESULTS FOR TASK 1 FLEX PIVOT AND TASK 2 MAGNETIC SUSPENSION SYSTEM

INPUT ANGULAR ACCELERATION, rad/sec^2	BULKHEAD DISTURBANCE AMPLITUDE, MILLIRAD, PEAK-TO-PEAK	TRANSMITTED ANGULAR VIBRATIONS, μrad PEAK-TO-PEAK	REJECTION RATIO	
			ABSOLUTE	DB
16	10.0	5.1	1958.3	65.8
32	20.5	6.5	3092.2	69.8
48	28.2	7.4	3786.8	71.5
64	40.5	8.5	4758.8	73.5
80	~56	7.7	7311.1	77.3
96	~72	8.8	8134.6	78.2
112*	~77	8.5	9047.5	79.1

*LIMIT OF SHAKER TABLE

FIGURE 3-6. TORSIONAL AMPLITUDE SWEEP TEST RESULTS

INPUT FREQUENCY, Hz	BULKHEAD (DISTURBANCE) AMPLITUDE, MILLIRAD, PEAK-TO-PEAK	TRANSMITTED ANGULAR VIBRATIONS, μrad PEAK-TO-PEAK	REJECTION RATIO	
			ABSOLUTE	DB
10	24.3	7.4	3263.1	70.3
20	8.01	12.7	627.4	55.9
50	1.09	6.8	160.8	44.1
100	0.735	7.9	92.1	39.3
200	0.106	5.3	5.0	26.0

FIGURE 3-7. TORSIONAL FREQUENCY SWEEP TEST RESULTS

The servo bandwidth was varied from a minimum of 82 Hz to a maximum of 120 Hz. A constant sinusoidal disturbance with a frequency of 10 Hz and an amplitude of 28.2 milliradians was applied. The results of the test is shown in figure 3-7. The angular vibrations transmitted to the seeker varied randomly from 6.0 microradians to 8.1 microradians. The conclusion reached from this test is that the amount of transmitted vibration is independent of lateral suspension stiffness.

3.2 LATERAL TESTS

The purpose of the lateral tests was to test the ability of the magnetic gimbal to remain operational during a severe lateral disturbance. As shown in figure 3-1, the magnetic gimbal assembly was placed directly on top of the shaker table.

As illustrated in figure 3-8, due to the extremely fast rise time of the simulated lateral thruster pulses (0 to maximum acceleration in less than 3 msec, and a maximum acceleration of 10 G's), the suspension servo alone could not handle pulses greater than approximately 0.8 G's. Above that amount, the shaft would strike its mechanical stop.

To improve this situation, acceleration feedforward compensation was added to the suspension control system that increased the effective bandwidth of the suspension servos from approximately 100 Hz to 500 Hz. With the compensation servo, the system could handle pulses of up to approximately 3 G's. Above 3 G's, the weight of the seeker structural model (16.5 lbs. total) and the high inductance of the magnetic bearing coils (.021 henries) became the limiting factors. The voltage amplifier saturated because of the high voltage levels required to overcome the coil inductance during the 3 msec disturbance pulse rise time.

The design modifications required to handle high lateral level, fast rise time accelerations are straightforward, low risk and utilize existing technology. They include increasing the effective speed of the suspension servo CPU's by a factor of 5 (accomplished by using a high speed digital signal processor to service all 5 servo systems or use a dedicated processor for each servo channel), incorporate acceleration feedforward compensation, design the magnetic suspension system to minimize electromagnetic coil inductance and increase the voltage headroom of the power driving system to overcome the remaining inductance. These modifications have been successfully implemented in subsequent systems.

SUSPENSION SERVO BANDWIDTH, Hz	TRANSMITTED ANGULAR VIBRATIONS, μrad PEAK-TO-PEAK	REJECTION RATIO	
		ABSOLUTE	DB
82	6.0	4883.3	73.8
91	8.0	3662.5	71.3
98	7.4	3934.6	71.9
105	6.9	4237.2	72.5
110	6.8	4303.4	72.7
120	8.1	3586.2	71.1

FIGURE 3-8. TORSIONAL SUSPENSION STIFFNESS TEST RESULTS

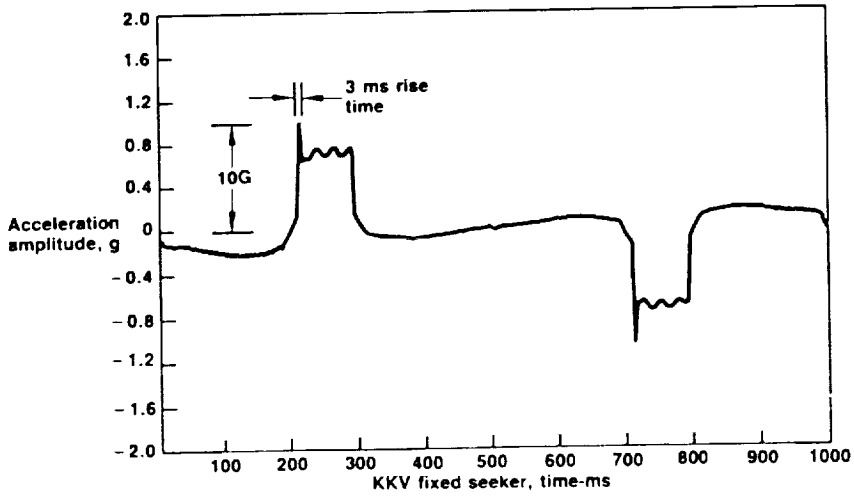

FIGURE 3-9. THRUSTER LATERAL PULSE WAVEFORM

4.0 CONCLUSIONS

Results from the the MGFT Program effort show that the magnetic suspension and pointing technology developed by IIS is highly suited for the gimballing requirements of systems requiring an extremely high degree of pointing accuracy in a severe vibrational environment. This effort also proved that digital magnetic suspension servos can be implemented quickly, reliably and inexpensively using commercially available hardware components.

The specific results and conclusions derived from the the MGFT Program for the Kinetic Kill Vehicle Weapon System indicate that magnetic suspension and pointing control will provide the following benefits when compared to alternative mechanically supported systems:

- Vastly superior angular vibration isolation due to the elimination of physical contact of the seeker with the interceptor's bulkhead (20 times better than spec)

- Elimination of the need for super-precise and repeatable machining (such as is required on high-accuracy pre-loaded ball bearing gimbal systems or flex pivot manufacturing)

- Ability to increase lateral stiffness of the gimbal without effecting its torsional stiffness

- Ability to automatically custom-tune the compliance of each individual gimbaled seeker system during assembly to relax required manufacturing tolerances

- High reliability and longevity in the space environment

The benefits of magnetic suspension and pointing control make this system a low cost, highly reliable and super-preforming gimbal that should be considered for use in any high precision pointing application.

omit

An Electromagnetically Levitated Two-Axis Gimbaless Pointing Mechanism

Gerald T. Volpe, University of Bridgeport

An Electromagnetically Levitated Two-Axis Gimbaless Pointing Mechanism

Gerald T. Volpe
University of Bridgeport
Bridgeport, Connecticut

Introduction

This is a brief description for a proposed new pointing mechanism which requires no mechanical gimbals, is virtually friction free, and is vibration isolated from a ground support system or vehicle. The device uses electromagnetic forces for support levitation and pointing, both being accomplished from a ground reference thereby leaving the payload virtually free from a remotely located command center. Solid pointing angles of almost 2π steradians are achievable, limited only by structural interference. A third degree-of-freedom tilt axis can be added at will, but will not be elaborated here. Although the system is primarily intended for space vehicles in a micro-gravity environment, earth-ground support is possible with superconducting electromagnets.

Description

Figure 1 shows the basic mechanism. The large ball or hollow sphere connected to ground contains 29 electromagnets for support (15 in each of two orthogonal planes with one being shared), and three mutually orthogonal winding loops (A, B, and C) which control pointing. Shown in the figure are 15 stator electromagnets, nine of which combine with the rotor's electromagnets to support the payload for rotation angle θ about the z axis (see key). Not shown are 14 additional stator electromagnets which circumvent the sphere in the x-z plane for rotation angle ϕ about the Y axis, and 8 rotor electromagnets in the same plane.

With winding loops A,B,C de-energized, consider the payload in the reference vertical position. Dc current sources drive all 29 stator electromagnets and 17 rotor electromagnets forming 17 north-north pole pairs. Repulsive levitation is generated by 16 electromagnets with the exception being magnet 5. The stator current in magnet 5 is driven with an opposite polarity current to provide a necessary attractive vertical component balancing force. The gravity vector shown also acts vertically downward. A sketch showing the flux line pattern for the levitating magnets in the aligned state is shown in figure 2. The north poles' flux lines return via a south pole sandwich. Each south pole is designed to be narrower than the main north pole to reduce the north-south attractive forces. The south pole material therefore must be specially selected to withstand the higher flux densities as illustrated in figure 2.

As the rotor turns, the aligned state is altered so that its north poles become temporarily positioned above stator's south poles and vice-versa so that undesirable attractive forces can be developed. To

reduce this effect, the south pole magnets may be scalloped, that is, material is removed from them, as shown in figure 3. This increases the air gap reluctance path between a north-south pole pair resulting in the flux line pattern shown in figure 3a.

Pointing Control

To establish the vertical reference position, winding loop A is energized with an ac voltage source. By transformer action this causes a voltage to be induced in magnet P located colinear with the north pole levitating magnet 5 on the rotor. With the winding of magnet P terminated in a resistor, an ac current flows which produces a self-aligning dc torque in the y direction. Demagnetization of the levitating magnets will not occur because they offer a very high impedance to ac current due to the steady dc current from the current source drive which maintains proper levitation independent of the ac pointing field. The ac pointing field frequency is to be selected so as to minimize core and eddy current losses. The heating losses due to the resistive termination of magnet P are used to control damping.

When loop B is energized in addition to loop A, the resultant pointing field will point in, say, the direction y' (loop C is still de-energized). Again by induction in magnet P only, the dc restoring torque causes the payload to rotate through an angle θ to align magnet P with the y' direction. As the rotor turns, the force balance remains intact except for a small unevenness due to north-south pole attraction as previously discussed. Any force unbalance caused by this unevenness is detected by the Hall effect sensors and is compensated for. It is worth noting that although such unbalances do produce velocity variations, pointing accuracy is not affected in an equilibrium position.

When loop C is energized a flux density component out-of-the-page gives a resultant B vector a ϕ pointing angle component to which the payload magnet P, and hence the payload, must align.

A crucial problem which is anticipated is the extent to which the resultant pointing flux field is localized. If it is perfectly localized along a straight line then it cannot couple into the aligning magnet P. As the field spreads or mushrooms then coupling becomes a reality. But if the mushrooming is too large, then pointing direction becomes ambiguous. For this reason, a detailed investigation is required for the optimum design of the pointing magnetic circuit design.

SUMMARY

To summarize, a mechanism has been described to support and point an instrument in a low gravity environment. Dc electromagnets provide a stiff electromagnetic levitating force field, whereas a moderately stiff ac pointing control system creates a rolling action of the moving member upon the dc electromagnetic field. Further, the possibility of using superconducting magnets allows for the possibility of non-contact ground support and control.

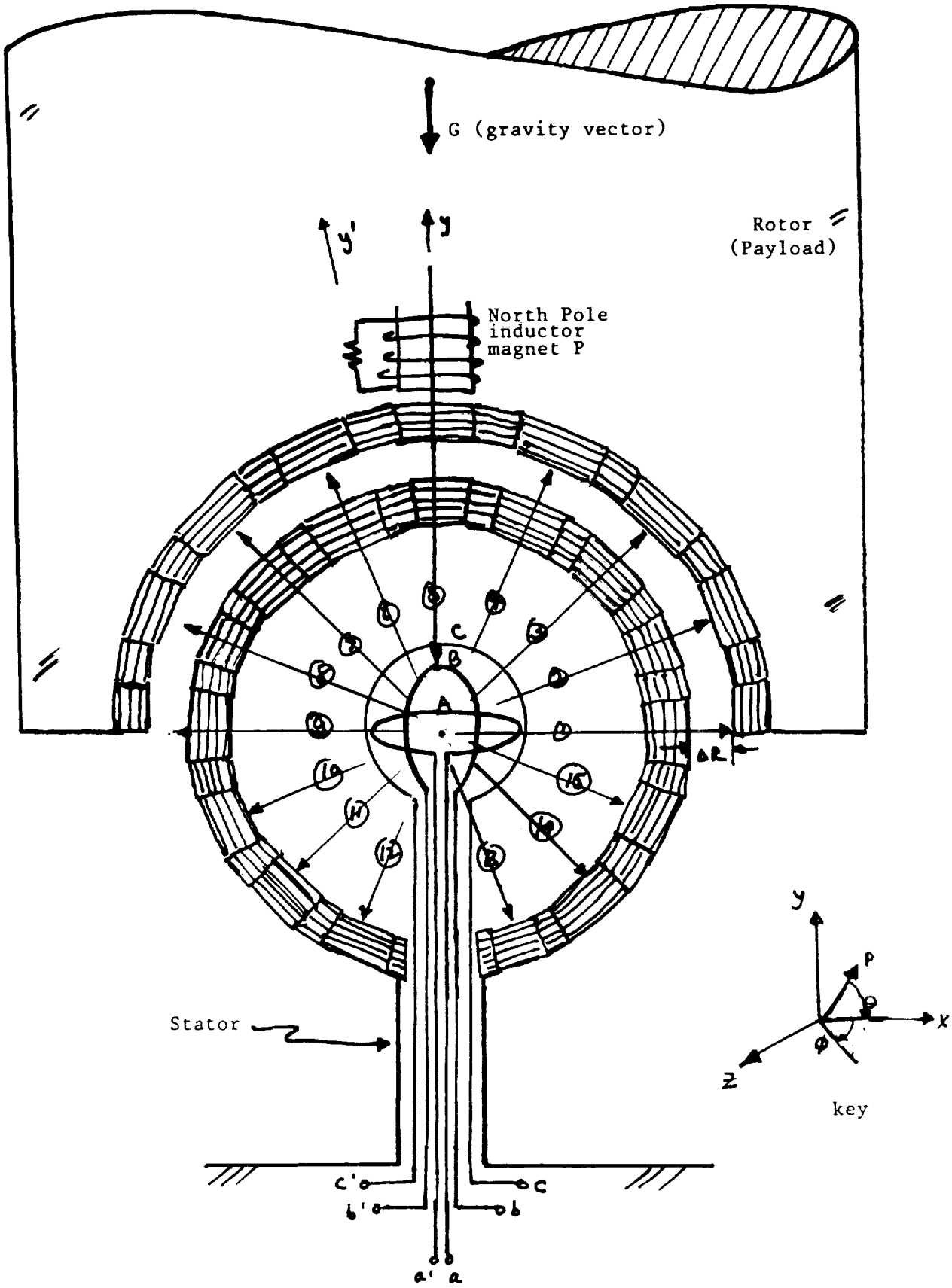

Fig 1 Electromagnetic Levitation Pointing Mechanism

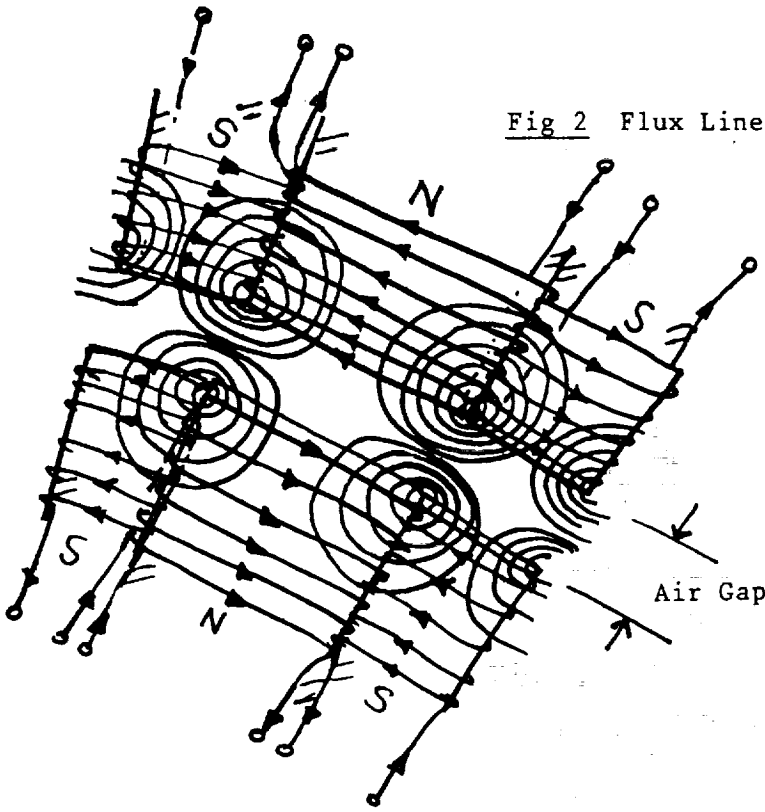

Fig 2 Flux Liner in Aligned State

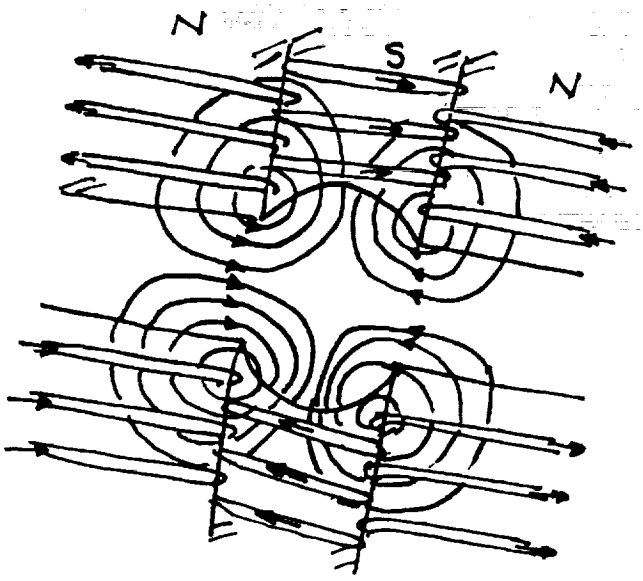

Fig 3 Scalloped South Poles in Aligned State

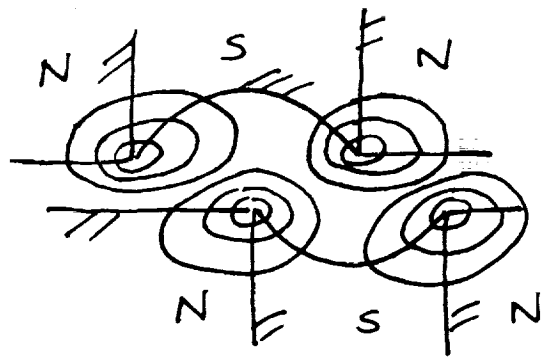

Fig 3a Increased Reluctance at South Poles reduces Attractive Forces in Quadrative State

omit

Multiple Degree-of-Freedom Force and Moment Measurement for Static Propulsion Testing using Magnetic Suspension Technology

Keith Stuart, Blake Bartosh,

Innovative Information Systems, Aura Systems Company

MULTIPLE DEGREE-OF-FREEDOM FORCE AND MOMENT MEASUREMENT FOR STATIC PROPULSION TESTING USING MAGNETIC SUSPENSION TECHNOLOGY

By
Keith Stuart
Blake Bartosh
Innovative Information Systems
an Aura Systems Company

1.0 INTRODUCTION

Innovative Information Systems (IIS), Inc. is in the process of designing and fabricating a high bandwidth Force and Moment Measuring device (i.e. the Magnetic Thruster Test Stand). This device will use active magnetic suspension to allow direct measurements of the forces and torques generated by the rocket engines of the missile under test. (See figures 1-1, 2-1, 2-2, 3-1 through 3-4, and 4-1 through 4.8.)

The principle of operation of the Magnetic Thruster Test Stand (MTTS) is based on the ability to perform very precise, high bandwidth force and position measurements on an object suspended in a magnetic field. This ability exists due to the fact that the digital servo control mechanism that performs the magnetic suspension uses high bandwidth (10 kHz) position data (via an eddy-current proximity sensor) to determine the amount of force required to maintain stable suspension at a particular point. This force is converted into required electromagnet coil current, which is then output to a current amplifier driving the coils. Figure 1-1 shows a conceptual diagram of the MTTS system components.

Section 2 contains a discussion of how the coil current and magnetic gap distance (the distance between the electromagnet and the object being suspended) is used to determine the forces being applied from the suspended assembly. If the suspended object contains a firing rocket thruster, the force of the thruster will create a motion that tends to drive the suspended object towards the opposite electromagnets. The proximity sensors will sense this motion, and the digital processor will command coil currents thus creating the servo force necessary to cancel the thruster force. The suspension servo will have the ability to cancel any forces that occur within the servo's closed loop bandwidth.

Any forces having frequency components above the servo bandwidth will cause the suspended assembly to accelerate. The motion caused by this acceleration will be tracked by the proximity sensors, and the acceleration will also be measured directly with accelerometers. Multiplying the acceleration with the suspended assembly's mass yields the force required to cause that motion. Summing the coil force with the acceleration force provides the required 10 kHz force data measurements for each pole assembly. The ability to measure high bandwidth forces well above the servo bandwidth has been demonstrated by the proof-of-concept demo, described in section 3. A 1,000 Hz sinusoidal motion disturbance was injected into a magnetically gimballed E-O seeker assembly, and measured accurately by the data acquisition and analysis system. Refer to figure 3-4.

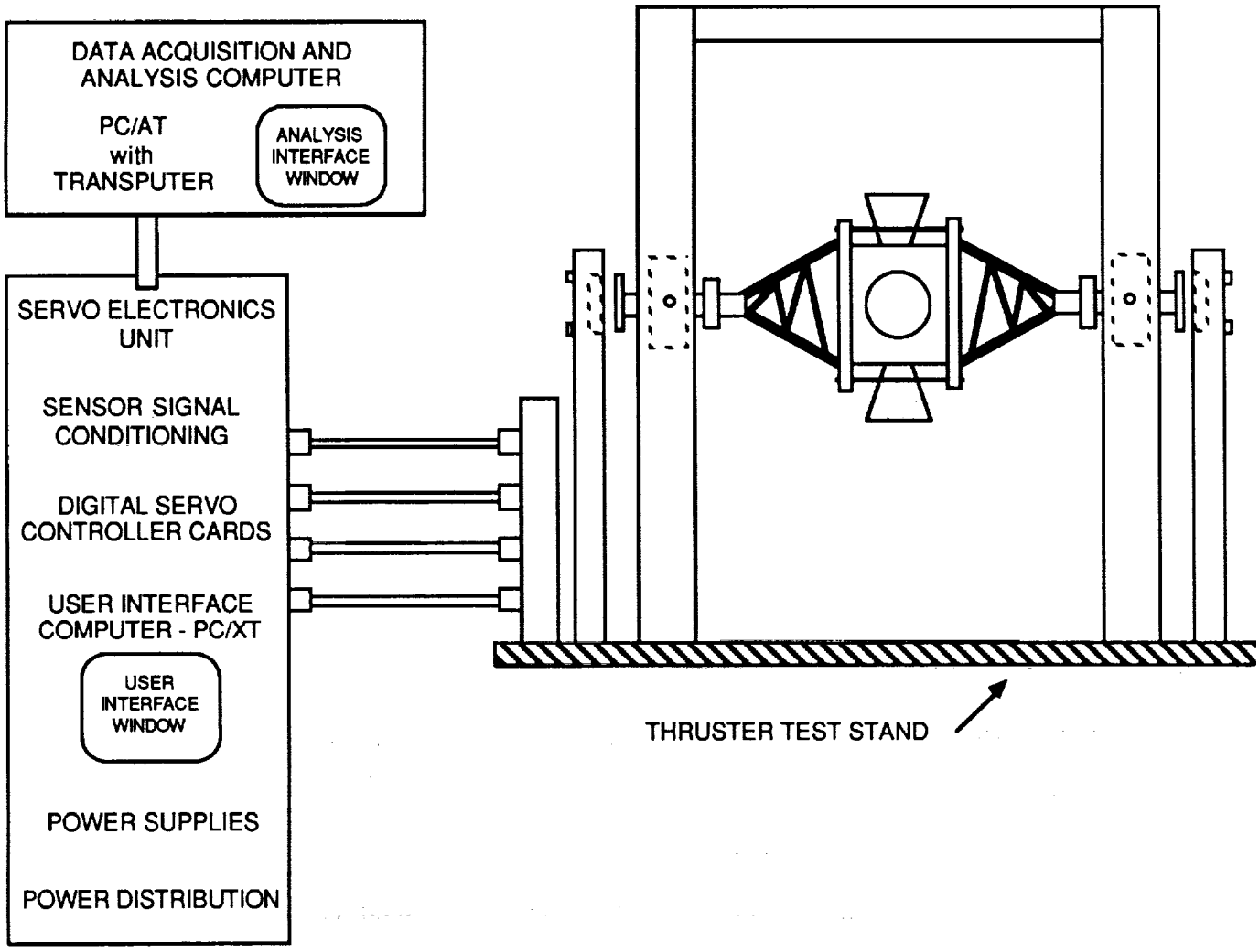

FIGURE 1-1: MTTS SYSTEM COMPONENTS

Individual coil forces can be summed in each of the lateral directions to provide 3 lateral force components, and differenced to provide the 3 angular torque components. Section 2 also contains a detailed discussion of the equations involved in this process.

It should be noted that the current and proximity sensor measurements taken by the data acquisition system reflect actual system conditions, not estimates of system conditions provided by the digital servo controller. The proximity sensor measurement reflects the actual gap distance, providing motion information up to its 10 kHz bandwidth. The current through the coils is measured by tracking the voltage across a resistor in series with the electromagnet coil. The digital processor is commanding that current level in discrete steps every 250 microseconds, but the actual system parameter of electromagnet coil current is the quantity that affects servo behavior, not the commanded level. By measuring the current directly, a much more accurate, higher bandwidth state of the system is obtained than would be possible if digital servo parameters were acquired.

SECTION 2: COMPUTING ELECTROMAGNETIC FORCE

Figure 1-1 showed a conceptual diagram of the MTTS system. The two radial magnetic bearings control the radial position of the vehicle in the support assembly, the axial electromagnets control axial position, and the two rotary actuators control the pitch angle.

When a divert thruster is fired, the vehicle/support assembly will be driven towards the radial electromagnets opposite to the firing thruster. The electromagnets opposite the direction of thrust will be activated by the servo, cancelling out the force of the thruster.

The amount of force being applied by the electromagnets during the thrust is dependent on the reluctance of the magnetic circuit, the number of turns in the electromagnetic coil and the current flowing through the coil.

Figure 2-1 contains a diagram of the closed magnetic "circuit" that is used for each of the pole assemblies. The magnetic circuit is analogous to an electric circuit. The material used in the pole pieces conducts magnetic flux, as wire conducts electrical current.

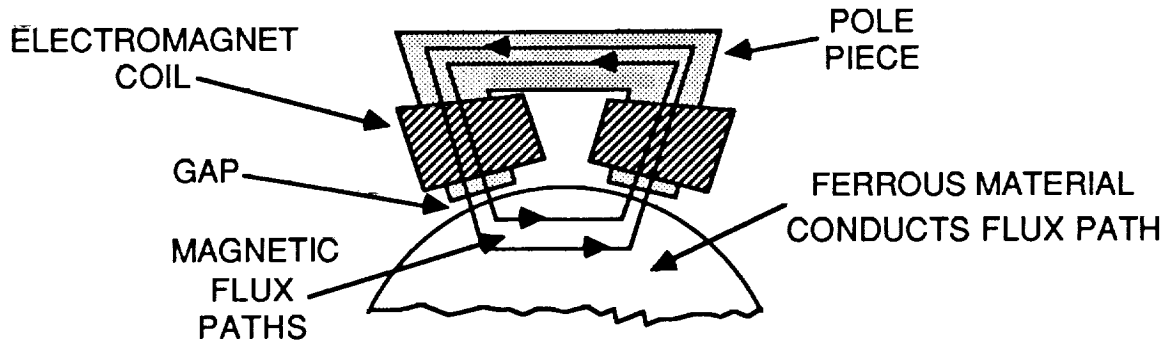

FIGURE 2-1: CLOSED MAGNETIC CIRCUIT

The reluctance of the pole assembly circuit in Figure 1-1 is computed as follows:

$$R_t = 2R_g + R_m$$

where: R_t is the total reluctance
R_g is the gap reluctance
R_m is the magnetic material reluctance

The reluctance of the material is a constant value that is measured during assembly. The reluctance of the magnetic gap is computed as follows:

$$R_g = \frac{l_g}{\mu_o A_g}$$

where: A_g is the cross sectional area of the gap
l_g is the gap length
μ_o is the permeability of free space

The magnetic flux density can now be computed:

$$B = \frac{Ni}{A_g R_t}$$

where: B is the magnetic flux density
Ni is the number of ampere-turns

With the flux density, the force that the electromagnet is applying to the rotor is computed:

$$F_c = \frac{B^2 A_g}{\mu_o} L_f$$

where L_f is the magnetic leakage factor

The data acquisition system will update the coil current and gap width measurements every 100 microseconds.

2.1 Computing Force of Motion

The electromagnetic coil can only respond and cancel forces whose frequencies are below the 200 Hz closed loop servo bandwidth. Any force components above that frequency will cause a force imbalance, which will in turn cause accelerations and thus motions to the vehicle and support assemblies.

The eddy current proximity sensors possess a bandwidth of 10 kHz, and therefore can track that residual motion. Figures 4-1 through 4-6 show examples of the various time waveforms during a thrust. In that example, when the truster is activated, the leading edge, high bandwidth component of the force will move the vehicle approximately 0.015 inches in about 5 msec until enough current has built up in the coil to balance the force and stop the motion. Accelerometers mounted on the suspended structure provide the acceleration levels. Multiplying the acceleration by the mass yields the high bandwidth force component that was not controlled by the servo.

Summing the electromagnet force computed above with the high bandwidth motion force yields a high bandwidth measurement of the force induced by the thruster.

2.2 Computing Total Thruster Forces and Torques

The above sections showed how high bandwidth force data was derived for an individual pole assembly. Figure 2-2 illustrates how the thruster force is distributed throughout the radial and axial poles of the system. By summing the force components of each pole assembly, the total force in the three lateral directions can be found as follows:

$$F_{x_t} = F_{x1} + F_{x2}$$

$$F_{y_t} = F_{y1} + F_{y2}$$

$$F_{z_t} = F_{z1} + F_{z2}$$

F_{x1} , F_{y1} and F_{z1} are the force vector components at bearing 1

F_{x2} , F_{y2} and F_{z2} are the force vector components at bearing 2

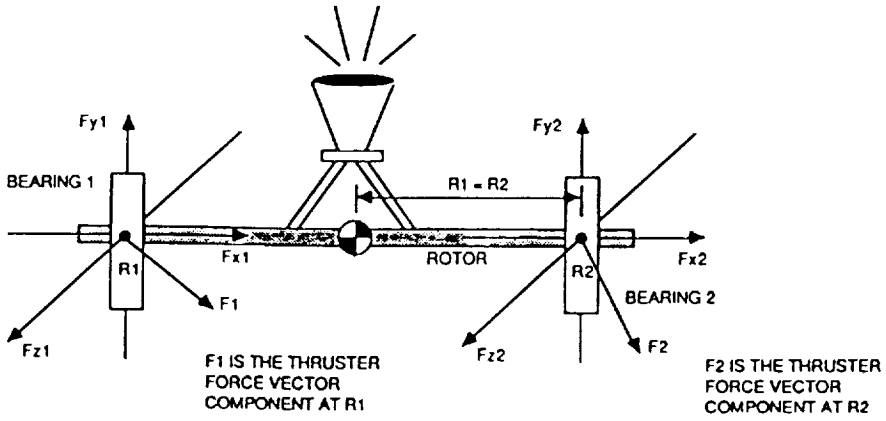

FIGURE 2-2: THRUSTER FORCE DISTRIBUTION

Similarly, the torques in the three angular directions can be found as follows:

$$T_{yaw} = (F_{z1} - F_{z2}) \times R$$

$$T_{roll} = (F_{y1} - F_{y2}) \times R$$

$$T_{pitch} = I_{act} \times K_{act}$$

where R is the moment arm
I_{act} is the current through the rotory actuator
K_{act} is the rotory actuator torque constant

Note that the torque in the pitch axis is measured directly from the angular actuator current.

3.0 Proof of Concept Feasibility Demo

In October, 1987, IIS modified the single axis magnetic gimbal hardware to demonstrate the feasibility of the MTTS engineering approach. The following paragraphs contain a description of the hardware and the results of the testing.

Figure 3-1 contains a diagram of the hardware configuration. The basic gimballing system consists of a pair of magnetic bearings which support a 16.5 pound structural model of a missile IR sensor mounted on an aluminum shaft. The axial direction is controlled passively by opposing Samarium Cobalt magnets on each end. The pitch angle is controlled by a rotary actuator.

The servo electronics consist of a single Motorola 68020 processor servicing the four radial suspension servos and the single rotary servo. This board is housed in a PC/AT computer, providing 5 channels of 12 bit A/D and D/A conversion.

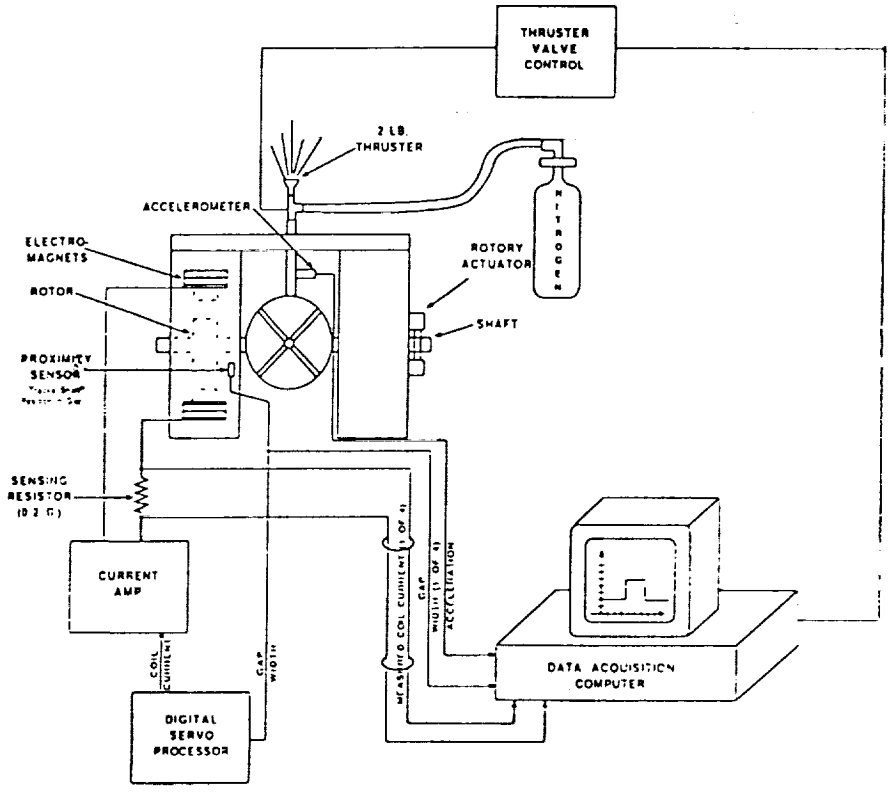

FIGURE 3-1: THRUST STAND FEASIBILITY DEMO SET-UP

A thruster support pedestal was designed and fabricated for the seeker, providing an attachment point for a 1.5 pound cold gas thruster. The thruster, associated valve driver electronics and high pressure nitrogen source was provided by Rocketdyne.

IIS constructed a rack-mounted electronic interface module providing the means to pick-off the appropriate servo signals for data acquisition. These signals were conditioned through an op- amp network, and included the following parameters:

- 4 channels of coil current data
- 4 channels of proximity sensor data
- 1 channel of accelerometer data

An 8-channel A/D converter printed circuit board was placed into the data acquisition computer (another PC/AT). To allow data acquisition of the accelerometer data, a multiplexing circuit was added to a channel of coil current data.

An additional electronic circuit was constructed to provide the means for the computer to command the thruster control valve on and off for user-defined intervals. The actual valve driver electronics was provided by Rocketdyne, commanding the high speed solenoid in the Moog thruster valve.

The software required to fire the thruster and acquire and process the data consists of 1,000 lines of assembly code to control the A/D card, 2,500 lines of "C" to un-interleave the A/D data that was dumped into computer RAM, and 3,000 lines of Fortran code to convert the raw data to engineering units and plot the results.

The fabrication of the mechanical interface, the electronic interface module and the development and debug of the software was accomplished in 3 weeks.

3.2 Results of Static Weight Testing

Figure 3-2 shows the data output of the feasibility hardware with no weight added, then with an additional weight of 1.63 lbs added. Since the weight of the seeker assembly itself contributes to the total force measured, the effect of the added weight is the delta between the weight measurements. A weight of 1.80 lbs was measured, and was within 0.17 lbs of the actual additional weight. The overall measurement accuracy is approximately 1% for static weight measurements $\left(\frac{.17\ lb}{16.77lb \times 100}\right)$.

The static force measurements were made with the nitrogen feed tube attached. Another static weight measurement was taken with this tube removed, providing a better accuracy of 0.01 lbs out of the 1.63 actual mass weight.

Figure 3-3 shows the resulting force from the firing thruster with a duty cycle of 50 msec on, 10 msec off. The thruster was being driven with nitrogen gas at 2,000 psi pressure.

The total force of the thruster varied from 2 to 2.3 lbs. The bumpiness seen on the waveforms could be caused from several factors, including:

- Line pressure variations: a pressure gauge attached to the feed line showed 200 lb pressure fluctuations during thruster firing.

- Feed line expansion/contraction: the terminal feed line was flexible, braided metal that got noticeably more stiff when it was pressurized.

- Feed line structural feedback: the firing of the thruster created an expected motion component onto the suspended seeker assembly. This motion caused the line to vibrate, providing the possibility of parasitic structural vibrations to be transmitted back to the seeker and sensed by the proximity sensors.

- Inaccuracies in the computation of seeker acceleration. Two methods of acceleration measurement were tried. The first used an accelerometer to sense the accelerations directly. Unfortunately, the "pinging" caused by the opening and closing of the thruster solenoid excited a 5 kHz structural mode in the accelerometer, setting up an electronic ringing component that buried the real thruster-induced accelerations. The second method used the proximity sensor data to derive the acceleration through double differentiation of the motion curve. Due to the coarseness of proximity sensor resolution (0.0002 inch sensitivity) and the 12 bit truncation, this signal had to be heavily filtered to provide reasonable data. Due to this, the acceleration was updated once every 1.0 msec rather than the 0.1 msec data acquisition rate. This filtering could have potentially removed some data, causing additional noise contributions.

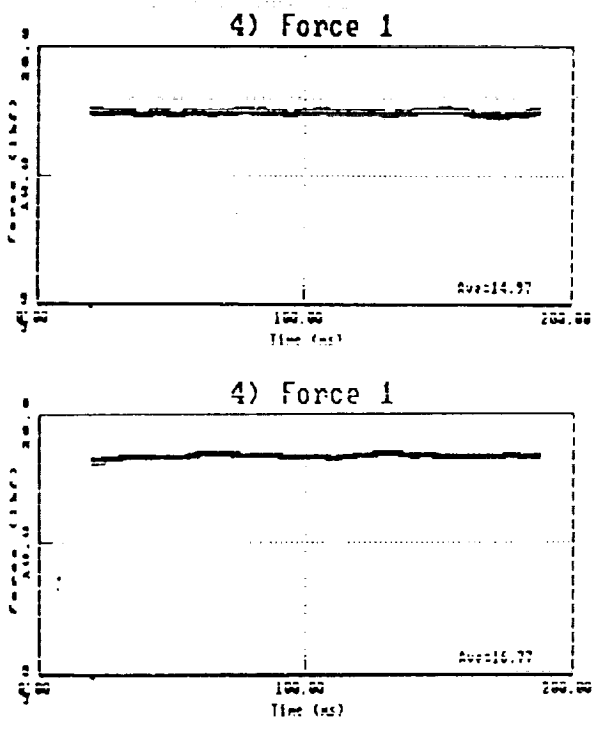

No Additional Static Weight Added

1.63 lb Static Weight Weight ASdded

Measured Weight :
16.77 lb - 14.97 lb = 1.80 lbs

FIGURE 3-2: FEASIBILITY DATA OUTPUT, STATIC TESTING

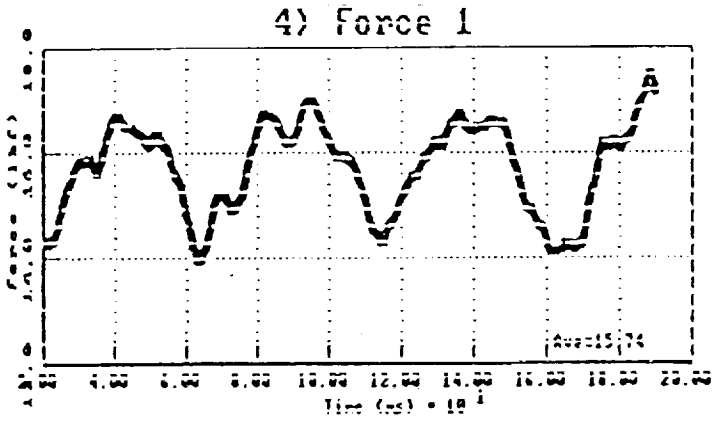

FIGURE 3-3: FEASIBILITY DATA OUTPUT, DYNAMIC THRUSTER TESTING

A major benefit of the MTTS system is its ability to measure events that occur at frequencies above the magnetic suspension's servo bandwidth. This capability was demonstrated on the feasibility hardware. A 1 kHz motion was induced electronically by injecting an open loop disturbance into the closed loop servo. The data in Figure 3-4 was acquired, tracking the 1 kHz disturbance induced into the seeker mechanical assembly.

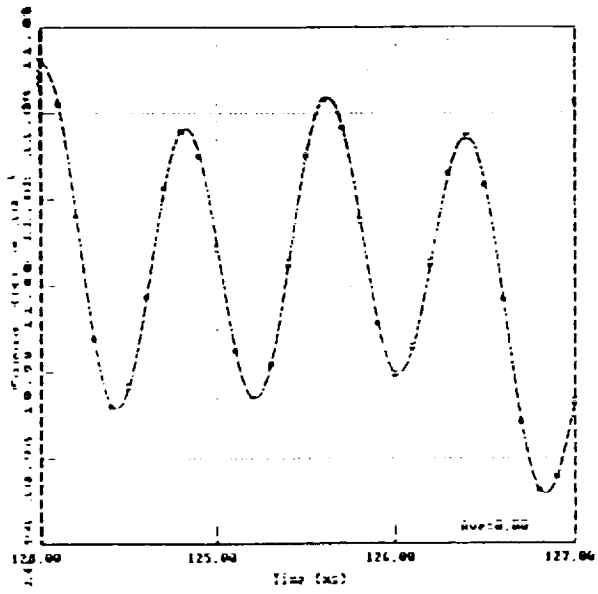

FIGURE 3-4: MECHANICAL JITTER DATA RESULTS

4.0 FORCE AND TORQUE MESAUREMENT RESOLUTION ANALYSIS

The force and torque measurement resolution is dependent on the system's ability to accurately measure electromagnet force, gap displacement and acceleration. The analysis that ties the subsystem hardware performance with these parameters follows.

4.1 System Resolution Analysis

Due to the non-linear nature of the system, a computer analysis was required to determine the overall force measurement resolution of the MTTS. The computer analysis modeled the reaction of the MTTS to user-specified thrust levels (see figure 4-1 for an example of a 222.5 Newton thrust force--the force one pole will see during a 100 lb thruster firing). This thrust level was then used to determine the force reaction to the coil (see figure 4-2). Subtracting the coil force from the thruster force yields the resultant force applied to the suspension shaft, on which the thruster resides (see figure 4-3). The shaft velocity and position change is then determined from the resultant force (see figures 4-4 and 4-5). The actual coil current can also be determined from the coil force curve (see figure 4-6).

Figures 4-1 through 4-6 show how the actual system parameters are determined from a thrust event. By using the position curve to emulate proximity sensor data, the coil current curve to emulate current measurement data, and shaft acceleration data to emulate the acceleration, the thruster force can be computed in the same way as it would be by the MTTS's data acquisition system. The thruster force is then re-computed with coil current measuring resolution, proximity sensor resolution and accelerometer resolution taken into account. These two results are used to determine the RMS error starting at 100 micro-seconds after thrust initiation, and ending 8 milliseconds into the thrust.

4.2 Analysis Results of Linear Thrust Case

Overall linear force errors were computed for 2 thrust levels: 2.5 lbs and 100 lbs. The results are given in figures 4-7 and 4-8, and in Table 4-I. In both cases, the total weight of the suspended object (vehicle plus associated fixture supports) was estimated to be 20 lbs. The resulting total RMS error combines the accumulated errors in two poles needed to obtain the total thruster force in a particular direction.

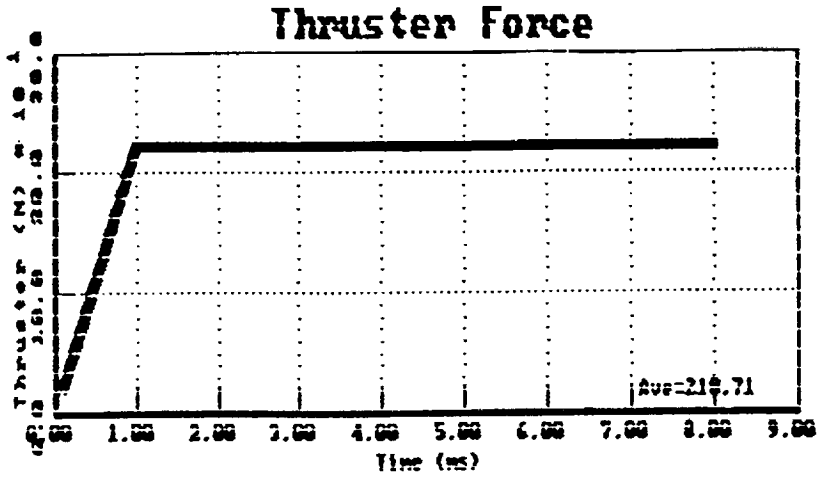

Figure 4-1: 100 lb Thruster Force On a Single Pole

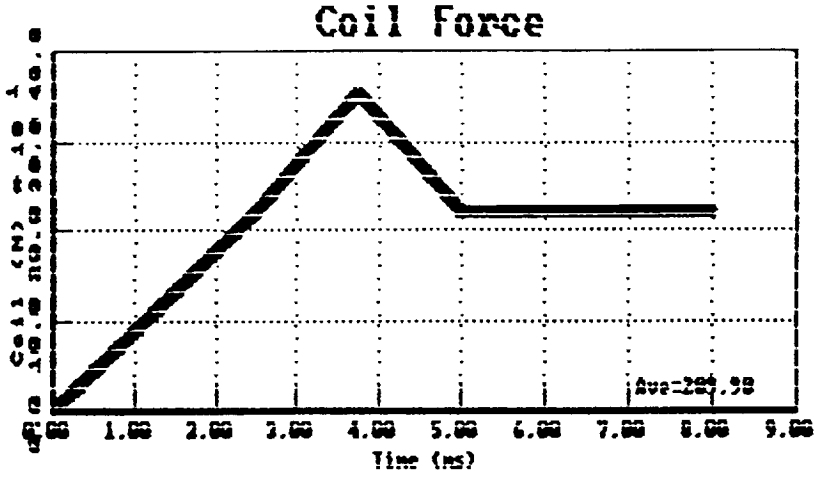

Figure 4-2: Resulting Coil Force from 100 lb Thrust

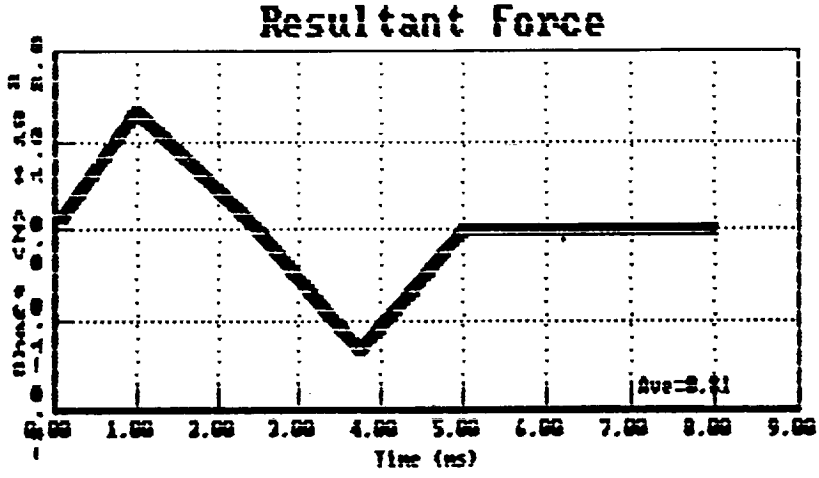

Figure 4-3: Resultant Shaft Force
(Thruster Force Minus Coil Force)

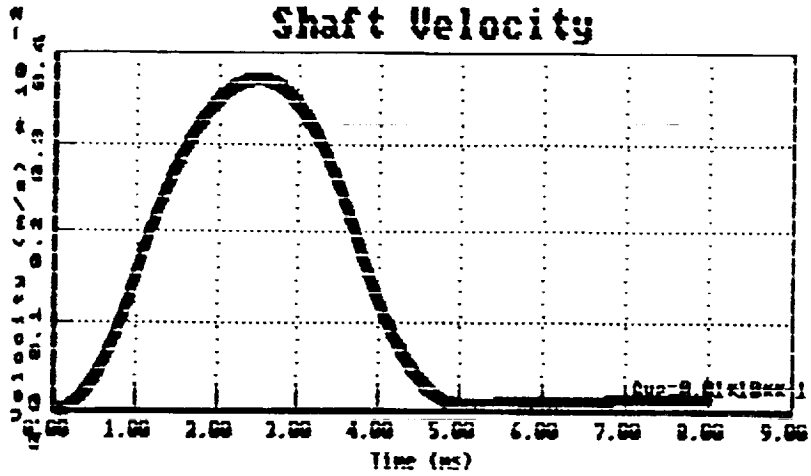

Figure 4-4: Shaft Velocity Due to Resultant Force

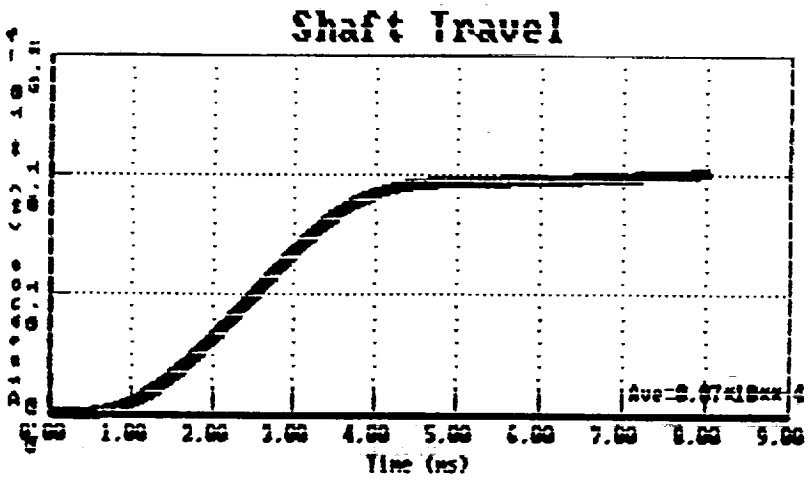

Figure 4-5: Shaft Travel Due to Resultant Force

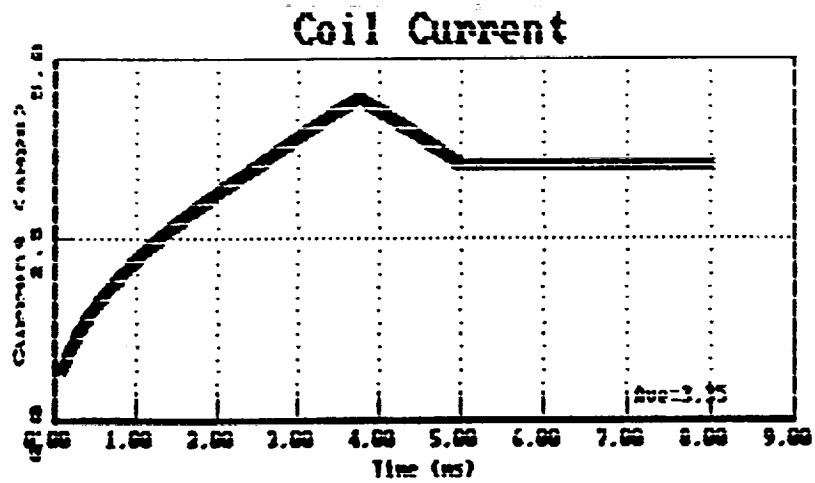

Figure 4-6: Coil Current

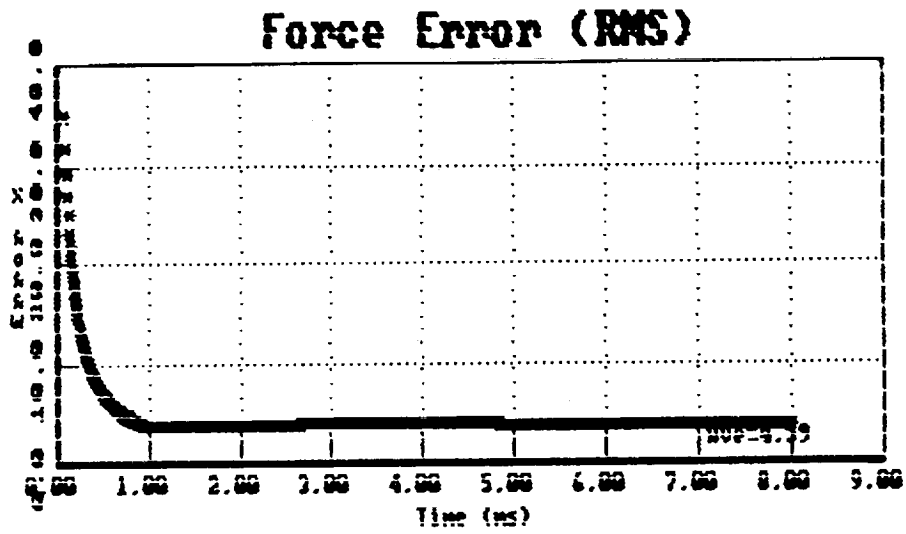

Figure 4-7: Total RMS Force Error for 2.5 lb Thruster

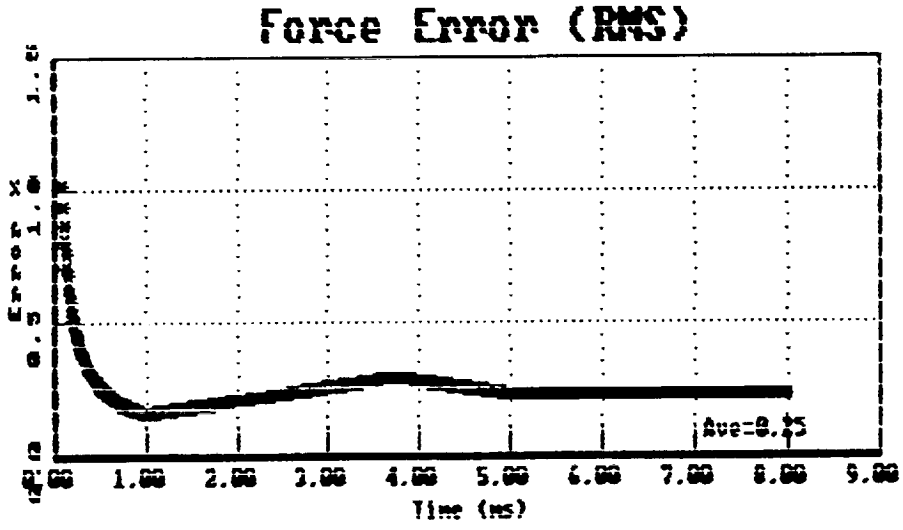

Figure 4-8: Total RMS Force Error for 100 lb Thruster

C3

TABLE 4-1: PERCENT TOTAL FORCE ERROR Vs. TIME

Time (MSec)	Percent Error* 2.5 lbs	100 lbs
0.1	34.9	1.03
0.2	17.7	.56
0.3	11.9	.40
0.4	9.0	.32
0.5	7.3	.27
0.6	6.1	.23
0.7	5.3	.21
0.8	4.6	.19
0.9	4.1	.18
1.0	3.7	.16
2.0	3.9	.21
3.0	4.0	.26
4.0	4.1	.29
5.0	4.0	.24
6.0	4.0	.24
7.0	4.0	.24
8.0	4.0	.24

*Current Measurement Resolution = 0.0005 Amps
Proximity Sensor Resolution = 1.27 x 10-7 Meters
Accelerometer Resolution = 3.0 x 10-4 G's

The torque measurement resolution is a function of the force resolution computed above, plus the physical distance between the two radial magnetic bearings and the various moments of inertia. These parameters will be determined during the design phase. Once the distance and moments of inertia are available, an analysis providing the torque measurement resolution of the MTTS will be performed.

omit

Session 4

Rotating Systems

Chairmen: Nelson J. Groom

NASA Langley Research Center

and

James F. Wilson

Honeywell Inc.

omit

Design and Test of a Magnetic Thrust Bearing

Paul E. Allaire, Bibhuti Banerjee, David W. Lewis, J. Imlach, University of Virginia

Andrew Mikula, Kingsbury Inc.

DESIGN AND TEST OF A MAGNETIC THRUST BEARING

P. E. Allaire, Professor (1)
A. Mikula, Director of Marketing (2)
B. Banerjee, Research Associate (1)
D. W. Lewis, Professor (1)
J. Imlach, Research Associate (1)

(1) Mechanical and Aerospace Engineering Department
Thornton Hall
University of Virginia
Charlottesville, VA

(2) Kingsbury, Inc.
10385 Drummond Road
Philadelphia, PA

ABSTRACT

A magnetic thrust bearing can be employed to take thrust loads in rotating machinery. This paper describes the design and construction of a prototype magnetic thrust bearing for a high load per weight application. The theory for the bearing is developed in the paper. Fixtures were designed and the bearing was tested for load capacity using a universal testing machine. Various shims were employed to have known gap thicknesses. A comparison of the theory and measured results is presented in the paper.

INTRODUCTION

Magnetic bearings are beginning to be used in significant numbers of rotating machinery. Industrial uses have included compressors, pumps, and turbines. Uses in space applications may include platform supports, telescopic pointing devices and flywheels. The type of magnetic bearing discussed in this paper is basically a single axis device which might be called either a thrust bearing or a magnetic suspension system.

Normally magnetic bearings for shaft support are employed in a set which includes a double acting thrust bearing and two radial bearings. The thrust bearings have not been discussed in the literature very much, in comparison to radial bearings. The first work by the authors on a magnetic support system of this type was reported in Allaire et al. [1]. This paper describes a single pole electromagnetic support system to verify the concept and compare it to some theoretical calculations. A second paper by Humphris, et al. [2] investigated the effects of control algorithms for magnetic support systems.

Some early work on magnetic thrust bearings was reported by Shimizu and Taniguchi [3,4]. They considered the control system required for operating the bearing. Some information on the S2M design of commercially available thrust bearings is given by Haberman, et al. [5,6] but few details are given. A drawing of a combination radial and thrust bearing is given in [6]. Applications of these bearings have been reported for pipeline compressors by Foster et al. [7] and Hustak

et al. [8]. Operation of the bearings in the industrial environment has been quite successful.

Work on an unusual magnetic bearing design was reported in [9,10]. The bearing was designed to be active axially but passive radially. Lewis and Allaire [11] investigated the potential use of magnetic thrust bearings for control of transmitted forces. The magnetic bearing would be used in conjunction with an oil thrust bearing.

Fairly extensive work has been reported on applications for satellite attitude control and energy storage. A three axis magnetic suspension system is described by Eisenhaure, et al. [12] employing high energy samarium cobalt permanent magnets. Anand, et al. [13] describes a flywheel magnetic bearing of combined active and permanent magnet design.

The purpose of this paper is to discuss the theory associated with active magnetic thrust bearings and present some experimental results on a prototype bearing. The theory describes the properties of the magnetic thrust bearing using electromagnetic principles. Design parameters associated with the bearing are then related to the bearing thrust and effective stiffness and damping parameters. A prototype bearing was constructed and the thrust capability measured. The measured results are compared to the theory.

NOMENCLATURE

A	Area
A_1	Area of inner pole face
A_2	Area of outer pole face
A_g	Area of air gap
B	Magnetic flux density
d	Depth of coil gap
D_1	Inner diameter of stator
D_2	Inner diameter of coil gap
D_3	Outer diameter of coil gap
D_4	Outer diameter of stator
F	Total force on thrust runner
F_p	Force on one pole face
h	Effective magnetic circuit gap
h_f	Effective gap of iron path
h_g	Air gap
i	Current in coil
K	Leakage correction factor
L	Axial length of stator
L_b	Axial length of stator base
L_f	Length of iron path
L_r	Axial length of thrust runner
L_t	Axial length of stator toroids
MMF	Magnetomotive force
N	Number of turns in coil
R	Total Reluctance of magnetic circuit
R_g	Reluctance of air gap
R_{Fe}	Reluctance of iron path
μ_o	Permeability of free space (air) $= 4\pi \times 10^{-7}$ Wb/A-turn-m
μ_r	Relative permeability of iron (4000)
ϕ	Magnetic flux

MAGNETIC THRUST BEARING DESCRIPTION

A magnetic thrust bearing has an electromagnetic stator and a thrust runner, as illustrated in Fig. 1. They are separated by an air gap or water gap when applied to

a pump. Because the electromagnet is attractive, the thrust bearing must be double acting to operate successfully for most applications. This is discussed in more detail later in the paper.

In its simplest form, the electromagnetic stator is formed by an inner and outer toroid connected by a common base. Figure 2 shows an exploded view of the stator, shaft, and thrust collar of a single acting bearing. All of the magnetic components are made of magnet iron. The inner and outer toroids and base may be constructed of separate pieces for ease of assembly. They may be held together by screws or other methods. Figure 3 gives a perspective view of the assembled stator. A coil of wire occupies the space between the inner and outer toroids. This produces the magnetic flux in the bearing. Magnetic flux paths are illustrated in Fig. 4 flowing through the inner and outer toroids as well as the thrust runner. It is important to provide a good flux path to avoid leakage from the magnetic components.

The rotating part of the bearing, in its simplest form, is a solid disk made of magnet iron and attached to the shaft. Fig. 2 illustrates this construction of the thrust runner. Unlike the rotating part of radial magnetic bearings, the thrust runner does not cross alternating magnetic flux lines so it does not have to be laminated to reduce eddy currents.

An electronic circuit controls the current in the coils of the stator, as illustrated in Fig. 4. The axial position of the thrust runner is continuously monitored by a sensor. The voltage from the sensor is fed into a sensor amplifier. This in turn enters a compensator, summer, and lead network or other network suitable for a given application. A current amplifier then supplies the appropriate current to the coils in the magnetic stator.

A steady state current provides the attractive force between the stator and runner which gives the bearing its steady load capacity. The bearing by itself has a negative stiffness (discussed later in [2]) so an automatic control circuit is required to give the bearing an effective positive stiffness. The position sensor is used to sense the axial position of the shaft and to provide the feedback signal to the control loop which creates the positive stiffness.

THEORETICAL MODEL

The theoretical model of the thrust bearing used in this paper is a one dimensional theory. It is assumed that the flux can be taken as varying only along the flux lines. No attempt is made here to do a finite element analysis of the magnetic flux in a two or three dimensional manner.

Several assumptions are made in this derivation for the sake of simplicity:

1. No leakage occurs between the toroids.
2. Flux levels are always below saturation.
3. Changes in the current are small compared to the steady state level.
4. Axial shaft motions are small compared to the steady state air gap.
5. A one dimensional model of the magnetic path may be used.

The first assumption is valid if the radial dimension of the space between the toroids is large compared to the air gap. If not, a leakage factor can be used as developed in Appendix A. The second assumption depends upon the proper design of the thrust bearing for the expected loads. Both assumptions 3 and 4 are generally valid

if the bearing is operating properly. The steady state current is usually large compared to oscillating thrust loads and the axial motions are small relative to the large magnetic bearing gap thickness. Finally, a one dimensional model of the magnetic path provides a reasonable first approximation.

All of the above assumptions may be violated to some extent by actual magnetic thrust bearings and probably are. However, that means that more complex analysis needs to be carried out to supplement the analysis given here. This approach can be used for preliminary design purposes.

MAGNETIC CIRCUIT RELUCTANCE

The pole face areas A_1 and A_2 are given by (see Figure 5)

$$A_1 = \frac{\pi}{4} (D_2^2 - D_1^2) \tag{1}$$

$$A_2 = \frac{\pi}{4} (D_4^2 - D_3^2) \tag{2}$$

These areas are made equal so that the magnetic flux has the same level in each torroid. The pole face area then equals the air gap area Ag. Also, the location of the most restrictive area in the stator base is the perimeter at the outer diameter of the inner toroid. Thus the length of the base is given by

$$L_b = L - L_t = \frac{A_g}{\pi D_2} \tag{3}$$

The thrust runner has thickness L_r equal to this value.

The reluctance of each air gap is given by

$$R_g = \frac{h_g}{\mu_o A_g} \tag{4}$$

and the reluctance of the iron path is

$$R_f = \frac{L_f}{\mu_o \mu_r A_g} \tag{5}$$

Let the length of air gap magnetically be equal to the iron path h_f with value

$$h_f = \frac{L_f}{\mu_r} \tag{6}$$

The total reluctance of the magnetic circuit is

$$R = 2R_g + R_f = \frac{1}{\mu_o A_g} [2h_g + h_f] \tag{7}$$

Thus the effective magnetic gap is h where

$$h = 2h_g + h_f \tag{8}$$

including both air gaps and the iron path.

MAGNETIC FLUX

A magnetomotive force (MMF) is equal to the number of turns in the coil times the current

$$MMF = Ni \tag{9}$$

The magnetic flux is then found from

$$\phi = \frac{MMF}{R} = \frac{\mu_o A_g N i}{h} \tag{10}$$

and the flux density is

$$B = \frac{\phi}{A_g} = \frac{\mu_o N i}{h} \tag{11}$$

This must not exceed the saturation level for the particular magnetic material involved. Typical values for silicon iron are 1.2 to 1.6 tesla and for rare earth materials up to 2.0 tesla.

Often the steady state (also called bias flux level) is chosen as one half of the saturation flux level. This value gets the operating point of the thrust bearing up in the linear range of the flux but still leaves operating room for increased flux for higher load capacity as needed.

LOAD CAPACITY

Each pole face develops an attractive force with value

$$F_p = \frac{\phi^2}{2\mu A_g} = \frac{\mu_o A_g N^2 i^2}{2h^2} \tag{12}$$

There are two pole faces so the total force is

$$F = 2F_p = \frac{\mu_o A_g N^2 i^2}{h^2} \tag{13}$$

The actual force is somewhat reduced by leakage effects. A leakage parameter k is calculated for the thrust bearing geometry. The thrust bearing load capacity is then modified to include k as

$$F = \frac{\mu_o A_g N^2 i^2}{k^2 h^2} \tag{14}$$

Appendix A gives the calculation method for k.

In most industrial applications, the thrust bearing must be made double acting. Figure 6 illustrates the geometry when a single thrust runner is employed in a double acting bearing. Other rotating machines employ a split double acting thrust bearing. An example is a canned motor pump with one thrust bearing at the pump end of the canned motor and the other thrust bearing at the opposite end of the motor. The load capacity (force acting on the thrust runner) of the double acting thrust bearing is

$$F = \left[\frac{\mu_o A_g N^2 i^2}{k^2 h^2}\right]_2 - \left[\frac{\mu_o A_h N^2 i^2}{kh^2}\right]_1 \tag{15}$$

where 1 denotes the left side and 2 denotes the right side. Clearly, if the two sides are identical the thrust load is zero. However, as a thrust load is applied,

the runner will move in the axial direction creating a difference in air gaps. The automatic control circuit insures that this thrust bearing will have positive effective stiffness and damping dynamic coefficients.

PROTOTYPE THRUST BEARING

A prototype single acting thrust bearing was constructed for load capacity testing. Figure 7 shows the assembled thrust bearing but without a thrust runner (which would be attached to a shaft). Figure 8 presents the prototype bearing disassembled. Also shown is the thrust runner on the left side of the photograph. The lead wires for the coil come out of holes in the stator base for connection to the control circuit.

Some of the dimensions of the prototype are

Axial length	L = 50.800 mm (2.00 in)
Inner diameter of stator	D_1 = 40.945 mm (1.612 in)
Inner diameter of coil gap	D_2 = 64.414 mm (2.536 in)
Outer diameter of coil gap	D_3 = 71.272 mm (2.806 in)
Outer diameter of stator	D_4 = 93.345 mm (3.675 in)
Depth of coil gap	d = 39.116 mm (1.54 in)
Axial length of thrust runner	L_r = 10.160 mm (0.40 in)
Air gap	h_g = 0.508 mm (20 mils)

LOAD CAPACITY TESTING

It was desired to measure the load capacity of the thrust bearing for comparison to the calculated values. A standard tensile testing device was used to apply loads to the bearing. First, the stator was mounted on a test base as shown in Figure 9. Second, a thin nonmagnetic shim was placed on top of the stator. Third, the thrust runner was attached to the movable part of the tensile tester. The assembled test setup is illustrated in Fig. 10. The prototype thrust bearing is shown in the bottom of the photograph. Immediately above the thrust bearing is a load equalizing device to avoid cocking of loads higher on one side than the other. At the top of the photograph is the load cell used to measure the bearing load capacity.

Testing was accomplished by turning on the current in the coil and applying a load to the tester. The gap thickness is known because of the nonmagnetic shim in the normal air gap region of the bearing. The permeability of the aluminum shim is essentially the same as that of air so the effect is that of having air in the gap. Two shims were used: 0.37 mm (14.5 mils) and 0.50 mm (19.5 mils). The current in the coil is increased and the thrust load capacity measured.

A number of difficulties were encountered with using the tensile tester. Basically, it is designed as a materials test device. It proved impossible to construct a bearing holder which had zero axial tolerances. With the clearances of the testing machine and those of the magnetic bearing test device, there was always a certain amount of initial force takeup before the steady state load was attained on the thrust bearing and actual test data was taken. In short, this procedure did not produce good, reproducible test results.

Another type of test, called the drop test, was performed on the thrust bearing. In this test, a known dead load is brought up to a specific distance (separation) to the face of the thrust bearing. This separation is determined by the particular aluminum shim used for the test. Current is then applied to the bearing of sufficient level such that the dead load is captured. The dead load and the bearing is raised by the universal testing machine so that the bearing alone is carrying the dead load. Then the current level to the bearing is slowly reduced to the point at which the bearing can no longer support the load. The dead load then drops from the bearing. The current level at this point is recorded with the value of the dead load and this yields one point on the LOAD vs CURRENT curve for the particular shim (or equivalent air gap of the bearing).

Figure 11 gives the results for the measured load capacity with 0.37 mm (14.5 mils). Figure 12 shows similar results with a 0.50 mm (19.5 mil) shim. The theory used is one dimensional and considers unrolling the toroids and not producing sufficiently accurate leakage factor for this geometry. More consideration needs to be done to generate more precise leakage factors.

For a significant range (close to our operating range) the slope of the simplified theory curve agrees fairly well with the experimental work (drop test). The theory is of proper sign in that there are losses that have not been considered so when further delineation of the flux leakage is produced, the theoretical curve will be shifted to the right and the slope will decrease.

The theory for the larger gap (clearance) understates the current by some 18 percent which is sufficient for design purposes because the sign of the error is known. The design conditions for this bearing called for a 0.508 mm ($\simeq$ 20 mil) gap. This prototype bearing was designed to carry a maximum load of 136 kg (300 lbs) at 0.9 amps. A redesign has been made with the new design handling up to 1.8 amp and with capacity to handle the maximum load.

INDUSTRIAL APPLICATION

The above theory was employed to design and construct a double acting magnetic thrust bearing for a canned motor pump. The pump has a single stage overhung centrifugal impeller and the canned motor is centrally mounted between the bearings. Figure 13 is a photograph of the pump. Both radial and thrust bearings were originally made of carbon. Unfortunately these bearings have relatively short operating life, less than one year, in hydrocarbon and other service. The objective of replacing the original product-lubricated bearings with magnetic bearings is to produce an extension of life. The objective is five years. As yet there is no data available on the extremely few applications of magnetic bearings to pumps. It is the authors' understanding that magnetic bearings have been installed in a vertical pump for the French Navy but that no results have been made public.

The thrust bearing is split for this canned pump so that one side is between the impeller and motor and the other side is outboard of the motor. The magnetic bearings have the same configuration. They fit in the same components that the original bearings do except for modified bearing housings at both ends. All other components such as the impeller, casing, motor, and shaft have not been replaced or substantially modified. Actually, the radial bearings are being replaced also but this paper is concerned with thrust bearings.

The status of this project at this point in time, January 1988, is that the bearings have been designed and are being constructed. Construction will be completed and testing done over the spring of 1988. A complete pump test loop has been constructed for this purpose. Full operational flow and vibration measurements were made on the pump with the original bearings before any modifications were made. These will serve as the benchmark measurements.

CONCLUSIONS

This paper describes the theoretical modeling of a magnetic thrust bearing. The theory is a one dimensional model of the magnetic flux path through the bearing and resulting forces acting on the thrust runner. Some simplified leakage effects were included in the model. No attempt has been made to develop a more accurate two or three dimensional finite element model of the bearing as yet.

A single acting prototype was designed with this theory and tested for load capacity. The theory over-predicted the load capacity by a significant fraction but did give a good feel for the trends in the bearing. Some problems were encountered with the initial testing which probably resulted in some measurement errors. The drop testing procedure has produced more reliable and repeatable results so that the relatively simple theory employed gives a good starting place for design purposes.

Bearings of this type have been designed for a canned motor pump. They are currently being constructed and will be tested in the pump in the near future.

ACKNOWLEDGMENTS

This work was funded in part by Kingsbury, Inc. and the Center for Innovative Technology of the Commonwealth of Virginia.

REFERENCES

1. Allaire, P. E., Humphris, R. R., and Kelm, R. D., "Magnetic Bearings For Vibration Reduction and Failure Prevention," Mechanical Failures Prevention Group, 40th Meeting, April 16-18, National Bureau of Standards, Gaithersburg, Maryland.

2. Humphris, R. R., Kelm, R. D., Lewis, D. W., and Allaire, P. E., "Effect of Control Algorithms on Magnetic Journal Bearing Properties," Journal of Engineering for Gas Turbines and Power, Trans. ASME, Vol. 108, October 1986, pp. 624-632.

3. Shimizu, H. and Taniguchi, O., "Research on the Control Systems of Magnetic Bearing," Bulletin of J. S. M. E., Vol. 11, No. 46, 1968, pp. 699-705.

4. Shimizu, H. and Taniguchi, O., "Research on the Self-Exciting Vibration of Thrust-Type Magnetic Bearing (Cylindrical Mode)," Bulletin of J. S. M. E., Vol. 14, No. 72, 1971, pp. 541-549.

5. Haberman, H. and Liard, G., "An Active Magnetic Bearing System," Tribology International, April 1980, pp. 85-89.

6. Haberman, H. and Brunet, M., "The Active Magnetic Bearing Enables Optimum Damping of Flexible Rotor," ASME Paper No. 84-GT-117, ASME Gas Turbine Conference, Amsterdam, June 1984.

7. Foster, E. G., Kulle, V., and Peterson, R. A., "The Application of Active Magnetic Bearings to a Natural Gas Pipeline Compressor," ASME Paper 86-GT-61, Presented at International Gas Turbine Conference, Dusseldorf, June 8-12, 1986.

8. Hustak, J. F., Kirk, R. G., and Schoeneck, K. A., "Analysis and Test Results of Turbocompressors Using Active Magnetic Bearings," American Society of Lubrication Engineers, Preprint No. 86-AM-1A-1, Presented at 41st Annual Meeting, Toronto, May 12-15, 1986.

9. Walowit, J. A. and Pinkus, O., "Analytical and Experimental Investigation of Magnetic Support Systems. Part I: Analysis," Journal of Lubrication Technology, Trans. ASME, Vol. 104, No. 3, July 1982, pp. 418-428.

10. Albrecht, P. R., Walowit, J. A., and Pinkus, O., "Analytical and Experimental Investigation of Magnetic Support Systems. Part II: Experimental Investigation," Journal of Lubrication Technology, Trans. ASME, Vol. 104, No. 3, July 1982, pp. 429-437.

11. Lewis, D. W., and Allaire, P. E., "Control of Oscillating Transmitted Forces in Axial Thrust Bearings with a Secondary Magnetic Bearing," ASLE Transactions, Vol. 30, No. 1, January 1987, pp. 1-10.

12. Eisenhaure, D. B., Downer, J. R., Bliamptis, T. E., and Hendrie, S. D., "A Combined Attitude, Reference and Energy Storage System for Satellite Applications," AIAA Aerospace Sciences Meeting, Reno, Nevada, January 9-12, 1984.

13. Anand, D. K., Kirk, J. A., and Bangham, M. L., "Simulation, Design and Construction of a Flywheel Magnetic Bearing," Design Engineering Technical Conference, ASME, Columbus, Ohio, October 5-8, 1986.

APPENDIX A

A.1 Introduction

The flux path that has been assumed is not the only one for the magnetic thrust bearing, even though it is the only effective one for our needs. There are a number of other flux paths across the air gap which are traversed by leakage flux. This reduces the thrust capability of the bearing, since a part of the magnetomotive force is wasted to sustain the leakage flux.

A.2 Calculation of Permeances

Before the leakage coefficient can be calculated, it is necessary to compute the permeance of all the significant flux paths in the air gap. A quite comprehensive analysis for the estimation of these permeances has been presented by Roters [12]. The following material is based on his treatment of the matter.

Figure 14 identifies by number the various flux paths in the air gap that are being considered here. The two basic formulae that we need are those for the permeance of a magnetic field between parallel plane surfaces of infinite extent, and

that of a magnetic field between *non*-parallel plane surfaces of infinite extent. For the former, with reference to Figure 15, the permeance Λ is given by

$$\Lambda = \mu \frac{S}{l} \qquad (A.2.1)$$

where

S is the surface area of each of the two plane surfaces,
l is the length of the gap between the surfaces,
μ is the permeability of the medium separating the surfaces.

For a pair of non-parallel surfaces, as shown in Figure 16, a cylindrical shell of flux of radial thickness dr and axial length l may be considered. Application of equation (A.2.1) and subsequent integration over dr gives us

$$\Lambda = \frac{\mu l}{\theta} \ln \frac{r_2}{r_1} \qquad (A.2.2)$$

where

l, θ, r_2, and r_1 are as shown in Figure 16.

The permeances of the four flux paths of interest can now be determined.

Path 1: Equation (A.2.2) can be used, with

$l = \pi D_4$, $\theta = \pi$, $r_1 = h_g/2$, and $r_2 = L_r + h_g/2$

to give us

$$\Lambda_1 = \mu_0 D_4 \ln \left[1 + 2L_r/h_g\right] \qquad (A.2.3)$$

where

D_4 is the outer diameter of the bearing,
L_r is the thickness of the thrust collar, and
h_g is the air gap between the bearing and the collar.

Path 2: This flux path is a semicircular cylindrical volume. The mean length of the path is that of a line drawn midway between the diameter and the circumference of the semicircle. This equals $1.22h_g$ by graphical measurement. The mean area of the flux path is estimated by dividing the volume of the path by this mean length. On applying equation (A.2.1) now, we get

$$\Lambda_2 = \frac{\mu_0}{1.22h_g} \frac{\pi h_g^2 (\pi D_4)}{8 \times 1.22h_g} = 0.26\pi\mu_0 D_1 \qquad (A.2.4)$$

Path 4: This path has twice the length of path 2 and is identical to it in every other respect, so that it has twice the permeance:

$$\Lambda_4 = 0.52\pi\mu_0 D_3 \qquad (A.2.5)$$

Path 3: This is the only path for the useful flux. Equation (A.2.1) can be used with $S = \pi\left[D_4^2 - D_3^2\right]/4$ and $l = h_g$, to give us

$$\Lambda_3 = \frac{\pi\mu_0}{4}\,\frac{D_4^2 - D_3^2}{h_g} \qquad (A.2.6)$$

where

D_3 is the inner diameter of the outer pole.

A.3 The Leakage Factor

The ratio of the total gap permeance to the useful gap permeance is defined as the leakage factor. Thus, for the outer pole of the magnetic thrust bearing, we have

$$k_{outer} = \frac{\Lambda_1 + \Lambda_2 + \Lambda_3 + \Lambda_4}{\Lambda_3} \qquad (A.3.1)$$

The leakage factor for the inner pole, k_{inner}, can be found in the same way, with D_4 ,D_3 replaced respectively by D_1 ,D_2. The higher of these two values is chosen as the effective leakage factor, since the useful flux at one of the two poles is determined by this, and the flux intersecting each of the two pole faces is assumed to be the same. Therefore, in equation (10), ϕ must be divided by the effective leakage factor k. Since the force developed is proportional to the square of the flux, this means that the right hand side of equation (13) must be divided by the square of k to get the effective value of thrust capacity. This is what has been done in equation (14).

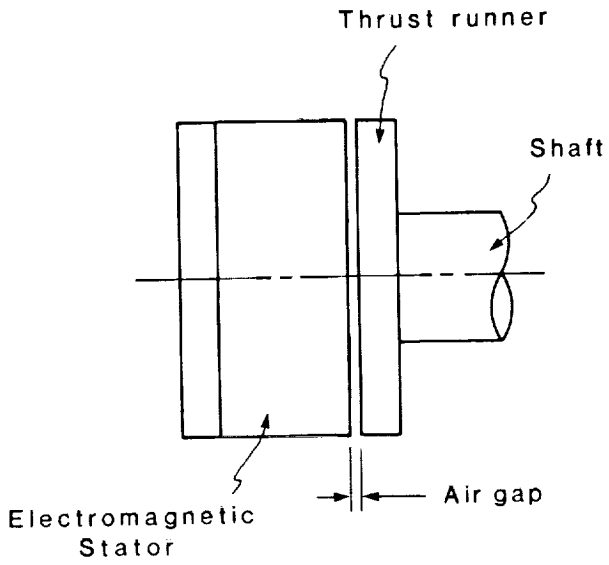

Figure 1. Basic Magnetic Thrust Bearing Geometry

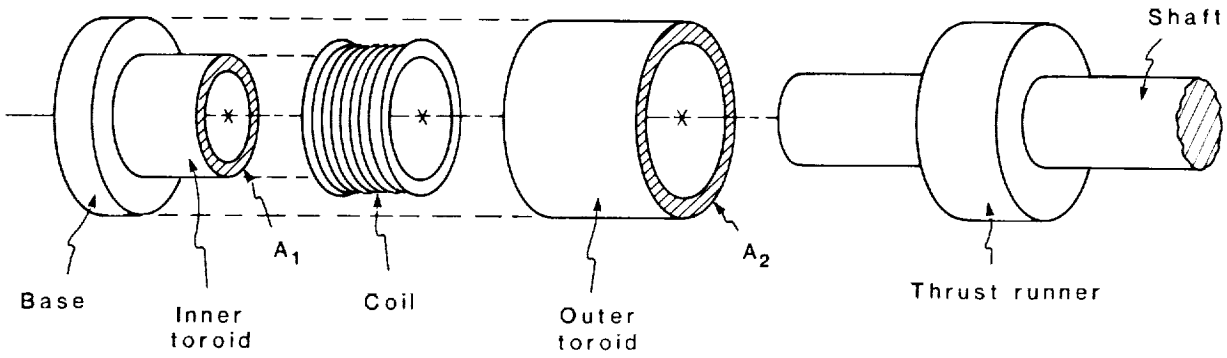

Figure 2. Exploded View of Single Acting Magnetic Thrust Bearing

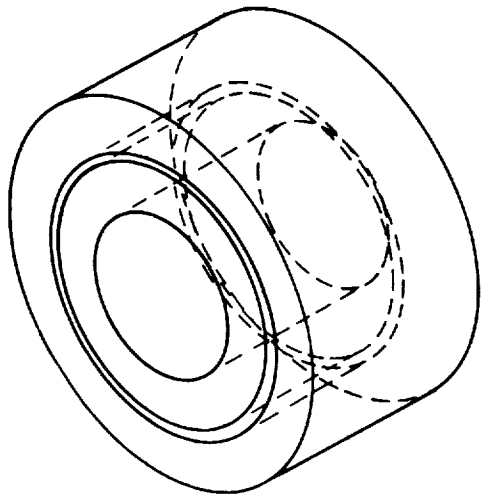

Figure 3. Perspective View of Stator for Magnetic Thrust Bearing

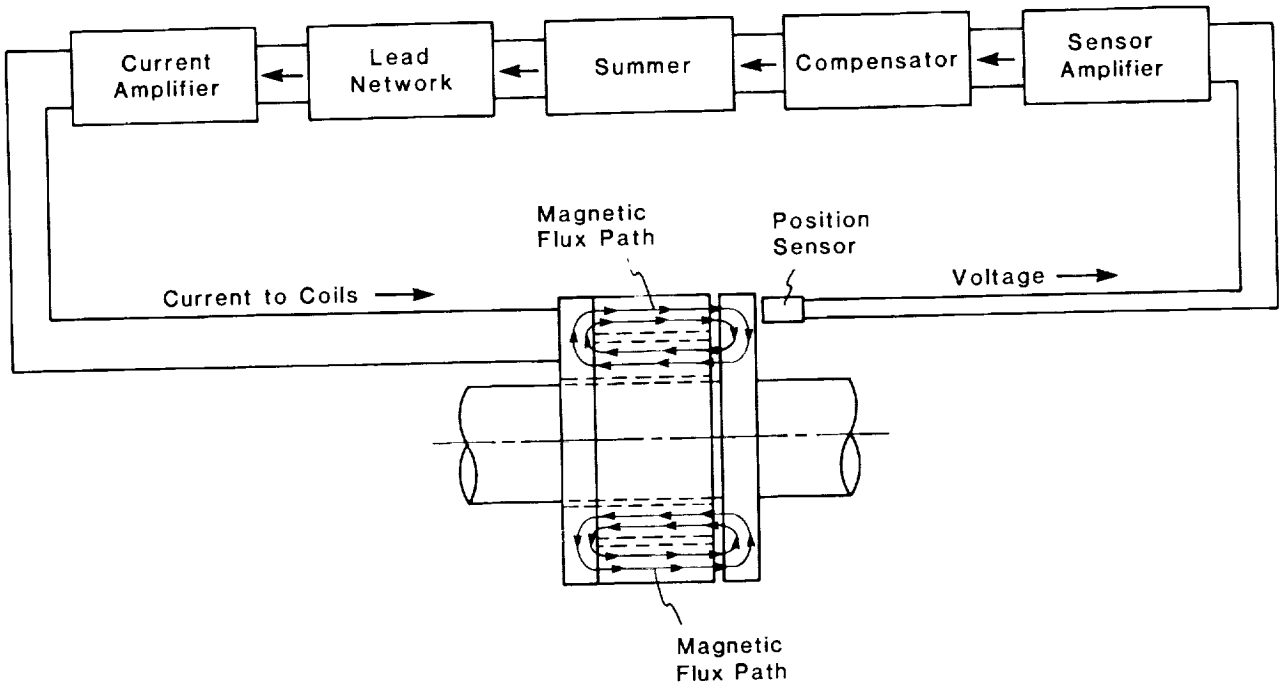

Figure 4. Magnetic Flux Paths and Control Loop in Single Acting Magnetic Thrust Bearing

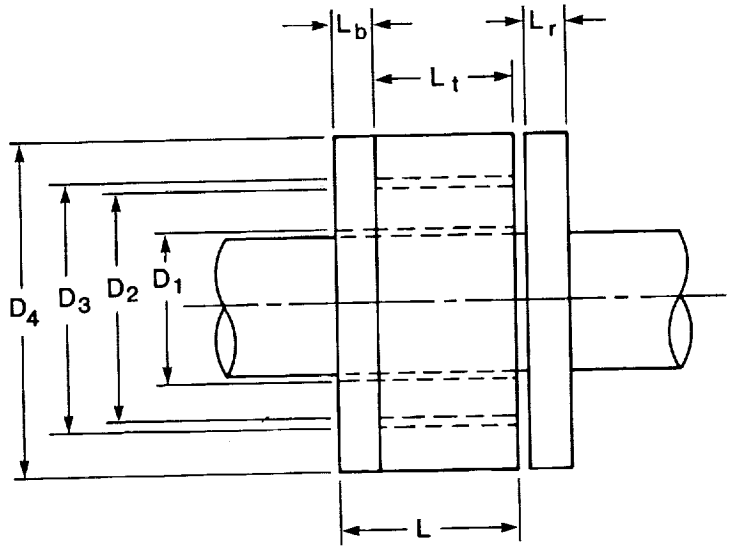

Figure 5. Geometry of Single Acting Magnetic Thrust Bearing

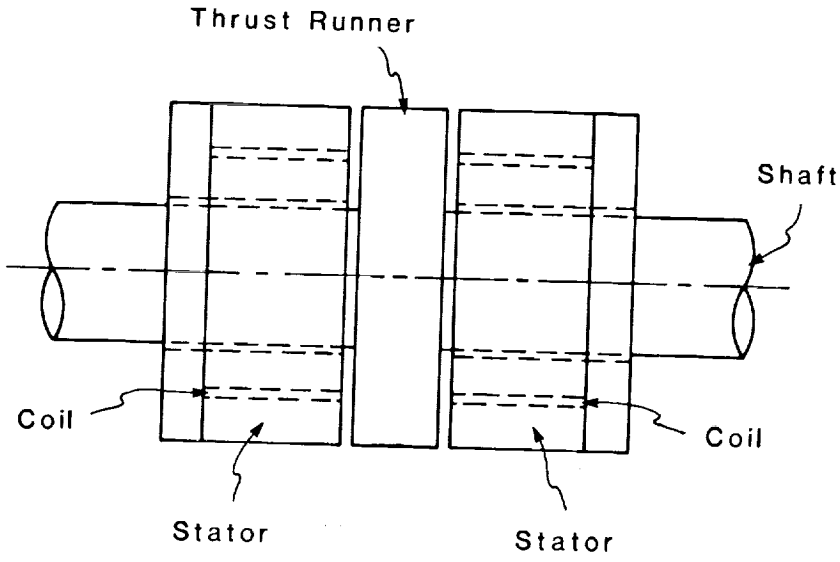

Figure 6. Geometry of Double Acting Thrust Bearing

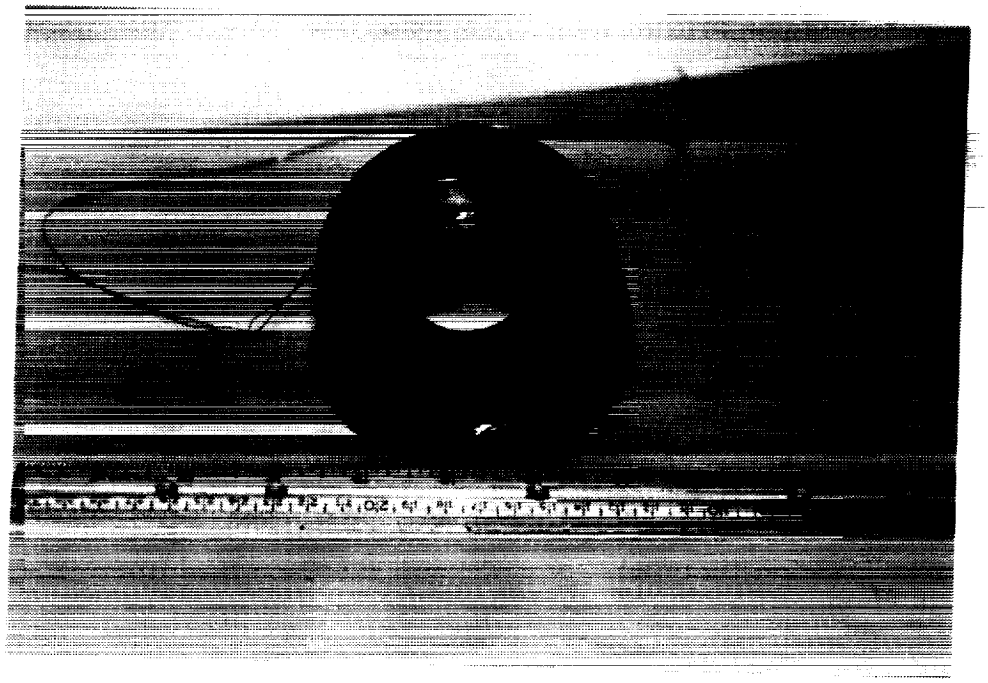

Figure 7. Prototype Thrust Bearing

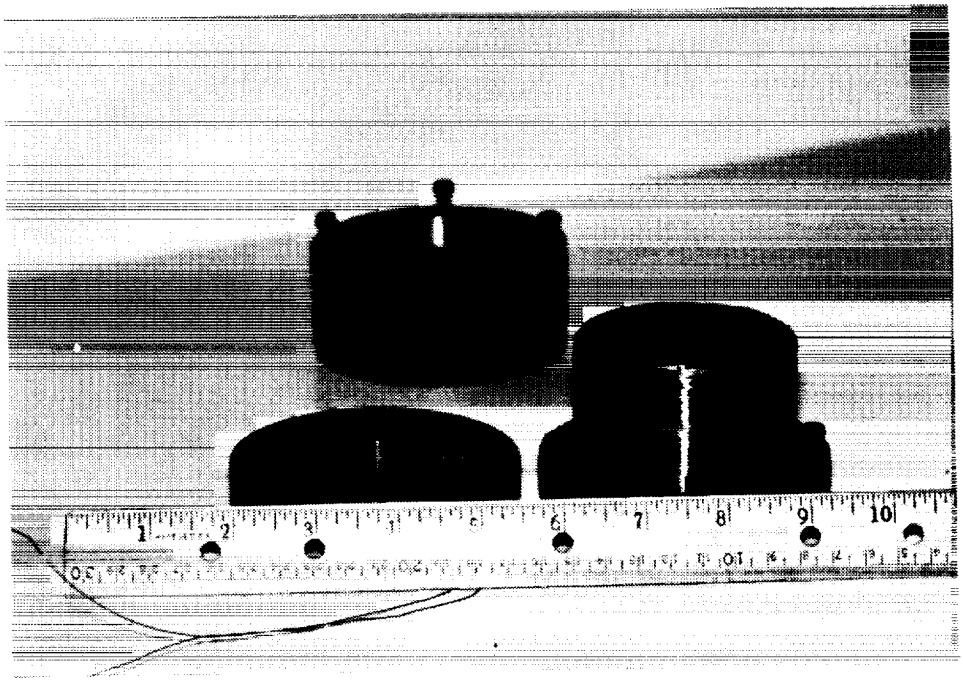

Figure 8. Disassembled Thrust Bearing

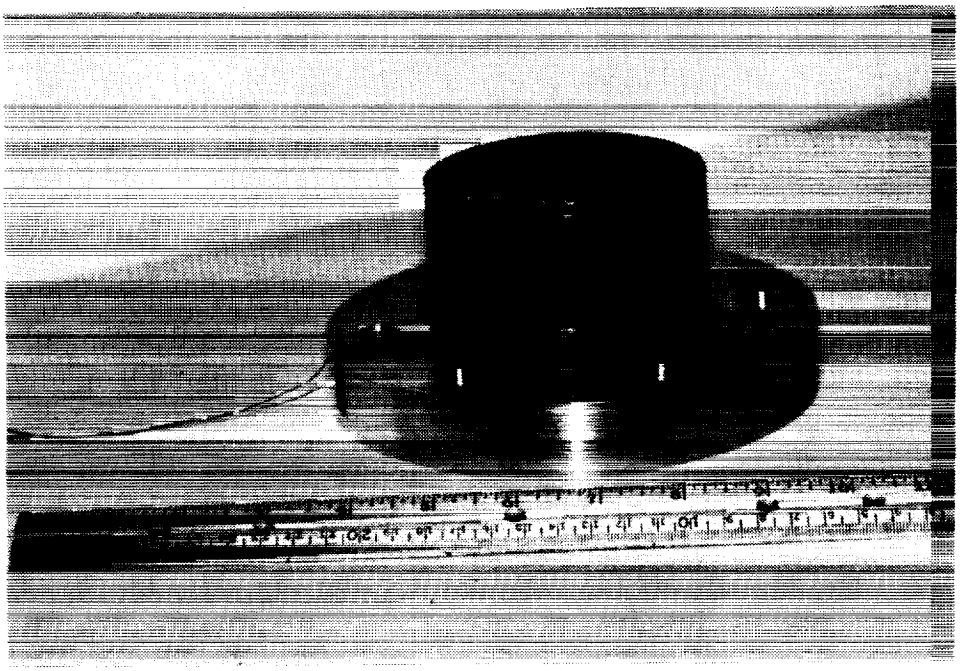

Figure 9. Thrust Bearing Mounted on Test Base

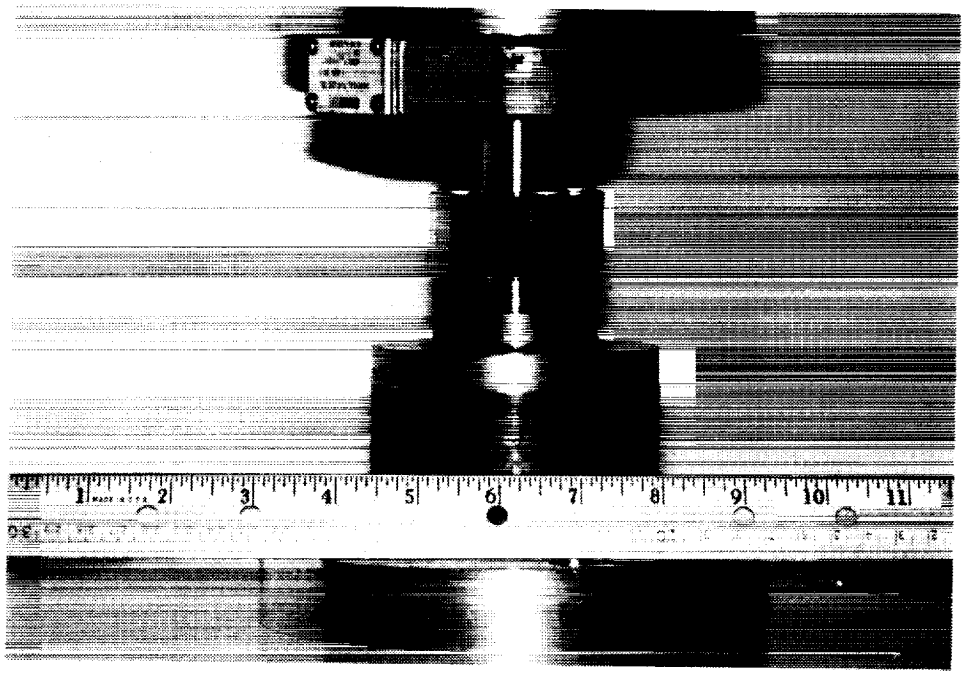

Figure 10. Thrust Bearing in Tensile Test Device

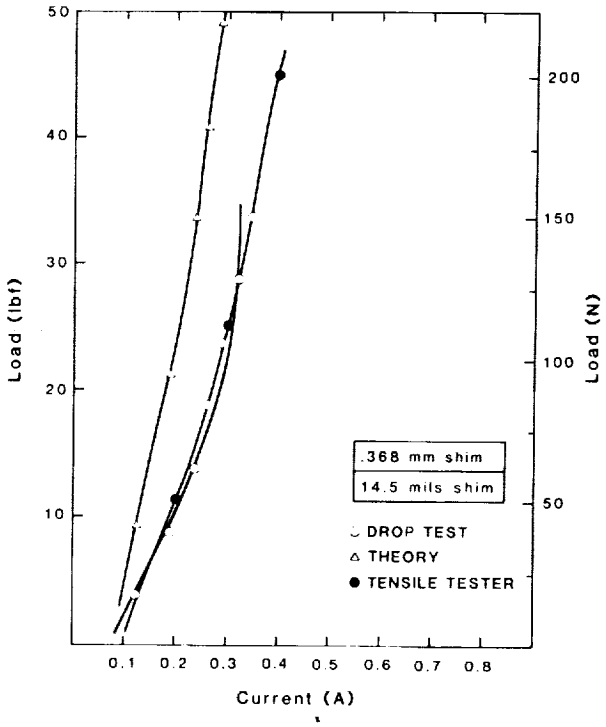

Figure 11. Thrust Force vs. Current for Magnetic Thrust Bearing with Gap Thickness of 14.5 mils.

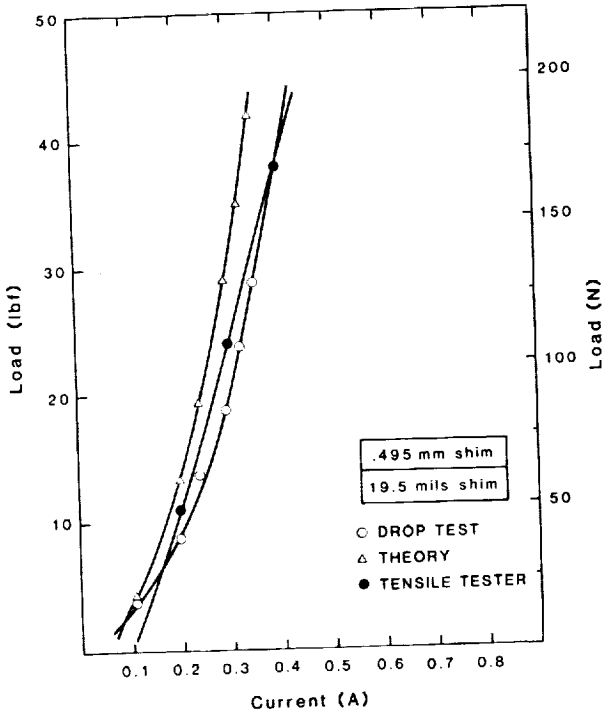

Figure 12. Thrust Force vs. Current for Magnetic Thrust Bearing with Gap Thickness of 19.5 mils.

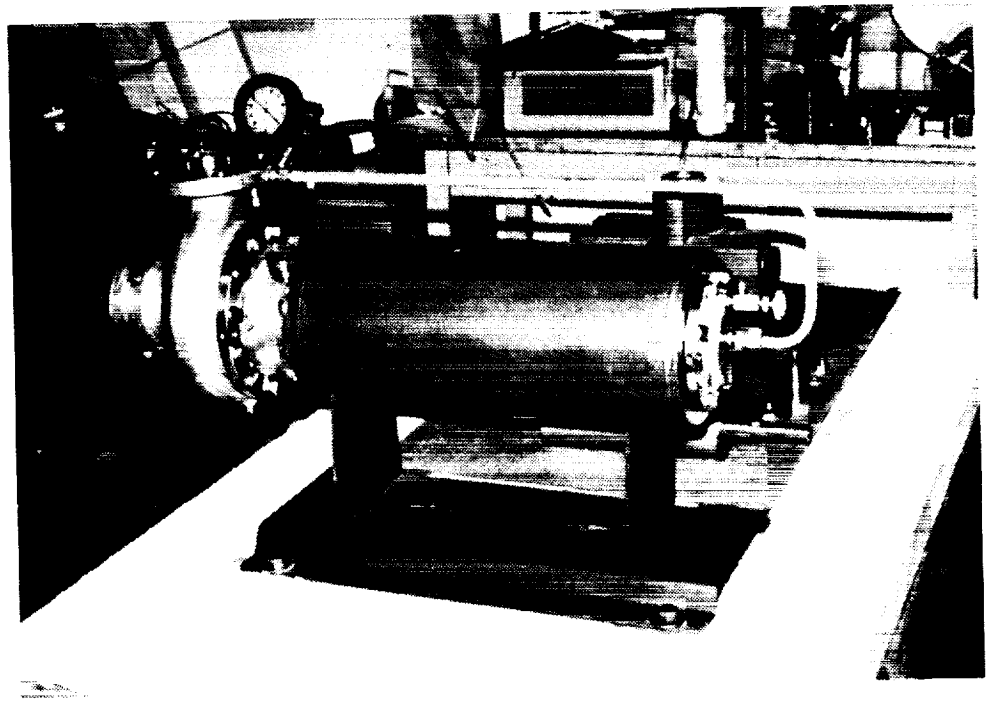

Figure 13. Canned Motor Pump Being Converted to Magnetic Bearings

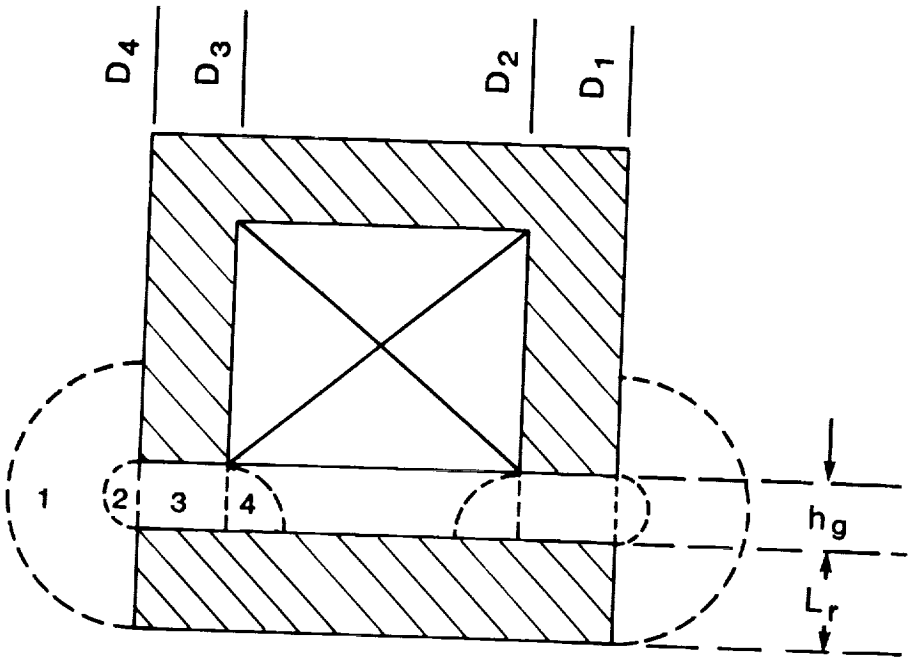

Figure 14. Section of Thrust Bearing System Showing Flux Paths

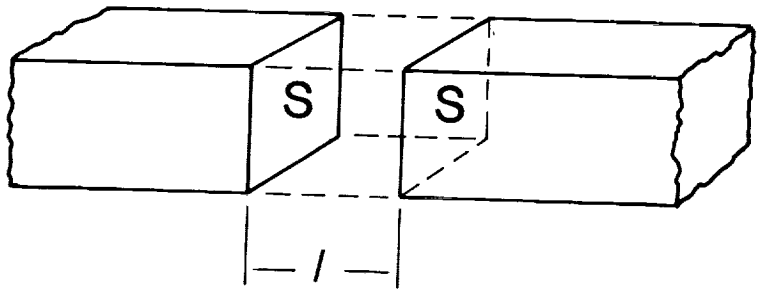

Figure 15. Parallel Plane Surfaces

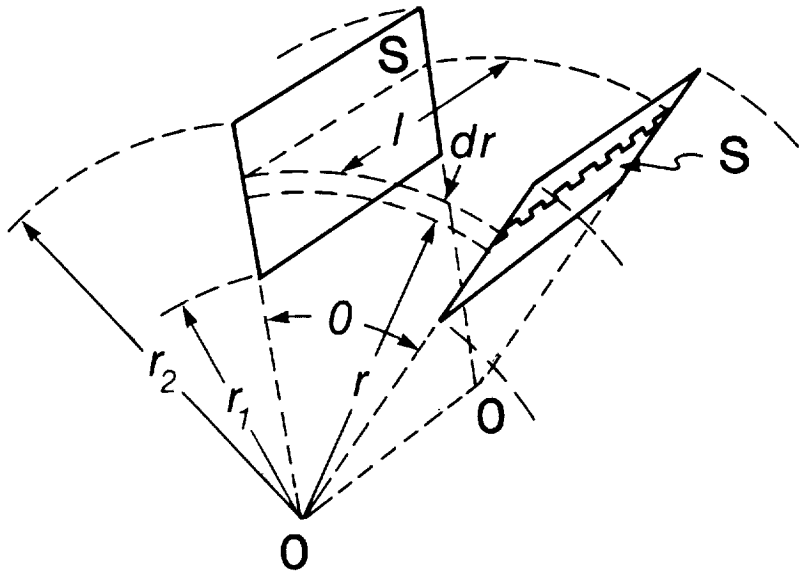

Figure 16. Non-parallel Plane Surfaces

OMIT

A Conventional Point of View on Active Magnetic Bearings

H. Ming Chen, James Dill, Mechanical Technology Incorporated

A CONVENTIONAL POINT OF VIEW ON ACTIVE MAGNETIC BEARINGS

By
H. Ming Chen
Jim Dill

MECHANICAL TECHNOLOGY INCORPORATED
968 ALBANY-SHAKER ROAD
LATHAM, NEW YORK

SUMMARY

Active magnetic bearings used in rotating machinery should be designed as locally controlled, independent devices similar to other types of bearings. The functions of control electronics and power amplifiers can be simply and explicitly related to general bearing properties such as load capacity, stiffness, and damping. In this paper, the dynamics of a rotor and its supporting active magnetic bearings are analyzed in a modified conventional method with an extended state vector containing the bearing state variables.

INTRODUCTION

Active Magnetic Bearings (AMBs) have been slow to show acceptance in the rotating machinery industry, and to machinery designers, they remain somewhat a mystery. AMBs have been developed over the decades by researchers in electrical engineering and systems control. Consequently, progress in their development is often presented in a language that is alien to the mechanical designers. The design engineer, whose major discipline is mechanical engineering, is likely to be unfamiliar with the concept that AMB stiffness and damping are functions of excitation frequency. In addition, the designer does not commonly use terminology such as control bandwidth, phase compensation, control spillover, etc. Not only does the AMB's electrical presentation hinder its acceptance, but also the fact that it is such a small component of a sophisticated machine; most design engineers will question whether it warrants the time and effort needed to gain familiarity with it. Consequently, greater understanding of the AMB is imperative in increasing its use in conventional rotor-bearing applications. With these observations in mind, the authors herein attempt to describe the key elements and properties of AMBs in a general engineering language that includes rotor dynamic notation which mechanical engineers are more accustomed to using.

BASIC PRINCIPLES

The principles of an AMB are well explained by Habermann and Liard (1980). The practical AMBs generally adopt an 8-pole stator configuration as shown in Figure 1. Both the stator and journal are made up of stacks of laminations of ferromagnetic material. The journal is shrunk on a shaft without windings. Laminations reduce eddy currents that not only create a power loss but also degrade the performance of the bearing. The eddy currents generate magnetic fields that oppose the flux needed for regulating the journal motion. The eight poles of the stator are separated into four quadrants (Weise, 1985). In each quadrant, the electromagnetic windings are

wound in such a way that the magnetic flux will circulate mainly inside the quadrants (Chen and Darlow, 1987). In other words, the magnetic forces of the poles in any quadrant can be varied by changing the amount of current in the windings of that quadrant without causing force changes in other quadrants. Therefore, each quadrant of poles can be controlled independently.

It is well known that the magnetic force is proportional to the current to air gap ratio squared (see Figure 2). Engineers conscientiously try to avoid nonlinear design and analysis. The linearization of AMB dynamics is achievable by making the air gap large relative to the journal normal excursion and by providing a relatively large steady state current (called bias current hereafter) through each quadrant. The bias current produces I^2R loss, which is a major power loss in AMB. However, the total resistance including the windings and other parts in current path is not large; the AMB power loss in general is insignificant when compared to the conventional bearings, such as the hydrodynamic oil-film type.

It is noteworthy that all poles exert attractive forces on the journal. Two opposite quadrants of poles are used to center the journal in one direction. While generating cancelling forces may seem to waste electric power, the AMB stiffness and damping are directly proportional to the bias current.

The journal floating in a magnetic field that is produced only by the bias currents is not stable. This situation is analogous to supporting a vertical stick at the bottom by a hinge without controlling the hinge. To create stability at the AMB center, the journal motion must be sensed and corrected instantaneously and continuously by superimposing a small control current to each bias current. For example, when the journal moves upward off the center by a small displacement, Y, the current in the top quadrant will be reduced by a small amount, i, and the bottom quadrant increased by i. The control currents produce a net downward force (-F) that pulls the journal back to the center. From sensing Y to producing -F, a series of AMB components become involved. It is the authors' preference to separate them into two groups:

- Sensor and control electronics
- Power amplifiers and electromagnets.

Before examining them in detail, presenting basic statics and dynamics will specify the function of these components.

AMB STATICS AND DYNAMICS

To support a static load, W, in Y-direction, the net attractive force caused by the bias currents is

$$W = f(I_1^2 - I_3^2)/C^2 \qquad (1)$$

where f is a magnetic pole constant for a given number of windings.

Choosing an I_3, I_1 can be determined by equation 1. I_3 must be larger than the control current, i, at any anticipated transient situation so that no current saturation can occur.

Assuming that

$$I_1, I_3 \gg i \quad \text{and} \quad Y \ll C$$

and that the AMB sees a dynamic mass, M, then a linearized equation of motion is

$$M\ddot{Y} - K_m Y = K_i\ i \tag{2}$$

where K_i and K_m are respectively called the current stiffness and the negative spring of the magnetic field due to the bias current. Without the small control current, i, equation 2 represents an unstable dynamic system. To make it stable, it is simple and sufficient to have

$$i = G\ E \tag{3}$$

and

$$E = -C_d\ Y - C_v\ \dot{Y} \tag{4}$$

where E is the controller output voltage signal and the input to the amplifiers, and G is the power amplifier gain (amp/volt). In other words, the small control current should be made proportional to the journal displacement and velocity. The minus sign is indicative of negative feedback, which is a common regulating mechanism. C_d and C_v are constants, and called proportional and derivative control gains.

Substituting equations 3 and 4 into 2 produces

$$M\ddot{Y} + GK_iC_v\ \dot{Y} + (GK_iC_d - Km)\ Y = 0 \tag{5}$$

If C_d is large enough, such that $GK_iC_d > K_m$, we achieve a stable one degree of freedom system in Y-direction which has damping coefficient GK_iC_v and stiffness coefficient $(GK_iC_d - K_m)$.

If the static load W, is miscalculated, or there is an occasional slowly varying load, (as can be caused by the gyroscopic effect of a manuvering spacecraft) the journal will sag or drift off the bearing center. To correct this potential problem, a third corrective mechanism called the integral control, as depicted in Figure 3, can be added to equation 4. That is,

$$E = -C_d\ Y - C_v\ \dot{Y} - C_e \int Y dt \tag{6}$$

As shown in Figure 3, the accumulated journal position error over a period of time will produce a part of the control voltage. The integral control does not respond to high frequency vibrations.

SENSOR AND CONTROL ELECTRONICS

For AMB journal displacement measurements, three practical sensors exist: the capacitance probe, inductance probe, and eddy current probe. Each has advantages and disadvantages, but they all relate the small distance (in mils), from the stationary sensor to the rotating shaft, to an output electrical signal in volts.

No inexpensive and reliable sensors are available yet for measuring the journal velocity ($\dot{Y}$). Consequently, different control circuit designs have been developed to produce a psuedo velocity from the displacement measurements. The feedback of velocity is in essence a corrective action of anticipation. If the vibration displacement is sinusoidal, the corresponding velocity is also sinusoidal,

$$Y = Y_o \sin(\omega t)$$

$$\dot{Y} = \omega Y_o \sin(\omega t + \pi/2)$$

but peaks 90° earlier on an oscilloscope. The logical way of obtaining the velocity from the measured displacement is by performing differentiation with an analog circuit. However, inevitable error or noise signals occur in this measurement; a small displacement error at high frequency will become a large erroneous velocity at the same frequency by differentiation, which may overhelm or bury the real velocity signals. Therefore, a practical differentiator always applies a certain "low-pass filtering", which reduces the high frequency signal content. A conflict arises between reducing the high frequency signal and keeping the lead time for the low frequency signal. The filtering aspect of circuit design may become awkward at times.

A more popular method of generating the velocity component of controllers is to use an analog circuit called phase-lead network. Each phase-lead network provides lead time or phase advance for the displacement signal in a reasonably large frequency range. The maximum phase advance per stage network is less than 70°. Two networks may be needed to cover a large spread of critical speeds. The output of a phase-lead network is a combination of displacement and velocity signals. Thus, its feedback produces the damping and contributes to the stiffness.

An alternative method, called the Velocity Observer, was recently developed and used by Chen and Darlow (1987) for producing the appropriate control signals. It integrates journal force, (equivalently, acceleration) to obtain velocity. The observer takes the displacement and the small control current as input. The Velocity Observer has an advantage over the phase-lead approach in that it covers much wider frequency range with phase advance > 90°.

The integral feedback term in equation 6 is straight forward in analog circuit design. The integral control is a time delay action. To confine its effect below 1 or 10 Hz, where system resonance seldom occurs, low-pass filtering may be included in the integrator circuit. A comparison of the mathematical expressions of the three types of circuits are presented in Figure 4.

The control electronics, which take the displacement Y as input, is generally called a Proportional-Integral-Derivative (PID) controller. There are many ways to implement the controller. Humphris et al. (1987) used a single path proportional derivative (PD) controller with two phase-advancing circuits in series. Fukata et al. (1986) used a PID controller with three parallel paths and a differentiator. Chen and Darlow (1987) used another PD controller using two parallel paths and a Velocity Observer.

The parallel-path approach is preferable because the adjustments of the stiffness and damping are less dependent on each other. A controller example is shown in Figure 5 using a single stage of phase-lead network. The transfer function of the controller can be expressed in the following closed-form formula:

$$-E/Y = C_d + C_v\,(s + a)/(s + b) + C_e/(s + \omega_1) \qquad (7)$$

From (2), the AMB dynamic force is

$$F = K_i\, i + K_m\, Y. \qquad (8)$$

Assuming the amplifiers provide control current as much as demanded with no delay, and for simplicity G = 1 (amp/volt), then

$$i = E \qquad (9)$$

Combining equations 7, 8, and 9, we have (for s = jw)

$$-F/Y = K + j\omega B \tag{10}$$

where

$$K = K_i[(C_d - K_m/K_i) + C_v(ab+\omega^2)/(b^2+\omega^2) + C_e\omega_1/(\omega_1^2+\omega^2)] \tag{11}$$

$$B = K_i[C_v(b-a)/(b^2+\omega^2) - C_e/(\omega_1^2+\omega^2)] \tag{12}$$

Equations (11) and (12) show that AMB stiffness and damping are functions of excitation frequency, ω. An example of the stiffness and damping using this controller is presented in Figure 6. It may appear unusual that bearing damping in Figure 6 is negative in the low frequency range. The fact is, that as long as no system vibration mode exists in that range, there should be no instability. Note that for every ω, a damped frequency value ω_n can be calculated from the bearing parameters M, K and B. A natural vibration modal frequency exists at $\omega = \omega_n$.

POWER AMPLIFIERS AND ELECTROMAGNETS

The physical size of an AMB journal and stator can be determined (Chen 1988) by first calculating the pole surface area:

$$A_p = F_{max}/250 \tag{13}$$

The formula was derived in American units for silicon steel laminations (saturation flux 110 x 10^3 lines/in.^{2}). A_p is taken as the smallest cross-sectional area (in.^{2}) along the pole. F_{max} is the maximum force (lb) that two opposite pairs of poles can take without flux saturation. Choosing the axial length L_p, the circumferential pole width is A_p/L_p. Then, the radial dimensions can be decided outward from a given shaft diameter at the AMB. The sizing guidelines are

- The cross-sectional area at any point of the flux path is not less than A_p.
- Adequate wiring space and cooling surface are provided.
- The axial length is no greater than the journal outer diameter.
- As a rule, the air gap should be ten times the expected journal excursion. The smaller the gap, the less power is required.

Converting a low power control voltage signal to a high power control current and actuating the electromagnets requires current source or power amplifiers. Two types of power amplifiers, the linear type and the pulse-width-modulation (PWM) type, have been studied and used by MTI in their magnetic bearings. The linear type applies the control signal to a power transistor in "active" mode. The transitor continuously regulates the current through the windings from a DC source. In this mode of operation, the voltage drops across the transitor, and thus the power loss is high. The PWM type applies the control signal to generate high voltage output pulses at a frequency above audible range. The on-time period of each pulse is proportional to the input signal. The high voltage pulse train produces current in the windings. The PWM amplifier is electrically noisy but much more efficient in providing the required power with low power loss. The power transitors in it operate in "saturation" mode and have small resistances. Schweitzer and Traxler (1984) had indicated that the borderline in favoring one type over the other is about 0.5 kVA.

The inductance of electromagnet windings can cause a problem of control current delay. The inductance, L, is proportional to N^2A_p/C. A time constant, L/R, is associated with the power amplifier-electromagnet system. A controller signal at $\omega >$

R/L will have a phase delay > 45°, which is one-fifth of a cycle. Also, the inductance limits the permissable rate of change of current, dI/dt (called slew rate) to V_S/L (V_S = DC supply in volts). The delay problem is more severe in systems with PWM amplifiers. An experience was recently reported and well explained by Bradfield, et al. (1987). To take into account this effect of inductive phase lag on the system dynamics, an approximate linear transfer function is

$$G = I/E = 1/[(L/R)S + 1] \qquad (14)$$

In the above, we neglected the component of back emf, due to variations of inductance as a result of changes in the air gap. For clarity, the maximum amplitude of the transfer function G has been assumed to be one. According to equation 14, it is only close to one at $\omega < R/L$. Above R/L, the control current is attenuated and delayed. The phase advance by the controller is cancelled by the phase lag in the amplifier system. This means negative AMB damping can occur in the high frequency range, and the control of flexible rotor criticals can be in jeopardy.

ROTOR-AMB SYSTEM DYNAMICS

AMB dynamic stiffnesses are generally lower than ball bearings or oil-film bearings. On a typical critical speed map, as shown in Figure 7, one can expect that the first two criticals will have rigid mode shapes, and they can be easily controlled. The higher modes (particularly the third and the fourth modes) with bending mode shapes must be given careful consideration in the design of the AMB controls. The first requirement is to assure the existence of positive damping for these modes, if the AMBs are responsive to the modal frequencies. Although oil-film bearings always provide positive damping, there is no guarantee of this for AMBs. Because of the inductance mentioned above, the control current at the high frequencies may lag behind the displacement measurement. If the operating speed is well below the bending critical, one can reduce the lagging current to a minimum at that frequency through electronic means. Then, the AMB would not be responsive to the modal resonance.

If the operating speed is above the bending critical, it is imperative to provide enough leading current at the appropriate frequency. Even once the proper control response has been achieved, the ability of the AMBs to control rotordynamic response will be significantly affected by rotor mechanical design. Care must be taken in mechanical design to ensure that the AMB locations are not at nodes of the vibrational modes of interest.

This system design challenge can be aided by performing conventional rotor-bearing dynamic analyses, such as calculating undamped critical speeds, unbalance response, and stability, which have been performed by MTI as part of the magnetic bearing design analysis. Hustak, et al. (1985) have performed similar analyses for two compressor rotors supported by AMBs. They have shown measured AMB stiffness and damping coefficients as functions of excitation frequency. A modified but more rigorous rotordynamics approach, which has the inherent advantage of integration of controller dynamics into the system equations, is described below.

The state vector of the conventional rotor model is extended to include the state variables of the AMBs. The controller dynamics of each AMB axis, such as shown in Figure 5, and the amplifier dynamics (equation 14) can be represented to be a set of first-order linear differential equations in terms of the extended states. The coupling terms between the rotor model and the AMB model exist in the AMB dynamic force, which is represented by equation 8. The resultant electomechanical model

using finite element formulation for the rotor part, can be used for eigenvalue/eigenvector and force response analyses. The rotor model input is the same as conventional model including sections of shaft with specified inner diameter, outer diameter, length, and concentrated mass and inertias. The input for each bearing would be the bearing station number, the measurement station number, and the parameters K_i, K_m, a, b, C_d, C_v, C_e, ω_l, and L/R. For properly sized AMBs, the feedback gains, C_d and C_v, are the key parameters that can be optimally determined by performing the eigen and response analyses. This approach to integrated rotordynamic analysis has been applied to typical magnetic bearings developed at MTI.

CONCLUSIONS

The essence of control and the properties of active magnetic bearings have been described and quantified in a language that is more adaptable to mechanical engineers. In doing so, the following viewpoints on AMB development have been emphasized:

1. AMB should be treated as a locally controlled and independent device similar to other types of bearings.

2. AMB control axes should be made independent from each other, with identical but tunable electronics.

3. Parallel circuits for stiffness and damping control should be implemented to permit more versatility in the application of these bearings.

4. Pitfalls exist in controlling the rotor bending critical modes; the reasoning, and design guidelines can be explained easily in mechanical terminology.

5. Modified rotordynamics analysis method with a state vector extended to include the AMB state variables are needed for rigorous system performance prediction.

These mechanical engineering viewpoints are long overdue in gaining prominence and influencing the development of AMB technology.

NOMENCLATURE

AMB	Active magnetic bearings
A_p	Pole cross-sectional area
a	Phase-lead zero parameter
B	AMB damping coefficient
b	Phase-lead pole parameter
C	Radial air gap
C_d	Proportional feedback gain
C_v	Derivative control gain; Phase-lead feedback gain
C_e	Integral feedback gain
E	AMB controller output voltage signal
F	AMB perturbed magnetic force
G	Power amplifier gain
L	Self-inductance of electromagnets
L_p	AMB axial length
I	Bias current
i	Control current

j	$\sqrt{-1}$
K	AMB stiffness coefficient
K_i	Current stiffness
K_m	Magnetic stiffness due to bias currents
M	Dynamic mass
N	Number of winding turns
Q	Integrator output
R	Resistance in current path
s	Laplace variable
t	Time
W	AMB static load
Y	AMB journal displacement in Y-direction
Z	Phase-lead circuit output
ω	Excitation frequency
ω_n	AMB critical frequency
ω_1	integrator cut-off frequency
$\dot{}$	d/dt
$\ddot{}$	d^2/dt^2

REFERENCES

1. Chen, H. M., and Darlow, M. S.: Design of Active Magnetic Bearings with Velocity Observer. 1987 ASME 11th Biennial Conference on Mechanical Vibrations and Noise, Boston: September 27-30.

2. Chen, H. M.: An Active Magnetic Damper for Rotor Vibration Control. Accepted for Presentation at the 2nd International Symposium on Transport Phenomenon, Dynamics, and Design of Rotating Machinery, Honolulu, Hawaii: April 4-6, 1988.

3. Bradfield, C. D., Roberts, J. B., and Karunendirkan, R.: Performance of an Electromagnetic Bearing for the Vibration Control of a Supercritical Shaft. Proceedings - Institution of Mechanical Engineers, vol. 201, No. C3, 1987, pp. 201-211.

4. Fukata, S., et al.: Dynamics of Active Magnetic Bearings Composed of Solid Cores and Rotor. Memoirs of the Faculty of Engineering, Kyushu University: vol.46, No.3, September 1986, pp.279-295.

5. Habermann, H. and Liard, G.: An Active Magnetic Bearing System. Tribology International, April 1980, pp. 85-89.

6. Humphris R. R., et al.: Effect of Control Algorithms on Magnetic Journal Bearing Properties. ASME 86-GT-54, 1986.

7. Hustak, J. F., Kirk R. G., and Schoeneck, K. A.: Analysis and Test Results of Turbocompressors Using Active Magnetic Bearings. Journal of ASLE, Lubrication Engineering, vol. 43, May 1987, pp. 356-362.

8. Schweitzer, G. and Traxler, A.: Design of Magnetic Bearings. Proceedings of International Symposium on Design and Synthesis, Tokyo, Japan: July 11-13 1984, pp. 423-428.

9. Weise, D. A.: Active Magnetic Bearings and Their Industrial Applications. 5th Annual Rotating Machinery and Controls Industrial Research Conference, San Antonio, Texas, 1985.

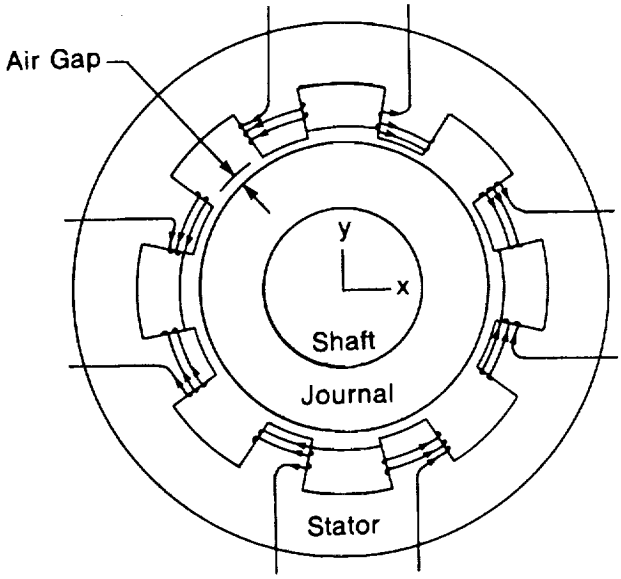

Fig. 1 8-Pole Active Magnetic Bearing Configuration

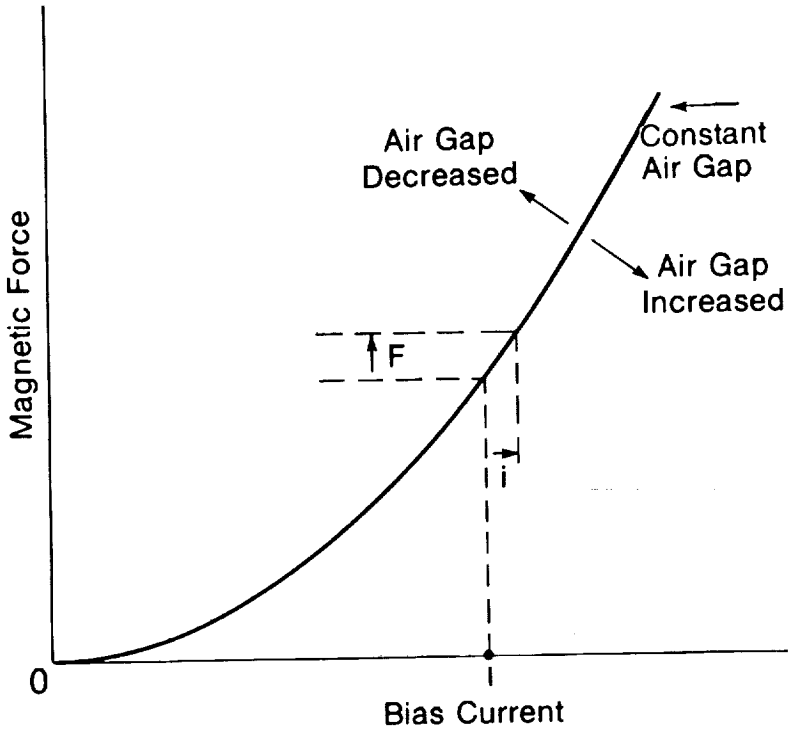

Fig. 2 Nonlinearity of Magnetic Force

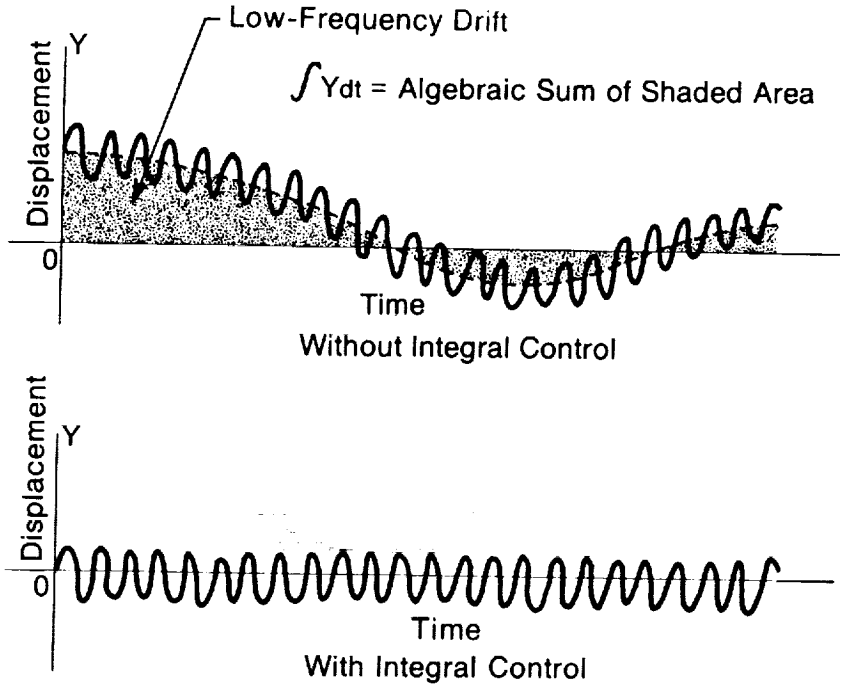

Fig. 3 Elimination of Low-Frequency Drift through Integral Control

	Transfer Function $\frac{V(s)}{Y(s)}$	Vector Diagram
Practical Differentiator	$\frac{s}{s+b}$	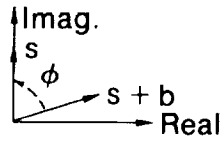
Phase-Lead Network ($b > a$)	$\frac{s+a}{s+b}$	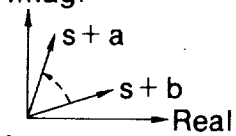
Velocity Observer Equivalence	$\frac{s-a}{s+b}$	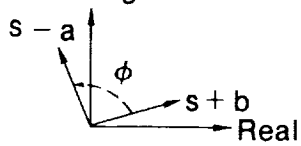

Notes:

ϕ = Phase Advance Angle

$s = j\omega$

$a > 0, b > 0$

Fig. 4 Comparison of Three-Phase Advancing Circuits

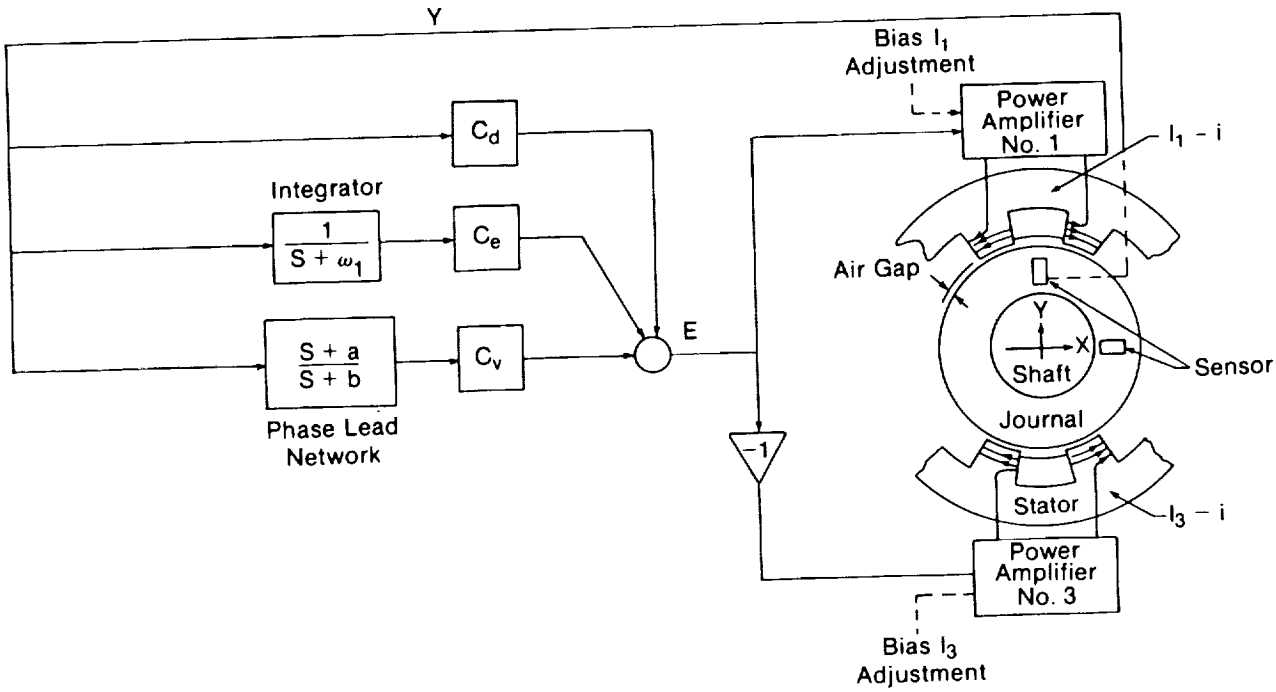

Fig. 5 Proportional-Integral-Derivative (PID) Controller

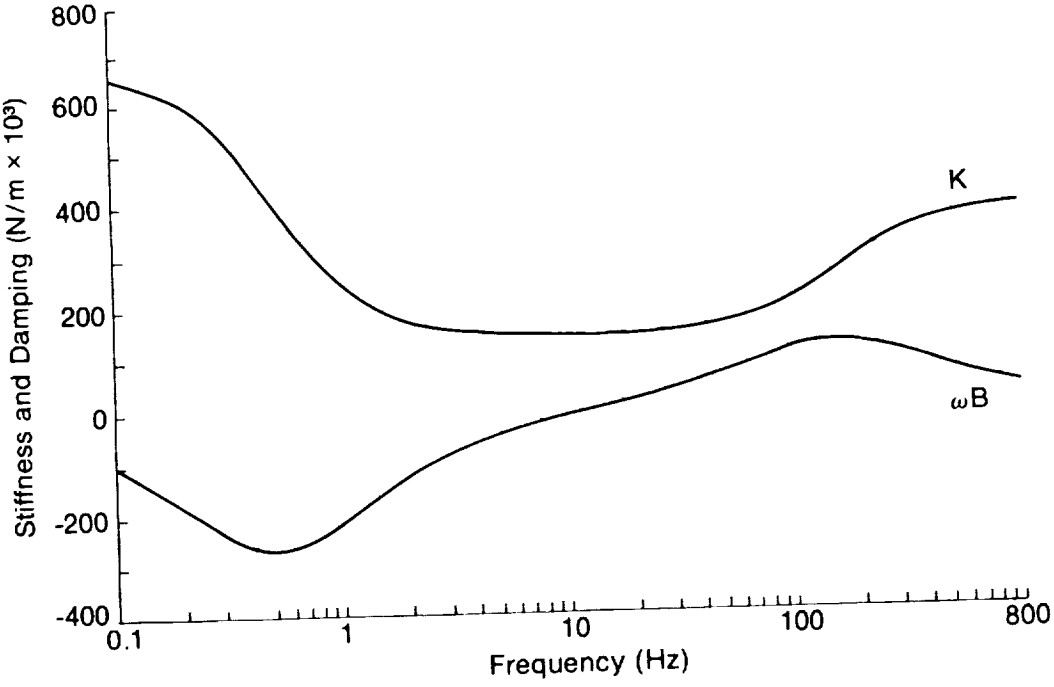

Fig. 6 Stiffness and Damping of a Typical Active Magnetic Bearing

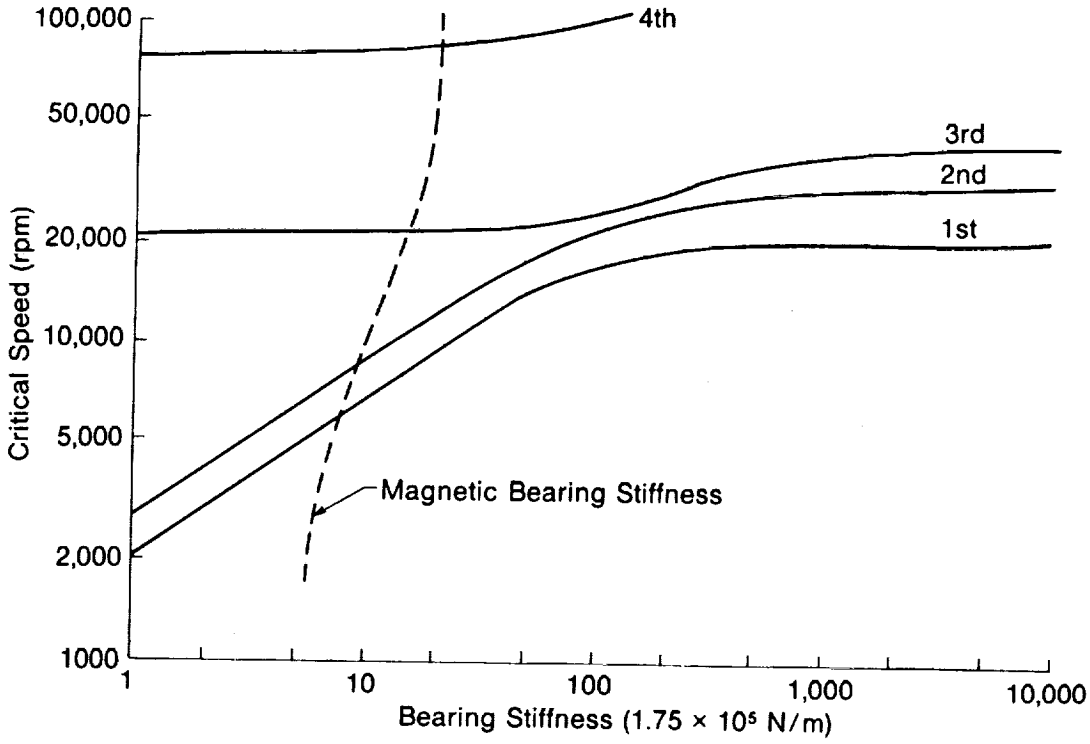

Fig. 7 Rotor Critical Speed Map

omit

Magnetic Bearings for a High-Performance Optical Disk Buffer

Richard Hockney, Timothy Hawkey, SatCon Technology Corporation

Magnetic Bearings for a High-Performance Optical Disk Buffer*

Richard Hockney and Timothy Hawkey

SatCon Technology Corporation
71 Rogers Street
Cambridge, Massachusetts

ABSTRACT

An optical disk buffer concept can provide gigabit-per-second data rates and terabit capacity through the use of arrays of solid state lasers applied to a stack of erasable/reusable optical disks. The RCA optical disk buffer has evoked interest by NASA for space applications. The porous graphite air bearings in the rotary spindle as well as those used in the linear translation of the read/write head would be replaced by magnetic bearings or mechanical (ball or roller) bearings. Based upon past experience, roller or ball bearings for the translation stages are not feasible. Unsatisfactory, although limited experience exists with ball bearing spindles also. Magnetic bearings, however, appear ideally suited for both applications.

The use of magnetic bearings is advantageous in the optical disk buffer because of the absence of physical contact between the rotating and stationary members. This frictionless operation leads to extended life and reduced drag. The manufacturing tolerances that are required to fabricate magnetic bearings would also be relaxed from those required for precision ball and gas bearings. Since magnetic bearings require no lubricant, they are inherently compatible with a space (vacuum) environment. Magnetic bearings also allow the dynamics of the rotor/bearing system to be altered through the use of active control. This provides the potential for reduced vibration, extended regions of stable operation, and more precise control of position.

INTRODUCTION

The advent of optical disk recording technology has made possible a family of high data rate, high capability memory devices. These devices provide gigabit-per-second data rates and terabit capability through the use of arrays of solid state lasers applied to an optical disk stack. Bearings are an enabling technology area where improvements are required to allow these systems to be utilized in space applications. Air bearings, utilized in ground based systems, are impractical in space. Experience with rolling element bearings has been unsatisfactory. With proper development, magnetic bearings represent an ideal candidate for both the translational and rotation stages of these devices.

---

*This work was supported by NASA SBIR contract number NAS5-30058.

The purpose of this study was to define specifications and determine candidate magnetic hardware, sensor, and electronics specifications for the translator magnetic bearings to be retrofit into the optical disk buffer system. The work consisted of the determination of detailed performance requirements, the analyses of the capabilities of various bearing configurations, the selection of a baseline hardware and sensor configuration, and the determination of controller and electronics requirements. Successful completion of these tasks is considered evidence of the technical feasibility of applying magnetic bearing technology to this device.

It was found that the retrofit of magnetic bearings into the current system is very feasible with only minor modifications to the current system. A permanent-magnet biased, asymmetrical three-pole design was chosen for the translator bearing. The required electromagnetic hardware fits easily inside the available volume and has reasonable power consumption. The capacitive position sensors are small and have excellent resolution and linearity. The controller requirements are modest as are the remaining analog electronic functions which need to be implemented. The extension of this design definition to the detailed design required for prototype development would appear to be an extremely straightforward effort.

SPECIFICATIONS

Definition of the specifications for the magnetic bearings for the optical disk buffer was facilitated by the decision to make the baseline design capable of retrofit into the existing NASA/RCA buffer design. This then determined both the maximum dimensions and allowed volume for the electromagnetic hardware and the amount of suspended mass. The stiffness required was determined from a calculation of the static stiffness of the existing air bearings.

The structural modes of the supported structures were established by RCA using finite-element model analysis of the existing devices. Since the linear motor on the translator head would be replicated, its velocity and acceleration profiles were required. Finally, the maximum level of stray magnetic fields both in the area of the recording head and near the disk were established from knowledge of the sensitivity of the magnetic domains in the recording material. The detailed specifications for the translator magnetic bearings are listed in Table 1.

MAGNETIC DESIGN

The prime objective of the translator bearing design was the definition of a magnetic-bearing alternative requiring minimal modifications of the existing system. The current system is shown in Figures 1 and 2. The read/write head is mounted in the aluminum carriage between the linear motors, which are the heart of the whole assembly. Producing high forces, the linear motors use large samarium-cobalt magnets that create large magnetic fields in the air-gap (1.2 Tesla). The shafts that carry the return flux are therefore large and double as air bearing surfaces. Actually, the air bearings

Table 1. Specifications

Stiffness	
Parallel to disk	4.6×10^5 N/m
Normal to disk	7.0×10^5 N/m
Suspended mass	0.45 kg
First-mode frequency	1967 Hz
Maximum dimensions	
Length	3.8 cm
Width	4.4 cm
Height	4.4 cm
Maximum stray field	
At read/write head	3 mT
At disk surface	0.2 T
Maximum acceleration	21 m/s^2
Maximum velocity	1.2 m/s

are made by milling slots in the iron shaft and covering them with porous graphite. Air is then pumped through the slots and graphite, forming a cushion of air between the graphite and the aluminum carriage which it supports.

For an easy retrofit, the entire bearing and shaft structure cannot occupy more space than the current air bearing shaft does. As such, the geometric constraints were the most restrictive. The tight spacing drove many of the design parameters and eliminated many configuration options. A second major restriction was imposed by magnetic flux of the linear motors. The twin voice-coil motors must move the read/write heads at high acceleration and, as such, require large magnetic flux density. This means that there must be a large pole face facing the linear motor magnet (for uniform flux), and that the shaft must have sufficient cross sectional area to carry the return flux of the motor magnet back to its other pole.

Together these restrictions quickly narrowed the design options to the two shown in Figures 3 and 4. Normally, a radially symmetrical four- or eight-pole design is used for magnetic bearings, but the linear motor magnet flux prevented pole placement on one side. Fortunately, all five controlled degrees of freedom can be controlled with a three-pole design because the two bearing sets are mirror images of each other and can be coupled to provide the proper support. The design shown in Figure 4 was chosen as the candidate configuration because its layout is both simpler mechanically and had lower predicted internal flux density (0.8 T as opposed to 1.8 T). In both cases, a permanent magnet providing bias flux has been included. The bias flux is used because it provides a linear operating point and because it reduces power consumption while increasing force capability.

The detailed mechanical design was determined mainly by force requirements. It was assumed that under worst case loading (one gravity), the transient force requirements for stabilization would not exceed twice the weight of the translator-plus-bearing assembly (6.4

N). The pole face area (A) and bias magnetic field (B_o) are related to the force required through

$$F = \frac{2B_o^2 A}{\mu_o} \quad (1)$$

The pole face area is constrained by available space, so B_o is determined at the modest value of 0.14 Tesla. The other major variable to be determined was the air gap length, the trade-off being between reduced coil size and ease of construction - a smaller gap length allowing smaller coils to be used, but also requiring better part tolerances and more difficulty of production. Air bearings often use gaps as small as 0.013 mm, and magnetic bearings usually use air gaps between 0.2 and 0.4 mm. A median value of 0.3 mm was chosen as a compromise, being small enough to allow reasonable size coils, but large enough not to present great difficulties in manufacturing.

The magnetic design began with the permanent magnet which provides bias flux in the air gaps. The flux travels through three separate paths with two air gaps on each path. Since the translator is very light, the force and flux-density requirements are modest. However, finding a magnet to provide the low magnetic field while being large enough to be easily produced was a challenging task. A ceramic Indox V grade magnet was selected for its low energy product and linear demagnetization curve.

Knowing the pole face areas, the desired gap flux, and the demagnetization curve for Indox V, the magnet dimensioning became straightforward. H_m and B_m define the operating point of the magnet on the demagnetization curve. Normally, the magnet operating point is chosen such that the product $B_m \cdot H_m$ is greatest. This is where the magnet produces the most energy and hence, requires the least volume. In this case, however, it was desired to make the magnet somewhat larger than minimum to ease production problems. The operating point was set at $B_m = 0.36$ T and $H_m = 1.6 \times 10^4$ amp·turns/meter. B_g has already been set at 0.14 T, the leakage factor σ_L was estimated at 1.1 and the reluctance factor σ_p at 1.25. The leakage factor is used to compensate for the fact that there are both leakage and fringing fields in the magnet circuit and reluctance factor, σ_p, to compensate for the drops in magneto-motive force (the magnetic equivalent to voltage) in the back iron. The final dimensions of the Indox V magnet are 14 mm long x 6.2 mm wide x 5.3 mm high. The magnet fits easily in the available space and is large enough to be easily manufactured.

The bias flux is modified by control coils to produce the differential forces that center the assembly. There are six coils per bearing set, one for each air gap. The basic coil design is simple - there are several issues that complicate matters, however. These are the packing factor, the leakage factor, and coil temperature use. The packing factor is only important when the final coil dimensions are determined. The factor, typically $\pi/4$, is used to account for the fact that not all of the area in a coil is occupied by copper.

Leakage, unlike packing, is a very serious issue in magnetic circuit design. The leakage factor is typically defined as the ratio of coil flux to gap flux:

$$\sigma_l = \frac{\sigma_{coil}}{\sigma_{gap}} \qquad (2)$$

where σ_{coil} is the magnetic flux produced by the coil, and σ_{gap} is the magnetic flux in the gap. A leakage factor for very efficient designs is about 1.05, but factors of 2 or more are not uncommon in large magnetic circuits. Initially, an estimate of 1.1 was used, and computer modelling using magnetic analysis software was performed for verification. The software operates by producing a finite element mesh over the user-entered magnetic structure and then solving for the magnetic potential on this mesh, subject to prescribed boundary conditions. The computer results supported initial estimates, giving leakage factors of 1.1 to 1.2. This is indicative of an efficient design with little flux loss.

Though the packing and leakage factors influence the coil design in an important way, the primary determinant of coil size is the limit on temperature rise. Though copper wire can carry significant currents under ideal conditions, the allowable current density is much smaller in practice. The limit in reality is power, more specifically the equilibrium temperature the wire will attain under steady current and whether the insulation and surrounding equipment can tolerate it. In other words, after the ampere-turns requirement is determined, the current density is set so that the steady state temperature of the coil is acceptable; this, in turn, sets the size of the coil. For this application, the final temperature rise should not be more than 50 C or so. Though a detailed thermodynamic analysis was not carried out, a value of $4 \cdot 10^6$ Amps/meter^2 was chosen for experience as a conservative estimate. The resulting power consumption for maximum force is 0.25 Watts for coil 1, and 0.15 Watts for coil 2.

The final step in the design procedure was selection of the magnetic materials to be used. The poles must be resistant to eddy current losses and so are designed to be made of silicon steel laminations. The shaft, however, must be able to carry the linear motor magnetic bearing flux. For this reason, Vanadium Permandur is the material of choice; it has very high saturation flux density.

Overall, the translator bearing design is simple and effective. The final design is shown in Figure 5. Though the size constraints are tight, the entire mechanism comfortably fits in available space. It appears that retrofit of this bearing into the current system is feasible and practical.

CONTROLLER CHARACTERISTICS

The attribute of the magnetic bearing configuration which has the largest influence on the controller design is the type of force employed. As discussed earlier, the choices are the primary

attraction force, or the secondary attraction force. The secondary attraction force is inherently stable and requires no external controller. The translator stage magnetic bearing employs the primary attraction force. This force is an unstable effect by its physical nature. A small change in the air-gap length (δG) produces a small change in force (δf_p) that tends to increase the change in the air gap at constant excitation. When this force is exerted on a body of mass m_b, application of Newton's law produces a differential equation for the position of the suspended body (x). If an increase in the position of the body is defined as a decrease in the air-gap length:

$$(\delta x) = -(\delta G) \tag{3}$$

the linearized differential equation about a nominal position (x_o) becomes the following:

$$m_b \frac{d^2(\delta x)}{dt^2} - c_g(\delta x) = c_i(\delta i) \tag{4}$$

Taking the Laplace transform and rearranging shows that an unstable plant results.

$$\frac{\delta x}{\delta i}(s) = \frac{c_i}{m_b s^2 - c_g} \tag{5}$$

The plant is characterized by a natural rate of growth (ω_u, typically called the "unstable frequency") which is calculated as follows:

$$\omega_u^2 = \frac{c_g}{m_b} = \frac{B_{go}^2 A_{go}}{\mu_o m_b G_o} \tag{6}$$

The unstable frequency of a given configuration is thus determined by the nominal (or bias) flux density.

The unstable plant that is represented by Equation (5) is characterized by a pair of real poles that are equally spaced about the imaginary axis ($s = +/- \omega_u$). The frequency response of the plant is characterized by both constant 180 degrees of phase lag over the entire spectrum and finite dc gain as shown in Figure 6. Stabilization of the closed loop response using classical lead-lag compensation of this plant is illustrated in Figure 7. Here the lead is introduced at the unstable frequncy (ω_u) and the lag occurs at $10\omega_u$. As shown, this results in approximately 45 degrees of phase margin. Since this technique is only successful above the unstable frequency, closed-loop stability requires a minimum bandwidth above ω_u.

POSITION SENSOR

The position sensors are probably the most vital element of the control system. In general, the controller can only be as accurate as its input information. Thus, for the high stiffness and accuracy

requirements of the magnetic bearing to be met, sensors of high resolution and accuracy are needed. Three types of non-contact position sensors were investigated to determine their suitability.

Photo-electric sensors are devices that use light to make distance measurements. Normally, they operate by measuring the intensity of light from a reflective target surface. As the target moves, the intensity of the reflected light changes, a change which is quasi-linear and can be measured. In static measurements, resolutions of one micron can be obtained. However, with surfaces of less than fine and uniform finish, or with a moving target, performance degrades rapidly. Another disadvantage to photo-electric systems is that two units (a transmitter and a receiver) are needed for each measurement. These two factors render these sensors inappropriate for the translator bearings.

Inductive sensors are very commonly used in metal sensing applications. They operate by using a high frequency oscillator to produce eddy currents in the target. As the target moves, the change in loss in the sensor circuit is measured. Resolutions of 0.025 mm are possible, and the sensors are readily available in small sizes. However, when measuring ferrous or moving targets, performance degrades rapidly. Since the sensors will be mounted in the moving translator, both of these conditions apply. This renders inductive sensors unsuitable for the bearings.

Capacitance sensors operate on a similar principle to that of inductive sensors, utilizing a high frequency alternating electric field (about 50 Khz). They do not require a metallic target and are free from the performance degradation problems of the inductive sensors. They are commercially available in a variety of very small packages and have resolutions to ten microns. Additionally, capacitive sensors offer excellent linearity and stability. For these reasons, capacitive sensors are the best choice for this magnetic bearing configuration.

The particular sensor chosen is model number ASP-20-PCR Pancake Radial Sensor from Mechanical Technology Instruments. It has an accuracy rating of +/-0.1% of range or 0.5 microns, and a resolution of 0.5 microns also. The specific model was selected such that the nominal air-gap length of 0.3 mm falls close to the middle of its linear range (0.5 mm). The overall dimensions of the sensor are 7.9 mm diameter and 2.5 mm thickness. Its extremely small size and high resolution make it an ideal candidate for this bearing system.

The proposed sensor locations are shown in Figure 8. The sensors will be epoxy mounted in depressions milled in the aluminum carriage and measure the distance between the carriage and the shaft (which is also the distance between the pole and the shaft). Small holes for the lead wires will also be needed, but these are minor modifications. Eight sensors will be used in total (two for each pole piece), providing double redundancy of information and hence more accurate support.

ELECTRONICS

The electronic functions required to close the control loops on the magnetic bearings are as follows:

(1) Position sensor interface
(2) Sensor signal processing
(3) Loop compensation
(4) Actuator signal processing
(5) Coil power driver

High reliability and low quiescent power dissipation dictate the goals of circuit simplicity and minimal part-count. These goals are best achieved with the use of analog circuitry. In addition, the lack of digital circuitry will eliminate the interference produced by high-speed switching and allow better signal-to-noise performance. The implementation of each of the above functions is described in the following paragraphs.

The position sensor interface provides the functions necessary to measure the variation in the capacitance of the sensor with displacement of the sensed object and to produce a linear voltage per displacement output. This is accomplished by exciting the sensor with a high-frequency ac current and measuring the ac voltage developed across the sensor. This voltage is then demodulated and filtered and corrected for its inverse proportionality to displacement. It is currently planned to purchase the unit which has been specially designed by the sensor manufacturer to interface to the selected position sensors.

The sensor signal processing must process the output of the eight sensors into the information required to control the five constrained degrees of freedom of the suspended translator head. The use of eight sensors results in the existence of redundant information. This redundancy will be accommodated by averaging signals with analogous information. The resultant signals will then be added to or subtracted from one another to produce translation and rotation information respectively. Implementing this function will require five operational amplifiers, one to produce the position signal for each of the five degrees of freedom.

The loop compensation circuitry multiplies the position signal for each control loop by the frequency dependent transfer function required to achieve the required stiffness and ensure loop stability. The specified integration is achieved with capacitive feedback around the operational amplifier resulting in approximately 120 db of open loop gain at dc. The remaining four poles and zeroes are produced by combinations of resistors and capacitors in either the input or feedback paths. Thus, again implementation will require only five op-amps, one per loop.

The actuator signal processing performs roughly the converse function to the sensor signal processing, i.e., it turns the five outputs from the control loop compensation stages into the six signals required to drive the actuator coils. Again addition and subtraction

of the signals is required and could be accomplished with six op-amps; however, the use of power op-amps in the coil power driver stages will allow implementation of both these functions in a single device per actuator.

The coil power drivers simply provide the voltage and current capability necessary to drive the actuator coils over their full force range. In order to keep the output-current requirement reasonable, it is planned to use +/-30 Volt power supplies for this stage. The use of separate power supplies for the power and signal stages also reduces the coupling of output power disturbances into the signal channels, thereby preventing parasitic feedback oscillations.

CONCLUSIONS

The overall technical objective of this program was to establish the technical feasibility of developing magnetic bearings for an optical disk buffer. The approach taken was to develop the specifications for the magnetic bearings and define the hardware configuration, controller characteristics, position sensors, and electronic functions required. Successful completion of these tasks is considered evidence of the technical feasibility of applying magnetic bearing technology to this device. The required electromagnetic hardware fits easily inside the available volume, and has reasonable power consumption. The position sensors are small and have excellent resolution and linearity. The controller requirements are modest as are the remaining electronic functions which need to be implemented. The extension of this design definition to the detailed design required for prototype development would appear to be an extremely straightforward effort.

BIBLIOGRAPHY

1. Downer, J.R., "Design of Large Angle Magnetic Suspensions," ScD Thesis, Massachusetts Institute of Technology, May 1986.

2. Levine, M.L., "A High Data Rate, High Capacity Optical Disk Buffer," 7th IEEE Symposium on Mass Storage Systems, Tucson, Arizona, November 4-7, 1985.

3. Roters, H., Electromagnetic Devices, New York: John Wiley & Sons, Inc., 1941.

4. Sabnis, A., "Analytical Techniques for Magnetic Bearings," PhD Thesis, University of California, Berkeley, June 1974.

5. Spin and Space Systems, Inc., Magnetic Suspension for Rotating Equipment, SBIR Phase I Final Report, Phoenix, Arizona, March 1980.

6. Studer, P.A., Magnetic Bearings for Instruments in the Space Environment, NASA Technical Memorandum 78048, Goddard Space Flight Center, Greenbelt, Maryland, 1978.

7. Watson, E.G., "Modal Analysis of Air Bearing Translator," RCA Internal Correspondence, January 1986.

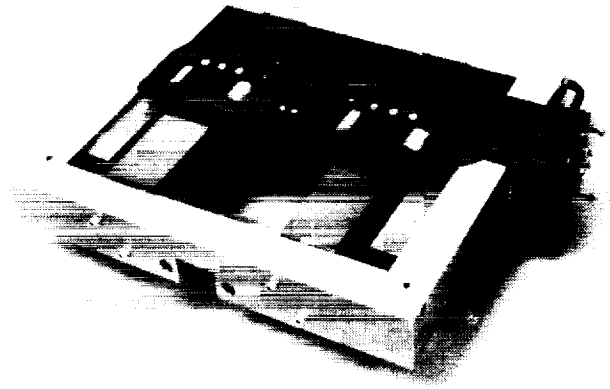

Figure 1. NASA/RCA translator assembly.

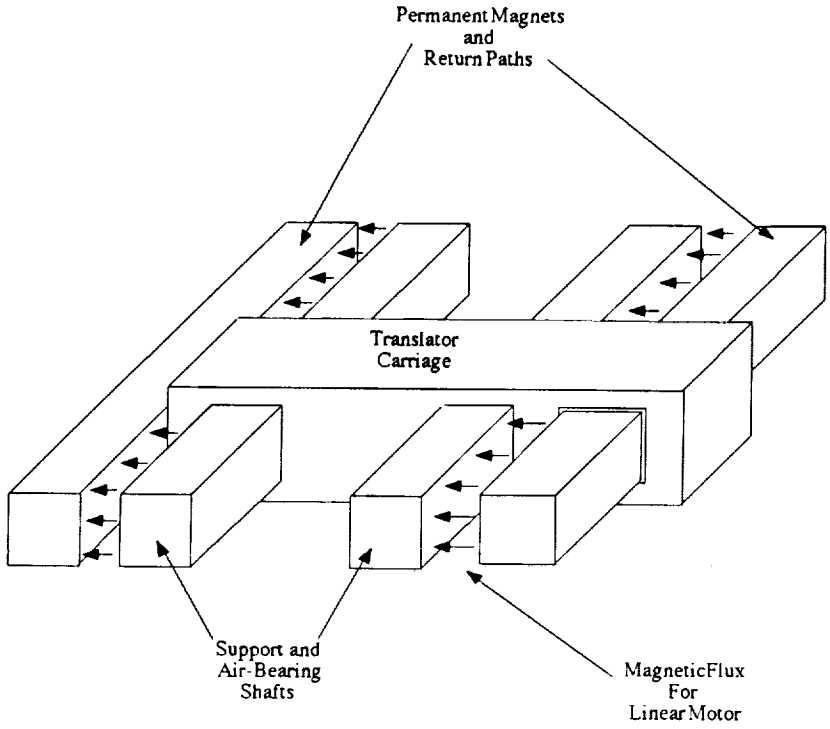

Figure 2. Existing magnetic structure.

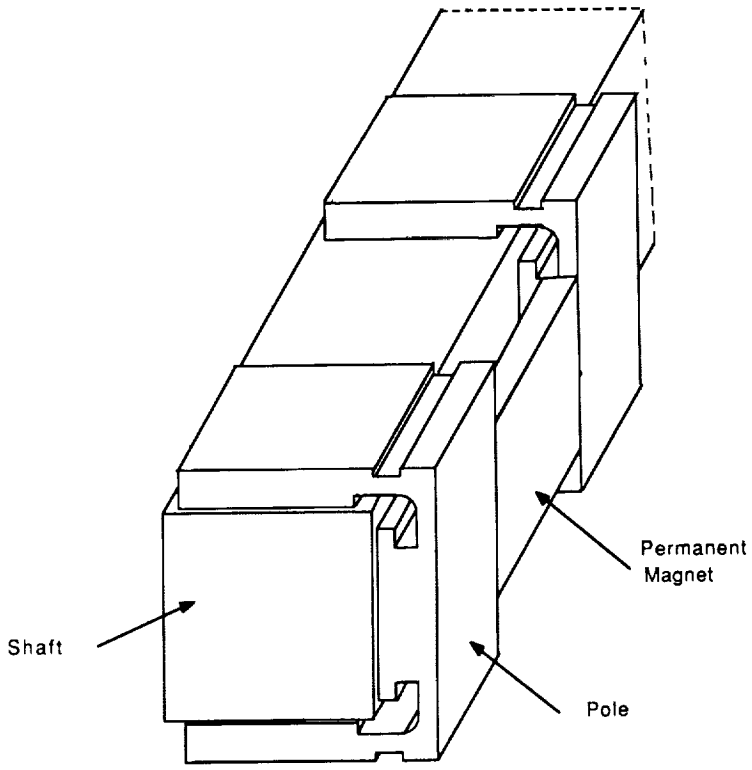

Figure 3. Preliminary bearing concept.

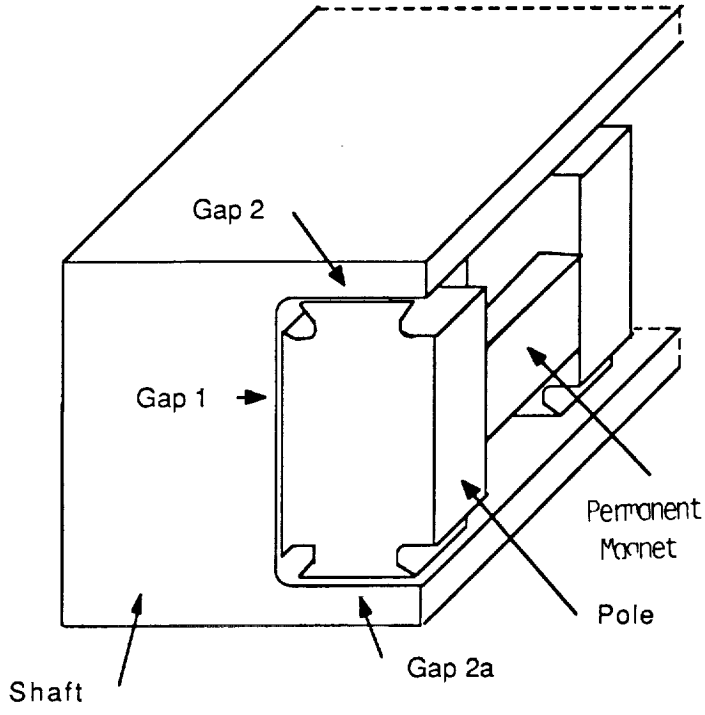

Figure 4. Candidate bearing concept.

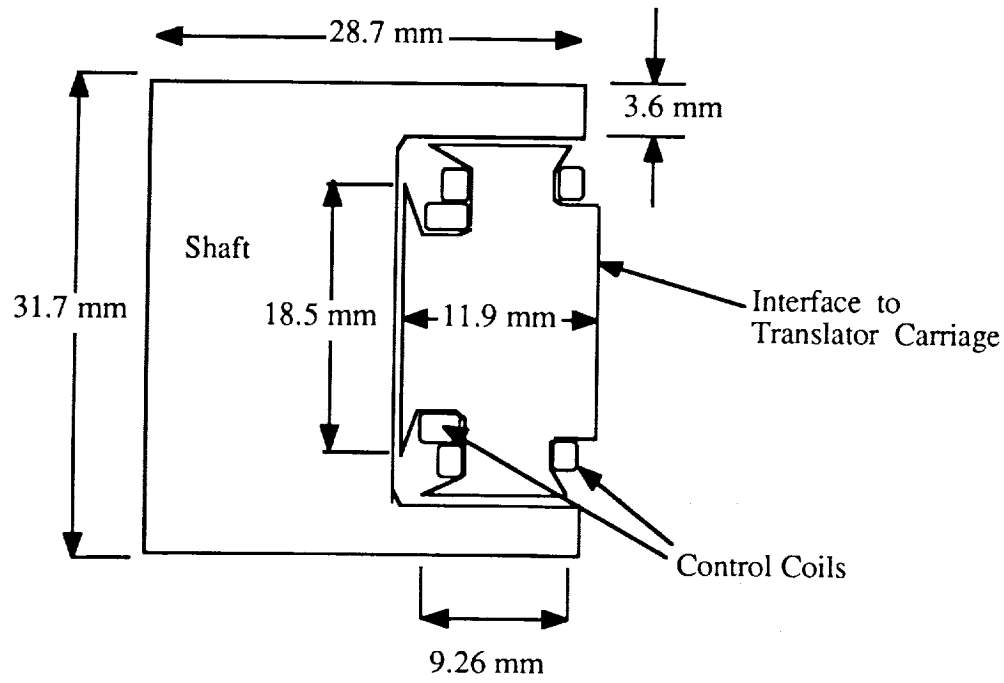

Figure 5. Translator bearing dimensions.

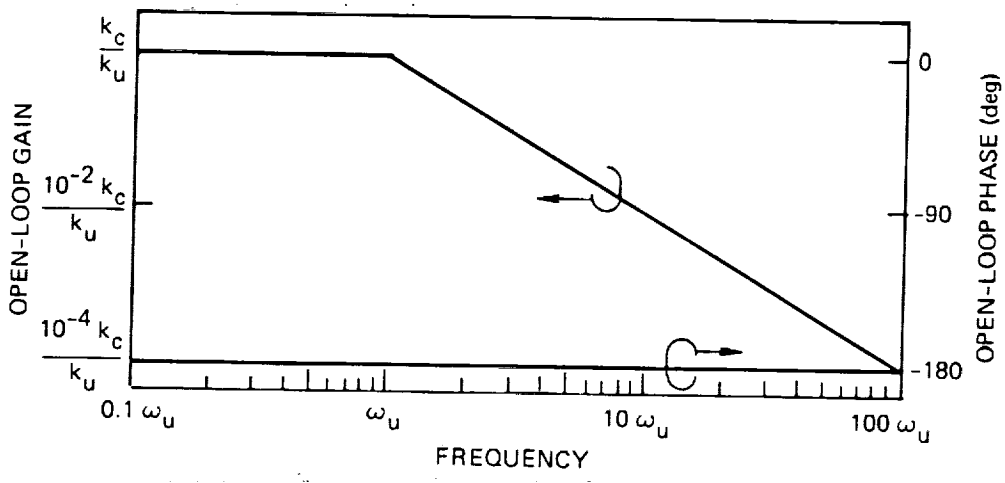

Figure 6. Unstable-plant frequency response.

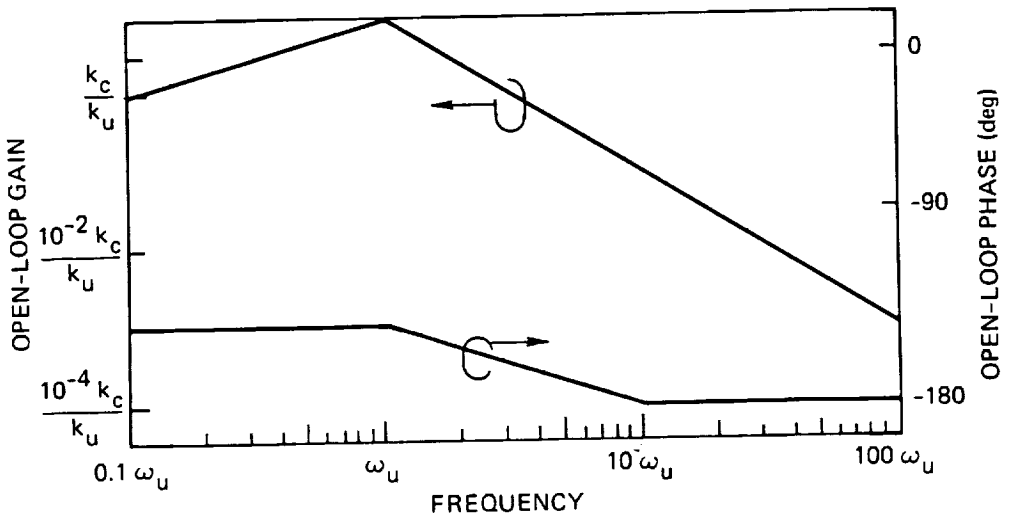

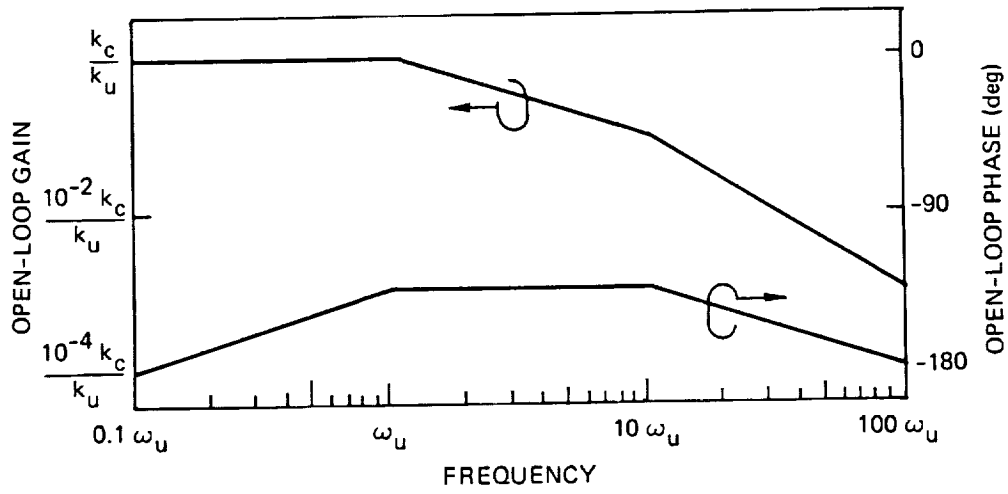

Figure 7. Lead-lag compensation of plant.

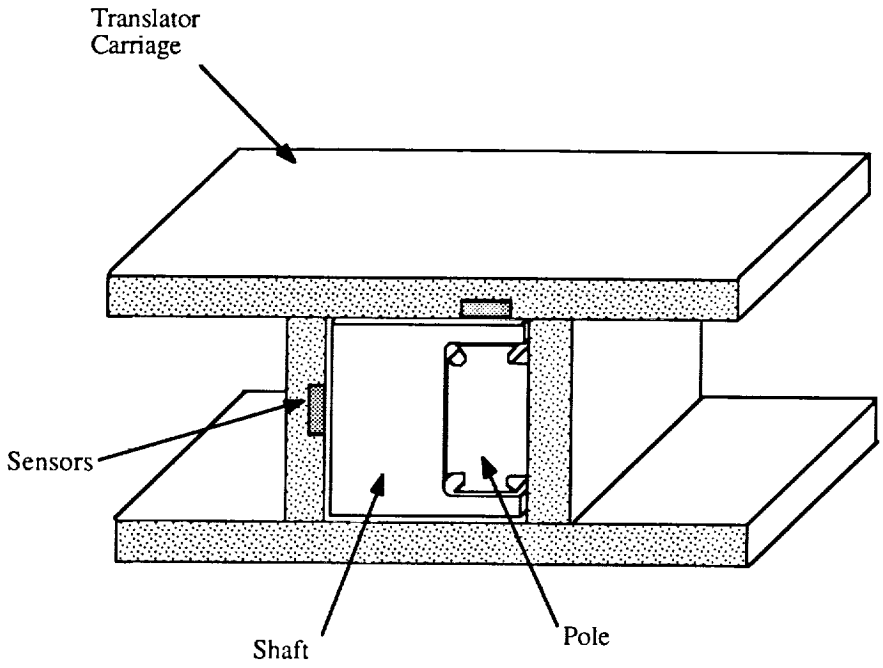

Figure 8. Position sensor locations.

OMIT

Active Magnetic Bearings Applied to Industrial Compressors

R. Gordon Kirk, Virgina Polytechnic Institute and State University

Jerry F. Hustak, Kenneth A. Schoeneck, Dresser-Rand Turbo Division

ACTIVE MAGNETIC BEARINGS APPLIED TO INDUSTRIAL COMPRESSORS

R. G. Kirk
Virginia Polytechnic Institute and State University
Blacksburg, Virginia 24061

J. F. Hustak
K. A. Schoeneck
Dresser-Rand Turbo Division
Olean, New York

SUMMARY

The design and shop test results are given for a high-speed eight-stage centrifugal compressor supported by active magnetic bearings. A brief summary of the basic operation of active magnetic bearings and the required rotor dynamics analysis are presented with specific attention given to design considerations for optimum rotor stability. The concerns for retrofits of magnetic bearings in existing machinery are discussed with supporting analysis of a four-stage centrifugal compressor. The current status of industrial machinery in North America using this new support system is presented and recommendations are given on design and analysis requirements for successful machinery operation of either retrofit or new design turbomachinery.

INTRODUCTION

A new technology in the form of active magnetic bearings (AMB) is being introduced into the marketplace for use on individual turbomachinery. The features of this technology, when applied to turbocompressor design, result in several economic, performance, and versatility improvements unavailable to the industry at the present time. Active magnetic bearings used in conjunction with dry gas seals and dry couplings now enable both the manufacturer and user to think in terms of oil-free centrifugal compressors.

Patent activity on passive, active, and combination magnetic bearing systems spans 150 years. The bulk of the initial investigations centered on permanent magnetic systems because they were easy to fabricate. It was later shown, however, that a passive magnetic suspension for three axes of displacement is unstable. This theory, first stated by Earnshaw (1) in 1842 is still valid today. The first totally active magnetic suspension system was described (2) and documented in a patent issued in 1957, but application to practical design conditions were not possible due to a lack of suitable electronic circuitry to switch the large DC currents required. In 1970, a totally active magnetic suspension system was developed for a communications satellite and in 1976, a new company was formed to further develop and commercially market active magnetic bearing systems internationally (3,4).

PRINCIPLE OF ACTIVE MAGNETIC BEARING OPERATION

The AMB is composed of two major mechanical parts consisting of the rotor and the stator. Both are made of ferromagnetic laminations. The rotor laminations are placed on the machine shaft at the selected journal location. The stator laminations are slotted and include windings to provide the magnetic levitation and position control. For each degree of freedom, two electromagnets are required since they operate by attraction only. Figure 1 shows the stator laminate construction of a radial bearing with the rotor laminate sleeve in the background.

Rotor position is monitored by sensors, and this signal is compared to a nominal reference signal with a closed loop controller which supplies a command signal to the power amplifier. These amplifiers provide power to the electromagnets to resist rotor movement from the nominal position. The design of the control loop gives the option to select the effective bearing damping and stiffness. The details of this design procedure are not the subject of this paper but the values of stiffness and damping must be carefully selected to give the rotor system the desired optimum dynamic response and stability.

This design concept can be applied to both radial and axial thrust bearings to give total control of a rotating rotor system. The load capacity of the AMB using standard materials can be made equal to standard fluid-film bearing designs. The overload condition for the AMB is controlled by auxiliary bearings which must be designed to provide rotor constraint in the event of system power failure or momentary transient overload.

The many advantages and detailed design requirements for the AMB are discussed in greater detail by Haberman (3,4). The application of the AMB to industrial compressors with proper evaluation of the rotor dynamic response and stability is essential for success of this new technology. This latter concern will be addressed in the following discussion.

DEVELOPMENT CENTRIFUGAL COMPRESSOR WITH AMB

Figure 2 is a view of an eight-stage, horizontally split, back-to-back centrifugal compressor equipped with magnetic radial and thrust bearings and gas seals on test at the authors' former company, 1980. The eight-stage rotor housed inside the compressor, originally designed to run at 167 Hz (10,000 rpm) on hydrodynamic bearings, has since operated successfully for 750 hours at speeds up to 217 Hz (13,000 rpm) on magnetic bearings. The compressor is shown attached to two closed loops constructed for the purpose of operating the rotor in a pressurized environment over a wide range of pressures and flows from choke to surge.

One unique feature of this compressor was the installation of the thrust and journal bearings located on the free end of the rotor directly into the gas (nitrogen) pressurized environment, thereby eliminating the need for one shaft seal. To illustrate the concept of a nonlubricated centrifugal compressor, a gas seal was chosen as the main shaft seal on the coupling end of the rotor. Table I summarizes some of the important design features of the eight-stage back-to-back rotor while Fig. 3 illustrates the appearance of the fully assembled test rotor.

Before power is applied to the bearings, the rotor is supported on two auxiliary ball bearings located in close proximity to the AMB. The clearance between the rotor and the inner race of the ball bearing is selected to prevent rotor contact with the AMB pole pieces or the internal seals of the compressor while the rotor is at rest or during an emergency shutdown. Typical shaft radial clearances in the AMB, internal seals, and auxiliary bearing inner race are 0.3 mm (0.012 in.), 0.254 mm (0.010 in.), and 0.15 mm (0.006 in.), respectively. When power is applied to the electronic controls, the electromagnets levitate the rotor in the magnetic field and rotation of the driving source, such as a motor or turbine, can be started. The sensors and control system regulate the strength and direction of the magnetic fields to maintain exact rotor position by continually adjusting to the changing forces on the rotor. Should both the main and redundant features of the AMB fail simultaneously, the auxiliary bearings and rotor system are designed to permit safe deceleration.

Magnetic bearing stiffness and damping properties are controlled by a PID (Proportional, Integral, Derivative) analog control loop that allows some flexibility for adjustment. The stiffness and damping characteristics are axi-symmetric, i.e., identical in both the horizontal and vertical directions. The resultant dynamic bearing stiffness, KD, is a complex number represented by the vectorial summation of a "real" stiffness component (K) and an "imaginary" stiffness component ($c\omega$).

$$KD = \sqrt{K^2 + (c\omega)^2} \tag{1}$$

The phase relationship (α) between the "real" (K) and "imaginary (cw) components is given by

$$\alpha = \arctan (c\omega/K) \tag{2}$$

where K = static real stiffness (N/m), ω = angular velocity of journal vibraton (sec^{-1}). Variation of the phase angle ranges from 0 to 90 degrees with typical values in the 30 to 40 degree range. Adjusting the amount of bearing damping is accomplished by changing the passive elements of the compensation circuit in the PID control loop. The amount of gain applied to the circuit through a potentiometer provides a proportional increase in the resultant dynamic stiffness, KD.

The undamped critical speed map shown in Fig. 4 compares the standard fluid film bearing/oil seal design to the magnetic bearing/gas seal design for the 8-stage development compressor. The magentic bearing design increased the first rigid bearing mode by reducing the bearing span but decreased the second, third, and fourth modes due to the additional weight of the ferromagnetic journal sleeves and the larger diameter thrust collar. Superimposed on this map are the stiffness and damping properties of the electromagnetic bearings as a function of rotor speed. For a design speed of 167 Hz (10,000 rpm), Fig. 4 indicates the rotor would have to pass through three critical speeds and operate approximately 20 percent above the third critical and 40 percent below the fourth critical. Furthermore, since both the first and second criticals are rigid body modes, only a significant response at approximately 133 Hz (8000 rpm) would be expected as the rotor passed through its third (free-free mode) critical. Subsequent unbalance forced response calculations verified these expectations with acceptable operations of the compressor to 233 Hz (14,000 rpm) (see Figs. 5 and 6).

The damping required for optimum stability may be arrived at by plotting the systems' calculated damped natural frequencies versus growth factors (5), (6), (7), For the first mode stiffness of 22.8 N/μm (130,000 lb/in), Fig. 7 shows the movement of the eigenvalues as the bearing damping varies. Increased damping levels cause the first and second modes to become critically damped. The third mode

increases in stability up to a point of 87.7 N-s/mm (501 lb-s/in.) but then decreases as damping is increased further. Since the first and second modes become critically damped, a second study was undertaken to determine if the third mode would go unstable at its corresponding stiffness of 40.1 N/μm (229,000 lb/in). The results of that analysis are presented in Fig. 8 and indicate the third mode becomes critically damped as the damping is increased, while the first mode damping would be at an optimum for 112.9 N-s/mm (645 lb-s/in.). The behavior of the first and third modes, resulting from the increase in bearing stiffness, is similar to results presented by Lund (5). These results indicate that a level of 70-87.5 N-s/mm (400-500 lb-s/in.) would be ideal for all modes up to and including the fourth.

The stiffness and damping characteristics for the magnetic bearing are given in Fig. 9. Active magnetic bearings have an important difference when compared to conventional fluid film bearings. Typical preloaded five-shoe tilt-pad bearings have characteristics generated predominantly by operating speed, with little influence from nonsynchronous excitations (8). The active magnetic bearing characteristics, shown in Fig. 9, are dependent on the frequency of excitation regardless of operating speed. For a given stiffness value selected to minimize unbalance forced response, the damping characteristics at subsynchronous excitation frequencies can be specified to assure optimum stability (3), (4).

The test program outlined for the compressor was directed toward confirming the analytical predictions for the dynamic behavior of the rotor and experimentally demonstrating the reliability of the complete system under typical operating conditions. The fully assembled compressor was installed on the test stand and operated at a maximum discharge pressure of 4.1 MPa (600 psig) with speeds up to 217 Hz (13,000 rpm). The results for a deceleration as recorded at the bearing probe locations are given in Figs. 10 and 11. The test results indicate well-damped rotor responses at 67 Hz (4000 rpm) and 133 Hz (8000 rpm). In comparison, the synchronous response to unbalance shown in Figs. 5 and 6 displays well-damped rotor response at 67 Hz (4000 rpm) and 133 Hz (8000 rpm). The amplitude of vibration is difficult to predict since the actual rotor unbalance configuration is made up of varying amounts of unbalance at different axial locations along the rotor. The predicted peak response frequencies are considered to be in good agreement with the test results.

DESIGN EVALUATION OF A FIELD RETROFIT

The economic advantages of gas seals and/or magentic bearings have prompted interest in retrofit of existing units. For either retrofit or new machinery, attention must be given to placement of critical speeds for both main and backup bearings, response sensitivity, and overall stability considerations. The preliminary design study for a four-stage high-speed centrifugal compressor will illustrate in more detail the parameters that must be considered for total system dynamic analysis. The basic design parameters for this rotor are indicatd in the second column of Table 1.

The undamped critical speed map for the four-stage compressor and dynamic stiffness values are shown in Figs. 12 and 13. The magnetic bearing stiffness is positioned such that the compressor must pass through three critical speeds before reaching a maximum continuous operating speed of 241.7 Hz (14,500 rpm). Due to the rigid body nature of the second and third modes, the actual damped critical speeds will occur from the first and fourth modes. The frequencies at which these modes respond, shown in Figs. 14 and 15, are 71.7 Hz (4300 rpm) and 305 Hz (18,300 rpm).

A plot of the systems calculated damped natural frequencies versus growth factor for a constant first mode stiffness of 15.1 N/μm (86,300 lb/in.) is shown in Fig. 16. The first forward mode typically goes unstable while the second and third modes become critically damped as the bearing damping is increased. For this compressor design, the first mode increases in stability as the damping increases up to 39.4 N-s/mm (225 lb-s/in.) but then decreases as the damping is increased further. The damping value initially supplied, 24.5 N-s/mm (140 lb-s/in.), should be increased by 61 percent based on the results of this analysis.

The optimum damping for stabiity was also calculated by an approximate method using the modal mass, rigid bearing critical frequency, and bearing stiffness (see Table_1). The equation from Ref. (9) can be written as follows (valid for high K ratios):

$$C_o = 2.893 \times 10^{-2} N_{cr} \left[M_m + \frac{4.98 \times 10^5 K_b}{N_{cr}^2} \right] \quad (3)$$

Example for four-stage first mode:

$$C_o = 2.893 \times 10^{-2} \times (90.39) \times (649 + (4.98 \times 10^5) \times (15.1)/(90.39)^2)$$

$$= 45.4 \text{ N-s/mm}$$

This quick calculation gives an answer 15 percent higher than the lengthy optimum damping method used in Fig. 16.

Figure 17 shows a comparison of stability versus aerodynamic excitation between the conventional fluid film design and the magnetic bearing retrofit design. The increase in stability due to the magnetic bearing and dry gas seal design moves the log dec from near zero to a value of 1.41.

Current Status of Active Magnetic Bearings

The application of magnetic bearings for industrial installations in North America has progressed to the point that both retrofit and new, original design applications have been initiated with successful operation on test and in the field. Table 2 shows the current status of new and retrofit turbomachinery in North America. The use of this new method of turbomachinery support and control has not been totally free of test stand problems. Machinery must withstand extremes of temperatures for various design applciations which must be properly evaluated to assure adequate bearing materials selection. In addition, loading from rotor system balance variations due to initial build and transient excitation resulting from process upsets must be accounted for in the initial design considerations.

These potential problems make the design prediction capability and initial design studies for rotor dynamics analysis just as important for AMB as it has been for machinery supported on fluid-film bearings.

CONCLUSIONS AND RECOMMENDATIONS

The capability of an active magnetic bearing system to support a flexible turbocompressor rotor and simultaneously influence its vibrations has been successfully demonstrated. During 750 hours of accumulated operating time for the development compressor equipped with active magnetic bearings, the following observations were made:

1. The rotor behaved in a stable manner at all times when accelerating/decelerating through its first three critical speeds.
2. The rotor behaved in a stable manner while undergoing surge cycles at maximum discharge pressure.
3. The magnetic bearings were able to suppress rotor amplitude to avoid contact between rotational and stationary components through the first three modes up to a speed of 271 Hz (13,000 rpm). Speeds beyond this point were limited by impeller stress considerations.

The following recommendations can be made for the design and analysis of magnetic bearing suspension turbomachinery:

1. Bearing stiffness should be selected by evaluation of shaft stiffness ratio with typical placement at the beginning of the third mode ramp on the undamped critical speed map.
2. Bearing damping should be specified to give the optimum stability with consideration given to all modes below maximum operating speed.
3. Consideration must be given to the next mode above operating speed (typically the fourth mode) to avoid interference between operating speeds and system natural frequencies.
4. The machinery must be engineered such that the shaft critical speeds are at least 10 percent lower or higher than any continuous operating speed when the rotor system is assumed to be operating on the auxiliary bearings.

ACKNOWLEDGMENTS

The authors wish to thank Mr. Howard Moses and Mr. David Weise of Magnetic Bearings Incorporated, Radford, VA for their assistance in the preparation of this paper and the permission to publish the information given in Table 2.

REFERENCES

1. Earnshaw, S., "On the Nature of the Molecular Forces," Trans. Cambridge Phil. Soc. 7, 97-112, 1842.

2. Tournier, M., and Laurenceau, P., "Suspension magnetique d'une maquette en soufflerie," La Recherche Aeronautique 7-8, 1957.

3. Haberman, H., "The Active Magnetic Bearing Enables Optimum Damping of Flexible Rotors," ASME Paper 84-GT-117.

4. Haberman, H., and Brunet, M., "The Active Magnetic Bearing Enables Optimum Control of Machine Vibrations," ASME Paper 85-GT-22, Presented at Gas Turbine Conf., Houston, TX, March 18-21, 1985.

5. Lund, J. W., "Stability and Damped Critical Speeds of a Flexible Rotor in Fluid-Film Bearings," J. of Eng. for Industry, Trans. ASME, Series B. 96, 2, pp. 509-517, May (1974).

6. Bansal, P., and Kirk, R. G., "Stability and Damped Critical Speeds of Rotor-Bearing Systems," J. of Eng. for Industry, Trans. ASME, Series B, 98, 1, pp. 108, February (1976).

7. Kirk, R. G., "Stability and Damped Critical Speeds--How to Calculate and Interpret the Results," CAGI Technical Digest, 12, 2, pp. 1-14 (1980).

8. Wilson, B. W., and Barrett, L. E., "The Effect of Eigenvalue-Dependent Tilt Pad Bearing Characteristics on the Stability of Rotor-Bearing Systems," Univ. of Virginia, Report No. UVA643092/MAES5/321, January 1985.

9. Barrett, L. E. Gunter, E. J., and Allaire, P. E., "Optimum Bearing and Support Damping for Unbalance Response and Stability of Rotating Machinery," Trans. ASME, J. of Eng. for Power, pp. 1-6 (1978).

Table 1--Centrifugal Compressor Design Parameters and Nomenclature

Parameter, Nomenclature SI Units (US Units)	Eight-Stage		Four-Stage	
Operating Speed, N, Hz, (rpm)	217.7	(13 000)	241.7	(14 500)
Total Weight, W, N, (lb)	3678	(827)	1237	(278)
Bearing Span, mm, (in.)	1269	(49.97)	886	(34.88)
Shaft Length, mm, (in.)	1902	(74.90)	1253	(49.32)
Coupling End Overhang, mm, (in.)	304.8	(12)	184.9	(7.28)
Shaft Stiffness K_s, N/μm ,(lb/in.)	61.1	(3.49E5)	21.4	(1.22E5)
Bearing Stiffness @ MCOS, K_b, N/μm ,lb/in.	63.9	(3.65E5)	28	(1.60E5)
Stiffness Ratio, $\bar{K}$, Dim., (Dim.)	0.74	(0.74)	1.41	(1.41)
Mid-Span Diameter, mm, (in.)	123.9	(4.88)	76.2	(3)
Journal Diameter, mm, (in.)	187.5	(7.38)	93	(3.66)
First Rigid Bearing Critical, N_{cr}, Hz,(rpm)	92.52	(5551)	90.39	(5423)
First Peak Response Speed, FPS1, Hz, (rpm)	129.5	(7700)	71.67	(4300)
Second Peak Response Speed, FPS2, Hz, (rpm)	271.7	(16,300)	305	(18 300)
First Mode Modal Mass, M_m, N, (lb_m)	1775.	(399)	649	(146)
Bearing Stiffness @ N_1, K_{b1}, N/μm ,(lb/in.)	22.8	(1.30E5)	15.1	(8.63E4)
Optimum Damping (9), C_o, N-s/μm , (lb-s/in.)	9.18E-2	(524)	4.54E-2	(259)

Note: Values are given in both SI and US customary units. The measurements and calculations were made in US customary units.

Table 2 AMB Industrial Compressor Applications in North America

MACHINE	TYPE	SERVICE	DUTY	COMM	ROTOR WEIGHT (lb) N	THRUST LOAD (lb) N	SPEED (rpm) Hz	JOURNAL DIAMETER (in) cm	DRIVER RATING (HP) kw	OPERATING HOURS (*)
MTA-824BB	CENT COMP	DEVELOP-MENT	INTERMIT	1980	(850) 3778	(3150) 14 000	(13 000) 217	(7.5) 19.0	(5360) 3997	750
CDP-230	CENT COMP	PIPELINE	SEASONAL	1985	(3200) 14224	(12 000) 52 340	(5250) 87.5	(10.6) 26.9	(12 800) 9545	6800
CDP-416	CENT COMP	PIPELINE	SEASONAL	1986	(280) 1245	(3370) 14 980	(14 500) 242	(3.7) 9.4	(4250) 3095	6700
1B26	CENT COMP	PIPELINE	CONTINUOUS	1986	(780) 3467	(4050) 18 000	(11 000) 183	(6.5) 16.5	(5500) 4101	4800
IB26	CENT COMP	PIPELINE	CONTINUOUS	1987	(780) 3467	(4050) 18 000	(11 000) 183	(6.5) 16.5	(5500) 4101	300
CBF-842	CENT COMP	REFINERY	CONTINUOUS	1987	(1420) 6312	(4590) 20 403	(10 250) 171	(6.0) 15.2	(4500) 3356	750
5P2	CENT COMP	PIPELINE	SEASONAL	NEW	(1540) 6845	(5500) 24 448	(7140) 119	(6.0) 15.2	(16 600) 12 379	

*AMB Cabinet operating hours as of December 15, 1987

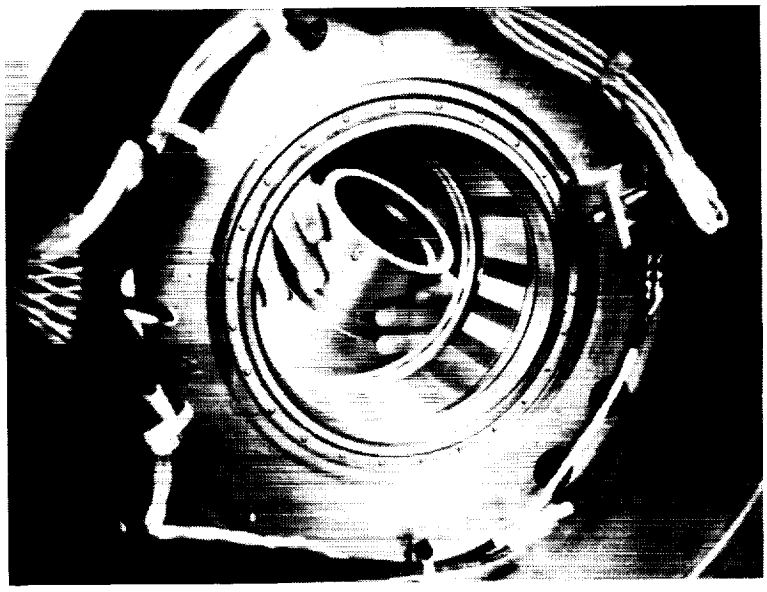

Figure 1. Active magnetic bearing stator with rotor sleeve in background.

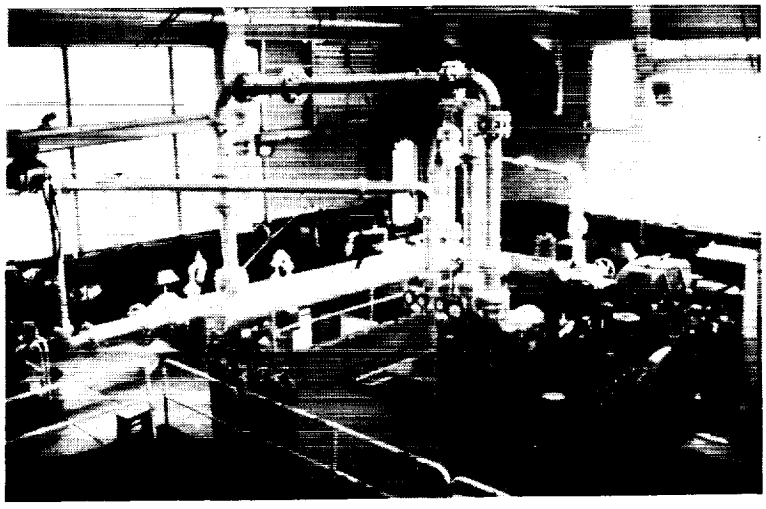

Figure 2. Eight-stage development compressor test setup.

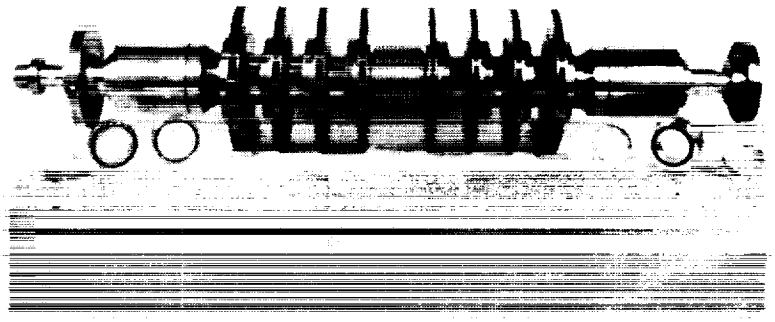

Figure 3. Eight-stage development compressor rotor.

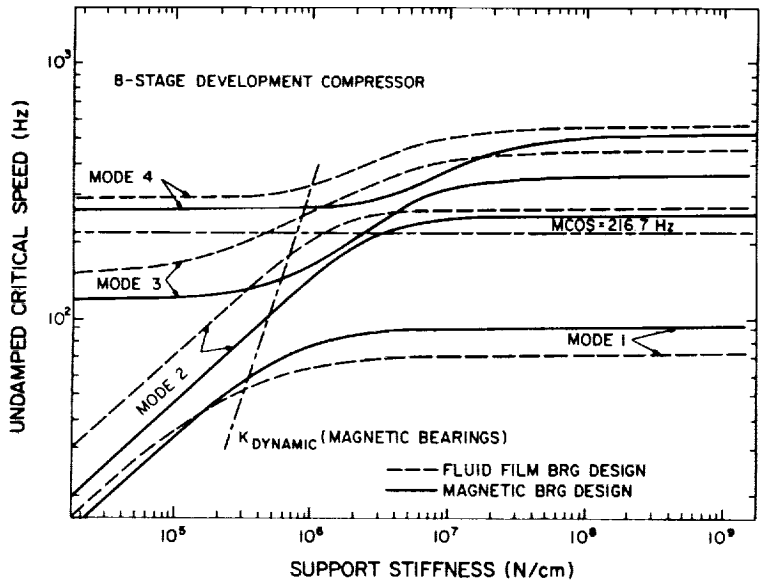

Figure 4. Eight-stage development compressor undamped critical speed map.

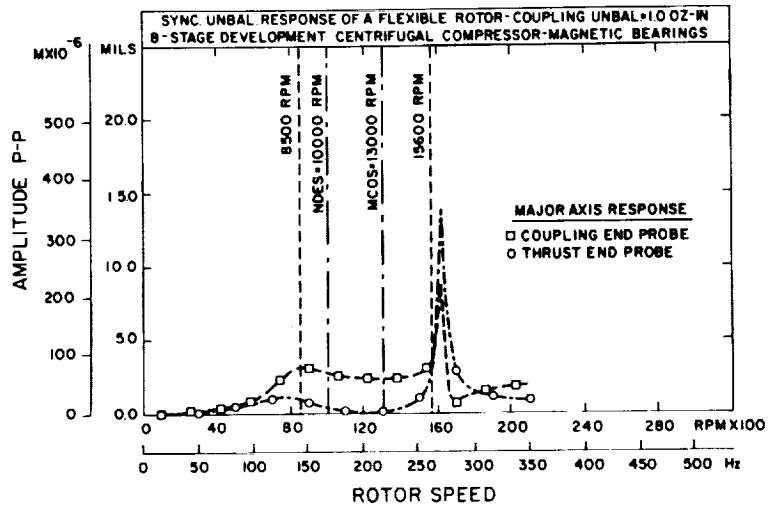

Figure 5. Eight-stage development compressor synchronous response to coupling unbalance.

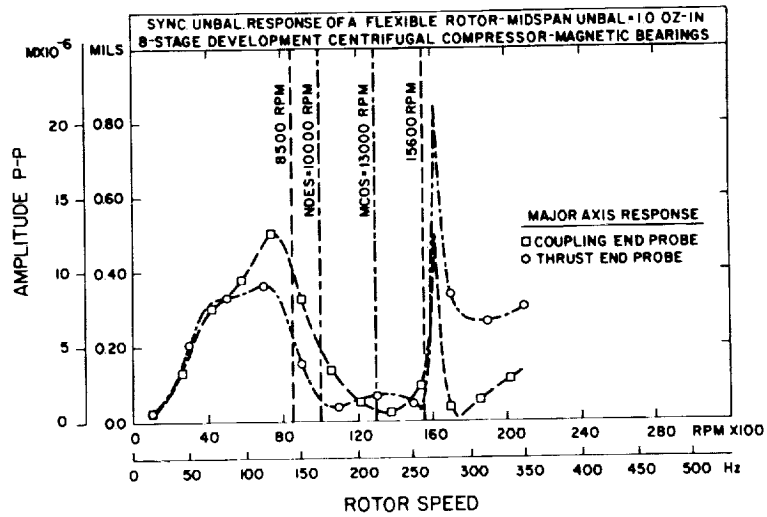

Figure 6. Eight-stage development compressor synchronous response to midspan unbalance.

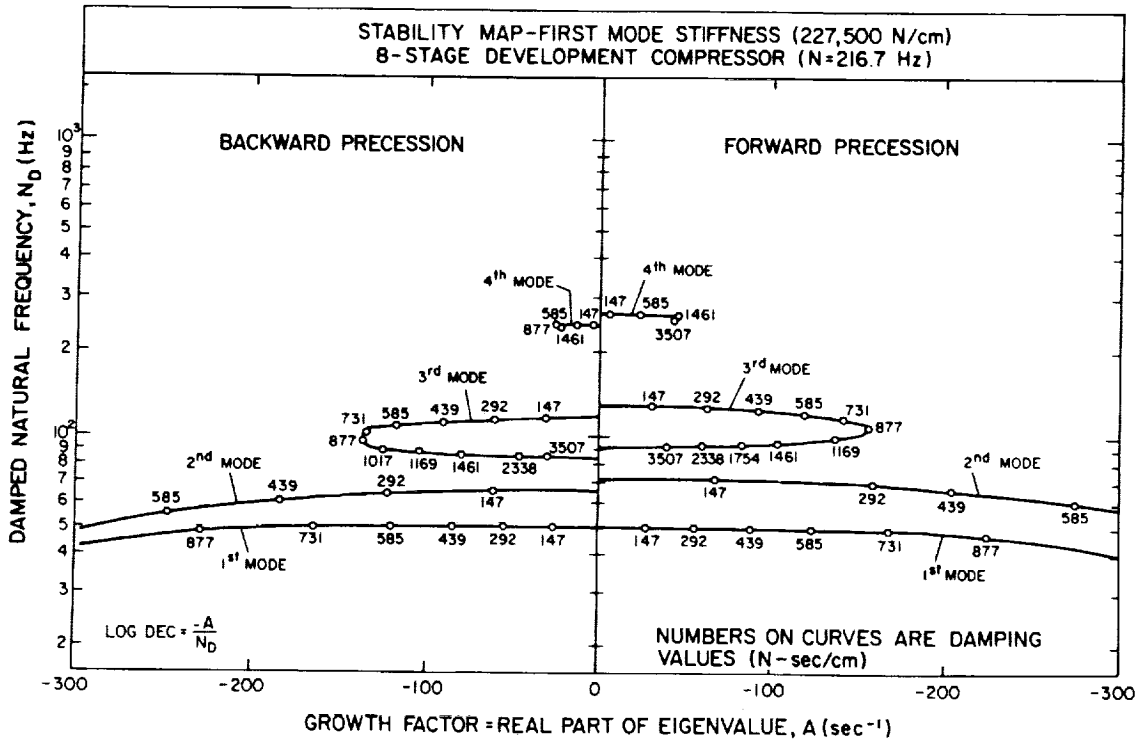

Figure 7. Eight-stage development compressor stability map for first mode stiffness.

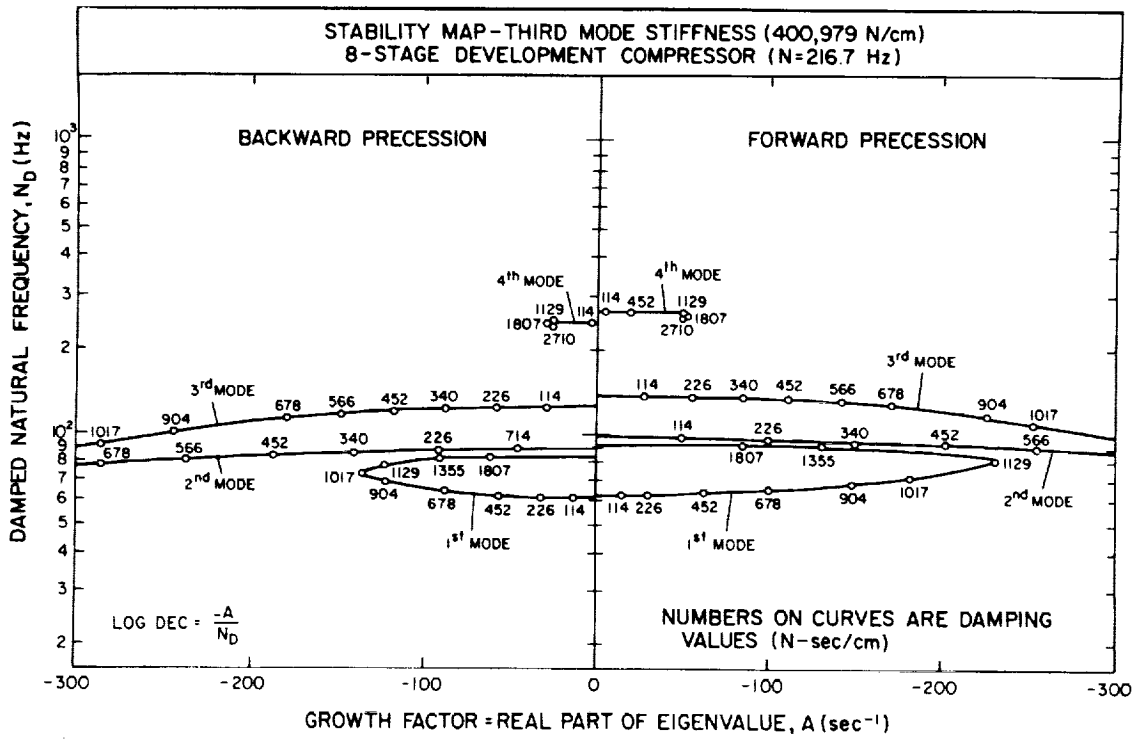

Figure 8. Eight-stage development compressor stability map for third mode stiffness.

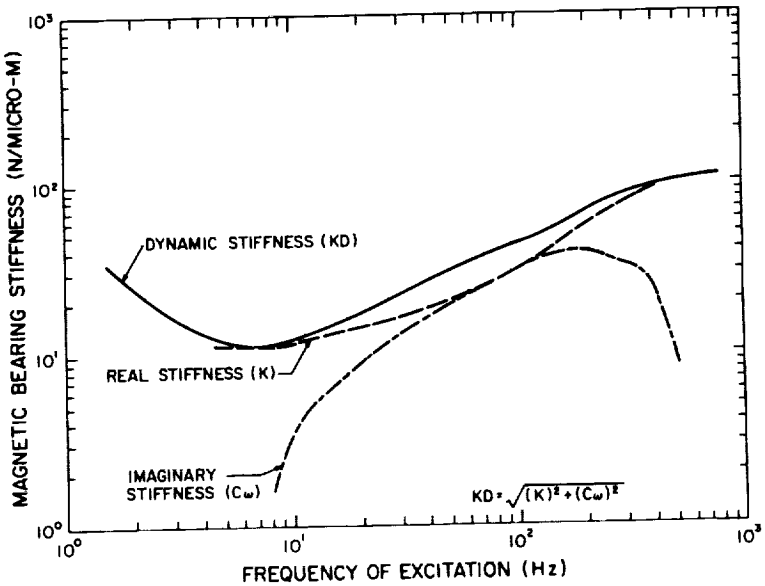

Figure 9. Eight-stage development compressor magnetic bearing characteristics.

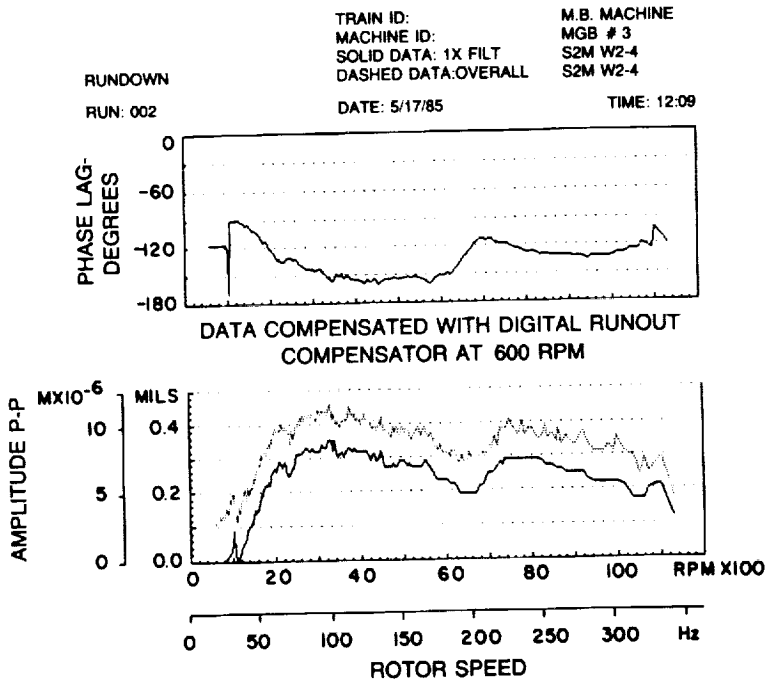

Figure 10. Eight-stage development compressor coupling end response from test results.

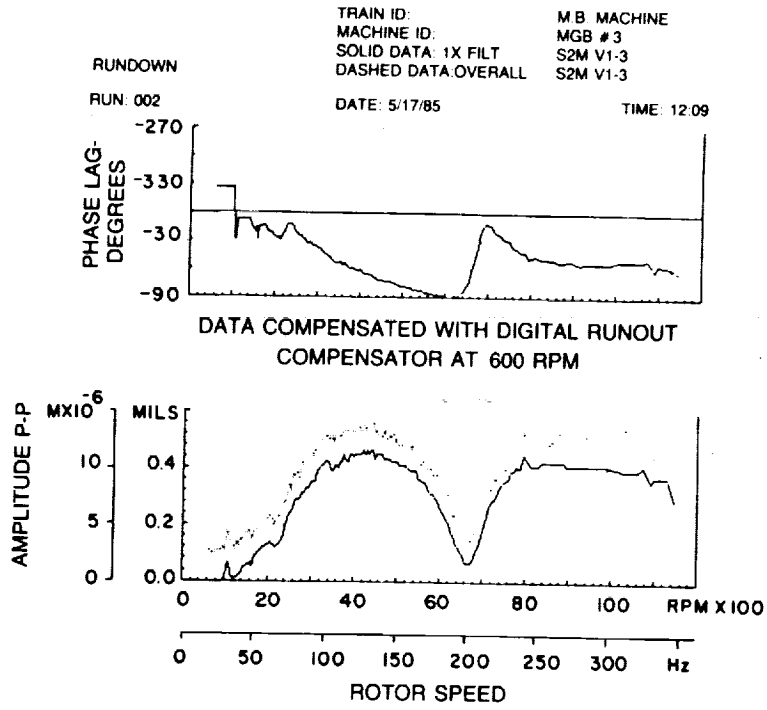

Figure 11. Eight-stage development compressor thrust end response from test results.

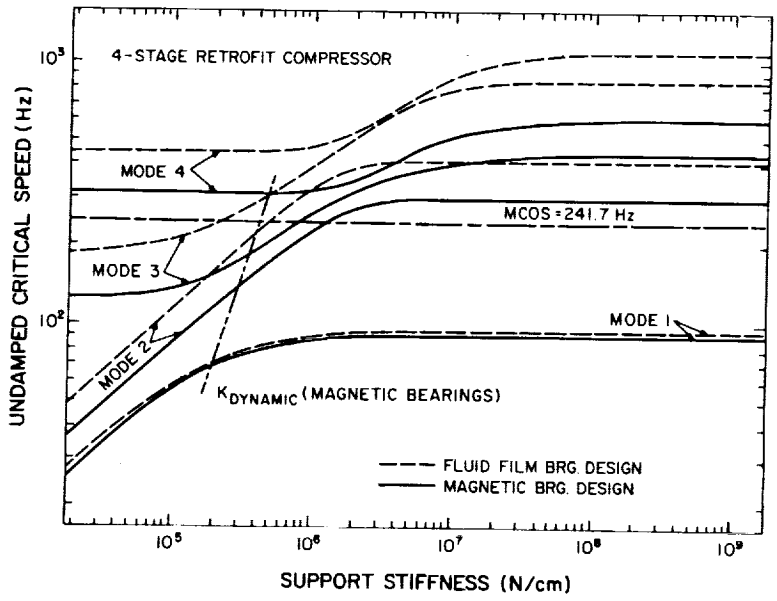

Figure 12. Four-stage retrofit compressor undamped critical speed map.

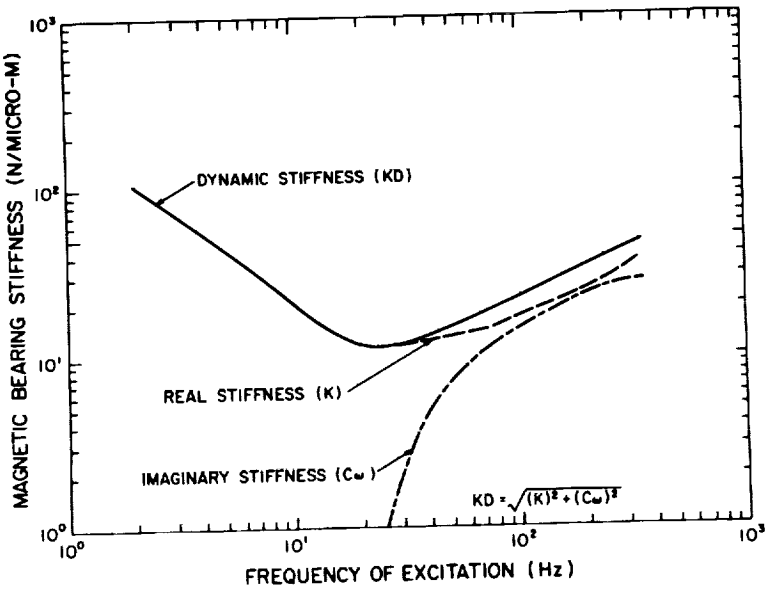

Figure 13. Four-stage retrofit compressor magnetic bearing characteristics.

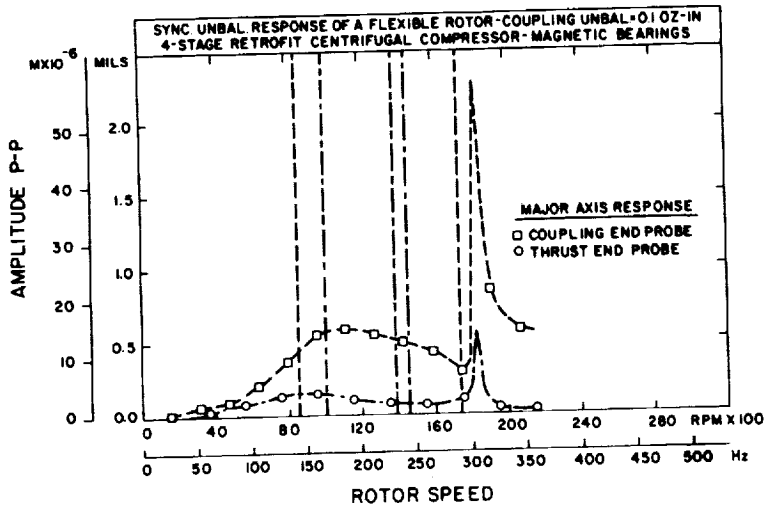

Figure 14. Four-stage retrofit compressor synchronous response to coupling unbalance.

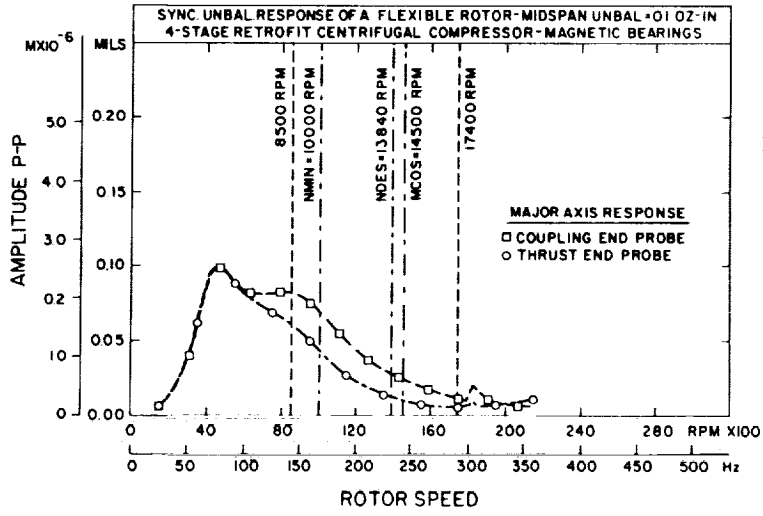

Figure 15. Four-stage retrofit compressor synchronous response to mid-span unbalance.

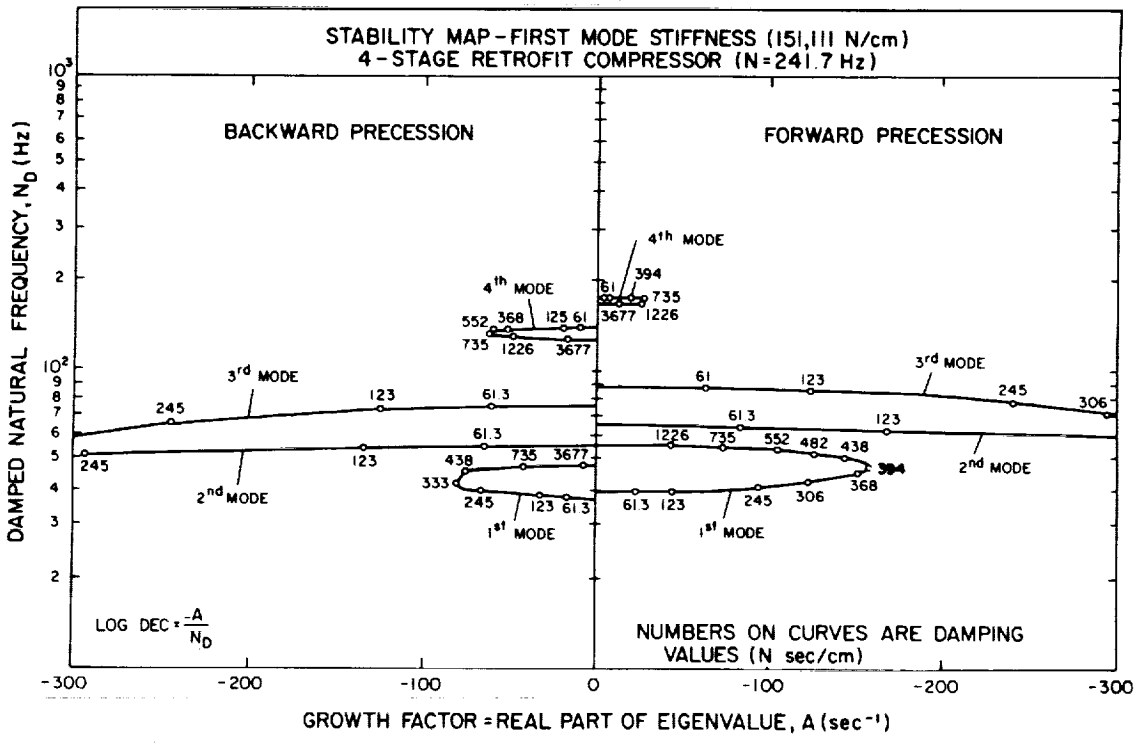

Figure 16. Four-stage retrofit compressor stability map for first mode stiffness.

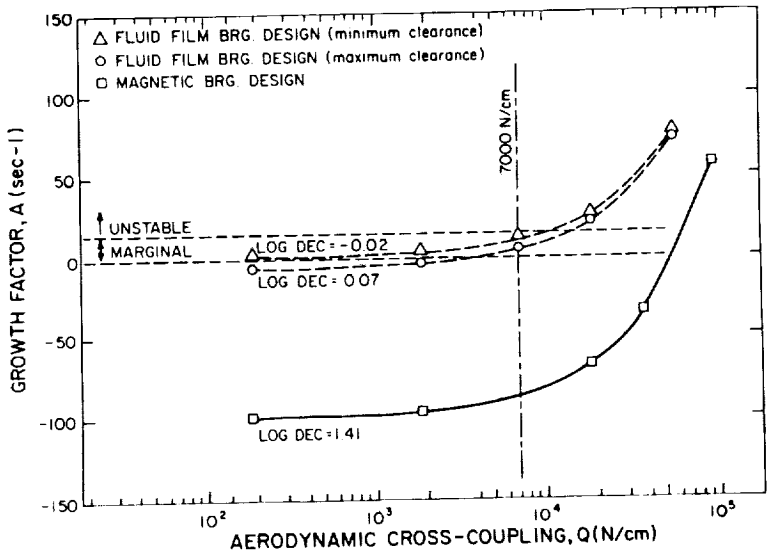

Figure 17. Four-stage retrofit compressor stability analysis results.

omit

Practical Limits to the Performance of Magnetic Bearings : Peak Force, Slew Rate and Displacement Sensitivity

Eric Maslen, Michael Scott, Robert R. Humphris, University of Virginia

Paul Hermann, Sundstrand Aviation Operations

Practical Limits to the Performance of Magnetic Bearings: Peak Force, Slew Rate, and Displacement Sensitivity[1]

E. Maslen, Research Associate (1)
P. Hermann, Chief - Rotating Machinery Research Mechanical (2)
M. Scott, Research Associate (1)
R. R. Humphris, Research Professor (1)

(1) Mechanical and Aerospace Engineering Department
Thornton Hall
University of Virginia
Charlottesville, VA

(2) Sundstrand Aviation Operations
4747 Harrison Ave.
Rockford, IL

Abstract

Magnetic bearings are subject to performance limits which are quite different from those of conventional bearings. These are due in part to the inherent nonlinearity of the device and in part to its electrical nature. Three important nonideal behaviors are presented: peak force capacity, force slew rate limitation, and sensitivity to rotor motion at large displacements. The problem of identifying the dynamic requirements of a magnetic bearing when used to support a known structure subject to known loads is discussed in the context of these limitations. Several simple design tools result from this investigation.

Introduction

Magnetic bearings are moving from the realm of science fiction into that of practical engineering. Not only is their feasibility being widely demonstrated, but many advantages over conventional bearings are becoming apparent. Amidst this atmosphere of optimism, it is important to recognize and understand the shortcomings of this class of devices. Hopefully, if our understanding of the limitations of magnetic bearings can at least keep pace with our concept of their advantages, premature disappointment can be avoided.

To the engineer accustomed to conventional bearings, the limiting behavior of magnetic bearings will be very unfamiliar. In stark contrast to fluid film bearings, these bearings become softer (less stiff) as the shaft excursion approaches the bearing clearance. Additionally, and perhaps even more alien, the rate at which the bearing force can change is strictly limited. This phenomenon is referred to as

[1]This work was supported in part by the Sundstrand Corporation Aviation Operations Division for study of aviation compressors. Partial funding was also provided by the Center for Innovative Technology of the Commonwealth of Virginia.

force slew rate limitation. Like the force slew rate, the peak force which can be generated is also subject to strict limits. These characteristics, which represent nonlinearities, are especially insistent because their onset can be quite abrupt.

Very little attention has been focused on these limitations in the literature. Britcher (ref. 1) and Sarma and Yamamura (ref. 2) have discussed operation of bearings in the magnetically saturated regime, for applications where field strength requirements are sufficiently stringent to justify the complexity of compensating for the resulting nonlinearity. Hebbale (ref. 3) presents a fairly thorough investigation of nonlinear performance in the unsaturated regime, but the study concentrates on eddy current effects in unlaminated rotors. Lamination of the rotor has become common practice and the eddy currents are readily reduced to where their contribution to nonlinear effects is minimal.

This paper represents an effort to describe some aspects of the limiting behavior of magnetic bearings and to suggest methods by which the required dynamic capacity of the bearing may be estimated.

Nomenclature

A_g	area of each air gap perpendicular to the magnetic flux	L_c	coil electrical inductance
A_p	minimum pole cross sectional area perpendicular to the magnetic flux	N	number of coil turns per pole pair
B	magnetic flux density	R_c	coil electrical resistance
B_{sat}	saturation flux density	R_f	current sensing resistance
F_x	bearing force in the x direction	t	time
F_{max}	bearing load capacity		
f	force slew rate: dF/dt	V_c	voltage across coil
g	length of the air gap	V_s	power supply voltage
G	nominal air gap: g(x = 0)	x	displacement of the rotor from the centered position
I_b	coil bias current: invariant	x_o	geometric clearance
i_p	coil perturbation current	β	sensitivity of the air gap to shaft displacement: $\partial g/\partial x$
K_i	magnetic actuator gain: $\partial F_x/\partial i_p$	τ	nondimensional bearing parameter
K_{nom}	nominal bearing stiffness	δ	bearing characteristic length
k_o	feedback gain: i_p/x	μ_o	magnetic permeability of air
K_x	open loop bearing stiffness	σ	nondimensional displacement: x/δ
$K_{x,cl}$	closed loop bearing stiffness	Φ	magnetic flux

Bearing Description

A wide variety of magnetic configurations has been proposed for accomplishing magnetic levitation. In applications where load capacity must be maximized relative to the size of the bearing package, the configuration described by figures 1 and 2 is the most commonly used.(refs. 3,4,5,6) For such a bearing, the force generated is a

nonlinear function of the current in the coils and the rotor displacement:

$$F_x = \frac{1}{4}\mu_o \beta N^2 A \left[(i_1/g_1)^2 - (i_2/g_2)^2 \right] \quad (1)$$

where the gap lengths have been assumed to vary linearly with rotor displacement:

$$g_1 = G - \beta x, \quad g_2 = G + \beta x \quad (2)$$

The bearing is made to do useful work on a system by varying the currents i_1 and i_2 in a manner correlated to the rotor displacement. Various methods have been proposed for linearizing the relation between a control signal and the resulting bearing force. These include establishing a bias flux and using the control signal to perturb it (refs. 5 and 6), relating i_1 and i_2 to the square root of the control signal (ref. 5), and using feedback of the actual magnetic flux level (ref. 4). In the discussion which ensues, the bearing is assumed to be bias flux linearized. The resulting performance and nonlinearities are similar to what would be obtained with square root linearization. Flux feedback has the potential to greatly reduce flux saturation nonlinearities and eliminate softening of the bearing with large displacements. However, no actual applications of this linearization have been reported; it seems more useful to discuss the prevalent designs.

Two methods have been reported for accomplishing bias flux linearization. The more common of the two is to establish a bias current in each of the bearing coils and then modulate it by adding a perturbation current proportional to the control signal. The other scheme is functionally identical except that the bias flux is established by linking the flux from a set of permanent magnets to that of the bearing coils in the air gaps. The latter scheme is somewhat more complicated to construct but can be substantially more energy efficient. Either scheme, however, is governed by the same operating equation and is subject to the same limiting behavior.

If bias flux linearization is employed, then equation (1) can be recast as

$$F_x = \frac{\mu_o A_g N^2 \beta}{4} \left[\frac{(I_b + i_p)^2}{(G - \beta x)^2} - \frac{(I_b - i_p)^2}{(G + \beta x)^2} \right] \quad (3)$$

As mentioned above, permanent magnets can be used to establish the bias flux rather than bias currents. In this case I_b would be replaced by the field strength of the permanent magnets, scaled appropriately.

Maximum Bearing Force Limits

The most immediately apparent limiting behavior of magnetic bearings is that of peak force limitation. This limitation is primarily due to nonlinearity in the magnetization curve of the electromagnet core material. Equation (1) is based on the assumption that the core magnetic flux is simply proportional to the magnetomotive force (MMF: coil turns x coil current). The actual relationship between these two quantities is depicted in the magnetization curve for the core material. Figure 3 shows a typical curve for conventional magnet iron. The significant feature is the leveling of the curve at high MMF's; beyond a certain point, the flux density ceases to increase substantially. This phenomenon is referred to as magnetic saturation and the flux density at which it occurs is the saturation flux density. Typically, this

number ranges between 1.2 and 1.6 Tesla, while some special materials push this limit slightly over 2.0 Tesla. The effect of magnetic saturation is that, once a certain coil current is reached, further increases in current will produce relatively little increase in bearing force.

The peak force which can be developed by a given magnetic bearing is determined in the following manner. The maximum flux in the most restricted cross section of the pole structure is

$$\Phi_p = B_{sat} A_p \tag{4}$$

The maximum flux in each air gap of the magnetic circuit is

$$\Phi_g = \mu_o N I_{sat} A_g / 2G \tag{5}$$

Since these two fluxes must be equal, equations (4) and (5) can be combined to obtain

$$NI_{sat} = 2GB_{sat} A_p / \mu_o A_g \tag{6}$$

Combining equations (6) and (3) by setting $i_p = I_b$, $I_b = \frac{1}{2} I_{sat}$, and $x = 0$ yields

$$F_{max} = \beta B_{sat}^2 A_p^2 / \mu_o A_g \tag{7}$$

It is readily shown that F_{max} is maximized by setting $I_b = \frac{1}{2} I_{sat}$. Throughout the remainder of this paper, it will be assumed that this design rule is followed.

As an example, consider a bearing designed with a pole face area of 10 cm^2 (1.6 in^2), a minimum pole cross sectional area of 7 cm^2 (1.1 in^2), and a geometry factor of 0.93. If the saturation flux density is 1.2 Tesla, equation (7) indicates that the peak force which can be developed is 524 N (118 lb).

Force Slew Rate Limits

The bearing force slew rate is limited because the magnet coils have a high inductance and the power supply to the driving amplifier is at a fixed voltage. For small displacements about $x = 0$, equation (3) can be linearized as

$$F_x = K_i i_p - K_x x \tag{8}$$

where

$$K_i = \mu_o A_g N^2 I_b \beta / G^2 \quad \text{and} \quad K_x = - \mu_o A_g N^2 I_b^2 \beta^2 / G^3 \tag{9}$$

If x is held constant so that we can investigate how rapidly the bearing force can be changed by varying the current then

$$dF_x/dt \,|_{x=0} = K_i \, di_p/dt \tag{10}$$

The voltage across the electromagnet coil is

$$V_c = (I_b + i_p) R_c + L_c di_p/dt \tag{11}$$

If the output stage of the amplifier which drives the coil is described by figure 4, where it is essentially a variable resistance between the coil and ground (the resistance being variable between about 0.5 ohms and nearly infinity), then the fastest possible positive force slew rate is

$$dF_x/dt < K_i \left[V_s - (I_b + i_p)(R_c + 0.5 + R_f) \right] / L_c \qquad (12)$$

For this output stage configuration, the largest negative force slew rate is determined by the reverse breakdown voltage of the output transistor. This limitation is typically larger (in magnitude) than that imposed by equation (12). Similar arguments apply to P-channel or bipolar output devices, push-pull configurations, and pulse-width-modulated amplifiers; the slew rate limitation is inherent in the fixed power supply voltage V_s.

Figure 5 illustrates this effect. The trace shown is of the coil current actually delivered to the bearing coils when the slew rate of the sinusiodal control signal exceeds the maximum slew rate permitted by the power supply voltage (200 VDC) and the coil inductance (0.95 H). Notice that the wave form is distorted only on the ascending portion. Distortion begins in the region where the positive slew rate is greatest, but is more evident as time proceeds because the current error is the time integral of the slew rate error. Once the slew rate limitation sets in, the current simply increases at the rate set by equation (12) until the demanded current and actual current once again coincide. In the case illustrated by figure 5, this occurs slightly after the peak. The descending portion of the waveform is undistorted because the reverse breakdown voltage of the output transistor (900 V) is far in excess of the 200 V power supply.

Slew rate limitation has two effects on the performance of the bearing. First, since it causes the bearing force to change more slowly than the control signal demands, it introduces phase lag. This is shown in figure 6, where the phase shift through the amplifier is plotted as a function of frequency for various power supply voltages. This produces a sudden loss of damping at high amplitudes, which can be catastrophic. The other effect is due to the asymmetry of the distortion relative to the bias level. This effectively reduces the bias current which, in accordance with equation (9), reduces the actuator gain, K_i. The result is a reduction in both stiffness and damping of the bearing.

In order to understand how to design around the force slew rate limitation, equation (12) must be examined with an eye to what the significant design parameters are. The inductance of the magnet coil is defined by

$$L_c = (N\Phi)/I \qquad (13)$$

where I is the coil current required to produce a magnetic flux Φ. Equations (4), (5), (7), and (13) can be used to convert equation (12) to the form:

$$dF_x/dt < \frac{2\beta B_{sat} A_p}{\mu_o A_g N} \left[V_s - (I_b + i_p)(R_c + 0.5 + R_f) \right] \qquad (14)$$

In general, the term $(I_b + i_p)(R_c + 0.5 + R_f)$ is on the order of 5% of V_s. The ratio A_p/A_g should be 1.0 for a thrust bearing ($\beta = 1$) and about 0.99 for radial bearings

($\beta \approx 0.93$). Thus the controlling design parameters are the power supply voltage and the number of coil turns. Requiring a large power supply voltage will degrade the thermal efficiency of the power amplifier which drives the bearing. However, space restrictions and thermal requirements will generally limit the usable number of coil windings. Both parameters must be carefully juggled in order to obtain adequate slew rate capacity.

Displacement Sensitivity

Displacement sensitivity of magnetic bearings is most evident as a softening of the bearing, or reduction of its spring rate, as the shaft approaches the radial clearance. This is a consequence of the nonlinear nature of equation (3). In order to readily describe this behavior, it will be assumed that the bearing has been designed to operate as a simple spring, without damping. To accomplish this, the perturbation current, i_p, is controlled by feedback of the shaft position:

$$i_p = -k_o x \tag{15}$$

The force equation (3) becomes

$$F_x = \frac{\mu_o A_g N^2 \beta}{4} \left[\frac{(I_b - k_o x)^2}{(G - \beta x)^2} - \frac{(I_b + k_o x)^2}{(G + \beta x)^2} \right] \tag{16}$$

The effective spring rate is the negative derivative of the bearing force with respect to deflection:

$$K_{x,cl} \equiv -\partial F_x / \partial x = \frac{\mu_o A_g N^2 \beta}{2} (k_o G - \beta I_b) \left[\frac{I_b - k_o x}{(G - \beta x)^3} + \frac{I_b + k_o x}{(G + \beta x)^3} \right] \tag{17}$$

Equation (17) is more tractable when nondimensionalized. To do this, two bearing characteristics are introduced: the maximum force or load capacity, F_{max}, and the nominal stiffness, K_{nom}. Noting that the nominal stiffness is that where $x = 0$,

$$K_{nom} = \mu_o A_g N^2 B I_b (k_o G - \beta I_b) / G^3 \tag{18}$$

If the bias current is half of the saturation current then the maximum force will be generated when $x = -I_b/k_o$:

$$F_{max} = \mu_o A_g N^2 \beta I_b k_o / (k_o G + \beta I_b)^2 \tag{19}$$

Note that equation (19) will predict a lower maximum force than will equation (7), where the maximum force was found at $x = 0$ and without defining a feedback law. Equations (18) and (19) define a characteristic length of the bearing

$$\delta \equiv F_{max} / K_{nom} \tag{20}$$

If the following nondimensional quantities are defined:

$$\tau \equiv \beta I_b / k_o G \ , \quad r(\tau) \equiv (1+\tau)^2 (1-\tau)/\tau \ , \quad \sigma \equiv x/\delta \ , \quad \kappa \equiv K_{x,cl} / K_{nom} \tag{21}$$

then equation (17) can be nondimensionalized as

$$\kappa = \frac{r^2}{2\gamma}\left[\frac{\gamma r - \sigma}{(r-\sigma)^3} + \frac{\gamma r + \sigma}{(r+\sigma)^3}\right] \tag{22}$$

The definitions of equation (21) lead to a useful expression for the air gap in terms of the characteristic length, δ, and the bearing parameter, γ:

$$G = \beta\delta\ (1+\gamma)^2(1-\gamma)/\gamma \tag{23}$$

Equation (22) is particularly useful because it describes the variation of bearing stiffness in terms of the nondimensional shaft displacement, σ, and the bearing parameter, γ, in such a way that σ and γ are entirely independent. This permits comparison of a wide variety of bearings having the same stiffness and load capacity but different clearances.

Figure 7 illustrates the family of curves defined by equation (22) for $0 \leq \gamma \leq 0.66$, $0 \leq \sigma \leq 1.0$. Stiffness curves for γ = .64, .50, .40, and .10 are shown separately in figure 8. The geometric requirement that $G \geq \delta$ dictates [by equation (23)] that $0 < \gamma < 0.755$. Further, since magnetic saturation sets in for $|\delta| > 1$, equation (22) is not valid for values of δ outside this range. Clearly, the bearing is most linear in the region of $\gamma = 0.5$ and as γ approaches zero. In interpreting these graphs, it is important to recognize that equation (22) implies that, as γ approaches zero, the air gap, G, becomes very large. This means that establishing the required magnetic flux in the air gap will require very high coil currents with the accompanying high I^2R power losses. Leakage flux losses are also accentuated by large air gaps.

To illustrate the use of these equations consider the design of a thrust bearing ($\beta = 1.0$) which is to have a nominal stiffness of 2×10^6 N/m (1.1×10^4 lb/in) and a load capacity of 500 N (112 lb). The characteristic length, δ, is 0.25 mm (0.010 in). If a bearing parameter, γ, of 0.5 is selected for high linearity and low I^2R losses, then the air gap would be [from equation (23)] 0.56 mm (0.022 in). At a rotor displacement of 0.20 mm (0.008 in), equation (22) predicts that the stiffness would be 88% of the nominal stiffness, or 1.8×10^6 N/m (9700 lb/in). At 0.25 mm, this figure would decrease to 64%.

Estimating Dynamic Requirements

The preceding discussion illustrates the importance of staying within the performance bounds of the magnetic bearing. Exceeding the peak force or slew rate limitations can introduce a sudden drop in bearing stiffness and damping. The resulting dynamic behavior can be disastrous. If the bearing is designed to minimize its displacement sensitivity, then it may be permissible to neglect this additional nonlinearity, especially if the design load capacity is somewhat greater than the actual dynamic requirement of the bearing. For any of these considerations, a careful assessment must be made of the actual forces that the bearing will be asked to deliver.

In estimating the dynamic requirements of a magnetic bearing, the designer may initially incline to set them equal to the worst dynamic characteristics of the anticipated loads. However, this is unrealistic and commonly demands far more performance of the bearing than is needed. In the following, two types of loads are discussed: step and sinusoidal. For the sake of simplicity, it will be assumed that the system being supported by the bearing is a simple mass. This assumption permits some fairly

general conclusions to be reached concerning slew rate and peak force requirements which will provide useful first pass design information and, more importantly, will help develop a sense of where these requirements come from. More exact estimates of the dynamic requirements placed on the bearing require detailed knowledge of the supported structure and the control algorithm.

Assume that a rigid body of mass m is supported by a control force, F_c. Because of geometric restrictions, the body cannot be permitted to move more than a distance x_o from its unloaded position. If a step force of F_s is applied to this body, then its time trajectory is described by

$$m\, d^2x/dt^2 = F_c - F_s \quad : \quad x(0) = x_o,\ dx/dt(0) = 0 \tag{24}$$

If, further, the control force is assumed to be initially zero and then changes at a fixed slew rate of f: $F_c = ft$, then equation (22) can be solved as

$$x = ft^3/6m - F_s t^2/2m + x_o,\ t \geq 0 \tag{25}$$

The body will collide with the geometric constraint if $x = 0$ for some $t > 0$. It can readily be shown that equation (25) has no positive real roots in t if

$$f > (2F_s^3/3mx_o)^{1/2} \tag{26}$$

For such a simple control scheme (essentially the integral of bang-bang), the peak force required of the controller is twice the applied load. If the force slew rate were unrestricted, then the peak force need be only slightly greater than F_s.

As an example, consider a body having a mass of 0.5 Kg (1.1 lbm). If the largest allowable excursion from its undisturbed position is 0.5 mm (0.020") and a step load of 100 N (22.5 lb) is applied, then a force slew rate of at least 52,000 N/sec (11,600 lb/sec) is required to prevent a collision. Figure 9 shows the time response of this system. The control algorithm used in this simulation consisted of delivering a constant force slew rate of ±52,000 N/sec or zero.

When the same system is excited by a sinusoidal force at frequency ω, then the analysis is even simpler. The best control force will obviously be sinusoidal, 180° out of phase with the load. The time response of the system is

$$x = (F_c - F_s)/(m\omega^2)\ \sin\omega t \tag{27}$$

The restriction that $|x| < x_o$ implies that

$$F_s - x_o m\omega^2 < F_c < F_s + x_o m\omega^2 \tag{28}$$

For a sinusoidal control force, the peak force slew rate is simply ω times the peak force:

$$\omega F_s - x_o m\omega^3 < f < \omega F_s + x_o m\omega^3 \tag{29}$$

If the same mass as in the preceding example were acted upon by a force of constant amplitude 50 N (11.2 lb) but over a frequency range of 100 rad/sec to 1000 rad/sec (955 RPM to 9550 RPM) then the control force actuator would have to be capable of delivering a force as large as 47.5 N (10.7 lb). The maximum required slew rate would occur at

$$\partial(\omega F_s - x_o m\omega^3)/\partial\omega = 0 \Rightarrow \omega = 258.2 \text{ rad/sec}$$

Thus, the actuator must be able to provide a slew rate of 8,607 N/sec (1,934 lb/sec).

Conclusion

This paper has treated three forms of nonideal behavior found in magnetic bearings. These include peak force limitation due to magnetic saturation, force slew rate limits due to magnet coil inductance and finite power supply voltages, and displacement sensitivity due to the nonlinear dependence of the bearing force on rotor position. The mechanisms which give rise to these limitations have been explored in some detail with the purpose of developing several relatively simple equations which can be employed in the design process.

As a complement and, perhaps, to motivate this interest in bearing limitations, a very simple discussion was given of the minimum dynamic requirements made on a bearing by a sinusoidally or step excited mass. The intent here was twofold. First, it was desired to demonstrate that the dynamic requirements do not necesarily match the characteristics of the external loads. Second, this simple analysis provides some useful guidelines for estimating the requirements of actual systems.

When working with a mechanism as readily tailored as a magnetic bearing, it is easy to lose sight of its limitations. These devices present the engineer with a solution to a vast range of difficult bearing problems, but if misapplied, their performance can be very disappointing. Hopefully, this investigation will help provide methods for ensuring that magnetic bearing designs will perform as intended.

References

1. Britcher, C.P. "Progress Toward Magnetic Suspension and Balance Systems for Large Wind Tunnels". Journal of Aircraft, Vol. 22, No. 4, April 1985.
2. Sarma, M.S. and Yamamura, A. "Nonlinear Analysis of Magnetic Bearings for Space Technology". IEEE Trans. on Aero. and Elec. Systems, Vol. AES-15, No. 1, Jan. 1979.
3. Hebbale, K.V. "A Theoretical Model for the Study of Nonlinear Dynamics of Magnetic Bearings", Masters Thesis, Cornell University, Jan. 1985.
4. Kral, K.D. and Havenhill, D.D. "Magnetic Suspension and Pointing System with Flux Feedback Linearization", U. S. Patent number 4,642,501; Feb. 10, 1987.
5. Bleuler, H. "Decentralized Control of Magnetic Rotor Bearing Systems", Ph.D. Dissertation, Swiss Federal Institute of Technology, ETH report number 7573, 1984.
6. Allaire, P.E., Humphris, R.R., and Kelm, R.D. "Magnetic Bearings for Vibration Reduction and Failure Prevention". Proceedings of the 45th Meeting of the Mechanical Failure Prevention Group, April 16-18, 1985, NBS, Gaithersburg, MD.

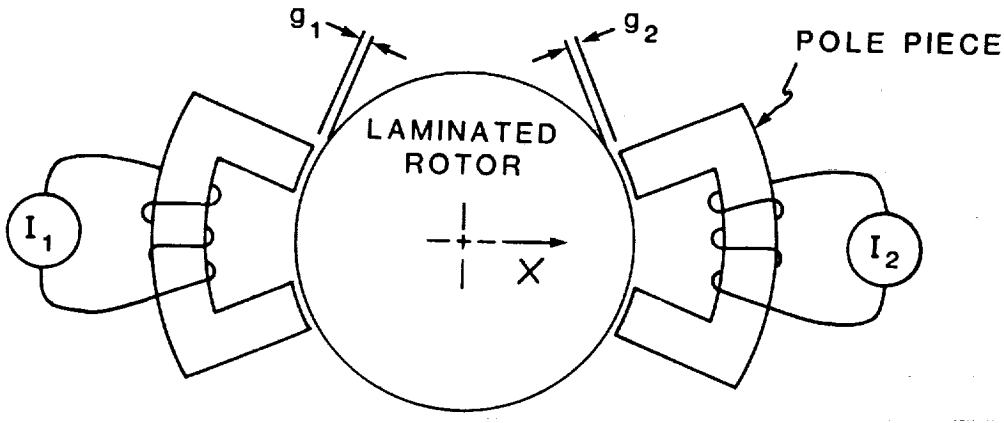

FIGURE 1. BEARING SCHEMATIC

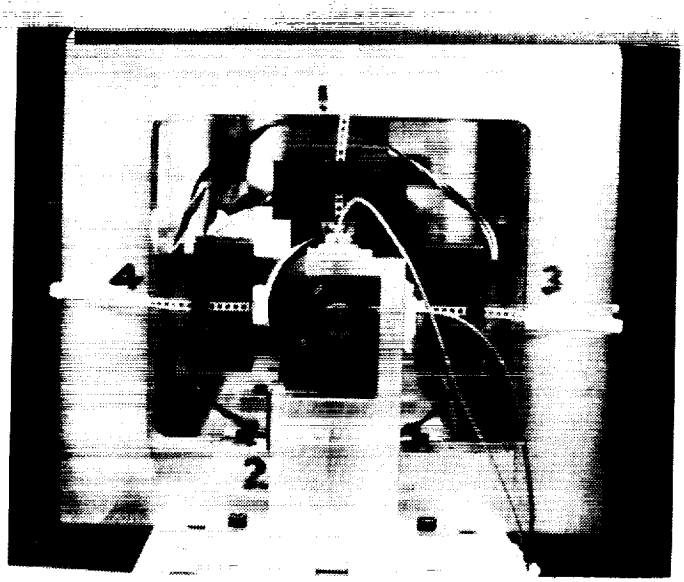

FIGURE 2. LABORATORY BEARING (ROMAC)

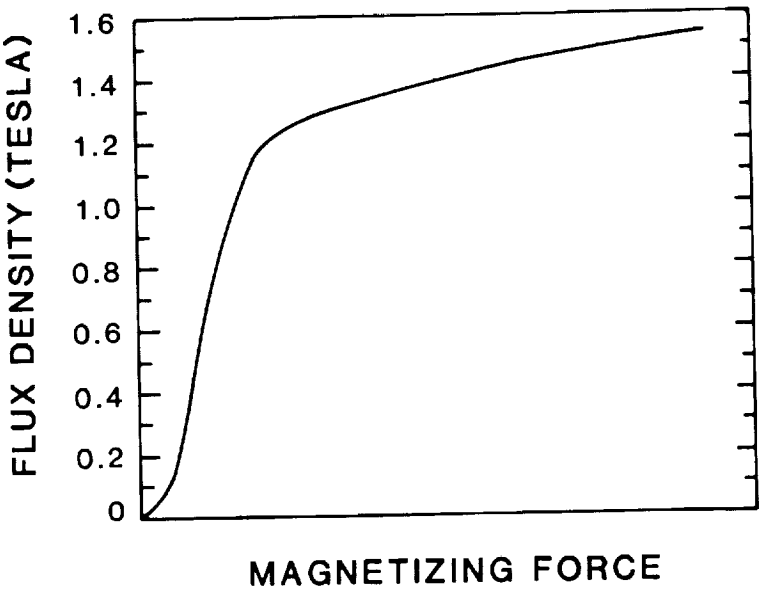

FIGURE 3. MAGNETIZATION CURVE

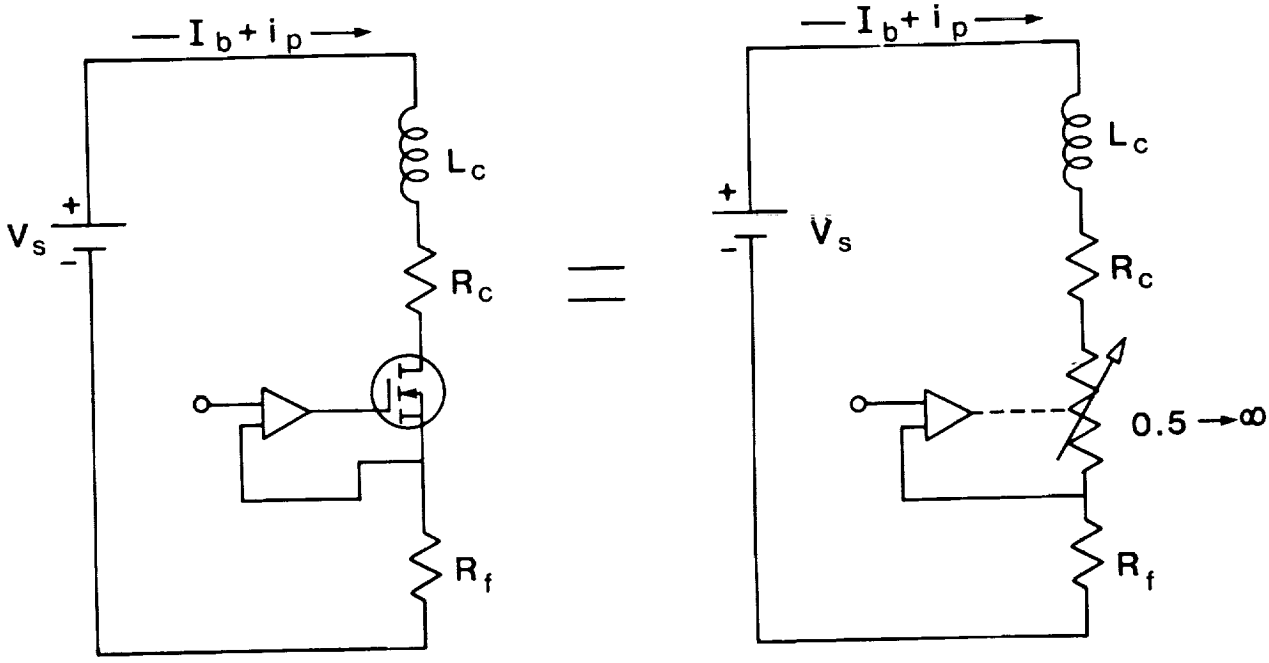

FIGURE 4. SIMPLIFIED AMPLIFIER SCHEMATIC

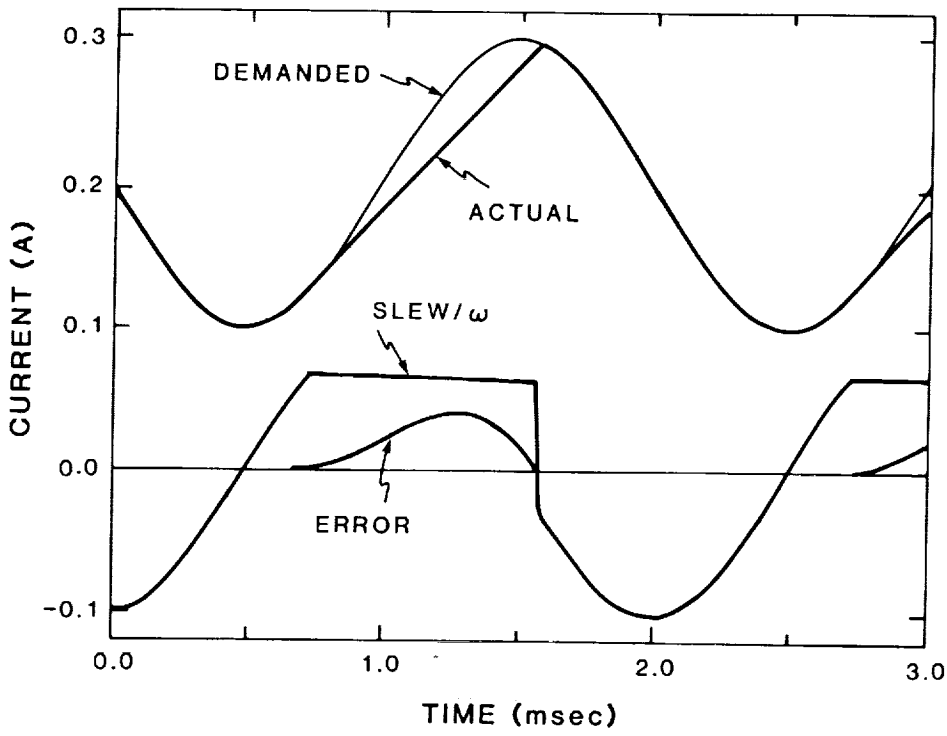

FIGURE 5. CURRENT DISTORTION DUE TO SLEW RATE LIMITATION

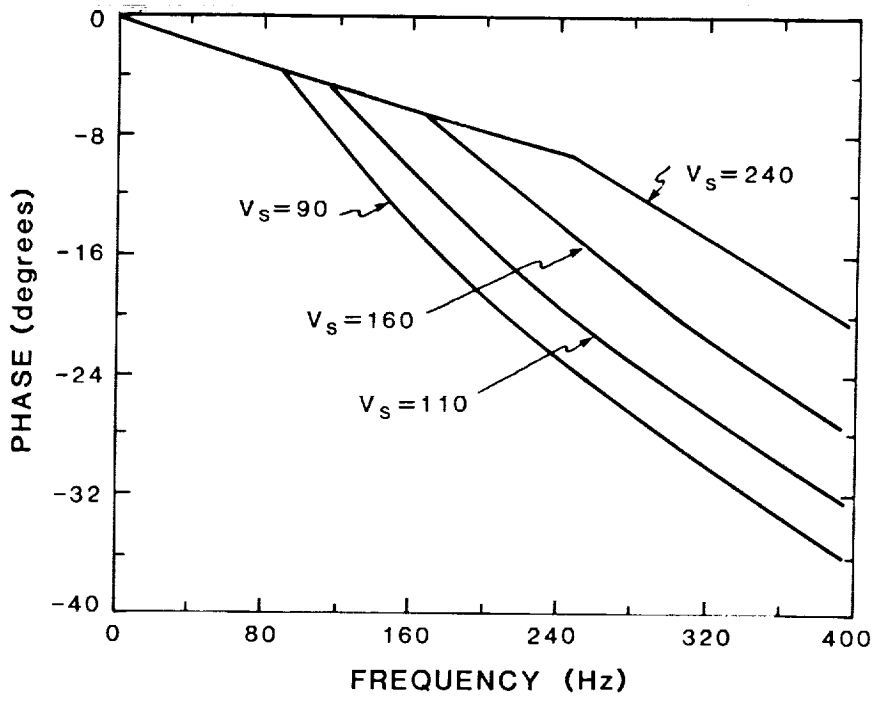

FIGURE 6. PHASE SHIFT: CONTROL SIGNAL TO COIL CURRENT

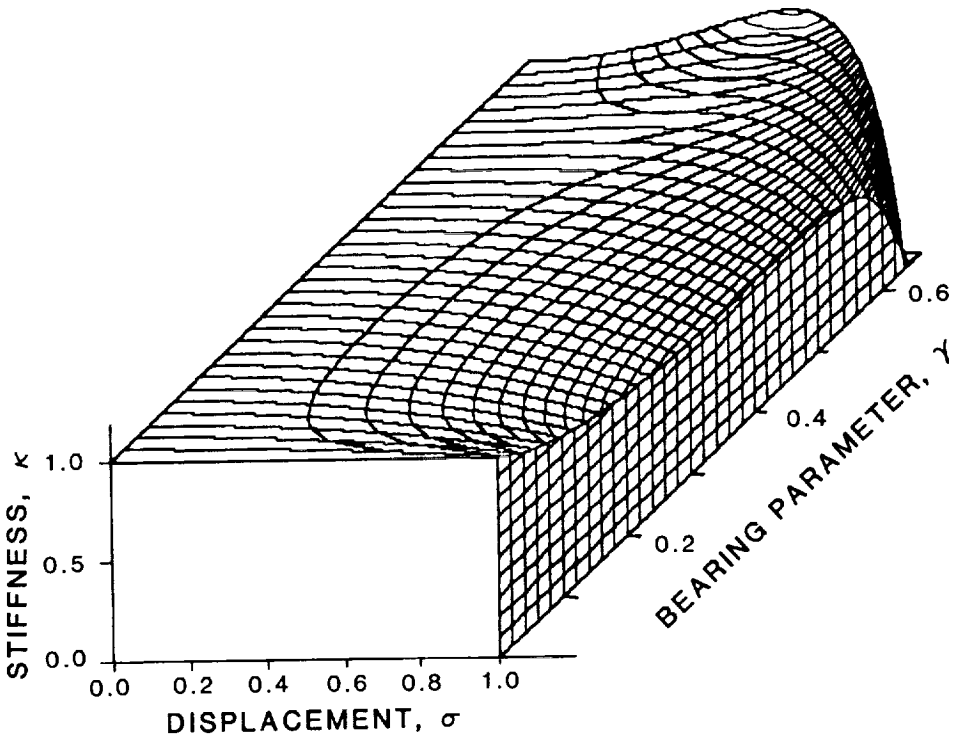

FIGURE 7. DISPLACEMENT SENSITIVITY

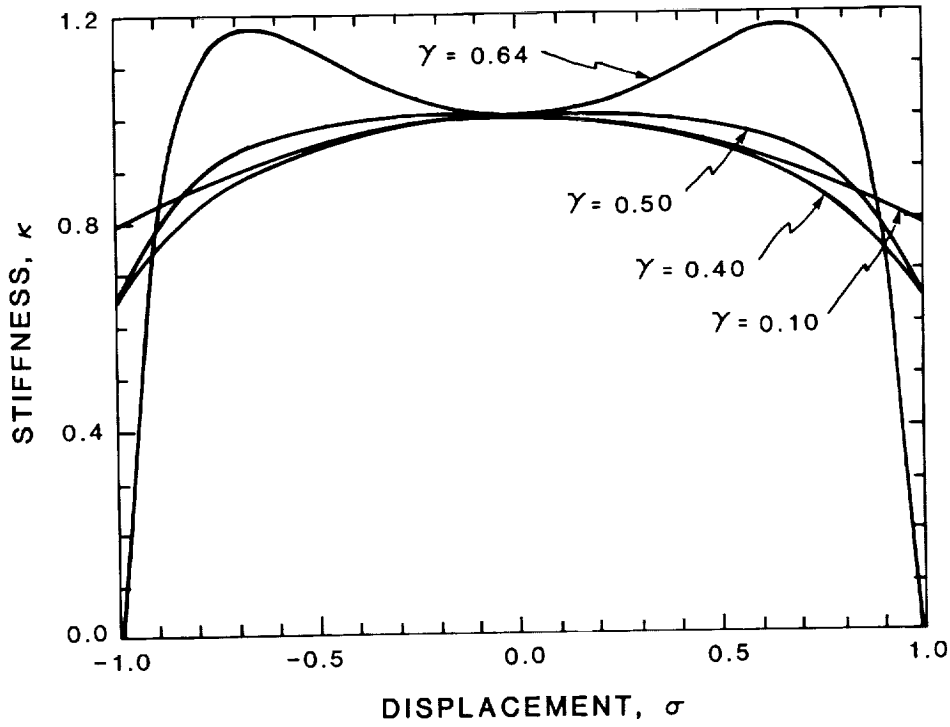

FIGURE 8. DISPLACEMENT SENSITIVITY

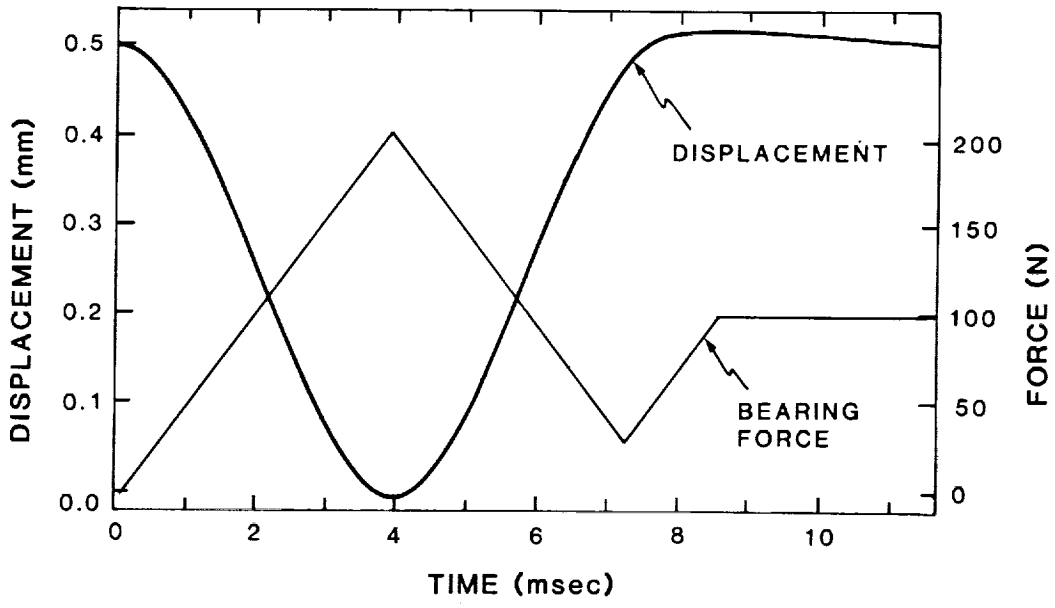

FIGURE 9. SLEW RATE LIMITED CONTROL: STEP RESPONSE

omit

Advanced Actuators for the Control of Large Space Structures

James Downer, Richard Hockney, Bruce Johnson, Kathleen Misovec

SatCon Technology Corporation

S/B-18

N93-27572

ADVANCED ACTUATORS FOR THE CONTROL OF LARGE SPACE STRUCTURES[1]

James Downer, Richard Hockney, Bruce Johnson, Kathleen Misovec

SatCon Technology Corporation
71 Rogers St.
Cambridge, MA

ABSTRACT

The objective of this research was to develop advanced six-degree-of-freedom actuators employing magnetic suspensions suitable for the control of structural vibrations in large space structures. The advanced actuators consist of a magnetically suspended mass that has three-degrees-of-freedom in both translation and rotation. The most promising of these actuators featured a rotating suspended mass providing structural control torques in a manner similar to a control moment gyro (CMG). These actuators employ large-angle-magnetic suspensions that allow gimballing of the suspended mass without mechanical gimbals. Design definitions and sizing algorithms for these CMG type as well as angular reaction mass actuators based on multi-degree-of-freedom magnetic suspensions were developed. The performance of these actuators was analytically compared with conventional reaction mass actuators for a simple space structure model.

INTRODUCTION

New spacecraft designs feature large structures characterized by low natural frequencies, lightly damped structural modes, and stringent pointing and vibration performance requirements. These large space structures (LSS) pose unique and difficult control problems. An important part of the solutions to these control problems in the development of actuators that allow the application of force and/or torque to the space structure.

The purpose of this research is to develop multi-directional actuators which employ magnetic suspensions and to assess their performance compared to conventional actuators. A baseline conventional linear reaction mass actuator is used in conjunction with a flexible structure model to size and evaluate the advanced actuators. The most promising actuator designs feature a rotating suspended mass providing control torques in a manner similar to a control moment gyro. Two small-stroke actuators were designed, one with a composite flywheel and the other with a steel flywheel. Several large-stroke actuators were designed which included both attraction force and Lorentz force designs. In addition, a large stroke actuator was designed which employs a superconducting coil.

The major advantages of these advanced actuators include high bandwidth compared to conventional CMG's and large momentum storage

1 This work was performed under NASA grant NAS1-18426

capability, low mechanical noise, and multi-degree-of-freedom actuation compared to conventional linear reaction mass actuators. The combination of high bandwidth and large momentum storage allow these advanced actuators to be used in applications such as space robotic arms that have both slewing and vibration requirements. Because of their six-degree-of-freedom actuation characteristics, these advanced actuators were shown to be capable of replacing numerous linear reaction mass actuators.

LARGE SPACE STRUCTURE MODEL

Because a beam can be an appropriate simplified model for many different types of flexible structures, such as a robotic arm or a deployable truss structure, actuator performance was evaluated in conjunction with a finite element cantilevered beam model.

A beam of length 60 m with a lowest natural bending frequency of 1.15 rad/sec (0.184 Hz) was chosen for this analysis. A 247 kg mass with a moment of inertia of 20 kg m^2 was situated at the tip of this model (Misovec, 1987). Figure 1 is a plot of the first four mode shapes. The lowest mode in this plot has a large transverse deflection at the tip. As the excitation frequencies get higher, more energy is required to move the large tip mass, and the tip increasingly behaves like a pinned end.

Table 1. Lowest Four Natural Frequencies of 35 Element Model.

0.184 Hz
1.83 Hz
5.7 Hz
11.7 Hz

ACTUATOR SIZING AND PLACEMENT

Baseline Conventional Actuator

The SatCon actuators were sized to give comparable performance to that of a conventional linear reaction mass actuator. These conventional actuators produce control forces by accelerating the actuator mass. The conventional actuator is capable of producing forces in only one direction. The magnitude of the actuator force is limited by how fast the mass can be accelerated and by how far the mass is allowed to travel (the stroke).

The conventional actuator that will be used to size SatCon actuators has the characteristics listed in Table 2 (Davis, 1986). It is capable of producing a maximum of 30 N of force with an 11 kg reaction mass. The maximum stroke is 15 cm (7.5 cm in each direction). This stroke has a limiting effect on the force for excitation frequencies less 1 Hz. For the beam considered in this paper, only the forces produced to control the lowest mode are reduced because of stroke limitations. The maximum force production in this mode is 1.1 N. SatCon torque actuators were designed for equivalent performance with a force actuator which can produce 1.1 N to control a mode 1 excitation and 30 N of force for all the other excitation

modes.

Table 2. Conventional Actuator Characteristics.

Maximum Force Capability	=	30 N
Maximum Stroke	=	15 cm
Reaction Mass	=	11 Kg
Total Mass per Direction	=	20 Kg

Actuator Sizing Issues

Actuator Torque Sizing

Because the advanced actuators are capable of both force and torque production while the baseline conventional actuator is only capable of force production, a sizing relationship between force actuation and torque actuation was developed. Assuming that torque and force actuators act as dampers and remove equal amounts of power from a vibrating structure, an expression relating torque capability and force capability can be established (Misovec,1987):

$$\frac{\tau}{F} = \frac{x_{max}}{\theta_{max}} = l_b \qquad (1)$$

x_{max} = Maximum Transverse Displacement for a Given Mode
θ_{max} = Maximum Rotational Displacement for a Given Mode
l_b = Beam Lever Arm

The relationship between torque and force will be referred to in this paper as the beam "lever arm". The required torque for an advanced actuator is the beam lever arm times the force used by the conventional actuator. An implicit assumption in the use of the beam lever arm is that each type of actuator is situated such that it removes the maximum possible amount of power from the vibrating beam. A force actuator is optimally located at the point of maximum transverse displacement, while a torque actuator is optimally located at the point of maximum rotation (Misovec, 1987). For example while the tip is a good location for force control of a mode 1 excitation, it is not a good location for control of a mode 2 excitation. These findings were verified by simulation (Misovec,1987). An effective force actuation scheme would require a number of actuators strategically placed along the beam. Analysis showed that a torque actuation scheme, on the other hand, would require only one torque actuator located at the tip (Misovec, 1987). Thus for this particular application, a torque actuation scheme has potential advantages over a conventional actuation scheme because it would require fewer actuators.

The beam lever arm is a strong function of mode. This is shown in Figure 2(a). This plot shows that at lower frequencies the torques that are required to give the same performance as conventional force actuators can be quite high (40 times the required force). By taking into account that at frequencies less 1 Hz, the force of the conventional actuators used for comparison is limited by stroke, the

'effective' lever arm is reduced. Figure 2(b) is a plot which shows the effect of limited stroke. Because the lowest frequency mode is the only mode with a frequency less than 1 Hz, limited stroke effectively reduces the beam lever arm for this mode.

As an estimate, 10 m will be used as a baseline effective beam lever arm. By multiplying this value by the maximum force capability of the conventional actuator (30 N see Table 2), SatCon actuators were designed to have a torque capability of approximately 300 N-m.

Actuator Stroke Sizing

Using the beam lever arm concept, a reaction mass torque actuator was sized for compatible performance with the baseline conventional reaction mass force actuator. The result of this analysis indicated that the required moment of inertia for the actuator would be unreasonably large for application to the beam model (Misovec,1987).

A CMG type actuator can be sized by considering Newton's Law which relates angular momentum (H), torque (τ), frequency (w) and angular stroke, (θ_s).

$$H = \tau / w \theta_s \qquad (2)$$

Because the actuator will be sized to give the same performance as the conventional actuators described previously, the torque used in this calculation is the force capability of the conventional actuator multiplied by the effective beam lever arm, which is a frequency dependent quantity. Thus, the required angular momentum is not a simple function of frequency. The required angular momentum is plotted versus angular stroke for the first three modes in Figure 3. A control moment gyro has large momentum storage capacities, and these values of angular momentum are reasonable. This plot was used to find the specifications for a small stroke and a large stroke actuator.

ACTUATOR CONCEPT SELECTION

Two baseline CMG type actuator designs were identified for comparison. One is a small stroke, high angular momentum design, and the other is a large stroke, low angular momentum design. The characteristics of these designs are presented below.

Table 3. Actuator Requirements

	STROKE	
	SMALL	LARGE
TORQUE (Nm)	300	300
MOMENTUM (Nms)	4000	400
STROKE		
(radians)	0.015	0.15
(degrees)	0.9	9

For the small stroke actuator, the air gap of the magnetic bearing (the clearance between the rotor and the stator) allows a sufficient angular stroke. Several small-stroke, magnetically-gimballed actuator

designs [Anderson, 1975; Sindlinger, 1977; Murakami, 1982] with gimbal angles up to about 2 degrees have been reported. For applications which require a larger stroke (greater than about 3 degrees), the length of the air gap which would be required causes the magnetic bearing design to be inefficient. The power required to establish the air-gap magnetic field is proportional to the square of the air-gap length. In addition, as the length of the air gap increases relative to other dimensions of the magnetic bearing, the amount of leakage flux also increases. Leakage flux is that flux which does not link the rotor and stator. It therefore does not contribute to the amount of force which is applied to the rotor and may even reduce it.

The large stroke actuator can be designed using a large-angle magnetic suspension (LAMS). A LAMS is a five-axes, actively-controlled magnetic bearing which is designed to accommodate relatively large angular motion of the rotor without an excessively long air gap. Actuation in the sixth degree of freedom can be provided by allowing the LAMS motor/generator to have gimballing capability.

Small-stroke Actuator

Flywheel.

Table 4 presents the characteristics for flywheels for the small-stroke actuator. A graphite/epoxy flywheel is compared to a high-strength steel flywheel. The mass of the composite flywheel is smaller than that of the steel flywheel by a factor of two and a half. The lower rotational speed of the steel flywheel results from its higher mass density. The advantage of the steel flywheel is that it may act as a portion of the magnetic circuit for the magnetic bearing.

Table 4. Flywheels for the Small-stroke Actuator

	COMPOSITE	STEEL
ASPECT RATIO	0.50	0.60
DIMENSIONS (cm)		
INNER DIAMETER	70	106
OUTER DIAMETER	35	64
AXIAL LENGTH	4	1.1
MASS (kg)	20	50
SPEED (krpm)	25	4

Small-gap Magnetic Bearings.

Figures 4(a) and 4(b) show the arrangement of eight magnets for flywheels which are either relatively large in diameter (an axial-air-gap magnetic bearing) or long (a radial-air-gap magnetic bearing). The figure also shows the lever arm (l) which relates bearing force (f) and torque (τ).

$$\tau = f \cdot l \tag{3}$$

A single expression relating the angular stroke (δ_{max}) to the air-

gap length (G) can be written.

$$G = \frac{1}{2} \sin(\delta_{max}) \tag{4}$$

This equation is used to determine the air-gap length from the dimensions of the flywheel and the angular stroke requirement. The horseshoe-shaped core and coil which are shown in Figures 5(a) and 5(b) respectively were used to approximate the performance of a single magnetic bearing element [Anderson, 1975]. The design procedure is summarized here; more detail may be found in Misovec, 1987.

The air-gap area (A_g) is related to the force by the magnetic pressure (p_m). The magnetic pressure is determined from the flux density in the air gap (B_g).

$$f = p_m \cdot A_g \tag{5}$$

$$p_m = \frac{(B_g)^2}{2 \cdot \mu_o} \tag{6}$$

Magnetic pressure is typically low. For an air-gap flux density of 1 Tesla, the pressure is approximately 400 kPa (58 psi).

The magnet design procedure (Figure 5) is to give the core of the magnet a constant cross section which is equal to the area of the air gap. The poles of the magnetic core are assumed to have a length which is equal to that of the section thickness. The coil completely fills the available space. The volumes of iron and copper used for each magnetic bearing can be determined from these dimensions. Given the mass densities of the core material and the windings, the mass of each bearing is found by adding masses of these components. The total bearing mass is that of twelve bearing elements. The assumption is that eight bearing elements are required for torquing and an additional four are required to provide either radial or axial forces.

The current density (J) in the coil which is required to produce the air-gap magnetic field is determined from Ampere's law.

$$J \frac{A_g}{2} = \frac{2 B_g G}{\mu_o} \tag{7}$$

The power consumed by each bearing during torquing and the total power consumed by the bearing system (P_b and P_t) are then determined from the current density, the volume of a bearing coil (V_c), and the conductivity of the material (σ).

$$P_b = \frac{J^2 V_c}{\sigma} \tag{8}$$

$$P_t = 4\ P_b \qquad (9)$$

Table 5 contains the performance data for magnetic bearing elements for use with the flywheels from Table 4. A baseline power consumption during torquing of 100 W was assumed.

Table 5. Magnetic Bearings for the Small-stroke Actuator

	COMPOSITE	STEEL
FLUX DENSITY (T)	1.0	0.6
AIR-GAP LENGTH (cm)	4.0	0.6
CURRENT DENSITY (MA/m^2)	4.4	3.4
BEARING ELEMENT MASS (kg)	2.2	3.5
TOTAL BEARING MASS (kg)	26.4	42.0

Small-stroke Actuator Summary.

Table 6 summarizes the performance of the two alternatives which were considered for the small-stroke actuator. Although the mass of the actuator which employs a steel flywheel is twice that of one which employs a graphite/epoxy flywheel, this might be a viable candidate for a laboratory-scale demonstration. The advantage of the steel flywheel is that it may act as part of the magnetic circuit for the bearing.

Table 6. Small-stroke Actuator Performance

FLYWHEEL TYPE	Gr/ep	STEEL
MASSES (kg)		
FLYWHEEL	20	50
BEARING SYSTEM	26	42
	--	--
TOTAL	46	92
POWER (W)	100	100

Large-stroke Actuator

Several types of actuators using large angle magnetic suspensions (LAMS) were examined. The conventional technology LAMS studied for this actuator application include two types of attraction force LAMS as well as a Lorentz force LAMS. In addition, a LAMS using superconducting technology was also studied.

Conventional-technology LAMS.

Flywheel.

The angular momentum storage capacity which is required for the large-stroke actuator is one tenth that of the small-stroke actuator. For both of the conventional technology LAMS concepts which are considered in this analysis, the rotating magnetic components will

C-4

store sufficient angular momentum for this actuator.

Conventional LAMS Torque Actuation Requirements

In addition to free rotation about the spin axis (SA), a LAMS provides controlled (but limited) angular motion about each of the orthogonal lateral axes. A reference frame based on the spherical coordinates shown in Figure 6 is employed for analysis.

A LAMS be analyzed in terms of forces that are spherically radial (f_R), azimuthal (f_α), elevational (f_β), or some combination of these as is shown in Figure 6. At the k^{th} point of force application, which is located at position (R_k,α_k,β_k), the net torque resolved in orthogonal coordinates is as follows.

$$\begin{aligned} \tau_k = {} & R_k(-f_{\alpha k}\cos\alpha_k\sin\beta_k + f_{\beta k}\sin\alpha_k)\, u_x \\ & - R_k(f_{\alpha k}\sin\alpha_k\sin\beta_k + f_{\beta k}\cos\alpha_k)\, u_y \\ & + R_k f_{\alpha k}\cos\beta_k\, u_z \end{aligned} \tag{10}$$

To meet the control torque requirements, the forces at each of N_1 points must satisfy the following.

$$\tau_x = \sum_{k=1}^{N_1} R_k(-f_{\alpha k}\cos\alpha_k\sin\beta_k + f_{\beta k}\sin\alpha_k) \tag{11}$$

$$\tau_y = \sum_{k=1}^{N_1} -R_k(f_{\alpha k}\sin\alpha_k\sin\beta_k + f_{\beta k}\cos\alpha_k) \tag{12}$$

$$0 = \sum_{k=1}^{N_1} R_k f_{\alpha k}\cos\beta_k \tag{13}$$

Equation (13) precludes first order interaction between the LAMS and the drive. Similar equations can be derived for LAMS actuation forces [Downer, 1986].

Examination of Equations (11) through (13) provides some insights into possible ways to design a LAMS. The simplest way to satisfy the "no-SA-torque" requirement (Equation (13)) is to not employ forces that act in the azimuthal direction ($f_{\alpha k} = 0$, for all k). With this constraint satisfied, it becomes clear that, for torquing, elevational forces alone will be a satisfactory configuration. The following two sections illustrate how elevational forces and thus control torques can be obtained in the LAMS systems analyzed in this study.

Attraction Force LAMS Designs

In order to use an attraction-force magnetic bearing in a large-angle configuration, the attractive surfaces on the rotor and stator are shaped to approximate concentric spheres. Figure 7 shows the forces exerted by one pole of an attraction-force LAMS that employs both primary and secondary attraction forces. The primary force acts in a direction that is spherically radial, while the secondary force

acts in the elevational direction. If the nominal air-gap length (G_o) is small in comparison to other dimensions, the forces may be approximated by assuming that the interacting surfaces are nearly parallel flat plates. The elevational attraction-force is readily evaluated for a spherical geometry.

$$f_{\beta k} = c_{a\beta} B_{gk}^2 \tag{14}$$

where $c_{a\beta}$ is a geometrical constant and B_{gk} is the flux density in air gap.

The components of the torque vector that is applied to the rotor by the k^{th} pole are found by substituting Equation (14) into Equations (11) and (12).

$$\tau_{xk} = R_o c_{a\beta} \sin\alpha_k B_{gk}^2 \tag{15}$$

$$\tau_{yk} = R_o c_{a\beta} \cos\alpha_k B_{gk}^2 \tag{16}$$

where R_o is the nominal spherical radius.

The two attraction-force LAMS designs are biased electro-magnets. Both employ two wound, four-pole disks on the stator. A magnetic field is maintained in the air gap when no mechanical load is present. The LAMS designs, however, differ in the manner through which the magnetic field is produced. The LAMS design which is shown in Figure 8(a) employs a heteropolar field maintained by current in control coils wound on salient poles. The second design alternative (Figure 8(b)) utilizes a permanent magnet to produce a homopolar bias field. The permanent magnet is shown as a part of the rotor, but it could also be incorporated in the stator structure if stresses due to rotation are a concern. A more complete description may be found in Downer, 1986.

Lorentz Force LAMS Designs

The Lorentz-force LAMS design (Figure 9(a)) consists of two identical magnetic structures each containing a rotor and a stator. Each rotor contains an axially-oriented, permanent magnet and sufficient core material to yield an approximately spherically-radial magnetic field in the air gap.

$$B = B_g u_R \tag{17}$$

Each stator consists of a thin shell containing four control coils as is shown in Figure 9(b). The figure also shows the direction for positive current.

The elevational force density vector at a point (R_k, α_k, β_k) within the k^{th} coil is the cross product of the coil current and flux density vectors.

$$\rho_{fk} = J_k \times B = B_g J_{\alpha k} u_\beta \tag{18}$$

The net elevational force (f_k) exerted on the rotor by the k^{th} coil is found by integrating the negative of the force density over the fraction of the active region which contains wire.

The net torque vector (τ_k) and its Cartesian components (τ_{Xk}, τ_{Yk}) are found by integrating the moment of the force density over the active region. The complete analysis may be found in Downer, 1986.

Comparison of Conventional LAMS

Figure 10(a) shows that, for a fixed range of LAMS mass, the power consumption of a Lorentz-force LAMS is lower than that of either of the attraction-force suspensions. The power consumption of a heteropolar, attraction-force LAMS is nearly four times that of a PM-field, Lorentz-force LAMS with the same mass. The power consumption of a homopolar LAMS is 30-50% higher than for a Lorentz-force LAMS (Downer, 1986).

Figure 10(b) shows the increased mass of the two attraction-force LAMS design options over the Lorentz-force LAMS for a range of control-torque power consumption. For power consumption that is equal to that of a Lorentz-force LAMS, a heteropolar LAMS must have a mass that is between two and a half and three times that of the Lorentz-force LAMS. The mass of a homopolar LAMS is not as great; in the range of 25-50% more than that of a Lorentz-force LAMS with equal power consumption (Downer, 1986). A baseline Lorentz force LAMS actuator for this application would mass 100 kg and require 400 W of power.

Superconducting LAMS.

The superconducting LAMS, as its name suggests, employs a superconducting coil for the elimination of all conventional magnetic structures in order to produce an energy-efficient, light-weight design. Figure 11 is a partially cut-away view which shows the rotating components (superconducting coil and flywheel) and cryogenic housing of a two-degree-of-freedom CMG which employs a superconducting LAMS. The superconducting coil is a solenoid which operates in persistent-current mode (without an electrical input). The current in the solenoid persists because of the lack of resistance in the superconducting material. The spherical case which surrounds the rotating components also serves as the cryostat for the superconducting solenoid.

A high-strength graphite/epoxy composite flywheel is attached to the solenoid to provide angular momentum storage capacity. The outer diameter of the flywheel is machined to a spherical shape. This allows the flywheel to be completely gimballed without contact with the case.

The normal coils shown in Figure 12 are used to apply torques to the flywheel. The figure illustrates the torquing mechanism. Assuming that the spin axis is along the z-axis, the magnetic field (B), produced by the superconducting solenoid at the location of the torquing coils is approximately parallel to the z-axis and constant. The torque (τ) results from the interaction of the dipole moment (μ) produced by the current (I) in the normal coil and the magnetic field.

In order to estimate the performance of a superconducting LAMS, a

set of scaling laws have been developed to scale from the a 34,000 Nm design to a 300 Nm design appropriate for flexible structure control of the beam model (Misovec,1987). Table 7 presents the results obtained by scaling the performance of the high-torque LAMS described in Downer (1987) to a size appropriate to the present application. Eight additional normal coils are used in order to apply radial and axial forces on the rotor. Each of the other eight coils required for the LAMS is assumed to have a mass which is equal to that of a torquing coil.

Table 7. Performance of Superconducting LAMS

	CURRENT APPLICATION
TORQUE (Nm)	300
ANG. MOM. (Nms)	400
MASSES (kg)	
SOLENOID	33
TORQUE COILS (4)	16
OTHER COILS (8)	32
TOTAL	81
POWER (W)	380

There is room for optimization of the design to reduce the power consumption of the torquing coils at the expense of added coil mass.

Comparison of Actuator Designs

Both conventional-technology and superconducting LAMS were also shown to be feasible for flexible structure control although the mass of the LAMS designs are higher than the mass of the small stroke designs. For future large space structure actuator development, the LAMS is preferred over the small stroke approach because of its larger momentum transfer capability. The added momentum transfer allows the large stroke actuator to be used in a variety of systems applications where high frequency control of flexible structure vibrations combined with significant low frequency momentum storage for slewing or attitude control are required.

Although the superconducting LAMS is 20% lower in mass than the conventional LAMS, this difference is not significant as there is room for optimization in both designs. The difference becomes less significant as the torque capability of the actuator is reduced. A superconducting LAMS may be the best choice actuator for specific applications where high torques are required. In addition, the superconducting LAMS is a high risk development project. On the other hand, for a modest development cost, the conventional-technology LAMS actuator can have a wider range of applications.

Thus a conventional-technology LAMS, either attraction force or Lorentz force is recommended for further development for flexible structure control.

CONTROLLER DESIGN

The closed-loop performance of both the conventional and advanced actuators were analytically obtained on the baseline flexible beam model using full-state, linear-quadratic-optimal feedback. These closed-loop simulations were primarily used to validate the open-loop comparison of actuator force versus torque control effectiveness. The controller designs were done using linear quadratic design tools (Kwakernaak and Sivan, 1972), which are based on the minimization of a quadratic cost functional.

The force/torque tradeoff derived previously is verified here by simulations of a beam vibrating in mode 1. A controller, which used tip force actuation was designed to give a peak control force level of 1.1 N; this is the stroke-limited level of force of the conventional actuator. Then the level of damping for this mode was computed. Then a controller, using tip torque actuation, was designed to give the same level of damping performance. The peak force should be the beam lever arm for mode 1 (40 m) multiplied by 1.1 N (or equivalently, the effective beam lever arm multiplied by 30 N). Figure 13 shows the results of this analysis. The peak torque which must be used to achieve the same performance as the force actuator is approximately 45 Nm. These plots indicate that the beam lever arm concept was verified for closed loop control of mode 1.

CONCLUSIONS

This research has investigated the feasibility of advanced six-degree-of-freedom actuators employing magnetic suspensions for use in actively controlling large space structures. These advanced actuators consist of a magnetically suspended mass that has three-degrees-of-freedom in both translation and rotation. These torque and force producing actuators can be used in a similar manner to conventional linear reaction mass actuators to control spacecraft vibrations.

The major advantages of these advanced actuators include high bandwidth compared to conventional control moment gyros (CMG's) and both large momentum storage capability and multi-degree-of-freedom actuation compared to conventional linear reaction mass actuators. The combination of high bandwidth and large momentum storage allow these advanced actuators to be used in applications, such as space robotic arms, that have both slewing and vibration requirements. Other similar applications include the combined control of the attitude and flexible structure dynamics of small spacecraft with flexible appendages. Because of their six-degree-of-freedom actuation characteristics and torquing abilities, these advanced actuators were shown to be capable of replacing numerous linear reaction mass actuators.

Design definitions of four actuators were developed, two with small angular strokes (approximately 1 degree) and two with large angular strokes (approximately 10 degrees). Simple models of these actuators were developed that allowed first-order comparisons of their mass and power. The performance goal was to have equivalent control effectiveness of low frequency modes as a conventional, commercially

available linear reaction mass actuator. Of the advanced actuators, the large angle magnetic suspensions were best with the non-optimized designs massing about 100 kg for equivalent low frequency control effectiveness in two directions.

The key technology development required for these advanced actuators is the large-angle-magnetic suspensions and associated controllers.

REFERENCES

1. Anderson, W. and N. Groom, The Annular Momentum Control (AMCD) Device and Potential Applications, NASA TN-D 7866, 1975.

2. Davis, L., D. Hyland, T. Otten, and F. Ham, "Mast Flight System Dynamic Performance," First NASA/DOD CSI Technology Conference, Norfolk, Virginia, November 1986.

3. Downer, J. Design of Large-angle, Magnetic Suspensions, ScD Thesis, Massachusetts Institute of Technology, May 1986.

4. Downer, J., D. Eisenhaure, R. Hockney, and B. Johnson, "Applications of Magnetic Bearings to High-Torque, Satellite Attitude Control Wheels," Proceedings of the Twenty-second Intersociety Energy Conversion Engineering Conference, Philadelphia, PA, August 1987.

5. Downer, J., Hockney, R., Johnson, B., Misovec, K. " Advanced Actuators for the Control of Large Space Structures, " Final Report for NASA Grant NAS1-18426, SatCon Technology Corporation, R07-87, August, 1987.

6. Kwakernaak, Huibert, and Raphael Sivan, Linear Optimal Control Systems, Wiley-Interscience, New York, 1972.

7. Murakami, C., "Development Activities on Magnetic Bearings for Space Use in National Aerospace Laboratory of Japan," Proceedings of the Sixth International Workshop on Rare Earth Cobalt Permanent Magnets and Applications, Technical University of Vienna, August--September 1982.

8. Sindlinger, R. "Magnetic Bearing Momentum Wheels with Magnetic Gimballing Capability for 3-Axis Active Attitude Control and Energy Storage," Conference on Attitude and Orbit Control Systems, ESA SP-128, Noordwijk, November 1977.

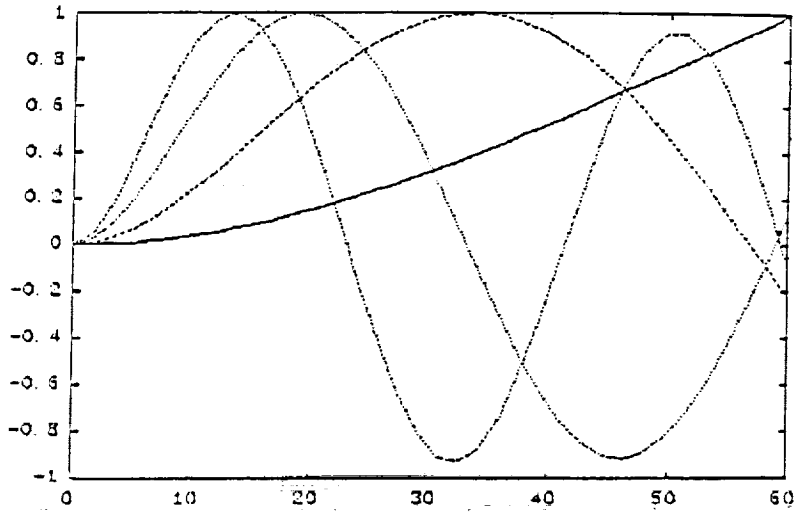

Figure 1. Mode Shapes

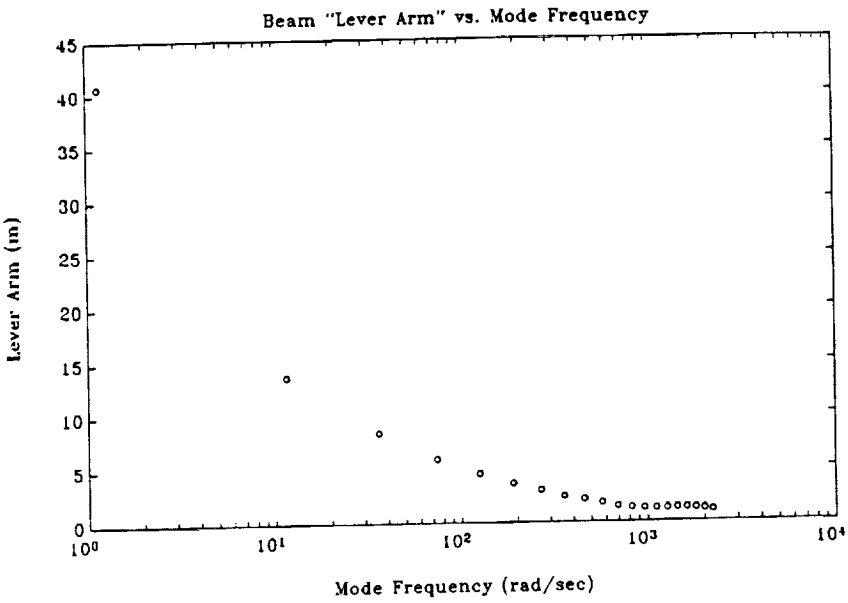

(a) Beam Lever Arm

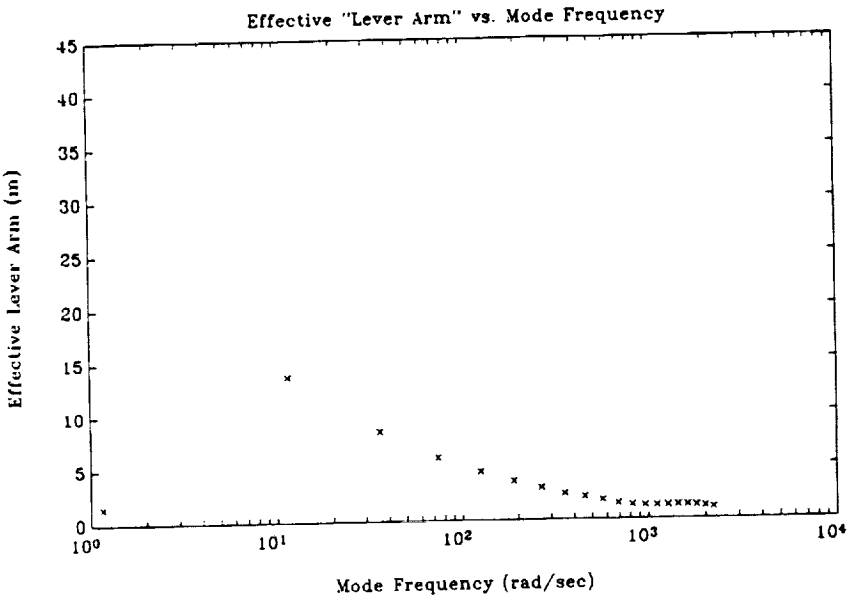

(b) Effective Beam Lever Arm

Figure 2.

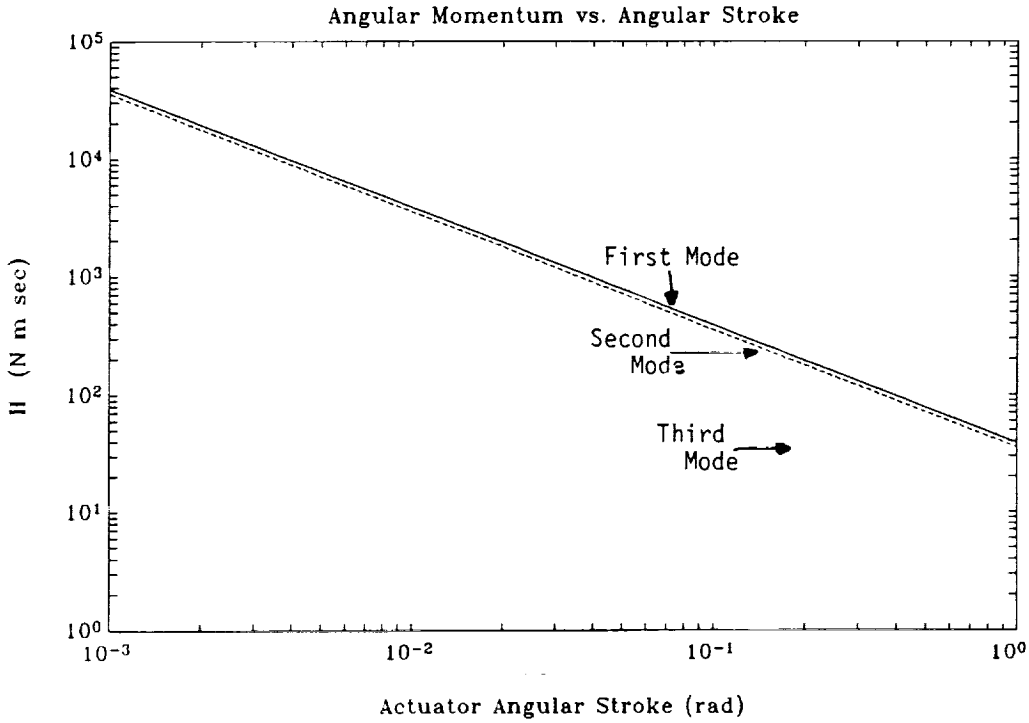

Figure 3. Required Angular Momentum vs Angular Stroke CMG Neglecting Effect of Beam Vibrations

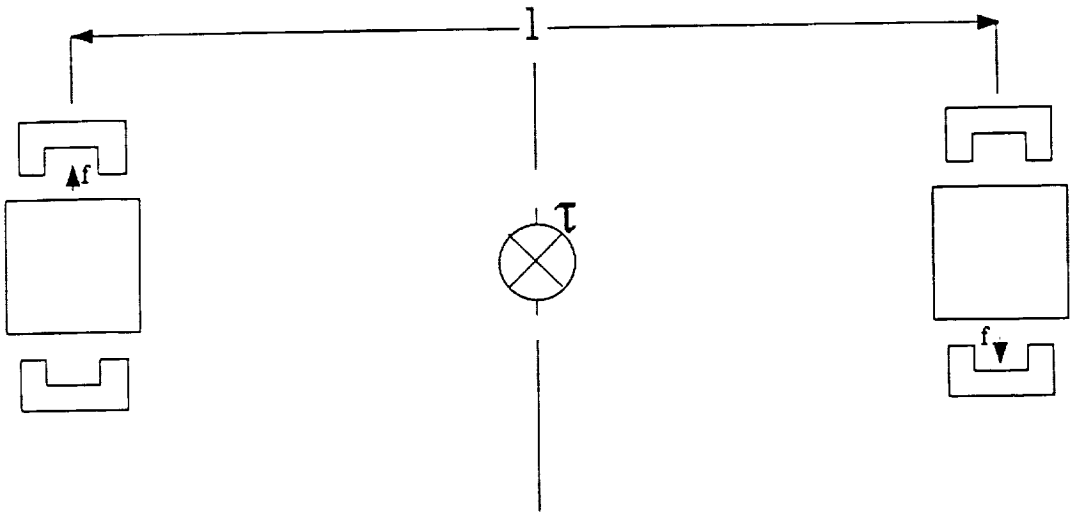

(a) Long Flywheels

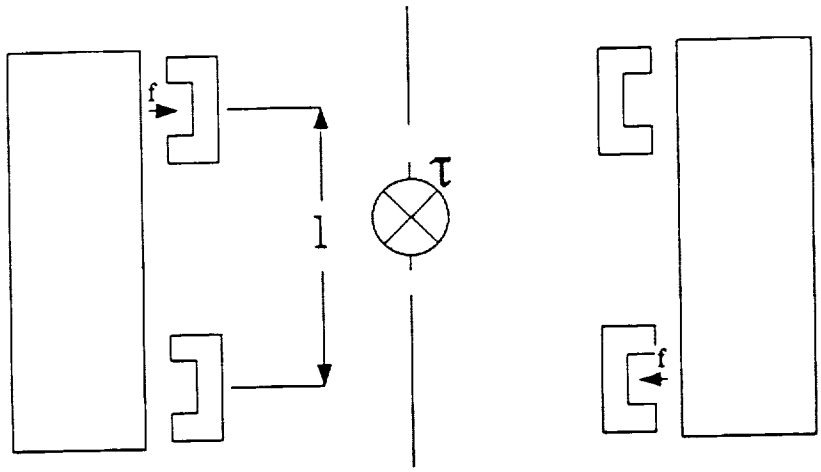

(b) Large-diameter Flywheels

Figure 4. Magnetic Bearing Configuration

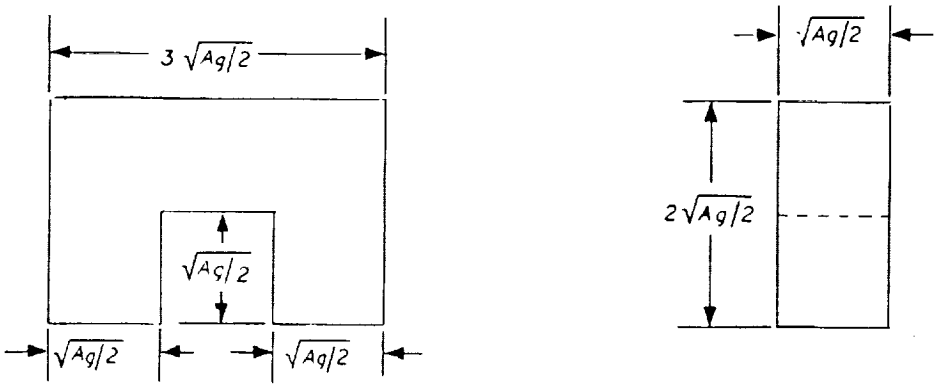

(a) Horseshoe Magnet Core

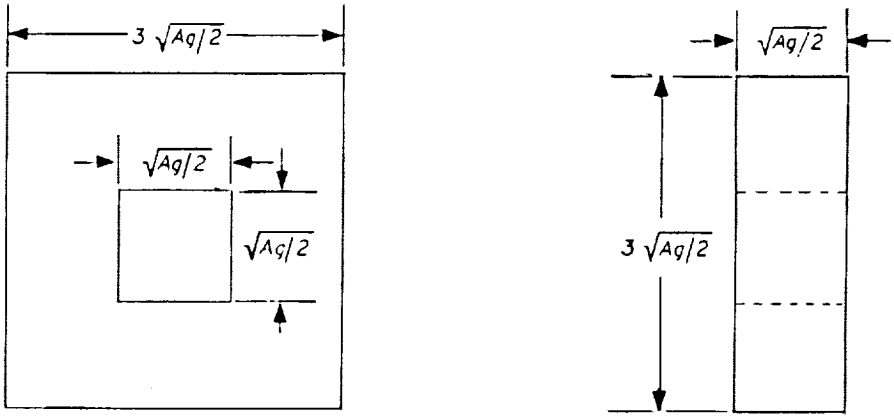

(b) Horseshoe Magnet Coil

Figure 5. Magnet Design

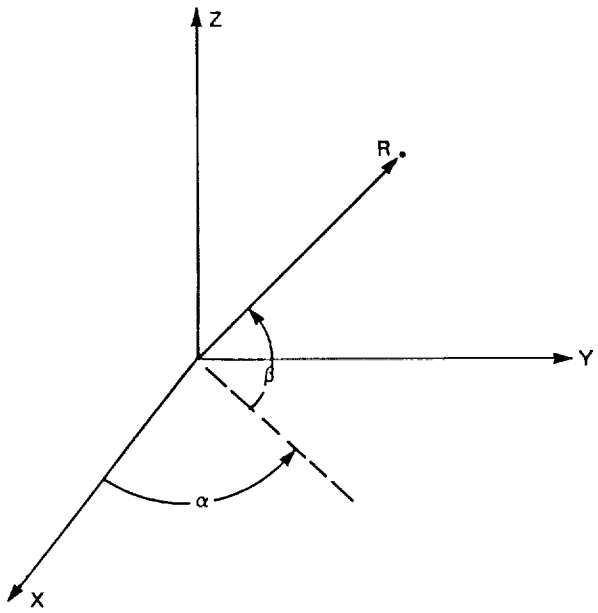

(a) Spherical Coordinate System

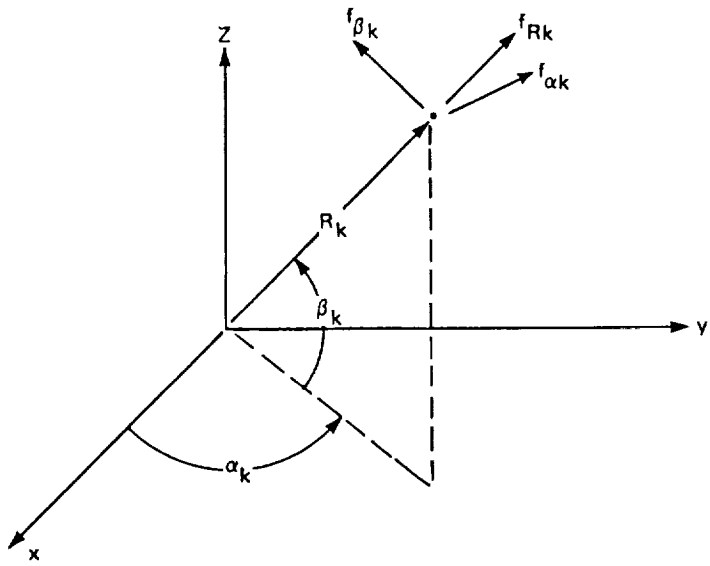

(b) LAMS Force Components

Figure 6. Geometric Symmetry Considerations for a LAMS

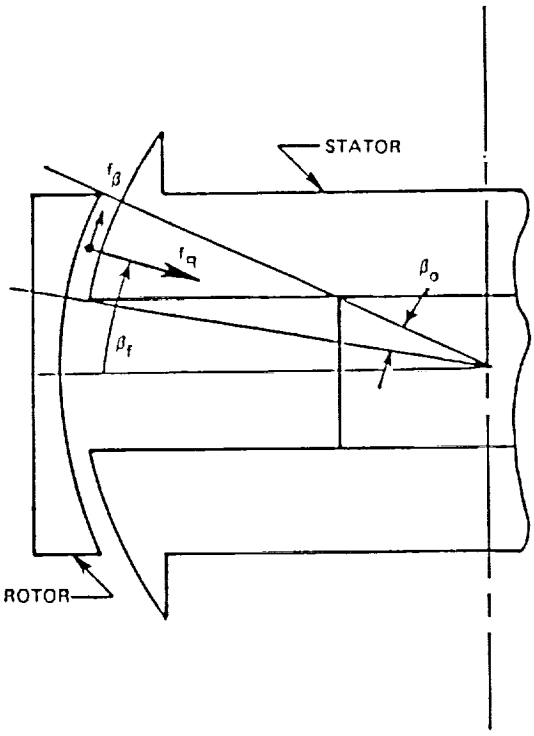

Figure 7. Forces in an Attraction-force LAMS

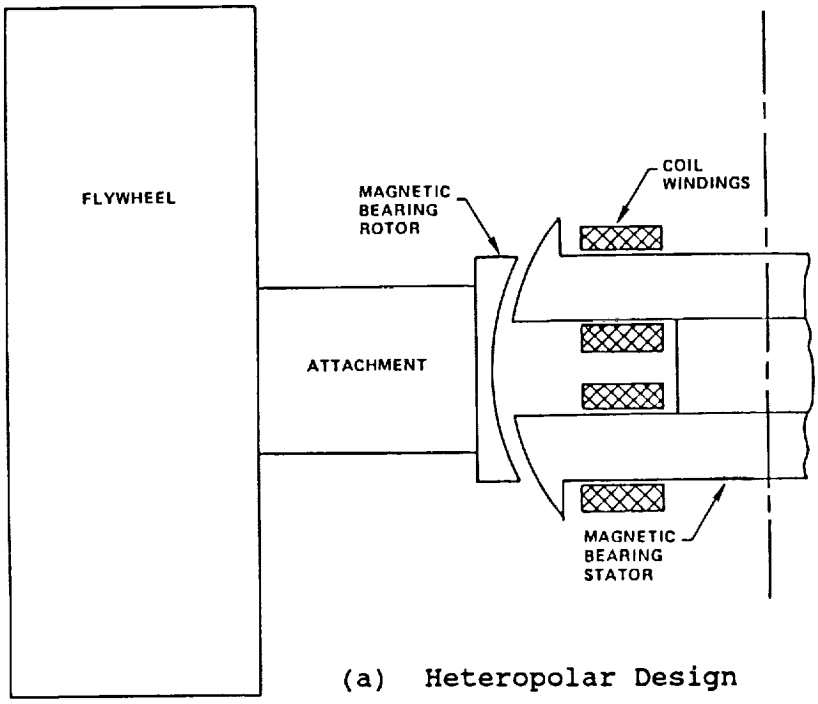

(a) Heteropolar Design

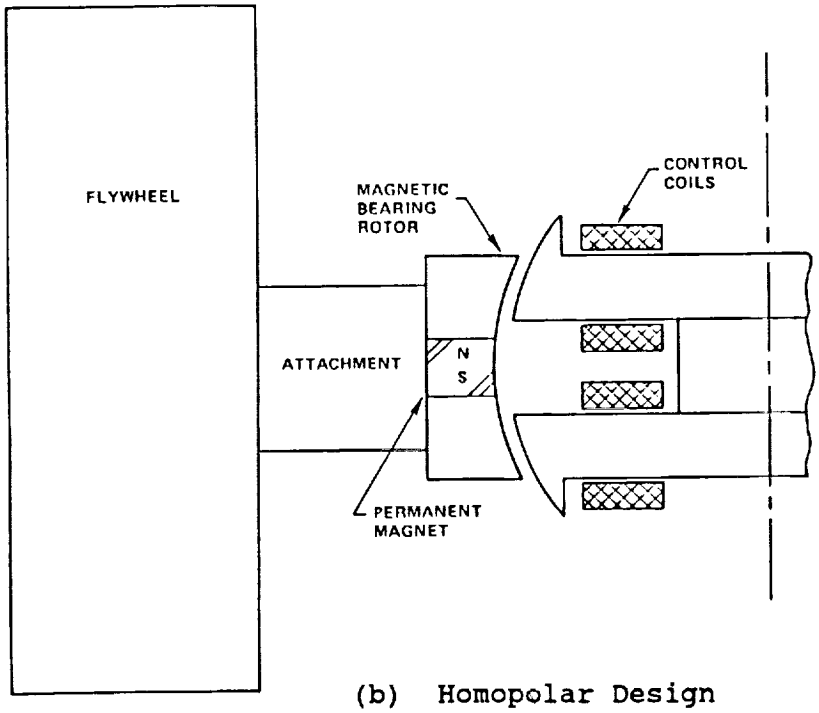

(b) Homopolar Design

Figure 8. Attraction-force MAMS Design Options

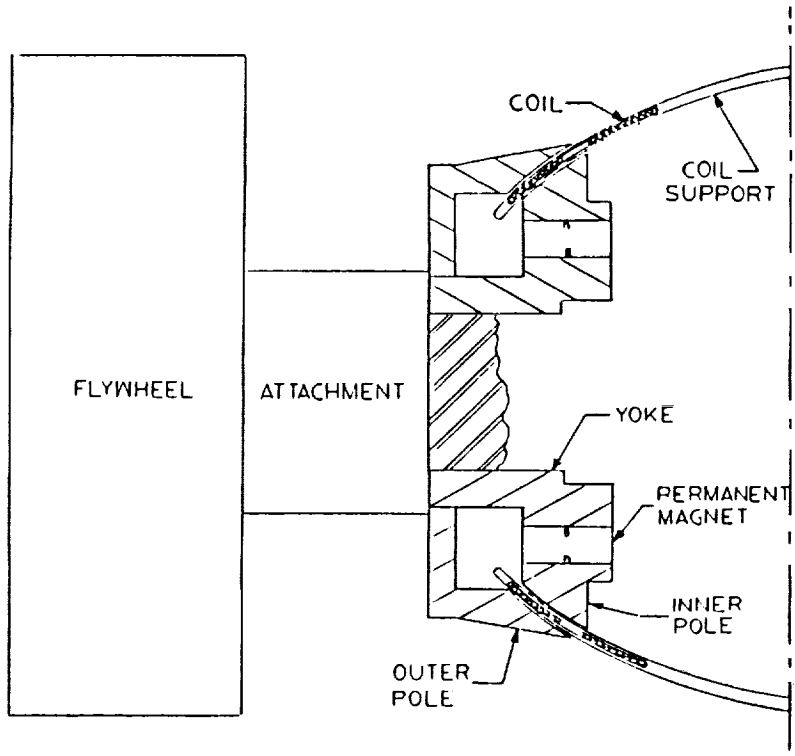

(a) Section View

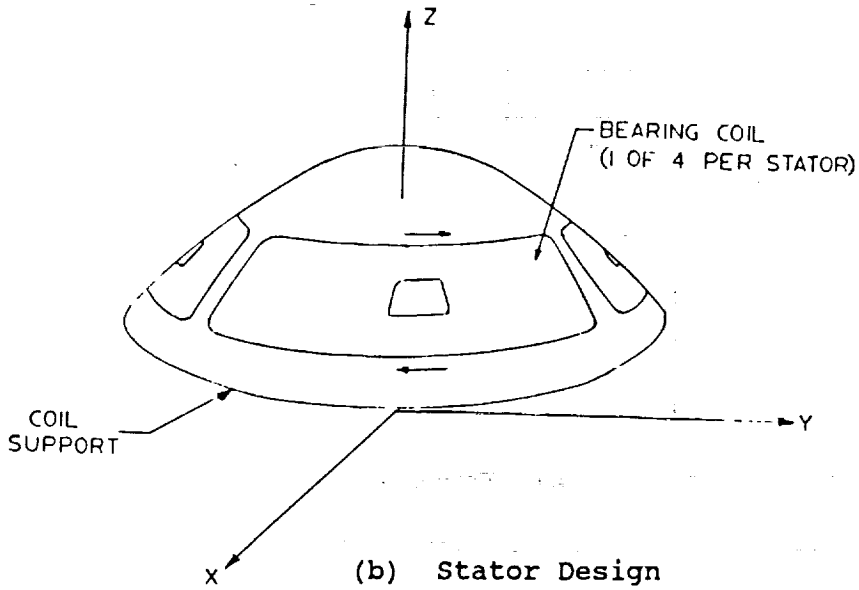

(b) Stator Design

Figure 9. Lorentz-force LAMS Design Option

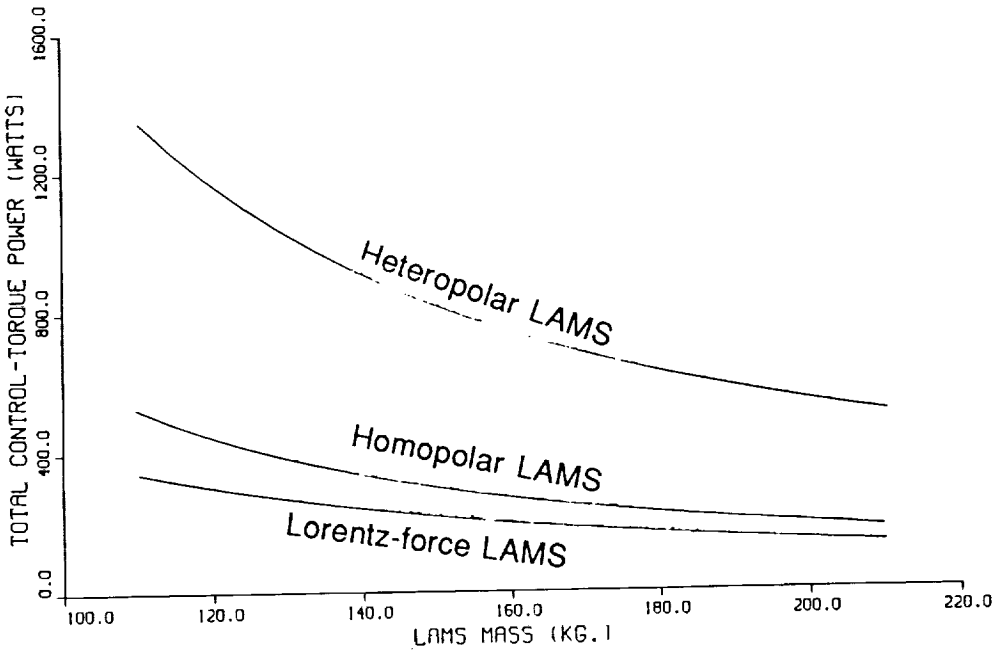

(a) Fixed Mass

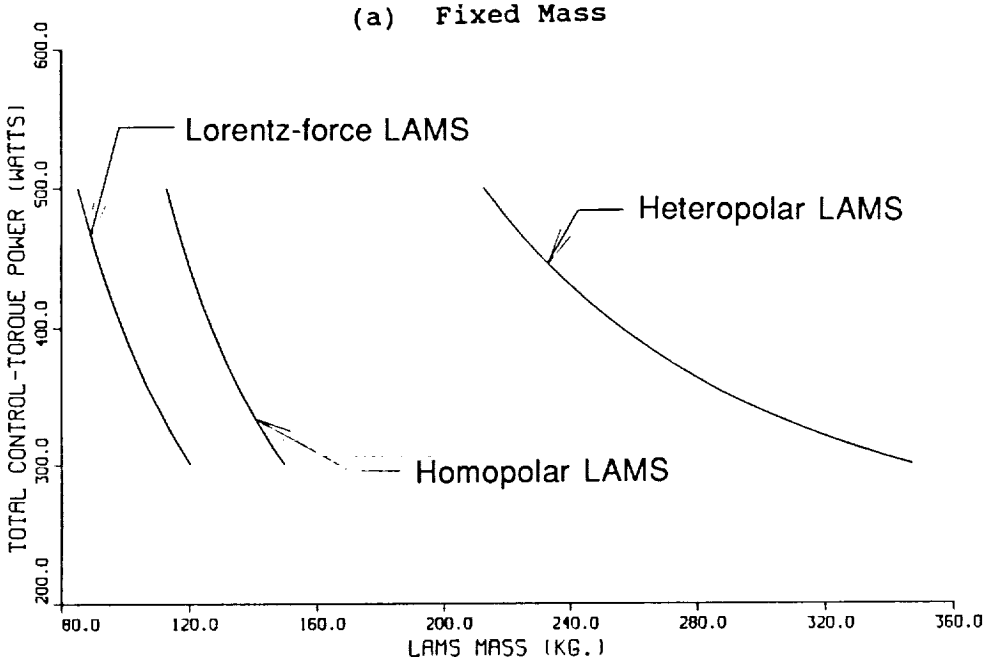

(b) Fixed Power

Figure 10. LAMS Trade-off Comparison

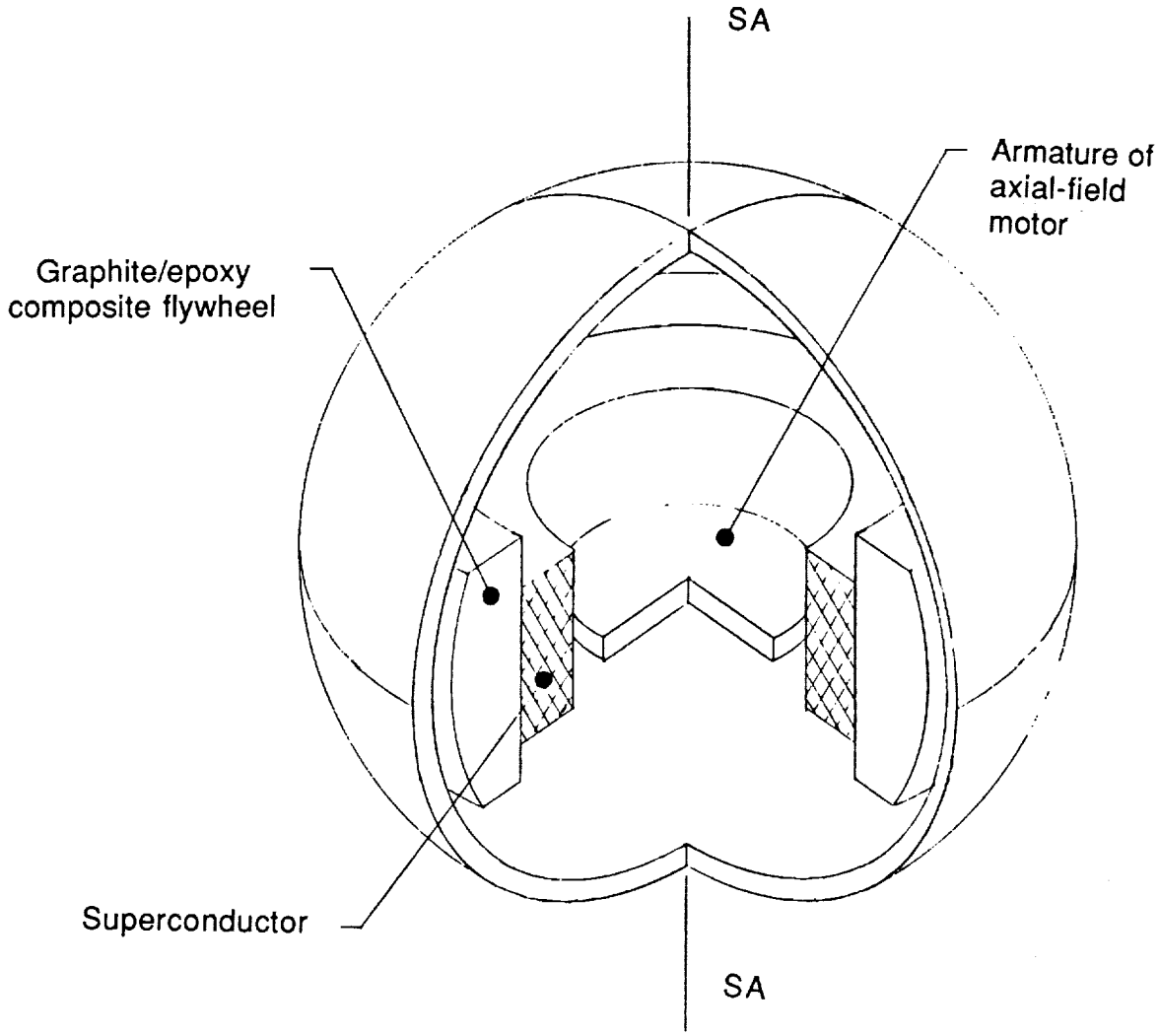

Figure 11. Superconducting CMG

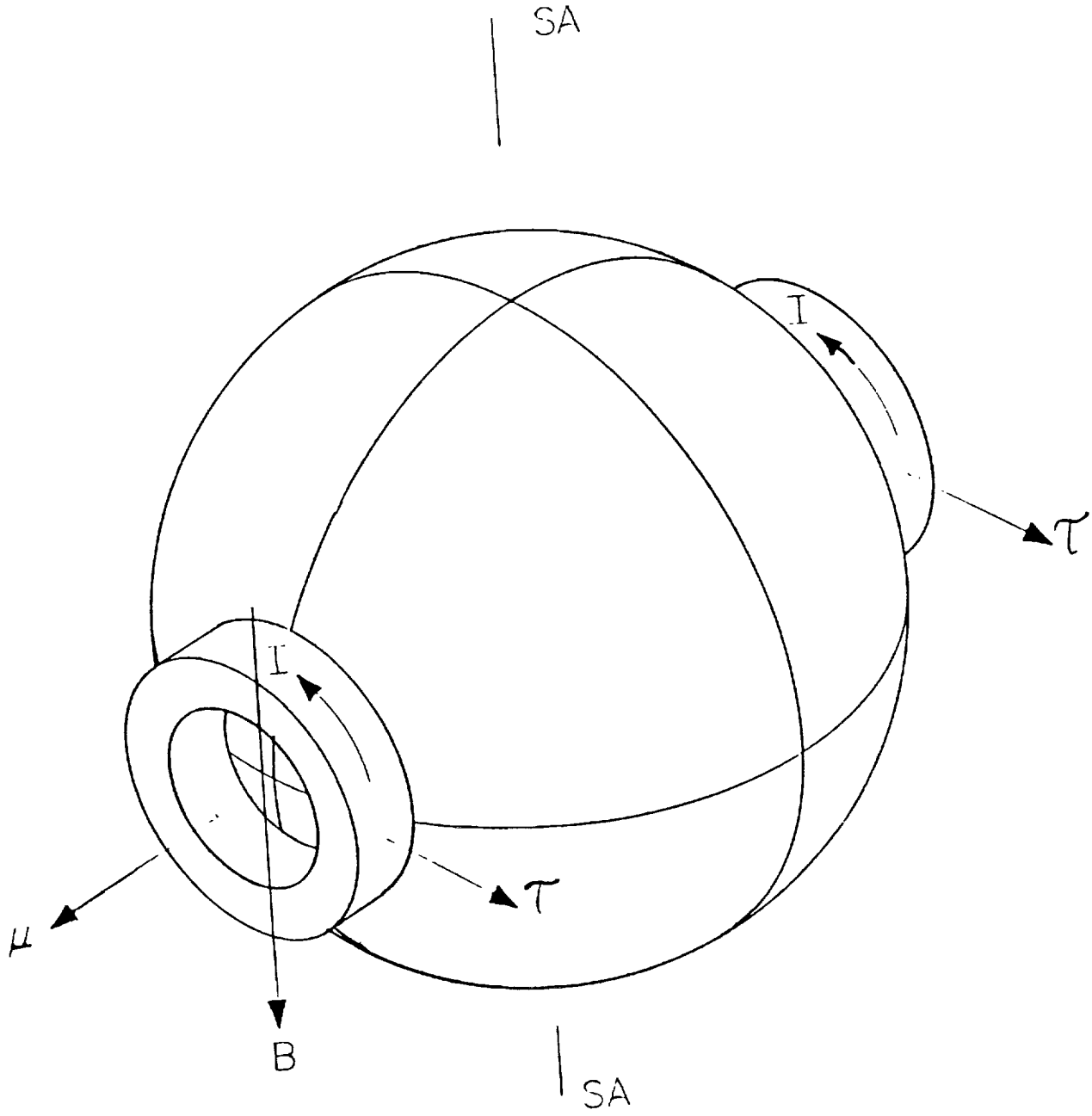

Figure 12. Torque Operation

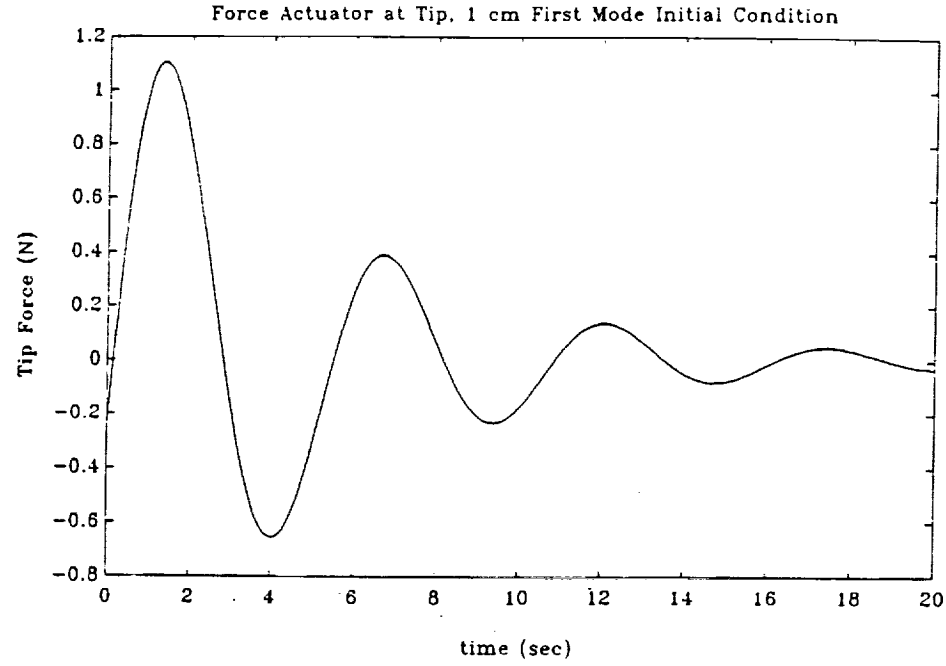

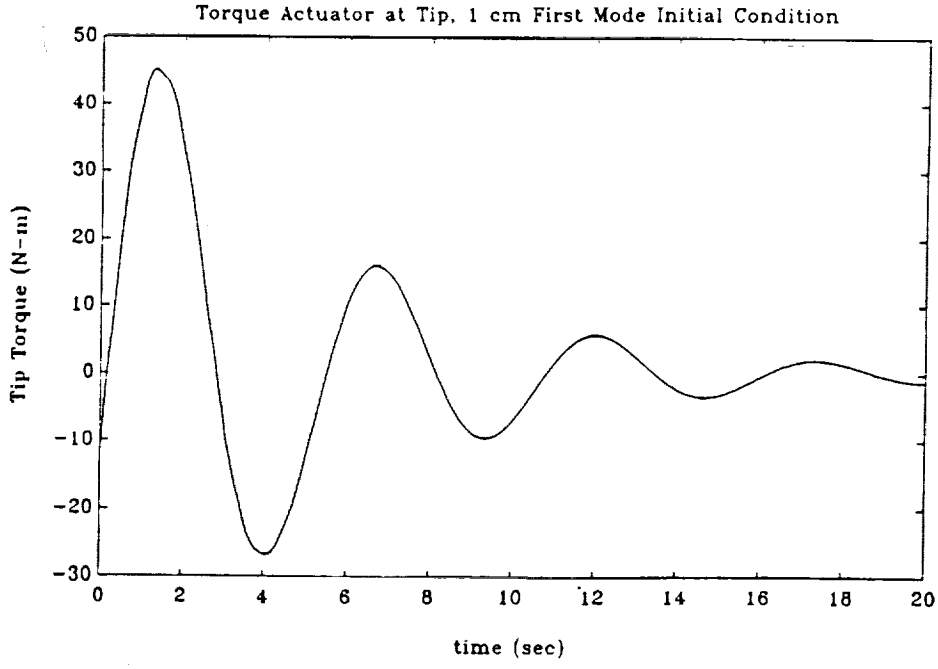

Figure 13. Beam Lever Arm Verification for Mode 1

omit

An AC-Electromagnetic Bearing for Flywheel Energy Storage in Space

Jorgen L. Nikolajsen, Texas A&M University

AN AC-ELECTROMAGNETIC BEARING FOR FLYWHEEL ENERGY STORAGE IN SPACE*

Jorgen L. Nikolajsen
Texas A&M University
College Station, Texas

SUMMARY

A repulsive type AC-electromagnetic bearing has been developed and tested. It was conceived on the basis of the so-called Magnetic River suspension for high-speed trains. The appearance of the bearing is similar to the traditional DC-type electromagnetic bearing but the operating principle is different. The magnets are fed with alternating current instead of direct current and the rotor is fitted with a conducting sleeve (e.g. aluminum) instead of a ferromagnetic sleeve. The repulsion is due to induction of eddy-currents in the conducting sleeve.

The bearing is inherently stable and requires no feedback control. It provides support in five degrees of freedom such that a short rotor may be fully supported by a single bearing. These capabilities have been demonstrated experimentally. On the down side, the load carrying capacity and the damping obtained so far have been quite low compared to the DC-type bearing. Also, significant heating of the conducting sleeve has been experienced.

The AC-bearing is essentially a modified induction motor and there are strong indications that it can be run both as a motor and as a generator with no commutator requirements. It is therefore considered to be a good candidate for support of energy storage flywheels in space.

INTRODUCTION

A new type of electromagnetic bearing, called the Eddy-Current Bearing, has been developed based on the so-called Electromagnetic River Suspension for high-speed ground transportation vehicles. See Eastham & Laithwaite [1]. The Magnetic River is shown in Figure 1. Suspension is achieved by repulsion between a set of AC-electromagnets and an aluminum plate.

---

*This work is supported by the Turbomachinery Research Consortium. Rig hardware was donated by International Minerals & Chemicals Corporation and by Magnetic Bearings Incorporated.

The repulsion is due to induction of eddy-currents in the plate. The Eddy-Current Bearing is simply a circular version of the Magnetic River as shown in Figure 2. This bearing was first proposed by Nikolajsen [2] in 1986.

Work on other types of AC-electromagnetic bearings has been reported by Bolton [3] in 1974, Iskierka [4] and [5] in 1984 and Connor & Tichy [6] in 1987.

Based on the reported work on the Magnetic River Suspension (see references quoted in Ref. [2]) the Eddy-Current Bearing was expected to have some unique capabilities which would make it a prime candidate for flywheel energy storage systems: (1) a single bearing would be sufficient to fully support the flywheel, (2) the bearing would be inherently stable with no need for a feedback control system, and (3) the bearing would have motoring and generating capabilities in addition to the support capabilities. The current paper reports on the experimental verification of capabilities (1) and (2). Verification of capability (3) is in progress.

THE PROTOTYPE BEARING

Analytical studies of a practical Eddy-Current Bearing design are difficult due to the three-dimensional interactions between the primary electromagnetic field set up by the magnets and the secondary field due to the eddy-currents in the conducting sleeve. It was therefore decided to base the prototype bearing design solely on the reported behavior of the Magnetic River suspension (see references quoted in Ref. [2]). This approach was expected to lead to a design with far from optimum capabilities but at least possessing the basic characteristics to be verified as mentioned in the Introduction.

Four U-shaped electromagnets are spaced 90° apart in a star formation to form a 4 inch diameter bearing as shown in Figures 2, 3, and 4. The magnets are mounted in a nonmagnetic stainless steel housing. The magnet cores are made of grain-oriented 0.014 inch laminations with a saturation flux density of about 2 Tesla. The coils have 58 turns each to achieve a peak flux density of about 1.5 Tesla. The inductance of two coils mounted on one core was measured to be about 3.2×10^{-3} Henry.

Each of the four magnets has an electric circuit as shown in Figure 5. Power is supplied from a 115V 60 Hz single phase outlet. The power is adjusted by means of the variable transformer. The variable capacitor is used to adjust the power factor to reduce the power requirements to cover only the I^2R losses in the coil and in the conducting sleeve. The result is that a large current circulates between the capacitor and the coil while a relatively small current is drawn from the supply. The variable capacitor consists of a bank of 13 250μF oil-filled capacitors in parallel which can be switched in and out of the circuit independently. Fine-tuning of the power factor is therefore not possible but the reactive power can be reduced sufficiently to permit the experimentation with the available equipment. It was generally found that 11 to 13 capacitors needed to be switched in to minimize the supply current.
The rotor to be levitated was an aluminum sleeve 6 inches long with an outer diameter of 3.75 inches and a weight of 2lb. 5oz.

EXPERIMENTS

The first two attempts to levitate the rotor were unsuccessful. The first problem was an underestimation of the coil inductance resulting in coils with too many turns and magnets with insufficient flux density. The second problem was a lack of stability of the rotor. It would oscillate radially and bounce off the bearing surfaces at close to the power frequency. The problem was solved by slightly reducing the outer diameter of the rotor. A likely explanation is that the rotor on its magnetic support had a natural frequency near 60 Hz which got excited by the 60 Hz magnetic flux oscillations.

The rotor was thereafter levitated successfully confirming the inherent stability of the bearing and the five degree-of-freedom support capability. During levitation, the current drawn from the power supply of each magnet was of the order of 10A at 50 VAC. The magnet currents were of the order of 50A with the highest current in the bottom magnet.

The supply current was limited to 18A by the variable transformers. Within that limit, a maximum weight of about 41b could be levitated with the bottom magnet current at 68A with a supply current of 16.5 A at 65 VAC. The side and top magnet currents were about 30 A with supply currents of about 10 A at 15 VAC. The corresponding maximum thrust capability was about 5oz. The power loss in the sleeve was calculated to be about 800W. Within a few minutes the sleeve got too hot to be hand held whereas the magnets remained cool with only a slight temperature increase to be felt. An increase in supply current to one circuit would result in a similar current in the other circuits indicating strong mutual inductance between the magnet's coils.

The thrust capability could be increased significantly by using a shorter sleeve but the radial support capability would then decrease. The radial support capability could be increased significantly by using a longer sleeve but thrust stability would then be lost and the sleeve would try to exit the bearing.

The stiffness of the support was quite low as indicated by natural frequencies of the order of 1Hz for the levitated sleeve. The sleeve vibrations would also take a long time to die out indicating that the damping is very low.

However, for flywheel energy storage applications in space, the high power loss in the sleeve is considered to be the most serious problem. Efforts are continuing to resolve it. It has been speculated that both the high power loss and the low lift capacity may be due to concentration of the eddy-current in 8 spots directly below the 8 magnet poles. It is likely that a design closer to a conventional motor will be needed to ensure adequate efficiency for flywheel energy storage.

PROPOSED FLYWHEEL CONCEPT

Figure 6 shows an example of how the Eddy-Current Bearing may be utilized in a flywheel energy storage system. The bearing has been inverted and supports the inside rim of the flywheel. During charging and discharging, the bearing acts

as an induction motor and as an induction generator respectively. The system is completely maintenance free. Two identical counter-rotating flywheels may be needed to cancel the reaction torque during energy transfer.

CONCLUSIONS

The reported experimental investigations have led to the following conclusions:

1. The Eddy-Current Bearing provides rotor support in five degrees of freedom: radial support and moment support in the horizontal and vertical directions plus thrust support in the axial direction. A single bearing is therefore sufficient to fully support a short rotor.

2. The Eddy-Current Bearing is inherently stable and does not require feedback control.

3. The damping capacity of the Eddy-Current Bearing appears to be low and is probably insufficient for most applications. Additional damping may be provided by a conventional eddy-current damper.

4. The I^2R loss in the rotor sleeve due to the eddy-currents is significant. Further work is needed to reduce this loss.

5. The unique capabilities of the Eddy-Current Bearing, demonstrated by this investigation, makes it a potential candidate for use in space based flywheel energy storage systems.

REFERENCES

1. Eastham, J.F., and Laithwaite, E.G., "Linear Induction Motors as Electromagnetic Rivers", Proc. IEE, Vol. 121, No. 10, 1974, pp. 1099-1108.

2. Nikolajsen, J.L., "A Magnetic Bearing Based on Eddy-Current Repulsion", NASA CP 2443, Rotordyn. Instab. Probl. in Hi-Perfom. Turbomach., 1986, pp. 461-465.

3. Bolton, H., "An Electromagnetic Bearing" IEE CP 120, Linear Electr. Machines, London, 1974, pp. 45-50.

4. Iskierka, S., "Influence of Irregularities of Exciting Current Density Distribution on Induction Bearing Work", Acta Technica Csav, No. 5, 1984, pp. 572-582.

5. Iskierka, S., "Analysis of an Induction Bearing by the Finite Element Method", Archiv fur Electrotechnik, Vol. 67, 1984, pp. 375-380.

6. Connor, K.A., and Tichy, J.A., "Analysis of an Eddy-Current Journal Bearing", ASME Pap. 87-Trib-10, 1987, p.7.

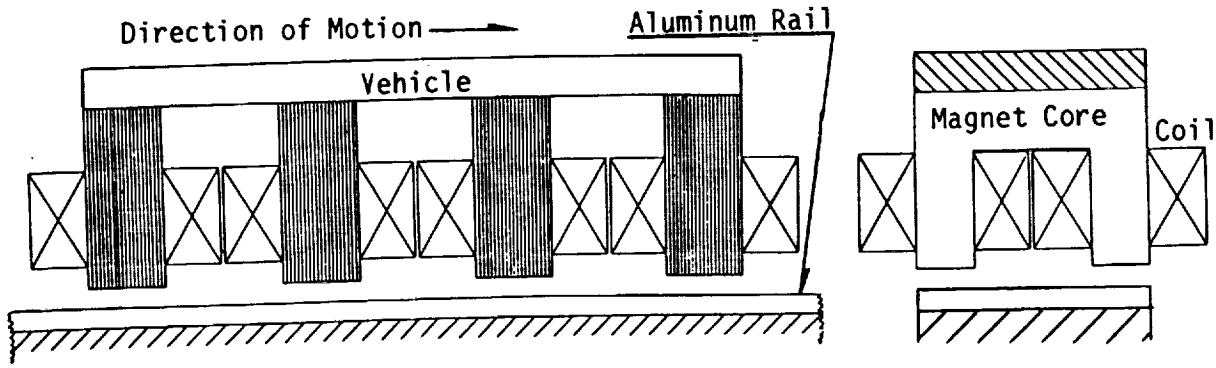

Figure 1 The Magnetic River Suspension (Schematic)

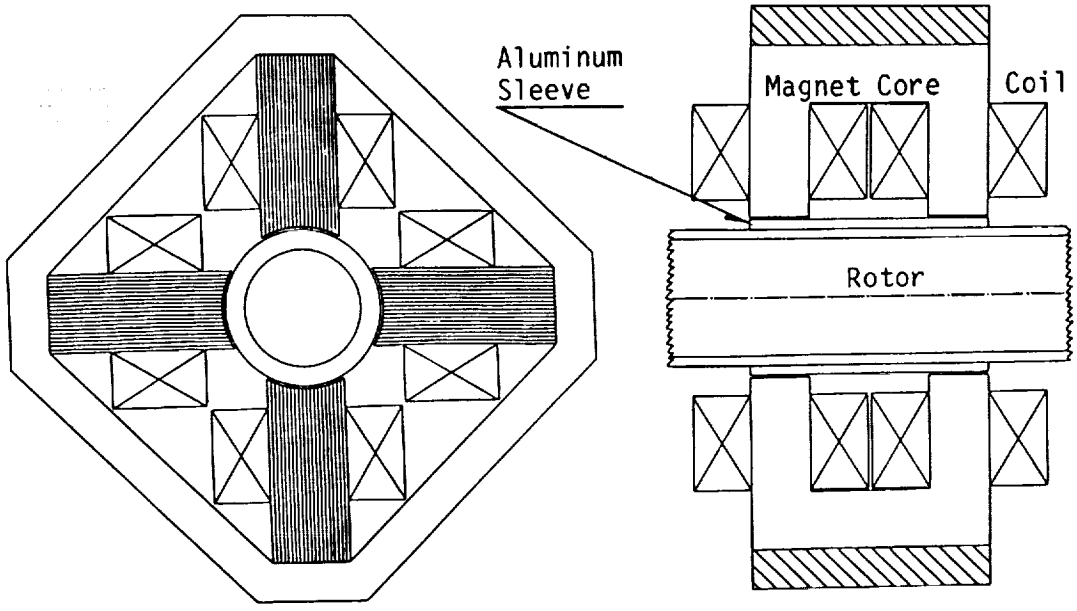

Figure 2 The Eddy-Current Bearing (Schematic)

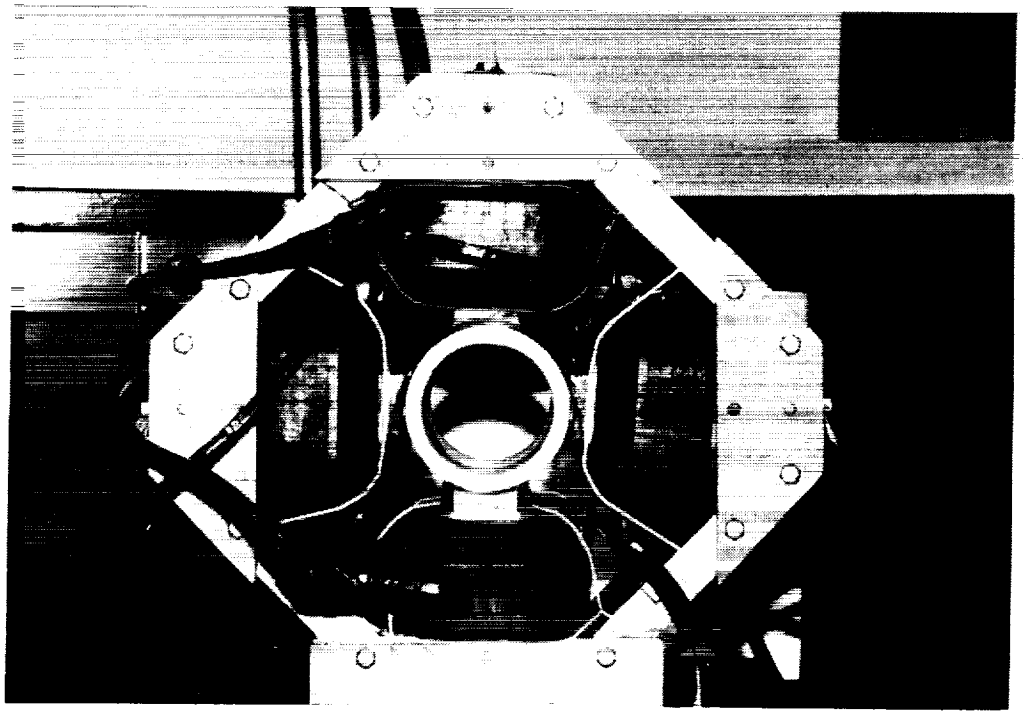

Figure 3 The Eddy-Current Bearing

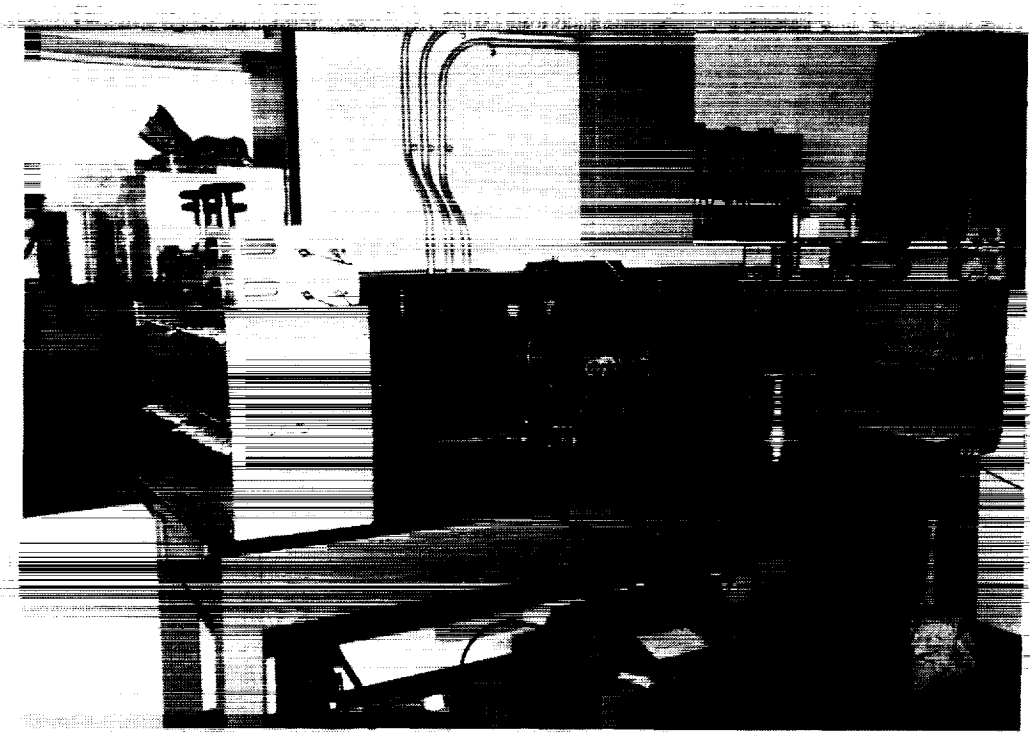

Figure 4 The Eddy-Current Bearing Rig

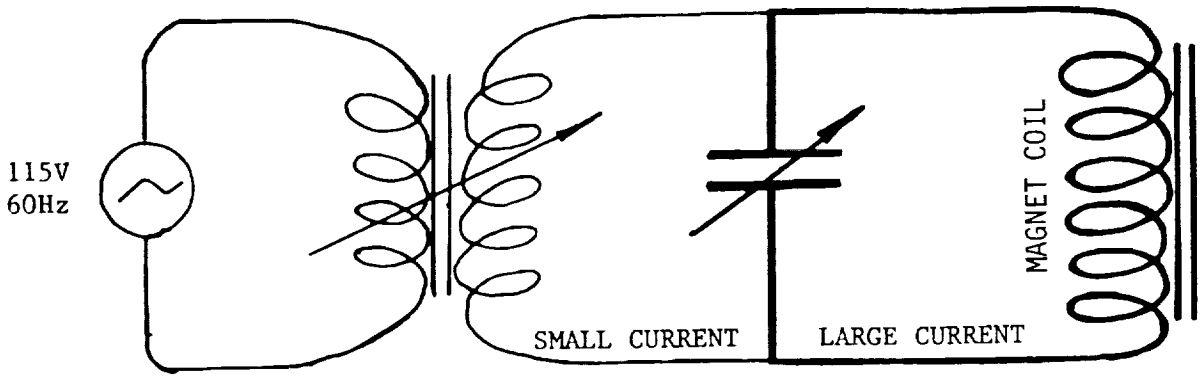

Figure 5 Magnet Circuit Diagram

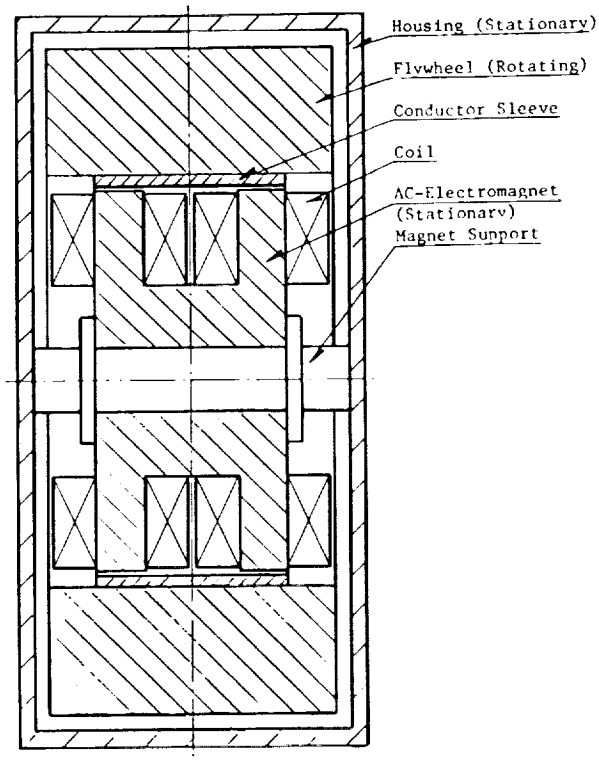

Figure 6 Proposed Energy Storage Flywheel Principle

OMIT

High Efficiency Magnetic Bearings

Philip A. Studer, TPI Inc.

Chaitanya P. Jayaraman, Davinder K. Anand and James A. Kirk,

University of Maryland

HIGH EFFICIENCY MAGNETIC BEARINGS*

Philip A. Studer, Manager, Electromagnetic R & D
TPI Inc.,
Bethesda, MD

Chaitanya P. Jayaraman, Graduate Research Assistant
Davinder K. Anand, Professor
James A. Kirk, Professor
University of Maryland
Mechanical Engineering Department
College Park, MD

SUMMARY

This paper reports on research activities concerning high efficiency permanent magnet plus electromagnet (PM/EM) pancake magnetic bearings at the University of Maryland.

The paper begins with a description of the construction and working of the magnetic bearing. Next, parameters needed to describe the bearing are explained. The paper then summarizes methods developed for the design and testing of magnetic bearings. Finally the paper discusses a new magnetic bearing which allows active torque control in the off-axes directions.

LIST OF SYMBOLS

A	magnetic bearing pole face area
B	magnetic flux density
c	control system sensitivity
F_A	active radial force
F_I	current force
F_X	passive radial force
g_0	width of airgap
i_{max}	maximum current in the electromagnetic coils
K_A	active radial stiffness
K_I	current force sensitivity
K_X	passive radial stiffness

*Supported by NASA Grant NAG5-396

N number of turns of wire in coils

x_{oper} maximum operational width of airgap ($< g_0$)

μ_0 permeability of free space

INTRODUCTION

Magnetic bearings evolved in the 1950s from the simple application of permanent magnets positioned to exert repulsive forces to electromagnets and then to present day magnetic bearings which utilize permanent magnets and electromagnets to achieve active control (ref. 1).

The magnetic bearings currently under development at the University of Maryland are of the permanent magnet plus electromagnet (PM/EM) type (ref. 2-5). These bearings use permanent magnets to provide bias flux and electromagnets to provide a modulating control flux so as to keep the clearance in the magnetic bearing constant. This modulation is necessary to provide active control in the radial direction and in the presence of unbalance or external forces. Control in the axial direction is passive. The bearing system consists of a central stator and a concentric rotor which in one application is a flywheel. The stator is made up of Samarium-Cobalt magnets which are contained between two bias flux plates. Four control coils are located at the top and bottom of the bias flux plates as shown in fig. 1. Bias flux produced by the magnets flows across the airgap and through the suspension ring in the flywheel (fig. 2); thus making the system unstable in the unpowered condition. Two feedback control systems one in the E-W and other in the N-S directions, are provided to stabilize the flywheel and hold the gap constant. When the rotor displaces radially, the motion is sensed by the position sensors and the control system responds by sending a measured current through the coils which results in the generation of a corrective magnetic flux. This flux adds to the permanent magnet flux on the side of the increasing gap and subtracts from the permanent magnet flux on the side of the decreasing gap as shown in fig. 3. The net result is a stabilizing force which moves the flywheel back to the central position.

There are three parameters which characterize the magnetic bearing. They are K_X, K_I and K_A. K_X is a measure of the destabilizing force produced by the permanent magnets and is measured in lbs./in. The amount of corrective force produced by the coils in response to a current is characterized by K_I which is measured in lbs./Amp. K_A represents the total stiffness of the stabilized magnetic bearing measured in lbs./in. These parameters are necessary in the design of magnetic bearings since they are directly related to stability, linear range of operation and load capacity of the bearing.

MAGNETIC BEARING DESIGN

Numerous computer programs have been developed as tools for the design of magnetic bearings. These programs are capable of simulating the working of the magnetic bearing for a given set of input dimensions (ref. 6,7). Theoretical predictions of K_X, K_I and K_A may be made in this manner. These programs also allow the user to observe the effects of various dimensional parameters on K_X, K_I and K_A and to select the optimal choices of bearing dimensions and permanent magnet size. Another useful feature of these programs is their capability to identify magnetic saturation in critical parts of the bearing and suggest ways to prevent it.

The general approach to designing a magnetic bearing is to compute the stiffness K_X based upon permeance modeling (ref. 7). Fig. 4 shows the half-plane representation of the permeance model. Magnetic flux produced by the permanent magnet is redistributed into useful flux and fringing flux based on this model. If B is the corresponding useful

flux density at the pole faces then K_X can be shown to be:

$$K_X = \frac{A * B^2}{g_0 * \mu_0}$$

If N is the number of turns of wire in the coils then the current force sensitivity K_I can be shown to be:

$$K_I = \frac{A * B * N}{\sqrt{2} * \pi * g_0}$$

This shows that a large radial flux (B) is beneficial for providing a large corrective force. This is an important and somewhat unexpected point. A large radial flux indicates the presence of a large destabilizing force. However, the nature of the control system is such that the destabilizing force is harnessed beneficially.

Once K_X and K_I are known the suspension operating range may be found from the following inequality.

$$K_I * i_{max} > K_X * x_{oper}$$

The physical meaning of this condition is that the stabilizing force produced by current through the electromagnet coils should exceed the destabilizing force generated by the permanent magnets.

Current in the coils is produced by the control system in response to displacement sensed by the position sensors. If c denotes the amount of current in the coils for a unit displacement at the position sensors then K_A can be written as

$$K_A = c * K_I - K_X$$

C, which is measured in Amps/inch is dependent on the control system. It must be noted that this equation for K_A is valid only in the linear range of operation of the control system and under steady state conditions.

An important characteristic is the maximum axial force carrying ability. Both the maximum axial force, and the curve shape (axial force vs. displacement) are important parameters. To prevent excessive sag, it is desirable to have a large slope at smaller displacements. Also, a large peak axial force prevents the loss of suspension under external axial overloads.

TESTING OF MAGNETIC BEARINGS

Theoretical formulation of K_X, K_I and K_A have been developed at the University of Maryland. Therefore there existed a need to verify theory with experiment. This was accomplished via an experimental apparatus developed by Frommer at the University of Maryland. The apparatus is shown in fig 5. In this apparatus the stator is held stationary on the bearing support while the rotor is clamped to the mounting plate which is allowed to move on a set of linear bearings. Force is measured via a strain ring and displacement is read as voltage from the position sensor. A more detailed description of the apparatus is presented in reference 8.

TESTING AND SIMULATION RESULTS

Fig 6 is a typical set of curves of radial force vs. displacement for different values of bias current. The linearity of the curve especially around the centered position suggests an absence of magnetic saturation. The slope of the force curve at 0 amps bias current is the K_X of the bearing. Fig 7 shows the variation of F_A which is the total restoring force produced by the bearing, with displacement. F_A can be shown to be a combination of two forces, F_I which is the stabilizing force produced by the coils and F_X which is the destabilizing force produced by the permanent magnets. This

is clearly seen in fig 7. The variation of F_X with displacement is fairly linear at smaller values of displacement, however the F_I curve clearly shows the effect of magnetic saturation and current limit of the control system. Current limit and magnetic saturation are to be avoided as far as possible so that the complete system is linear. A large linear range assures a larger range of controllability leading to a stable magnetic bearing.
Tests on magnetic bearing led to an improved understanding of the working of the bearing and these were reflected in the simulation programs. Changes were made to account for saturation and magnetic flux paths were revised so as to arrive at theoretical predictions which were consistent with test results (ref. 9).

OFF-AXES TORQUE CONTROL MAGNETIC BEARING

Another configuration of EM/PM magnetic bearing currently under development is an off-axes torque control magnetic bearing (ref. 10). The arrangement of permanent magnets and electromagnet coils in this bearing gives it an added degree of control i.e. capability of controlling the tilt in the off-axes direction. Bias flux at the air gap is provided by two sets of permanent magnets as shown in fig 8. Modulation of the control flux is provided by electromagnetic coils. These coils are capable of controlling the radial position as well as the off-axes tilt of the flywheel with respect to the bearing. Radial control is possible when radial-control electromagnetic coils at opposite ends of the central permeable disk introduce magnetic flux. This flux aids the bias flux of the magnets on one side while opposing it on the other resulting in radial movement of the flywheel. The angular-control electromagnetic coils on the upper and lower permeable disk quadrants are connected to produce a magnetic flux circulating around the periphery of the magnetic path. When this flux circulates in the clockwise direction as shown in fig 8, it aids the permanent magnet flux at the upper-right and the lower-left airgaps and opposes the permanent magnet flux at the upper-left and the lower-right airgaps. This flux pattern does not introduce a net right or left force, but the inequalities of forces at the corner airgaps produce a net torque on the rotor, tilting it counterclockwise about the y-axis. Similar arrangement exists in the y-z plane of the stator to control the rotor motion along the y-axis and rotor tilt about the x-axis. Control along the z-axis is passive.

Fig 9 illustrates a feedback control system for one plane of the bearing. The control circuitry varies the currents in the radial- and angular-control coils in response to the outputs of the radial- and angular- position sensors. An angular command bias to the angular differential amplifier sets the equilibrium angular position.

CONCLUSIONS

Both 3" and 4" diameter EM/PM magnetic bearings have been successfully designed and tested at the University of Maryland. Under initial tests the 3" magnetic bearing flywheel was maintained at a speed of 2000 rpm for a total time period of 200 hours. In addition this bearing was successfully spun to a maximum rpm of 10,000.

During the commissioning of these bearings many problems were encountered both with the actuator and the control system. These problems centered around magnetic saturation in the metallic parts and the modeling of permanent magnet leakage fluxes. The development of testing procedures helped shed light and alleviate many of the problems.

Continuing work includes the use of Vanadium Permendur which is a material with an extremely high saturation level (2.3 Teslas) as compared to Nickel Iron (1.5 Teslas) which is currently used. There is also a need to improve bearing performance with superior position transducers and power amplifier systems. Newer bearing configurations such as the one described in this paper are also being developed.

REFERENCES

1. Rodriguez G. E. and Eakin, V., "Magnetic Bearings for Inertial Energy Storage", Proceedings of the 22nd Intersociety Energy Conversion Engineering Conference", August 10-14, 1987, Philadelphia, Pa., Vol. 4, pp 2070-2076.

2. Kirk, J. A., "Flywheel Energy Storage - Part I, Basic Concepts", International Journal of Mechanical Sciences, Vol. 19, 1977, pp. 223-231.

3. Kirk, J. A. and Studer, P. A., "Flywheel Energy Storage - Part II, Magnetically Suspended Superflywheel", International Journal of Mechanical Sciences, Vol. 19, 1977, pp. 233-245.

4. Kirk, J. A. and Huntington, R. A., "Energy Storage - An Interference Assembled Multiring Superflywheel", Proceedings of the 12th IECEC Conference, Washington, D.C., September 2, 1977, pp. 517-524.

5. Kirk, J. A. and Anand, D. K., et al., "Magnetically Suspended Flywheel System Study", NASA Conference Publication 2346, "An Assessment of Integrated Flywheel System Technology". Dec. 1984, pp. 307-328.

6. Anand, D. K., Kirk, J. A. and Bangham, M., "Simulation, Design and Construction of a Flywheel Magnetic Bearing", ASME Paper 86-DET-41.

7. Iwaskiw, A. P., "Design of a 500 Wh Magnetically Suspended Energy Storage System", University of Maryland, M. S. Thesis.

8. Frommer, D. A., "Mechanical Design Considerations for a Magnetically Suspended Flywheel", University of Maryland, M. S. Thesis.

9. Plant, D. P., Jayaraman, C. P., Frommer, D. A., Kirk, J. A. and Anand D. K., "Prototype Testing of Magnetic Bearings", Proceedings of the 22nd IECEC Conference, Aug. 10-14, 1987, Philadelphia, Pa., pp. 835-839.

10. Studer, P. A., "Magnetic Bearing with radial and Angular Control", NASA Tech. Briefs, March 1987, pp. 62,63.

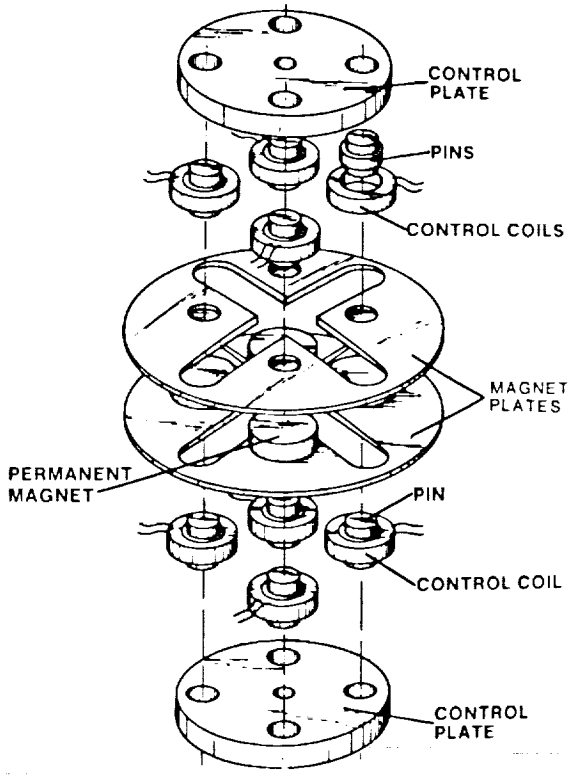

Fig. 1 Exploded View of Stator of Magnetic Bearing

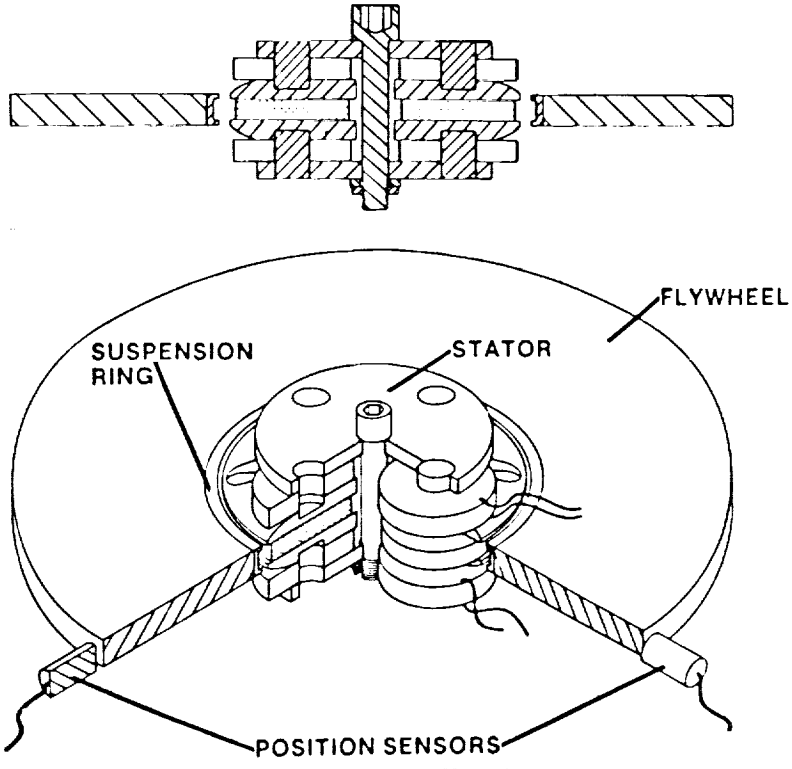

Fig. 2 Pancake Magnetic Bearing

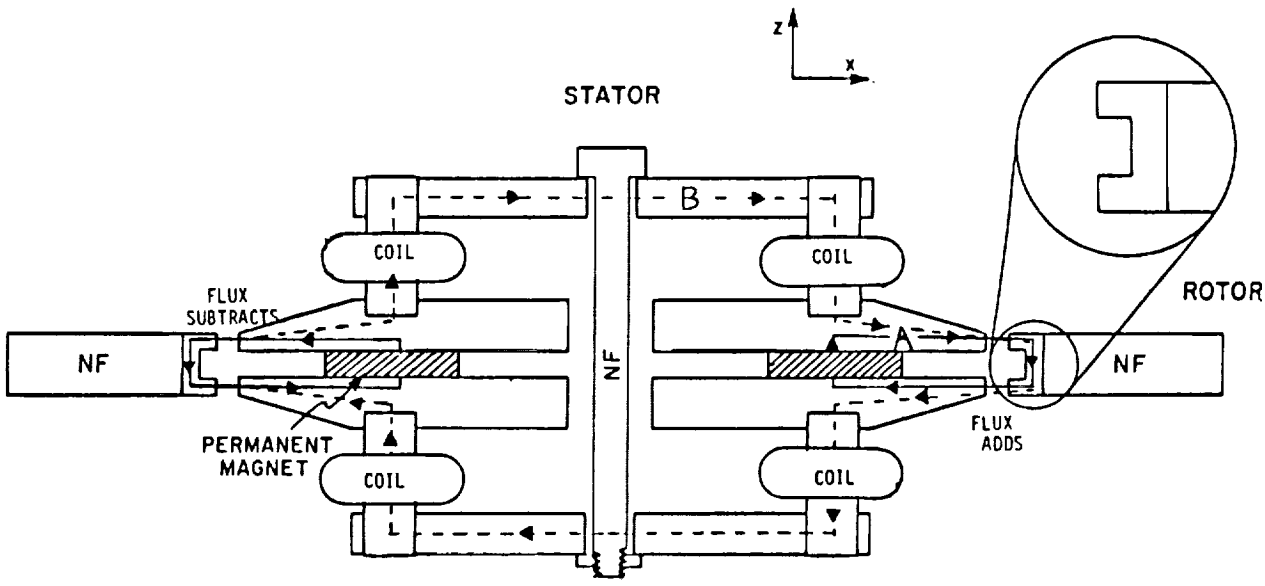

* All materials are Ni-Fe unless marked NF (non-ferromagnetic)

Fig. 3 Flux Paths in Magnetic Bearing

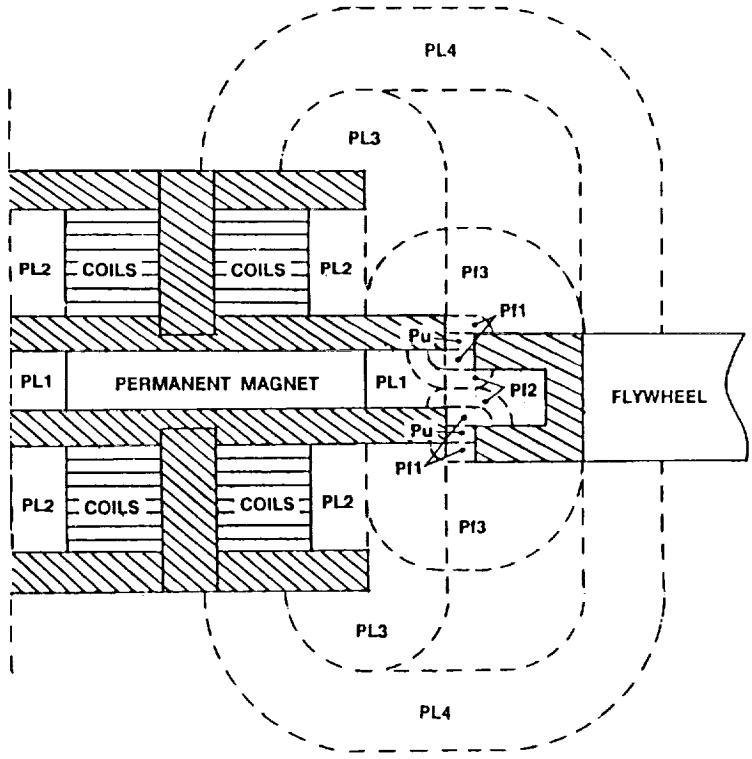

Fig. 4 Flux Paths in Permeance Model

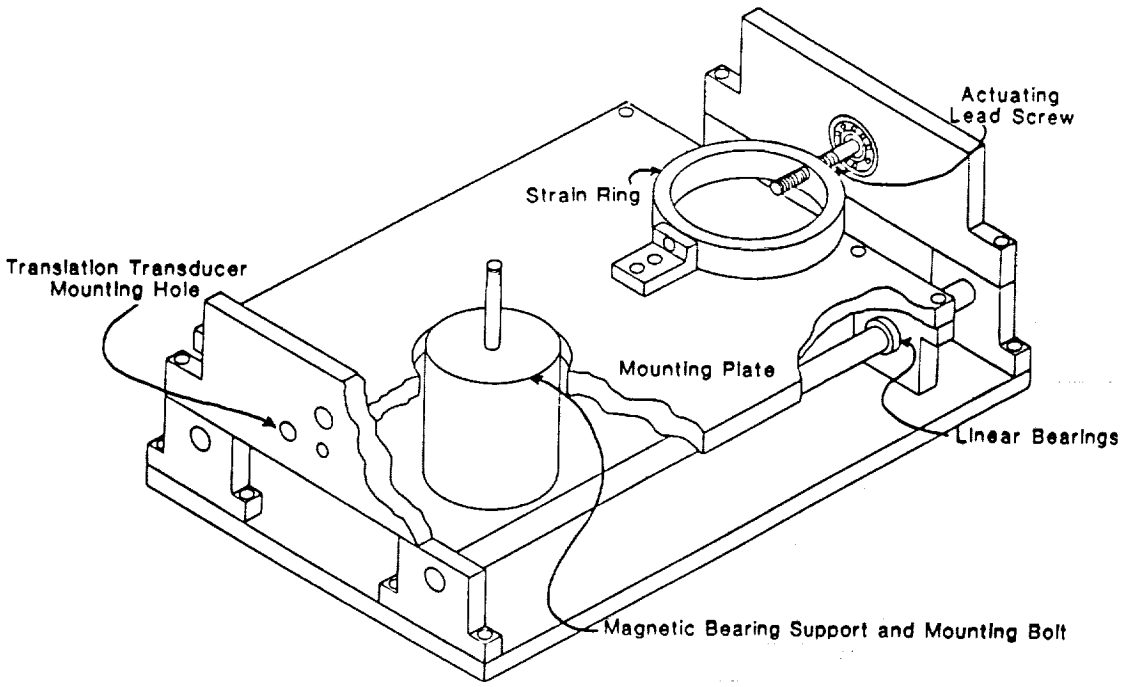

Fig. 5 Magnetic Bearing test apparatus

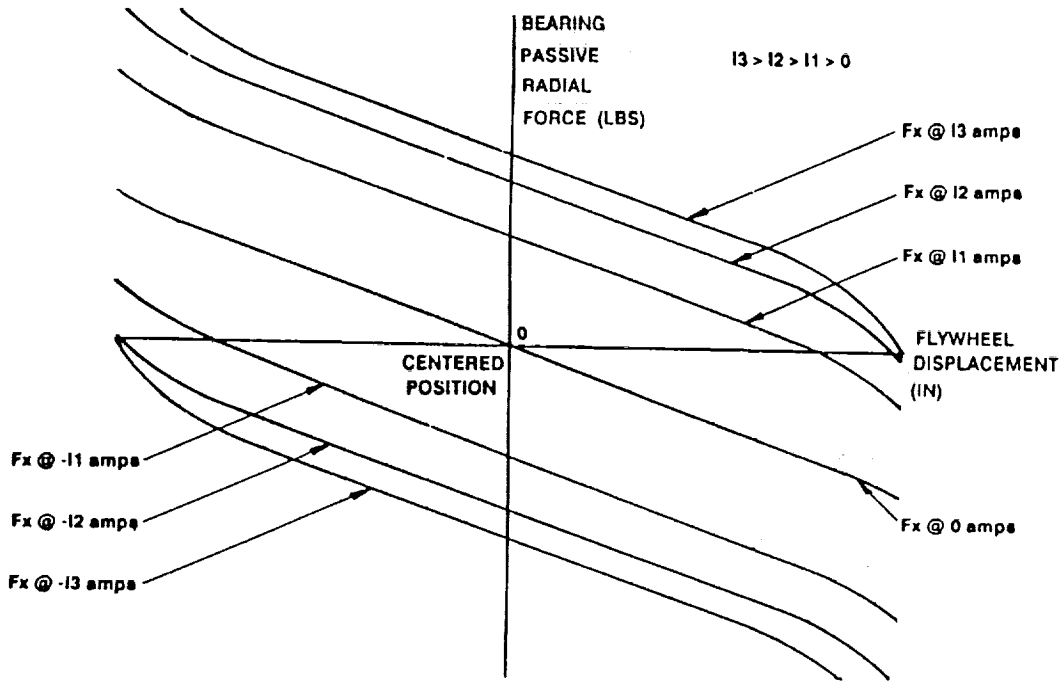

Fig. 6 Radial Bias Force vs. Displacement

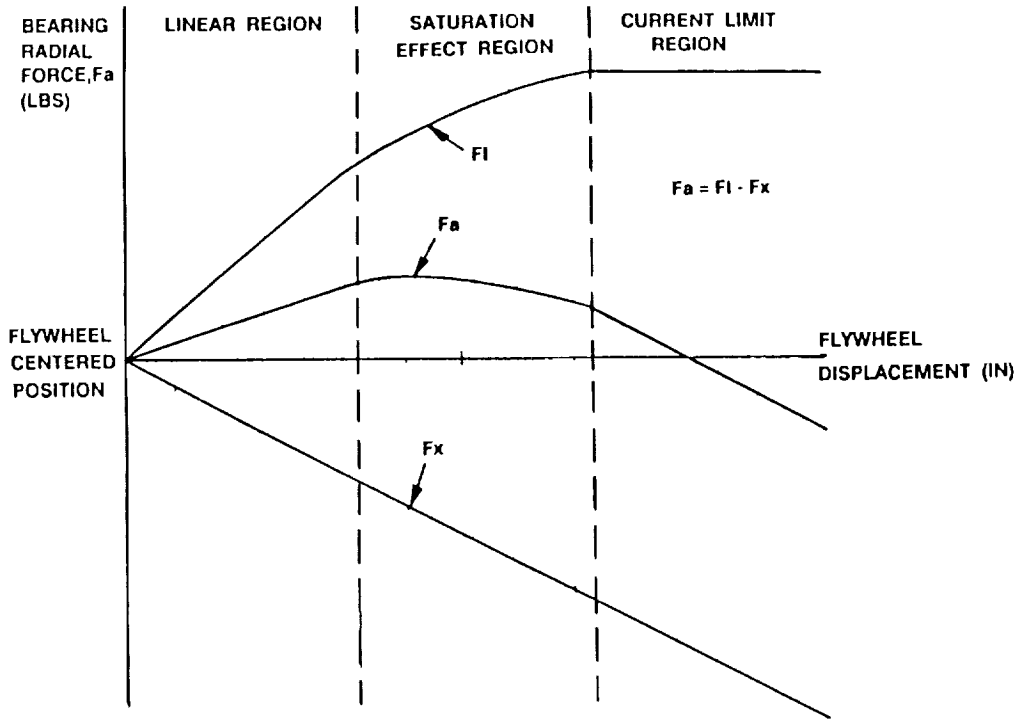

Fig. 7 Bias, Coil and Restoring Force vs. Displacement

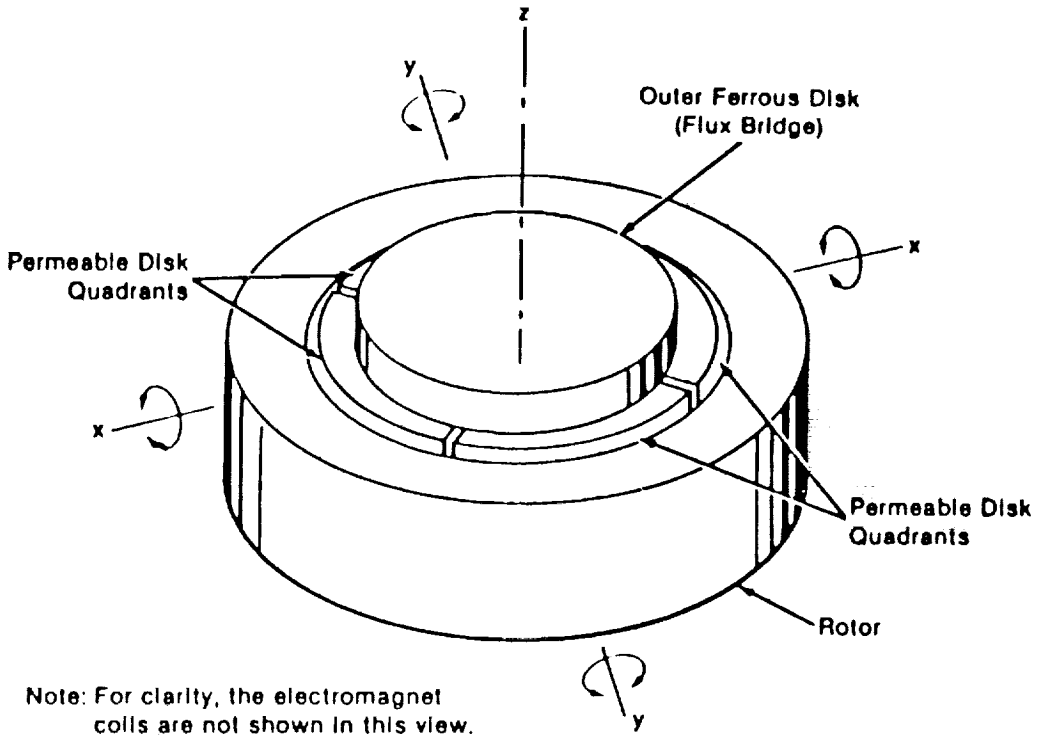

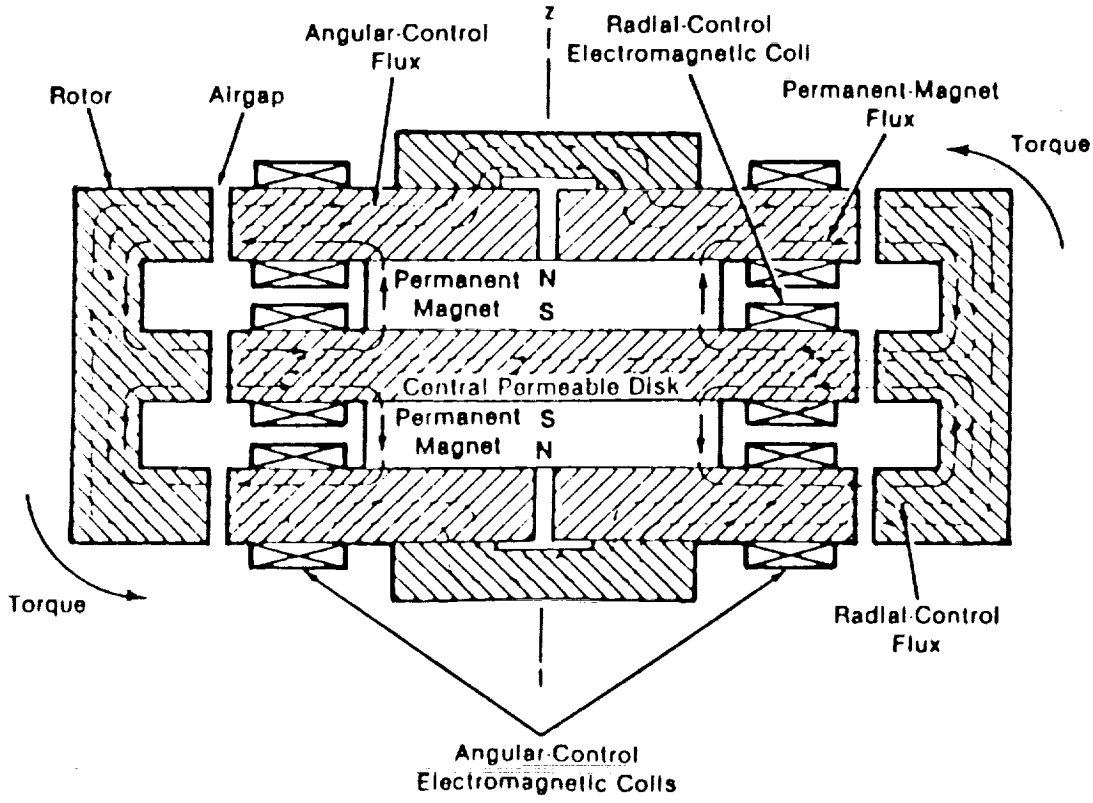

Fig. 8 Off-Axes Torque Control Magnetic Bearing

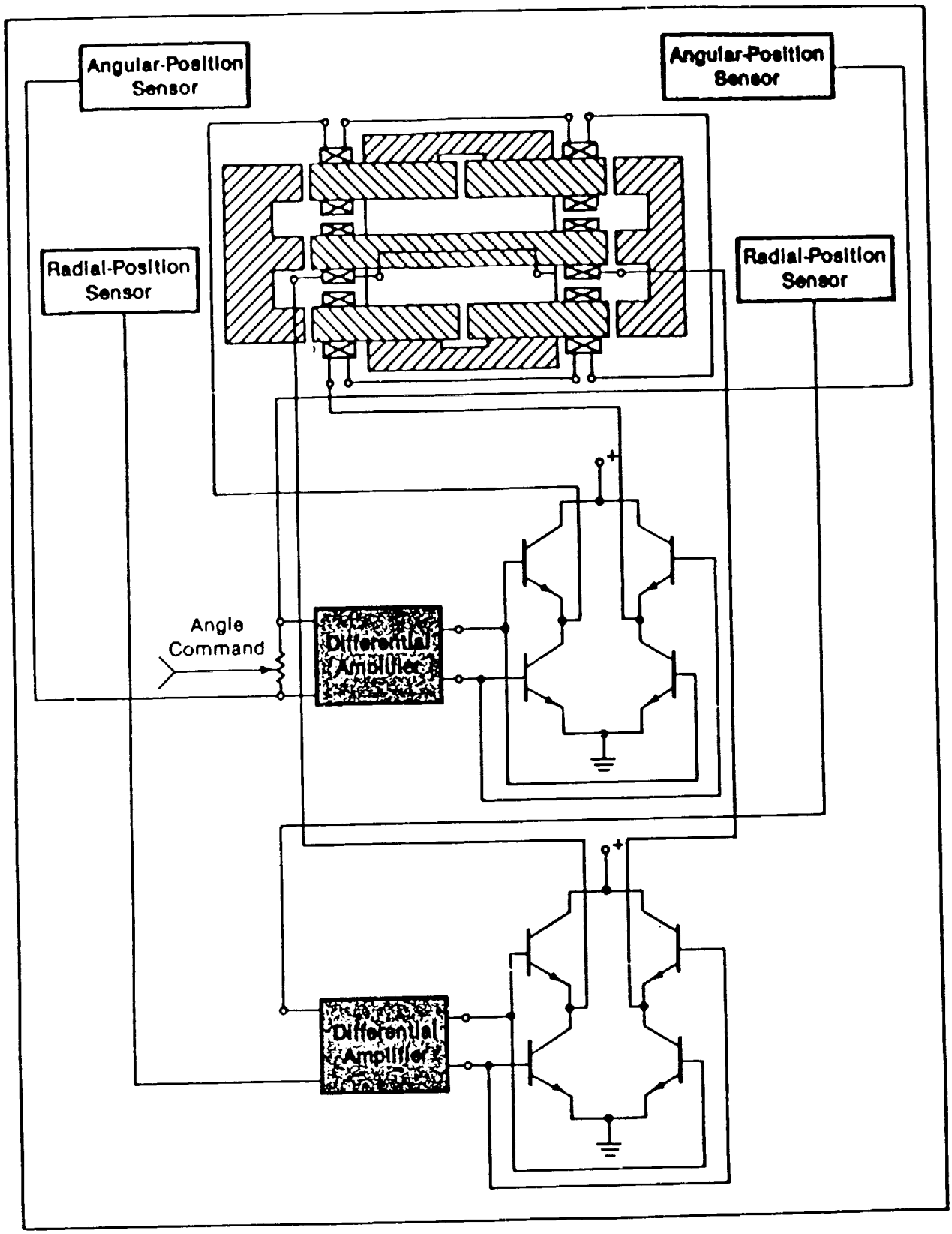

Fig. 9 Control System for Off-Axes Torque control Bearing

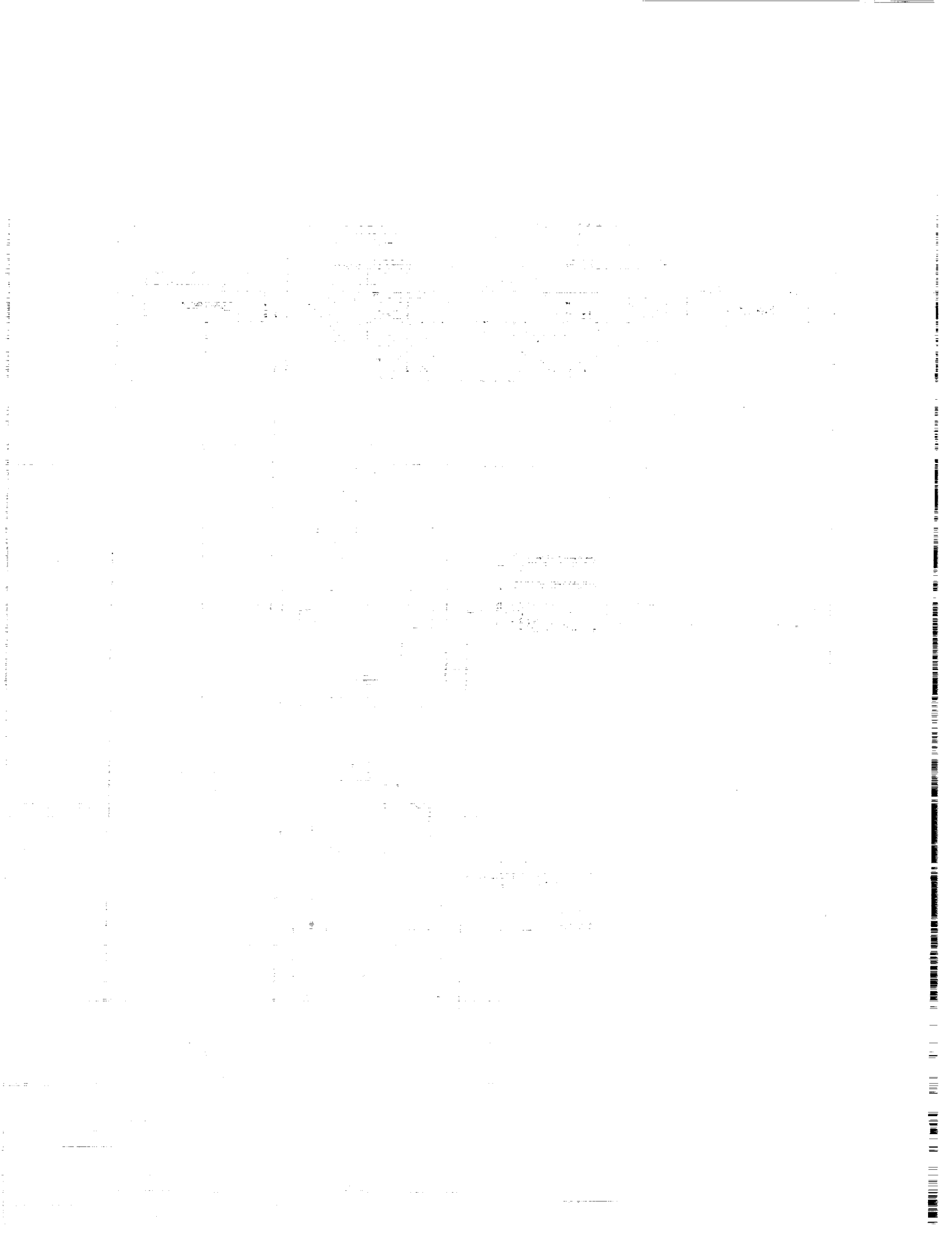

omit

Session 5

Superconductors

Chairman: David B. Eisenhaure

SatCon Technology Corporation

OMIT

Development of Superconducting $YBa_2Cu_3O_x$ Wires with Low Resistance Electrical Contacts

R. Caton, R. Selim, Christopher Newport College

B.I. Lee, V. Modi, M. Sherill, H.D. Leigh, C.C. Fein, Clemson University

A. Martin Buonocristiani, Charles E. Byvik, NASA Langley Research Center

DEVELOPMENT OF SUPERCONDUCTING $YBa_2Cu_3O_x$ WIRES WITH LOW RESISTANCE ELECTRICAL CONTACTS

R. Caton* and R. Selim*
Christopher Newport College
Newport News, Va

B. I. Lee**, V. Modi**, M. Sherrill**, H. D. Leigh**, C. C. Fain**
G. Lewis**, and C. H. Barron**
Clemson University
Clemson, SC

A. M. Buoncristiani† and C. E. Byvik
NASA Langley Research Center
Hampton, VA

SUMMARY

Materials exhibiting superconductivity above liquid nitrogen temperatures (77 K) will enable new applications of this phenomena. One of the first commercial applications of this technology will be superconducting magnets for medical imaging. However, a large number of aerospace applications of the high temperature superconducting materials have also been identified. These include magnetic suspension and balance of models in wind tunnels and resistanceless leads to anemometers. The development of superconducting wires fabricated from the ceramic materials is critical for these applications. The progress in application of a patented fiber process developed by Clemson University for the fabrication of superconducting wires is reviewed. The effect of particle size and heat treatment on the quality of materials will be discussed. Recent advances made at Christopher Newport College in the development of micro-ohm resistance electrical contacts which are capable of carrying the highest reported direct current to this novel material is presented.

*Supported by NASA Grant NAG 1-796
**Supported by NASA Grant NAG 1-820
†National Research Council Resident Research Associate

INTRODUCTION

The high temperature superconductivity research program at Langley Research Center is focused on developing technology required for the early application of the new high temperature superconducting materials to aerospace systems. The near term effort addresses the fabrication of superconducting wires utilizing a process proven successful for making wires from ceramic materials. Superconducting wires will find use in airborne and spacecraft platforms as interconnects between electronic devices and to ground planes at 77 K(liquid nitrogen temperatures). Important to the exploitation of the effort to develop electronic devices (detectors, etc.) is the development of low resistance contacts which are compatible with existing electronic technology. The long term objective will merge these efforts into the development of a Superconducting-Insulating-Superconducting (SIS) thin film detector for 100 micron radiation for atmospheric remote sensing.

The following report summarizes the results of the research efforts on sample preparation techniques, the development of low-resistance contacts to the new superconducting material and the progress in forming superconducting wires using c-shaped carbon forms.

SAMPLE PREPARATION TECHNIQUE

This section focuses on the procedure for preparing $YBa_2Cu_3O_x$ (YBCO) superconducting samples using the sintering (solid-state reaction) method. The starting materials for our samples are oxide and carbonate powders. The purities of the starting materials are as follows: $BaCO_3$ - 99.997%; Y_2O_3 - 99.999%; CuO - 99.999%. The sintering method involves several steps of mixing, grinding and heat treatment (ref. 1). Systematic studies for producing better quality samples (capable of carrying relatively larger current densities) resulted in the following procedure:

1) Mixing powders of $BaCO_3$, Y_2O_3 and CuO using a mixer/mill machine.
2) Pressing pellets of 1/2" diameter using a 10 ton hydraulic press, and treating these pellets in a split tube furnace at 950 C for 8-12 hrs in air.
3) Regrinding the material in alcohol slurry using the mixer/mill machine; heating the slurry to remove alcohol, and repeating step 2.
4) Regrinding the material in alcohol slurry using the mixer/mill machine, heating the slurry to remove alcohol, and pressing the resulting powder to form 1/2" pellets for the final O_2 treatment.

5) Retreating the pellets in oxygen flow (0.2 lpm in a 1" diameter quartz tube) at 950 C for 24 hrs, cooling down the pellets to 700 C and treating for 16 hrs, then cooling to 400 C and treating for 5 more hours.

The resulting samples are hard, black and brittle. Resistance measurements indicate a sharp superconducting transition with an onset temperature of 93 K and a transition width of 1 K.

Figure 1 shows the resistance of two samples after air treatment. One sample was pressed into a pellet before the air treatment while the other was treated as compacted powder. They were subsequently given an additional air treatment as pellets. It is clear that we get better results by pressing the samples before the air treatment.

Figure 2 shows the effect of duration of the air treatment. All samples were given the initial air treatment indicated on the graph followed by a 24 hour air treatment and oxygen treatment. The resistance results suggest that treating samples for periods of 8 to 12 hrs is sufficient to produce a transition temperature of 92 K and little improvement for samples treated for longer periods. Similar results were obtained for the time of the second air treatment.

Figure 3 shows the effect of hand grinding (HG) where the sample was ground by hand using a mortar and pestle, machine grinding (MG) using a mixer/mill machine, and machine grinding in alcohol (AG). All samples underwent two air treatment and a final oxygen treatment. Alcohol ground sample has a higher transition temperature.

We have found that using the results in figures 1-3 to develop the sample preparation procedure described earlier results in dense samples with mass density of 5.7 g/cm^3 (90% of the theoretical value) and a relatively larger current density that is limited only by grain effects present in polycrystalline bulk superconductors (ref. 2). Using this procedure we obtained critical current density J_c of 200 A/cm^2 at 77 K and J_c of 480 A/cm^2 at 20 K.

LOW-RESISTANCE CONTACTS

Since the new high T_c superconductors are ceramics, electrical contact to these novel materials presents a challenge. While silver paste and pressure

contacts can be used to measure the resistive transition, their inability to carry large currents without burning out make them unsuitable for determining large critical currents directly or for use in high current carrying applications (refs. 3 and 4).

Following previous work on gold contacts to sapphire (ref. 5), we form the contacts by placing small squares of gold foil on the surface of a shaped resistivity sample that has been cut from a fully oxygen treated pellet. The gold squares are ≈ 1 mm on a side (or less) and 0.1 to 0.3 mm thick (the thicker pieces for current contacts and thinner for voltage contacts). We then bring the sample to ≈ 1065 °C in air in from one half to one hour. The gold melts and diffuses into the sample pores. The sample is removed from the oven once it has cooled to ≈ 900 °C. At this point the gold bead that is formed is slightly oxidized and firmly connected to the sample; however, the contact resistance is high (≈kohms). Since some of the oxygen is lost from the sample during this process, retreatment in oxygen is necessary.

Restoration of the superconducting properties and good electrical contact are achieved by the following: expose to flowing oxygen (≈ 0.2 lpm) at 900 °C for 24 hr, 700 °C for 16 hr, and 400 °C for 8 hr. The slight oxide coating remaining on the gold bead after retreatment is abraded off before soldering wires to the bead for measurement. It is easy to solder external leads to the beads making good electrical contact. Lead-tin solder can be used if the temperature of the soldering iron is kept to a minimum. This relatively simple technique promises to be of practical use in many applications of high T_c superconductors.

Figure 4 shows a macroscopic scanning electron microscope (SEM) picture of a typical bead of diameter ≈ 1 mm with a copper wire soldered in place. All measurements of resistance were made in a closed cycle refrigerator capable of covering the temperature range of 15 to 300 K. The samples were mounted on a copper block with GE varnish for thermal contact and lens paper soaked in GE varnish for electrical insulation. A calibrated platinum thermometer (good to 0.1 K) mounted in a well directly below the sample was used to measure the temperature. A four probe dc method was used to measure the resistance of the sample and the contact resistance (see inset of figure 5). Each data point represents an average of twenty readings with the current reversed each time to eliminate thermal offsets (with a precision of ≈0.1%). Figures 5 and 6 show typical resistance vs temperature runs using gold bead contacts and silver epoxied leads bonded to sputtered gold films. Each figure

displays the resistance of the sample only (curve a) and the resistance of the sample plus two current contacts (curve b) after adjusting for the different length of sample between the current and voltage leads. Our best sample contacts show resistances of < 50 $\mu\Omega$ below the superconducting transition and < 18 $m\Omega$ at room temperature. We can only report an upper limit since the resistance we measure includes the solder and gold bead. Since the area of the beads is typically 0.01 cm^2 the surface resistivities are < 0.5 $\mu\Omega cm^2$ and 180 $\mu\Omega cm^2$ respectively. Figure 6 shows that the contact resistances for epoxied leads bonded to sputtered gold films is considerably higher: $\approx$ 0.2 Ω per contact at 77 K. The gold bead contacts are clearly superior.

Poor contact hampers direct measurement of critical current densities. With silver paint contacts we were typically obtaining critical current densities up to 30 A/cm^2 which did not vary much with temperature. Feeling that these were spurious due to the local heating effects of the high resistance of the silver paste contacts (especially once they burn out), we made measurements on similar samples with the gold bead contacts. We obtained 200 A/cm^2 at 77 K and > 480A/cm^2 at 20 K. A current of 7.5 ampere was passed through the sample while making the critical current measurement at 20 K in vacuum with the sample bonded to a copper block. If the contacts can perform that well in vacuum, they should present no problem in high current carrying applications where the devices will most likely be immersed in liquid nitrogen.

The strength of the contact was determined by measuring the force necessary to cause shear failure of a contact of given area. The results varied among the samples so we report the range, the average value, and the standard deviation of the shear strength. The gold beads ranged from 5 to 23 MPa with an average of 13 $\pm$ 6 MPa; the epoxy ranged from 4 to 11 MPa with an average of 8 $\pm$ 3 MPa; and the silver paste ranged from 0.6 to 1.7 MPa with an average of 1.2 $\pm$ .8 MPa. The gold bead contacts were the strongest, having a shear strength about 1/20 that of iron while that of the silver paste was about the same as concrete. In some cases the sample failed before the gold bead contact.

The contacts have the clear advantage of being reasonably robust making it possible for the leads attached to the contacts to withstand mechanical stress without need for support.

DEVELOPMENT OF SUPERCONDUCTING WIRE

Clemson University has recently demonstrated a technique to produce ceramic fibers using its C-shape carbon fibers (reference 6). In this technique, ceramic fibers are formed by filling c-troughs of the carbon fibers (CF) (fig. 7) with a ceramic precursor sol or a fine slurry followed by pyrolyzing the CF. This technique was thought to be equally applicable in fabricating superconducting fibers from the new ceramic oxide superconductor.

Since the discovery of the new ceramic high Tc superconductor, Clemson University has also developed a simple way (refs. 7 and 8) to produce high quality YBCO powder. Moreover, it has developed a method to produce a YBCO material by way of a homogeneous solution called a sol-gel technique. Thus, it is the objective of this study to develop methods to obtain strong and flexible fibers or wires which are superconducting above the temperature of the boiling point of liquid nitrogen.

The C-shape of CF were produced by the procedure described in reference 6. Two kinds of C-shape CF were used. One is heat treated at 240 C for crosslinking and the other one is carbonized at 1500 C. YBCO sol was prepared by dissolving alkoxides of yttrium and barium and copper cyclohexanebutyrate in an organic solvent in a nitrogen atmosphere under refluxing conditions: A YBCO powder dispersion (b) was prepared in the following steps. The carbonized CF were pretreated to improve wetting by YBCO A or B. The pretreatments included soaking the CF in concentrated HNO3, heating in air @400 C, or soaking in ethanolic 3-aminopropyltriethoxysilane. Bundles of the uncarbonized CF and the surface treated carbonized CF were dipped into YBCO A or B. The wet fibers were dried in air followed by heat treatments in air, oxygen or nitrogen at 500 C, 600 C or 900 C. To prevent CF from oxidizing, the YBCO coated fibers were heat treated in nitrogen gas at 900 C followed by oxygen annealing at 400 C. In some cases, silver oxide powder (10-50 V/O) was added to YBCO B to furnish oxygen in situ for firing in nitrogen gas and the resulting silver to increase ductility of the fibers. Cotton threads in various lengths were impregnated with YBCO A or B followed by direct heat treatments at 910 C in air, or the impregnated threads were coated with silver paint prior to heat treatments. Resistance vs temperature curves were obtained by using AC four-point probe and silver paste and indium pads.

Figure 8 shows an SEM micrograph of the YBCO powder used in the slurry B. It shows submicron size of particles after 8 hrs. ball-milling in ethanol.

Figure 9 shows the superconducting transition temperature of 94 K where the resistance is zero. As shown in figure 10, a wafer derived from YBCO sol A after firing in air has no transition above 77 K. This is thought to be the incorrect stoichiometry of the sol. The composition of the sol is currently being determined. Figure 11 shows the CF after coated with YCO A or B with or without silver oxide followed by heat treatments in nitrogen at 940 C for 2 hours and oxygen annealing at 400 C for 8 hours. The YBCO containing CF were too brittle and showed little strength. These poor mechanical properties should be caused by the reactions between carbon and YBCO during nitrogen firing and/or the oxygen annealing at 400 C. It is conceivable that carbon provides a reducing condition during the firing in nitrogen gas. In that case, oxygen annealing should have no effect in restoration of the superconductivity of the fibers.

Figure 12 shows wires produced by impregnating a cotton thread and coated with silver paint followed by firing in air for 6 hours at 910 C. The wires are flexible and mechanically moderately strong. However, the surface is not so uniform resulting from the all manual process. Figure 13 shows a resistance versus temperature curve indicating the wires are superconducting above 77 K. The low resistance throughout the temperature region is due to the silver conductivity. It clearly shows the superconducting transition above the liquid nitrogen temperature. The wire showed good ductility originating from the silver. Refinement of the technique to produce more uniform surface of the wire is underway.

ACKNOWLEDGMENTS

We wish to acknowledge the efforts of Raquel Caton and Robert Harvey for preparing samples.

REFERENCES

1. Xiao-Dong Chen, Sang Young Lee, John P. Golben, Sung-Ik Lee, R, McMichael, Yi Song, Tae W. Noh, and J.R. Gaines, Rev. Sci. Instrum. **58**, 1565 (1987).

2. D.S. Ginley, E.L. Venturini, J.F. Kwak, R.J. Baughman, B. Morosin, and J.E. Schirber, Phys. Rev. B **36**, 829 (1987).

4. Caton, R.; Selim, R.; Buoncristiani, A.M.; and Byvik, C.E.: "Rugged Low-Resistance Contacts to the High Tc Superconductor YBa2Cu3Ox." Meeting of the American Physical Society, March 1988.

5. Caton, R.; Selim, R.; Buoncristiani, A. M.; and Byvik, C. E.: "Rugged Low-Resistance Contacts to YBa2Cu3Ox," Applied Physics Letters, Vol. 52, March 21, 1988, pp. 1014-1016.

6. C. Varmazis, R. Viswanathan, and R. Caton, Rev. Sci. Instrum. **49**, 549 (1978).

7. N. Mack, C. C. Fain, T. D. Taylor, J. Cogburn, and D. D. Edie, "Piggybacks: A Unique Process for Forming Ceramic Fibers and Ceramic/Carbon Bicomponent Fibers," NASA Conf. Pub. 2482, Metal Matrix, Carbon, and Ceramic Matrix Composites, 1987, J. D. Buckley, ed, p.169.

8. B. I. Lee, V. Modi, and M. Sherrill, "YBCO Superconductor Via Nitrates," Accepted for Presentation at 90th Am. Ceramic Soc. Annual Meeting, May 1-5, 1988, Cincinnati, OH.

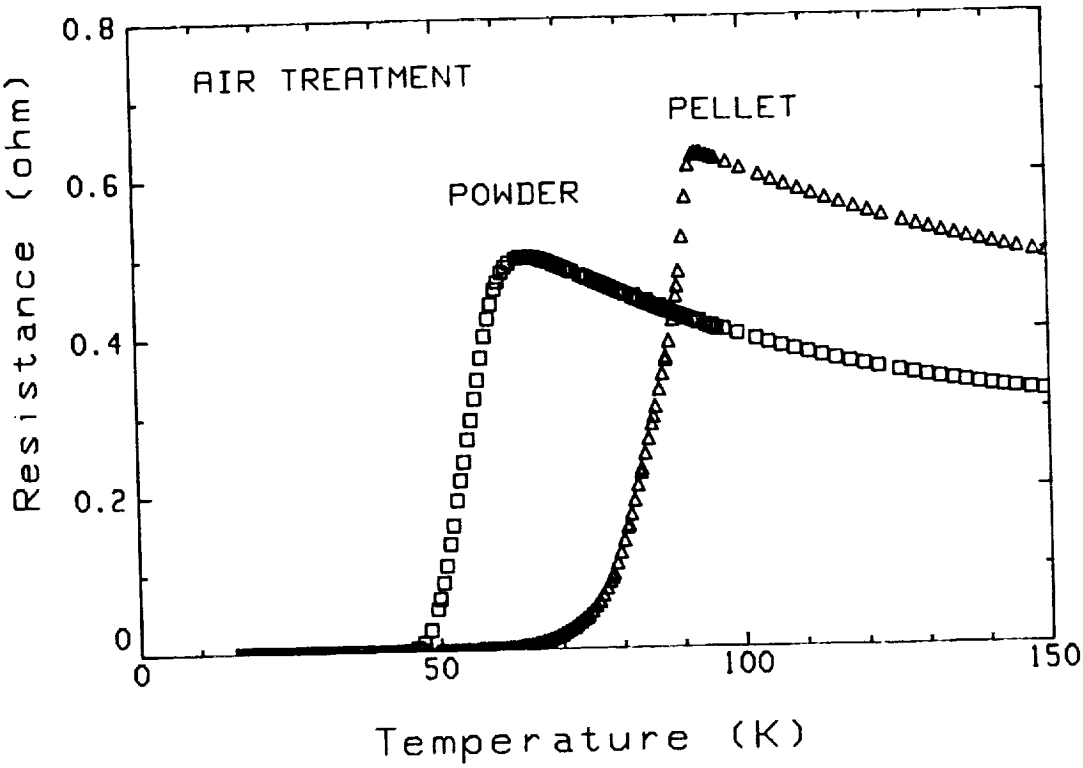

1. Resistance vs temperature for a pressed pellet and a compacted powder sample.

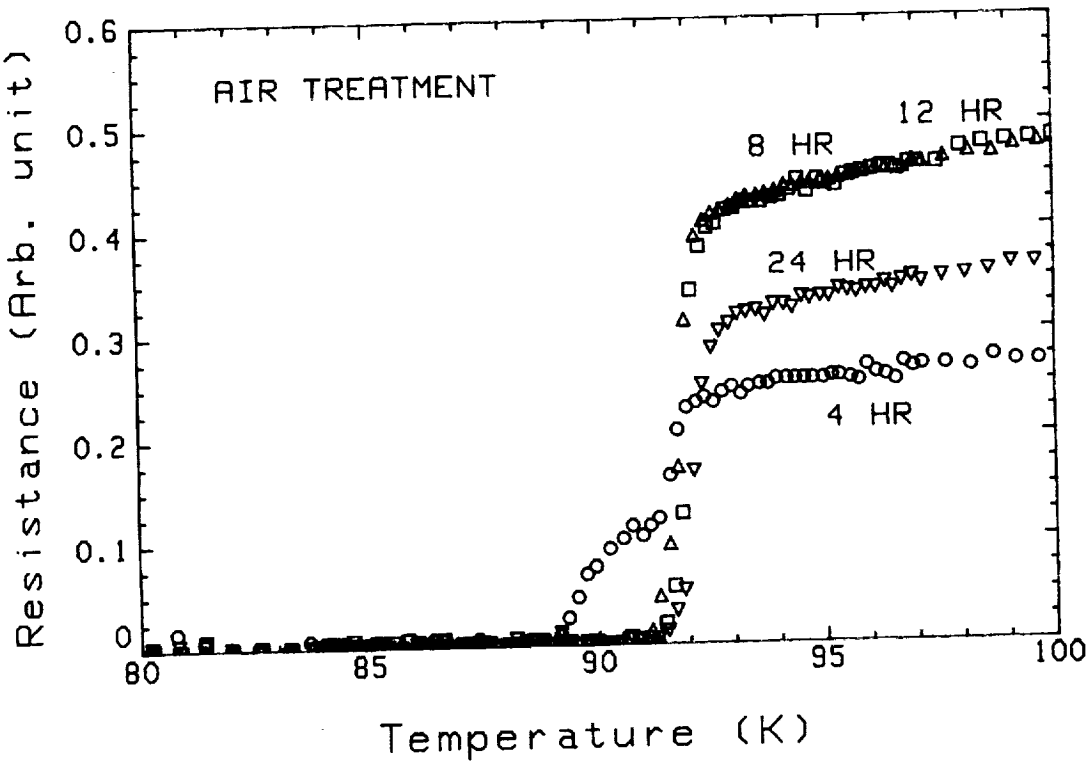

2. Resistance vs temperature for 4 samples showing the effect of air treatment for 4, 8, 12 and 24 hours.

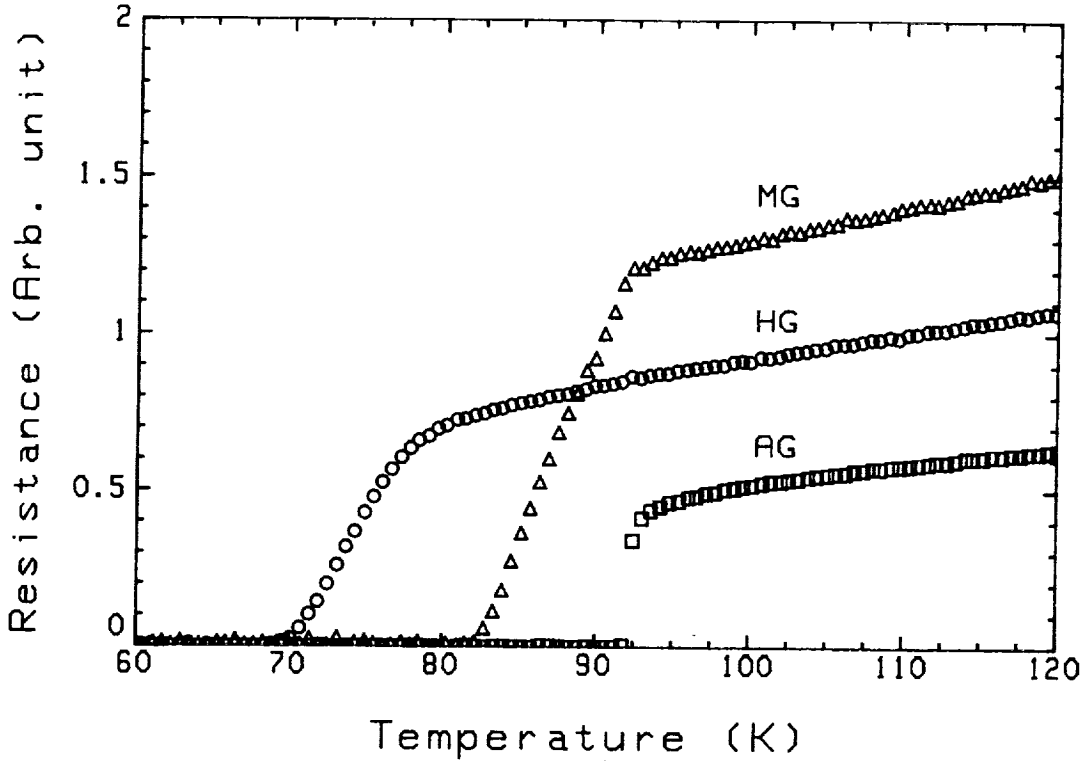

3. Resistance vs temperature for 3 samples showing the effect of hand grinding (HG), machine grinding (MG) and grinding in alcohol slurry (AG).

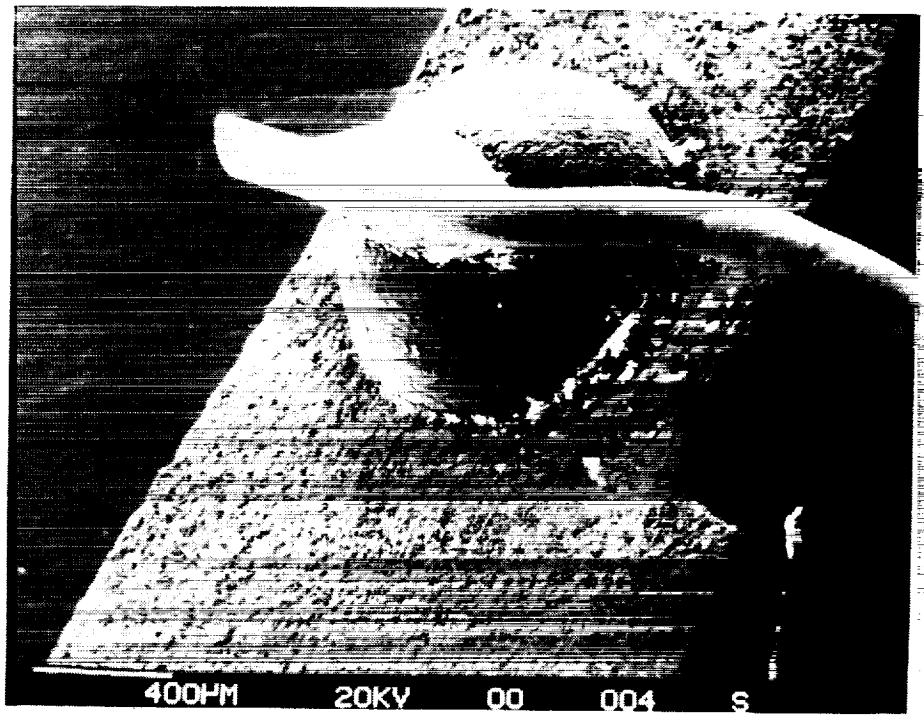

4. Macroscopic SEM picture of a gold bead contact with a soldered copper lead.

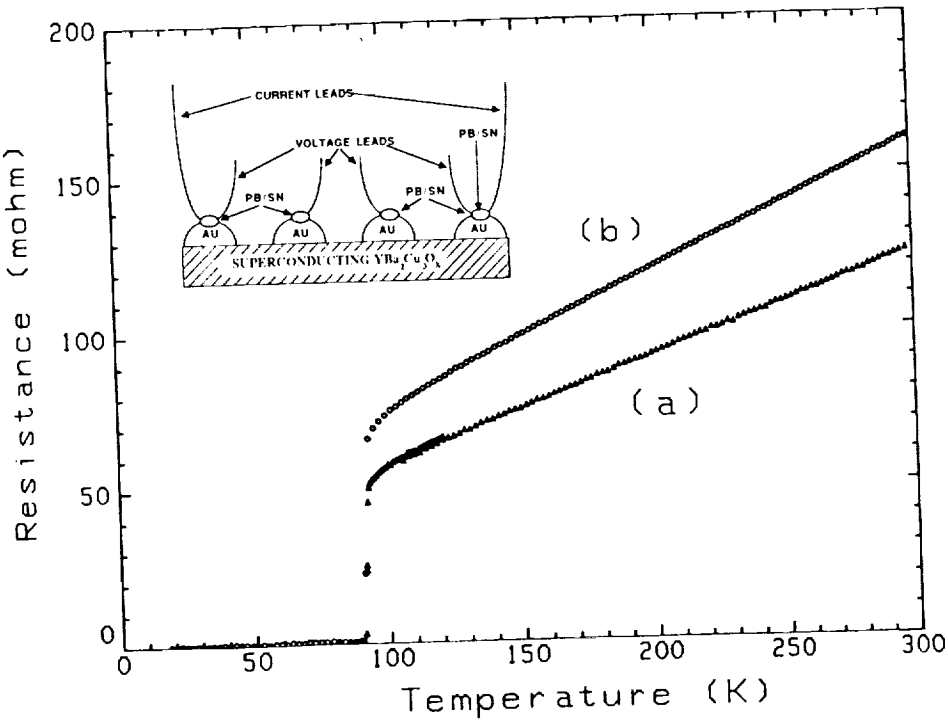

5. Resistance vs temperature for the gold bead contacts. Curve a is the resistance of the sample only. Curve b includes the resistance of two contacts. The inset is a schematic diagram of the contacts made to the sample for resistance measurement.

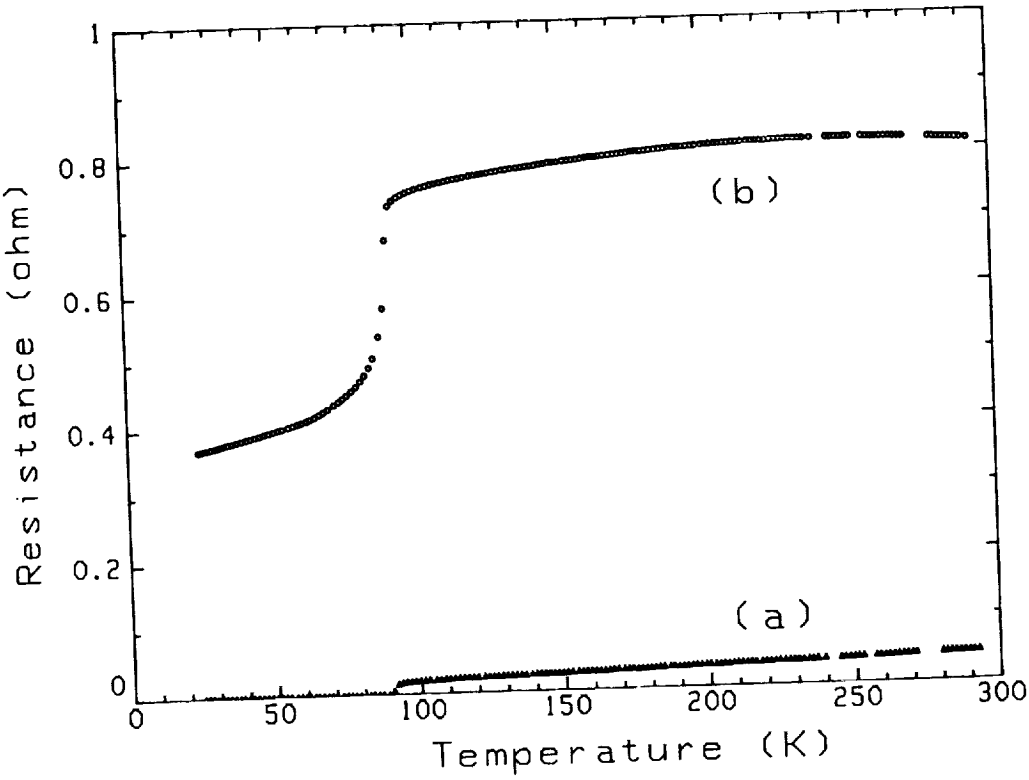

6. Resistance vs temperature for the epoxy to metal film contacts. Curve a is the resistance of the sample only. Curve b includes the resistance of two contacts.

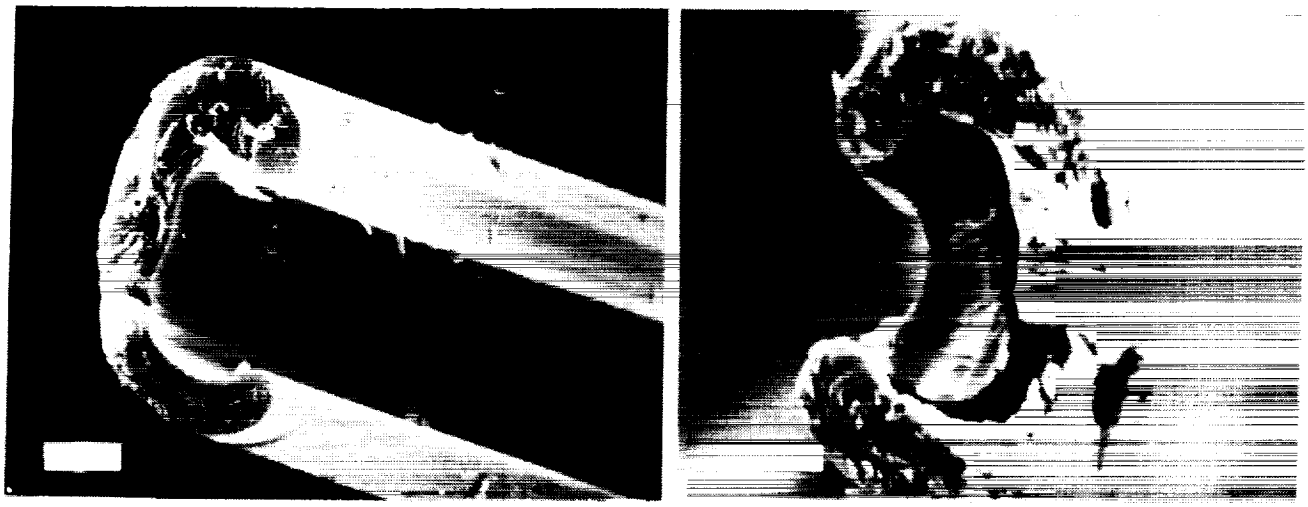

Figure 7. A C-shape carbon fiber derived from a petroleum pitch (left), the C-trough filled by a silica precursor sol (right).

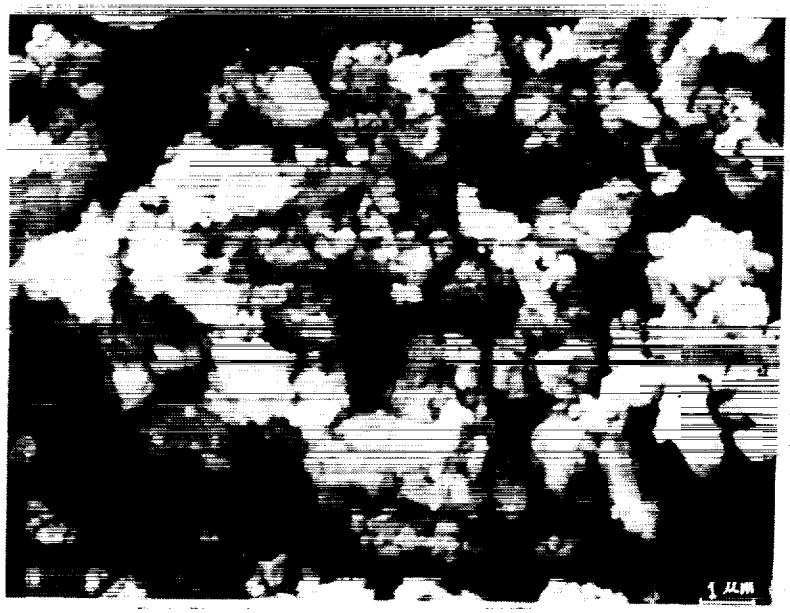

Figure 8. A scanning electron micrograph of YBCO powder after ball milling.

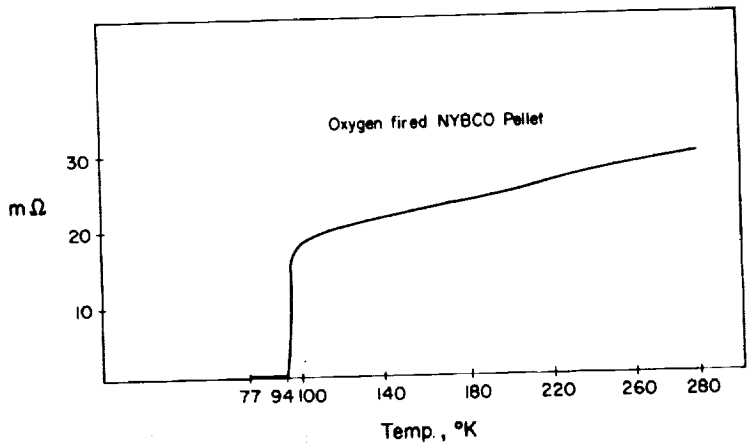

Figure 9. Resistance as a function of temperature for YBCO powder derived directly from nitrates of yttrium, barium and copper.

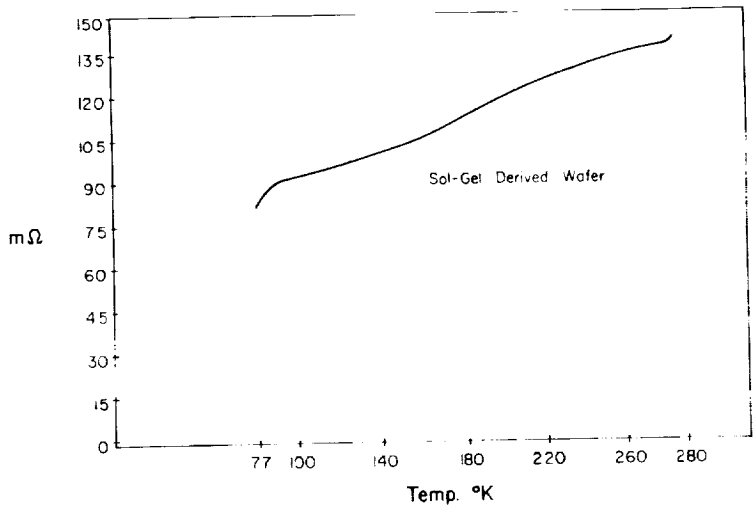

Figure 10. Resistance as a function of temperature for Sol A.

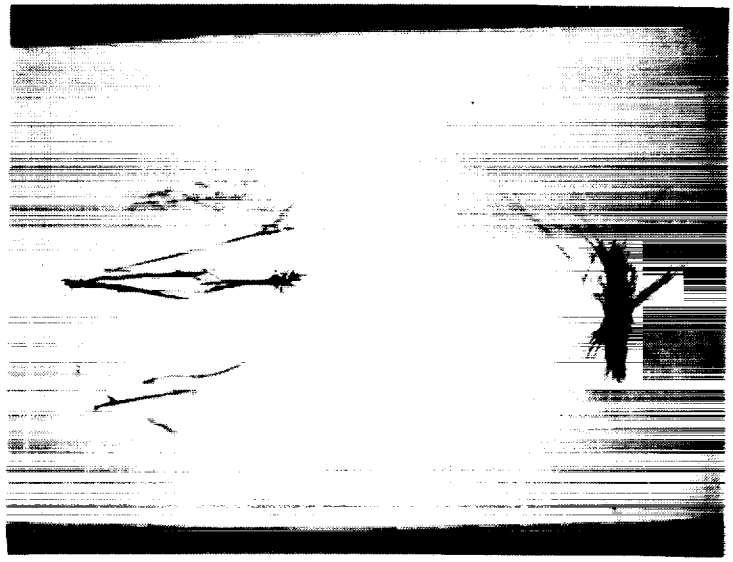

Figure 11. CF before dipping in YBCO Sol (left) and after dipping and firing (right).

Figure 12. Superconducting wires produced by impregnation of cotton threads.

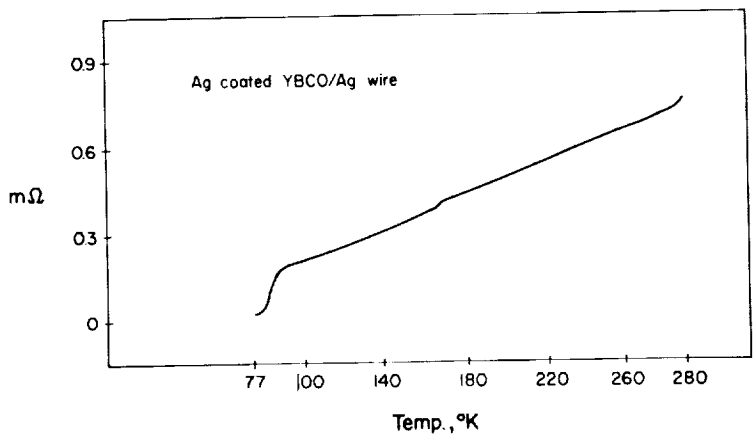

Figure 13. Resistance as a function of temperature for wires in figure 12.

omit

The Role of Superconductivity in Magnetic Bearings for High-Load Applications

James Downer, David B. Eisenhaure, SatCon Technology Corporation

S22-37

N93-27562

THE ROLE OF SUPERCONDUCTIVITY IN MAGNETIC BEARINGS FOR HIGH-LOAD APPLICATIONS*

James Downer and David Eisenhaure
SatCon Technology Corp.
Cambridge, MA

SUMMARY

Slewing of large payloads will require control torque and angular momentum storage capacities that are large in comparison to the capabilities of available control moment gyros (CMGs). SatCon Technology Corporation is currently designing a CMG which may be employed as a slew actuator for large spacecraft or other payloads. The slew actuator employs a novel type of magnetic bearing which may be used in high load applications. The magnetic bearing is also used to fully gimbal the suspended rotor of the slew actuator.

The use of magnetic bearings in angular momentum exchange actuators has the primary advantage that physical contact between the rotor and stator is eliminated. This leads to greatly extended life, increased reliability, and reduced vibrations. Several actuators operating on magnetic bearings have been demonstrated in previous research efforts. These were sized for use in small satellites. For conventional magnetic bearings, which employ magnetic cores, high torsional loading may require that the magnetic structure be excessively massive.

This paper discusses an alternative magnetic bearing design which employs a superconducting coil and eliminates conventional magnetic structures. The baseline approach is to replace the field coil of a conventional magnetic bearing with the superconducting coil.

INTRODUCTION

This paper discusses a novel approach to the design of magnetic bearings in which a superconducting coil is employed in order to eliminate conventional magnetic cores and permanent magnets. The design was motivated by recent progress in superconducting materials and by the requirements for an advanced control moment gyro (CMG) type of slew actuator which is currently under development at SatCon Technology Corporation. The slew actuator is intended for use with large spacecraft.

In order to present the superconducting magnetic bearing, a chronological description of the design process is presented. First, the application and specifications for the slew actuator are derived. Next, a brief discussion of the operating principles for a CMG is presented. A discussion of recent advances in superconducting

*This research was supported by the NASA Langley Research Center

materials, particularly "high-temperature" superconductors is used to motivate the decision to apply this technology to a high-performance magnetic bearing. A baseline superconducting magnetic bearing design is presented. Finally, the performance of the magnetic bearing is compared to that of more conventional approaches. These results show that substantial improvements in mass and power consumption are obtainable through the use of superconducting technology.

SLEWING MANEUVERS FOR SPACECRAFT

Many civilian and military space missions require that the angular orientation (attitude) of a spacecraft be controlled over large angles. The purpose of a slew maneuver is to reorient a spacecraft (with moment of inertia I) through an angle (θ) in a time period (T). This section analyzes a typical slewing maneuver in order to provide specifications for the design of the slew actuator.

Bang-bang Slew Profile

One approach for accomplishing a slew maneuver is to apply a constant torque on the spacecraft for half of the maneuver time. During this acceleration period, the spacecraft will gain angular momentum. An equal but opposite torque is then applied in order to decelerate the spacecraft. Angle, angular momentum and torque profiles for this type of slew profile are shown in Figure 1.

Torque Shaping

The above analysis assumes that the spacecraft is a rigid body. In applications where this assumption is not valid, a smoother torque profile is typically employed to reduce vibrations (ref. 1). Possible torque profiles include sine-wave, double versine (1 - cosine), and sine-wave cubed. The primary effect of torque shaping on the requirements for the slew actuator is an increase in the peak control torque which is required for a given slew maneuver. During the early stages of the slew actuator design program, nine torque shapes were identified and analyzed. For the purposes of the present discussion, an eight percent increase in the peak control torque requirement will be used to account for the effect of torque shaping.

Slew Actuator Requirements

Table 1 presents the parameters (spacecraft moment of inertia, slew angle, and slew time) which define the slew. The table also presents the requirements (control torque and angular momentum storage capacity) for the slew actuator.

ANGULAR MOMENTUM EXCHANGE ACTUATORS

One approach for controlling the attitude of a spacecraft is to apply equal and opposite torques to the craft and a flywheel. The net angular momentum of the flywheel and the spacecraft will remain constant. This type of device is referred to as an angular momentum exchange effector since any angular momentum which is gained (lost) by

the spacecraft is lost (gained) by the flywheel. This type of actuation has several advantages over reaction control systems (thrusters). These include reduced maintenance and improved compatibility with optics. Thrusters operate by expelling a fluid which is stored, in tanks, on-board the spacecraft. These stores of fluid must be periodically replaced. Another advantage of angular momentum exchange effectors is that there are no effluents to disturb the on-board optics. The operating principles for the most common type of momentum exchange effector, the control moment gyro, are described below.

Control Moment Gyros (CMGs)

This type of actuator exchanges angular momentum by varying the angular orientation of a constant-speed flywheel through the use of gimbals. Figure 2 describes the acceleration phase of the slew maneuver in terms of applying a torque to a spacecraft over a fixed period of time. The torque is applied through the azimuth-axis torquer. The flywheel precesses about the elevation axis to conserve angular momentum.

Magnetic Gimballing

The use of a mechanical gimbal structure such as the one shown in Figure 2 is the conventional approach for CMG design. An alternative approach which consolidates the functions of conventional bearing and gimbal systems has been demonstrated. A large-angle magnetic suspension (LAMS) is a five-axes, actively-controlled magnetic bearing which is designed to accommodate a certain amount of angular motion about the lateral axes of the flywheel (ref. 2). An early study (ref. 3) indicated that the mass of conventional gimbal systems is approximately equal to that of the gimballed rotor. Later research (ref. 4) indicates that the mass of a LAMS can be made to be less than that of a gimbal system by a factor five (depending on the amount of angular freedom). The magnetic bearing which is described in this paper is an extension to this technology.

MOTIVATION FOR THE USE OF SUPERCONDUCTORS

The decision to employ superconductors in the design of the magnetic bearing for the slew actuator was motivated by recent progress in superconducting materials and by the drawbacks (power and mass) associated with meeting the control torque requirement for the slew actuator through the use of conventional technology. This section provides further discussion of these issues.

Recent Advances in Superconductors

Recent advances in superconducting materials have sparked new interest in a technology formerly restricted to sophisticated laboratory applications. In fact, the potential of these advances is so far reaching that numerous articles on the subject have recently appeared in the popular press (refs. 5, 6, and 7). The renewed interest in superconductivity is a result of the discovery of a new

class of materials with significantly higher transition temperature (the temperature at which superconductivity occurs). Progress on this front has been so rapid that a better than four-fold increase in transition temperature has been achieved in the past year with a new record of 98 degrees Kelvin. This temperature allows cooling to be accomplished using inexpensive liquid-nitrogen as opposed to the exotic and expensive liquid-helium previously required, thus improving the economic feasibility of numerous applications. The new materials are a class of rare-earth ceramics and are thus very brittle and fragile. In addition, at the present time they are limited in operation to current density approximately one percent of that for conventional superconductors, or roughly equivalent to normal household wiring. However, the level of intensity of research world-wide is expected to overcome these obstacles and produce usable devices in a few short years.

Deficiency of Current Approaches

Based on the results of preliminary analyses, it became obvious that conventional approaches to the design of the magnetic bearing would be excessively massive and inefficient. Thus, it was decided to turn the design toward a magnetic bearing based on superconducting technology. This decision promised significant reductions in power and weight for the following reasons:

1) The current density in a superconductor can be extremely high (on the order of 10^8 A/m^2);

2) No field-shaping iron is required;

3) Higher flux density increases the force-producing capability of conventional coils.

DESCRIPTION OF THE MAGNETIC BEARING

A superconducting magnetic bearing is an advanced design for a magnetic bearing which may be used in a CMG to deliver large torques to a spacecraft without the need for an excessively massive magnetic core or the consumption of a large amount of power. The superconducting magnetic bearing, as its name suggests, employs a superconducting coil and thus eliminates all conventional magnetic structures in order to produce an energy-efficient, light-weight design. The following paragraphs describe the construction and operation of a superconducting magnetic bearing when it is used in a large CMG.

Overall Slew Actuator Design

Figure 3 is a partially cut-away view which shows the rotating components (superconducting coil and flywheel) and cryogenic housing of a two-degree-of-freedom CMG which employs a superconducting magnetic bearing. The superconducting coil is a solenoid which operates in persistent-current mode (without an electrical input). The current in the solenoid persists because of the lack of resistance

in the superconducting material. The spherical case which surrounds the rotating components also serves as the cryostat for the superconducting solenoid.

Flywheel. A high-strength graphite/epoxy composite flywheel is attached to the solenoid to provide angular momentum storage capacity. This material is currently being used for advanced energy storage flywheels for space power applications (ref. 8). The outer diameter of the flywheel is machined to a spherical shape. This allows the flywheel to be completely gimballed without contact with the case.

Spin Motor. Figure 4 shows one phase of the multi-phase stator (armature) of an axial-field electric machine in the center (bore) of the solenoid and illustrates the operation of this device as a motor. Radial currents (I) in the stator interact with the axial flux density (B) produced by the solenoid to apply torques about the spin axis (SA) of the flywheel. Torque is applied to the rotating components of the CMG until the rotor reaches its operating speed. Drag losses will be sufficiently small that the motor need not operate continuously in order to maintain the nearly constant rotational speed required of a CMG.

Magnetic Bearing Loading

This section discusses the mechanisms which are used to apply forces and torques to the flywheel of the slew actuator. The design employs a total of twelve (12) normal (non-superconducting) coils in conjunction with the superconducting solenoid in order to apply forces and torques.

Radial Forces. Figure 5 shows two coils which are attached to the outer surface of the case of the superconducting CMG. The interaction of the magnetic field (B) produced by the solenoid and the current (I) in each differential section (dV) of the coil produces a differential force (**df**). The net force (f) produced by the two coils is perpendicular to the spin axis of the flywheel (shown as being along the x axis). Two additional sets of concentric coils are shown in Figure 6. The y-axis coils operate in the same manner as the x-axis coils in order to produce forces along the y-axis. The third set of coils is used to provide radial forces when the spin axis has a large angular displacement from the z-axis.

Axial Forces. Figure 7 shows six additional control coils. These coils are used to apply either axial forces or torques about the lateral axes. In the discussion which follows, the spin axis of the flywheel is assumed to coincide with the z-axis.

Figure 8 shows the interaction of the current (I) in the axial-force coil and the magnetic field (B) produced by the superconducting solenoid. Each differential segment (dV) of the coil has applied a differential force (**df**) to the rotor. The net result of this interaction is a force (**f**) which acts along the z-axis as is shown in Figure 8.

Torques. The coils shown in Figure 7 which are not coaxial with the spin axis of the flywheel are used to apply torques to the flywheel. Figure 9 illustrates the torquing mechanism. Assuming that the spin axis is along the z-axis, the magnetic field (B), produced by the superconducting solenoid is nearly parallel to the z-axis and constant. The torque (τ) results from the interaction of the dipole moment (μ) produced by the current (I) in the normal coil and the magnetic field.

PERFORMANCE OF THE MAGNETIC BEARING

Although the design of the superconducting magnetic bearing is not yet finalized, some preliminary estimates of the mass and power consumption of the magnetic bearing as a torquer are available. Table 2 presents these performance characteristics and compares them to the comparable characteristics for other types of CMG torquers. The performance of a conventional gimbal torquer (ref. 9), a conventional magnetic bearing (ref. 10), and a LAMS (ref. 4) are scaled from previous designs. The increased mass and power consumption of the other types of torquers result from the mass of the backiron required to shape the magnetic fields and from the power dissipated in copper coils. It should be noted that this table compares only the mass and power consumption of these torque-producing mechanisms and is not intended to show detailed system-level trade-offs.

RESULTS

A unique type of magnetic bearing has been presented. The bearing, when incorporated in a magnetically-gimballed CMG-type of slew actuator, produces an energy efficient, lightweight device. When compared to other types of torquers, the superconducting magnetic bearing produces superior performance in terms of mass and power consumption.

REFERENCES

1. Breakwell, J. "Optimal Feedback Slewing of Flexible Spacecraft," AIAA Journal of Guidance and Control, Vol. 4, No. 5, Sept-Oct 1981, pp. 472-479.

2. Downer, J., D. Eisenhaure, R. Hockney, B. Johnson, and S. O'Dea, "Magnetic Suspension Design Options for Satellite Attitude Control and Energy Storage," Proceedings of the 20th Intersociety Energy Conversion Engineering Conference, pp. 2.424-430.

3. Gross, S. "Study of Flywheel Energy Storage for Space Stations," D180-27951-1, Boeing Aerospace Corp, February 1984.

4. Downer, J., Design of Large-angle Magnetic Suspensions, ScD Thesis, Massachusetts Institute of Technology, May 1986.

5. Business Week, April 6, 1987, pp. 94-97.

6. Time Magazine, March 2, 1987, p. 62.

7. Time Magazine, May 11, 1987, pp. 64-75.

8. Olszewski, M. and D. O'Kain, "Advances in Flywheel Technology for Space Power Applications," Proceedings of the 21st Intersociety Energy Conversion Engineering Conference.

9. "Model 4500 CMG," CMGs and Momentum Wheels, Sperry Flight Systems, pp. 6.0-6.5.

10. Anderson, W. and N. Groom, "The Annular Momentum Control Device (AMCD) and Potential Applications", NASA TN-D 7866, 1975.

TABLE 1. - SLEW PARAMETERS AND ACTUATOR REQUIREMENTS

Slew Angle (θ)	1 rad.
Slew Time (T)	4 sec.
Inertia (I)	100 $kNms^2$
Control Torque (τ)	27 kNm
Angular Momentum (H)	45 kNms

TABLE 2. - RELATIVE PERFORMANCE OF THE SUPERCONDUCTING MAGNETIC BEARING AS A TORQUER (27 kNm)

Torquer Mass (kg)

Superconducting Magnetic Bearing	530
Conventional Gimbal Torquer	12,700
Conventional Magnetic Bearing	2,500
Large-angle Magnetic Suspension	5,300

Power Consumption (kW)

Superconducting Magnetic Bearing	7
Conventional Gimbal Torquer	60
Conventional Magnetic Bearing	200
Large-angle Magnetic Suspension	12

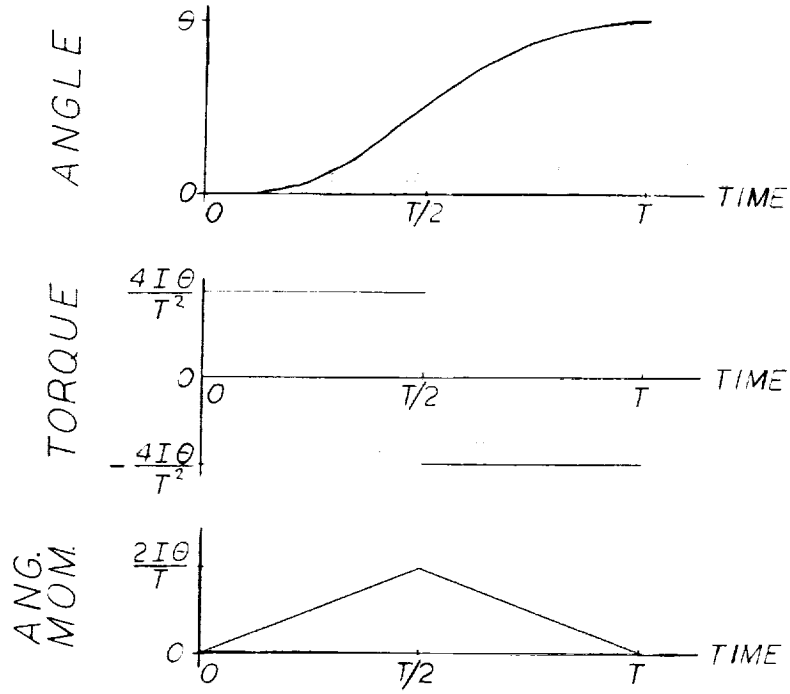

Figure 1.- Slew trajectories.

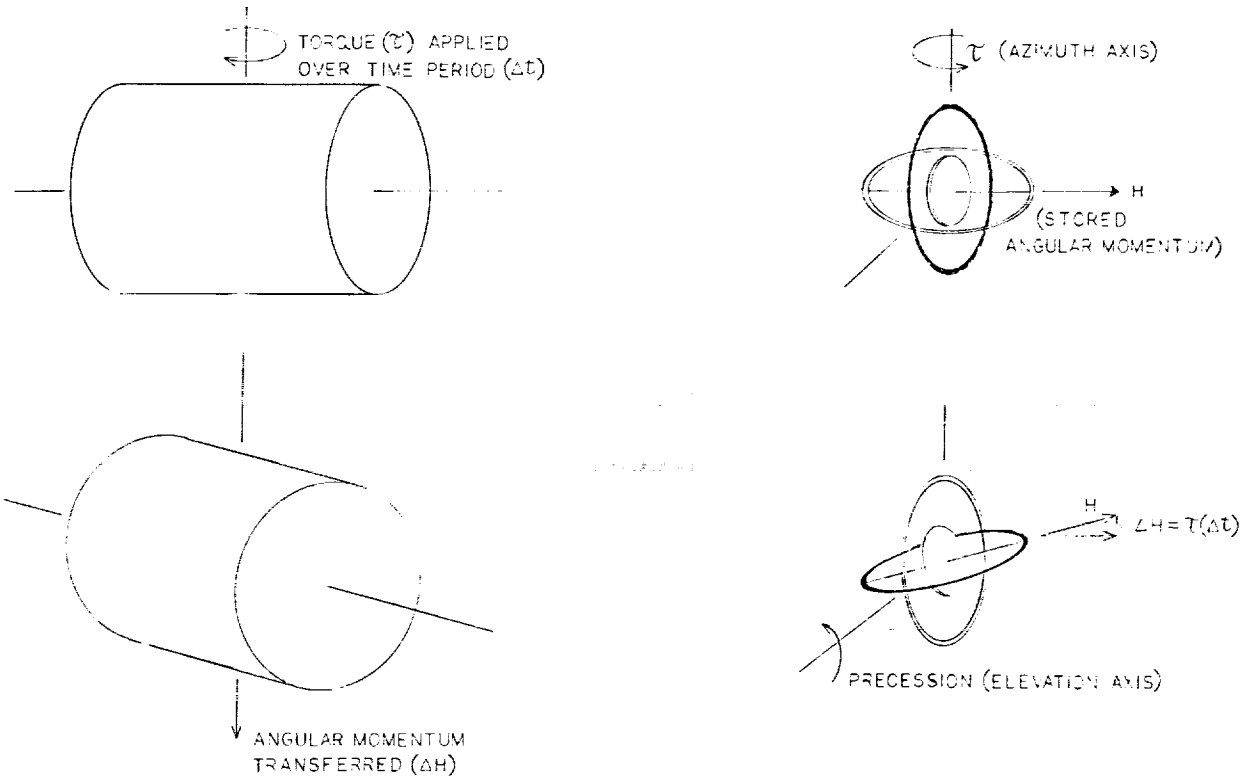

Figure 2.- CMG operating principle.

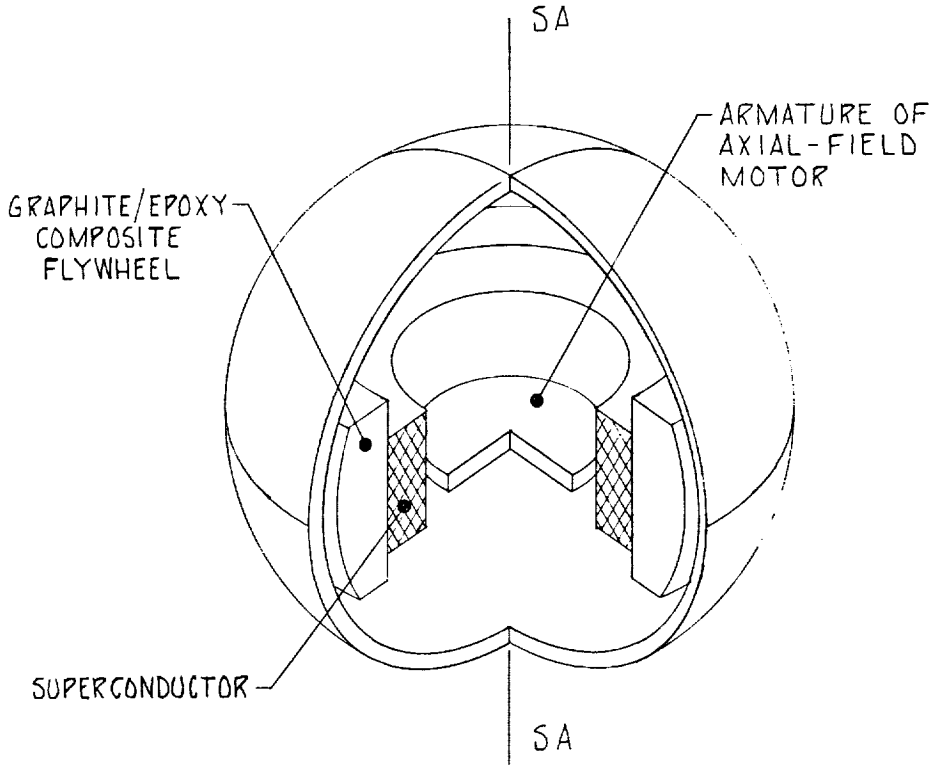

Figure 3.- Slew actuator.

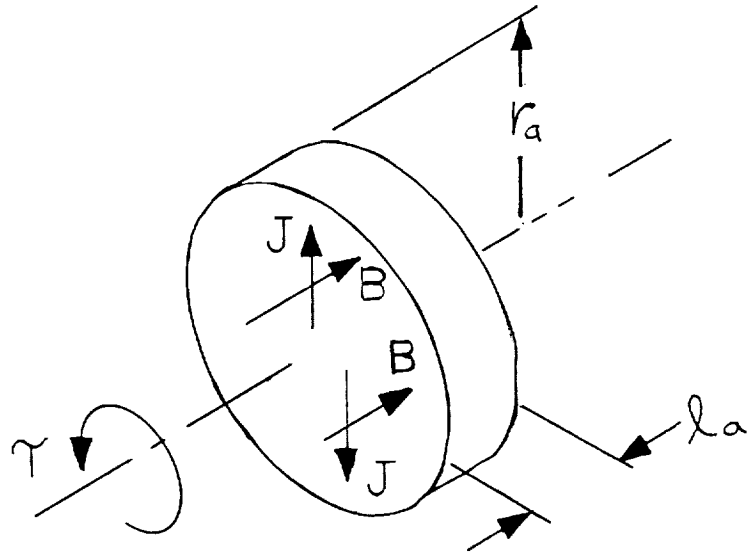

Figure 4.- Spin motor.

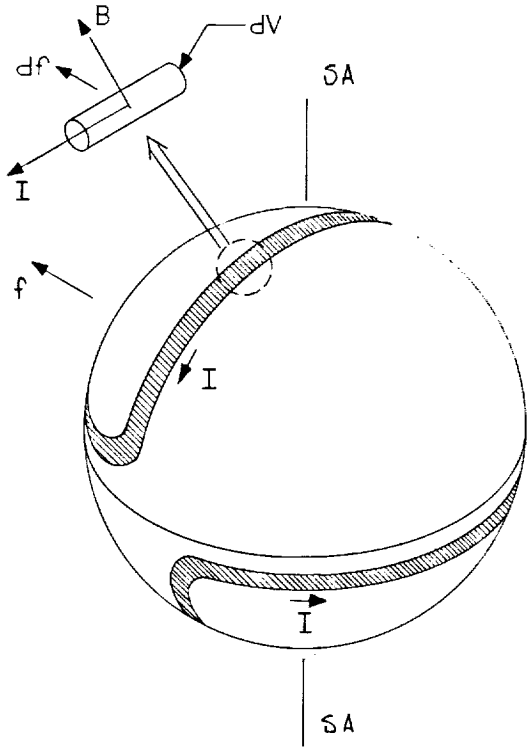

Figure 5.- Radial-force loading.

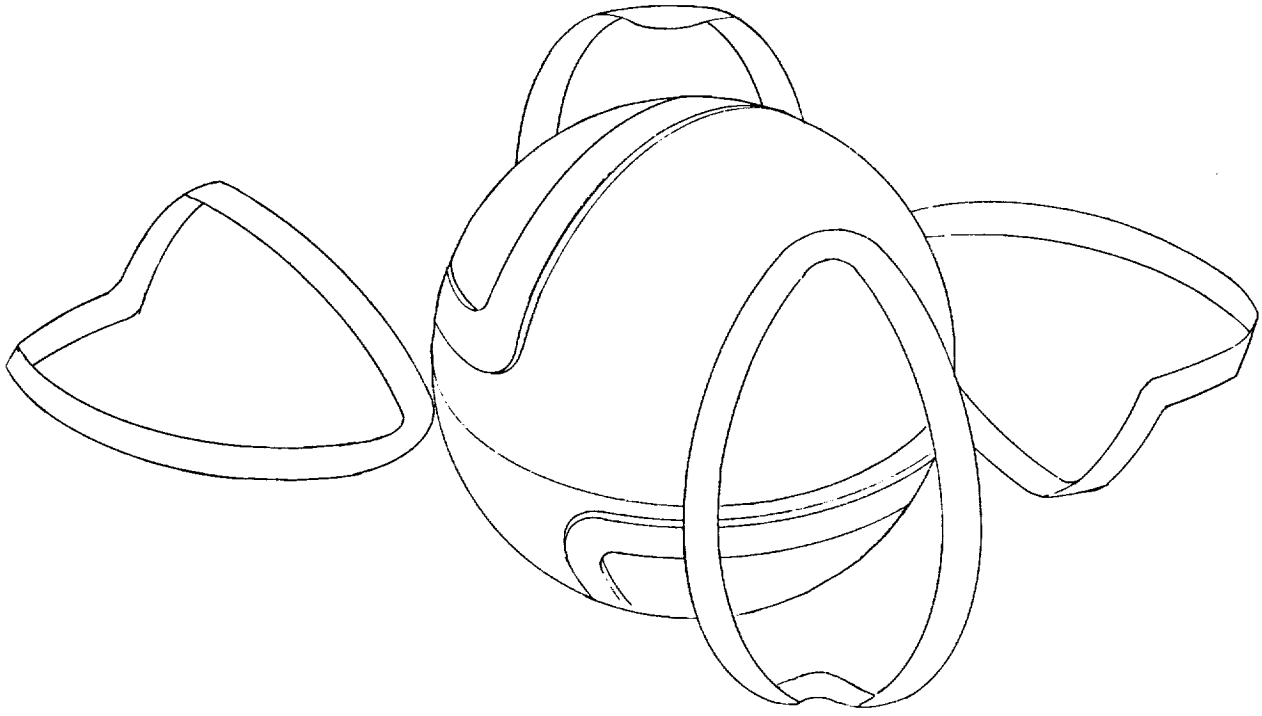

Figure 6.- Radial-force coils.

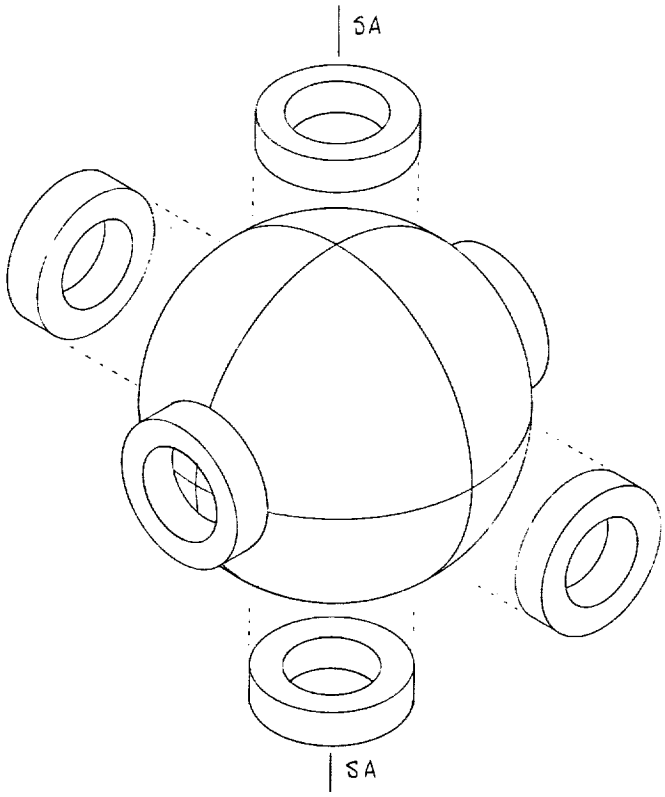

Figure 7.- Axial-force/torque coils.

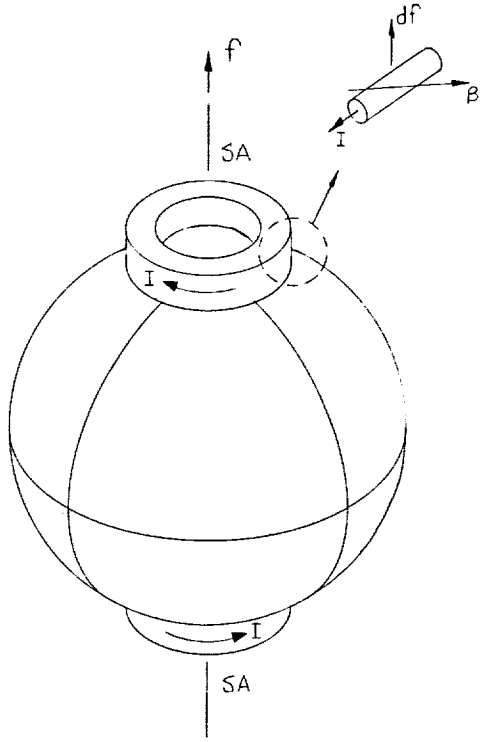

Figure 8.- Axial-force loading.

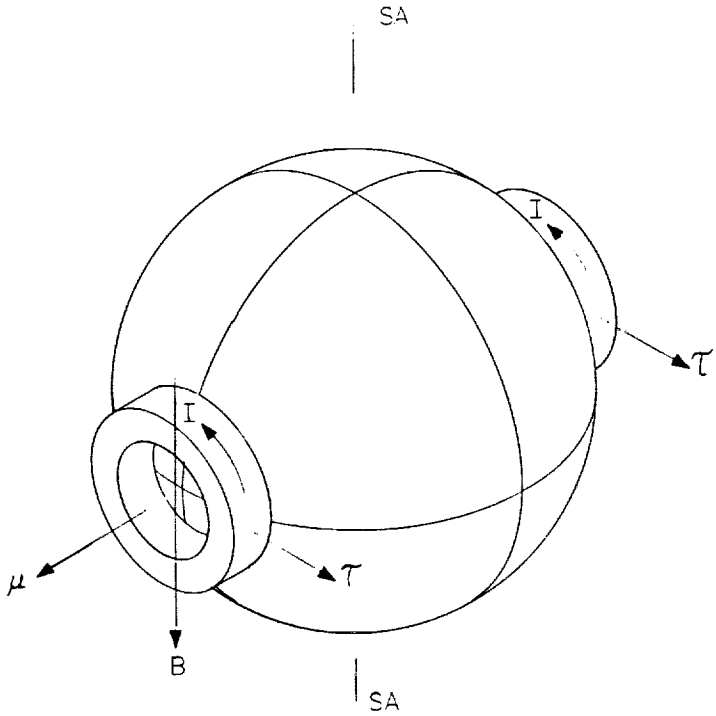

Figure 9.- Torque loading.

omit

Superconducting Linear Actuator

Bruce Johnson and Richard Hockney, SatCon Technology Corporation

SUPERCONDUCTING LINEAR ACTUATOR

by

Bruce Johnson and Richard Hockney
SatCon Technology Corporation
Cambridge, MA

ABSTRACT

Special actuators are needed to control the orientation of large structures in space-based precision pointing systems. Electromagnetic actuators that presently exist are too large in size and their bandwidth is too low. Hydraulic fluid actuation also presents problems for many space-based applications. Hydraulic oil can escape in space and contaminate the environment around the spacecraft. A research study was performed that selected an electrically-powered linear actuator that can be used to control the orientation of a large pointed structure. This research surveyed available products, analyzed the capabilities of conventional linear actuators, and designed a first-cut candidate superconducting linear actuator.

The study first examined theoretical capabilities of electrical actuators and determined their problems with respect to the application and then determined if any presently available actuators or any modifications to available actuator designs would meet the required performance. The best actuator was then selected based on available design, modified design, or new design for this application. The last task was to proceed with a conceptual design.

During this study, no commercially-available linear actuator or modification capable of meeting the specifications was found. A conventional moving-coil dc linear actuator would meet the specification, but the back-iron for this actuator would weigh approximately 12,000 lbs. A superconducting field coil, however, eliminates the need for back iron, resulting in an actuator weight of approximately 1000 lbs.

INTRODUCTION

SatCon Technology Corporation has performed a study directed toward selecting an electrically-powered linear actuator which could be used to control the orientation of a large, space-based precision pointed structure. This paper reports the findings of that research including the baseline design, a superconducting dc linear actuator. This introductory section provides background, specifications, and selection criteria.

In this application, linear actuators are used to rapidly orient (slew) a large (25kg) space structure. Reaction masses (counterweights) are driven in the opposite direction to conserve momentum. Figure 1 shows two possible laboratory tests for one of the linear actuators (with and without a reaction mass). The laboratory test is sized to simulate the load on the actuator in actual orbital operation. The actuator must step the position (x) of the mass at constant step period (T) and varying amplitude (x_s). The desired acceleration profile for the load mass is defined by the cube of a

sine-wave. The desired position, velocity (v), and acceleration (a) trajectories as a function of time (t) are defined by the following equations.

$$a(t) = (3\ x_s/T^2)\sin^3[2\ (t/T)]$$

$$v(t) = [x_s/(2T)]\{2 - 3\cos[2\ (t/T)] + \cos^3[2\ (t/T)]\} \qquad (1.1)$$

$$x(t) = x_s\{(t/T) - (1/2\ )\sin[2\ (t/T)] - (1/12\ )\sin^3[2\ (t/T)]\}$$

Table 1 presents the kinematic parameters (length and time for the step) which define the time profiles. The maximum step length is used to size the capacity for the actuator while the rms value determines the steady-state requirements.

Table 1. Kinematic Parameters

Step Period		0.016 sec.	
Step Length	(max.)	5.0 cm	(2 in.)
	(rms)	2.5 cm	(1 in.)

As shown in figure 2, the net load (f) acting on the actuator is the sum of the inertial (D'Alembert), viscous friction, and coulomb friction forces. Table 2 presents the parameters which determine the load on the actuator.

Table 2. Load Parameters

Load Mass (m_L)	25 kg	(54 lb_m)
Viscous Friction Coefficient (b)	73 N/m/s	
Coulomb Friction (f_c)	454 N	(100 lb_f)

The following equation defines the load profile.

$$f(t) = m_L \cdot a(t) + b \cdot v(t) + f_c \cdot \mathrm{sgn}[v(t)] \qquad (1.2)$$

Figure 3 shows the load profile that the actuator must produce during the maximum length step. The final specifications for the actuator are derived from this analysis and are presented in Table 3.

Table 3. Actuator Specifications

Maximum Total Travel	25 cm	(10 in.)
Maximum Velocity	6.3 m/s	(20 ft/sec)
Maximum Acceleration	1830 m/s^2	(6,000 ft/sec^2)
Maximum Force	45,000 N	(10,000 lb_f)
First Mode Structural Frequency	500-1000 hz	

The acceptability of each electrically-driven linear actuator was determined by its performance relative to that of an alternative hydraulic actuator. The performance parameters which were used to determine acceptability are listed below.

1) Energy Efficiency
2) Volume and Weight
3) Interface Requirements (Electrical and Cooling)
4) Environmental Compatibility

The final criterion implies that the actuator must be compatible with both laboratory and exo-atmospheric environments unless a design which is intended for Earth-based applications can be readily modified for space.

CONVENTIONAL LINEAR ACTUATORS

The first phase of the research examined conventional linear actuators, both commercially available and custom designs. The survey of over fifty manufacturers, including telecons with leading linear actuator manufacturers, indicated that the only commercially available technology that could come close to meeting the specifications was a motor/lead screw combination. The state-of-the-art in lead-screw technology for these loads is a few inches a second, however, compared to the 20 feet per second required. The conclusion of the product survey was that neither an existing design nor a modification of an available actuator design would meet the performance requirements for this application. The study next proceeded to the analysis or the theoretical capability of known types of linear actuators.

The various conventional linear actuators that were examined can be divided into three categories.

1) Rotary motors with transmissions
2) Linear motors
3) Linear actuators

The distinction between the second and third categories is that a linear motor requires commutation and its stroke is limited only by the length of its stationary component. The stroke of a linear actuator is limited by some combination of the length of the stationary and moving components, and no commutation is required.

For each type of actuator, first order models that predicted the geometry, moving mass, and stationary mass were developed. These models all had common assumptions with regard to magnetic materials, conductive materials, and mechanical impedance. A summary of the results of this study are listed below. A more detailed description of the results and development of the models is found in [Hockney 1986].

Rotary Motors Both axial and radial air-gap motors were examined. The axial air-gap motor could produce sufficient torque and an adequate torque/inertia ratio only a high (18,000 rpm) speeds. As mentioned earlier, the problem with rotary motors is that no mechanical method of transmission to linear motion exists that can meet the specifications, especially the 20 ft/sec speed.

Linear Synchronous Motor This is a linear analog of a brushless dc motor. It was found to be impractical because of the large gap required (11 cm).

Linear Induction Motor This linear analog of a common induction motor would require an armature of 3.8m length and 1.6 cm radius. This long, thin rod is impractical for this application.

Reluctance Linear Actuator As for the linear synchronous motor,

this approach is impractical because of the large air gap required.

Solenoid This approach requires too much moving mass to produce the required force and cannot, therefore, meet the acceleration requirement.

DC Linear Actuator DC linear actuators (voice coils) are typically used in fixed-based applications such as shaker tables where large forces and relatively long strokes are required. Of all the conventional options examined, this device was the only one that could meet the specifications. It would require nearly six metric tons of soft iron, however, to shape the magnetic field, which is grossly excessive for any space-based application.

SUPERCONDUCTING ACTUATOR

Based on the results of the above analysis, a linear actuator utilizing conventional technology would weigh approximately two orders of magnitude more than its hydraulic counterpart. Thus, the investigation toward an actuator was based upon superconducting technology. This decision was motivated by two factors. First, a superconducting actuator could be built using the same principle as the conventional dc linear actuator which, except for the weight of its back-iron, was shown to be the "best" electrical linear actuator for this application. Second, the application of superconducting technology to this actuator type held the promise of significantly reducing its weight. This is true for the following reasons:

1) The current density in the field coil can be extremely high (roughly 10^8 A/m^2);

2) This level of current density allows the system to be constructed without the use of back-iron;

3) The lack of back-iron allows higher operating flux density in the area of the moving coil armature by about a factor of two.

As stated above, the superconducting actuator concept is based upon the same principle as the dc linear actuator. The concept drawing is shown in Figure 3. In this cross-sectional drawing, the cross-hatched area represents the superconductor volume. There are a pair of oppositely excited, mechanically attached armature coils shown operated at current density J. The vectors B and f represent the field flux density and the Lorentz force, respectively. Thus there is a large net force acting to the right on the armature as well as two smaller forces tending to compress one coil and expand the other. Obviously the direction of the forces may be reversed by changing the direction of the current density in both coils.

As shown in Figure 4, the two armature (moving) coils are attached by a shaft that runs through the center of the superconductor dewar. The load mass is attached to the end of this shaft. For baseline system sizing, simple models were developed that relate the geometry and placement of the armature (moving) coils and superconductor to system performance. A minimization procedure was then used to arrive at the minimum mass design. An example of the results of this

analysis are shown in Figure 5. Shown is a plot of subcomponent (structure (st), armature coil (c), superconductor (s)) and total (t) system mass versus radial magnetic flux density at the armature. For small fields, the mass of armature coil needed increases dramatically. At larger fields, the armature coil mass decreases but at the cost of more superconductor (field coil) mass. As shown, these two effects result in a minimum mass design of approximately 300 kg.

After the preliminary design was developed using simple subcomponent models, a more detailed design was begun. The major areas of design effort are briefly presented below. A more detail discussion can be found in Hockney [1987].

Structural design The moving structure must transmit a peak force of 15,900 lb_f with a first mode frequency greater than 500 hz. The moving structure must be as light as possible. Because of the 200 g acceleration of the moving mass, each additional lb_m of moving structure increases the peak actuator force requirement by 200 lb_f. After extensive design and modelling, a beryllium moving structure was chosen. Sectional views of half of the structure are shown in Figure 6. The moving structure consists of shaft sections attached to the armature assembly. The armature assembly contains the wound aluminum tape armature coil connected to the shaft by a conical shaped web.

Superconductor design The superconductor design, of course, is central to this actuator. A variety of superconducting design issues arose, some common to any superconducting coil and some unique to this application.

Any low-temperature (conventional) superconductor requires a cryostat to maintain the superconducting temperature with a minimum of power consumption. This cryostat design is made more difficult when it must also support the large loads (10000 lb_f) required for dc force testing of this actuator. The resulting design has the superconducting solenoid contained in a stainless-steel coil housing which holds liquid helium. Several inches of aluminized mylar insulation (also called "super-insulation") surrounds the inner dewar in an evacuated space. An aluminum or stainless-steel vacuum jacket surrounds the insulating layer. The coil housing is supported with respect to the vacuum jacket by a series of stainless-steel spokes. For this superconductor run in the laboratory, the expected heat loss is about 3 watts of power at 4.2 degrees Kelvin. This would require a liquid helium refrigeration system that consumes less than 10 kW.

Another, more unique design issue is posed by the high frequency magnetic fields produced by the armature coils. The superconductor must be shielded from these fields or else large circulating currents in the superconductor would be generated, causing the superconductor to go normal. This shielding requires the placement of a conductive, eddy current shield around the ends of the superconductor. The eddy currents generated in this shield will partially attenuate the forces and fields which are experienced by the superconducting solenoid.

The superconducting solenoid required for this application is relatively large compared to the usual, commercially available solenoids. Because of its size, both the self-induced stresses in the solenoid and the large stored energy require special design considerations. The size and field requirements also drive the design to high-performance niobium-tin (NbSn) superconductor versus the more conventional niobium-titanium (NbTi) superconductor.

Interaction with Earth's Magnetic Field The large dipole moment of the superconductor, approximately 500 kAm^2, will produce relatively large torques, on the order of 10 Nm, due to interaction with the Earth's magnetic field. Three approaches were investigated to ameliorate this problem.

1) The use of a control moment gyro
2) The use of an equal and opposite dipole
3) The use of magnetic shielding

The first two approaches are possible, with the magnetic shielding requiring too much mass. Control moment gyros are available in this size range, however, the approach of using an equal and opposite dipole appears the best. This is a natural approach for this application since dummy actuators moving reaction loads will be required to counterbalance the moving load.

Electrical Power The armature requires a peak current of over 1000 Amps, as shown in Figure 7. The corresponding armature voltage waveform is shown in Figure 8. The armature voltage consists primarily of inductive and back-emf voltage. The volt-amp waveform, which sizes the power electronics, is shown in Figure 9. The peak volt-amperage required is approximately 2 MVA. About 600 kW of peak power is mechanically delivered to the load. These requirements can be met with commercially available components. The electrical connection to the armature must be extremely flexible to accommodate the 10" total stroke and must be very strong to withstand the 200 g acceleration with a large cycle-life. The solution was to use a commercially available high-current, flexible strap.

SUMMARY

SatCon Technology Corporation has performed a study directed toward selecting an electrically-powered linear actuator which could be used to control the orientation of a space-based, precision pointed structure. After an extensive review of existing and conventional electromagnetic actuators, none of which could meet the specifications, a superconducting design was developed that could. The candidate linear actuator has a total mass of 447 kg, a rms power requirement of 174 kVA, and an occupied volume of 0.6 m diameter by 0.82 m long.

REFERENCES

[Hockney 1986] James Downer and Richard Hockney Linear Actuator Engineering Study. SatCon Technology Report R01-86, Cambridge, MA: August 1986.

[Hockney 1987] Richard Hockney, et al. Design Definition for a Superconducting Actuator. SatCon Technology Report R10-87, Cambridge, MA: November 1987.

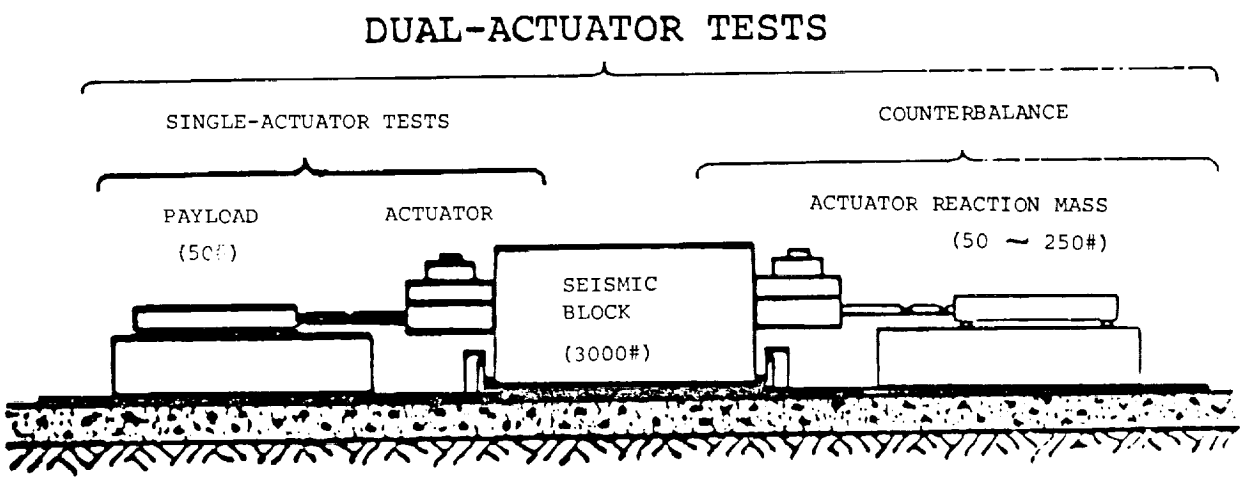

Figure 1. Actuator Test Bed.

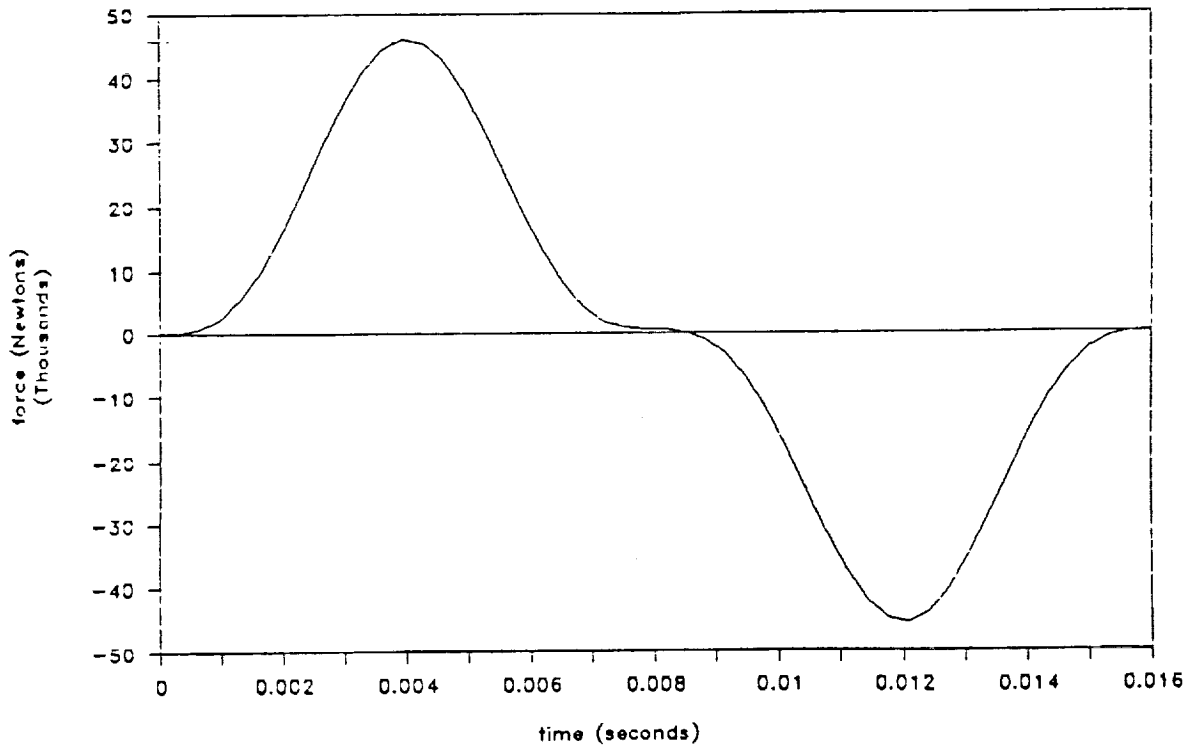

Figure 2. Required Force Profile.

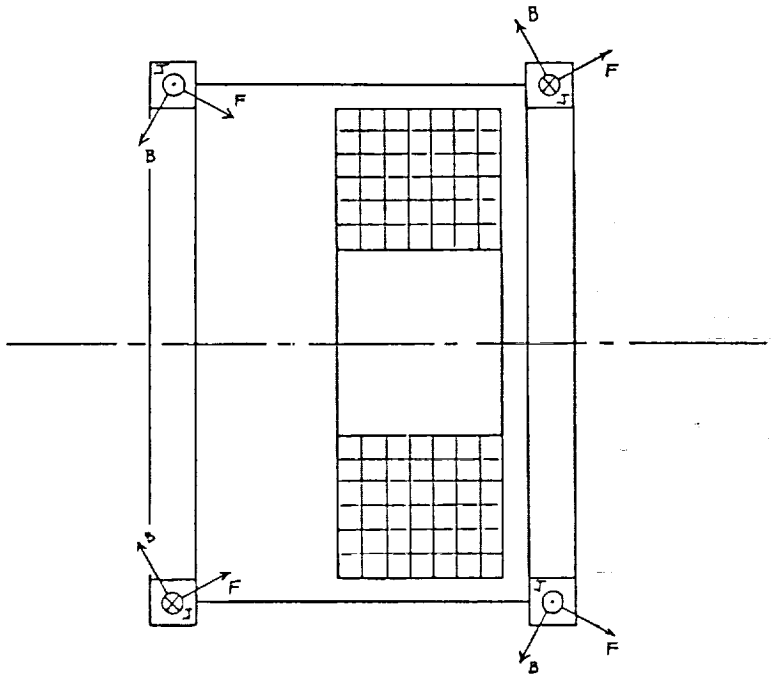

Figure 3. Superconducting Linear Actuator Concept.

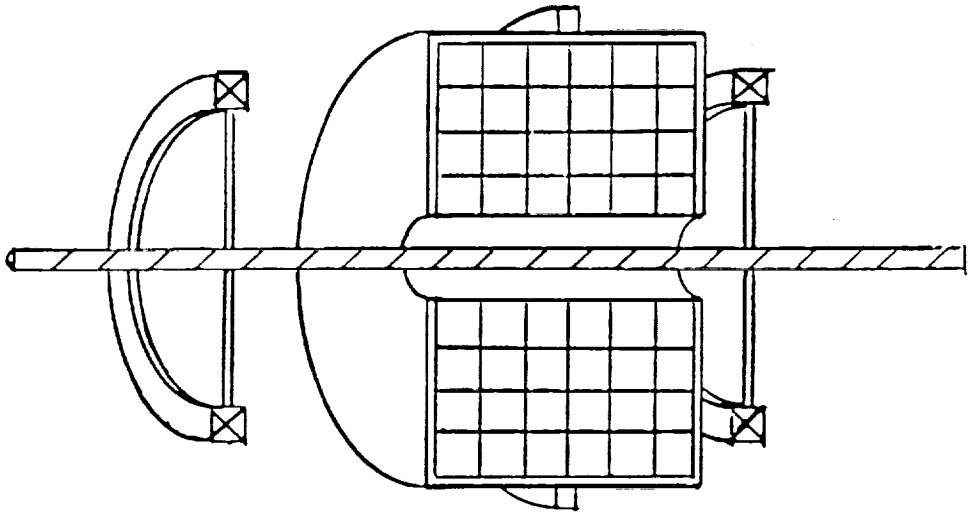

Figure 4. Baseline Configuration.

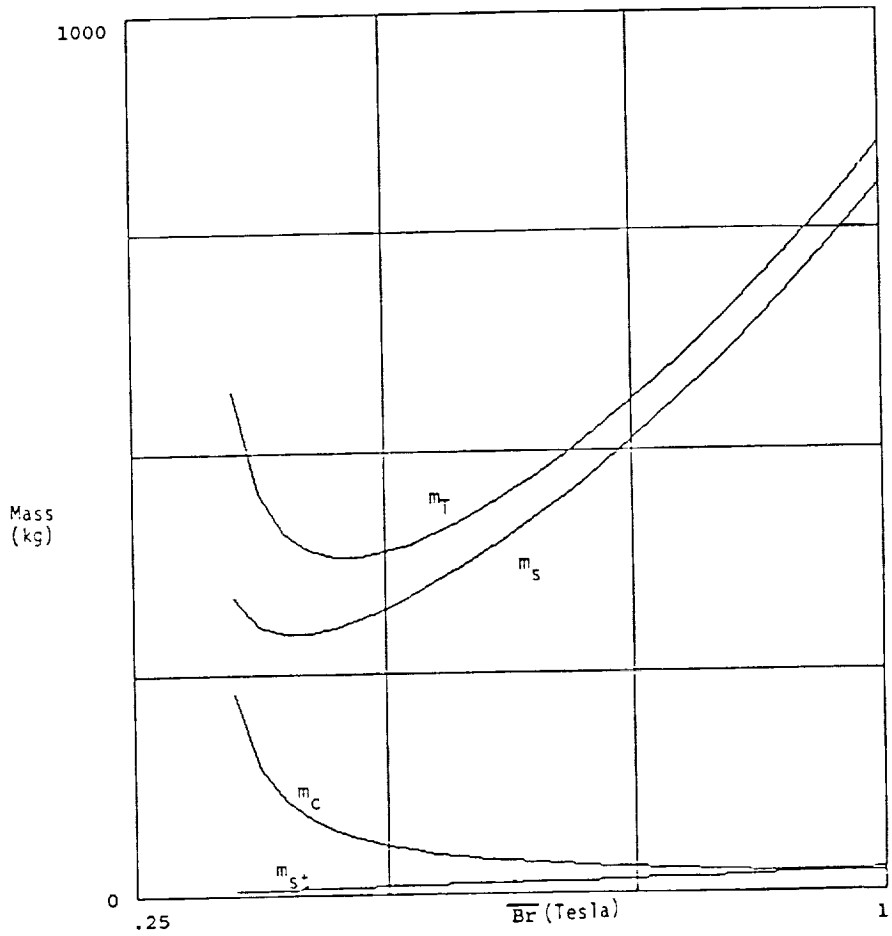

Figure 5. Mass vs Radial Flux Density at the Armature.

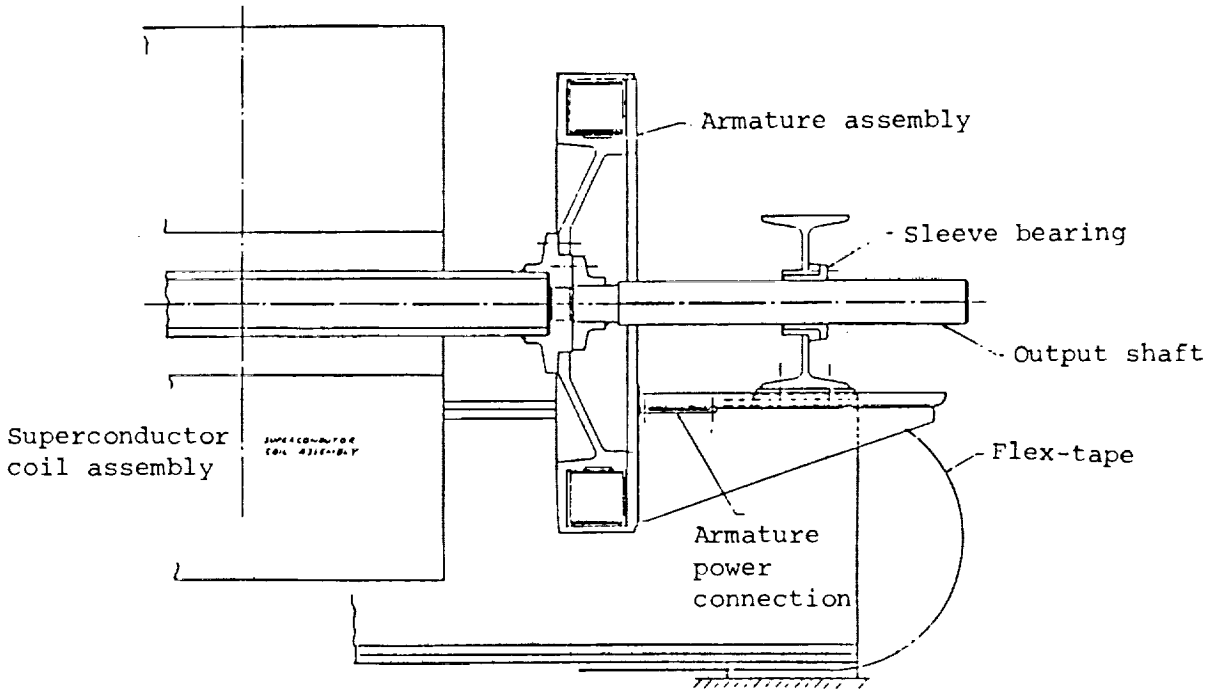

(a) Section View

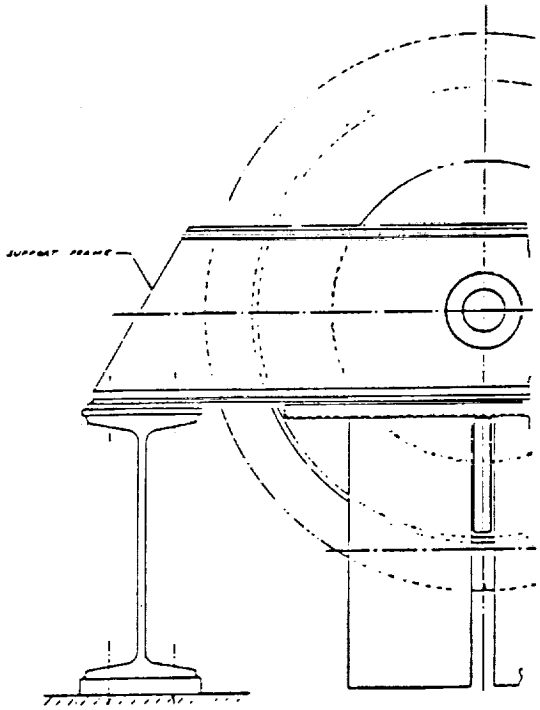

(b) View Along Output Shaft

Figure 6. Overall Linear Actuator Design.

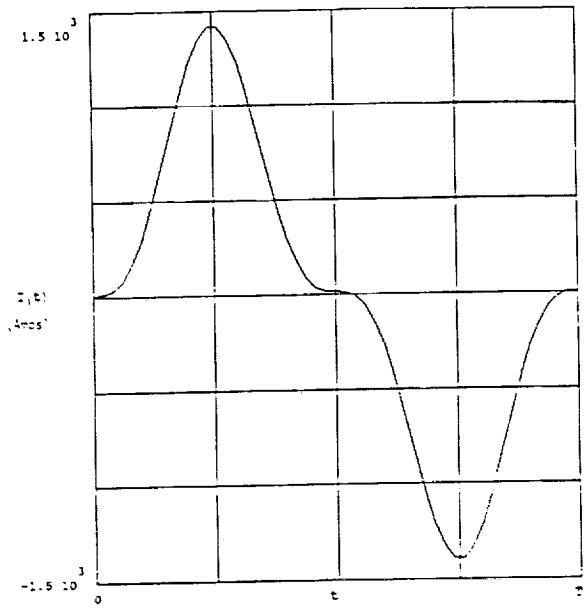

Figure 7. Armature Current Waveform.

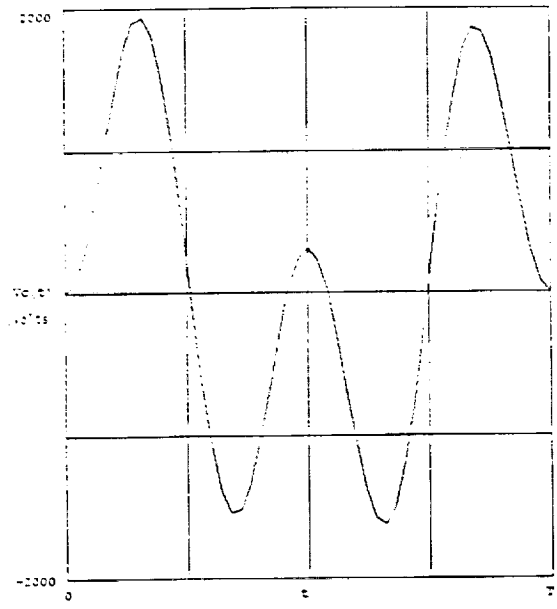

Figure 8. Armature Voltage Waveform.

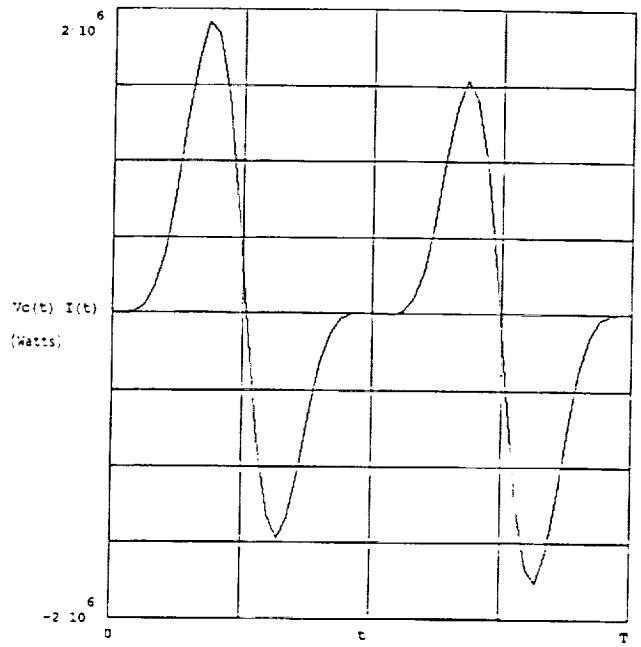

Figure 9. Armature Volt-amperage Waveform.

omit

Performance of Ceramic Superconductors in Magnetic Bearings

James L. Kirtley Jr., Massachusetts Institute of Technology

James R. Downer, SatCon Technology Corporation

PERFORMANCE OF CERAMIC SUPERCONDUCTORS IN MAGNETIC BEARINGS*

James L. Kirtley, Jr.
Massachusetts Institute of Technology
Laboratory for Electromagnetic and Electronic Systems
Cambridge, MA

James R. Downer
SatCon Technology Corporation
Cambridge, MA

SUMMARY

Magnetic bearings are large-scale applications of magnet technology, quite similar in certain ways to synchronous machinery. They require substantial flux density over relatively large volumes of space. Large flux density is required to have satisfactory force density. Satisfactory dynamic response requires that magnetic circuit permeances not be too large, implying large air gaps.

Superconductors, which offer large magnetomotive forces and high flux density in low permeance circuits, appear to be desirable in these situations. Flux densities substantially in excess of those possible with iron can be produced, and no ferromagnetic material is required. Thus the inductance of active coils can be made low, indicating good dynamic response of the bearing system.

The principal difficulty in using superconductors is, of course, the deep cryogenic temperatures at which they must operate. Because of the difficulties in working with liquid helium, the possibility of superconductors which can be operated in liquid nitrogen is thought to extend the number and range of applications of superconductivity. Critical temperatures of about 98 degrees Kelvin have been demonstrated in a class of materials which are, in fact, ceramics. Quite a bit of public attention has been attracted to these new materials.

There is a difficulty with the ceramic superconducting materials which have been developed to date. Current densities sufficient for use in large-scale applications have not been demonstrated. In order to be useful, superconductors must be capable of carrying substantial currents in the presence of large magnetic fields.

This paper investigates and discusses the possible use of ceramic superconductors in magnetic bearings and identifies requirements that must be achieved by superconductors operating at liquid nitrogen temperatures to make their use comparable with niobium-titanium superconductors operating at liquid helium temperatures.

---

*This research was partially sponsored by the National Science Foundation under the Small Business Innovation Research Program.

INTRODUCTION

This paper analyzes the performance of ceramic superconducting materials in a magnetic bearing application. The use of superconducting materials in magnetic bearings is justified when high performance (reduced runout) is required. The design, operation, and performance of a magnetic bearing system which employs a low temperature superconducting material (niobium-titanium) is presented as a baseline (ref. 1). The general characteristics of high temperature ceramic materials are discussed and current density is seen as the primary limit of this technology. Using the laws of electromagnetic component scaling, the performance of the baseline magnetic bearing system is estimated as a function of the achievable current density. The scaling of the auxiliary components of the bearing system to liquid nitrogen temperatures is also considered. An operating current density on the order of one tenth that of niobium-titanium superconductors appears to provide an equivalent system cost.

USE OF SUPERCONDUCTORS IN MAGNETIC BEARINGS

An opportunity exists for innovative bearing concepts to be employed in machine tool spindles. These advanced bearings concepts will allow the rotor to be more accurately positioned with respect to the stator. This reduced runout is particularly desirable in high-precision machining applications such as the manufacture of large-scale optical surfaces where rotor position accuracy on the order of a micro-inch is desired (ref. 1).

Magnetic bearings employing conventional technology have been employed in many rotating applications which require modest performance levels. Actively controlled magnetic bearings will maintain the position of the rotor to the accuracy level which can be measured by the sensors. Conventional approaches to magnetic bearing design, however, are limited in position accuracy by non-linearities, bandwidth, and the ability to apply large forces and torques.

SatCon Technology Corporation has recently completed a study directed toward investigating the role of superconducting materials in a machine tool magnetic bearing system and defining a design which could be used to roughly duplicate the air bearing system of an existing machine tool spindle in a high-precision machining operation. Superconducting magnetic bearings were shown to offer advantages in terms of linearity, bandwidth, weight, and load-carrying capability which make them superior to more conventional approaches.

The lack of a soft-iron magnetic circuit leads to a linear force versus control current characteristic and improved response time (lower inductance). The lack of soft-iron allows the weight of the magnetic circuit to be drastically reduced. The power consumption of normal control coils in a superconducting magnetic bearing is relatively modest due to the high magnetic fields produced by the superconducting source coil. There is no power consumed in maintaining this magnetic field, and the control coils which interact with it become more effective because of the elevated field levels. The development of this magnetic bearing design will provide a necessary element for high-precision machining systems when it is integrated with high resolution sensing elements.

BASELINE MAGNETIC BEARING (ref. 1)

Figure 1 shows the combination of a single superconducting coil (the "source coil") and eight non-superconducting coils (the "control coils") which comprises the system. The axis of the source coil is along the spin axis of the rotor. Four control coils are located at each end of the rotor displaced radially from the spin axis of the rotor and are spaced 90 degrees from each other. The axis of each control coil is perpendicular to that of the source coil.

The source coil operates in persistent mode (without an electrical input). This is a condition in which the current in the coil persists because of the lack of resistance in the superconducting material. Forces and torques are produced by the interaction of the current in the control coils and the magnetic field produced by the source coil.

The electromechanical interaction is independent of which of the two components (source coil or control coils) rotates. Other engineering considerations, however, affect this decision. If the superconducting coil is fixed to the rotor, then some mechanism for transporting cryogenic fluids, such as liquid helium, across the rotating interface must be designed. In addition, the stresses due to rotation will superpose on those due to the excitation of the source coil and will have to be supported by an additional structural member. If, however, the control coils are fixed to the rotor, then electrical excitation must cross the rotary interface. Signal- and power-level couplings (slip rings and brushes) have been developed for a number of applications and are considered a state-of-the-art technology. In addition, the sensors for the control system will also rotate. This simplifies the design of the control system and avoids an additional transformation of coordinates. These decisions will add some mass to the rotor.

OPERATION OF THE SYSTEM

Figures 2 and 3 show the excitation of the control coils which leads to a pure thrust force on the rotor. Figure 2 shows a section through the x-z plane, while Figure 3 shows the equivalent y-z plane section. The z-axis is defined as the spin axis of the rotor (the axis of the source coil). The figures also show the north and south poles of each of the coils. One way to visualize the interaction of the coils is to think of the attraction of opposite poles and repulsion of like poles. Figures 4 and 5 show equivalent diagrams for the cases of pure lateral loading along the x-axis and pure torsional loading about the y-axis. In these two cases, the coils whose axes lie in the y-z plane are not excited. The excitation for lateral loading along the y-axis and torsional loading about the x-axis are similar and are not shown.

PERFORMANCE OF THE BASELINE SYSTEM

Table 1 presents working and ultimate loads for the baseline superconducting magnetic bearing. These were derived from the rated loads for two typical air-bearing machining spindles at a nominal operating pressure of ten atmospheres. Table 2 presents the performance characteristics (weight and power consumption) for the

superconducting magnetic bearing system. Loads of the magnitude required here would require a substantial conventional magnetic bearing structure to carry the magnetic fields at the saturation flux density of common core materials. In addition, a great deal of power would be consumed in order to provide the source field.

CERAMIC SUPERCONDUCTING MATERIALS

The most common superconducting material in use today is niobium titanium. This is a strong, ductile material which is commonly fabricated into composite conductors with pure copper or mixed copper alloy matrices. At the boiling point temperature of liquid helium (4 degrees Kelvin) critical current and flux densities are on the order of 100 MA/m^2 and 5 Tesla respectively. There is a great deal of design experience with this material. The less commonly used niobium-tin material will maintain a superconducting state up to a critical flux density of about 12 Tesla. This material, however, is extremely brittle and therefore much more difficult to fabricate into coils than niobium titanium. Extremely high performance is available from niobium germanium aluminum superconductors. This material has a critical temperature which is slightly greater than 20 degrees Kelvin, but it is virtually impossible to fabricate into wires (ref. 2).

The principal difficulty in using available superconductors is, of course, the deep cryogenic temperatures at which they must operate. Because it takes several hundred Watts of refrigerator input power to remove one Watt of thermal dissipation of heat leak from a space operating at the temperature of boiling liquid helium, the use of superconductors operating at that temperature is impractical for all but the most demanding applications.

Recent advances in "high-temperature" superconducting materials have prompted engineers to consider the use of this emerging technology in many applications including magnetic bearings. Superconducting materials could have a substantial impact on the design of these devices. Figure 6 shows a timeline of the development of superconducting materials in terms of the critical temperature (ref. 3). Since the winter of 1987, the technical (ref. 4) and popular literature (refs. 5, 6, and 7) have contained many articles which discussed progress in "high-temperature" superconductors. Critical temperatures greater than 90 degrees Kelvin have been demonstrated in a newly discovered class of superconducting materials which are, in fact, ceramics. The possibility of operating these materials in boiling liquid nitrogen (a temperature of 77 degrees Kelvin) has been raised. Physicists are quick to note that there is currently no theory which precludes a material from being a superconductor at room temperature and research continues toward that goal.

The promise of higher operating temperatures is tempered by the relatively low useful current densities which have been demonstrated and by the nature of the materials themselves. In order to be useful, superconductors must be capable of carrying substantial currents in the presence of large magnetic fields. Being ceramics, they are brittle and difficult to form into useful conductors. In addition, the class of materials which has been demonstrated is highly reactive, sensitive to water and difficult to make connections to.

Clearly there are a number of technical barriers to be overcome before ceramic superconductors may be employed in actual engineering designs. We do not focus on these technological issues however, but rather on the useful current density. We will show that substantial but not spectacular current densities are required to make useful magnetic bearings with ceramic superconductors operating at the boiling point temperature of liquid nitrogen.

SCALING STUDY

Based on the results of a detailed sizing study of the superconducting bearing, a baseline source coil design was established. This niobium-titanium source coil for the machine tool spindle bearing is described in Table 3. It is used as the "base case" for this study. For the purpose of this study it was assumed that a suitable figure of merit for the magnet is its dipole moment. Thus, the ceramic superconductors studied here all had the same dipole moment. We also assumed the same magnet shape (radius and length ratios), so that all magnet linear dimensions vary as the inverse fourth root of the current density. In this way it was possible to estimate required magnet size as a function of current density. In this exercise, no attention was paid to flux density. This is thought to be alright because the reference case operates at a relatively low flux density (a maximum of about 4 Tesla).

Coil Sizing and Conductor Cost

Figures 7 and 8 present the dimensions for the coil and the dewar as a function of the current density in the conductor. A constant insulation thickness of two inches (5 cm) in all directions is assumed. The magnet becomes quite large at current density levels less than a few thousand Amps per square centimeter.

The effective conductor density and cost were estimated to be 8900 kilograms per cubic meter and $ 220 per kilogram respectively. There is no reliable data, of course, on what stabilized ceramic composite conductor might weigh or cost. Modern metallic conductors come in a wide variety of configurations, but these numbers are thought to be not terribly far from correct. Figures 9 and 10 show the mass and material cost for the magnet coil as a function of the conductor current density. A horizontal line in Figure 10 shows the material cost for the baseline niobium-titanium coil.

Refrigerator Sizing and Cost

The refrigerator capacity was estimated by calculating the heat leak from the dewar. The largest components of the heat leak rate are thermal conduction in magnet supports (assumed to be stainless steel wires) and thermal radiation between the inner and outer walls of the dewar. Support cross-sectional area was estimated by using the maximum loads to be delivered by the bearing plus the weight of magnet and shaft system. The support length was estimated based on the thickness of the magnet and its insulating system. No intermediate support cooling was assumed. Figure 11 shows estimates for these two heat leak components and their sum.

Refrigerator input power and cost were estimated from available commercial data. It should be pointed out that there is not a lot of data on refrigerator efficiencies or costs, particularly in the very small sizes of liquid nitrogen temperature refrigerators that are predicted here. The estimates that have been made are, however, quite conservative and are shown in Figures 12 and 13. Figure 13 also shows the cost of the refrigerator for the baseline niobium-titanium coil. It should be possible to reduce the liquid helium system heat leak by careful engineering, and this would tend to reduce the apparently substantial advantage of the higher temperature materials. The bottom line seems to indicate that the cost of refrigeration does not dominate this bearing system.

Total System Cost

Figures 14 and 15 show the total cost of the ceramic superconducting source coils (conductor and refrigerator) and compares them with that of the niobium-titanium coil. Figure 14 attempts to answer the question: "What performance would a high temperature superconductor have to have to make it as attractive as niobium titanium for this application?" By trial and error, we estimate that the conductor would have to exhibit a useful current density of 9,000 Amps per square centimeter, or a little less than one tenth that of the niobium-titanium coil. Figure 15 shows that even if it were possible to make a superconductor with an operating temperature of 77 degrees Kelvin but otherwise having the properties of niobium-titanium, there would be a benefit in the refrigeration system, but that benefit would not be overwhelming.

Low performance but high temperature superconductors do not seem to be applicable here. Even at 1,000 Amps per square centimeter, the amount of superconductor required is large enough to dominate the cost of the refrigerator and make the liquid helium temperature system more attractive. It should, of course, be pointed out that this conclusion relies on the cost of superconductor. If it turns out that the high temperature superconductor can be made for, say $ 50 per kilogram, this conclusion would be different.

RESULTS

This study was only a first cut at this particular problem. We made, for example, no attempt to optimize the magnets for the high temperature materials, and it is possible that a more thorough design would have found a solution more favorable to high temperature materials. On the other hand, we were quite conservative in our estimates of low temperature heat leak in the liquid helium temperature base case.

It is also important to consider the fact that, aside from the costs which can be quantified relatively easily, there are engineering costs which increase because of the difficulties in using liquid helium. It always involves high vacuum systems, thermal radiation shields and transfer piping which is complicated. Liquid helium systems are vulnerable to contamination because all other substances are solid at such low temperatures. Air is either abrasive or obstructive, depending on which is more inconvenient. We have not

attempted to estimate the increased costs associated with the complexity of the liquid helium system, nor the effects on reliability of the lower temperatures.

A most important result, however, is due to the fact that thermal isolation techniques are quite advanced, so that even coils operating at liquid helium temperatures can have very low heat loss. Because of this, the penalty associated with low temperature operation is relatively weak. The result is that, in order to offer practical benefits over niobium-titanium, ceramic superconductors must exhibit reasonably high current densities.

REFERENCES

1. Anastas, G., A. Bennett, J. Downer, and R. Hockney, Superconducting Magnetic Bearings for Machine Tools, R11-87, SatCon Technology Corporation, January 1988.

2. Wilson, M., Superconducting Magnets, Clarendon Press, Oxford, 1983.

3. Pokorny, B, "The frenetic worldwide race for ultimate superconductor," The Boston Globe, April 20 1987, Page 35.

4. Lerner, E., "Superconductors heat up aerospace," Aerospace America, The American Institute of Aeronautics and Astronautics, Vol. 25, No. 10, October 1987, pp. 14-17.

5. Business Week, April 6, 1987, pp. 94-97.

6. Time Magazine, March 2, 1987, p. 62.

7. Time Magazine, May 11, 1987, pp. 64-75.

TABLE 1. - MAGNETIC BEARING LOAD REQUIREMENTS

	Ultimate	Working
Thrust	5,340 N	2,670 N
Lateral	445 N	223 N
Torsion	180 Nm	90 Nm

TABLE 2. - BASELINE MAGNETIC BEARING PERFORMANCE

Weight		
Source Coil	57 kg	
Cryostat	24 kg	
Stator Total	81 kg	81 kg
Control Coils	105 kg	
Structure	26 kg	
Rotor Total	131 kg	131 kg
System Total		212 kg
Power Consumption		
Thrust Loading		750 W
Lateral Loading		390 W
Torsion Loading		425 W

TABLE 3. - BASELINE SOURCE COIL

Coil	
Inner Diameter	25.4 cm
Outer Diameter	31.0 cm
Axial Length	25.4 cm
Conductor Current Density	9,300 A/cm^2
Mass	57 kg
Dewar	
Insulation Thickness	5.1 cm
Mass	24 kg
Overall	
Clear Bore Diameter	15.2 cm
Outer Diameter	41.1 cm
Overall Length	34.3 cm
Mass	81 kg

C-5

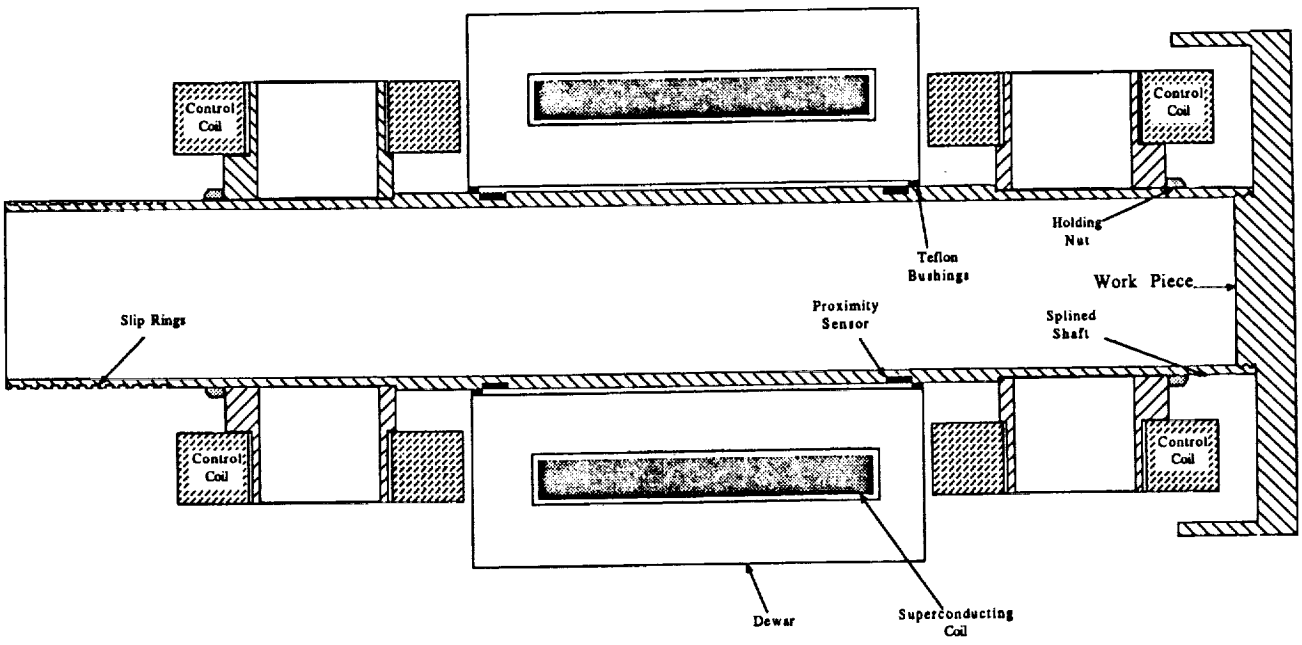

Figure 1. Baseline superconducting magnetic bearing.

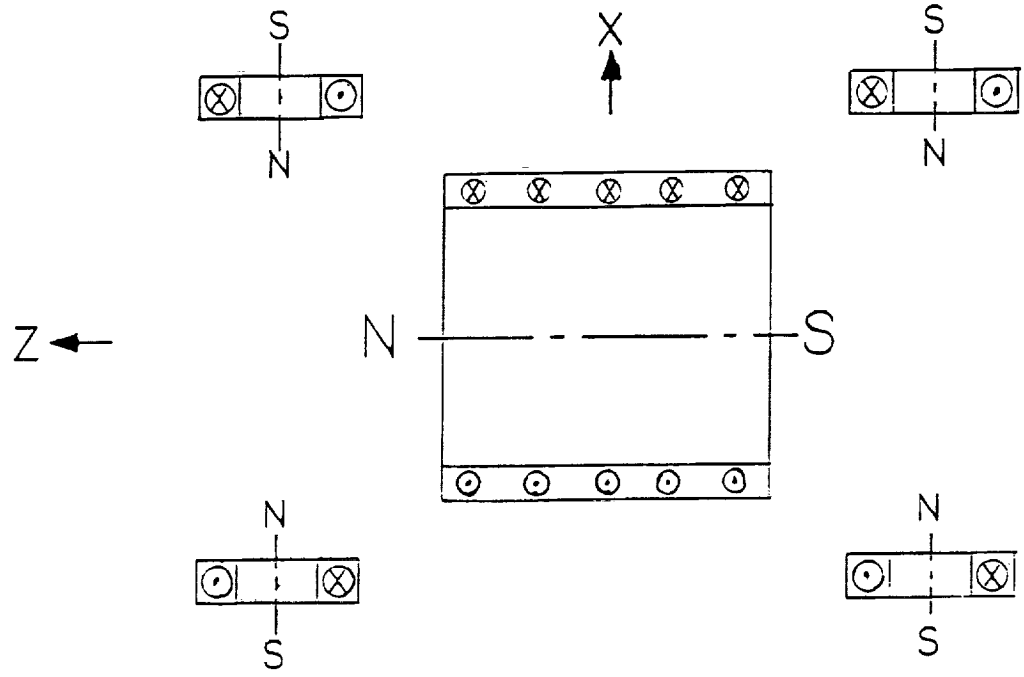

Figure 2. Coil excitation for thrust-force load (x-z plane).

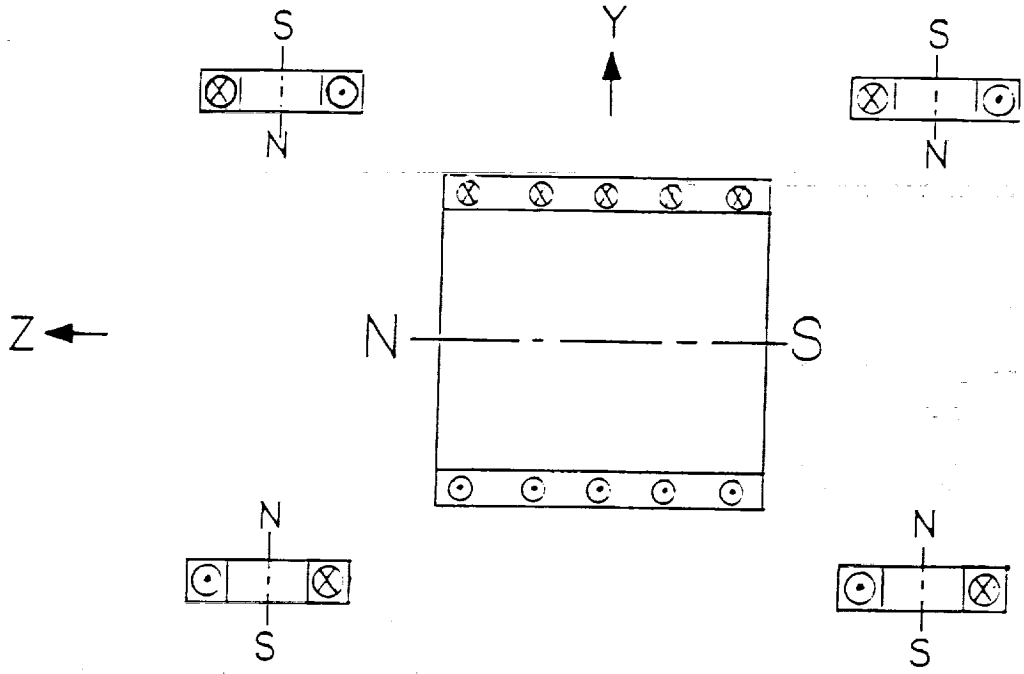

Figure 3. Coil excitation for thrust-force load (y-z plane).

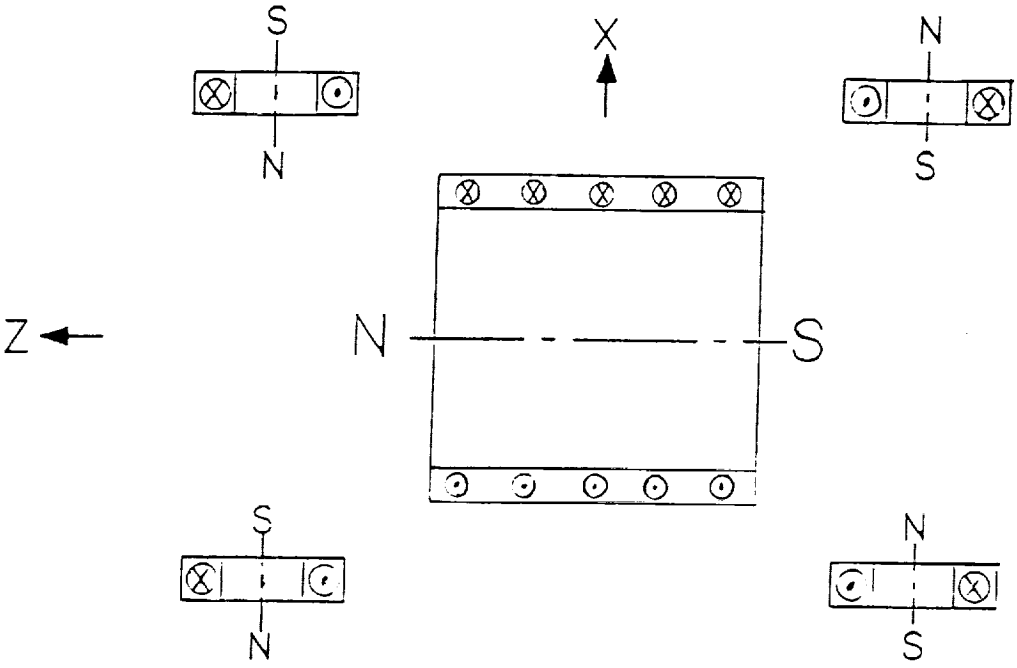

Figure 4. Coil excitation for lateral-force load.

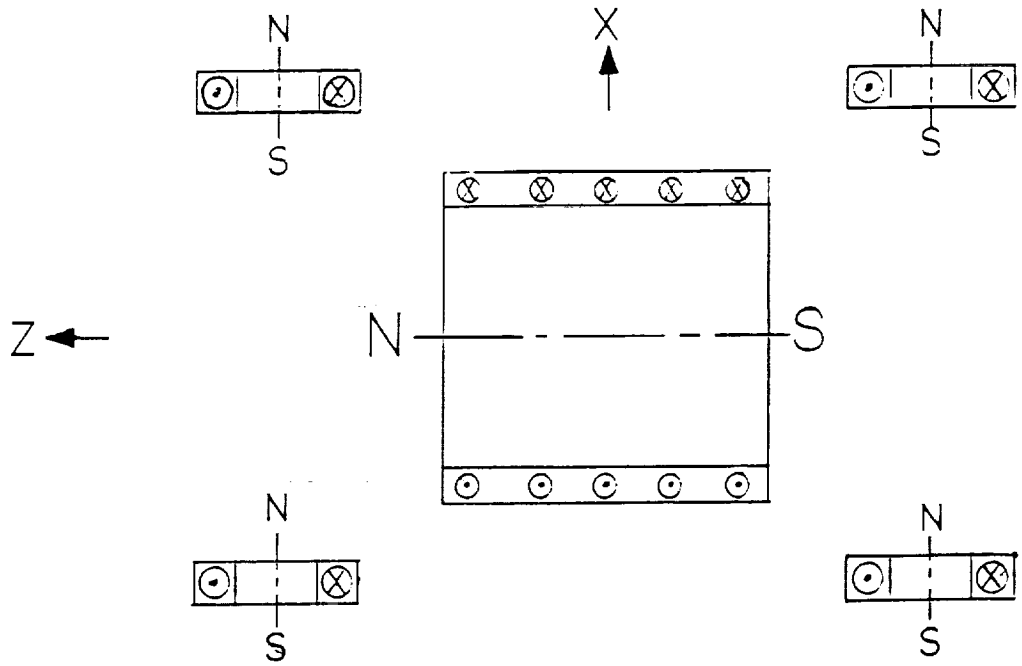

Figure 5. Coil excitation for torsion load.

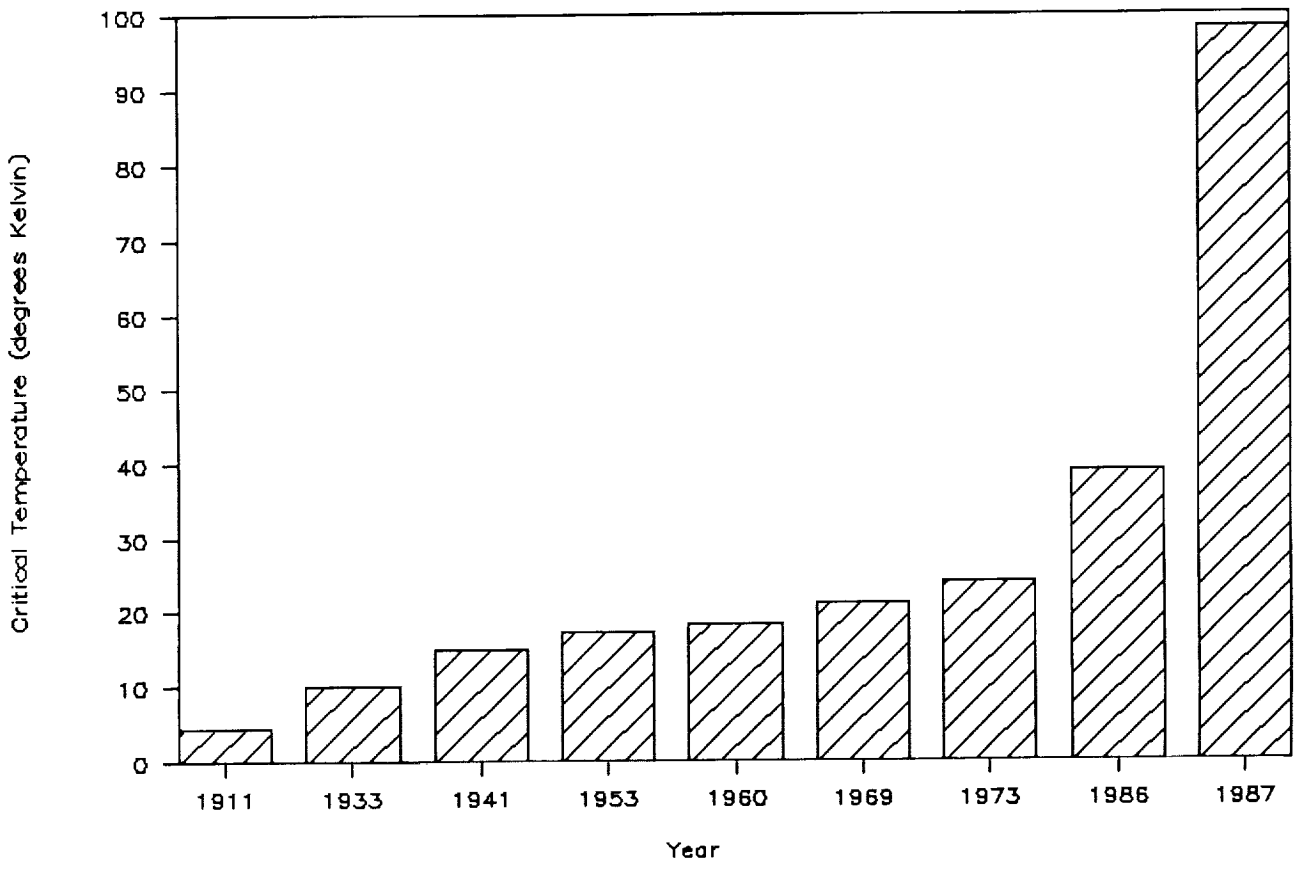

Figure 6. Progress in superconductivity.

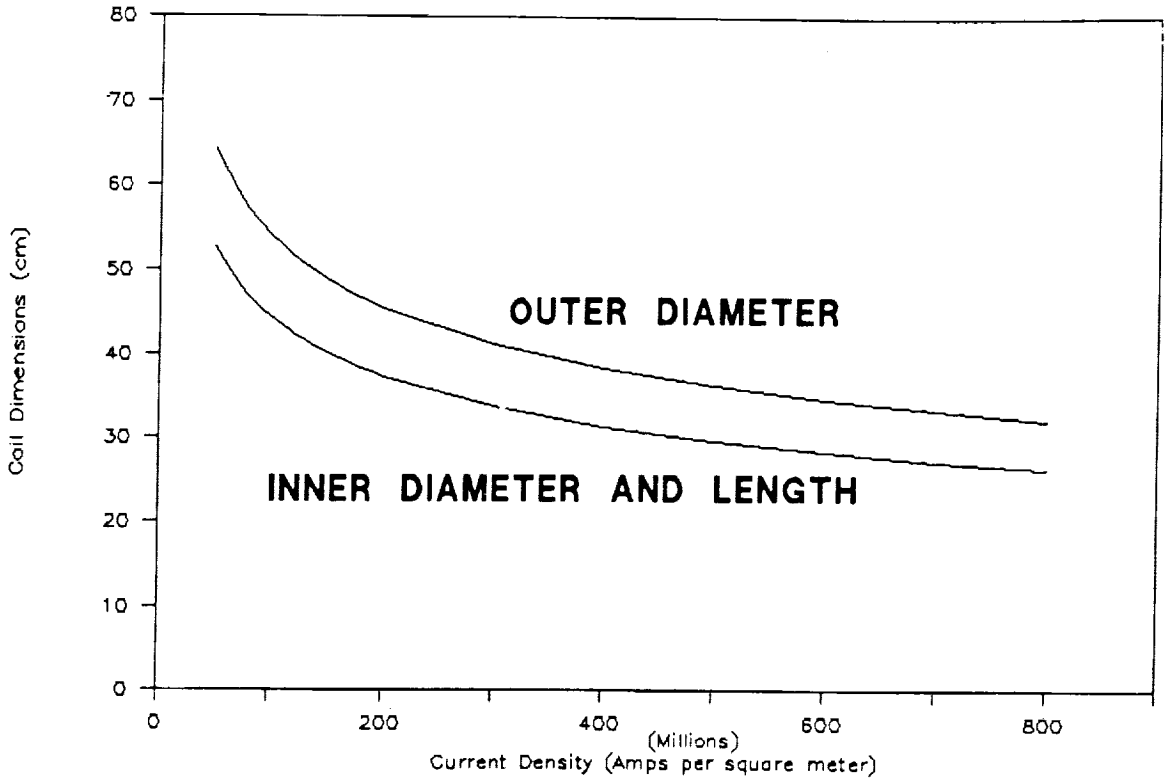

Figure 7. Source coil dimensions.

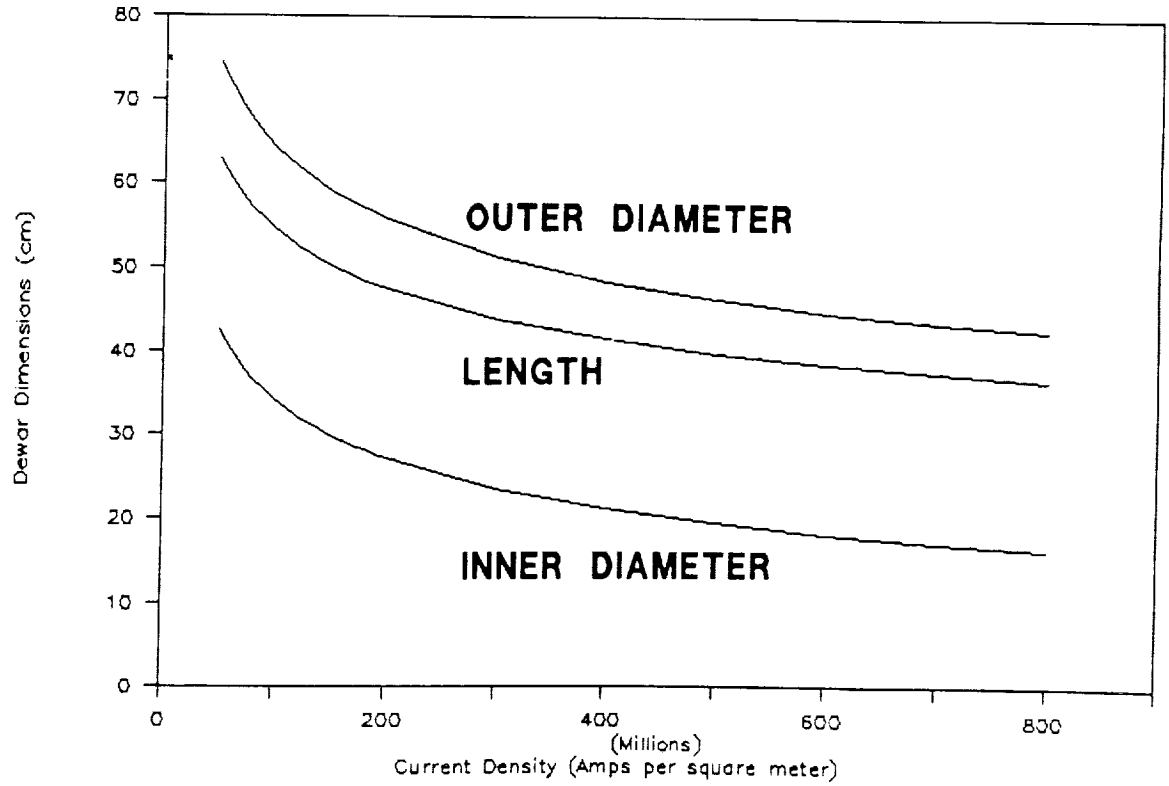

Figure 8. Dewar dimensions.

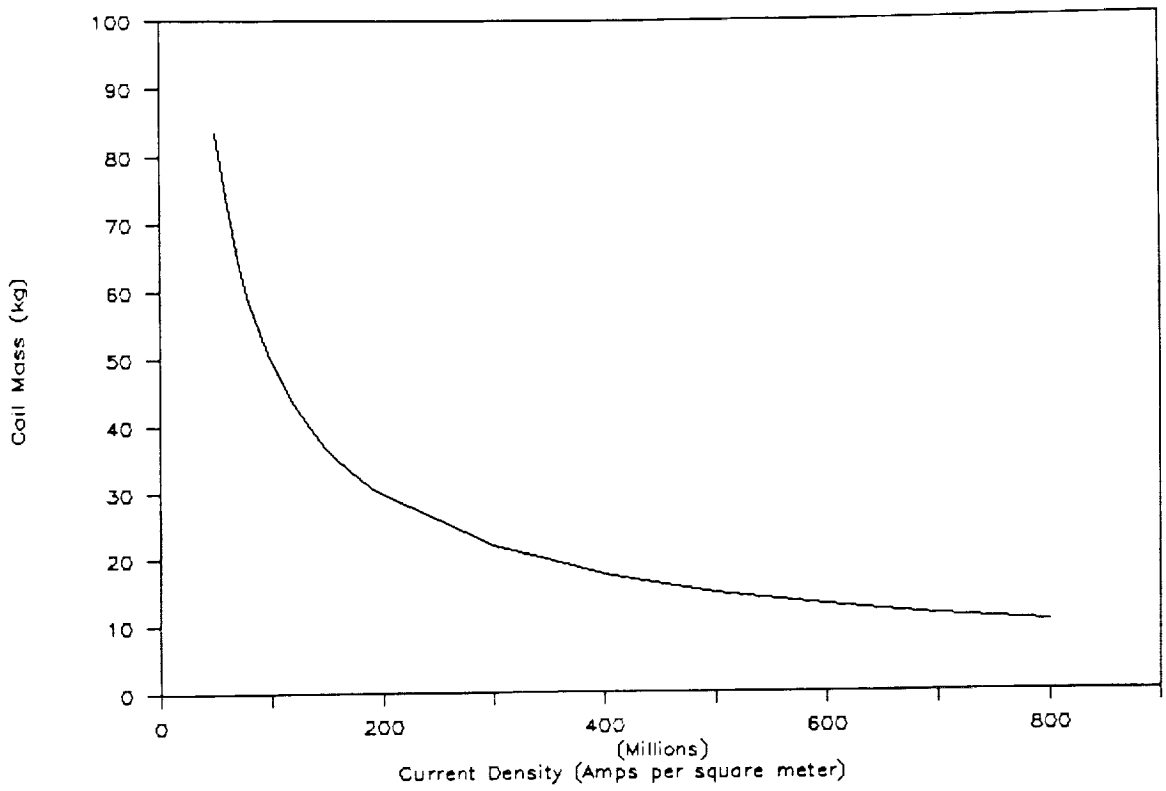

Figure 9. Source coil mass.

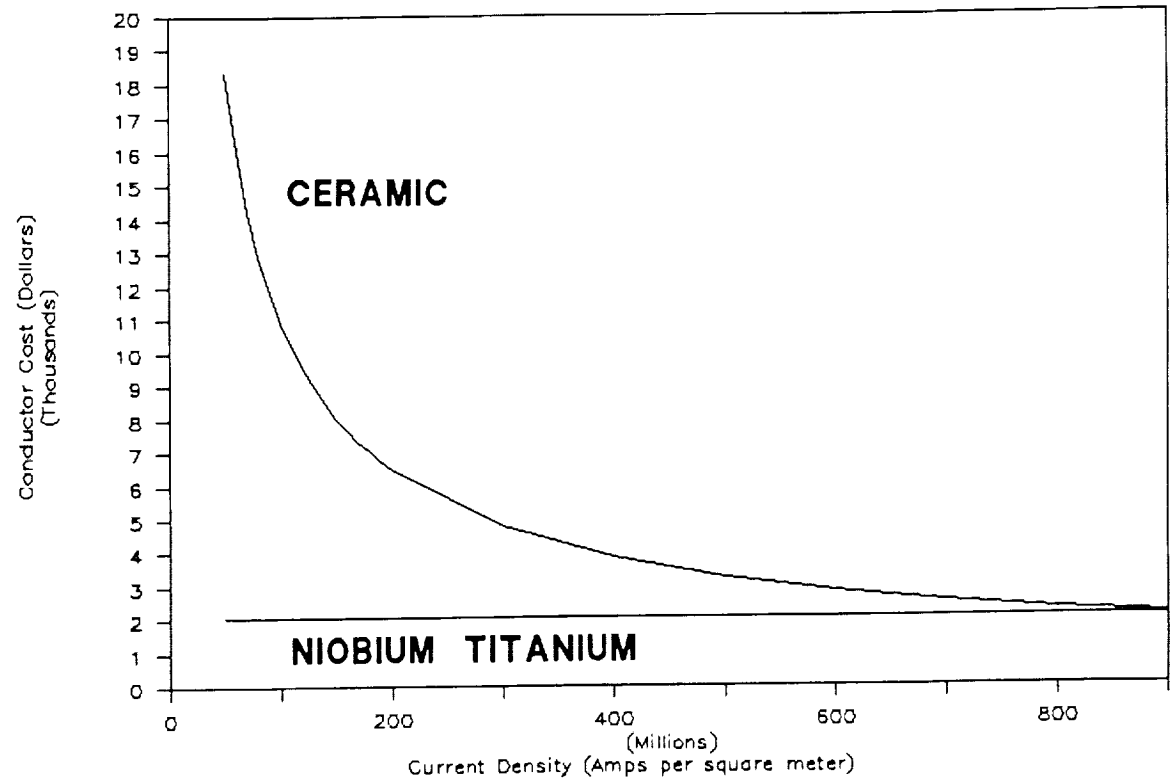

Figure 10. Source coil conductor cost.

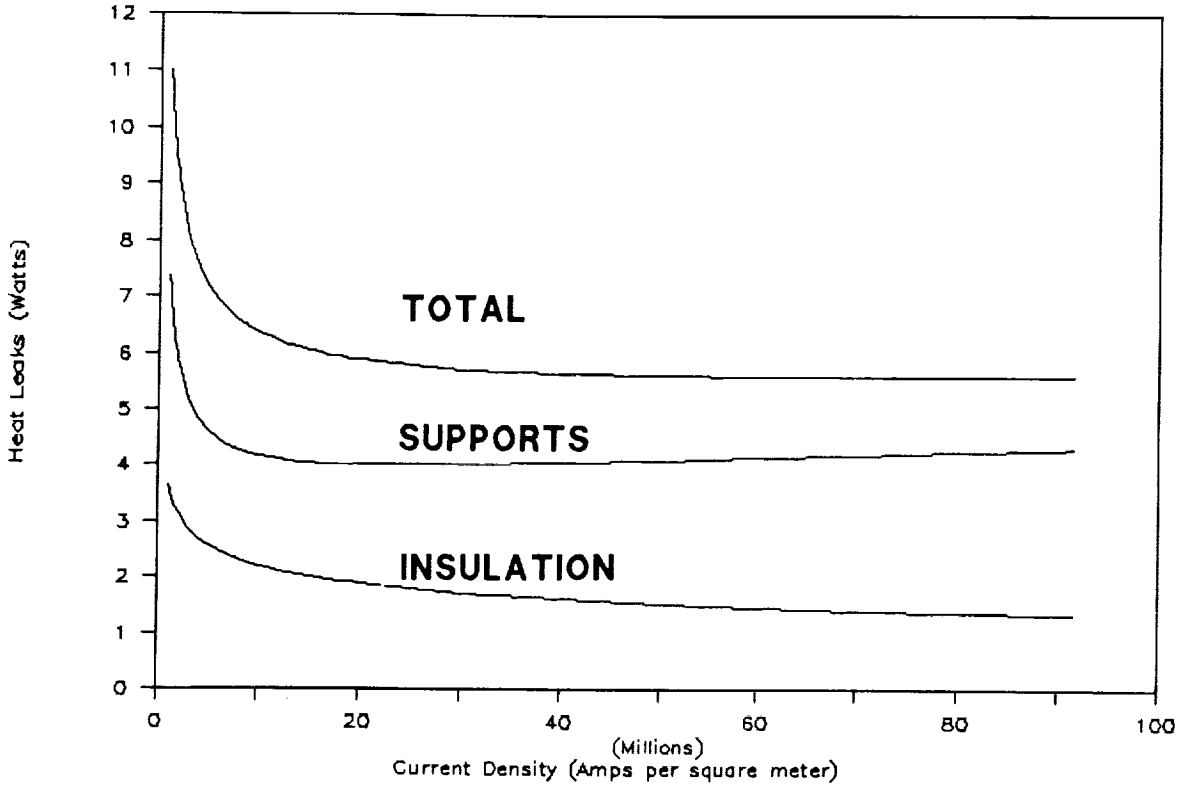

Figure 11. Dewar heat leaks.

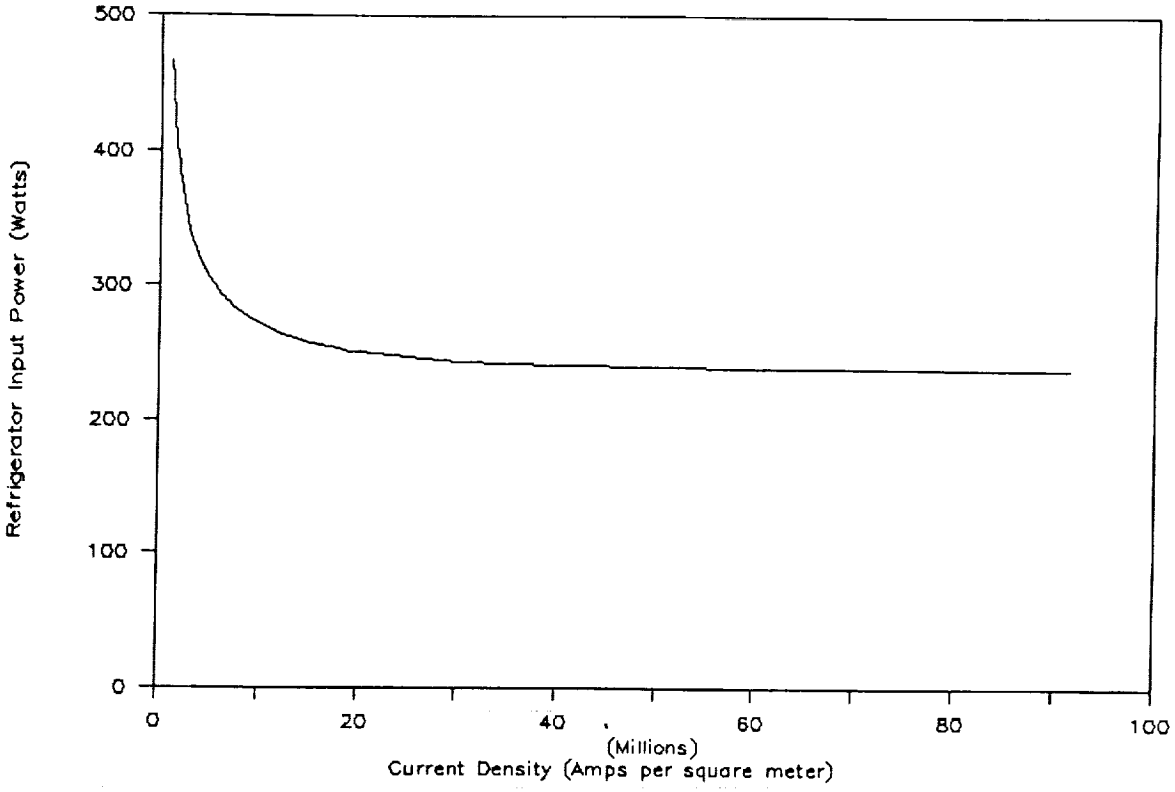

Figure 12. Refrigerator input power.

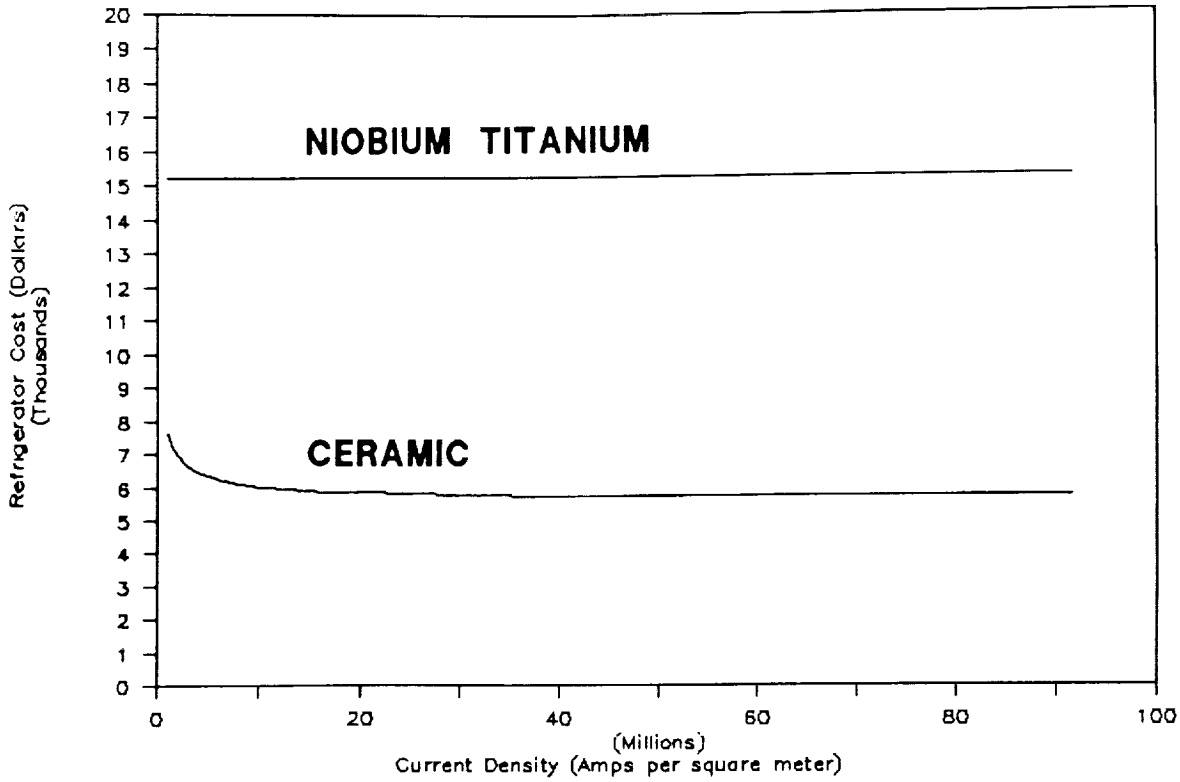

Figure 13. Refrigerator costs.

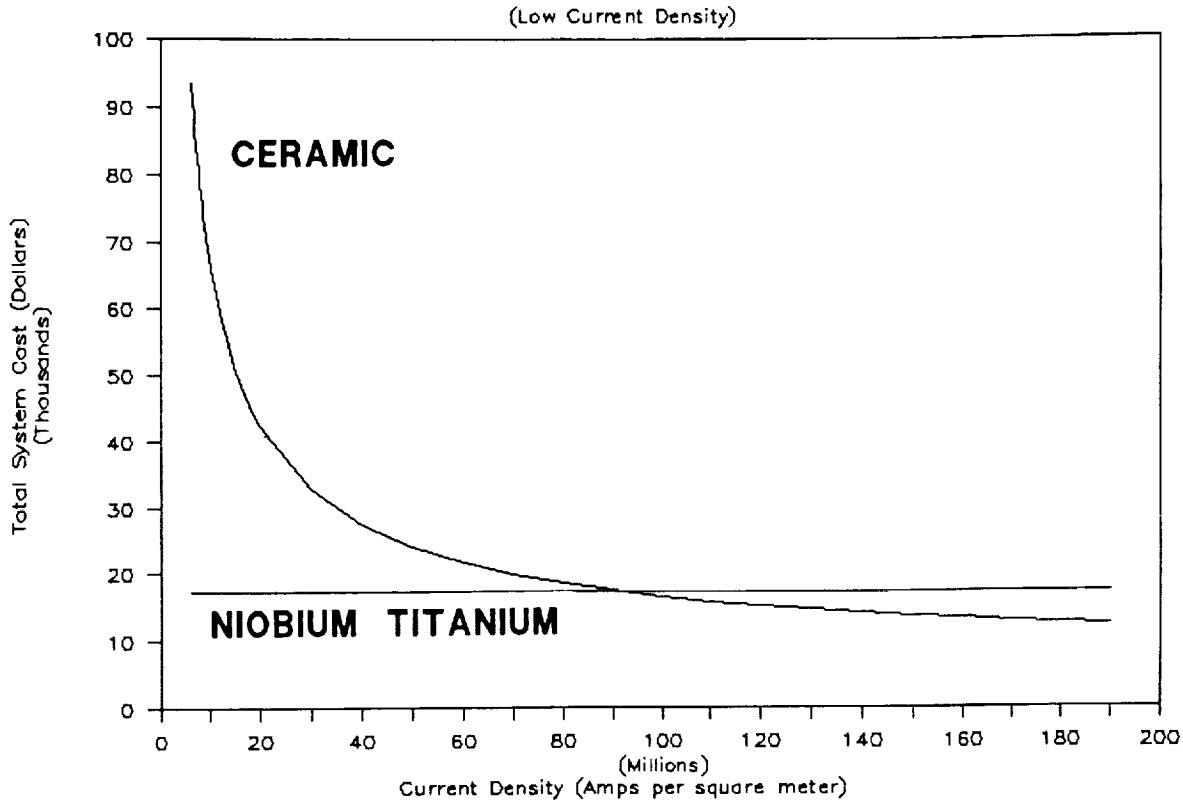

Figure 14. Total system cost, low current density.

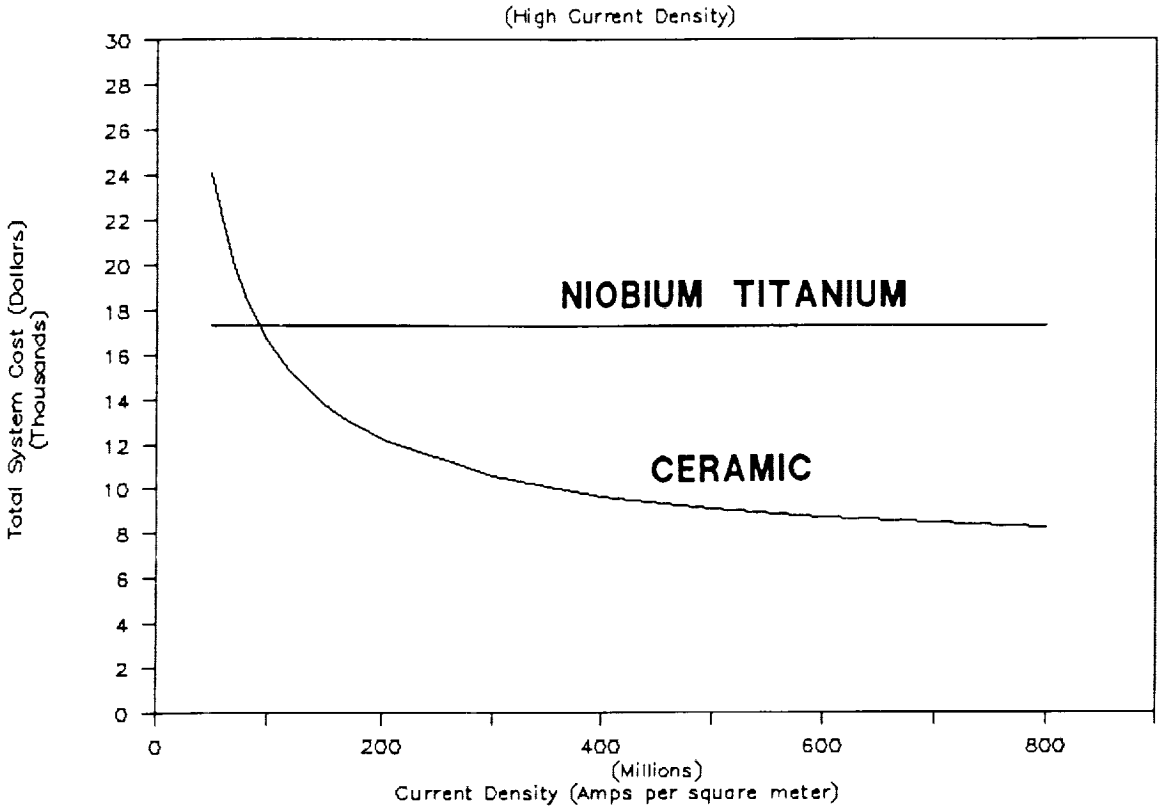

Figure 15. Total system cost, high current density.

OMIT TO END

List of Attendees

University of Virginia
Attn: Paul Allaire
Dept. of Mech & Aero Engineering
Thornton Hall, McCormick Road
Charlottesville, VA 22901

Newport News Shipbuilding Co.
Attn: Michael C. Beale
4101 Washington Avenue
E78/B600
Newport News, VA 23607

Vector Fields
Attn: Brent N. Anderson
1700 N. Farnsworth Avenue
Aurora, IL 60505

NASA Langley Research Center
Attn: Fred B. Beck
Mail Stop 490
Hampton VA 23681-0001

University of Virginia
Attn: Bibhuti Banerjee
ROMAC Labs, Mech & Aero Engrg.
Thornton Hall, McCormick Road
Charlottesville, VA 22901

Garrett AiResearch
Attn: Robert W. Bosley
2525 West 190th Street
P. O. Box 2960
Torrance CA 90509-2960

Proto-Technology Corporation
Attn: Steve Banwarth
591 Poquonnock Road
Groton, CT 06340

NASA Langley Research Center (ODU)
Attn: Colin P. Britcher
Mail Stop 161
Hampton, VA 23681-0001

ACA Systems
Attn: Gale Brown
20209 State Line Road
Harvard, IL 60033

W.J. Schafer Associates, Inc.
Attn: Charles E. Byvik
1901 N. Ft. Myer Drive, Suite 800
Arlington, VA 22209-1681

NASA Langley Research Cen. (CNU)
Attn: Alfred M. Buoncristiani
Mail Stop 231
Hampton VA 23681

Newport News Shipbuilding Co.
Attn: Brian J. Campbell
4101 Washington Avenue
E-72/B600
Newport News, VA 23607

Sundstrand Fluid Handling
Attn: Lee Cameron
14845 West 64th Avenue
Arvada, CO 80004

NASA Marshall Space Flight Center
Attn: James L. Cannon
Mail Stop EP-62
Marshall Spc Flt Cnt, AL 35812

TRW Inc.
Attn: Robert A. Cash
Mail Station 1070/Bldg. 82
One Space Park
Redondo Beach, CA 90278

University of Virginia
Attn: Santosh Chitakki
ROMAC Labs, Mech & Aero Engrg
Thornton Hall, McCormick Road
Charlottesville, VA 22901

Christopher Newport University
Attn: Randall Caton
Physics Department
50 Shoe Lane
Newport News, VA 23606

Eastman Kodak Corporation
Attn: Paul Christian
Federal Systems Div., Research Labs
Bldg. 82A, 5th Floor
Rochester, NY 14650

Charles Stark Draper Laboratory
Attn: James H. Connelly
555 Technology Square
MS#20
Cambridge, MA 02139

National High Magnetic Field Lab
Attn: Jack E. Crow
Florida State University
1800 E. Paul Dirac Dr., B-223
Tallahassee, FL 32306

Jet Propulsion Laboratory
Attn: John B. Dahlgren
Mail Code 198-330
4800 Oak Grove Drive
Pasadena, CA 91109

Charles Stark Draper Laboratory
Attn: Edward M. Cusson
555 Technology Square
Cambridge, MA 02139

NASA Langley Research Center
Attn: Dr. Victor E. Delnore
Mail Stop 490
Hampton VA 23681-0001

NASA Langley Research Center
Attn: Taumi S. Daniels
Mail Stop 230
Hampton VA 23681

Magnetic Bearings Inc.
Attn: Debasish Dhar
5241 Valleypark Drive
Roanoke, VA 24019

SatCon Technology Corporation
Attn: James R. Downer
12 Emily Street
Cambridge, MA 02139-4507

SatCon Technology Corporation
Attn: David B. Eisenhaure
12 Emily Street
Cambridge, MA 02139-4507

TRW Inc.
Attn: Alan W. Fleming
One Space Park
Redondo Beach, CA 90278

NASA Langley Research Center
Attn: Nelson J. Groom
Mail Stop 161
Hampton, VA 23681-0001

Charles Stark Draper Laboratory
Attn: Edward J. Hall
555 Technology Square
Mail Stop 37
Cambridge MA 02139

Stanford University
Attn: Daniel DeBra
Department of Aero and Astro
Durand Building
Stanford, CA 94305-4035

University of Virginia
Attn: Patrick Depret-Guilliaume
ROMAC Labs, Mech & Aero Egnrg
Thornton Hall, McCormick Road
Charlottesville, VA 22901

Naval Sea Systems Command
Attn: George M. Drakeley
Department of the Navy
Washington DC 20362-5101

Newport News Shipbuilding Co.
Attn: Deborah E. Earnshaw
4101 Washington Avenue
Building 4633, 3rd Floor
Newport News, VA 23607

Bently Rotor Dynamics Research Corp.
Attn: Wesley D. Franklin
P. O. Box 2529
Minden, NV 89423-2529

NASA Langley Research Center
Attn: D. Ghosh
Mail Stop 161
Hampton VA 23681-0001

SatCon Technology Corporation
Attn: Richard Hockney
12 Emily Street
Cambridge, MA 02142

NASA Lewis Research Center
Attn: Carlos M. Grodsinsky
21000 Lewis Research Center
MS 500-205
Cleveland, OH 44135

NASA Langley Research Center
Attn: Neil Holmberg
Mail Stop 442
Hampton, VA 23681-0001

University of Virginia
Attn: Roy D. Hampton
ROMAC Labs, Mech & Aero Engrg
Thornton Hall, McCormick Road
Charlottesville, VA 22901

Newport News Shipbuilding Co.
Attn: H. Douglas Huebner
4101 Washington Avenue
Dept. E67/Bldg. 4633
Newport News, VA 23607

Northern Research & Engrng Corp
Attn: Arnold Heitmann
39 Olympia Avenue
Woburn MA 01801

University of Maryland
Attn: Chaitanya P. Jayaraman
Mechanical Engineering Department
College Park MD 20742

Pratt & Whitney
Attn: David H. Hibner
400 Main Street
MS 163-09
East Hartford, CT 06108

NASA Langley Research Center
Attn: Claude R. Keckler
Mail Stop 479
Hampton, VA 23681-0001

Kingsbury, Inc.
Attn: Joe Imlach
10385 Drummond Road
Philadelphia, PA 19154

University of Virginia
Attn: F. Joseph Keith
Electrical Engineering Department
Thornton Hall, McCormick Road
Charlottesville, VA 22901

Boeing Aerospace Company
Attn: A. Dean Jacot
P. O. Box 3999
MS 82-24
Seattle, WA 98124

NASA Langley Research Center
Attn: Pierce L. Lawing
Mail Stop 267
Hampton VA 23665

University of Virginia
Attn: Shankar Jannathan
ROMAC Labs, Mech & Aero Engrg
Thornton Hall, McCormick Road
Charlottesville, VA 22901

Ctr. for Mag Brgs/ROMAC Labs
Attn: Dr. David W. Lewis
University of Virginia
Thornton Hall/McCormick Road
Charlottesville, VA 22903 22903

SatCon Technology Corporation
Attn: Bruce G. Johnson
12 Emily Street
Cambridge MA 02142

Jet Propulsion Laboratory
Attn: Carl A. Marchetto
Code 251
4800 Oak Grove Drive
Pasadena CA 91109

NASA Langley Research Center
Attn: Dr. Suresh M. Joshi
Mail Stop 161
Hampton VA 23681-0001

Superconductor Week
Attn: Lisa McClain
1050 17th Street, N. W.
Suite 480
Washington DC 20036

NASA Langley Research Center
Attn: Warren C. Kelliher
Mail Stop 416A
Hampton, VA 23681-0001

AVCON
Attn: Crawford R. Meeks
19151 Parthenia Street
Suite G
Northridge, CA 91324

VPI & SU
Attn: Dr. Robley G. Kirk
Mechanical Engineering Department
Randolph Hall
Blacksburg VA 24061

Glacier RPB Inc.
Attn: William Michaud
12 Roosevelt Avenue
Mystic, CT 06355

Honeywell Inc.
Attn: John C. Kroeger
Satellite Systems Division
P. O. Box 52199
Phoenix, AZ 85072-2199

University of Virginia
Attn: Timothy Miles
ROMAC Labs, Mech & Aero Engrg.
Thornton Hall, McCormick Road
Charlottesville, VA 22901

NASA Langley Research Center
Attn: Anne MacKenzie
Mail Stop 490
Hampton VA 23681-0001

SatCon Technology Corporation
Attn: Kathy M. Misovec
12 Emily Street
Cambridge, MA 02142

Battelle Columbus Division
Attn: Kenneth Marken
505 King Avenue
Columbus, OH 43201

Magnetic Bearings, Inc.
Attn: Howard J. Moses
501 1st Street
Radford, VA 24141

University of Virginia
Attn: Eric Maslen
Mech and Aero Engr. Department
Thornton Hall, McCormick Road
Charlottesville, VA 22901

NASA Langley Research Center
Attn: Douglas B. Price
Mail Stop 161
Hampton, VA 23681-0001

Air Force Aeronautical Laboratory
Attn: Brian McKee

Edwards AFB, CA 93523-5000

Cornell University
Attn: Mark L. Psiaki
244 Upson Hall
Ithace NY 14853-7501

Honeywell Systems & Research Center
Attn: Armin Metze
P. O. Box 1361, M/S MN65-2600
3660 Technology Drive
Minneapolis, MN 55418

Attn: Rhonda C. Raffi
12 Emily Street
Cambridge MA 02142

Kingsbury, Inc.
Attn: Andrew M
10385 Drummond
Philadelphia, PA 1

Booz, Allen & Hamilton
Attn: Ann Reimers
1725 Jefferson Davis Highway
Arlington, VA 22202

Sundstrand Corporation
Attn: Mokadam
4747 Harrison Avenue
P. O. Box 7002
Rockford IL 61125-7002

DoD - Air Force
Attn: Lewis Rosado
AFWAL/POSL
Wright Patterson AFB, OH 45433-6563

NASA Langley Research Center
Attn: D. S. Naidu
Mail Stop 161
Hampton, VA 23681-0001

Dresser-Rand Co.
Attn: Kenneth A. Schoeneck
Turbo Machinery Division
P. O. Box 560
Olean, NY 14760

Texas A&M University
Attn: Jorgen Nikolajsen
Mechanical Engineering Dept.
College Station, TX 77843

NASA LaRC
Attn: Michael A.Scott
MS 230
Hampton VA 23681-0001

FARE, Inc.
Attn: David P. Plant
4716 Pontiac Street, Suite 304
College Park, MD 20740

NASA Langley Research Center
Attn: Thomas A. Shull
Mail Stop 488
Hampton, VA 23681-0001

NASA Langley Research Center
Attn: William C. Poole
Mail Stop 490
Hampton VA 23681-0001

Massachusetts Institute of Tech.
Attn: Alexander Slocum
Building 1 Room 143
77 Massachusetts Avenue
Cambridge, MA 91109

Mechanical Technology Inc.
Attn: Dr. Dantam K. Rao
968 Albany-Shaker Road
Latham, NY 12110

Newport News Shipbuilding Co.
Attn: Randall R. Stowe
4101 Washington Avenue
E-77/B800
Newport News, VA 23607

Pratt and Whitney
Attn: Gregory E. Reinhardt
400 Main Street
East Hartford, CT 06108

Magnetic Concepts
Attn: Phillip A. Studer
10313 Ridgemoor Drive
Silver Spring, MD 20901

Sundstrand Corporation, ATG 741-6
Attn: Katsumata Shin
4747 Harrison Avenue
P. O. Box 7002
Rockford, IL 61125-7002

Naval Surface Warfare Center
Attn: Michael J. Superczynski
Carderock Division, Code 2712
Annapolis Detachment
Annapolis, MD 21402-5067

Kaman Science Corporation
Attn: D. Robert Smith
P. O. Box 7463
Colorado Springs, CO 80933

Cornell University
Attn: Dean L. Taylor
219 Upson Hall, M&AE
Ithaca, NY 14853

Aura Systems, Inc.
Attn: Christopher Sortore
2335 Alaska Avenue
El Segundo, CA 90245

AlliedSignal Aerospace
Attn: Anil Trivedi
2525 West 190th Street
M/ST-41
Torrance, CA 90509

AURA Systems, Inc.
Attn: Keith Stuart
2335 Alaska Avenue
El Segundo, CA 90245

University of Bridgeport
Attn: Gerald T. Volpe
Department of Electrical Engrng
University Avenue
Bridgeport, CT 06601

TRW Inc.
Attn: Kevin J. '
Mail Station 107(
One Space Park
Redondo Beach, C

U.S. GOVERNMENT PRINTING OFFICE: 1993-728

REPORT DOCUMENTATION PAGE

Form Approved
OMB No. 0704-0188

1. AGENCY USE ONLY (Leave blank)	2. REPORT DATE	3. REPORT TYPE AND DATES COVERED
	April 1993	Conference Publication

4. TITLE AND SUBTITLE
Magnetic Suspension Technology Workshop

5. FUNDING NUMBERS
WU 506-59-61-04

6. AUTHOR(S)
Claude R. Keckler, Nelson J. Groom, and Colin P. Britcher, Editors

7. PERFORMING ORGANIZATION NAME(S) AND ADDRESS(ES)
National Aeronautics and Space Administration
NASA Langley Research Center
Hampton, VA 23681-0001

8. PERFORMING ORGANIZATION REPORT NUMBER
L-17252

9. SPONSORING/MONITORING AGENCY NAME(S) AND ADDRESS(ES)
National Aeronautics and Space Administration
Washington, DC 20546-0001

10. SPONSORING/MONITORING AGENCY REPORT NUMBER
NASA CP-3202

11. SUPPLEMENTARY NOTES
Claude R. Keckler and Nelson J. Groom: Langley Research Center, Hampton, VA; Colin P. Britcher: Old Dominion University Foundation, Norfolk, VA

12a. DISTRIBUTION/AVAILABILITY STATEMENT
Unclassified-Unlimited
Subject Category 18

12b. DISTRIBUTION CODE

13. ABSTRACT *(Maximum 200 words)*

In order to identify the state of magnetic suspension technology in such areas as rotating systems, pointing of experiments or subsystems, payload isolation, and superconducting materials, a Workshop on Magnetic Suspension Technology was held at the Langley Research Center in Hampton, Virginia, on February 2–4, 1988.

The workshop included five technical sessions in which a total of 24 papers were presented. The technical sessions covered the areas of pointing, isolation, and measurement, rotating systems, modelling and control, and superconductors. A list of attendees appears at the end of the document.

14. SUBJECT TERMS
Magnetic bearings; Magnetic suspension; Small gap magnetic suspension; Superconducting magnetic suspension systems; Control systems

15. NUMBER OF PAGES
419

16. PRICE CODE
A18

17. SECURITY CLASSIFICATION OF REPORT	18. SECURITY CLASSIFICATION OF THIS PAGE	19. SECURITY CLASSIFICATION OF ABSTRACT	20. LIMITATION OF ABSTRACT
Unclassified	Unclassified	Unclassified	